The Hydrodynamic and Hydroelastic Responses of Rigid and Flexible Surface-Piercing Hydrofoils in Multi-Phase Flows

by

Casey Mackenzie Harwood

A dissertation submitted in partial fulfillment
of the requirements for the degree of
Doctor of Philosophy
(Naval Architecture and Marine Engineering)
in The University of Michigan
2016

Doctoral Committee:

Professor Yin Lu Young, Co-Chair
Professor Steven L. Ceccio, Co-Chair
Professor Carlos E. S. Cesnik
Assistant Professor Kevin J. Maki

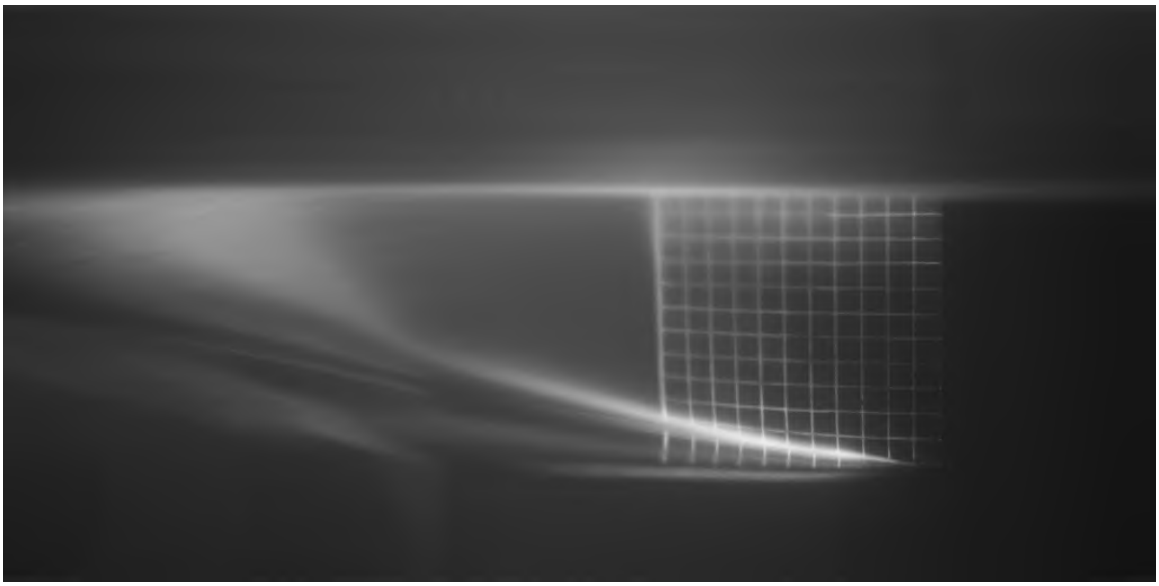

For Grandpa: I strive to engineer and to live by your example.

ACKNOWLEDGEMENTS

The work in this thesis was made possible by the financial support of Dr. Ki-Han Kim and Dr. Thomas Fu from the Office of Naval Research under grant numbers N00014-09-1-1204, N00014-10-1-0170 and by the Naval Engineering Education Center (NEEC) (Award number N65540-10-C-003). Support also came from National Science Foundation Graduate Student Research Fellowship program under grand number DGE 1256260. This work was also supported in part by the National Research Foundation of Korea (NRF) grant funded by the Korean government (MEST) through the GCRC-SOP grant number 2012-0004783. Facility and staff time for a portion of this work was provided by the Italian National Research Council Marine Technology Research Institute (CNR-INSEAN). In addition to funding, I want to thank Drs. Kim and Fu for the professional support that they have been so generous in providing throughout my interactions with them.

It is difficult to enumerate the people to whom I owe my success. My years as a graduate student have been filled with challenges and equally filled with people to help me overcome them. First and foremost, I want to thank my advisors, Julie Young and Steve Ceccio. It is hard to imagine how Julie finds time for her students among her many pursuits, but she has never failed to make time to read my papers, to review my presentations, and to provide judicious and well-reasoned guidance whenever I came up against a tough decision. Likewise, Steve has allowed me to abuse his open-door policy for five years, and has always provided council and perspective when I became overwhelmed. To you both, thank you for helping me grow as a researcher and scholar.

I want also to thank my family for their constant presence and support, even from across the country. Mom, Dad, and Mara, I could not have it made here without your encouragement, love, and care-packages. I also owe Deema Totah a debt of gratitude for her unerring support of my goals, and her equally steadfast companionship during late-night work sessions.

To Dr. Steve Zalek, Nick Wild, David Parsons, Brent Cragin, and the other staff of the Marine Hydrodynamics Lab: thank you for moving heaven, earth, and a whole

lot of water to help make these experiments happen, and I appreciate the access you gave me to the towing tank – even after I crashed the carriage.

I want to extend a heartfelt "Grazie!" to my collaborators at CNR INSEAN, Dr. Mario Felli, Dr. Massimo Falchi, Dr. Emilio Campana, and the facility staff that treated us with such hospitality. The access to the cavitation tunnel was an incredible opportunity, and I hope to work with you all again in the near future.

The staff of the Naval Architecture and Marine Engineering department helped with every aspect of these experiments. Sallie, Nicole, Kimberly, Susan, Amanda, and Nathalie kept my work running smoothly through a host of crises. From expediting purchase orders to bilingual shouting matches with Italian customs officers, your efforts kept the whole project from going off the rails.

Thanks to Dr. Kyle Brucker, who performed beautiful simulations of the experiment described in this work, and to Dr. Antoine Ducoin, who gave me my first lessons on CFD.

Thanks are owed to my other committee members, Professor Carlos Cesnik and Professor Kevin Maki for agreeing to serve on my committee. I appreciate the time and feedback you gave to me.

The success of my graduate career due in no small part to the influence of Jacques Hadler and Dr. Richard Royce, who gave me my first tastes of experimental hydrodynamics during my time at the Webb Institute.

Finally, my I would be remiss if I failed to thank the coffee roasters of greater Ann Arbor for keeping my mug and spirits full.

TABLE OF CONTENTS

LIST OF FIGURES

Figure

LIST OF TABLES

Table

LIST OF APPENDICES

Appendix

LIST OF ABBREVIATIONS

1-D One-Dimensional

2-D Two-Dimensional

3-D Three-Dimensional

A/D Analogue to Digital Converter

AC Aerodynamic Center

BEM Boundary Element Method

CFD Computational Fluid Dynamics

CG Center of Gravity

CP Center of Pressure

DAQ Data Acquisition

DMD Dynamic Mode Decomposition

DOF Degree of Freedom

EA Elastic Axis

FEM Finite Element Method

FPS Frames Per Second

FRF Frequency Response Function

FSI Fluid Structure Interaction

FV Fully Ventilated

FW Fully Wetted

ILES Implicit Large-Eddy Simulation

LDV Laser Doppler Velocimetry

LE Leading Edge

LES Large-Eddy Simulation

LL Lifting Line

MDOF Multi-degree-of-freedom

MHL Marine Hydrodynamics Laboratory

NA Neutral Axis

NFA Numerical Flow Analysis

PC Partially Cavitating

PIV Particle Image Velocimetry

POD Proper Orthogonal Decomposition

PV Partially Ventilated

QUICK Quadratic Upwinded Interpolation for Convective Kinematics

RFP Rational Fraction Polynomial

RMS Root Mean Square

RMSE Root Mean Squared Error

SC Shear Center

SC Supercavitating

SDOF Single-degree-of-freedom

TE Trailing Edge

VOF Volume of Fluid

LIST OF SYMBOLS

EI	Flexural rigidity
GJ	Torsional rigidity
L, D, M	3-D lift, drag, and moment (F_Y, $-F_X$, M_Z)
L_c	Cavity Length
P	Local pressure
P_0	Ambient pressure at the free surface
P_∞	Free-stream pressure
P_c	Cavity pressure
P_v	Fluid vapor pressure
P_{atm}	Atmospheric pressure (101 kPa)
S	Span
T	Maximum foil thickness
U	Free stream velocity
a_0	Section lift curve slope $\partial C_{l_{2D}}/\partial \alpha_{2D}$
c	Chord
f	Cyclic frequency
f_0, f_d	Undamped, damped natural frequencies (cyclic)
g	Gravitational acceleration
h	Immersion depth
l, d, m	2-D section lift, drag, moment
z'	Distance measured downward from the free surface

Δ	Influence distance
Γ	Sectional bound circulation
Φ	Local angle of cavity-closure line
α	Geometric angle of attack
α_0	Angle of attack for zero lift
α_e	Effective angle of attack, including elastic twist
α_i	Induced downwash angle
α_{eff}	Effective sectional angle of attack,$\alpha_{eff} = \alpha_{2D} - \alpha_0 - \alpha_i$
α_{2D}	Sectional effective angle of attack
$\bar{\Phi}$	Angle of straight-line fit through cavity-closure line
δ	Bending deflection
δ	Lateral bending deflection
$\epsilon_{x,y,z}$	Normal strain in x,y,z
η	Damping loss-factor
γ	Surface tension
λ	Root compliance factor
ν	Fluid kinematic viscosity
ω	Angular frequency
ω_0, ω_d	Undamped, damped natural frequencies (angular)
ρ_f, ρ_s	Fluid density; Solid Density
θ	Twisting deflection
ξ	Viscous damping ratio
AR_S	Geometric aspect ratio S/c
AR_h	Immersed aspect ratio,h/c
C_P	Pressure coefficient, $\frac{P-P_\infty}{\rho_f U^2/2}$
St_x	Strouhal number, based on length scale x, $\frac{fx}{U}$
We	Weber Number, $\frac{\rho U^2 c}{\gamma}$

$C_{D_{3D}}$ 3-D drag coefficient, $\frac{D}{\rho_f chU^2/2}$

$C_{L_{3D}}$ 3-D lift coefficient, $\frac{L}{\rho_f chU^2/2}$

$C_{M_{3D}}$ 3-D moment coefficient, $\frac{M}{\rho_f c^2 hU^2/2}$

$C_{d_{2D}}$ Section drag coefficient, $\frac{d}{\rho_f cU^2/2}$

$C_{l_{2D}}$ Section lift coefficient, $\frac{l}{\rho_f cU^2/2}$

$C_{m_{2D}}$ Section moment coefficient, $\frac{m}{\rho_f c^2 U^2/2}$

Fn_c Chord-based Froude number, $\frac{U}{\sqrt{gc}}$

Fn_h Depth-based Froude number, $\frac{U}{\sqrt{gh}}$

Re_c Chord-based Reynolds number, $\frac{Uc}{\nu}$

μ Solid-to-fluid mass ratio, $\sqrt{\frac{4m}{\rho_f \pi c^2}}$

σ_c General cavitation index, $\frac{P_\infty - P_c}{\rho U^2/2}$

σ_v Vaporous cavitation index, $\frac{P_0 - P_v}{\rho U^2/2}$

e Dimensionless distance from elastic axis to center of pressure, $\frac{X_{EA} - X_{CP}}{c}$

$[\boldsymbol{C_s}]$ Structural damping matrix

$[\boldsymbol{C_{fl}}]$ Fluid damping matrix

$[\boldsymbol{K_S}]$ Structural stiffness matrix

$[\boldsymbol{K_{fl}}]$ Fluid stiffness matrix

$[\boldsymbol{M_S}]$ Structural mass matrix

$[\boldsymbol{M_{fl}}]$ Fluid mass matrix

$[\boldsymbol{\Theta}]$ Matrix of normal mode shapes

$[\boldsymbol{\Omega}]$ Linear operator matrix for downwash computation

$\{\boldsymbol{F_{EX}}\}$ Vector of external forces

$\{\boldsymbol{F_{fl}}\}$ Vector of fluid forces

$\{\boldsymbol{F_{other}}\}$ Component of fluid force vector not proportional to structural motions (*e.g.* vortex shedding)

$\{\boldsymbol{F_{r,steady}}\}$ Steady fluid load on a rigid lifting geometry

$\{\boldsymbol{U_{jet}}\}$ Re-entrant jet velocity vector

$\{\boldsymbol{X}\}$ Vector of bending and twisting displacements

ABSTRACT

The Hydrodynamic and Hydroelastic Responses of Rigid and Flexible Surface-Piercing Hydrofoils in Multi-Phase Flows

by

Casey Harwood

Co-Chairs: Yin Lu Young and Steven L. Ceccio

Ventilation and vaporous cavitation are multi-phase flows with critical effects upon the performance, stability, and controllability of high-speed marine vessels. The entrainment of air from the free surface (ventilation) or the formation of water-vapor-filled voids (cavitation) can cause dramatic reductions in the efficiency of lifting surfaces, large dynamic loads, and strongly hysteretic flows. This thesis investigates the hydrodynamic and hydroelastic performance of surface-piercing hydrofoils through experiments on three hydrofoil models (one rigid and two flexible), which were tested in a towing tank and in a free-surface cavitation tunnel.

The results reveal four distinct flow regimes, which are defined by their parametric stability regions. The concept of flow stability is used to describe transitional flow and resulting hysteresis to yield a holistic description of ventilation on surface piercing hydrofoils. These concepts are used to develop scaling relations for the washout of ventilated cavities. Hydrodynamic loads are shown to vary as functions of the attack angle, immersion depth, forward speed, cavitation number, and flow regime. Flexibility of the hydrofoil model modifies the hydrodynamic loads and stability regions through hydroelastic coupling. Flow-induced vibration and lock-in are shown to result from coherent vortex shedding at all speeds tested. Fitted transfer functions are used to develop reduced-order models and to estimate modal parameters of a flexible hydrofoil, demonstrating that both modal resonance frequencies and modal damping ratios are dependent upon immersion depth, forward speed, and flow regime. A robust shape-sensing strut is also developed to measure the *in-situ* structural motions of deformable lifting-surfaces in real time.

The work presented in this thesis contributes significantly toward the study of multi-phase flows and fluid-structure interactions through the establishment of experimental methodologies, the construction of a versatile experimental platform with original instrumentation, and the collection and thorough interpretation of a large, rich dataset. The insights gained from the work significantly improve our understanding of ventilation, cavitation, and their interactions with structural dynamics, thereby aiding future researchers and designers to perform robust experiments, validate numerical solvers, and design safe, efficient, and controllable marine devices.

CHAPTER I

Introduction

1.1 Background and Motivation

Ventilation is a multi-phase flow characterized by the entrainment of non-condensable gas into the liquid flow around a fully or partially immersed body. An individual observing the vigorous stroke of a paddle in the water may notice the depression of the water's surface, which exposes one face of the paddle to the air. Similarly, those familiar with high-speed water-craft are likely acquainted with the notion of a dry transom, where the flow around a hull forms a pocket of air in the hull's wake above a certain speed, leaving the transom completely exposed. Both are examples of atmospheric ventilation, or naturally-ventilated flow, where air displaces liquid in some portion of a flow-field. Both are also examples of bluff-body flows. Ventilation becomes significantly more nuanced and complex when it occurs in the flow around streamlined bodies, particularly those designed to generate lift.

In order for ventilation to occur on a fully or partially submerged body, the local pressure near the body must be lower than the pressure of the impinging gas, a region of separated flow must exist for the gas to occupy, and a continuous path of ingress by which gas enters the cavity must be available (*Wetzel*, 1957; *Wadlin*, 1958; *Breslin and Skalak*, 1959) – conditions upon which later sections will elaborate. Atmospheric ventilation, in particular, can occur on many marine systems operating at or near the free surface, including propellers, turbines, waterjets, dynamic positioning devices, hydrofoils, struts, rudders, fins, stabilizers, ship hulls (*Arndt et al.*, 2009), as well as narrow side hulls and hard chines of high-speed craft (*Amromin*, 2015), and even on aircraft components during ditching maneuvers (*Iafrati et al.*, 2015).

Through careful design, one can ensure a cavity closes well downstream of the body to which it is attached, forming a supercavity. Vaporous or ventilated supercavities can be levied for advantageous reductions to the frictional drag on lightly to

moderately loaded, high-speed bodies (*e.g.* , struts, hydrofoils, torpedoes, propellers, stepped hulls, etc.). For reasons given in §1.3, supercavities also tend to be much more stable than other cavity regimes because the cavity collapses well downstream of the body trailing edge – a fact that also helps to mitigate cavitation erosion, vibration, and noise issues. The uncontrolled or unanticipated formation of a ventilated cavity, on the other hand, can have an extremely deleterious effect on performance. Ventilation may lead to sudden and large changes in the forces acting on the body, and result in craft stability and/or structural concerns if it occurs unexpectedly or in off-design conditions. In some cases, lift-reversal has even been observed during the ventilation of high-speed hydrofoils (*Rothblum et al.*, 1969). These considerations lead naturally to concerns regarding controllability issues as well as structural and/or hydroelastic stability issues including divergence, flutter, transient or parametric resonance. In severe sea-states, where propeller emergence occurs, ventilation of propeller blades may cause a substantial loss of thrust and an accompanying reduction in shaft torque, resulting in an uncontrolled increase in propeller revolution rate that may damage engines or auxiliary systems. Moreover, a sudden imbalance between the lift of foils opposite one another about the centerline of a hydrofoil-supported craft could result in a large rolling moment, and may cause the vessel in question to capsize.

The large dynamic loads that can be induced by ventilation have implications not only upon the hydrodynamic performance and stability of affected systems, but also on their structural responses. In recent years, there has emerged an increased interest in light-weight and non-metallic construction materials for marine systems. Alternative construction materials offer a number of advantages, including weight-savings and corrosion resistance, over metals. Additionally, flexible marine systems may be tailored for desirable structural responses, or may be actuated to deform in a desired way. Improvements in the modeling, material science, and production of advanced or "smart" materials has enabled the design of more systems that deform or deflect under loads for purposes of active (*Caverly et al.*, 2016) or passive (*Motley et al.*, 2009; *Motley and Young*, 2011) control. The design of robust compliant marine systems requires a thorough knowledge of the magnitudes and frequency content of excitation forces that act on the system. Ventilated and wetted flows can behave so differently – and transition between them can occur so violently – that the structural response is a key topic of concern. Moreover, ventilation involves the displacement of liquid from the flow and its replacement with a much-lighter gas. The change in the fluid density field around a ventilated body can affect the inertial and restorative forces acting upon the body or the ability of the body to dissipate energy via damping.

An unmitigated case of unforeseen ventilation could conceivably lead to catastrophic failure of marine propulsors, hydrofoils, or control surfaces under the right (or wrong) circumstances as a result of unanticipated loads, rapidly changing loads, or dynamic instability. The many physics involved create a fascinating problem. Pragmatism and inquisitiveness, therefore, both demand a closer look at the physics governing ventilation and its interplay with structural motions.

This chapter contains a review of previous research on the ventilation of lifting-surfaces and hydroelasticity of hydrofoils. §1.2 clarifies some initial terminology, §1.3 reviews the hydrodynamics of cavities on foil sections in two dimensions, and §1.4 extends these concepts three-dimensional flows and reviews relevant research. A summary of research on the hydroelasticity of lifting-surfaces is given in §1.5. §1.6 frames the open questions to be addressed in this work and lays out the specific research objectives. Finally, §1.7 contains an outline of the thesis.

1.2 Types of Multi-Phase Flows: Vaporous, Natural, and Artificial Cavities

With the wealth of literature that exists in multi-phase flows, the terminology has become difficult to navigate without ambiguity. As an example, the terms "natural cavities," "vaporous cavities," or simply "cavitation," are all used to describe the vaporization of liquid into its gaseous phase, making them distinct from "artificial cavities," "ventilated cavities," "natural ventilation," "aeration," or simply "ventilation." To preempt a confusion of the various terminology, the language used in the recent review by *Young et al.* (2016) will be adopted.

Natural ventilation, or simply "ventilation" (as it applies in this thesis) describes the case when a cavity is filled with air entrained from a nearby free surface (*Acosta*, 1979; *Faltinsen*, 2005). They are so named because they can persist under the supply of gas naturally entrained from the atmosphere. As a result, the pressure inside of the cavity is everywhere atmospheric, notwithstanding small dynamic pressure variations due to gas velocities inside of the cavity.

It is also possible to support a cavity on a submerged body that does not naturally ventilate by artificially pumping gas around the body. The gas may be used to boost the cavity pressure in an existing vaporous cavity, to fill an otherwise-wetted region of flow separation, or to alter the character of the attached and separated flow entirely. This is referred to as forced or artificial ventilation, and is a useful technique for drag-reduction and flow-control (*Acosta*, 1979; *Pearce and Brandner*, 2012; *Schiebe*

and Wetzel, 1961; *Ceccio*, 2010). It is so named because the gas used to sustain and replenish a cavity must be intentionally pumped into the cavity.

Ventilation shares numerous similarities with another multi-phase flow phenomenon known as vaporous cavitation. Typically, cavitation occurs when the local absolute pressure decreases to the saturated vapor pressure of the liquid. Additional factors such as surface-finish and water quality (dissolved gas content or nucleation concentration) can modify incipient cavitation conditions (*Brennen*, 1995; *Franc and Michel*, 2004; *Morch*, 2009; *de Graaf et al.*, 2016). Cavitation involves bi-directional transitions between the liquid and vapor phases through vaporization and condensation. Ventilation, on the other hand, solely involves the transport of non-condensable gas around the submerged portion of a body as the primary mechanism of gas ingress and egress, and does not involve significant phase-change. As a result, the dynamics of unsteady ventilated and vaporous cavities can be very different.

Both ventilation and cavitation are complex multi-phase flows that involve multiple length and time scales, ranging from bubbly flows to continuous cavity sheets, and both can lead to large load fluctuations. Vaporous cavitation can also promote atmospheric ventilation in some situations (*Wadlin*, 1958; *Rothblum et al.*, 1969; *Waid*, 1968; *Swales et al.*, 1974), and can even occur simultaneously with both natural and forced ventilation (*Olofsson*, 1996; *Young and Brizzolara*, 2013). Detailed reviews of steady and unsteady cavitation processes may be found in *Brennen* (1995); *Franc and Michel* (2004); *Terentiev et al.* (2011).

"Ventilation," as it is used in this thesis, refers specifically to the phenomenon of natural ventilation. Vaporous cavitation will be discussed as well. The distinction between the two will be made clear whenever they are presented in the ensuing work. Forced ventilation is beyond the scope of this work, and will not be covered in this thesis, though excellent reviews are available by *Ceccio* (2010); *Terentiev et al.* (2011); *Young et al.* (2016).

1.3 Multi-Phase Flow on Two-Dimensional Foil Sections

The archetypal lifting geometry is a 2-D foil section, which is representative of a slice through a typical 3-D hydrofoil, control surface, or propeller blade. Additionally, the theories of 2-D cavitating flow are instructive in approaching 3-D flows. The 2-D hydrofoil section, therefore, is an ideal platform for introducing the typical flow regimes.

The coefficents of lift, drag, and moment on a foil section are defined as

$$C_{l_{2D}} = \frac{l}{\rho_f U^2 c/2}; \tag{1.1a}$$

$$C_{d_{2D}} = \frac{d}{\rho_f U^2 c/2}; \tag{1.1b}$$

$$C_{m_{2D}} = \frac{m}{\rho_f U^2 c^2/2}, \tag{1.1c}$$

where l, d, and m are respectively the the lift, drag, and pitching moment per unit span, U is the reference velocity, ρ_f is the density of the working fluid, and c is the chord-length of the hydrofoil. Most theoretical approaches to lifting sections in cavitating flows are based on free-streamline theory, wherein the location of the streamline forming the boundary between a gaseous phase and liquid phase is determined. Exact and nonlinear solutions to the free-streamline problem, utilizing methods such as the hodograph transformation are both informative and elegant. However, they are laborious to execute and their complexity precludes closed-form solutions for cavity length, lift, drag, and moment. For this reason, the far-simpler linearized theory has found widespread applications (*Tulin*, 1964), the results of which will be summarized in this section. For the interested reader, a wealth of literature exists, with excellent reviews by *Tulin* (1964); *Wu* (1972).

Linearized foil theory involves a decomposition of the foil section into a symmetric thickness problem and an asymmetric lifting problem, where the coefficients in equations 1.1 are determined by integrating the dimensionless pressure coefficient around the body (*Munk*, 1923; *Newman*, 1977; *Milne-Thomson*, 1973; *Abbott and Von Doenhoff*, 1959). The simplest lifting problem is that of a flat plate at an angle of attack. Flat-plate solutions, when superimposed with appropriate thickness distributions, can be used to describe a variety of appropriately thin, uncambered lifting sections. For this reason, flat-plate solutions form the basis of the 2-D cavitating foil theory in this section.

For a 2-D foil section, there exist three or four characteristic flow regimes: fully wetted, base-cavitating (in the case of a foil with a blunt trailing edge), partially cavitating, and supercavitating flows (*Brennen*, 1995; *Franc and Michel*, 2004). These regimes are illustrated in figure 1.1, and are individually described in the following sections. The same terminology is often used for both cavitation and ventilation. Regardless of the composition of gas inside of the cavity, the regimes are distinguished by the length of the cavity (L_c) relative to the chord length c of the lifting-section (*Brennen*, 1995). The nondimensional cavity length L_c/c is in turn governed by the

effective angle of attack of the section (α_{2D}) and the sectional cavitation number σ_c (also termed the cavity under-pressure coefficient by *Franc and Michel* (2004)),

$$\sigma_c = \frac{P_\infty - P_c}{\rho_f U^2/2}, \tag{1.2}$$

where P_∞ is the absolute free-stream pressure in the plane of the section, and P_c is the absolute pressure inside of the gaseous cavity.

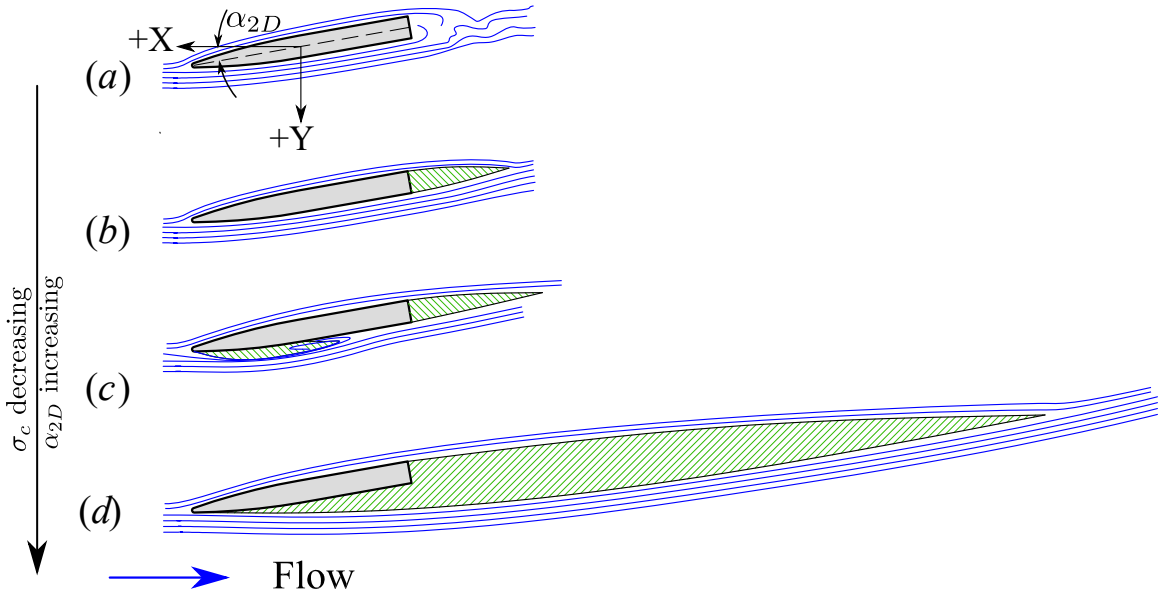

Figure 1.1: Cavitation regimes on a 2-D hydrofoil section. (a) Fully wetted, (b) Base-cavitation or base-ventilation, (c) Partial-cavitation or partial ventilation, (d) Supercavitation or super-ventilation. Figure reproduced from *Young et al.* (2016).

In the case of ventilation, P_c will approach the ambient pressure at the free surface (P_0), yielding

$$\sigma_c = \frac{P_\infty - P_0}{\rho_f U^2/2}. \tag{1.3}$$

In the special case of a vaporous cavity, P_c will be the sum of partial pressures of water vapor and any non-condensable gas contained in the cavity. In the limit of a vanishingly-small quantity of non-condensable gas, P_c will approach the saturated vapor pressure of the liquid (P_v). The vaporous cavitation number is defined as,

$$\sigma_v = \frac{P_\infty - P_v}{\rho_f U^2/2}. \tag{1.4}$$

Other variations of the above forms of cavitation number may be expressed by mea-

suring the free-stream pressure P_∞ at a location not necessarily in the section plane. Such alternate conventions will be defined in context when they are used in this work.

1.3.1 Fully Wetted and Base Cavitating Sections

For a streamlined hydrofoil at small angle of attack α_{2D} and/or large σ_c, both sides of the foil surface will be fully wetted, as shown in figure 1.1(a). According to classic linearized 2-D potential flow solution on a fully wetted flat plate (*Munk*, 1923; *Milne-Thomson*, 1973; *Tulin*, 1956; *Newman*, 1977), the hydrodynamic loads in this regime are,

$$C_{l_{2D}} = 2\pi\alpha_{2D}; \tag{1.5a}$$

$$C_{d_{2D}} = 0; \tag{1.5b}$$

$$C_{m_{2D}} = \frac{\pi}{2}\alpha_{2D}. \tag{1.5c}$$

These are classic results, with ubiquitous applications in aerospace and marine design. Note that when the foil section possesses a blunt TE like that in figure 1.1, a small cavity may develop abaft the foil's TE, as in figure 1.1(b). In the case of base-cavitation or base-ventilation, the cavity pressure acts on the foil TE, modifying the drag relative to the fully wetted case. For slim bodies, however, the change in drag will be relatively small, and the base cavity will not materially affect the hydrodynamic loading of the section (*Scherer and Auslaender*, 1964).

1.3.2 Partially Cavitating Sections

The length of a partial cavity is less than the chord length, as shown in figure 1.1(c). This may occur whenever the peak suction pressure on the hydrofoil surface reaches the cavity pressure, P_c, causing a gas/vapor bubble to form in the vicinity of the low pressure. The extent of the cavity is limited, however, and the flow will reattach somewhere along the chord length ($0 < L_c/c \leq 1$). The solution for a flat plate with a partial leading edge cavity was derived by *Acosta* (1955) and

is given by *Kerwin and Hadler* (2010) as,

$$L_c/c = \cos^2\beta; \tag{1.6a}$$

$$\frac{\sigma_c}{\alpha_{2D}} = 2\cot\beta\frac{1+\sin\beta}{1-\sin\beta}; \tag{1.6b}$$

$$C_{l_{2D}} = \pi\alpha_{2D}\left(1+\frac{1}{\sin\beta}\right); \tag{1.6c}$$

$$C_{d_{2D}} = \pi\alpha_{2D}^2\left(1+\frac{1}{\sin\beta}\right); \tag{1.6d}$$

$$C_{m_{2D}} = \frac{\pi\alpha_{2D}}{8}\left(-3-6\sin\beta+\sin^2\beta+4\sin^3\beta\right), \tag{1.6e}$$

where β is a transformation variable. In real flows, a re-entrant jet develops as a result of the flow-reattachment, with some liquid flow undercutting the cavity (see figure 1.1c). The momentum of the re-entrant jet is dependent upon the thickness of the jet, and therefore on the thickness of the partial cavity (*Franc and Michel*, 2004; *Callenaere et al.*, 2001). At small α_{2D}, the jet causes vortical structures to be shed from the trailing edge of the cavity. At large α_{2D}, the jet leads to large-scale periodic shedding and fluctuations of the attached cavity length and hydrodynamic loads. §1.3.5 elucidates upon the topic of partial cavity shedding.

1.3.3 Supercavitating Sections

For large α_{2D} and/or small σ_c, the pressures everywhere along the suction surface become small, and a cavity encloses the entire suction surface ($L_c/c > 1$). The displacement of the liquid flow by the cavity effectively establishes a lower limit on the suction pressure, which limits the forces that can be developed on the section. The solution for a supercavity on a flat plate was originally derived by *Tulin* (1953) as, and is given in the form below by *Kerwin and Hadler* (2010),

$$\frac{c}{L_c} = \cos^2\beta; \tag{1.7a}$$

$$\frac{\sigma_c}{\alpha_{2D}} = 2\cot\beta; \tag{1.7b}$$

$$C_{l_{2D}} = \pi\alpha_{2D}\frac{1}{\sin\beta(1+\sin\beta)}; \tag{1.7c}$$

$$C_{d_{2D}} = \pi\alpha_{2D}^2\frac{1}{\sin\beta(1+\sin\beta)}; \tag{1.7d}$$

$$C_{m_{2D}} = \pi\alpha_{2D}\frac{4+\sin\beta}{8\sin\beta(1+\sin\beta)^2}. \tag{1.7e}$$

For very small σ_c and large L_c/c, the value of a_0 (defined as the slope of $C_{l_{2D}}$ as a function of α_{2D}) approaches a limit of $\pi/2$ – a reduction of 75% relative to the fully wetted value, where $a_0 = 2\pi$ (see equation 1.5a). Supercavities are generally more stable than are partial cavities because the cavity closure – and the associated turbulence, re-entrant flow, and vortex shedding – occur downstream of the affected hydrofoil section (*Brennen*, 1995; *Franc and Michel*, 2004). However, supercavities with lengths of $1 \leq L_c/c \lesssim 1.5$ can exhibit periodic instability caused by the proximity of the cavity-closure to the hydrofoil's TE.

1.3.4 Theoretical Three-Quarter Chord Instability

Equations 1.6-1.7 are the linearized solutions to cavitating flow on a flat plate for dimensionless cavity lengths L_c/c less than unity and exceeding unity, respectively. When L_c/c approaches unity, the stagnation point of the cavity boundary interferes with the Kutta condition at the foil TE, and both solutions become pathological. The partial-cavity solution, when plotted as a function of σ_c/α_{2D}, has two branches, which bifurcate at $L_c/c = 0.75$. The branch for $L_c/c < 0.75$ is taken to be the valid one in most analyses. The resulting pathology is dubbed the three-quarter chord instability, and it has been a topic of debate whether the instability is a theoretical artifact or whether it belies a physical instability. Real cavities in the range of $3/4 \lesssim L_c/c \lesssim 4/3$ tend to be physically unstable (a phenomenon discussed in the following section), but a strong case is made in the literature (*Kerwin and Hadler*, 2010; *Brennen*, 1995; *Wu*, 1962) that the physical mechanism is unrelated to the theoretical instability.

Figure 1.2 shows the solutions of *Acosta* (1955); *Tulin* (1953), along with the experimental data of *Wade and Acosta* (1966), measured on a plano-convex hydrofoil. The theoretical three-quarter-chord instability is evident in the neighborhood of $L_c/c \approx 1$, indicated by a grey shaded band. The experimental results of *Wade and Acosta* (1966) indicate that cavities in this neighborhood are highly unsteady, but the cause of the physical unsteadiness is linked to re-entrant flow, as discussed in the following section. Note that the plano-convex foil was oriented such that the flat surface was the pressure side. As a result, the foil possesses a positive camber when fully wetted or partially cavitating. In the supercavitating regime, however, the suction surface is hidden from the flow, so the foil behaves like a flat plate. For this reason, the experimental measurements of $C_{l_{2D}}$ in figure 1.2 agree with the flat-plate solution in the supercavitating regime, but not in the partially cavitating or fully wetted regimes.

It was suggested by *Brennen* (1995) that the correct dimensionless length of a

2-D cavity could be inferred by blending the two solutions, effectively bridging the gap created by the three-quarter chord instability. This very approach was taken by *Harwood et al.* (2016c), who fitted the valid portions of equations 1.6b and 1.7b with rational polynomial functions of $\sigma_c/2\alpha_{2D}$ to yield equation 1.8. The valid portion of the solutions was taken to be the solutions outside of the grey-shaded band in figure 1.2 ($L_c/c \geq 1.25$ for supercavitation and $L_c/c < 0.5$ for partial cavitation). The lift coefficients in equations 1.6c and 1.7c may be similarly blended to yield 1.9.

$$\frac{L_c}{c} = \frac{1.36\frac{\sigma_c}{\alpha_{2D}} + 96.62}{0.125\left(\frac{\sigma_c}{\alpha_{2D}}\right)^3 - 1.76\left(\frac{\sigma_c}{\alpha_{2D}}\right)^2 + 24.71\frac{\sigma_c}{\alpha_{2D}} + 0.961} \tag{1.8}$$

$$C_{l_{2D}} = \pi\alpha_{2D}\frac{\frac{\pi}{2}\left(\frac{L_c}{c}\right)^3 - 2\left(\frac{L_c}{c}\right)^2 + 4.5\left(\frac{L_c}{c}\right) + 1}{\pi\left[\left(\frac{L_c}{c}\right)^3 - \left(\frac{L_c}{c}\right)^2 + 0.75\left(\frac{L_c}{c}\right) + \frac{1}{2\pi}\right]} \tag{1.9}$$

These rational-polynomial approximations are also shown as the solid black lines in figure 1.2. Fitted approximations of the drag and moment coefficients were not sought.

It should be noted that equations 1.8 and 1.9, and the accompanying curves in figure 1.2, are not themselves solutions to the linearized flat plate problem. Rather, they are fitted to the two sets of linear solutions, such that the behavior of both partial cavities and supercavities may be approximated without the pathological solutions near $L_c/c = 1$. Moreover, the preceding expressions represent only the mean or steady-state topology and forces on cavitating bodies, and do not reflect the periodic instability which arises in many physical flows, known as partial cavity shedding.

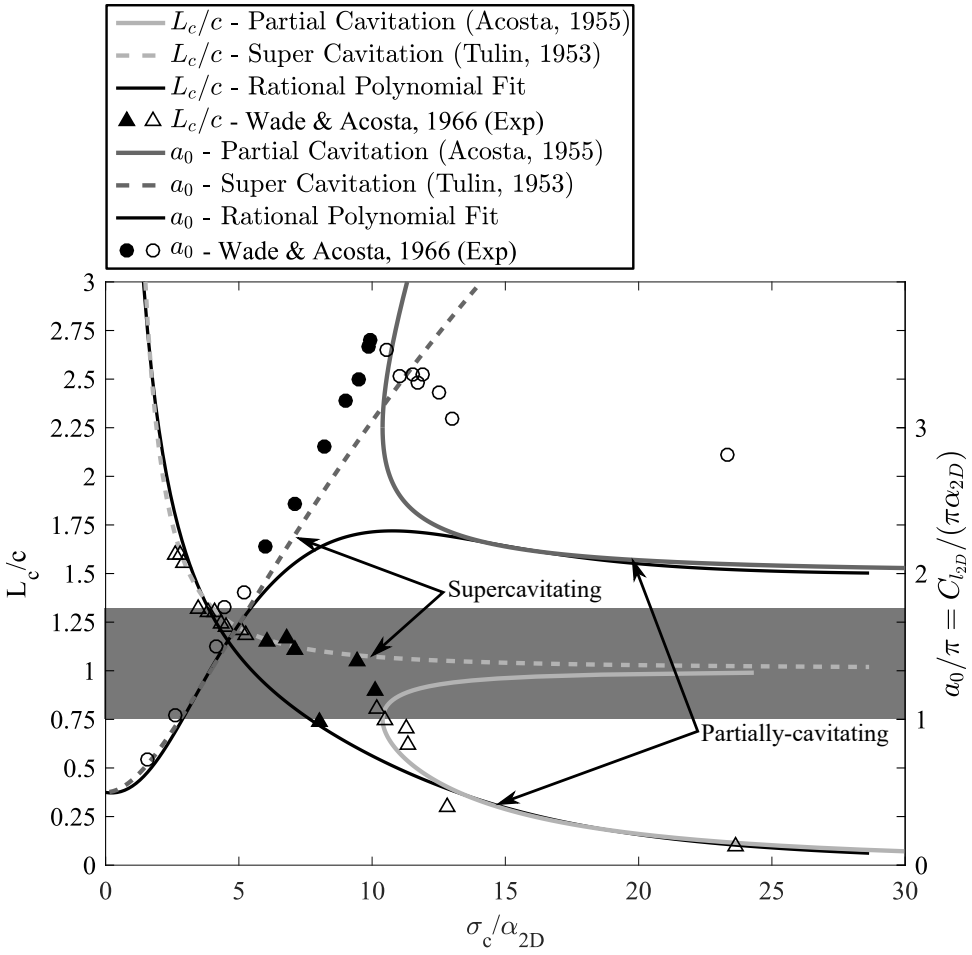

Figure 1.2: Cavity length (L_c/c) and section lift-slope (a_0), approximated with free-streamline theory and plotted as functions of σ_c/α_{2D} for $\alpha_{2D} = 4°$. Experimental results from *Wade and Acosta* (1966) are shown, with open symbols denoting steady cavity flow and filled symbols denoting unsteady cavity flow. The grey region indicates the neighborhood of $L_c/c \approx 1$, in which the linearized flat plate solutions are regarded as non-physical (*Brennen*, 1995). The theoretical three-quarter-chord instability develops where the partially cavitating solution bifurcates at the lower boundary of the grey-shaded region. Rational polynomial approximations to the linear theory are shown as solid black lines, which fair across the three-quarter-chord instability. Figure styled after *Brennen* (1995) and reproduced from *Young et al.* (2016).

1.3.5 Partial Cavity Shedding

Sheet cavities, both vaporous and ventilated, are subject to periodic shedding as a result of re-entrant jet flow. An attached cavity can become extremely unstable when the cavity length is roughly $0.75 \lesssim L_c/c \lesssim 1.3$ (*Brennen*, 1995; *Kawakami et al.*, 2008; *Wade and Acosta*, 1966). In this case, the cavity oscillates between a partial cavity and a supercavity in a well-documented mode of periodic instability known alternately as sheet-cloud cavitation or cloud-cavitation instability (*Brennen*, 1995; *Franc and Michel*, 2004; *Callenaere et al.*, 2001; *Kawakami et al.*, 2008). For specific mixtures of liquid, vapor, and non-condensable gas in which the speed of sound in the mixture is minimized, the instability can also be due to pressure shock waves generated by the growth and collapse of the liquid-vapor mixture (*Ganesh*, 2015; *Ganesh et al.*, 2016).

Cavity shedding on a 2-D foil section is most commonly caused by the re-entrant jet. In this case, reattaching flow on the solid surface creates a stagnation point near the cavity's trailing edge, leading some streamlines to turn underneath the attached cavity. The jet migrates forward until it intercepts the forward interface of the cavity, "pinching-off" the attached cavity and causing it to shed downstream in a bubbly vortical structure (*Brennen*, 1995; *Franc and Michel*, 2004). Shedding by the mechanism of re-entrant flow is regarded as a three-part process (drawn schematically in figure 1.3).

1. **Development of re-entrant flow:** The re-entrant jet migrates upstream from the cavity's trailing edge to the cavity's leading edge (a distance of L_c).

2. **Cavity shedding:** The sheet cavity detaches and is convected downstream as a bubbly vortex.

3. **Growth of the leading-edge cavity:** A leading-edge cavity develops and grows to the maximum attached cavity length of L_c, completing the cycle.

The development and forward-propagation of the re-entrant jet is generally considered to require about one-third of the cavity shedding period (*Franc and Michel*, 2004) (steps 2 and 3 are sometimes described as occurring concurrently, together requiring approximately two-thirds of the period to complete). The frequency of shedding cycle may therefore be approximated as,

$$f_c = \frac{1}{T_1 + T_2 + T_3} \approx \frac{1}{3T_1}, \tag{1.10}$$

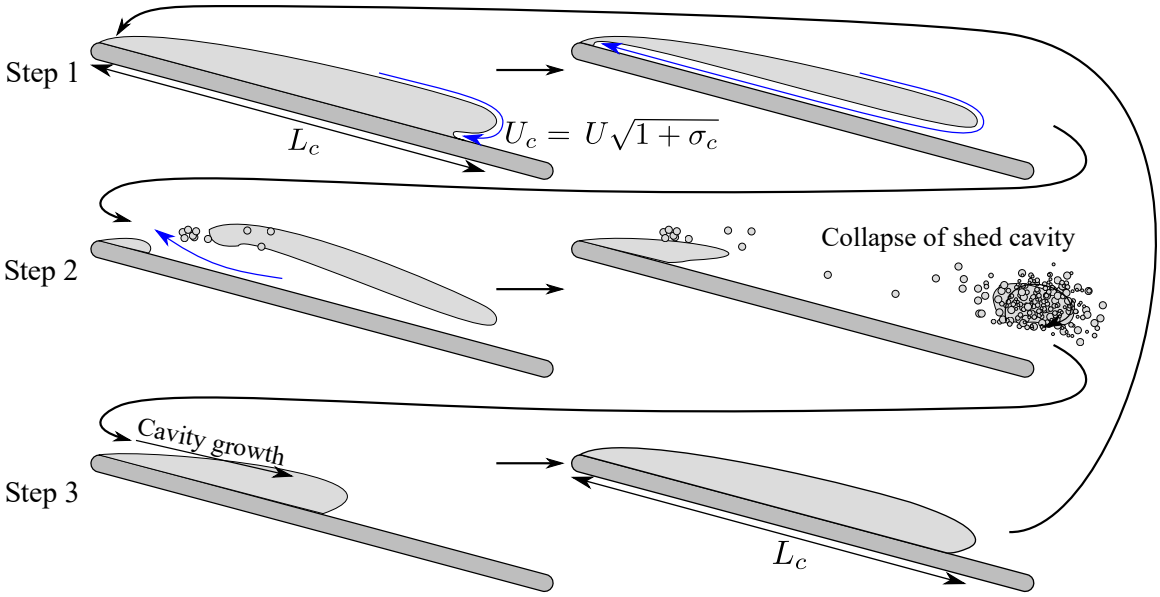

Figure 1.3: Schematic illustration of 2-D cavity shedding caused by a re-entrant jet. Horizontal rows indicate each of the three steps of the cycle, labeled on the left. Dark grey indicates the solid surface of a flat-plate hydrofoil, light grey represents the vaporous cavity, and blue arrows represent liquid streamlines. Figure reproduced from *Young et al.* (2016).

where $T_{1,2,3}$ indicate the timescales of the three processes listed above.

The time for step 1 to occur can be estimated by the convective timescale of the re-entrant jet. The velocity along the streamline forming the boundary of a gaseous cavity (and therefore the velocity of the re-entrant jet) is, from Bernoulli's equation,

$$U_{jet} = U\sqrt{1+\sigma_c}. \tag{1.11}$$

The length-scale of convection in step 1 is the maximum cavity length, L_c. Thus,

$$T_1 \approx \frac{L_c}{U\sqrt{1+\sigma_c}}. \tag{1.12}$$

The cavity-shedding Strouhal number, based on the cavity length, is given by *Arndt et al.* (1995),

$$St_L = \frac{f_c L_c}{U} = \kappa \quad \overline{(1+\sigma_c)}, \tag{1.13}$$

where κ is an empirical parameter, given by *Arndt et al.* (1995) to be $\kappa \approx 0.25$. Substituting equation 1.12 into equation 1.10 yields a value of $\kappa \approx 0.33$. *Franc and Michel* (2004) dispenses with the σ_c term entirely and approximates $St_L \approx 0.25-0.35$.

Alternatively, by using the chord-length c as a characteristic length scale, one may

write the Strouhal number as,

$$St_c = \frac{f_c c}{U} = St_L \left(\frac{L_c}{c}\right)^{-1}; \\ = \kappa \sqrt{(1+\sigma_c)} \left(\frac{L_c}{c}\right)^{-1}. \tag{1.14}$$

The relationship between c and L_c introduces variation with σ_c/α_{2D}, as described in the preceding section (see equations 1.8 and 1.9) (*Kawakami et al.*, 2008).

Figure 1.4 shows experimentally-measured Strouhal numbers (St_c) compiled by *Kawakami et al.* (2008) for three hydrofoils in three different cavitation tunnels, as well as numerical simulations of cavity shedding on a NACA66 hydrofoil by *Ducoin et al.* (2012b); *Akcabay et al.* (2014a). Strouhal numbers based on cavity length (St_L) were calculated using equation 1.14 and the cavity length approximation from equation 1.8. Value of the chord-based Reynolds number,

$$Re_c = Uc/\nu, \tag{1.15}$$

are given in the figure caption, where ν is the fluid kinematic viscosity.

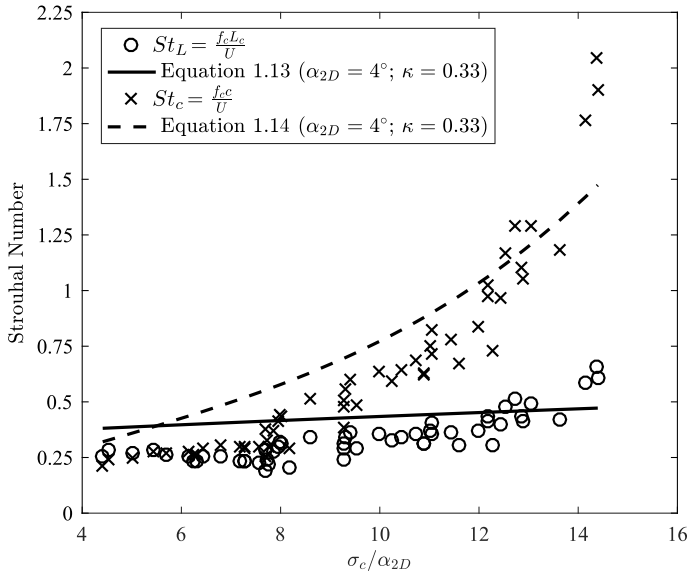

Figure 1.4: Cavity-shedding Strouhal number as a function of cavitation parameter. Data from experiments by *Kawakami et al.* (2008) ($3.5 \times 10^5 \leq Re_c \leq 1.02 \times 10^6$) and numerical simulations by *Ducoin et al.* (2012b); *Akcabay et al.* (2014a) ($Re_c = 7.5 \times 10^5$) are shown as symbols. Contours of equations 1.13 and 1.14 are shown, with σ_c estimated for $\alpha_{2D} = 4°$ and $\kappa = 0.33$. Data re-plotted from *Akcabay and Young* (2015) and figure reproduced form *Young et al.* (2016).

1.4 Multi-Phase Flows on Three-Dimensional Lifting Surfaces

1.4.1 Extending from Two-Dimensional to Three-Dimensional Ventilated Flows

Spanwise variations in 3-D cavity shapes arise from spanwise gradients in geometry, inflow conditions, cross-flow, proximity to the free surface or adjacent solid boundaries, buoyancy, and rotation. A schematic representation of some typical 3-D lifting systems is shown in figure 1.5, annotated with the geometric parameters used in the ensuing text. Included are surface-piercing hydrofoils with and without dihedral, fully submerged hydrofoils, propellers, and superventilated bodies. This is not an exhaustive list, and the examples shown are canonical, lacking skew, rake, taper, twist, or curvature. However, it represents a cross-section of typical lifting-systems.

The variation in absolute free-stream pressure P_∞, relative to the lifting surface in question, is one such source of non-uniformity For a steady-state ventilated cavity, the cavity pressure P_c in equation 1.2 may be considered constant everywhere inside of the cavity, while P_∞ may vary in space. In general, P_∞ must be computed on a case-by-case basis for the geometry and flow under consideration, although some simplified cases exist, which are informative to consider. For example, consider a surface-piercing lifting surface like those shown in figures 1.5(a,b). Assume that pressure gradients are dominated by gravity, such that the static pressure gradient in a rectilinear coordinate system with the z-direction defined positive downwards is $\{\boldsymbol{\nabla P}\} = \{0, 0, \rho_f g\}$, and the cavity pressure is given by $P_c = P_0 = P_{atm}$, where P_{atm} is atmospheric pressure (approximately 101 kPa). A section located at a depth z below the free surface then possesses a sectional cavitation number of (*Kiceniuk*, 1954; *Breslin and Skalak*, 1959; *Young and Brizzolara*, 2013),

$$\sigma_c(z) = \frac{P_{atm} + \rho_f g z - P_c}{\rho_f U^2/2} = \frac{2gz}{U^2}. \tag{1.16}$$

which causes σ_c to vary along the span of a hydrofoil, according to the spanwise pressure gradient. When the pressure gradient is hydrostatic, as in the case of surface-piercing hydrofoils, the variation is linear. One might imagine other cases, where the spanwise pressure gradient is not solely hydrostatic, but is induced by flow curvature, caused by rotating flow, or is absent. In the latter-most case, such as for horizontal hydrofoils, the cavitation number would be constant along the span.

Any lifting surface with a finite span will also possess a non-uniform distribution of

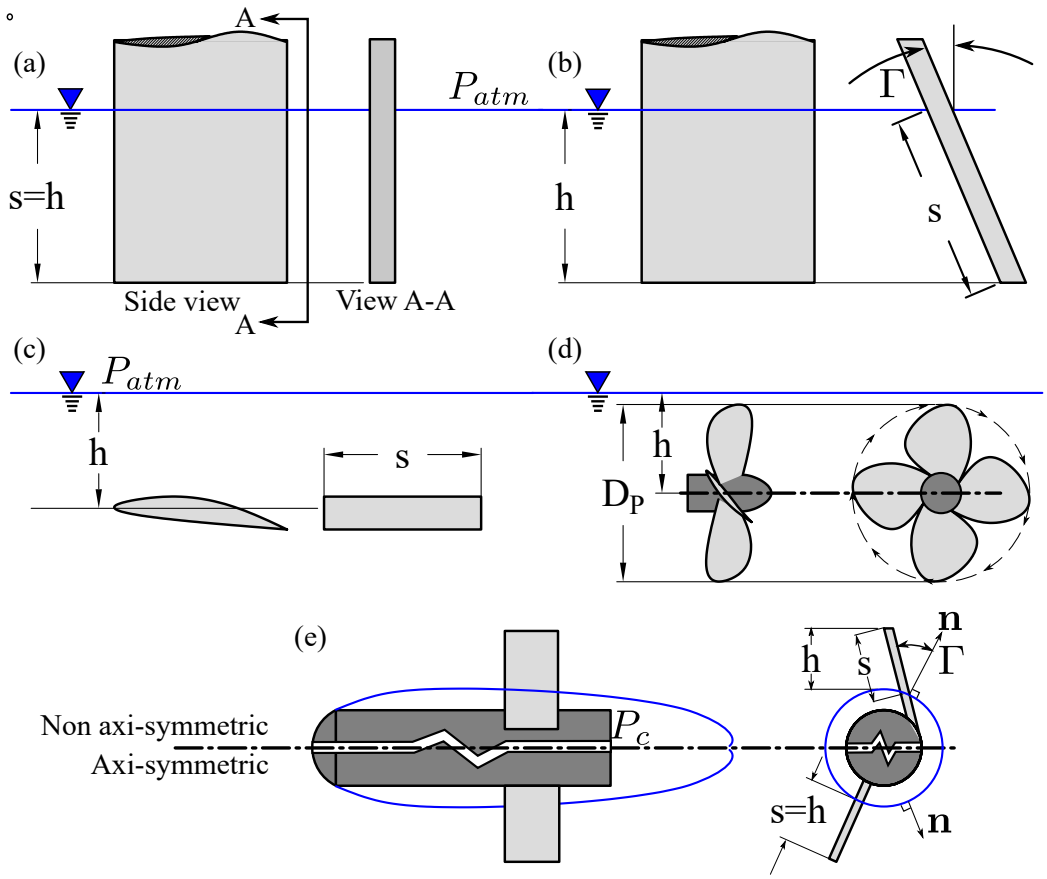

Figure 1.5: Schematic depictions of lifting surfaces that may be subject to ventilation. (a) Vertical surface-piercing hydrofoil/strut, (b) Surface-piercing hydrofoil with dihedral angle Γ, (c) Horizontal fully submerged hydrofoil, (d) Shallowly submerged propeller, (e) Super-ventilated or supercavitating body with control surfaces penetrating the cavity boundary. Note that (e) depicts two different appendage configurations-one axi-symmetric and one with a local dihedral angle Γ relative to the local cavity normal. In all cases, $S \equiv$ geometric span, $h \equiv$ normal distance from phase boundary to lifting surface tip or centerline, $\{\boldsymbol{n}\} \equiv$ unit normal vector on phase interface, directed toward dense fluid, $D_P \equiv$ propeller diameter. Figure reproduced from *Young et al.* (2016).

sectional angles of attack and sectional lift coefficients as a result of the free surface, tip flow, vortex shedding, and geometric variation. The 2-D sectional properties and 3-D distributions may be rectified by application of a suitable 3-D foil theory. The spanwise gradients of hydrostatic pressures, sectional angles of attack, lift, drag, inflow conditions, and cavity lengths have been modeled by a variety of methods, ranging from strip-theory (*Perry*, 1955; *Breslin and Skalak*, 1959) to simple lifting-line models (*Wadlin*, 1959; *Harwood and Young*, 2014; *Harwood et al.*, 2014, 2016c) to boundary element methods (*Young and Kinnas*, 2003a,b; *Young and Savander*, 2011; *Young and Brizzolara*, 2013). Depending upon the type of system being considered (hydrofoil, propeller, rudder, etc.), the impact of a cavity's three-dimensionality can range from negligible to important. Some systems (those at high speeds or without significant buoyancy effects) behave similarly to 2-D cavitating bodies. On the other hand, 3-D effects make the categorization or analysis of cavities on other types of system non-trivial (*Rothblum*, 1977b; *Harwood et al.*, 2014, 2016c).

The geometric aspect ratio of a lifting surface with a constant chord length is defined as,

$$AR_S = \frac{S}{c}, \tag{1.17}$$

where S is the submerged length of the hydrofoil. The submerged aspect ratio is defined as,

$$AR_h = \frac{h}{c}, \tag{1.18}$$

where h is the submerged depth of the hydrofoil, measured perpendicular to the phase-interface nearest to the body. For straight lifting surfaces piercing the free surface vertically, the two aspect ratios are equivalent. For surfaces with a dihedral angle Γ, the ratio of AR_h to AR_S is the cosine of Γ.

The right hand side of equation 1.16 takes the form of a Froude number, which is widely used as a scaling parameter in free surface flows. In fact, equation 1.16 may be re-written as

$$\sigma_c(z) = \frac{2}{{Fn_h}^2}\frac{z}{h}, \tag{1.19}$$

where

$$Fn_h = \frac{U}{\sqrt{gh}}, \tag{1.20}$$

is the depth-based Froude number, g is gravitational acceleration, h is the depth of a body below the free surface, measured vertically. Note that the depth-based Froude number is an indicator of the ratio of dynamic head over hydrostatic head and it may

be viewed as a ratio of the spanwise pressure gradient to the chordwise pressure gradient – an interpretation that will be informative during later chapters of this thesis. As will be shown in the following sections, Fn_h is a primary parameter in the natural ventilation of bodies at or near the free surface. For artificial ventilation, there could conceivably arise situations involving neither the free surface nor gravitational head. Consider the example of a high-speed cavitator with a nominally axi-symmetric cavity like that in figure 1.5(e). Here, S indicates the geometric length of the protruding control surface, measured from the nominal axi-symmetric cavity boundary and h denotes the distance measured along a vector normal to the cavity interface. An appendage piercing the gas-liquid interface of the cavity could be viewed as analogous to the free surface flow, but with disturbances on the cavity boundary restored by a normal pressure gradient not necessarily gravitational in origin. A more general form of Froude number was proposed by *Young et al.* (2016) to be

$$Fn = \frac{U}{\sqrt{|h\nabla P \cdot \mathbf{n}|}}. \tag{1.21}$$

For all cases of ventilation in this thesis, equation 1.21 and equation 1.20 are equivalent.

1.4.2 Re-Entrant Jets on 3-D Cavities

The angle of the cavity-closure line relative to the inflow has an interesting effect on the re-entrant jet kinematics. Figure 1.6 shows cases with a cavity-closure line normal and non-normal with respect to the incoming flow. If the inflow velocity is expressed in components normal and tangential to the cavity-closure line, then conservation of momentum can be used to show that the tangential component remains constant because the pressure at the cavity boundary is constant (*De Lange and De Bruin*, 1998; *Duttweiler and Brennen*, 1998). Equation 1.11 states that the magnitude of the jet's velocity will be equal to the magnitude of the inflow velocity along the cavity interface. Thus, 3-D re-entrant flows can be regarded as a reflection of the incoming flow about the boundary of separation. A streamline on the cavity surface, intersecting the cavity closure boundary at an angle Φ will emerge in the re-entrant jet at an angle 2Φ relative to the downstream direction of the inflow. As a result, re-entrant flow is not necessarily directed upstream.

The effects of spanwise re-entrant jets was studied on swept wings by *De Lange and De Bruin* (1998); *Duttweiler and Brennen* (1998); *Laberteaux and Ceccio* (2001b),

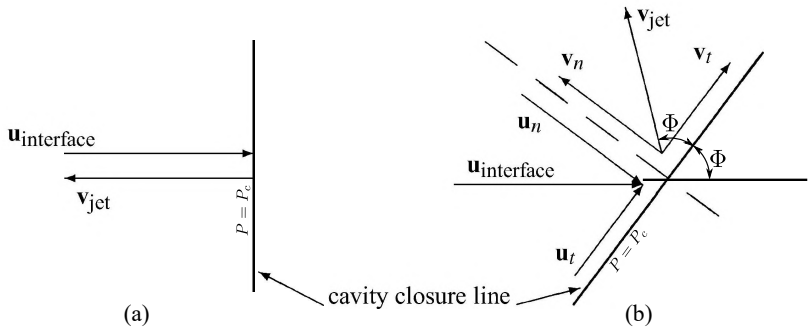

Figure 1.6: A depiction of the flow in the neighborhood of cavity-closure lines (a) normal to the inflow and (b) at an angle to the inflow. Conservation of momentum in the tangential direction causes incoming flow to be reflected about the local cavity-closure line. Figure reproduced with modifications from *De Lange and De Bruin* (1998).

where the non-orthogonality of the cavity closure to the incoming flow was caused by the sweep of the foil. In the case of surface-piercing hydrofoils and struts, the spanwise variation is a result of the hydrostatic pressure gradient and resulting variation in σ_c along the span. This is an important fact, and it will be used in chapter III to explain the stability of ventilated flow regimes.

1.4.3 Three-Dimensional Ventilated Cavity Flows

Ventilated flows around surface-piercing bodies were extensively studied in the 1950's, the 1960's, and the 1970's, spurred by interest in high speed hydrofoil-supported vessels. A summary of past experimental studies is tabulated in table 1.1 as a convenient reference for the parameter ranges examined in each study.

Perry (1955) found that the separated wake behind bluff bodies piercing the free surface became aerated readily, and that, given a suitable perturbation, a ventilated cavity could extend beyond the low-energy wake to envelop much of the body. *Kiceniuk* (1954) showed that ventilation could also occur on streamlined hydrofoils when the yaw angle (α, which is also the angle of attack for vertically-oriented hydrofoils and struts) exceeded the stall angle. Once a cavity was present, it remained stable across a wide range of angles, including those below the stall angle at which ventilation occurred. In both studies, air was initially entrained into low-pressure regions of separated flow, but with sufficiently large amounts of ventilation, a new stable state was reached, with a cavity extending beyond the original wetted zone of flow separation.

Wetzel (1957) performed experiments on partially immersed cylindrical rods with diameters between 0.8 mm and 5.1 cm (1/32 to 2 in) and vertical symmetric struts to study the scale-effects associated with the transition between wetted and ventilated flows. The Reynolds number and Weber number were varied independently from the Froude number by heating the water and adding detergents, respectively. While not directly reported, his data showed that the effect of Weber number was negligible above a critical value of $We = \rho_f U^2 l/\gamma \approx 250$, where l is the characteristic length (rod diameter, d, or strut section chord-length, c) and γ is the surface tension constant in N/m. For struts at a geometric yaw angle (α), ventilation at $\alpha \leq 21^\circ$ was hysteretic and dependent upon the yaw angle, sometimes occurring suddenly in what the author dubbed "flash" ventilation. Note that for vertical lifting surfaces, the yaw angle and angle of attack are equivalent. At angles exceeding the stall angle ($\alpha \geq 21^\circ$), ventilation occurred gradually through entrainment of air into the stalled wake (dubbed "creeping" ventilation). The latter type of ventilation was found to scale with the depth-based Froude number. Large-diameter cylinders for which $We \geq 250$ and hydrofoils at yaw angles of $\alpha \geq 21^\circ$ both ventilated via the "creeping" process at a constant Froude number of $Fn_h \approx 1.7$.

Wadlin (1958) studied an un-yawed, vertical, surface-piercing hydrofoil with a cambered section profile. Oil-smear visualizations on the suction surface indicated a laminar separation bubble near the TE, but the separated flow did not extend to the free surface. When air was artificially injected into the separated flow, it displaced the water to form a cavity of approximately the same size as the preceding separation zone. *Wadlin* (1958) concluded that both low pressures and separated flow are required for ventilation to occur. He referenced the experiment by *Coffee and McKann* (1953), in which vaporous cavitation occurred on the after-body of an un-yawed surface-piercing hydrofoil at speeds in excess of 23 m/s ($Fn_h > 16$). The presence of vaporous cavitation provided visual evidence of the necessary low pressures and flow separation, but ventilation did not occur of its own volition, as one might expect it to. In *Wadlin*'s experiment, ventilation was induced by "disturbing the water surface in the vicinity of the leading edge." The disturbance was likely a thin wire inserted into the flow, though the exact method was unspecified. The disturbance served to rupture the barrier of unseparated flow near the free surface, allowing air to enter and occupy the ventilation-ready flow. The ventilated cavity gradually disappeared once the disturbance was removed, leading *Wadlin* (1958) to conclude two things: first, that low-pressure paths (such as shear flows or the cores of shed vortices) must be available to permit the ingress of air into a ventilation-

ready flow before ventilation can occur, and second, that those air paths must remain available for ventilated cavities to persist.

Breslin and Skalak (1959) performed a series of experiments on yawed surface-piercing hydrofoils with and without cambered sections with chord lengths of $c = 7.6$ cm and $c = 6.4$ cm, respectively. They defined ventilation as a flow regime characterized by the entrainment of a smooth-walled, air-filled cavity along the entire immersed span of a hydrofoil. Ventilation caused a reduction of up to 70% in the measured lift coefficient, $C_{L_{3D}}$, relative to fully wetted flows at the same conditions. The appearance and disappearance of ventilated cavities were respectively termed ventilation "inception" and "closure." At post-stall angles of attack/yaw angles ($\alpha \geq 20°$), ventilation occurred spontaneously and gradually, with air entrainment occurring through eddies in the separated wake, similar to the base-flow behind bluff bodies and highly-yawed hydrofoils observed by *Wetzel* (1957). At angles approaching stall ($\alpha \approx 15°$ to $18°$), vortices were shed by the imminently-stalled flow. The shed vorticity intersected the free surface, aerating through the vortex cores and drawing air into locations of peak suction pressure on the hydrofoil to cause ventilation. At very small immersion depths and moderate angles of attack ($14° \leq \alpha \leq 18°$ and $AR_h = h/c = 0.5$), ventilation formation occurred through the ingestion of air into the tip vortex far downstream of the hydrofoil, at which point, the vortex core aerated, transporting air upstream to the hydrofoil's suction side.

Breslin and Skalak (1959) also showed that ventilation could be triggered at sub-stalled angles ($\alpha \leq 14°$) by breaching the free surface upstream of the hydrofoil's leading edge with a disturbing body (such as the point of a pencil). Unlike *Wadlin* (1958), who observed ventilated cavities triggered in this manner to disappear after the disturbance was removed, *Breslin and Skalak* (1959) found that such cavities remained stable, even as the yaw angle was decreased towards zero degrees, corroborating the observations of *Kiceniuk* (1954) and *Wetzel* (1957) and reinforcing the notion that the formation and elimination of ventilated cavities was, to some degree, a hysteretic process. *Breslin and Skalak* (1959) also used oil-film visualization to demonstrate that boundary layer separation did not extend to the free surface for yaw-angles below stall. *Breslin and Skalak* (1959) studied the conditions at cavity elimination with varying hydrofoil sections and immersed aspect ratios by decreasing the speed of a fully ventilated hydrofoil and recording C_{L_w} and Fn_h immediately following the elimination of the fully ventilated cavity, where C_{L_w} denotes the 3-D lift coefficient of the fully wetted hydrofoil at the conditions under which ventilation ceased to occur (discussed further in §4.6). When C_{L_w} was plotted against ${Fn_h}^{-2}$, a

number of boundaries were revealed for the different foil shapes and configurations. At the limit of small Fn_h^{-2} (large Fn_h) and small C_{L_w}, the boundaries faired into a line, suggesting that fully ventilated flows were stable only if,

$$C_{L_w} \geq 5Fn_h^{-2} \qquad \text{and} \qquad Fn_h \geq 3. \tag{1.22}$$

It should be noted that, at smaller Fn_h or larger C_{L_w}, the boundaries found by *Breslin and Skalak* (1959) deviated from the asymptotic fit and from one another, so equation 1.22 over-predicted the required lift coefficient at a given Fn_h and over-predicted the Fn_h for a given lift coefficient at which stable ventilation may occur.

Rothblum et al. (1969) performed a series of experiments at high speeds and Reynolds numbers ($5 \times 10^5 \leq Re_c \leq 1.7 \times 10^7$) on a family of symmetric biogive-section hydrofoils with chord lengths of 0.3 to 0.61 m, several leading edge radii, and zero TE thickness at varying yaw angles. He identified wetted and ventilated flow regimes, and noted the propensity of ventilated flow to remain stable at yaw angles much smaller than the conditions at formation. At speeds high enough to induce vaporous cavitation, ventilation occurred when the layer of liquid separating the vaporous cavity from the free surface was ruptured. The formation of a ventilated cavity occurred very suddenly, reducing or even reversing the action of lift. *Rothblum et al.* (1969) suggested that at moderate angles of attack, flow over the hydrofoil's suction surface induced a downward acceleration of the free-surface, creating Taylor instabilities on the free surface (*Taylor*, 1950; *Emmons et al.*, 1960). Air then entered ventilation-prone zones on the suction surface through low-pressure vortical paths created by the collapse of the Taylor instabilities.

The same family of biogival struts with a chord-length of $c = 0.3$ m was also tested by *Waid* (1968) in a depressurized towing tank to study the interactions of ventilated and vaporous cavities. Cavitation numbers as low as $\sigma_v = 0.162$ were tested. Here, $\sigma_v = (P_0 - P_v)/(\rho_f U^2/2)$ is the vaporous cavitation number, where the reference pressure P_0 is taken to be the ambient pressure at the free surface. The results suggested that the value of σ_v was a primary factor governing ventilation formation when vaporous cavities were present. Taylor instabilities in the thin layer of water between a vaporous cavity and the free surface were a primary mechanism of air-ingress into the low-pressure vaporous cavity.

Swales et al. (1973) used pressure taps and oil-film visualization on the suction surface of a yawed vertical hydrofoil with a 0.1 m chord biogival section to show that sub-atmospheric pressures and flow separation preceded ventilation formation

in all cases, consistent with previous studies. The oil-film indicated a long leading edge separation bubble on the suction surface, which, like those observed by *Wadlin* (1958) and *Breslin and Skalak* (1959), did not extend to the free surface at sub-stall yaw angles. This indicated that a thin layer of fluid near the free surface presented a barrier to the ingress of air. The researchers corroborated the claim of *Wadlin* (1958) that sub-atmospheric pressures and boundary layer separation are necessary pre-conditions of ventilation. However, they found no explicit relationship between spontaneous ventilation formation and the satisfaction of these pre-conditions, *i.e.* they were unable to show that the pre-conditions were sufficient to guarantee ventilation formation.

Swales et al. (1974) studied the same biogival model families as *Rothblum et al.* (1969) and *Swales et al.* (1973). In addition, struts with NACA-0012 and NACA-16-021 sections and 10 cm chords were used. They found that the Taylor-instabilities described by *Rothblum et al.* (1969) induced ventilation formation for streamlined sections (termed "tail inception"), while sharp-nosed sections ventilated through a long leading edge bubble and the associated leading edge vortex (termed "nose inception"). Leading-edge separation with subsequent reattachment of the flow is a feature of sharp-nosed sections known as thin-airfoil stall (*Gault*, 1957), which occurs when adverse pressure gradients induce laminar separation upstream of the turbulent transition point. *Chang* (1960, 1961) states that the laminar separation point is independent of free-stream Reynolds number on such section shapes. *Hecker and Ober* (1974) found that the length of separation bubbles on sharp-nosed hydrofoil sections grew as the angle of attack was increased, and depended only weakly on the Reynolds number in the range of $1 \times 10^5 \leq Re_c \leq 3 \times 10^5$. Air injected into a separation bubble by *Hecker and Ober* (1974) was entrained in the separated flow and formed a partial ventilated cavity, while air injected outside of the bubble was convected downstream without inducing ventilation.

Rothblum et al. (1974) studied the effects of surface roughness, surface wettability, and speed on the formation of ventilated cavities using a strut with a 10 cm chord and NACA-0012 section profile with different surface coatings and finishes. They determined that roughened surfaces and higher speeds acted to weaken the sealing-effect of the unseparated flow at the free surface by promoting turbulence and generating vorticity near the free surface. Surface wettability and surface tension were judged to have negligible influence at the scale tested.

One recurring conclusion from the studies is that ventilation must be preceded both by sub-atmospheric pressures and by boundary-layer separation. Another recur-

ring observation is that there exists an un-separated layer of flow near the free surface at angles of attack below stall. The condition of constant pressure at the free surface relieves chordwise pressure gradients on the hydrofoil, precluding flow separation. As a result, a thin layer of high-energy flow forms a seal between the ventilation-prone regions and the source of air, delaying ventilation, even beyond the point at which the flow could begin to sustain a ventilated cavity. This conclusion was supported by the observations of *Wadlin* (1958); *Breslin and Skalak* (1959); *Rothblum et al.* (1969) and *Swales et al.* (1974) that in some trials, sub-atmospheric pressures and separated flow were evident (inferred from pressure surveys and oil films, or indicated by the presence of vaporous cavities), even while the flow remained fully wetted. Likewise, the lack of sufficiency of sub-atmospheric, separated flow for predicting ventilation formation (*Swales et al.*, 1973) was thought to be a result of the free surface seal created by the un-separated layer of flow. *Fridsma* (1963) referred to this hysteretic range of operation as an "unstable" range, in which the flow – and the associated lift of the hydrofoil – was not uniquely determined by its angle of attack (see figure 1.7). *Brizzolara and Young* (2012); *Young and Brizzolara* (2013) referred to the same region as the "transitional range." This uncertainty with respect to the character of the flow has resulted in much research being devoted to ventilation suppression in an effort to increase the stability of the wetted flow *Swales et al.* (1974); *Rothblum* (1977b), especially because the developed lift can be catastrophically reduced by unanticipated ventilation. Fences and manipulation of the boundary layer are examples of ventilation suppression techniques (*Rothblum et al.*, 1976). An alternative approach is to encourage ventilation using air-injection, so that sudden transition from wetted to ventilated flow at high speed is avoided in favor of a controlled transition at low speed. This unstable/transitional region therefore merits further investigation in order to formalize its definition and understand what causes its associated hysteresis.

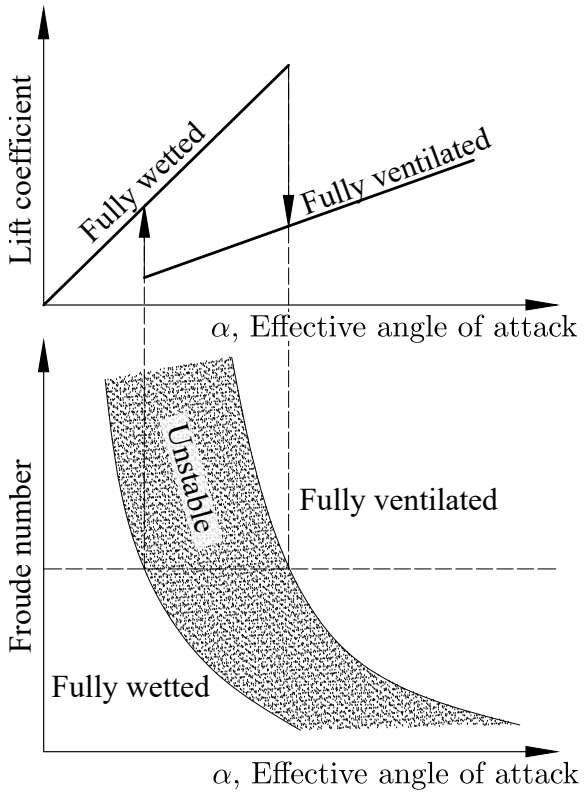

Figure 1.7: The characteristic lift curves for wetted and ventilated flows and the notional stability zones of a surface-piercing hydrofoil. The shaded overlapping range of angles of attack is referred to by *Fridsma* (1963) as the "unstable region," stemming from the fact flow is hysteretic and can transition unexpectedly from one flow regime to another. Figure styled after *Fridsma* (1963) and reproduced from *Young et al.* (2016).

Table 1.1: Summary of previous studies of natural ventilation on surface-piercing bodies. The facility types are keyed as follows: TT-Towing Tank, FSWC-Free surface water channel, RAT-Rotating arm tank, DPTT- Depressurized towing-tank, FSCT-Free surface cavitation tunnel. Where minimum or maximum parameter values were not given, they are inferred from the respective reports. Table adapted from *Harwood et al.* (2016c).

Citation	Section Shape	Facility Type	$c(d)$, cm	AR_h	Fn_c	Fn_h	σ_v
Coffee and McKann (1953)	NACA 66_1012	TT	10–20	1–6	6.5–24.4	2.6–24.4	0.3–2.3
	NACA 66_4021	TT	1	1–6	9.2–24.4	3.7–24.4	0.3–2.3
Kiceniuk (1954)	Circ. arc	FSWT	3	1.0–1.5	6.2–12.3	5.1–12.4	4.1–16
Perry (1955)	Rect. bars	FSWT	2.5	1.2–16.8	3.1–16.5	0.7–15.0	2.9–84
	Cyl. rods	RAT	0.1–5.1	1–100	1.3–65.3	0.1–65.3	5.3–>100
Wetzel (1957)	NACA 0012	RAT	5.1-7.6	0.5–5	1.1–8.6	0.5–12.2	5.3–>100
	NACA 0024	RAT	5.15	0.5–4.5	1.3–8.6	0.6–12.2	5.3–>100
	NACA 4412	RAT	7.6	0.5–2	0.9–10.6	0.6–15.0	2.3–>100
Breslin and Skalak (1959)	Circ. arc	RAT	6.4	0.5–2	1.0–11.6	0.7–16.4	2.3–>100
Fridsma (1963)	Wedge @ 30° dihedral	TT	5.1	1–3	4.3–17.3	2.5–17.3	1.3–21
Waid (1968)	Circ. arc family	DPTT	30.5	1–1.5	3.5–5.3	2.9–5.3	0.2–5.3
Rothblum et al. (1969)	Biogive family	TT	30.5	1–3	1.2–16.4	0.7–16.4	0.24–46
	Blunt biogive	TT	10	1–1.5	1.5–6.2	1.3–6.2	5.3–84
Mcgregor et al. (1973)	NACA 0012	TT	10	1.5	1.5–6.2	1.3–5.0	5.3–84
	6deg wedge	TT	7.5–10	1.5	1.5–7.1	1.3–5.8	5.3–84
Swales et al. (1973)	Biogive	FSWT	10	2	1.5–6.1	1.1–4.3	5.3–87
	Sharp Biogive	FSCC	10	2	1.5–6.1	1.1–4.3	0.1–87
Swales et al. (1974)	Naca 0012	FSCC	10	2	1.5–6.1	1.1–4.3	0.1–87
	NACA 16-021	FSCC	10	2	1.5–6.1	1.1–4.3	0.1–87
	Biogove	TT	30.5–61	2	0.8–14.6	0.6–10.3	0.3–54
Fuwa et al. (1993)	Circular Arc	TT	30	1.5	0.1–3	0.1–2.5	7.4–> 100
	Circular Arc	TT	80	1.5	0.1–3	0.1–2.5	2.8–> 100
Pogozelski et al. (1997)	Streamlined body at 0deg	TT	91.4	1.5	0.1–0.5	0.05–0.4	84–> 100

1.5 Hydroelasticity of Lifting Surfaces

Fluid dynamics and structural dynamics all too often become divided by dichotomous academic mindsets. Fluid Structure Interaction (FSI) is the re-pairing of the two disciplines, and concerns itself with the two-way interaction that occurs between a body moving in a fluid and the forces induced by the fluid on the body. The review thus far has dealt with the exclusively-hydrodynamic aspects of multi-phase flow on lifting-surfaces. In reality, all structures are flexible to some degree. Highly-loaded appendages of moderate-to-high aspect ratio, such as propeller blades, rudders, hydrofoil, and control surfaces, are particularly likely to deform under loads – especially with increasing use of non-metallic construction materials such as composites and plastics. Hydroelasticity is the sub-discipline of FSI dealing with deformable bodies in dense fluids. In this section, a brief review of the meaning, governing physics, and interpretations of relevant hydroelastic topics will be given. Much of this section borrows heavily from, or contains excerpts from, the text of *Young et al.* (2016).

Hydroelasticity shares many principles with the more-mature field of aeroelasticity, the literature of which is replete with authoritative sources such as *Bisplinghoff et al.* (2013); *Fung* (2002). The distinction between the two is usually made on the basis of the relative mass ratio, defined as,

$$\mu = \sqrt{\frac{4m}{\rho_f \pi c^2}}, \tag{1.23}$$

which may be interpreted as the ratio of the solid mass a foil section, m to the fluid mass contained inside of its circumscribed circle, both defined per unit length. Mass ratios of $\mu > 4$ are typical of aerospace systems, while marine systems typically fall into the range of $\mu < 2$. Operation in water poses a number of unique challenges not present in aeroelasticity. As implied by the value of μ, the density of the fluid tends to be much greater relative to that of the solid, increasing the importance of fluid inertia. Speeds tend to be smaller by one to two order of magnitude in water than in air, resulting in lower Reynolds numbers and increased viscous effects. Additionally, marine applications possess multiple fluids, in the form of a free surface and multi-phase flow. Numerical work (*Fu and Price*, 1987; *Akcabay et al.*, 2014b; *Akcabay and Young*, 2014; *Akcabay et al.*, 2014a; *Chae et al.*, 2013, 2016) and experimental work (*Besch and Liu*, 1971, 1973, 1974; *Blake*, 1972; *Blake and Maga*, 1975; *Fu and Price*, 1987; *Akcabay et al.*, 2014a; *Chae et al.*, 2016) have demonstrated that fluid inertia, damping, and disturbing forces can dominate the governing equations of motion for

lightweight lifting bodies in water. These large fluid forces, combined with the presence of a free surface, wave generation, and multi-phase flow, contribute to significant nonlinearity in the fluid-structure interactions. In some cases, particularly in steady flow, where inertial effects are unimportant, hydroelasticity can be described using the same tools derived for aeroelasticity. However, as flows become more dynamic, and as inertial, viscous, and other nonlinear forces become increasingly dominant, the tenets of classical linear aeroelastic analysis (such as frequency-domain methods) begin to break down.

The general equations of motion for the dynamical system (taken here to be a hydrofoil) may be written,

$$[\boldsymbol{M_s}]\left\{\ddot{\boldsymbol{X}}\right\} + [\boldsymbol{C_s}]\left\{\dot{\boldsymbol{X}}\right\} + [\boldsymbol{K_s}]\{\boldsymbol{X}\} = \{\boldsymbol{F_{EX}}\} + \{\boldsymbol{F_{fl}}\}, \tag{1.24}$$

where $[\boldsymbol{M_s}]$, $[\boldsymbol{C_s}]$, and $[\boldsymbol{K_s}]$ are respectively the solid mass, damping, and stiffness matrices, $\{\boldsymbol{X}\}$ is a vector of displacements in some finite number of degrees of freedom, $\{\boldsymbol{F_{EX}}\}$ is a vector of external perturbations, and $\{\boldsymbol{F_{fl}}\}$ is the hydrodynamic force vector, which includes all steady and unsteady fluid loads. In later chapters, assorted representations will be made of $\{\boldsymbol{F_{fl}}\}$, all of which conform to the model,

$$\{\boldsymbol{F_{fl}}\} = \{\boldsymbol{F_{r,steady}}\} - \left[\boldsymbol{M_{fl}}\right]\left\{\ddot{\boldsymbol{X}}\right\} + [\boldsymbol{C_{fl}}]\left\{\dot{\boldsymbol{X}}\right\} + [\boldsymbol{K_{fl}}]\{\boldsymbol{X}\} + \{\boldsymbol{F_{other}}\}. \tag{1.25}$$

$\{\boldsymbol{F_{r,steady}}\}$ is the steady fluid load on an rigid lifting geometry at the same (undeformed) attitude as the flexible structure, $[\boldsymbol{M_{fl}}]$, $[\boldsymbol{C_{fl}}]$, and $[\boldsymbol{K_{fl}}]$ are the fluid added mass, added damping, and added stiffness matrices, and $\{\boldsymbol{F_{other}}\}$ contains the assorted fluid force components not contained within the preceding terms (*e.g.* nonlinear forces, cavity shedding, or vortex shedding). Dynamical system models range widely in their fidelity and complexity, but for the sake of brevity in this review, let us consider a representative model with only two degrees of freedom.

1.5.1 Two-Dimensional, Two-DOF Model of a Wing Section

Consider the two-dimensional, two-degree-of-freedom (2-D, 2-DOF) model in figure 1.8, which depicts a section taken through a flexible hydrofoil at some spanwise station. For simplicity, we assume homogeneity and isotropy of the structural material throughout this work. Lift and drag act through the Center of Pressure (CP). The Center of Gravity (CG) of the section is located along the 3-D body's Neutral Axis (NA). Bending and twisting deformations are respectively denoted as δ and θ.

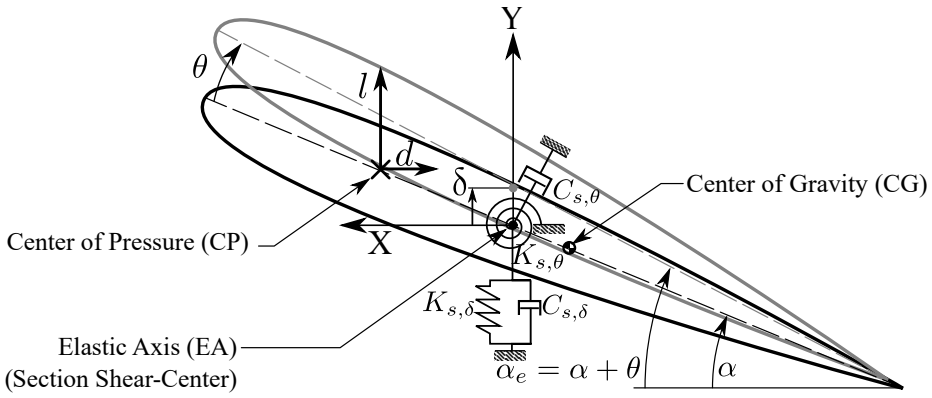

Figure 1.8: A 2-degree-of-freedom model of a flexible wing section.

Both are measured at the EA of the section, formed by the locus formed by the shear center of each section. The structural stiffness spring-rates of the hydrofoil in bending and twisting are respectively denoted $K_{s,\delta}$ and $K_{s,\theta}$, while damping coefficients (of linear dashpot representation) are denoted by $C_{s,\delta}$ and $C_{s,\theta}$.

With reference to equation 1.24, $\{\boldsymbol{X}\}$ denotes the section's bending and twisting deflections, $\{\boldsymbol{F_{EX}}\}$ is the vector of externally-applied forces and moments, and $\{\boldsymbol{F_{fl}}\}$ is the vector of fluid-induced forces and moments, respectively written as,

$$\{\boldsymbol{X}\} = \left\{ \begin{array}{c} \delta \\ \theta \end{array} \right\}; \qquad \{\boldsymbol{F_{EX}}\} = \left\{ \begin{array}{c} F_{y,ext} \\ M_{z,ext} \end{array} \right\}; \qquad \{\boldsymbol{F_{fl}}\} = \left\{ \begin{array}{c} l \\ m \end{array} \right\}. \tag{1.26}$$

The matrices may be expressed as,

$$[\boldsymbol{M_s}] = \left[\begin{array}{cc} m & S_\theta \\ S_\theta & I_\theta \end{array} \right]; [\boldsymbol{C_s}] = \left[\begin{array}{cc} C_{s,\delta} & 0 \\ 0 & C_{s,\theta} \end{array} \right]; \qquad [\boldsymbol{K_s}] = \left[\begin{array}{cc} K_{s,\delta} & 0 \\ 0 & K_{s,\theta} \end{array} \right]. \tag{1.27}$$

Here, $S_\theta = \frac{1}{2}mc(X_{CG} - X_{EA})$ is termed the static unbalance and $I_\theta = \frac{1}{4}r_\theta^2 c^2$ is the angular mass moment of inertia, where r_θ is the radius of gyration.

Note that these forms of the the matrices and vectors in equation 1.24 are strictly valid only for a 2-D section that is chordwise rigid. However, it constitutes a good foundation from which to build toward 3-D models, as well. Chordwise rigidity is a good assumption for most lifting-surfaces of moderate-to-large aspect ratios. This enables a separation-of-variable approach to be undertaken, wherein the 3-D motions of the lifting surface are taken to be the products of 2-D bending and twisting motions at a representative section (typically the free tip, if the foil is in a cantilevered configuration) and spanwise shape-functions (*Bisplinghoff et al.*, 2013; *Fung*, 2002; *Akcabay et al.*, 2014a; *Chae et al.*, 2016).

1.5.2 Steady-State Hydroelasticity

In steady conditions, the hydrodynamic force components in $\{\boldsymbol{F_{fl}}\}$ are given by steady-state hydrodynamic theory. Using linear theory, the lift per unit span is given by,

$$l = C_{l_{2D}} qc = a_0 \alpha_e qc, \tag{1.28}$$

where $C_{l_{2D}}$ is the 2-D lift coefficient, $q = \rho_f U^2/2$ is the fluid dynamic pressure, and a_0 is the linearized slope of the lift-coefficient as a function of the angle of attack, α. The twisting moment is given by,

$$m = C_{m_{2D}} qc^2 = a_0 \alpha_e qec^2/2, \tag{1.29}$$

where e is the distance from the elastic axis to the center of pressure (as shown in figure 1.8), nondimensionalized by the semi-chord. With equations 1.28 and 1.29 substituted into the right-hand side of equation 1.26 and equation 1.27, the steady-state deflections may be written,

$$\delta = \frac{a_0 \alpha qc}{K_{s,\delta}} \quad 1 + \frac{a_0 \frac{e}{2} qc^2}{K_{s,\theta} - a_0 \frac{e}{2} qc^2} \quad . \tag{1.30a}$$

$$\theta = \frac{a_0 \alpha \frac{e}{2} qc^2}{K_{s,\theta} - a_0 \frac{e}{2} qc^2} .. \tag{1.30b}$$

An alternate – but equivalent– expression may be written by eliminating all unsteady terms from equation 1.24, assuming steady hydrodynamic loading only (*i.e.* $\dot{\boldsymbol{X}} = \ddot{\boldsymbol{X}} = \{\boldsymbol{F_{EX}}\} = \{\boldsymbol{F_{other}}\} = \{\boldsymbol{0}\}$), and solving for the displacement to yield,

$$\{\boldsymbol{X}\} = \left([\boldsymbol{K_s}] + [\boldsymbol{K_{fl}}]\right)^{-1} \{\boldsymbol{F_{r,steady}}\} . \tag{1.31}$$

.

Equation 1.30b demonstrates that the feedback of the elastic twisting deflection into the hydrodynamic moment reduces the effective torsional stiffness of the system when the center of pressure is located ahead of the elastic axis ($e > 0$), as depicted in figure 1.8. As a result, the loads on – as well as the deflections of – flexible lifting bodies of isotropic and homogeneous construction tend to increase as the material becomes more compliant (particularly as $K_{s,\theta}$ decreases). Significant spanwise bending also reorients the direction of sectional lift forces. For this reason, both twisting and bending deflections of yawed surface-piercing hydrofoil or strut will affect the rolling moments on the supported craft.

1.5.2.1 Static Hydro-Elastic Instability: Divergence

The denominator of equation 1.30b is the effective total system stiffness in torsion, which takes into account the apparent reduction in stiffness caused by the two-way hydro-elastic coupling. In classical aero-elastic analysis, the static divergence of a wing is defined as the conditions at which the effective torsional stiffness vanishes (*Fung*, 2002; *Bisplinghoff et al.*, 2013), which occurs when the dynamic pressure exceeds a critical value ($q = \frac{1}{2}\rho_f U^2 \geq q_D$), where,

$$q_D = \frac{2K_\theta}{a_0 e c^2} = \frac{1}{2}\rho_f U_D^2. \tag{1.32}$$

Equation 1.32 suggests that divergence is possible at a finite dynamic pressure if and only if the aerodynamic center is located forward of the elastic axis ($e > 0$). Note that, according to linear theory, the center of pressure CP and the Aerodynamic Center (AC) are nearly coincident for thin, symmetric foils at small angles of attack. However, even when the AC and the EA are coincident, experiments by *Besch and Liu* (1971) and viscous simulations by *Chae et al.* (2013) have demonstrated that the actual center of pressure can migrate away from the AC as a result of viscous effects, particularly for thick foil sections, or when flow separation and/or cavitation develops. As a result, a moment may be developed about the AC, suggesting that static divergence can still occur in practice, even when the AC and EA coincide initially.

By substituting equation 1.32 into equation 1.30b, the following expression may be derived (*Liu and Young*, 2010),

$$\frac{1}{\theta} = \frac{1}{\alpha} q_D \quad \frac{1}{q} - \frac{1}{q_D} \quad , \tag{1.33}$$

which indicates a linear relationship between $1/q$ and $1/\theta$. The left hand side of equation 1.33 approaches zero as q approaches q_D. If $1/\theta$ is plotted against $1/q$, then the X-intercept equates to $1/q_D$. Figure 1.9 from *Young et al.* (2016) depicts equation 1.33 for wetted (FW) and ventilated (FV) surface piercing hydrofoils, predicted using a coupled lifting-line finite-element model, a partial description of which is given in §3.4.2, and which is further described in *Ward et al.* (2016). Figure 1.9 suggests that, as a result of reduced loading and an altered pressure distribution on the hydrofoil in ventilated flow, ventilation may actually delay static divergence. However, work by *Kaplan and Henry* (1960); *Kaplan* (1962); *Kaplan and Zeckendorf* (1964); *Kaplan and Lehman* (1966); *Rowe and Marvin* (1968); *Besch and Liu* (1973) indicate

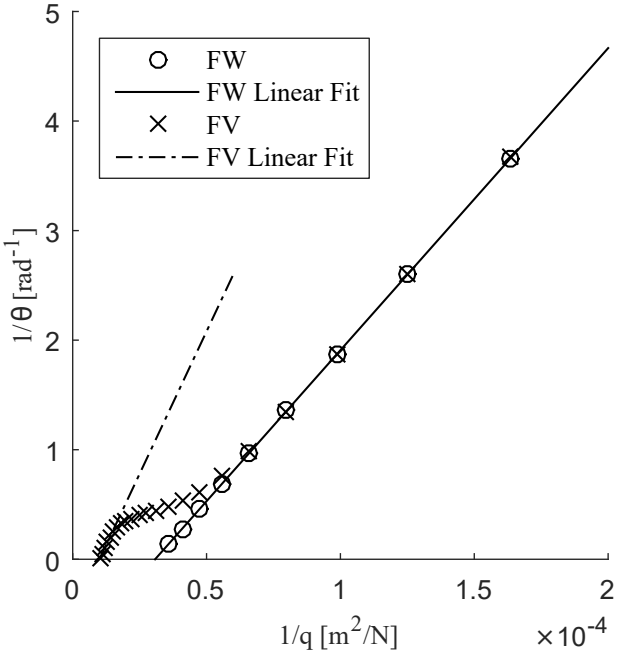

Figure 1.9: A plot of reciprocal elastic twist $1/\theta$ (measured at the tip of a flexible hydrofoil) against the reciprocal dynamic pressure $1/q$ for a hydrofoil in wetted and ventilated flows. The X-intercept is the reciprocal divergence dynamic pressure $1/q_D$. Figure reproduced from *Young et al.* (2016).

that unsteady cavitation and/or ventilation may accelerate flow-induced vibration and dynamic hydroelastic instability.

1.5.3 Dynamic Hydroelasticity

Dynamic FSI concerns the interactions between unsteady flows and the structural response of the body. The forces on the body may be externally-induced or the result of natural flow processes, so we speak of forced motions and flow-induced motions.

Forced motions, as the name implies, result from an external force, represented by $\{\boldsymbol{F_{EX}}\}$. Often, this force is harmonic, prompting a harmonic structural response at the same frequency. Resonance occurs when the frequency of the forced excitation matches a natural frequency of the excited system (or some harmonic or subharmonic thereof), resulting in a large-amplitude of motion in that structure's associated mode. External excitations include operational sources such as vibrations of engines, shafting, or propellers, or direct perturbations of a structure, such as a a shaker motor attached to a structure.

When the excitation is generated by the flow, the force is grouped into the fluid

force vector $\{\boldsymbol{F_{fl}}\}$, and the resulting motion is referred to as flow-induced vibration. Periodic cavity-shedding, vortex shedding, and boundary-layer instability are example causes of flow-induced vibration (*Ducoin et al.*, 2012a; *Akcabay et al.*, 2014a). Note that care should be taken that these types of excitations remain separate from the fluid lift and drag that make up the unsteady hydrodynamic forces in $\{\boldsymbol{F_{fl}}\}$. Flow-induced vibration leads to a subtle variation on resonance, known as "lock-in." Lock-in occurs when the flow phenomenon creating the force and the motions of the affected body interact – *e.g.* the motions of a body will interact with the shedding of partial cavities. When the excitation frequency falls within some finite band surrounding a natural frequency of the affected structure, the forcing frequency locks in to the natural frequency. A well-known example is the phenomenon of vortex-induced vibrations of cylindrical bodies. When the frequency of oscillation of a cylindrical body and the frequency of vortex shedding into the Von Kármán street approach one another, the motions of the body will – to some extent – drive the frequency at which vortices are shed, and the two phenomenon will lock in to a flow-induced resonance condition. When the forcing frequency is outside of this finite band, a lock-off condition prevails.

Multi-phase flows lead to a secondary type of resonance, as well. Periodic cavity shedding acts as a source of flow-induced excitation on the one hand, but on the other hand, the growth and collapse of the gaseous cavity periodically modifies the density and pressure fields around the body. As a result, the system's effective mass, damping, and stiffness matrices are modulated in time. The frequency of modulation or one of its subharmonics can excite the natural frequency of the flexible body – a situation known as parametric resonance. *Akcabay and Young* (2015) derived a SDOF model model of parametric excitation and lock in using a Van der Pol oscillator to model the modulation of system parameters with the cavity shedding frequency.

The dynamic interactions between the unsteady structural motions, $\{\boldsymbol{X}\}$, $\dot{\boldsymbol{X}}$, $\ddot{\boldsymbol{X}}$, and the hydrodynamic forces contained in the fluid force vector $\{\boldsymbol{F_{fl}}\}$ are particularly complicated because the unsteady motions of the body again feed back into the fluid loads. The instantaneous forces on a lifting-surface at a static attitude in the flow are functions of the body's position. When the undergoes unsteady motion, however, the instantaneous fluid loads represented by $\{\boldsymbol{F_{fl}}\}$ become the product of unsteady hydrodynamic theory, where α_{2D}, δ, θ, their first and second derivatives (rate effects), and their integrals (memory effects) contribute to the instantaneous lift and moment. A foil section subjected to an impulsive change in α_{2D}, for example, will experience an instantaneous lift force that gradually approaches the steady-state value as the foil starting vortex is convected downstream, creating an apparent lag in the instanta-

neous hydrodynamic load behind the motion of the body. Classic theories for computing the unsteady fluid loads typically come from the field of aeroelasticity. The most famous include the frequency-domain Theodorsen's equation (*Theodorsen*, 1935) and Sears' function (*Sears*, 1941) or the time-domain Wagner function (*Wagner*, 1925), in addition to quasi-steady (rate-only) forms. A detailed review of unsteady aerodynamic and hydrodynamic theories is beyond the scope of this thesis, but a number of comprehensive reviews and references exist, to which an interested reader may refer (*McCroskey*, 1982; *Bisplinghoff et al.*, 2013; *Fung*, 2002; *Dowell et al.*, 2004). In the special, but informative, case where the body motion is harmonic, the hydrodynamic force vector is also harmonic. The apparent time-lag of instantaneous forces manifest as phase-shifts between the body motion and the resulting hydrodynamic force. $\{\boldsymbol{F_{fl}}\}$ thus contains fluid force components proportional to structural motion, velocity, and displacement, commonly referred to as added mass, damping, and stiffness matrices, and which modify the effective system properties. Additionally, frequency modulation, and nonlinearities that can modify the effective system properties.

1.5.3.1 Dynamic Hydroelastic Instability: Flutter

Unsteady fluid loads may modify the effective system mass, damping, and stiffness matrices. As a result, dynamic modes of hydroelastic instability arise – chief amongst which is flutter, which is defined as a self-excited resonance in a flowing fluid. Flutter occurs when the damping of at least one mode of the structure in question becomes negative, known as the flutter mode. As a result, the flutter mode begins extracting energy from the flow and grows without bound. Flutter in coupled degrees of freedom involves a coalescence of two or more modal frequencies toward the so-called "flutter frequency." The instability occurs with the unbounded transfer of energy from one highly-damped mode into another, negatively-damped one, the latter being denoted the flutter mode.

Flutter analysis of systems with low mass ratios is notoriously difficult. Classic methods of predicting flutter *via* modal damping estimates, such as the K-method, P-method, or P-K method, are limited to the frequency domain, and are thus linear. Additionally, the coupling of structural dynamics and unsteady aerodynamics requires that harmonic or near-harmonic motions be assumed, which implicitly carries with it the assumption of small damping. *Abramson* (1969) succinctly summarizes three factors of hydroelasticity that de-rail most usage of aeroelastic techniques: the presence of a free surface, the presence of multiple phases (cavitation or ventilation), and low mass ratios. Indeed, for even fully submerged hydrofoils in uniform flow, no

modifications to aeroelastic theory have been generally successful at capturing experimental results (*Abramson*, 1969; *Chae*, 2015). For example, figure 1.10 shows that theoretical predictions of flutter are extremely un-conservative below $\sqrt{\mu} \leq 2.1$, and that theory predicted no flutter for $\sqrt{\mu} \leq 1.8$. The experimental data, on the other hand, demonstrate that flutter did occur, and at speeds significantly lower than at larger mass ratios.

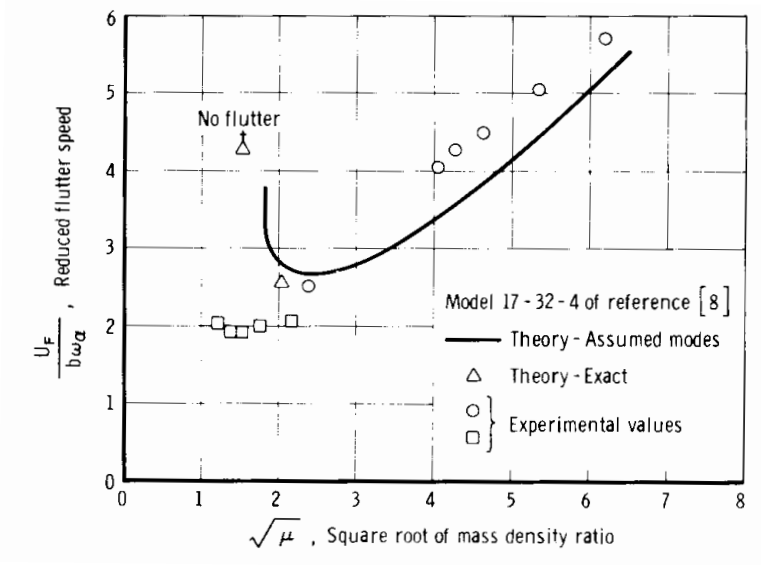

Figure 1.10: Flutter speed plotted as a function of μ. Figure reproduced from *Abramson* (1969).

These results are typical. Work by *Hilborne* (1958); *Besch and Liu* (1971, 1973, 1974) have explored and demonstrated, to varying degrees, the deficiencies in classical theory for reproducing the experimentally-observed flutter boundaries. *Besch and Liu* (1973) specifically noted that predictions were extremely un-conservative at low value of μ. The same study led to the conclusion that flutter predictions were most deficient as a result of poor hydrodynamic damping estimates, and that theory was entirely unable to capture the onset of flutter in cavitating conditions or with modified boundary-layer profiles. Again, more-detailed reviews of the hydrofoil flutter problem may be sought out by the interested reader, and include *Woolston and Castile* (1951); *Henry et al.* (1959); *Abramson and Chu* (1959); *Abramson* (1969).

The problem of cavitation and ventilation on a lightweight, flexible surface piercing hydrofoil is one possessing all three of factors described by *Abramson and Chu* (1959): a proximal free surface, multiple phases, and a low mass ratio. With linear frequency-domain analysis unable to accommodate these factor, most present-day researchers have turned to coupled time-domain simulations, which do not require the assumption

of harmonic motion. These simulations recruit a variety of fluid and solid models, including 1-D lifting-line analysis with 1-D beam-element FEM (*Ward et al.*, 2016), Boundary Element Method (BEM) fluid models coupled with 2-D and 3-D FEM solid models (*Motley et al.*, 2009; *Young*, 2010; *Young et al.*, 2010), and viscous Computational Fluid Dynamics (CFD) simulations coupled to FEM or reduced-order solid models (*Chae et al.*, 2013, 2016; *Akcabay and Young*, 2014, 2015). Even with the wealth of available tools, 3-D ventilating and cavitating flows are dominated by a panoply of physical phenomena that, considered individually, stress the capabilities of present numerical tools, so say nothing of simulating them together. Recent work by *Akcabay et al.* (2014a); *Chae et al.* (2016) have sought to synthesize the knowledge gained from experimental work into robust and meaningful simulations, but more progress is needed. Presently, the scientific community lacks the necessary knowledge of the physics governing unsteady FSI in the presence of ventilation, cavitation, and the free surface to have any confidence in the results of simulating such flows.

1.6 Open Questions and Research Objectives

The preceding review is intended to highlight some of the areas of interest in multi-phase flow and hydroelasticity, and to demonstrate a number of areas in which improvements may still be made. Depth-based Froude numbers in the range of $1 \leq Fn_h \leq 25$ were reported for studies of streamlined struts/hydrofoils in the previous work described in this chapter, but discussions of cavity topologies and stability were focused primarily on relatively large Froude numbers ($Fn_h \geq 4$), by testing at high speeds or by using very small models. In the range of $Fn_h \geq 4$, the flows tend to be unambiguously wetted or ventilated. The range of low-to-moderate Froude numbers ($0.5 \lesssim Fn_h \lesssim 4$) is an important one, however. Naturally ventilated cavities at low and moderate Froude numbers possess more-pronounced spanwise variation in the cavity topology than those at higher speed. The three-dimensionality of a lifting surface can blur the distinctions between the established 2-D cavity regimes shown in figure 1.1. In many cases, different sections along the span of a 3-D lifting surface may simultaneously be fully wetted, base-cavitating, partially cavitating, and supercavitating. The lack of a formalized set of criteria for separating one flow regime from another highlights the need for standardization of the definitions involved in natural ventilation.

The transitional flows that precede fully developed ventilation, especially at lower speeds, have been largely neglected as a result of the historical focus on high speeds.

It should be noted that the term "inception," used by several previous researchers, is replaced in this this by the term "formation." Inception will be assigned a specific definition, more consistent with its usage cavitating flows, in chapter IV. Likewise, "closure," as it has been defined in the literature, is replaced in this thesis by "elimination" to avoid confusion with the downstream extent of a gaseous cavity, known as a cavity "closure region." As shown by the results of *Wetzel* (1957) and *Breslin and Skalak* (1959), ventilation formation and elimination may occur at low Froude numbers, incurring sudden changes in loading and flow topology. Additionally, while a limited number of studies have investigated ventilation formation, the process of ventilation elimination has not been examined closely, with the exception of a brief treatment by *Breslin and Skalak* (1959). Any system designed to operate at high Froude numbers must necessarily transit the low-to-moderate Froude number range. From a scientific standpoint, it is desirable to better-understand ventilation in this range of Froude numbers, where hydrostatic and dynamic pressures are on the same order of magnitude. Therefore, a more thorough investigation of flow-stability and ventilation transition processes at moderate Froude numbers is of both practical and academic interest.

The topic of hydroelasticity adds additional complexity to the consideration of multi-phase flow. The static and dynamic hydroelastic response and stability of lifting surfaces depend strongly upon the forces applied by the fluid flow, cavity shedding, proximity to the free surface, and vortex shedding, as well as upon the effective system mass, damping and stiffness. Previous studies of hydrofoil hydroelasticity have demonstrated a gap between classical theory and physical observation. The combined complexity of multiple phases, flexible lifting surfaces, and free-surface effects renders classical theory inadequate, and even present numerical methods are insufficient to simulate hydroelastic and multi-phase flows with any degree of confidence. The range and complexity of physics also makes experimental measurement and study a challenging task, and as a result, most experimental studies of hydroelasticity have been limited primarily to single-phase flows, with some recent experimental work exploring the FSI of two-phase (cavitating) flows (*Ducoin et al.*, 2010; *Rodriguez*, 2012; *Ducoin et al.*, 2012b; *Akcabay et al.*, 2014a; *Chae et al.*, 2016).

It is the overall objective of this thesis to provide an improved understanding of the mechanics of atmospheric ventilation and vaporous cavitation on rigid lifting surfaces, as well as their interplay with the hydroelastic responses of flexible lifting surfaces at moderate Froude numbers. An experimental campaign has been performed to study ventilation on both rigid and flexible lifting surfaces, the findings of which will be

expanded upon in subsequent chapters of this thesis. It is useful at this point to motivate the following chapters by posing a number of questions to be addressed by this work:

- What are the characteristic steady flow regimes of surface-piercing lifting-surfaces and how are they formally defined?
- What physical processes dictate the hydrodynamic response and stability of steady flow regimes?
- How do hydrodynamic loads differ between flow regimes? How do the loads change with speed, immersion depth, and attack angle within each regime?
- How do flows transition between different regimes and how do transition mechanisms relate to the physics governing flow stability?
- What flow transition mechanisms occur on surface-piercing struts in subcavitating and cavitating flow?
- What effect does hydrofoil flexibility have upon the answers to the above questions? Are hydrodynamic response, stability, and flow regimes significantly modified by flexibility of the surface-piercing strut?
- What simple models can be derived to simulate the behavior of surface-piercing hydrofoils in multiphase flows?
- How does multi-phase flow affect the static and dynamic hydroelastic response and stability of the hydrofoil?
- How are the system natural frequencies, mode shapes, and damping coefficients altered by flow speed and multi-phase flow?
- Can ventilation and/or cavitation cause hydroelastic instability?
- Can scaling relations be developed to describe the static and dynamic loads, structural response, or stability conditions of surface-piercing hydrofoils?

1.7 Thesis Structure

The body of this thesis will be be organized into two introductory chapters, four results chapters, and a chapter for conclusions and future work. In chapter II, the

experimental methodology will be described, which involves multiple experimental campaigns, conducted in two facilities, using three geometrically-similar model hydrofoils with different flexibilities. The results and associated discussions are divided among four segments, comprising chapters III through VI. Chapter III describes the aspects of steady flows on the aluminum hydrofoil, which serves as an effectively rigid reference model. Chapter III lays out much of the terminology to be used in the remainder of the thesis, and scaffolds the discussion going forward. Unsteady flows on the rigid hydrofoil are described in chapter IV, including a taxonomy of the transitional flows that occur between flow regimes. Chapter V describes the differences between the hydrodynamic response of two flexible hydrofoils and that of the rigid hydrofoil in the preceding two chapters, including flow regime stability, hydrodynamic loads, and flow-induced vibration. Chapter VI presents a preliminary exploration of the vibratory characteristics of a flexible hydrofoil, which is tied back into the discussion of dynamic hydroelastic stability. A reflection upon the results, insights gained, and lessons learned concludes each individual chapter. A summary of findings, major contributions, and avenues for future research concludes the work in chapter VII.

CHAPTER II

Experimental Approach

Three hydrofoil models were tested in two facilities, with varying instrumentation suites and experimental protocols. In this chapter, the experimental program will be detailed for each set of testing undertaken. First, the hydrofoil models, their shared geometry, and their individual constructions will be described, along with the fixturing scheme for each of the facilities. Then, the facilities themselves will be described and the instrumentation suite will be covered according to measurement-type. Data acquisition architecture will follow, and a table of propagated uncertainties concludes the chapter.

2.1 Hydrofoil Models and Fixture

Three hydrofoil models were constructed from a shared baseline geometry, which is shown in figure 2.1. The geometry possesses a uniform semi-ogival section along the span, with an approximate chord length of $c = 27.94$ cm, approximate maximum thickness of $T = 2.8$ cm, a circular arc (ogival) forebody with a radius of curvature of 85 cm, and a rectangular after-body. The section has a leading edge radius of $0.01c$ (0.28 cm) and a blunt Trailing Edge (TE). Slight variations on sectional dimensions resulted from modifications made to the models, and specific dimensions are listed in table 2.2. This *semi-ogival* section geometry resembles that used in past studies, particularly the models of *Rothblum et al.* (1969); *Swales et al.* (1973, 1974); *Waid* (1968). Its advantages include a negligible pressure gradient over the aft-half of the section shape (due to a lack of curvature), an easy-to-instrument section with a thick after-body, into which sensors could be installed, and a sharp leading edge, which represents a mostly-fixed point of separation, reducing the need for turbulent tripping. The blunt TE, although a strange choice from a purely hydrodynamic standpoint, is also advantageous for a few reasons. First, the region of dead water or base-flow

abaft of the TE ventilates through the classic “creeping" mechanism described by *Wetzel* (1957), providing a convenient visual indication of the negation of hydrostatic pressure by the base pressure. Secondly, as a result of this base-flow and the smooth detachment of the suction- and pressure-side streamlines, sensors can be installed on the TE without disrupting flow along the suction and pressure faces. Finally, the thick afterbody resulted in a physically-strong model, capable of withstanding large side-loads, even with a non-metallic construction. The hydrofoil has a rectangular plan-form with a span of $S = 91$ cm (36 in), along which the section shape is constant. An additional mounting tang with a length of 7.6 cm (3 in) and a rectangular section shape was machined into the root of the hydrofoil.

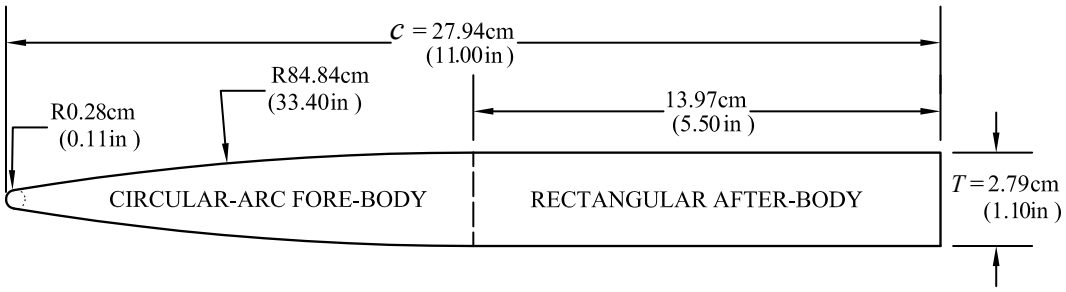

Figure 2.1: Cross-section shape shared by the hydrofoil models. Figure reproduced from *Harwood et al.* (2016c).

One rigid aluminum hydrofoil and two flexible variants of a PVC hydrofoil were built. Construction drawings for the models and fixture may be found in appendix A. The following sections describe the construction of each model. Table 2.1 lists the material properties of 6061 aluminum and Type 1 PVC and table 2.2 gives the mass and section properties of each of the three hydrofoil models. Table 2.2 also lists the first three *in-vacuo* natural frequencies of each hydrofoil model with the associated normal modes, which were determined by Finite Element Method (FEM) analysis (simulated with cantilevered boundary conditions) and verified experimentally.

Table 2.1: Tabulated material properties of hydrofoil construction materials.

Material	6061 Aluminum	Type 1 PVC
density, kg/m^3	2700	1486
Young's modulus E, GPa	69	3.36
Shear modulus G, GPa	26	1.2
Poisson ratio ν	0.33	0.4

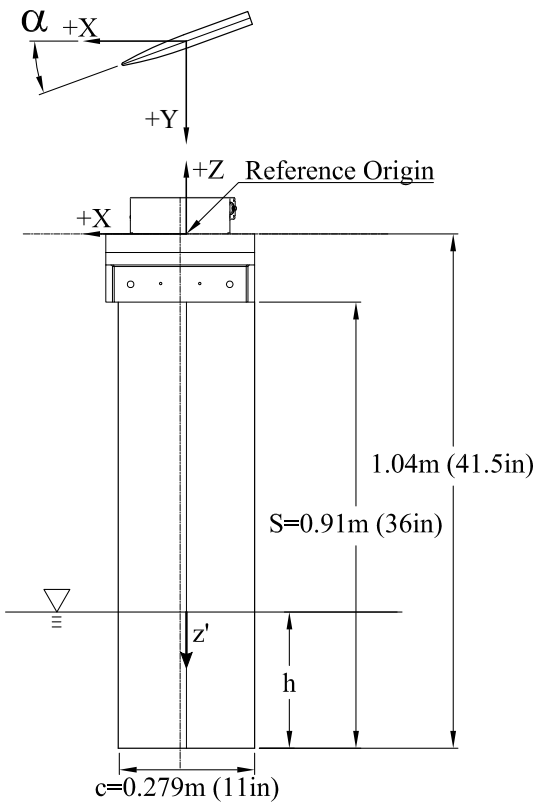

Figure 2.2: Dimensions of hydrofoil plan form. The root of the hydrofoil is shown installed into the lower portion of the model fixture, which will be described later. The coordinate system used in experiments defined with the X axis pointing upstream and the Y-axis pointing in the direction of positive lift. The direction of the Z axis follows from the right-hand coordinate system, and was varied to accommodate the orientation of the model in each facility. z' describes the distance measured downward from the free surface. Figure reproduced from *Harwood et al.* (2016c).

Table 2.2: Tabulated physical properties of hydrofoil model 0, model 1, and model 2.

Hydrofoil Model	Model 0	Model 1	Model 2
Material	6061 Aluminum	Type 1 PVC	Type 1 PVC with 6061 Aluminum Reinforcement Strip
Chord, cm	27.94	27.94	28.58
Section Area, cm^2	67.3	58.8	60.6
Section Mass, kg/m	18.2	8.7	9.2
Shear Center X_{SC}/c (fwd of mid-chord)	-0.136	-0.106	-0.259
Mass Center X_{CG}/c (fwd of mid-chord)	-0.06	-0.045	-0.068
Torsional Rigidity GJ, N-m^2/rad	46,670	1800	2450
Flexural Rigidity EI, N-m^2	25,450	1220	1950
Mode 1	1^{st} Bending: 21.2 Hz	1^{st} Bending: 8.0 Hz	1^{st} Bending: 9.9 Hz
Mode 2	2^{nd} Bending: 112.1 Hz	2^{nd} Bending: 48.3 Hz	1^{st} Twisting: 51.7 Hz
Mode 3	1^{st} Twisting: 170 Hz	1^{st} Twisting: 56.5 Hz	2^{nd} Bending: 63.3 Hz

2.1.1 Rigid Hydrofoil (Model 0)

The rigid model was machined as a monolithic piece from 6061 aluminum It is depicted in figure 2.3 prior to surface-finishing. The foil was hardcoat anodized for corrosion and abrasion resistance. As a result of the aluminum construction, the foil was extremely stiff. With the exception of limited free-vibration testing (discussed in chapter VI), the aluminum hydrofoil was assumed to experience no hydrodynamically significant deflections, *i.e.* is assumed to be rigid.

Figure 2.3: Photo of aluminum hydrofoil (Model 0), prior to hardcoat anodizing.

2.1.2 Flexible Hydrofoil (Model 1)

The flexible hydrofoil model (herein referred to as model 1), was constructed from PVC with outer dimensions identical to those of the aluminum hydrofoil. The choice of PVC was made because it is inexpensive, easily machined, has low water absorption, has relatively high ultimate strength (among thermoplastics), and possesses a density comparable to that of many composites. Specifically, Type 1 PVC was selected (also known as rigid PVC), which is available in sheet stock, and which has particularly good chemical resistance.

The PVC strut was machined in two halves, symmetric about the chord-line. Along the plane, two interior channels were machined, into which custom-built shape-sensing spars were installed, as shown in figure 2.4. More details on the shape-sensing spars are given in §2.5.

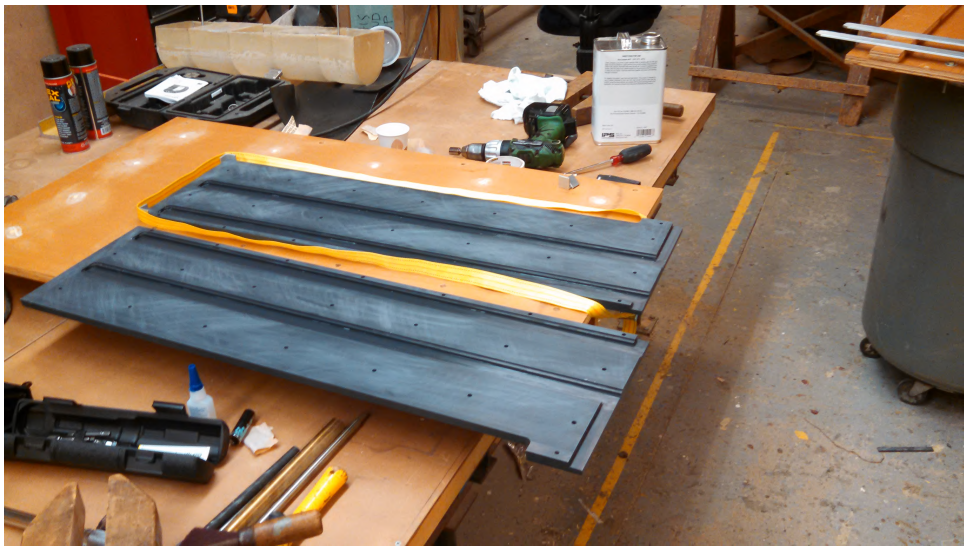

Figure 2.4: Photo of split PVC hydrofoil

Because a single, monolithic structure was desirable, and because the maximum shear stress occurs along the bonded plane, it was necessary to use a chemical solvent bond, which dissolves the material on both bonding surfaces, which are then pressed together. When the solvent evaporates, an ideally-bonded joint will behave as a single homogeneous material, with polymer chains joining the previously-separate parts. Type 1 PVC, however, is notoriously difficult to bond, and the solvent welding products used for PVC pipe do not work on Type 1 PVC sheets. In the end, the two halves of the foil were affixed using a solvent mixture of Tetrahydrofuran (THF) and Methyl Ethyl Ketone (MEK), sold as Weld-On® Scigrip 2007 Rigid Vinyl Cement. The foil halves were brushed with solvent and stacked together, using locating pins to align

the interior channels. A clamping jig was used to sandwich the two halves, on which bolts around the edge of the hydrofoil were uniformly torqued to a known specification to achieve the desired clamping pressure of approximately 690 kPa (100 psi). Female molds of the hydrofoil's section were machined from extruded polystyrene insulation foam and placed between the wood and the hydrofoil to evenly distribute the clamping pressure across the curved surface of the hydrofoil. Purely-solvent formulae are extremely volatile, so the entire process had to be completed in about 120 seconds. Figure 2.5 shows the hydrofoil being clamped immediately following the application of adhesives.

Figure 2.5: Photo of PVC hydrofoil being clamped during chemical weld.

Some small air pockets remained in the seam after the solvent-weld, which compromised the water-proofing of the hydrofoil. First, a second dose of solvent adhesive was injected by syringe into the seam, where capillary action wicked it into small air voids. Following that, a vacuum bag was applied to the top of the hydrofoil and the interior channels were placed under a vacuum. Cyanoacrylate glue, or "super glue," was used to back-fill the small voids by allowing the vacuum to pull the adhesive into the voids in the seam, where the glue hardened and sealed the capillary passages. Super glue is documented as an excellent bonding agent for most types of PVC. As a last step, the seams along the TE and the tip of the foil (where the width of the bond was a minimum and water leaks occurred) was milled out with a V-groove and back-filled with heat-welded PVC. Final waterproofing was verified by positively-pressurizing the interior channels and submerging the hydrofoil in a tank

of water to check for air bubbles. Two PVC hydrofoils were constructed in this way (one primary and one back-up), neither of which suffered from leakage.

As a last preparatory step, the Leading Edge (LE) of each foil was sanded with a precision-radiused block to smooth out inconsistencies in the sharp LE. The surfaces of the foils were treated with plastic epoxy filler, dry sanded, wet sanded, and polished with fine polishing compound to achieve a semi-glossy, hydraulically smooth surface, shown in figure 2.6.

Figure 2.6: Photo of surface-finish of PVC hydrofoil after LE treatment and polishing.

2.1.3 Flexible Hydrofoil with Reinforced Trailing Edge (Model 2)

A second variant of the PVC hydrofoil was constructed, denoted model 2. In reality, model 2 was simply a modification to model 1, wherein a strip of 6061 aluminum was affixed to the TE to modify the section properties of strut. Figure 2.7 shows a comparison of the sections of model 1 and model 2, with the locations of the mass-centers and shear-centers called out. The locations of the interior channels are

also shown, with shape-sensing spars represented as shaded blue and red rectangles. The spars will be described in §2.5.

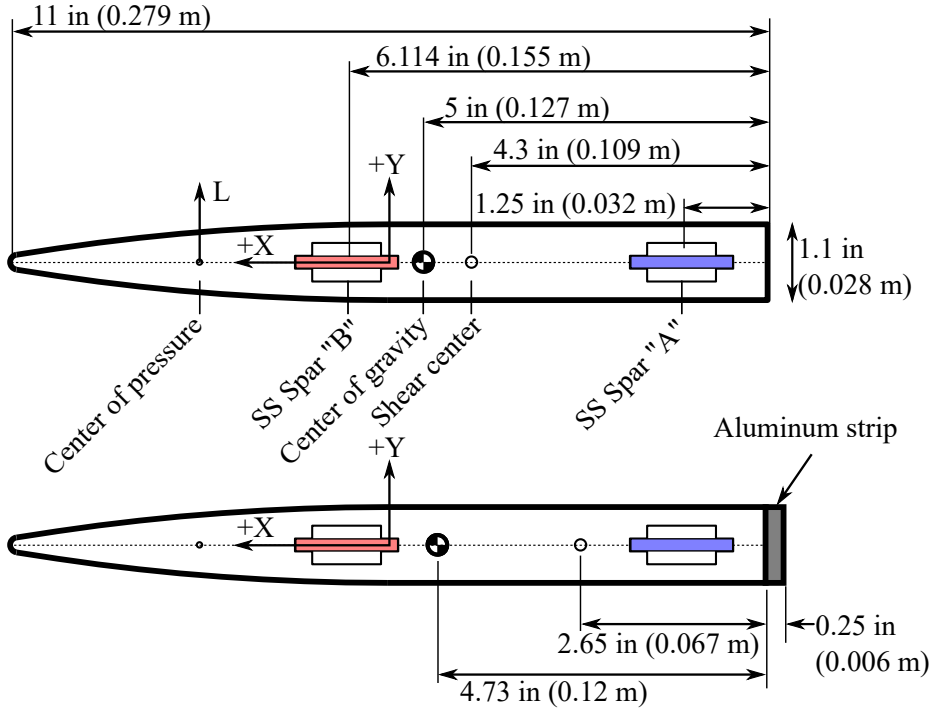

Figure 2.7: Cross-sections of PVC (model 1) and modified PVC (model 2) hydrofoil with section properties. More section properties are listed in table 2.2. Figure reproduced from *Harwood et al.* (2016b).

The aluminum reinforcement strip serves several purposes. First, as shown in figure 2.7, it moves the shear center aft by a distance of $0.15c$, increasing the moment arm of the lift force about the foil's elastic axis. Secondly, it increases the bending stiffness of the hydrofoil by approximately 60% and the torsional stiffness by approximately 36%, as indicated in table 2.2. The increased rigidity was beneficial for repeated and long-duration testing at highly-loaded conditions, like the cavitation-tunnel testing described in §2.2.2, because it substantially increased the margin of safety against yield or ultimate failure. It should be noted that, while the addition of the strip marginally increased the chord-length, the change is only $0.023c$, and is judged to be negligible. Therefore, the nominal chord was used for nondimensionalization of loads, immersion depth, *etc.*

The reinforcement strip was milled to match the width of the hydrofoil with a tolerance of -0.0127 cm (-0.005 in). The strip was affixed with 14 screws, countersunk into the aluminum and with holes tapped in the hydrofoil's TE. A strip of fiberglass double-sided tape was sandwiched between the screws and aluminum to improve the

load transfer between the two members. Figure 2.8 is a photo taken of the aluminum strip attached to the strut.

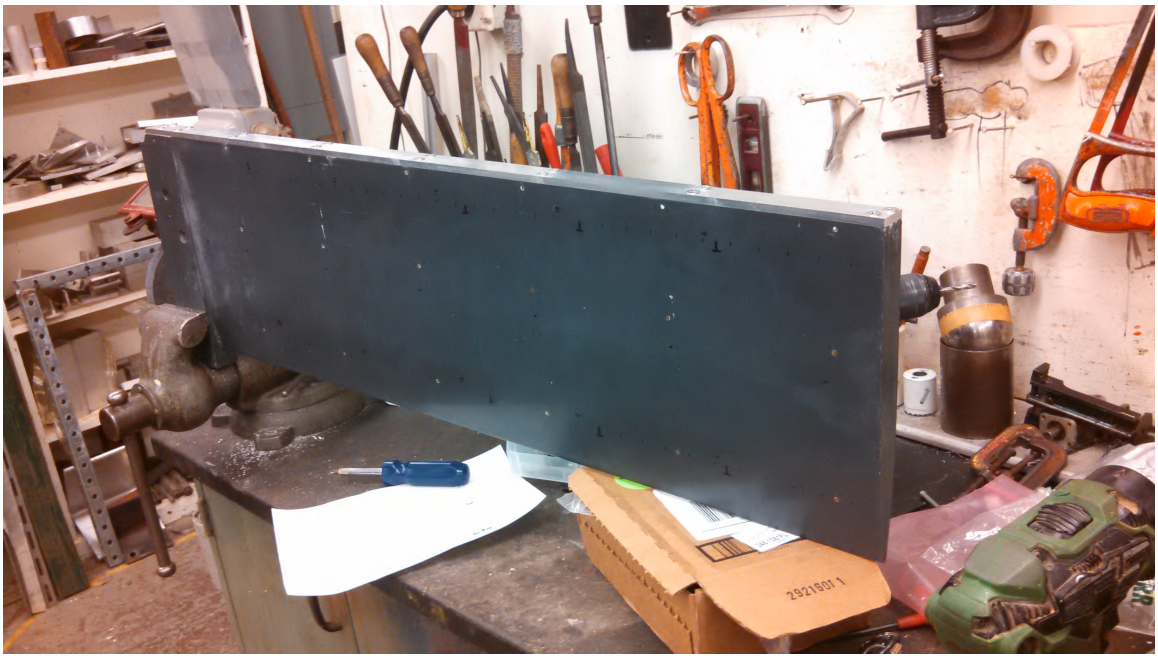

Figure 2.8: Photo of aluminum reinforcement strip on model 2

Each of the flexible hydrofoil models was treated as a beam in bending and torsion, with beam-section properties listed previously in table 2.2. The shear-center location, bending stiffness, and torsional stiffness were determined by a combination of FEM modeling and static load testing. For the aluminum model, an FEM analysis alone was used. One challenge with the PVC hydrofoils is that PVC sheeting is sold without precisely-quantified material properties. A relatively large range of material properties are provided by the manufacturer, leaving the customer to determine with greater accuracy what the density, elastic modulus, and shear modulus of the material are. Moving point-loads were applied to model 1 to experimentally determine the chordwise location of the elastic axis (the locus of sectional shear centers), as well as the effective bending and torsional stiffnesses. These were compared with the FEM model, in which the Young's modulus and the Poisson ratio were varied within the manufacturer's limits until the model predictions of shear-center location and static deflections matched well with experiments. The resulting material properties are listed in table 2.1. For model 2, FEM modeling alone was used to compute the modifications to the sectional properties with the addition of the aluminum strip.

2.1.4 Model Fixture and Foil Attitude

The hydrofoil being tested was clamped at the root and mounted vertically in a cantilevered configuration to pierce the water free-surface, as shown in figure 2.9. The apparatus was configured to allow the angle of attack α, the forward speed U, and the tip-immersion depth h to be independently varied. The supporting structure,

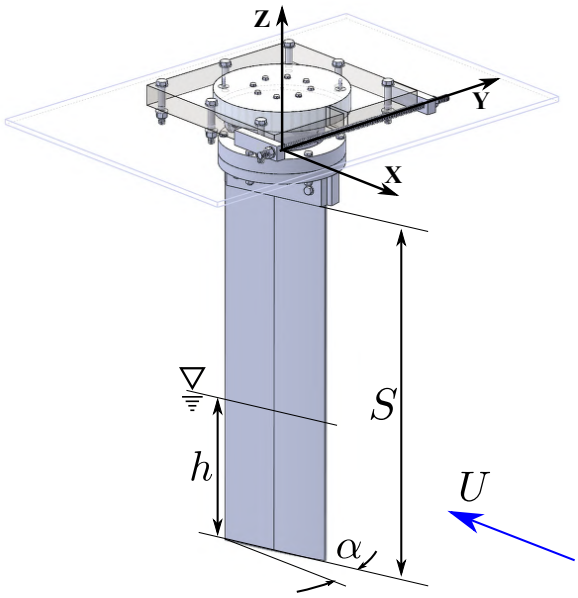

Figure 2.9: Depiction of the hydrofoil and the variables that describe its attitude in the flow.

shown in figure 2.9 as a transparent flat plate, was treated as the mechanical ground. Its design and anchoring in each of the facilities is described below.

The immersion depth of the hydrofoil was visually measured against tick-marks drawn on the surface of the hydrofoil at 0.5 inch (m cm) increments, as shown in figure 2.10. The maximum estimated uncertainty in the immersion depth is ± 0.25 inch, as the contact angle of the water with the foil surface causes some ambiguity in reading of the water level. Additionally, some natural fluctuation in water level occurred, due to evaporation, leaking, and filling of the towing tank, and due to near-constant adjustments in water level required at the INSEAN cavitation tunnel.

The hydrofoil was coupled to its mounting structure by way of a disk that rotated about a vertical axis, permitting the yaw angle α (angle of attack) to be varied. As depicted in figure 2.9, the machined aluminum disk is inset into a steel collar clamp. The yaw angle was set by hand by rotating the disk, which caused the hydrofoil and all attached instrumentation to rotate with it. Angle indicators, machined into the disk at one-degree intervals were used to visually sight the desired yaw angle with an

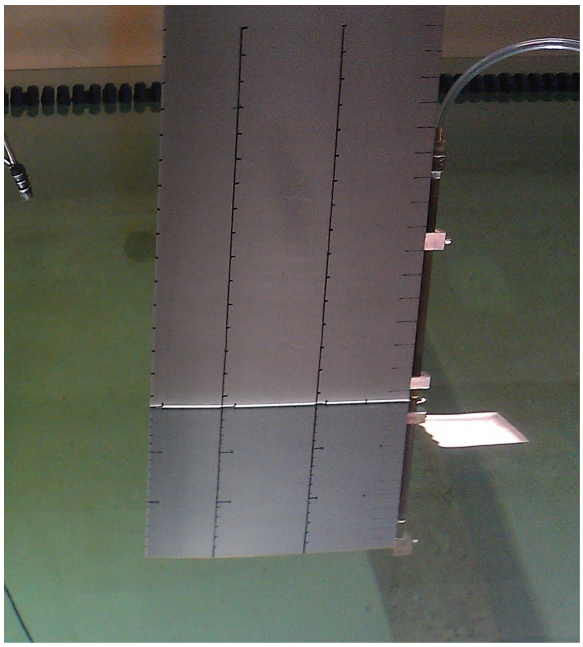

Figure 2.10: Tick marks on foil suction surface of model 0 in the towing tank. The marks were used to measure the immersion depth of the hydrofoil with an estimated uncertainty of ± 0.25 inch (0.635 cm).

estimated uncertainty of 0.25°. Once set, the hydrofoil's yaw angle was constrained by tightening a threaded rod across the steel collar clamp to apply clamping pressure around the circumference of the disk.

During testing, the large loads on the hydrofoil induced a large moment about the longitudinal axis (in the plane of the clamp), which could cause the disk lift on one side and become seized in the clamp. Checks were made after each run and, if the disk was found to be out-of-level, the disk was re-set into the clamp and the run performed again. For later testing, four flanged bolts were used to fix the yaw disk in the horizontal plane. The tapped holes, visible around the circumference in figure 2.11 were located such that the flange faces of the bolts provided a vertical clamping force to the top surface of the aluminum disk, preventing it from lifting at the interface and providing extra assurance against the angle of attack changing under load.

Figure 2.11: Rotating disk and clamp used to set yaw angle of hydrofoil. The disk rotates about the Z-axis of the hydrofoil shown in figure 2.9. The disk is machined from aluminum, while the clamp is machined from mild steel. A horizontal threaded rod on the opposite side of the clamp is used to apply clamping pressure around the circumference of the disk. Four additional flanged bolts are threaded into the tapped holes visible in the clamp, distributed around the disk's circumference, which apply a vertical clamping force to keep the constrain the vertical orientation of the hydrofoil.

2.2 Facilities

Experiments were conducted over the course of three years in two testing facilities: an atmospheric towing tank (TT) and a free-surface cavitation tunnel (FSCT). The details of each facility are discussed further below.

2.2.1 University of Michigan Towing Tank

Experiments were carried out in the towing tank at the University of Michigan Marine Hydrodynamics Laboratory (MHL), which has dimensions of 110 m (360 ft) long $\times$ 6.7 m (22 ft) wide $\times$ 3.05 m (10 ft) deep. The tank was originally constructed in 1905, and is among the largest academic towing tanks in the world. It is equipped with a gantry-type carriage, capable of speeds up to 6.1 m/s (20 ft/s). Speed is measured by an optical encoder and regulated by an on-board controller with constant acceleration and deceleration stages. The magnitudes of the acceleration and deceleration may be independently controlled, with software-limited maxima of 0.53 m/s^2. The ambient pressure is atmospheric and water temperatures varied between 15C and 20C.

A steel fixture-frame was mounted between two longitudinal structural members of

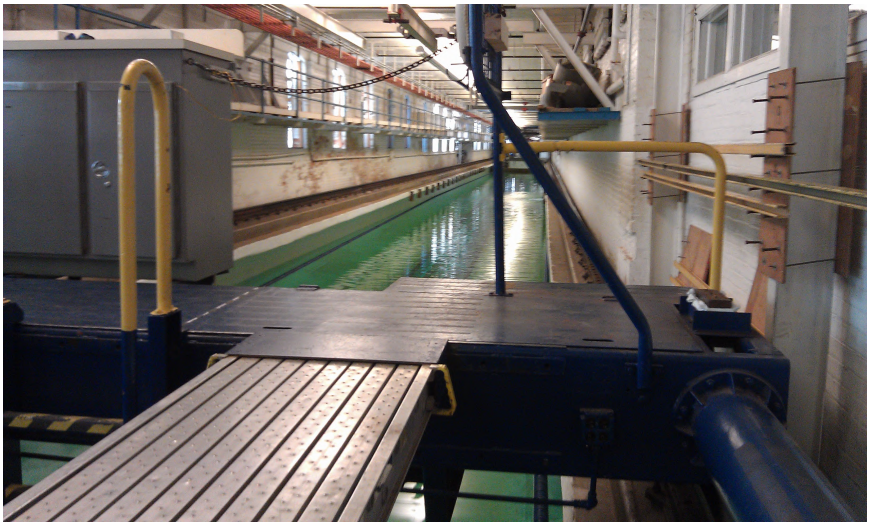

Figure 2.12: A view of the towing tank at the University of Michigan Marine Hydrodynamics Laboratory, looking upstream.

the towing tank carriage (see figure 2.13). Threaded feet were used to bring the frame to within $\pm 0.1^\circ$ of level, as measured in the X–Z and Y–Z planes. The steel box-frame carrying the foil model was mounted between two longitudinal steel members of the towing carriage, which comprise the lower catwalks. The frame was clamped to the carriage using large C-clamps and leveled to within $\pm 0.1^\circ$, measured along the longitudinal and transverse axes of the carriage.

During a run, the carriage accelerated to the specified speed ($U = U$) and decelerated again along a programmed speed profile. Trials were conducted by varying U for each configuration of α, AR_h, then varying α within each fixed value of AR_h, and varying AR_h once all values of α and Fn_h had been tested. For each trial, data collection was started while the carriage was at rest. For steady-state data collection, ramp-up and ramp-down times were minimized to increase the amount of data collected at the target condition of $U = U$. To study unsteady or quasi-steady ventilation (formation, elimination, and other transient processes), the ramp-up and/or ramp-down times were typically made longer to minimize inertial effects. Sufficient time (five to fifteen minutes) was permitted between runs to allow waves and currents in the tank to dissipate.

Additionally, some dry-land calibration and vibration-testing were performed with a specially-built steel frame, which serves as a mock-up of the carriage catwalks. The steel frame, which is shown in figure 2.14, was stiffened to make it a suitable for vibration and static load testing of the hydrofoil with all instrumentation installed.

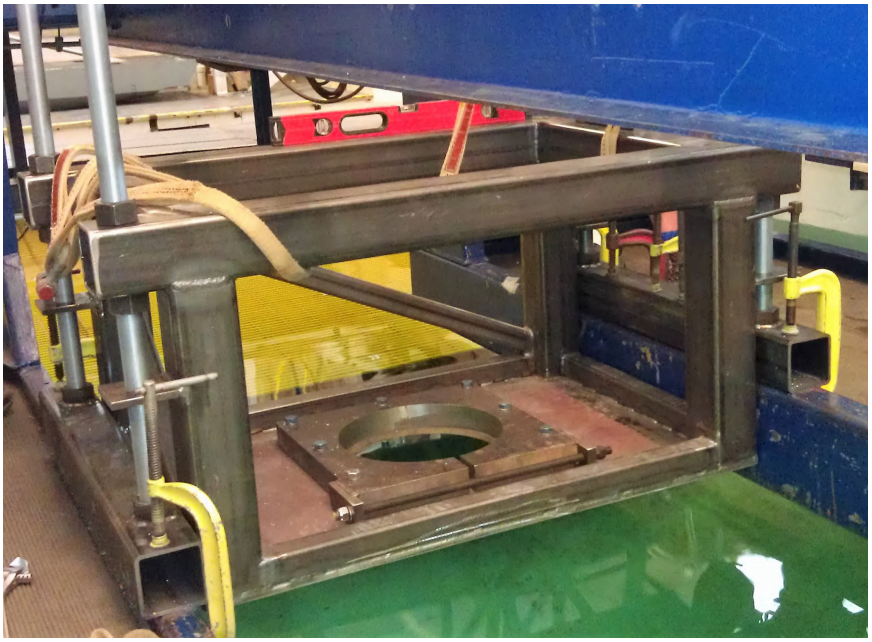

Figure 2.13: Steel frame used to support the hydrofoil between the carriage catwalks.

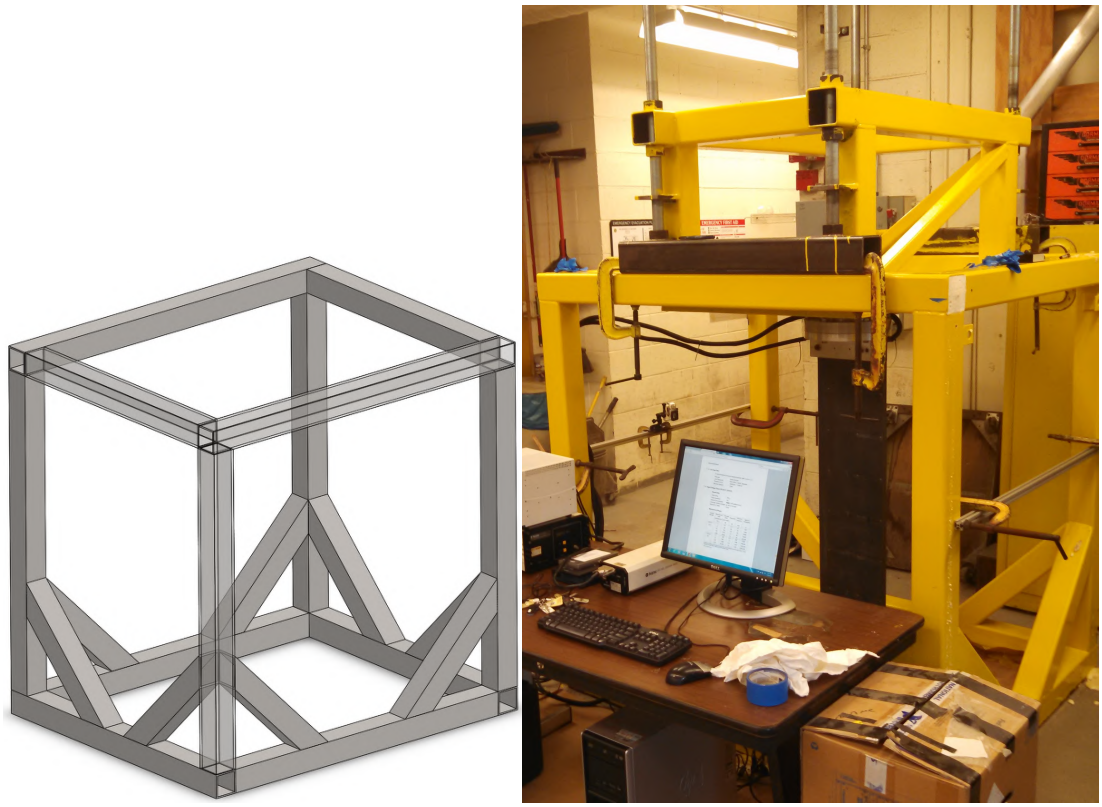

(a) (b)

Figure 2.14: (a) drawing and (b) photo of the steel frame used for calibration and dry-land testing.

2.2.2 INSEAN Cavitation Tunnel

The second facility used during the course of this work was the recirculating water tunnel at the National Research Council - Italian National Institute for Studies and Experiments in Naval Architecture (CNR-INSEAN) campus in Rome, Italy. With a test section measuring 10 m $\times$ 3.6 m$\times$ 2.25 m $L \times W \times D$, the channel is an uncommonly large one that permitted the installation of the hydrofoil model with very few modifications.

The tunnel is driven by dual 4-bladed axial impellers with delivered power of up to 435 kW (584 hp) apiece. A maximum tunnel velocity of 5 m/s also compares well to the speeds at which testing was performed at the MHL towing tank. Figure 2.15 shows the elevation view of the facility, which is housed in a four-story building.

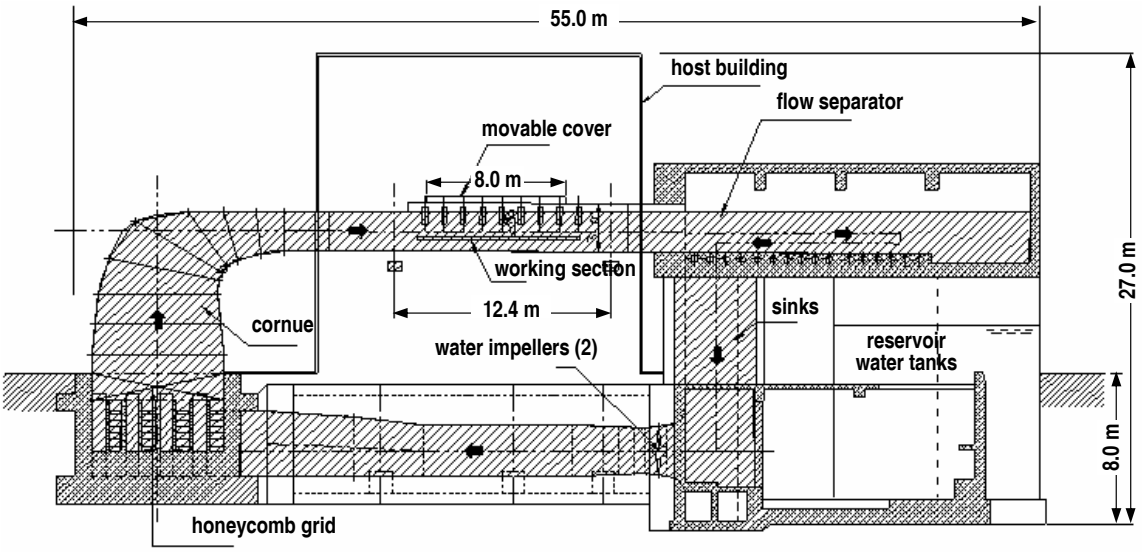

Figure 2.15: Elevation view of the depressurized free-surface recirculating water channel at CNR-INSEAN. Figure reproduced from *ITTC* (2002).

Figures 2.16 show the tunnel section of the INSEAN channel from both ends of the test section. Figure 2.16a conveys the size of the facility, The hydrofoil was installed near the upstream extent of the tunnel, along the centerplane of the section. A 1-cm thick steel plate was braced and clamped to transversely-oriented steel beams, as shown in figure 2.16b, to which the rest of the setup was attached. Apart from the flat steel plate and its grounding to the facility, the experimental setup was nearly identical to that used in the towing tank.

During operation, windows installed into both walls and the floor of the tunnel provided a range of viewing angles from which to observe the hydrofoil. Additionally,

(a) View from downstream end of the INSEAN tunnel section. The hydrofoil is visible near the center of the frame. The channel lid is the large beige structure visible on the left-hand side of the frame.

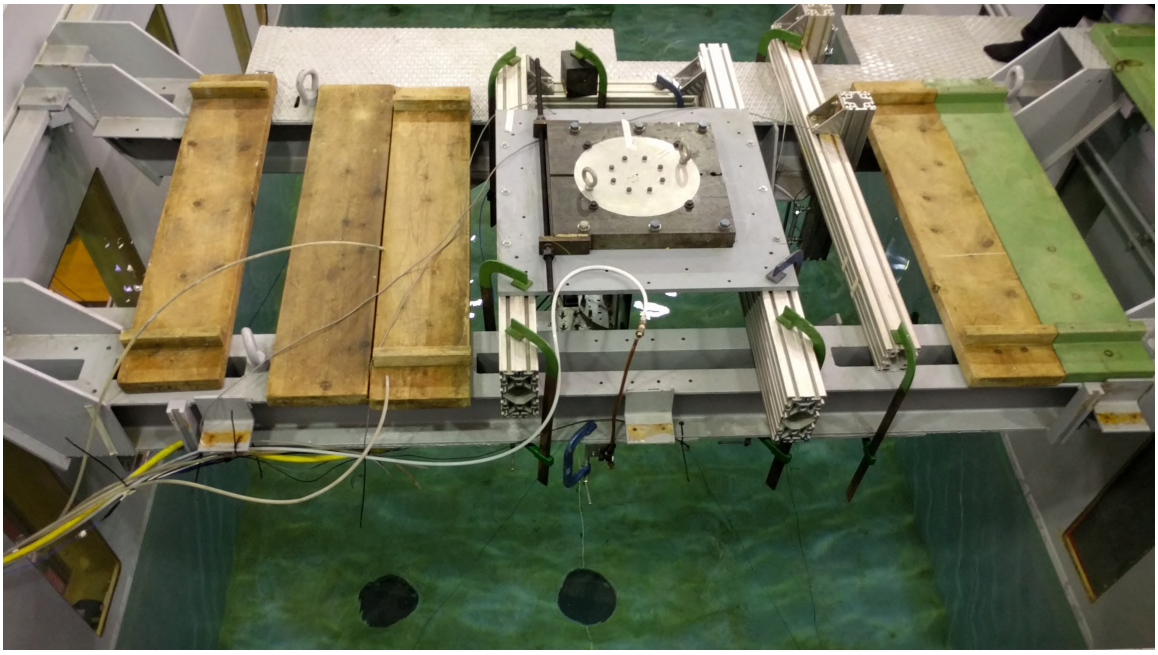

(b) View from the upstream end of the INSEAN tunnel section, looking at the hydrofoil mounting arrangement. Two heavy transverse beams span the tunnel, to which the rest of the mounting arrangementwas affixed.

Figure 2.16: Views of the test section of the CNR cavitation tunnel, taken from the shop floor above the model.

Figure 2.17: Photo of control room and observation windows at CNR-INSEAN re-circulating water channel. All control of tunnel speed and pressure, data acquisition, signal generation, and videography were performed inside of the control room.

the windows provided optical and lighting access for high-speed videography, detailed in a later section. All tunnel controls, data acquisition, and observations were performed from the control room, which runs the length of the test section, as shown in figure 2.17.

Most importantly, however, is the ability of the tunnel to operate with a stable free surface and under vacuum conditions. The ambient pressure at the free surface can be reduced to a value of approximately 40-50 mbar (0.04 - 0.05 ATM), which provided an opportunity to explore the behavior of surface-piercing hydrofoils with vaporous cavitation and natural ventilation occurring separately or simultaneously on the foils. A large steel cover (visible on the left hand side of figure 2.16a) was lifted by an overhead hoist onto the tunnel section to provide an airtight seal during depressurized testing. During Evacuation of air required between one and four hours (depending upon the target pressure), though an additional 12-24 hours of de-gassing was found to be desirable to improve the water quality.

During testing, all sensors were zeroed at the start of the day and reference sensor levels were recorded. The angle of attack was fixed, while the flow speed was adjusted from inside the control room. When the flow was on-condition, data were collected for the desired duration, and the flow speed was changed the next test condition. Unlike testing in the towing tank, testing in the cavitation tunnel did not permit the flow to be stopped between runs. Thus, sensors were not re-zeroed before collection of each dataset, as they were in the towing tank and the hydrofoil remained under

a nearly-constant load for hours at a time. Consequently, some sensor drift was observed, though bias recordings at the end of each period of testing indicated that drift was not too severe. Such long periods of high loads acting on the hydrofoil are demonstrative of why the TE reinforcement strip was required. Without it, stresses at the root of the hydrofoil would have been too near the yield strength to tolerate long periods of loading.

It was observed during testing that a component of cross-flow existed in the tunnel equivalent to a bias of $+2^\circ$ in the yaw angle of the hydrofoil. Thus, data collected in the cavitation tunnel were shifted during post processing to account for the bias.

2.3 Test Matrices

The following test matrices indicate the conditions of testing for each hydrofoil and facility. Additionally, a complete log of all experimental trials may be found in appendix B. A tabulation of all steady-state results may be found in appendix C.

Table 2.3: Test matrix for towing tank tests.

Foil Models	Al Model 0, PVC Model 1, PVC Model 2		
Tip Immersion	h	$0.14, 0.28, 0.41$ m	(5.5, 11, 16.5 in)
Immersed Aspect Ratio	$AR_h = \frac{h}{c}$	$0.5, 1.0, 1.5$	
Steady Velocities	U	0.6-6 m/s	(1.8 – 20 ft/s)
Depth Froude #	$Fn_h = \frac{U}{\sqrt{gh}}$	0.5 – 5	
Chord Reynolds #	$Re_c = \frac{Uc}{\nu}$	1.5×10^5 - 1.7×10^6	
Yaw Angle	α	$-5°$ – $30°$	
Weber Number	$We = \frac{\rho U^2 c}{\gamma}$	1.2×10^3 - 1.42×10^5	
Vaporous Cavitation Number	$\sigma_v = \frac{P_{atm} - P_v}{\rho U^2/2}$	5.4 – >> 10	
Shaker Motor Excitation	Aluminum: No; PVC Model 1: No; PVC Model 2: Some		

Table 2.4: Test matrix for tests at CNR-INSEAN cavitation channel.

Foil Models	Al Model 0, PVC Model 2		
Tip Immersion	h	0.28 m	(11 in)
Immersed Aspect Ratio	$AR_h = \frac{h}{c}$	1.0	
Steady Velocities	U	0.5-4.2 m/s	(1.64 – 14 ft/s)
Depth Froude #	$Fn_h = \frac{U}{\sqrt{gh}}$	0.3 – 2.5	
Chord Reynolds #	$Re_c = \frac{Uc}{\nu}$	1.8×10^5 - 1.2×10^6	
Yaw Angle	α	$-5°$ – $15°$	
Weber Number	$We = \frac{\rho U^2 c}{\gamma}$	830 - 6.7×10^4	
Vaporous Cavitation Number	$\sigma_v = \frac{P_0 - P_v}{\rho U^2/2}$	0.24 – >> 10	
Shaker Motor Excitation	Aluminum: Some; PVC Model 2: Yes		

2.4 Instrumentation

The instrumentation suite used in the hydrofoil testing was comprised of both purchased and custom-built sensors. Moreover, the sensor suite evolved over the course of multiple testing campaigns. The following sections break down and describe the instrumentation according to the measured quantities. An aggregated summary of measurements, derived quantities, and their estimated uncertainties may be found in table 2.7 at the conclusion of this chapter. The most significant changes in instrumentation occurred when switching between the rigid hydrofoil and the flexible hydrofoils. Figure 2.18 depicts the instruments and respective locations on the rigid hydrofoil (model 0). Figure 2.19 depicts the instrumentation used during testing of the flexible hydrofoils (models 1 and 2).

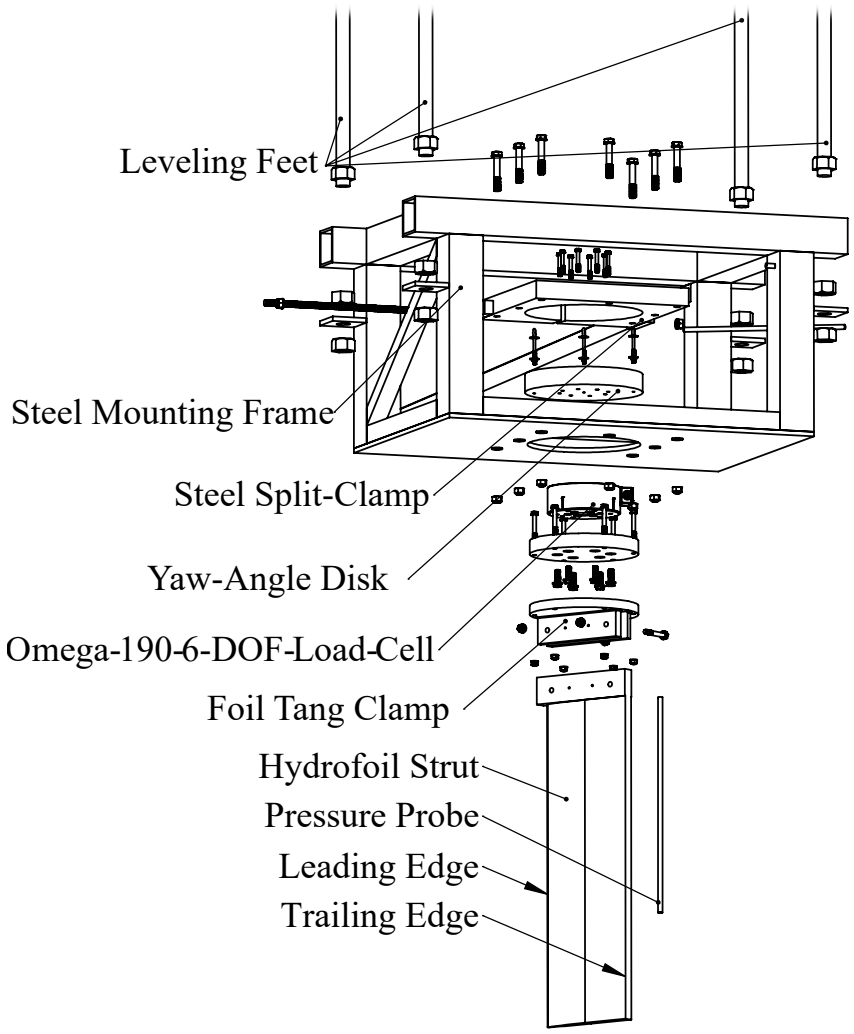

Figure 2.18: Exploded view of the components comprising the experimental rig and instrumentation used for the rigid hydrofoil experiments. Note that the drawing includes the steel frame used to mount the experiments on the towing tank, which was replaced with an alternate arrangement for testing at the INSEAN tunnel. Figure reproduced from *Harwood et al.* (2014).

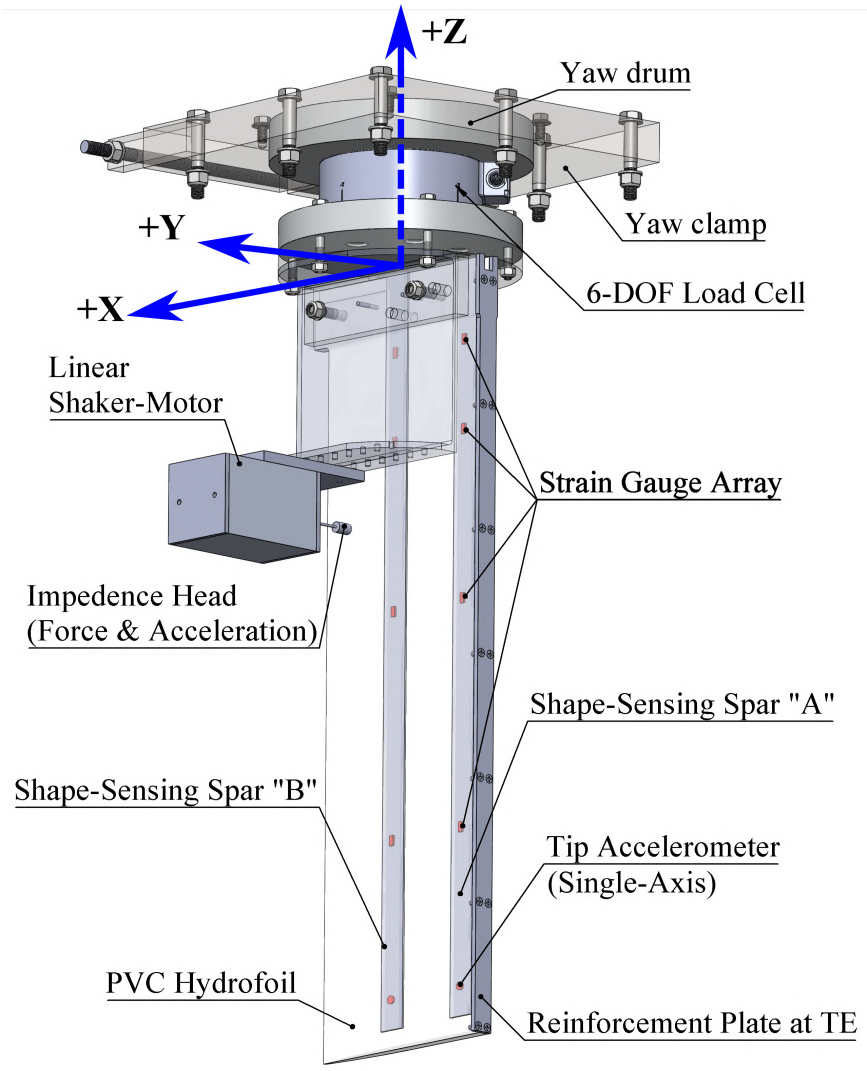

Figure 2.19: Labeled diagram of instrumentation on the flexible hydrofoil model. Specifically, model 2 is shown. Note that if the aluminum strip shown along the TE is omitted, then the figure corresponds to model 1. The near side of the hydrofoil and parts of the appended structure are made transparent, so that interior components (the yaw disk and the shape-sensing spars) are visible. Figure reproduced from *Harwood et al.* (2016b).

2.4.1 Force and Moment Measurements

Table 2.5: Characteristics of Omega-190 6-DOF load cell.

General Characteristics	
Manufacturer	ATI Industrial Automation
Model	Omega-190 US-800-6000
Ingress Protection	IP68 (10m immersion)
Overload safety factor	4.8-19.9 × sensing range
Load sensing ranges and resolutions	
F_x, F_y	±3550 N; $\Delta = 0.7$ N; ±800 lbf; $\Delta = 5/32$ lbf
F_z	±8900 N; $\Delta = 1.4$ N; ±2000 lbf; $\Delta = 5/16$ lbf
M_x, M_y	±8150 N; $\Delta = 0.4$ N-m; ±6000 in-lbf; $\Delta = 5/16$ in-lbf
M_z	±8150 N; $\Delta = 0.8$ N-m; ±6000 in-lbf; $\Delta = 5/8$ in-lbf
Maximum Quoted Uncertainty	
F_X	±3.25% Full Scale (FS) (±115N; ±26lbf)
F_Y	±3.25%FS (±115N; ±26lbf)
F_Z	±2.75%FS (±245N; ±55lbf)
M_X	±2.3%FS (±11.9N-m; ±8.75lbf-ft)
M_Y	±2.3%FS (±13.6N-m; ±10lbf-ft)
M_Z	±2.3%FS (±15.25N-m; ±11.25lbf-ft)

An ATI Omega-190 US 800-6000 six-Degree of Freedom (DOF) force-torque transducer was used to measure forces and moments at the root of the hydrofoil. The rated measurement ranges, step sizes, and maximum uncertainties are given in table 2.5 The load cell is IP-68 rated for immersion in fresh-water. It should be noted that the uncertainties are quoted maximum values from the manufacturer, and do not represent the individual transducer used. The NIST calibration sheet provided with the load-cell indicates that the uncertainty is closer to ±1% of the measured load for each axis, when *isolated*. Since the load cell is subjected to multi-axis loading in all testing, the uncertainty is estimated for all force and moment axes to be,

$$\epsilon_{F,M} = \sqrt{\sum_{i=1}^{6} \epsilon_i^2} = 2.6\%, \tag{2.1}$$

where ϵ_i is the Root Mean Square (RMS) of the proportional error for the i^{th} axis reported on the calibration sheet. This lower estimate, in addition to being much-more useful, is also far more consistent with observations of the load cell's performance over three years of frequent use.

2.4.2 Flow Speed Measurements

An optical encoder wheel was used to record the instantaneous carriage-speed in the MHL towing tank, the digital pulse output from which is transformed into a DC voltage recorded by the Data Acquisition (DAQ) system. During steady-state operation, the measured speed has an average bias error of -0.25% and a repeatability error not exceeding $\pm 0.25\%$, based on measured transit-times between precision-located markers. During acceleration and deceleration, the uncertainty is less well-quantified. During the three-year testing campaign, changes were made both to the optical encoder itself and to the method by which the digital pulse train was converted into an analog voltage. Early testing (pre-2014) made use of an analog pulse-counter, which suffered from some inherent phase lag. The lag became more pronounced at very low speeds (when the pulse period was longest), but became negligible for speeds of interest.

Later testing in the MHL towing tank used a higher-resolution optical encoder connected to a dedicated PC. The pulse period was estimated and the inferred carriage speed updated with each pulse period. Offset "A-B" pulses were used both to improve the speed resolution and to determine the sign of the instantaneous speed (such that forward and reverse motion of the carriage could be differentiated). The PC translated the estimated carriage speed into a DC voltage output, which was measured with the DAQ system designed for the surface-piercing foil tests. The newer method yielded a much-improved time-resolution of the instantaneous carriage velocity, with negligible lag at all speeds of interest, but small artifacts in the optical encoder signal caused the dedicated PC to infer rather noisy velocity estimates, which had to be filtered to yield reasonably clean time-traces of the carriage velocity. The noisy signal is not seen by the on-board carriage controller, which uses the optical encoder output directly, so the artifacts are confined to the measurement, and were assumed not to affect the performance of the speed controller.

Finally, testing at the INSEAN cavitation tunnel did not utilize any direct measurement of flow speed. Rather, detailed Particle Image Velocimetry (PIV) surveys of the mean flow-field were performed to yield an *a priori* mapping between the pump revolution rates and the channel velocity profiles. Thus, the tunnel was run in a purely feed-forward configuration, with a specified pump speed prescribed to achieve a desired velocity at the point of the surface-piercing foil. Following the hydrofoil testing, another detailed PIV survey of the proximal velocity field was performed in the absence of the hydrofoil. The results of the PIV survey are still undergoing final processing by collaborators at CNR-INSEAN, and are not presented in this thesis.

For expediency, a value of 3% is used as an estimated uncertainty for flow-speed measurements for both towing-tank and cavitation tunnel testing.

2.4.3 Pressure Measurements

Trailing edge pressures were measured during testing on the rigid hydrofoil only. A slender copper tube with a 1/8-inch inner diameter (ID) was fastened to the bluff TE of the strut by aluminum brackets, as shown in figure 2.18. The height of which could be adjusted by sliding the tube through the aluminum brackets and tightening a set-screw against the tube's outer surface. The bottom of the tube was left open, and acted as a probe for point-measurements of gage pressure. The top of the tube was connected to a dry-dry differential pressure sensor, with the opposite side left open to the atmosphere, so that the setup was able to measure the gage pressure at the location of the tube's open end. To avoid errors associated with trapped liquid and surface-tension, a three-way solenoid valve was attached between the copper tube and the pressure-transducer. The third leg of the valve was connected to a needle valve on an air tank, adjusted to provide a slow air bleed that kept the copper tube primed with air. At the time that a pressure measurement was desired, the data acquisition PC provided a voltage to the three-way solenoid that halted the air bleed and connected the pressure transducer to the copper tube to measure the gage pressure.

A PX26-001DV low-frequency transducer, manufactured by Omega engineering, was used for pressure measurements. The sensor has a $\pm$ 1 psi range ($\pm$6.9 kPa) with a maximum quoted nonlinearity error of 1% and maximum random error of 0.2%.

During depressurized testing at INSEAN, several methods of pressure measurement were available. An electronic pressure transducer was used to estimate the pressures with an approximate uncertainty of $\pm$5 mbar. When the pressure reached a steady value, a mercury manometer was used to verify the tunnel pressure with an estimated uncertainty of $\pm$1 mbar. The tunnel pressure tended to vary with time, because the operators had to balance the air leakage into the tunnel against the flow-rate of the vacuum pumps in order to maintain a steady tunnel pressure – a nearly impossible task for more than a few minutes at a time. However, none of the phenomena discussed in this thesis are very sensitive to such small pressure variations, so excursions of a few mbar from the nominal tunnel pressures were were not cause for great concern.

2.4.4 Acceleration Measurements

Accelerometry constituted a significant part of the instrumentation during this experimental campaign, and several accelerometry configurations were used. Most accelerometry was performed using ceramic shear-type accelerometers (models 357C10 and 357B06), manufactured by PCB Piezotronics. The accelerometers generate a electrical charges, which were converted into AC voltage signals using Bruel and Kjaer charge amplifiers (Model 2635).

The arrangement and mounting of the accelerometers varied between tests. The various configurations and characteristics of the accelerometry measurements are summarized in table 2.6.

Table 2.6: Properties of the piezoelectric accelerometers used in experiments on the rigid and flexible hydrofoils.

Manufacturer	PCB Piezotronics	PCB Piezotronics
Model	PCB 357C10	PCB 357B06
Measurement Type	Single-Axis	Single-Axis
Sensing Element	Piezoelectric - Ceramic Shear Type	Piezoelectric - Ceramic Shear Type
Output Type	Charge	Charge
Sensitivity	0.17 pC/(m/s^2)	0.51 pC/(m/s^2)
Measurement Range	$\pm$ 4905 m/s^2	$\pm$ 4905 m/s^2
Nonlinearity error	<1%	<1%
Off-axis sensitivity	<5%	<5%
Half-power frequency limit	<25000 Hz	N/A
MHL Testing - Model 0	Foil Tip at TE, Foil Root at TE, Box-Frame	-
MHL Testing - Model 1	-	-
MHL Testing - Model 2	-	Shape Sensing Spars
INSEAN Testing - Model 0	Foil Tip at TE	-
INSEAN Testing - Model 2		Shape Sensing Spars

2.4.5 Vibrometry Measurements

Structural velocities used to characterize the vibrations of the aluminum and PVC (model 1) hydrofoils during hammer testing. Surface velocities were measured using a fixed point PolyTec OFV-353 Laser Doppler Velocimetry (LDV) head, equipped with a low power HeNe laser, lens, and interferometer. Information regarding the uncertainties was unavailable from the manufacturer. Scaled values from the interferometer were never used; rather, only frequency content was analyzed. As a result, the measurement accuracy of the LDV isn't particularly impactful.

2.4.6 Surface-Flow Visualization by Paint-Streaks

For towing-tank testing of the rigid hydrofoil only, a limited number of surface-flow visualizations were conducted. The method used a grid of paint dots, following the method of *Green* (1988); *Green and Acosta* (1991). Eight parts yellow artist's oil paint and one part white oil primer were mixed with five to twelve parts refined linseed oil to achieve a range of shear-thinning behaviors, suitable for trials conducted at different speeds. 10 μL droplets were applied as a grid on the suction surface of the hydrofoil with a repeating pipette, with a grid spacing of approximately 1 to 2.5 cm (0.5 to 1 inch), totaling between 50 and 150 dots. Figure 2.20 depicts the suction surface of the aluminum strut before and after a run performed with a grid of paint dots applied. Between each trial, the foil was wiped clean and the dots were reapplied.

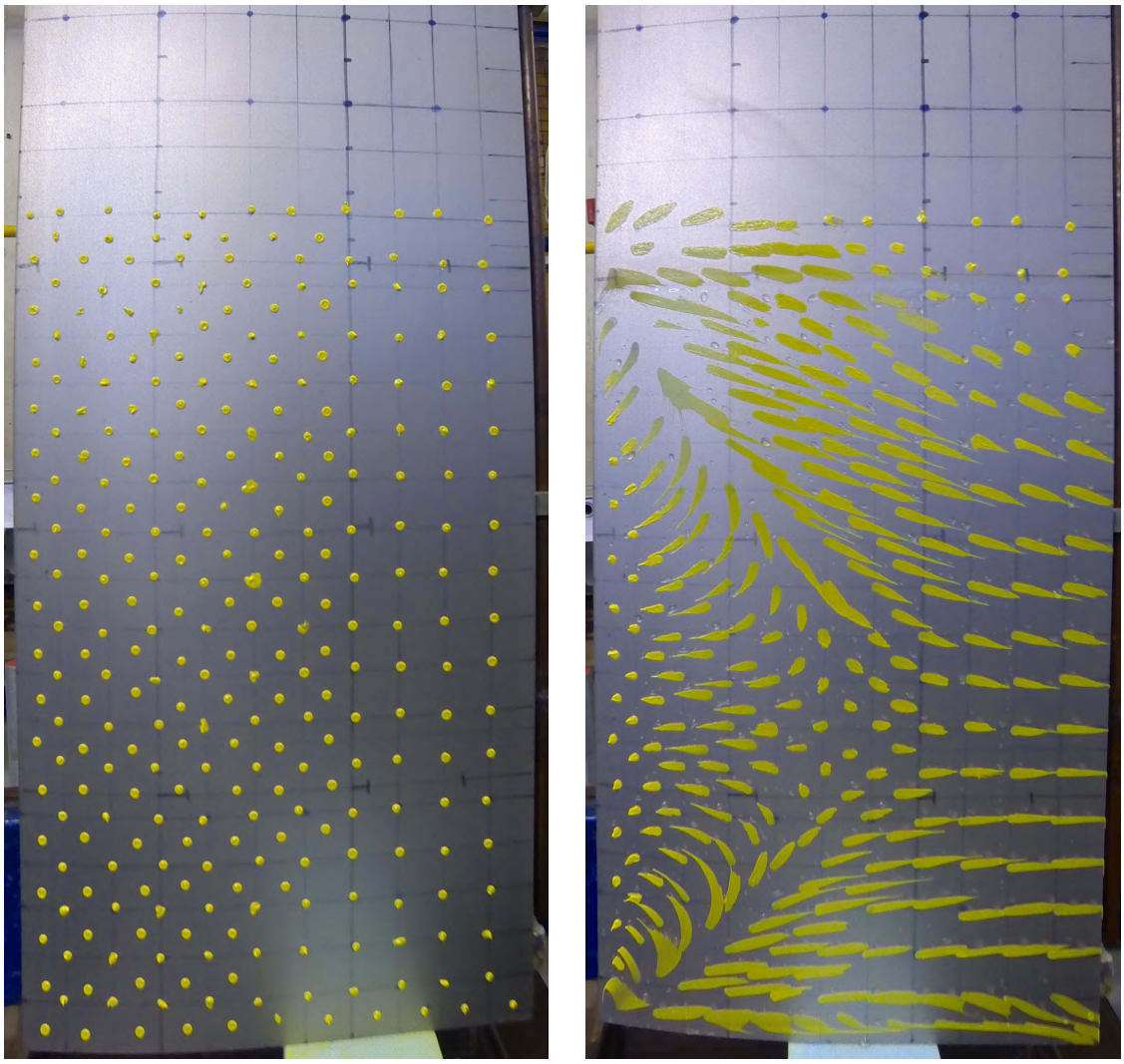

(a) Grid of paint dots before run.

(b) Sheared paint dots following run.

Figure 2.20: Before-and-after photos of paint-dot grid applied to aluminum hydrofoil, showing streak pattern. The paint mixture for the case shown was 8 parts yellow artist's oil paint - 1 part white oil primer - 5 parts refined linseed oil. The run was conducted at $\alpha = 15°$; $U = 4$ m/s. The leading edge is located on the left-hand side of both photos. The forward-swept streaks of paint indicate a large region of reversed flow, characteristic of "thin-airfoil stall" (*Gault*, 1957).

2.4.7 Videography

2.4.7.1 Camera Systems and Synchronization

Low-speed videography during towing-tank testing was performed using GoPro® cameras (HERO3 Black®, HERO4 Silver®, and HERO4 Black® models) in waterproof housings. Video was recorded with a resolution of 1920×1080 pixels at a rate of 60 Frames Per Second (FPS). Lighting was provided by commercial halogen work-lamps mounted below the carriage and aimed at the hydrofoil. Between two and four video angles were acquired at a time, including the submerged suction surface, the suction and pressure surfaces above the still waterline, the TE, and the leading edge. The locations of the underwater and trailing-edge cameras are indicated in figure 2.21. Views from each camera are depicted in figure 2.22. Video was recorded continuously during testing. An LED was placed in the field of view of each camera, which illuminated in synchronization with the beginning of data-collection. During post-processing, a script was used to trim the respective video clips, with the illumination of the LED marking the first frame, and to match them to the correct run numbers in a master log file. All video manipulations were completed using a combination of MATLAB® and the open-source library FFmpeg®.

A collection of videos were also recorded at the MHL, using a Phantom V9.0 high-speed camera in a waterproof housing. More details on the underwater recording setup may be found in *Lee* (2015). The camera was installed on the tank's bottom, off-center with its view directed upward and at an angle to capture the hydrofoil's tip and suction surface. Lighting was provided by a submerged bank of LED lights located below the carriage track rails. The lights and camera remained stationary, illuminating and recording images of the hydrofoil as the carriage passed by their location. A set of triggers were installed at pre-determined locations on the carriage track to initiate the video capture and to turn the lights on and off. Videos were not synchronized to the rest of the DAQ, and frame rates were varied between 200 and 500 FPS.

In cavitation tunnel testing, low speed videography was performed with GoPro® cameras inside of the flow channel. High-speed videos were recorded using two Photron® brand high-speed cameras (FASTCAM® SA-Series) aimed through windows in the test section – one aimed horizontally at the submerged suction surface and one aimed vertically upward at the foil's free tip. The camera's locations relative to the hydrofoil are shown in figure 2.23. Figure 2.24 shows the view from each camera. Both cameras acquired monochrome video at a resolution of 1024×512 pixels, 12-bit

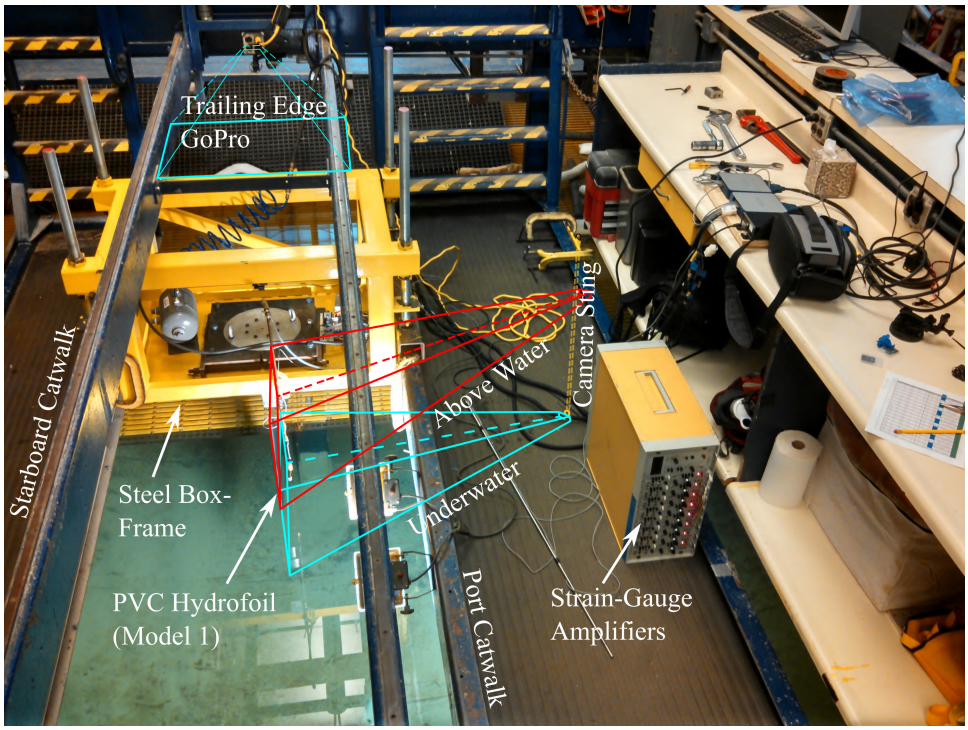

Figure 2.21: PVC Hydrofoil (model 1) installed on towing tank carriage, viewed from upstream. Camera positions for the underwater and TE cameras are indicated, as are visible pieces of the instrumentation. The underwater sting used to support the underwater GoPro® is drawn as a dashed yellow line.

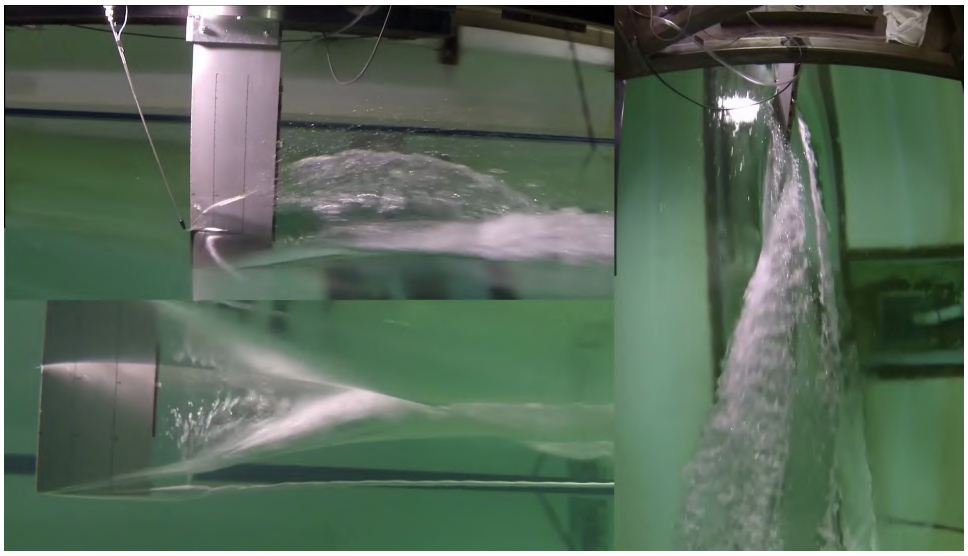

Figure 2.22: Views from GoPro® cameras installed during towing-tank tests. Clockwise from top right: Suction surface above waterline, trailing edge, and suction surface below waterline.

greyscale, and a rate of 500 FPS. The suction surfaces of model 0 and model 1 were marked with 2.54 cm (1 inch) grids. A reference sampling clock was routed from the host DAQ to a timing controller, with which tunable delay was affected on the timing signal. Both cameras were synchronized to this timing signal such that the DAQ's sample clock pulse occurred precisely in the middle of each 1 ms exposure. The cameras were, in this fashion, effectively phase-locked to the DAQ's sample clock, with a one-period delay at the beginning and ending of each acquisition. Camera recording was manually triggered, and a TTL pulse train was routed to the DAQ for each camera exposure, appearing in the logged voltages as a "boxcar" voltage pulse spanning the samples corresponding to video acquisition. Lighting was accomplished using tripod-mounted Arri® lights aimed through the viewing windows.

Figure 2.23: Illustration of camera perspectives in the cavitation tunnel at CNR INSEAN. Only the high-speed cameras are shown – one on the suction surface, and one below the tunnel.

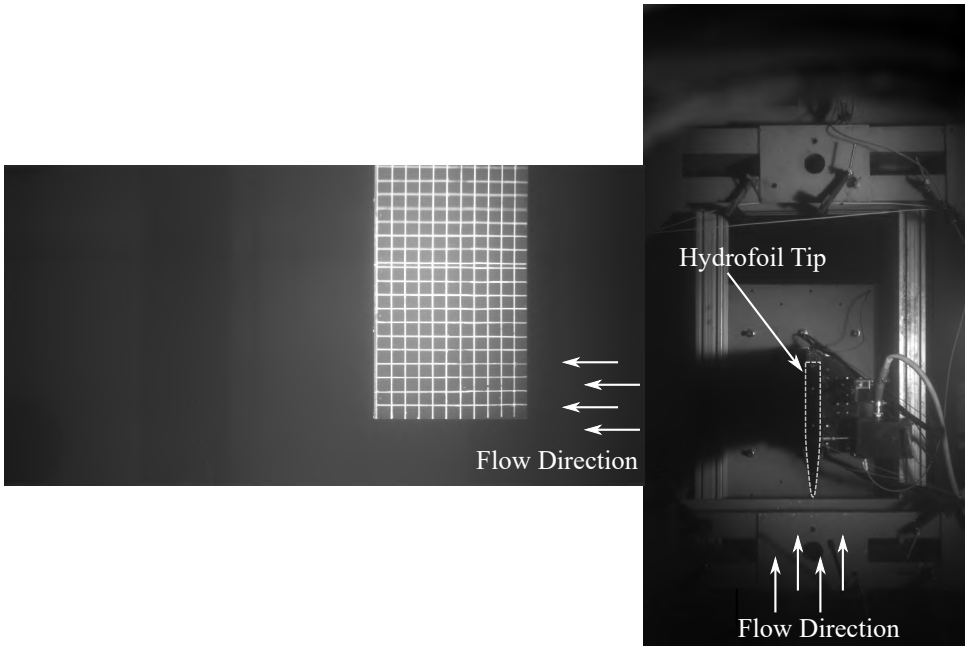

Figure 2.24: Views from high-speed cameras used in cavitation tunnel testing at INSEAN's recirculating water channel. Left: submerged suction surface. Right: View of hydrofoil free tip.

2.4.7.2 Optical Measurement of Foil Motions

For the experiments performed at INSEAN only, video recorded from below the flow channel was used to track the motion of the foil's tip. Dots were painted on to the free tip of the flexible hydrofoil (model 2), with white paint. A script was written to perform sequential image segmentation and contrast stretching to locate the boundaries of the dots. Finally, the locations of the dots were inferred from the brightness-weighted centroid of each separate regions identified as a marker. Figure 2.25a shows the view from the camera and an enlarged view of the image interrogation region, with the inferred dot locations overlaid as red "X" markers. The locations are mapped from pixel coordinates to real-world coordinates *via* a predetermined transformation matrix (mapped loci of marker locations are shown in real-world coordinates in figure 2.25b).

The script was run on individual frames of acquired video to create a time history of marker locations. These time-traces were linked using a MATLAB® implementation of the Hungarian method (*Munkres*, 1957) and were used to infer the time-resolved motion of the foil tip. For the linking of particle locations across time steps, a third-party MATLAB® function was used (*Tineves*, 2016). Figure 2.26 shows an example of the tracked motions of the hydrofoil at $\alpha = 5°$ and $U = 3.3$ m/s. This method of

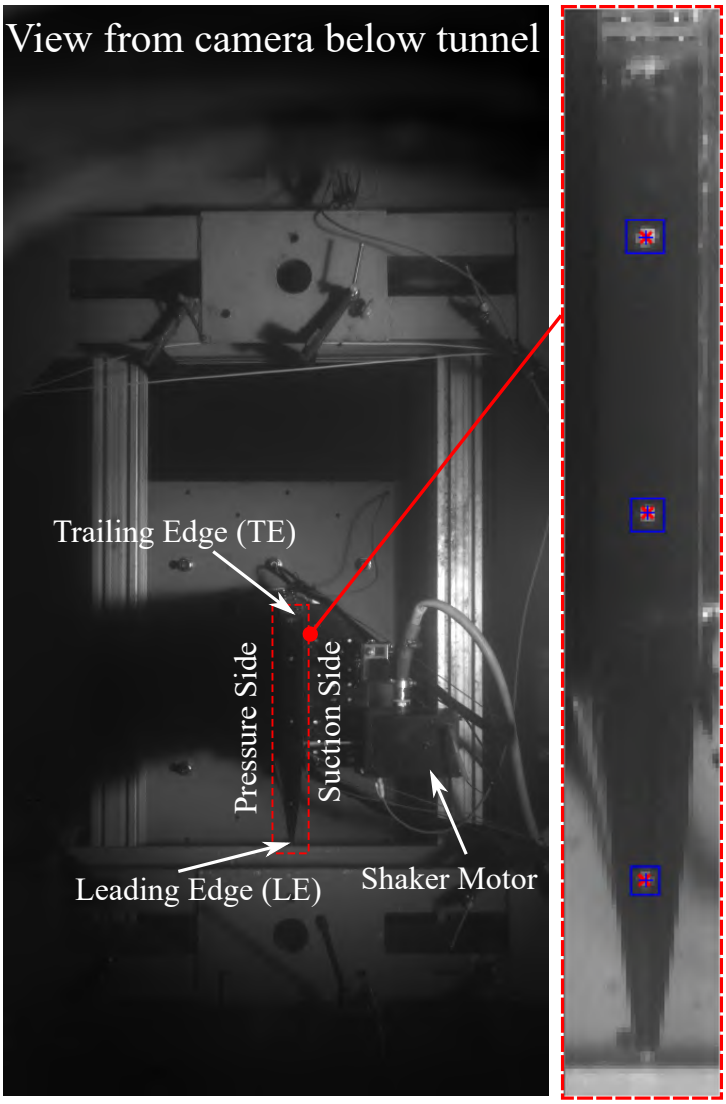

(a) View from the high-speed camera below the tunnel section. An enlarged view of the hydrofoil's tip is shown on the right. The boundaries of the white dots are indicated by blue boxes, the geometric centroids of white pixels are indicated by blue + symbols, and the brightness-weighted centroids of the white dots are indicated by red X markers.

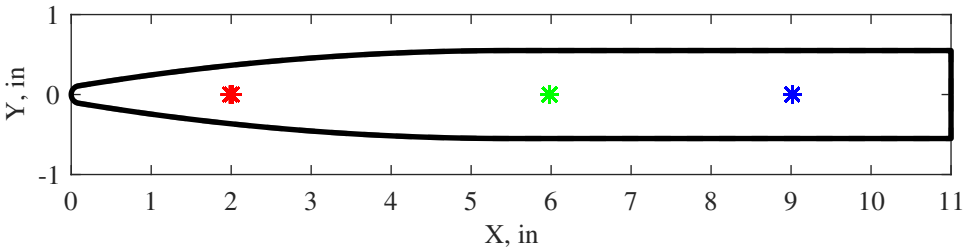

(b) Points mapped from the image shown in (a) to real-world coordinates. A locus of 1000 points (2 seconds of data) are shown for each dot

Figure 2.25: View of hydrofoil tip and identification of markers used for motion tracking.

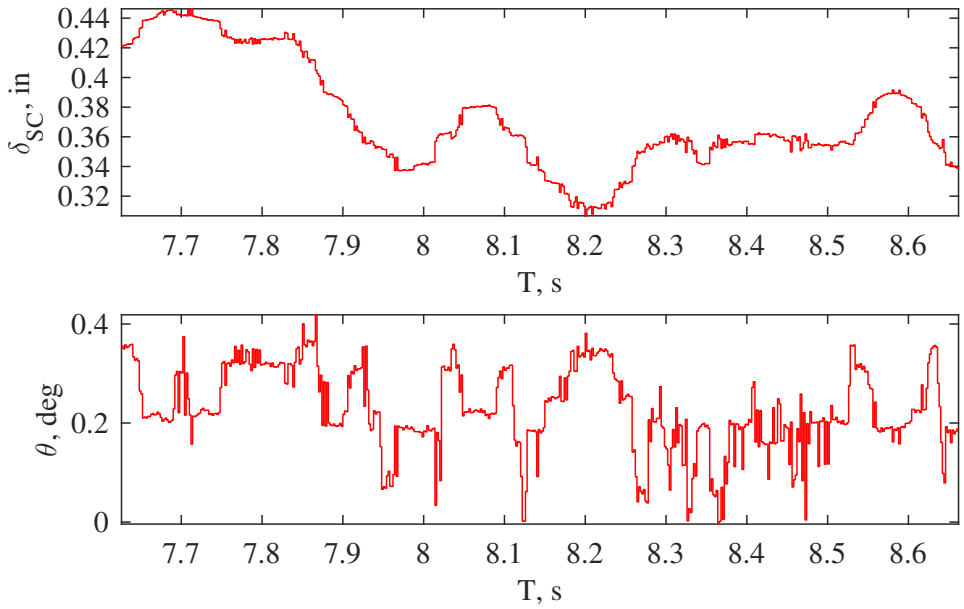

(a) Time history of bending and twisting deflections, tracked by high-speed camera.

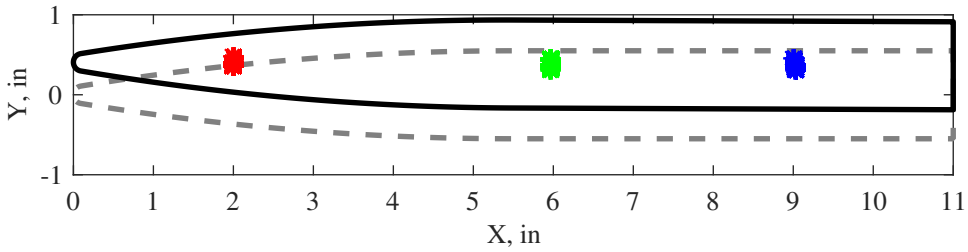

(b) Point loci of tracked markers and mean deflected position of foil tip in real-world coordinates. The undeformed position is indicated by a dashed grey outline.

Figure 2.26: Motions of hydrofoil tip tracked by camera for a run at $\alpha = 5°$, $U = 3.3$ m/s.

optical tracking is admittedly rudimentary. Far more advanced correlation-based algorithms are regularly applied in research and industry. The particle-tracking scheme, however, offers the advantage of flexibility and transparency, as it was coded from scratch and easily adapted to the application or integrated with other elements of the post-processor.

2.5 Displacement Measurements using Custom Shape Sensing Spars

Inferring motions of flexible structures typically requires accelerometry and/or optical methods. The former method encounters problems for non-harmonic motions, while the latter cannot operate in environments where fluid interfaces cause refraction (such as in the case of a ventilated cavity). In this section, an alternative method of measuring the deflections of flexible struts is developed and validated.

2.5.1 Design of Shape Sensing Spars

A non-optical means of tracking structural deflections was developed in the form of shape-sensing spars, pictured in Figure 2.27.

The shape-sensing methodology invokes the beam bending equation,

$$\epsilon_z \approx \frac{-t}{2}\frac{\partial^2 Y}{\partial Z}, \tag{2.2}$$

where ϵ_z is the surface bending strain on a beam of thickness t, Y is the coordinate in the direction of lateral beam deflection and Z is the coordinate along the initial (undeformed) length of the beam. The slim aluminum spar is instrumented with N strain gauges in a half-cosine spacing. The boundary condition, $\epsilon_z|_{Z=L} = 0$, permits

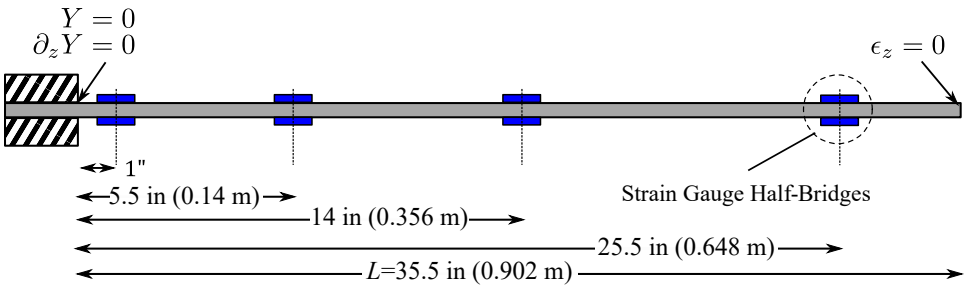

Figure 2.27: A dimensioned sketch of one instrumented spar. Figure reproduced from *Harwood et al.* (2016a).

an N^{th}-order polynomial may be fitted to the measured strains.

$$\hat{\epsilon_z}(Z) = \sum_{i=0}^{N} a_i Z^i. \tag{2.3}$$

Equation 2.3 may be substituted into equation 2.2 and twice-integrated to yield a polynomial approximation of the lateral deflection. The process is diagrammatically represented in figure 2.28.

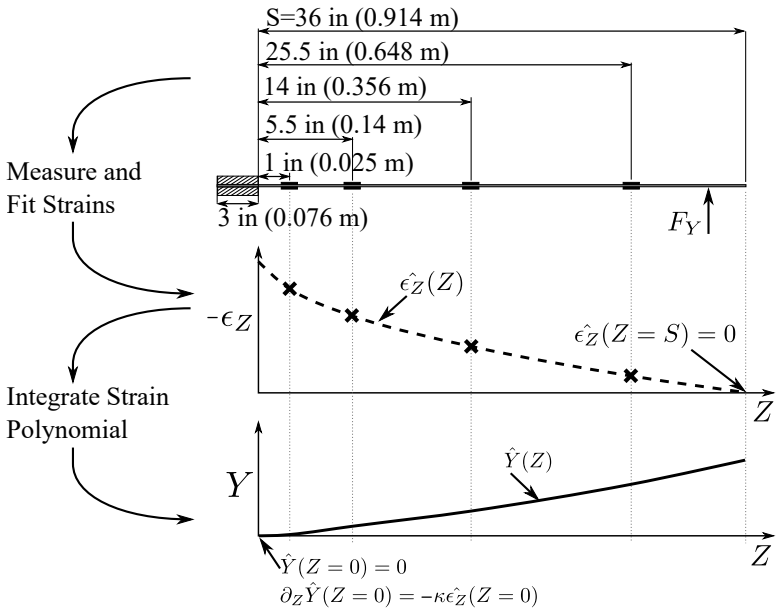

Figure 2.28: A schematic illustration of shape-sensing using an instrumented spar. Figure reproduced with modifications from *Harwood et al.* (2016b).

$$\hat{Y}(Z) = \sum_{0}^{N+2} A_i Z^i. \tag{2.4}$$

The integration yields two additional coefficients, A_0 and A_1, which must be determined from the beam's boundary conditions. For an ideal cantilever, $A_0 = A_1 = 0$. Thus:

$$A_i = \begin{cases} 0, & j = 0, 1 \\ \dfrac{a_i(j-2)!}{j!}, & j = 1, 2, \ldots, N+2 \end{cases} \tag{2.5}$$

Under the assumption that bending along the chord is negligible (chordwise rigidity), the deflections along the two spars – respectively $\hat{Y_A}(Z)$ and $\hat{Y_B}(Z)$ – may be used to reconstruct the deformed centerline plane of the strut. It is convenient to recast

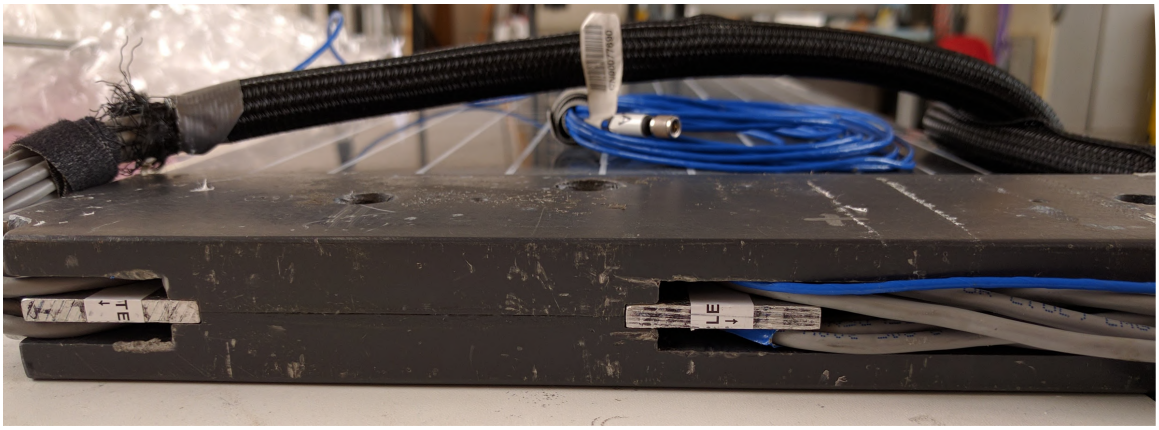

Figure 2.29: Photo of spars inserted into flexible hydrofoil until flush with the mounting tang.

the deformations into the decoupled angular and lateral deflection of each spanwise section along the elastic axis:

$$\hat{\theta}(Z) = \arcsin \quad \frac{\hat{Y_A}(Z) - \hat{Y_B}(Z)}{X_A - X_B} \tag{2.6a}$$

$$\hat{Y_{EA}}(Z) = \hat{Y_A}(Z) + (X_{EA} - X_A)\sin(\theta(Z)), \tag{2.6b}$$

where X_A and X_B respectively denote the chordwise positions of the spars inside of the strut and X_{EA} denotes the chordwise location of the elastic axis.

Referring back to figures 2.7 and 2.19, one can now see that the shape-sensing spars are located at two chordwise positions along the centerplane of the hydrofoil. Figure 2.29 depicts the root of the hydrofoil. The spars are inserted at the root and pushed into the machined channels until flush with the root. The edges of each channel are sized for a relatively tight interference fit with the spars, and the middle portion of the channel is widened to permit the passage of the strain gauges and cabling. The interference fit ensures that the hydrofoil's motions are transferred to the interior spar, and the spars may be removed through the root, which permits in-field repairs or replacements to be made.

Figure 2.30 shows an example of how bending and twisting deformations are inferred. A combined bending and twisting load was applied by hand to the strut, with a photo taken of the leading edge and the tip of the hydrofoil. The inferred deflections were mapped into image coordinates and overlaid onto the image to demonstrate that the deflections are, in fact, correctly inferred. The twisting deformation at the tip does not match perfectly with the photo, due to a number of factors. With the close

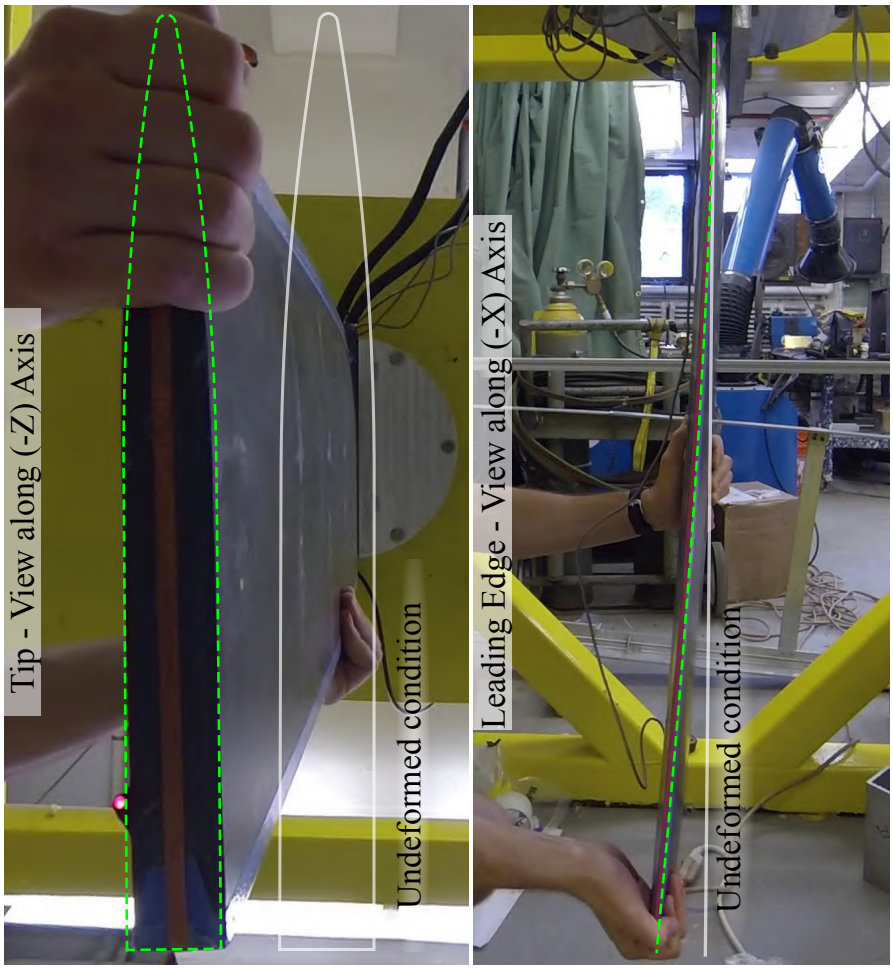

Figure 2.30: The (post-calibration) tip-deflection and the leading edge deflection inferred from the pair of shape-sensing spars are overlaid as green dashed lines onto photos of the strut subjected to a combined bending/twisting load. White solid lines indicate the initial undeformed geometry of the strut's tip and leading edge. Figure reproduced from *Harwood et al.* (2016a).

proximity of the camera to the foil tip, perspective and lens distortions make it challenging to map between real-world and image coordinates accurately, so some error is undoubtedly attributable to an imperfect mapping. More importantly, however, the spars require careful calibration to correct for linearizable sources of error. The case shown in figure 2.30 is a preliminary test, and only a preliminary calibration had been performed. The calibration procedure, and a more-rigorous characterization of the accuracy of inferred deflections, are described in the following sections.

2.5.2 Spar-Level Calibration and Validation

Independent calibrations were first performed on each individual spar to correct for small errors in the values of surface bending-strain caused by small differences in the strain gauge mounting (gauge orientation, adhesive thickness, *etc.*) or other linearizable sources of variation. A calibration rig (shown in figure 2.31) permitted each spar to be deformed in a controlled manner while being recorded by a camera. The root of the spar was clamped and point loads were applied to the beam to achieve various static deflections. This process is shown in figure 2.32. A calibrated camera was used to measure the lengthwise deflections with an estimated uncertainty of 1/32 in (0.79 mm), from which the surface strains were calculated *via* equation 2.2. This was conducted for a N_{trials} different conditions. A calibration matrix, $[\boldsymbol{A}]$, unique to each spar, was fitted to satisfy, in a least-squares sense, the equation,

$$\begin{bmatrix} \{\boldsymbol{\epsilon_{z,SG}}\}_1 \\ \{\boldsymbol{\epsilon_{z,SG}}\}_2 \\ \dots \\ \{\boldsymbol{\epsilon_{z,CAM}}\}_{N_{trials}} \end{bmatrix} [\boldsymbol{A}] = \begin{bmatrix} \{\boldsymbol{\epsilon_{z,CAM}}\}_1 \\ \{\boldsymbol{\epsilon_{z,CAM}}\}_2 \\ \dots \\ \{\boldsymbol{\epsilon_{z,CAM}}\}_{N_{trials}} \end{bmatrix}, \tag{2.7}$$

thus minimizing the strain energy contained in the error between the strain values inferred optically and those measured by the strain gauges. Using the calibrated vector of strain measurements, a corrected beam deflection was inferred. The difference between pre- and post-calibration inferences of the deflected shape of a beam are shown in figures 2.32a and 2.32b. Figure 2.32c shows a summary of the pre- and post-calibration error in tip deflections for all single-load calibration cases. The plotted symbols, and the linear trends fitted to them, make it clear that the calibration significantly reduced both the mean error and the variance of the error.

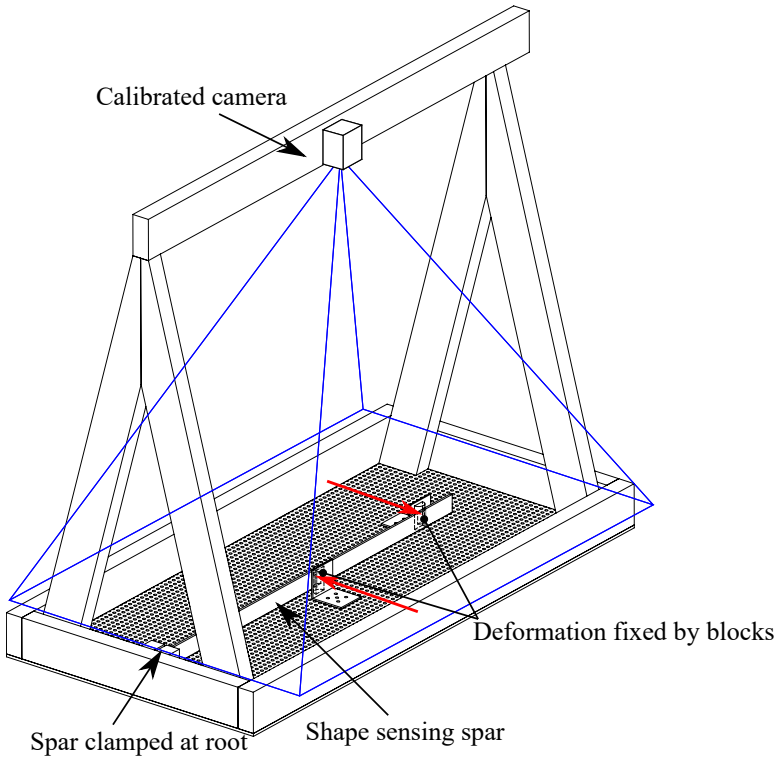

Figure 2.31: Photo of A-frame setup used for optical calibration of strain measurements on spar. A lens model was used to correct camera lens distortion for a rectilinear image. The resulting image was used to track the edge of the spar, subjected to a number of constrained static deformations. The deformations were imposed by blocking the spar with a number of movable blocks, fitted into the peg-board base.

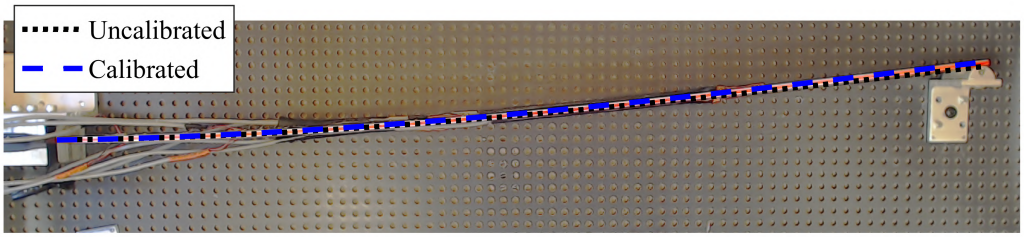

(a) View from the camera. The inferred deflections (pre- and post-calibration) are overlaid onto the photo.

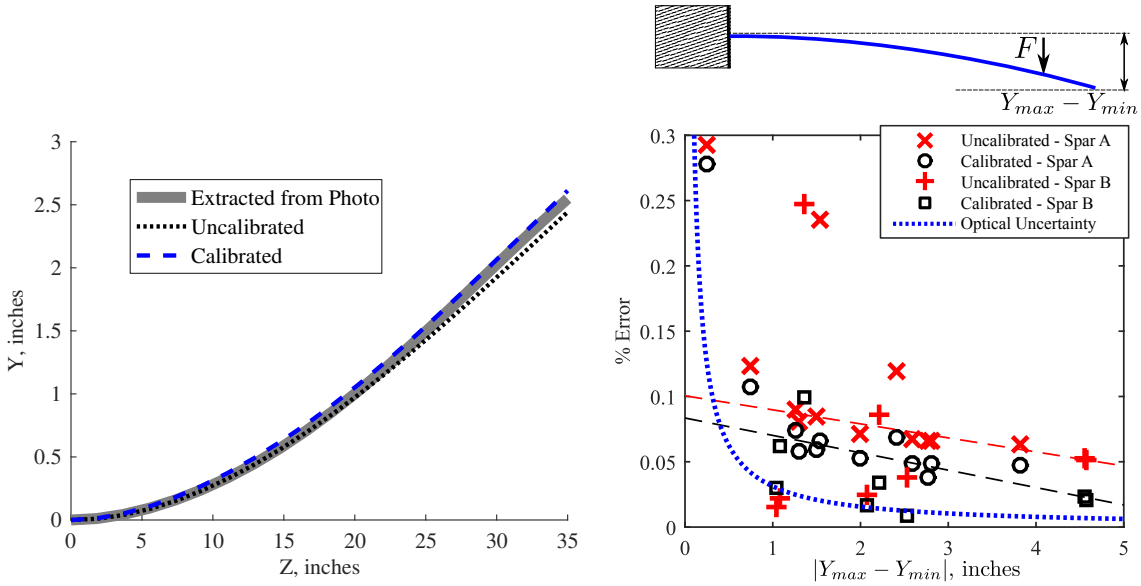

(b) View of reference deflection and strain-gauge(c) Error in bending for spars A and B for all measurements, magnified in the direction of bend-single-point-load calibration cases.
ing.

Figure 2.32: Photo of spar-level calibration procedure. A point load is applied by fixing a block into the pegboard. The “true" deflection of the beam is extracted by tracking the red striping tape on the edge of the spar. The pre- and post- calibration bending inferred by the strain gauges are shown to scale in (a) and magnified in (b). The measured strains are corrected by a $N \times N$ calibration matrix, such that the strain energy contained in the error is minimized. The resulting calibration matrix quantifiably reduces the error in simple (single node) bending, as shown in (c). Figure reproduced in part from *Harwood et al.* (2016a).

2.5.3 In-Situ Calibration and Validation of Spars

Once the spars were installed into the hydrofoil, a second calibration was performed. In equation 2.5, it was assumed that the boundary condition of each beam's root was perfectly clamped, enabling the first two A coefficients to be nullified. In practice, the root of each spar was judged to be imperfectly clamped as a result of the compliance of the surrounding PVC, such that $Y(Z) = 0$ but $Y'(Z) \neq 0$ at $Z = 0$. Early testing demonstrated that the root boundary condition of the spars *in-situ* was better-described by a torsional spring, which permits a nonzero slope at the root, while no displacement occurs at the root. $A_0 = 0$ satisfies the zero-displacement conditions, and A_1 is defined as,

$$A_1 = -\lambda \hat{\epsilon}_Z|_{Z=0}, \tag{2.8}$$

where λ is dimensionless root compliance factor. A series of controlled loading experiments was performed as follows. The hydrofoil was clamped into the dry-land testing frame as depicted in figure 2.33. Point loads were applied at a known spanwise position and the deflections were measured at the LE and TE at another spanwise position. Loads were applied using ratcheting tie-downs, affixed at chordwise positions aft of, coincident with, and forward of the elastic axis. Pure-bending responses were recorded by applying the load at the elastic axis. Combined bending and twisting responses were achieved by applying loads eccentrically, or on a line of action not coincident with the elastic axis. Finally, pure-twisting deflections were achieved by applying two opposing loads in a couple about the elastic axis, such that the elastic axis did not move from its unloaded location.

Deflections at the LE and TE were measured at another known spanwise condition using linear rules, shown in figure 2.33b. These measurements were translated into bending and twisting motion about the shear center at the known spanwise station, respectively δ_{SC} and θ. The shape-sensing spars were used to infer the bending and twisting deflections at the same spanwise station at which reference measurements were made. The vector of compliance factors, denoted

$$\{\boldsymbol{\lambda}\} = \left\{ \begin{array}{c} \lambda_A \\ \lambda_B \end{array} \right\},$$

was selected to minimize the combined L_2 norm of the error in bending and twisting across approximately 100 loading cases. Several optimization algorithms were used, including both gradient-based and gradient-free methods, all of which converged to

an final value of

$$\{\boldsymbol{\lambda}\} = \left\{ \begin{array}{c} 7.56 \\ 4.77 \end{array} \right\}.$$

It was later pointed out in peer-review that the torsional spring model may have been necessitated by the presence of the load cell, rather than by compliance in the PVC surrounding the roots of the spars. The load cell is, by the very nature of its operation, a multi-DOF spring. In either case, however, the compliance vector accounts for at least some of the compliance in the parent structure, whether that compliance arises from the load cell or the foils material.

(a) Loads being applied to the hydrofoil during calibration. The tension is being applied forward of the elastic axis, leading to a combined bending and twisting response.

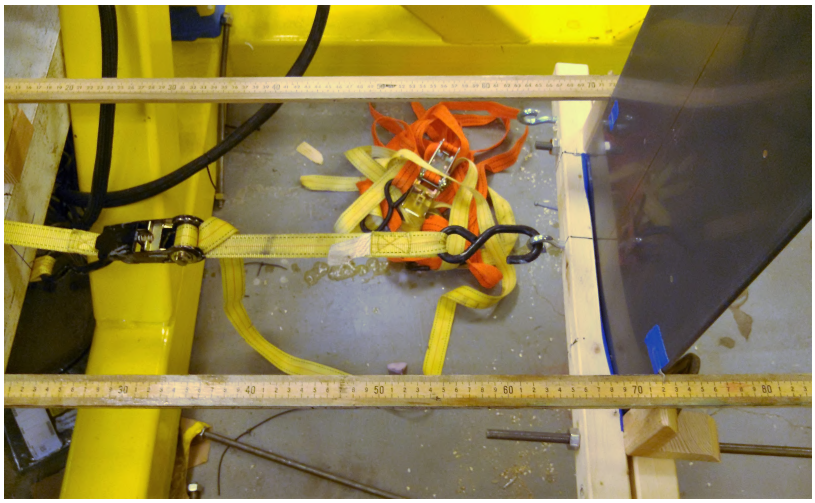

(b) Jig used to apply point loads and to measure deflections at LE and TE. The tension load is being applied along the elastic axis in order to minimize the amount of twist. Razor blades along the LE and TE are used to precisely measure the deflections at each location on a meterstick.

Figure 2.33: Photo of loads being applied to clamped PVC hydrofoil during *in-situ* calibration.

2.5.4 Characterization of Error in Shape-Sensing Spars

The following figures show a comparison of the foil's deflections in bending and twisting inferred by the shape-sensing spars and measured against the linear rules. in each figure, the absolute Root Mean Squared Error (RMSE) and proportional RMSE are given for bending and twisting, based on the data shown. Error bars visually indicate the same RMSE bounds. The proportional RMSE is computed as,

$$\% \text{ Error (bend)} = \frac{RMS\ \ \{\boldsymbol{\delta_{ref}}\} - \ \hat{\boldsymbol{\delta}}}{RMS\left(\{\boldsymbol{\delta_{ref}}\}\right)}; \tag{2.9}$$

$$\% \text{ Error (twist)} = \frac{RMS\ \ \{\boldsymbol{\theta_{ref}}\} - \ \hat{\boldsymbol{\theta}}}{RMS\left(\{\boldsymbol{\theta_{ref}}\}\right)}, \tag{2.10}$$

where $\{\boldsymbol{\delta}\}$ and $\{\boldsymbol{\theta}\}$ are respectively $(N_{Trials} \times 1)$ vectors of bending and twisting deformations (N_{Trials} being the number of points shown in the accompanying figure). The subscript $(\quad)_{ref}$ denotes the reference measurements obtained from the linear rules and $(\ \hat{}\ )$ denotes measurements obtained from the shape-sensing spars.

Figure 2.34 shows a compilation all loading cases. Bending deflections are plotted against force and twisting deflections are plotted against the twisting moment, measured about the elastic axis. The performance in bending is extremely good, while the uncertainty in twisting is significantly higher. Some insight into the larger error in the twisting measurements can be gained from Figure 2.35, which shows the performance of the spars in pure-bending. While the agreement in bending is excellent, the shape-sensing spars suffer from an apparent nonlinear error in the inferred twist angles. More specifically, a negative twist angle is inferred, even when one is not present in the reference data.

Figures 2.36 and 2.37 respectively show the results in combined bending-twisting and in pure twisting. Again, the performance in twisting is variable, but the trend indicates that the absolute error in twisting increases as the lateral bending deflections increase. The proportional error decreases with an increase in the actual twisting response of the hydrofoil. Both observations are consistent with the idea that a spurious "apparent" twist angle is being inferred as a result of large bending deflections.

The specific causes of the error are not known, though a few candidate causes may be named. First is the possibility of an imperfectly-applied strain gauge – an air bubble in the adhesive between the gauge and substrate, for example, may cause a nonlinear error in the transfer of strain from substrate to gauge, which could produce this type of error, and which would not be corrected by the spar-level calibration in

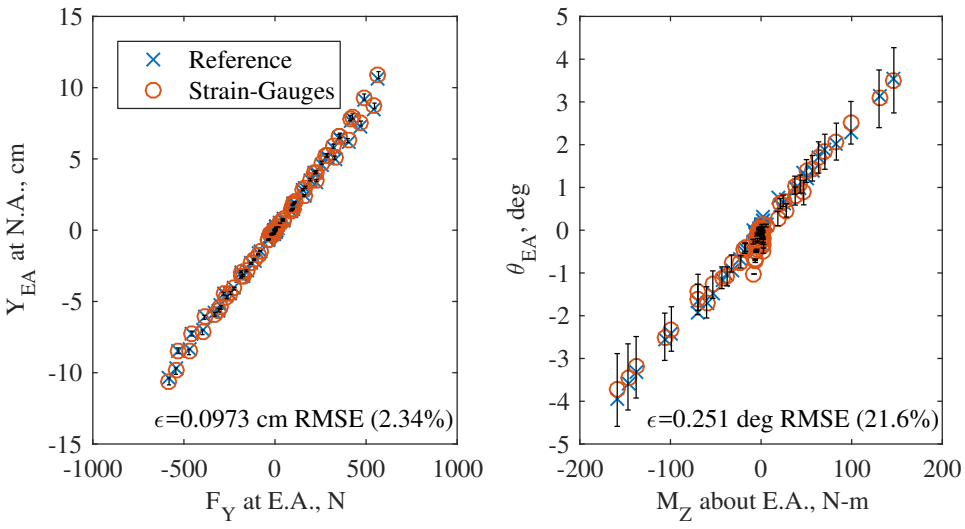

Figure 2.34: Characterization of shape-sensing spar uncertainty in pure bending, pure twisting, and combined bending-twisting (all load cases).

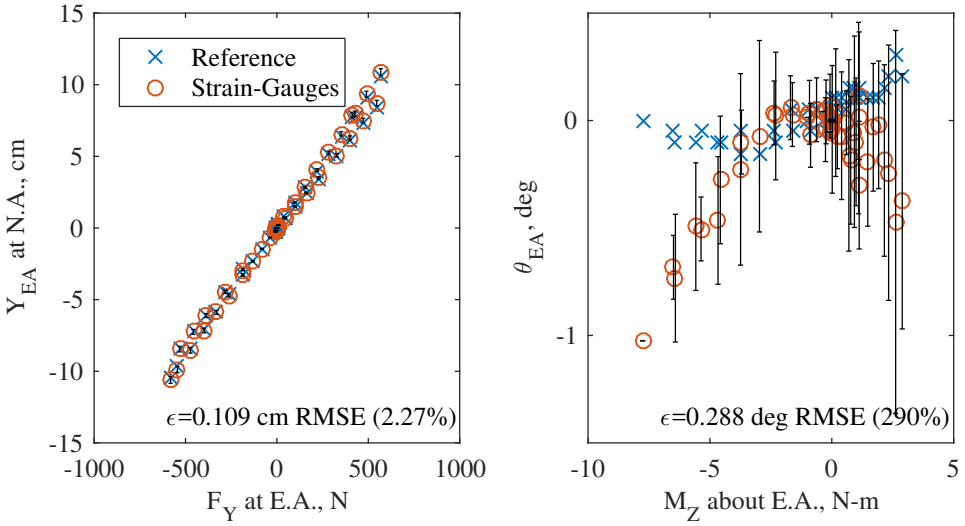

Figure 2.35: Characterization of shape-sensing spar uncertainty in pure bending only (loads applied along elastic axis).

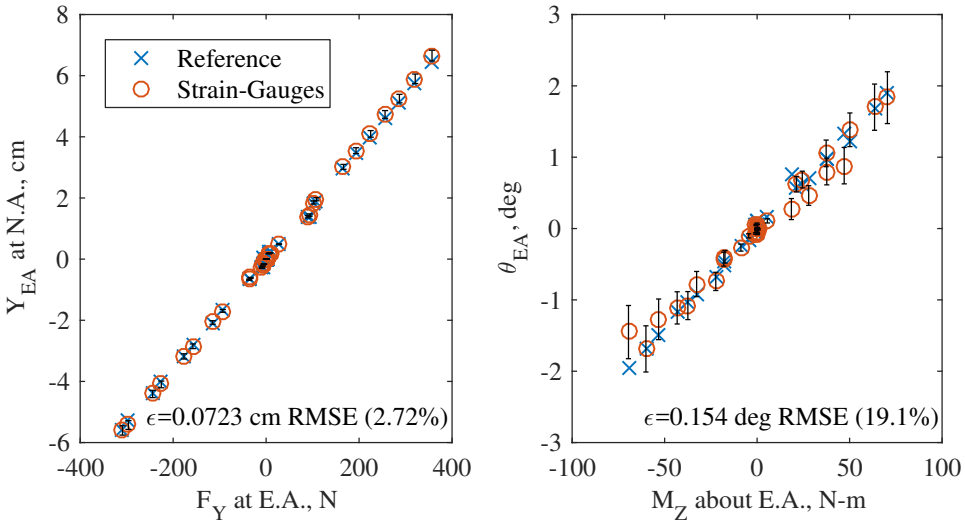

Figure 2.36: Characterization of shape-sensing spar uncertainty in combined bending and twisting (eccentric loads only).

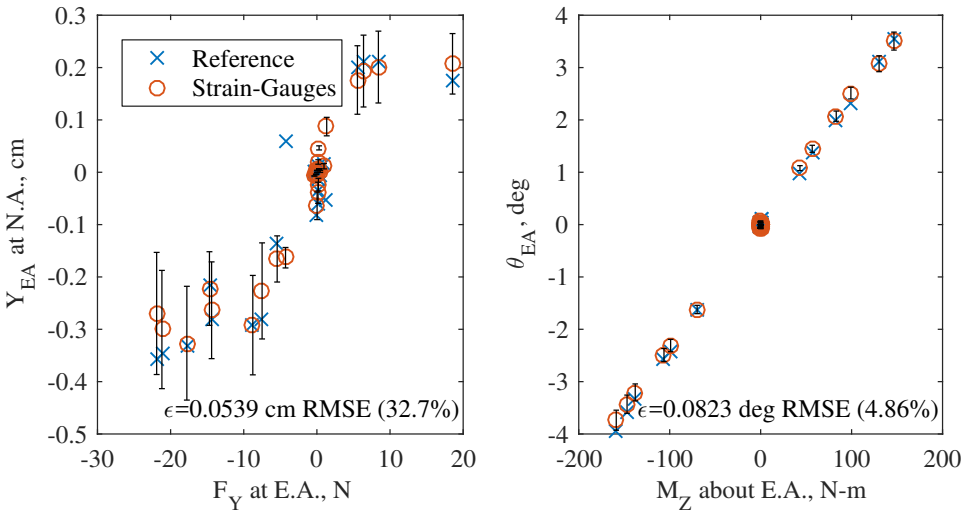

Figure 2.37: Characterization of shape-sensing spar uncertainty in pure twisting only (couple applied about elastic axis).

§2.5.2. This, or other sources of measurement error, could be compounded by the root compliance model, which uses different root compliance factors for each of the two spars. Finally, the method of measuring twist is fundamentally problematic. In essence, the twist is inferred as the small difference between two large numbers, a scenario in which even negligible errors in bending may amplified into a large error in the inferred twist.

In any case, the results shown in figure 2.34 are judged to be a robust – if conservative – representation of the spars' performance under a wide range of loading conditions, with uncertainty of 2.5% in bending and 22% in twisting. Despite the large proportional uncertainty in twisting, the dimensional RMSE of 0.25° is actually highly competitive with optical methods such as digital image correlation (DIC). It's important to note, as well, that the loads on the hydrofoil during towing tank and cavitation tunnel testing were, in most cases, smaller than those used in the calibration tests. Thus, we can expect the characteristic uncertainties to be valid in the range of testing.

2.5.5 Comparison of Shape-Sensing and Optical Methods of Tracking

It is a natural next step to compare the performance of the optical motion tracking to that of the shape-sensing spars. Figure 2.38 shows a baseline case, with the foil in a quiescent fluid. The two measurement methods agree favorably, though it should be noted that the random errors in the optically-inferred quantities are significantly higher than those for the shape-sensing. The shape-sensing spar results, in particular, demonstrate a strikingly low noise floor.

Figure 2.39 shows a comparison of the two motion-tracking methods with the foil vibrating in a quiescent fluid. A shaker motor (described in §2.6.2) was used to excite the first bending mode of the hydrofoil, which results in a sinusoidal motion at the hydrofoil's tip. The two methods produce another excellent agreement, with the shape-sensing spars again producing much lower noise and random error.

Figure 2.40 shows a comparison of the two methods with the hydrofoil yawed at $\alpha = 5°$ in a moving fluid with a velocity of $U = 4.2$ m/s. In the middle of the run, a ventilated cavity was induced on the hydrofoil, (a vertical black line indicates the time of cavity formation). Prior to the formation of the cavity, the two methods agreed very favorably once again, with the exception of what appears to be some bias offset between the two (probably a result of sensor drift). However, following the formation of the cavity, the cavity's interface causes refraction and optical drop-outs that render the optically-inferred deflections useless. Additionally, if the frequency content of the

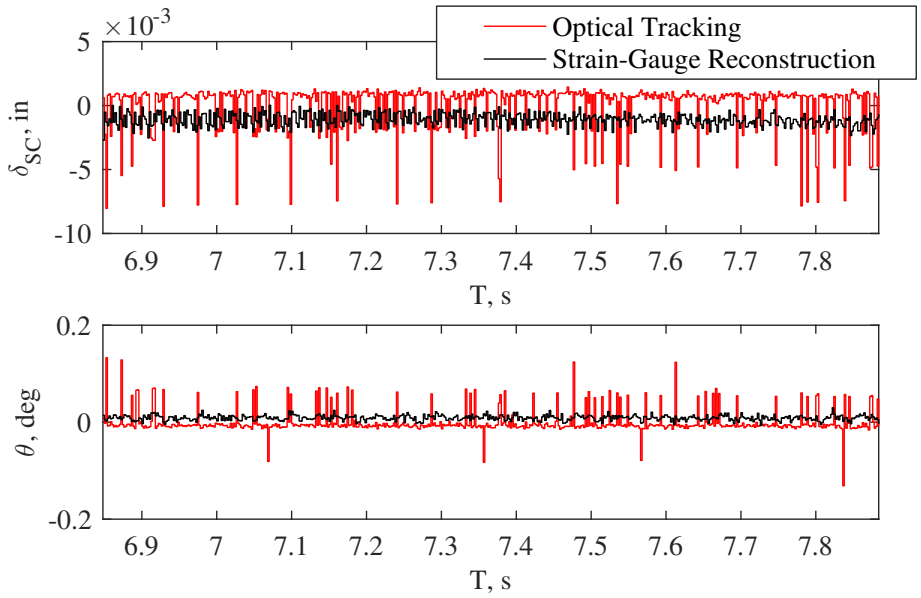

Figure 2.38: The foil tip motions are shown for the two methods of tracking. Model 2 was set at $\alpha = 0°$ in a quiescent fluid to obtain a zero-reference.

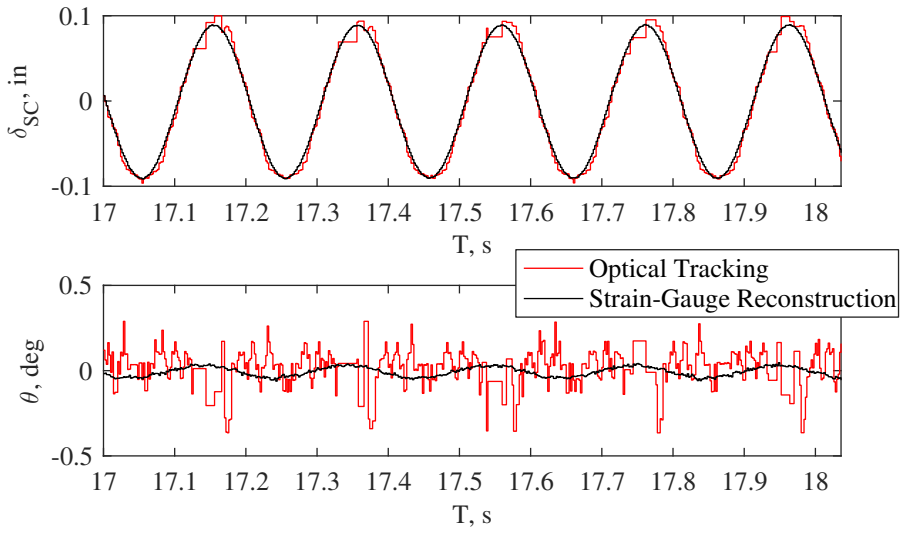

Figure 2.39: Comparison of model 2 tip motions for a zero-speed trial. The first bending mode of the hydrofoil was excited, resulting in a sinusoidal deformation at the foil tip – primarily in bending, with some small twist angle. The comparison between the two methods is excellent in bending, and quite acceptable in twisting.

response is important, the optically-measured deflections will be contain spurious broadband spectral content as a result of the noisy time-domain signal.

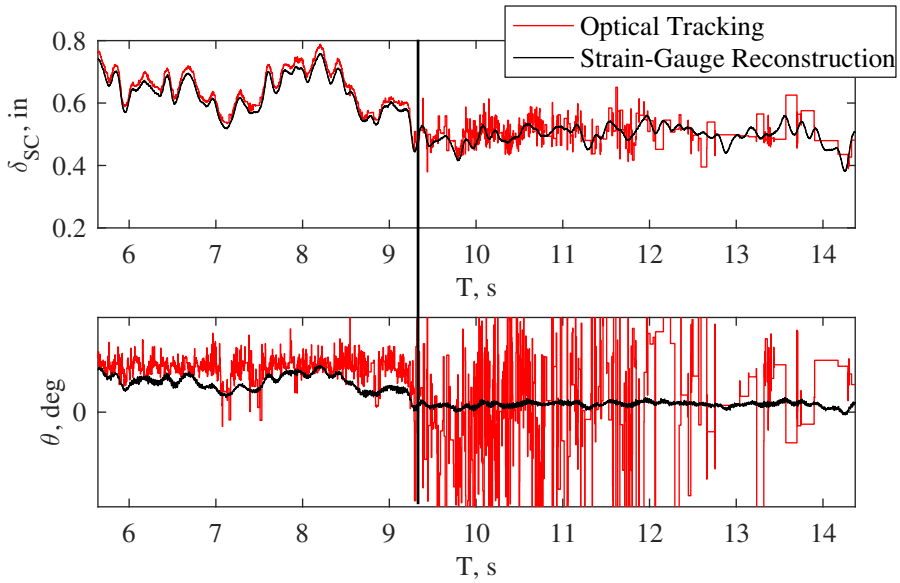

Figure 2.40: Comparison of model 2 tip motions for a run at $\alpha = 5°$; $U = 4.2$ m/s. Ventilation occurred during the run, at the location marked by the vertical black line. When ventilation occurred, the loss of optical access makes the optical tracking method very noisy.

The three figures in this section demonstrate the strengths of the shape-sensing spars developed for this project. They are simple, low-cost, robust, and accurate, when compared to optical motion tracking. Moreover, and of particular importance to this work, they are unaffected by loss in optical access, and can be used to accurately infer the motions of flexible wing-like structures where optical methods cannot.

2.6 Actuation

In addition to the various sensing instruments described in §2.4, several components provided inputs to the hydrofoil and/or flow as a means of perturbing or controlling the experimental conditions.

2.6.1 Air-Injection

Under certain flow conditions, it was observed by *Breslin and Skalak* (1959); *Wadlin* (1958); *Rothblum et al.* (1969), among others, that ventilation could be perturbed by disrupting the inflow. Inserting a small object, such as a thin wire, into the flow just upstream of a foil's leading edge resulted in ventilation, presumably

the free surface seal is penetrated by the wire's intrusion, and by eddying, separated flow behind the wire, which allow air to enter into the ventilation-prone flow along the hydrofoil suction surface. In the present work, a high-pressure, focused jet of air was used to affect the same disruption to the flow. The jet, pictured in figure 2.41 was aimed at the junction of the LE and the free surface. When a disturbance was desired, a pulse was generated on a DAQ output channel, which closed a 110 VAC circuit *via* an optically-isolated relay. The newly-closed circuit in turn opened a solenoid-controlled valve to allow air to flow from the jet nozzle. Air was provided from a small compressed-air tank kept at approximately 860 kPa (125 psig). Under certain conditions, the jet of air was sufficient to produce a ventilated cavity. It is important to note that the duration of air injection was typically less than 1 second, so the jet did not provide the air needed to *sustain* the cavity. Instead, it was simply a perturbation to the otherwise-undisturbed free surface seal. Further discussion will be dedicated to the effect of this perturbation on the flow in §IV. Note that a second, three-way valve, was similarly (but separately) actuated to switch the submerged pressure probe at the TE (described in §2.4.3) from a slow air-priming circuit to the differential pressure transducer.

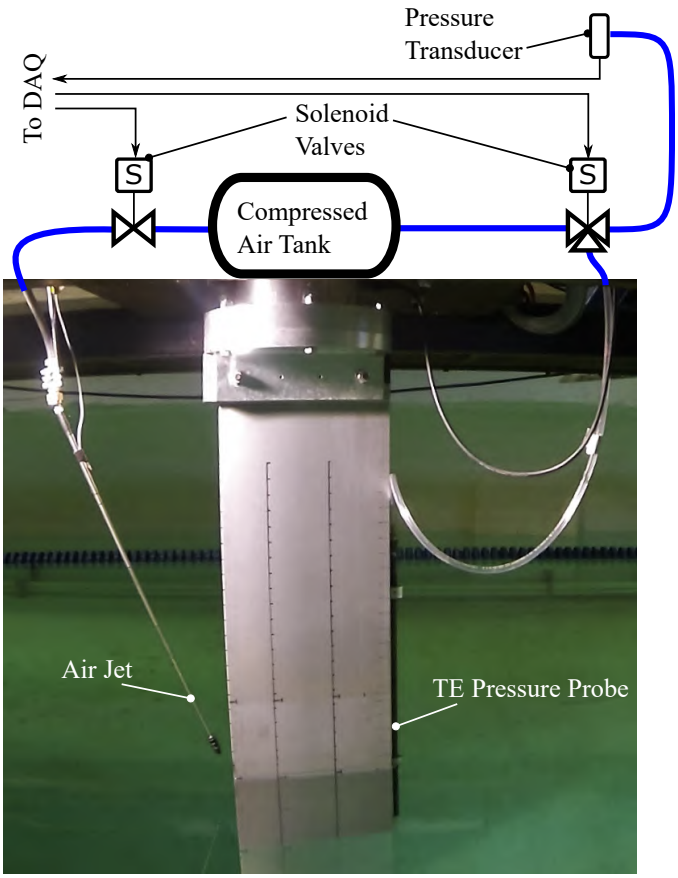

Figure 2.41: Depiction of solenoid-controlled air jet used to trigger ventilation. The jet is fed from a compressed air tank at approximately 860 Pa (125 psig). The valve is a normally-closed design that is actuated by a 5 VDC signal from the DAQ computer, *via* an optically-isolated relay.

2.6.2 Shaker-Motor Excitation

For tests on the reinforced flexible hydrofoil (model 2), a shaker motor was used to excite the hydrofoil. The location of the shaker motor is depicted in figure 2.19. The motor used was a model 2007E "mini-shaker," manufactured by The Modal Shop. The unit has a frequency range of 0-10 kHz and a maximum sinusoidal force amplitude of 31 N (7 lbf). The motor was housed inside of a machined aluminum case, both of which are shown in figure 2.42. All seams of the housing were sealed and the housing was positively-pressurized from a compressed air source to preclude water ingress. An air-bleed line was included to provide some convective cooling for operation inside of the vacuum tunnel. The shaker motor was coupled to the hydrofoil models *via* a

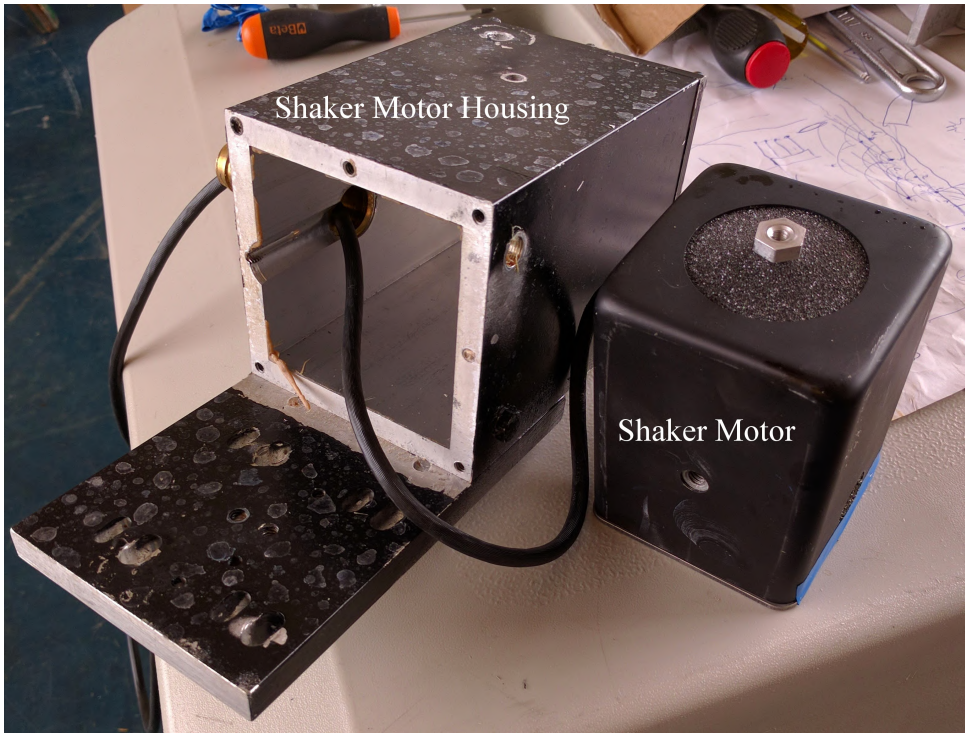

Figure 2.42: Shaker motor (right) and waterproof housing (left).

nylon stinger to avoid off-axis excitation. The point of excitation was located 24.1 cm (9.5 in) from the root of the hydrofoil and 3.8 cm (1.5 in) aft of the leading edge. The excitation force at the drive-point of the shaker motor was recorded as the system input, to be used in the ensuing modal analysis (more details in §VI). For drive-point measurements, a Model 288D01 impedance head was used, manufactured by PCB Piezotronics. The impedance head measured AC-coupled loads and accelerations with a frequency response of 1 to 5000 Hz and a maximum nonlinearity error of $\pm 1\%$.

The shaker motor was controlled from the DAQ host system in the following

manner, which is shown pictorially in figure 2.43. The data-acquisition PC was used to generate a pulse train at the desired frequency, to which a pair of lock-in amplifiers (Stanford Research Systems SR830) were phase-locked. The signal-generator portion of the master SR830 was used to generate a sinusoid at the commanded frequency, which was amplified through a conventional analogue power-amplifier (The Modal Shop E2100E21-100) to drive the shaker motor. The accelerometers at the tip of each shape-sensing spar (PCB 357B06) were connected to inputs of the lock-in amplifiers, permitting the magnitude and phase of the structural accelerations to be monitored on-line. For most trials, a linearly- or logarithmically-swept sine wave with a fixed amplitude was used as the excitation signal, although it was possible to manually specify an arbitrary excitation frequency as well.

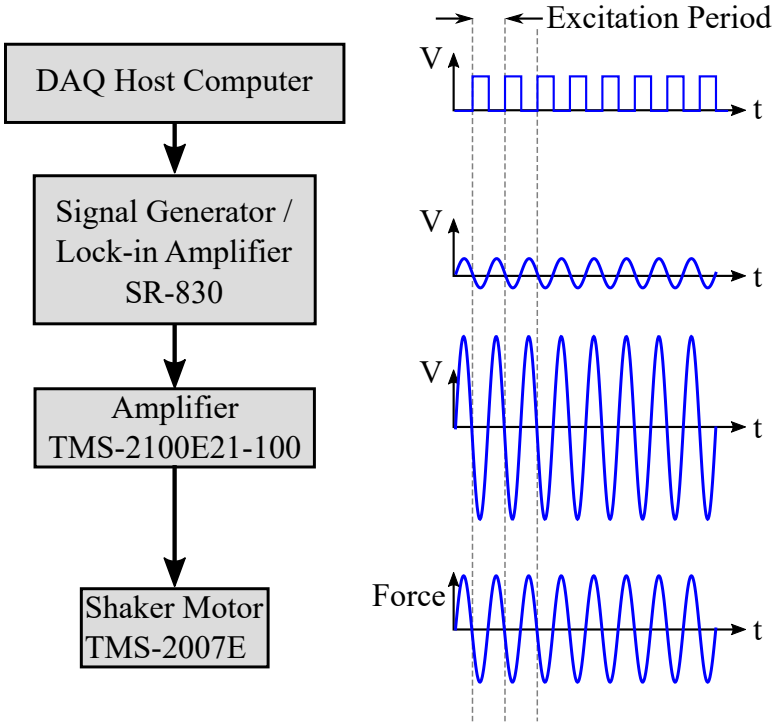

Figure 2.43: Pictorial depiction of signal flow from DAQ host PC to the shaker motor output.

2.7 Data Acquisition System Architecture

The numerous permutations and expansions of the experimental program necessitated an evolution of the DAQ system to accommodate increasingly complex input, output, and timing requirements. All data acquisition used National Instruments® multifunction DAQ devices for input and output, hosted on a Hewlett Packard Z400

workstation PC. The arrangement, interconnections, and additions to the hardware are summarized in the following subsections. All signals were measured as analog voltage and, after preliminary signal on-line signal processing (for user feedback, etc), were written as ASCII data files (ASCII format, though inefficient, was chosen over binary formats to improve the portability of the data). Control of the DAQ, on-line signal processing, and logging were performed in National Instruments LABVIEW software.

Finally, it bears mentioning that no anti-aliasing filters were used between the signal sources and the Analogue to Digital Converter (A/D) inputs on the DAQ. Most experimentalists are very familiar with the aliasing of signals at frequencies above the Nyquist frequency, which informs the choice of minimum sampling frequency to be used. The purpose of anti-aliasing frequencies is to prevent the unintentional aliasing of signals that are not of interest, but reside above the Nyquist frequency, back into the frequency band being investigated, which occurs whenever signal sources are not inherently band-limited. The aliasing of high-frequencies into the frequency-bands of interest is a real concern for rigorous frequency-domain analysis, but a few considerations alleviate concerns about this issue. In the steady-state testing on the hydrofoil the effect of the aliased signals is to increase the noise floor somewhat – a nuisance, but not a severe detriment. For the dynamic testing, such as the modal analysis detailed in chapter VI, the input of the shaker motor into the vibratory system was band-limited to the commanded frequencies. As a result, the output from the system was *approximately* band-limited, in that most of the energy was concentrated into the band of excited frequencies.

2.7.1 Testing Prior to April 2014: PCIe-Based System

The first stage of testing used an entirely PCI-based DAQ system. A dedicated PCIe-6320X card provided excitation to, and measured the signals from, the load cell on differential channels. A second, PCIe-6323X card with 16 differential / 32 single-ended voltage inputs, 4 analog outputs, and 48 digital I/O lines was used in various configurations to measure the remainder of the instruments. All connections were made *via* SCB-68A binding-post connection terminals.

Both cards used muxed configurations, where the A/D scans across the physical channels with a switching asynchronism of less than 1 μs introduced by each switch. Sample rates between 500 Hz and 2 kHz were used, with 1 kHz being the most common. A batch-buffered approach was used to read buffered segments of data from the on-board buffers for processing and writing to disk without interrupting the

hardware-timed sampling.

One disadvantage of the PCI-based system was a lack of rigorous synchronization between the two physical cards. While muxing and sampling was controlled by precise onboard hardware clocks, the phasing between the two cards was controlled *via* a software clock. This was not a major concern for the collection of slowly-varying or steady-state data, but subsequent testing demanded more-rigorous control over system timing.

2.7.2 Testing Between April, 2014 and March, 2016: PXIe-Based System

To improve the timing performance, an external PXI express chassis from National Instruments® was used. The chassis, which is remotely controlled by the same host computer used previously, acts as an extension to the native PCI-express bus of the host system. Unlike the PCIe bus, however, it contains built-in hardware clocks and dedicated synchronization channels, as well as a modular design that permits extensibility and reconfigurability of DAQ modules.

Two multifunction DAQ cards were used in the chassis. A model PXIe-6341 was dedicated to powering and measurement of the load-cell. A model PXI-6363 was used as the input-output hub for the remainder of the instrumentation. The only difference between the implementation of PXI-based system and that of the PCI-based system was the introduction of a master synchronization clock, which permitted the two DAQ cards to be phase-locked for improved and consistent phasing of time-resolved measurements across the multi-card system.

2.7.3 Testing at INSEAN in May, 2016: Multiple DAQ Systems

Testing at INSEAN presented a number of challenges that required further re-vamping of the DAQ system. First, the number of inputs and outputs exceeded the available number of channels on either the PXI or PCI systems alone, requiring the two to be aggregated without compromising the synchronization between channels. Secondly, a number of the signals to be measured (*e.g.* thermistors, pressure gauges, and pump-speed encoders) were not available as analog voltages, and were thus not measurable using the NI system. Finally, the collaborating scientists at INSEAN wished also to collect data on their in-house DAQ (manufactured by Prosig®), which lacked the output channels required to actuate certain components of the hydrofoil rig (*e.g.* lights, shaker motor, and camera control).

In order to bridge the PCI and PXI DAQ systems, a master-slave setup was

adopted. A 10 MHZ reference clock (TTL pulse train) was exported from the PXI chassis to a counter line on each of the PCI DAQ cards, along with the PXI sampling clock and sampling start-trigger. With these three signals imported, each of the PCI DAQ cards was set to use the imported signals in place of their on-board clocks and triggers, so that all cards began data collection synchronously and remained phase-locked. In this way, the two National Instruments® systems were aggregated, allowing more channels to be added.

To solve the second and third issues, data were logged on both DAQ systems simultaneously. An analog voltage output was run from the NI DAQ to an input on the Prosig DAQ, which in turn was used to trigger the Prosig's acquisition. After triggering, the voltage signal was linearly ramped between two known values, allowing the time-delay of the Prosig's sample clock, relative to that of the NI DAQ, to be determined within one sampling period. Data logged on the Prosig DAQ were time-shifted and aggregated with those logged on the NI DAQ during post-processing. In this manner, multiple signal types were collected, and a number of channels were redundantly logged. Finally, the Prosig® DAQ was equipped with anti-aliasing filters on all inputs, so a direct comparison between the unfiltered data and filtered data for identical signals was made possible. It was a comparison of two such signals that indicated the lack of input filtering was not a significant shortfall in data collected with the National Instruments® DAQ.

2.8 Propagated Uncertainties

The estimated uncertainty bounds of measured and derived quantities are summarized in table 2.7.

Table 2.7: Tabulated uncertainties in baseline variables, measured quantities, and derived quantities.

Baseline Variables		**Description**	**Uncertainty**		
h, m		Tip immersion depth	0.0065 m (1/4 in)		
α		Yaw angle	0.25°		
ν		Kinematic viscosity	8%		
T_s		DAQ synchronization time	1.6×10^{-5}s		
Measured Quantities	**Description**	**Measurement Method**			
U	Flow speed	Optical encoder / pump impeller speed	3%		
F_X	X Force component	Load cell	2.6%		
F_Y	Y Force component	Load cell	2.6%		
M_Z	Z Moment component	Load cell	2.6%		
δ_{SC}	Bending deflections	Shape-sensing spars	2.5%		
θ_{SC}	Twisting deflections	Shape-sensing spars	22%		
P_{ATM}	INSEAN tunnel pressure	Absolute pressure transducer	5%		
P_{TE}	Trailing edge base pressure	Differential pressure transducer	1%		
F_{EX}	Shaker excitation force	AC-coupled load cell	1%		
A_{EX}	Drive-point accelerations	AC-coupled accelerometer	1%		
$a_{X,Y,Z}$	Structural accelerations	Piezoelectric accelerometers	1%		
T_w	Water temperature	Thermocouple	1°C		
Derived Quantities	**Description**	**Formula**	$AR_h = 0.5$	$AR_h = 1.0$	$AR_h = 1.5$
Fn_h	Froude number	$Fn_h = \frac{U}{\sqrt{gh}}$	3.8%	3.2%	3.1%
Re_c	Chord-based Reynolds number	$Re_c = \frac{U_\nu}{c}$	6%	6%	6%
AR_h	Immersed aspect ratio	$AR_h = \frac{h}{c}$	5%	2%	1.5%
σ_v	Vaporous cavitation number	$\sigma_v = \frac{P_T - P_V}{\rho U^2/2}$	8%	8%	8%
$C_{P_{TE}}$	Trailing edge pressure coefficient	$C_{P_{TE}} = \frac{P_{TE} - P_\infty}{\rho U^2/2}$	6%	6%	6%
$C_{L_{3D}}$	Lift coefficient	$C_{L_{3D}} = \frac{F_Y}{\rho U^2 hc/2}$	8%	7%	7%
$C_{D_{3D}}$	Drag coefficient	$C_{D_{3D}} = \frac{F_X}{\rho U^2 hc/2}$	8%	7%	7%
$C_{M_{3D}}$	Yawing moment coefficient	$C_{M_{3D}} = \frac{M_Z}{\rho U^2 hc^2/2}$	8%	7%	7%

CHAPTER III

Steady State Flows with the Rigid Hydrofoil

This chapter will elucidate upon the nominally-steady flows around the rigid aluminum strut. It is the goal of this chapter to address the following questions, originally posed in §1.6:

- What are the characteristic steady flow regimes of surface-piercing lifting-surfaces and how are they formally defined?
- What physical processes dictate the hydrodynamic response and stability of steady flow regimes?
- How do hydrodynamic loads differ between flow regimes? How do the loads change with speed, immersion depth, and attack angle within each regime?
- What simple models can be derived to simulate the behavior of surface-piercing hydrofoils in multiphase flows?

3.1 Steady-State Flow Regimes

Consider figure 3.1, which depicts natural ventilation of the aluminum hydrofoil (Model 0). Sectional cuts taken through the three spanwise locations called out in the figure are classified by the Two-Dimensional (2-D) flow regimes defined in chapter I as fully wetted, partially cavitating, and supercavitating. The previous half-century of literature have failed to produce a standardized vernacular for 3-D cavity flows, which has complicated the matter of describing the various flow regimes and physics attendant on a surface piercing hydrofoil or strut. In order to establish such a desired standardization of the terminology, let us first revisit the re-entrant jet, which plays an important role in dictating flow stability. We will then define the

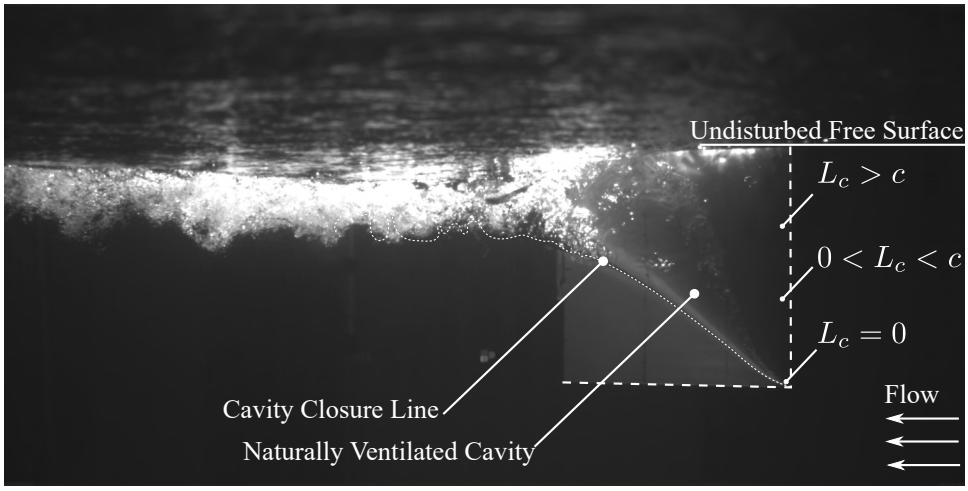

Figure 3.1: Example of a naturally ventilated cavity flow at $\alpha = 15°$, $Fn_h = 1.25$, $AR_h = 1.0$. At different points along the span, sections are fully wetted, partially cavitating, and supercavitating, making it unclear how to define the flow regime of the 3-D cavity.

four flow regimes observed in the present experiments: fully wetted flow, partially ventilated flow, partially cavitating flow, and fully ventilated flow.

3.1.1 The Re-entrant Jet and its Impact on Flow Regimes

Where a cavity closes on a solid surface, streamlines inside of the stagnation streamline form a jet spray that undercuts the cavity, known as a re-entrant jet (*Laberteaux and Ceccio*, 2001a). In 2-D flows, the re-entrant jet may impinge on the upstream cavity boundary, causing "pinch-off." A well-known example is the phenomenon of sheet-cloud cavitation, which occurs when a re-entrant jet induces periodic shedding of vaporous partial cavities, and which was reviewed in §1.3.5. It was discussed in §1.4.3 that when the line of cavity closure is non-normal to the incoming flow, the re-entrant jet is a reflection of the incoming flow about the cavity closure line (*De Lange and De Bruin*, 1998; *Franc and Michel*, 2004; *Laberteaux and Ceccio*, 2001b). This is shown in figure 3.2 in the context of the surface-piercing strut. If incoming flow encounters a cavity closure-line at a local angle of Φ from the horizontal plane, the jet flow will be directed at an angle of 2Φ, as shown by the arrows in figure 3.2. Let z' be a distance measured downward from the free surface, as shown in figure 2.2. At a given depth z', the magnitude of the jet velocity vector $\vec{U_j}$) may be obtained by applying the steady Bernoulli equation between the upstream flow (known velocity) and the cavity boundary (known pressure) to obtain,

$$||\vec{U_j}(z')|| = U \quad \overline{1 + \sigma_c(z')}. \tag{3.1}$$

The respective stream-wise (u_j) and spanwise (w_j) components of the re-entrant jet velocity are,

$$u_j(z') = U_0 \quad \overline{1 + \sigma_c(z')}\cos\left(2\Phi(z')\right), \tag{3.2a}$$

$$w_j(z') = U_0 \quad \overline{1 + \sigma_c(z')}\sin\left(2\Phi(z')\right). \tag{3.2b}$$

Note that these velocities are derived from the steady Bernoulli equation, which neglects viscosity, and so may be valid only at the cavity closure line where the jet develops.

The notion of re-entrant as a reflection of incoming flow is reinforced by the surface-flow visualization shown in figure 3.3. Paint dots were applied as described in §2.4.6, and the hydrofoil was accelerated along a ramped velocity profile at a yaw-angle (α) sufficiently large for a ventilated cavity to spontaneously develop ($\alpha = 14°$). As the forward speed increased, the ventilated cavity grew in size. At different instants in time, shown as frames to the right of the figure, the cavity profile was observed, and theoretical re-entrant trajectories was estimated from equations 3.2. The resulting

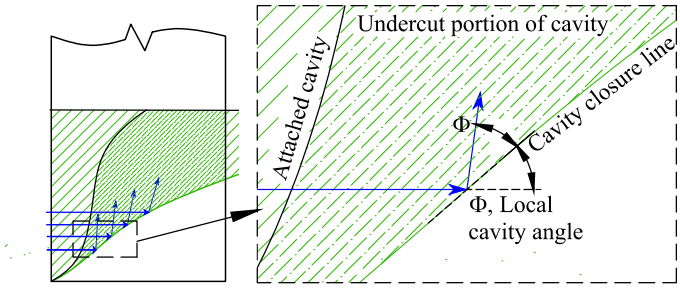

Figure 3.2: Schematic representation of the re-entrant jet on a spanwise-varying cavity. When incoming flow (arrows) encounters an oblique line of cavity closure at a local angle Φ, the flow is reflected about the normal to the cavity closure line so that the resulting jet spray is directed along an angle of 2Φ from the horizontal plane.

trajectories were superimposed as arrows onto the respective cavity profile. The re-entrant jet at the cavity closure line was swept over the paint dots, causing the dots to shear in the direction of the local jet spray. Some smearing of the dots was unavoidable, as the dots experienced some shear stress in the stream-wise direction prior to their interaction with the re-entrant jet; nevertheless, the primary directions of streaking clearly coincide with the superimposed arrows. This indicates that the local velocity of a streamline encountering the cavity closure line is well-captured by a rotation of the inflow velocity through an angle of 2Φ.

The re-entrant jet is an important feature that affects the stability of a ventilated cavity. If a configuration, or regime, of the flow remains unchanged following any perturbation to the flow, then that regime is considered exclusively and globally stable. If small perturbations do not affect the flow regime, but large perturbations cause transition to another flow regime, then the regime is considered locally stable. The coexistence of a locally stable regime and another locally- or globally–stable regime constitutes a bi-stable set of conditions. For given flow conditions, a flow regime is considered unstable if it cannot be sustained, even if left unperturbed.

When the local angle of the cavity closure line is $\Phi > 45°$, the re-entrant jet will possess an upstream velocity component. With enough momentum, the jet impinges on the leading edge of the ventilated cavity, causing a large-scale shedding of the cavity *via* pinch-off (as in the case of sheet/cloud cavitation, described earlier). If this occurs over a significant portion of the span, then a ventilated cavity becomes unstable. If the cavity has a shallow closure line ($\Phi < 45°$), then re-entrant flow is redirected along a trajectory that still carries it downstream, where it cannot impinge upon the cavity's leading edge.

To verify that $\bar{\Phi}$ is a suitable metric for judging the stability of the flow, images

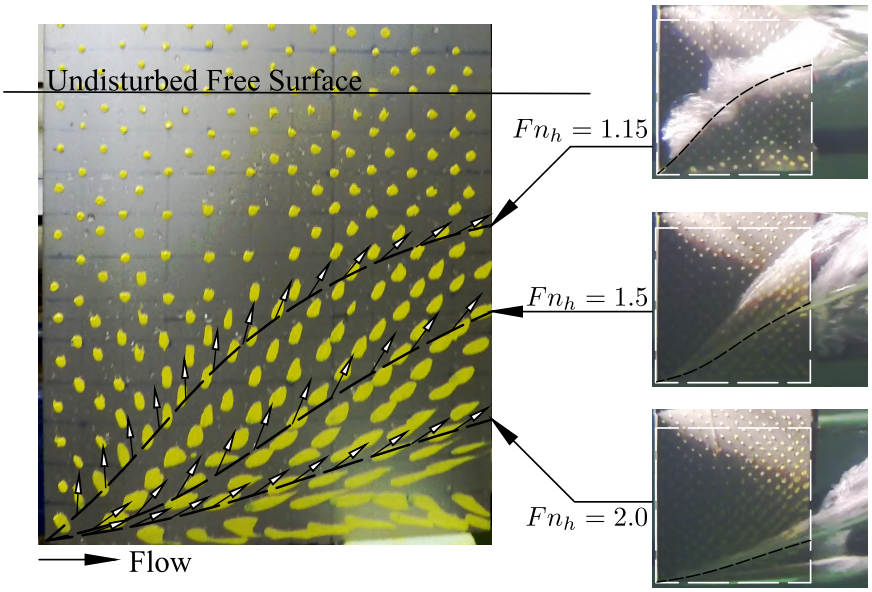

Figure 3.3: Paint streaks on the suction side of a hydrofoil in accelerating flow at $\alpha = 14°; AR_h = 1$. As the speed increased, the cavity grew (see photos to right), sweeping the re-entrant jet over the surface of the foil and shearing the paint in the direction of the jet. Cavity length distributions are drawn for $Fn_h = 1.15, 1.5$, and 2.0. Superimposed on each cavity profile are arrows indicating the local theoretical re-entrant jet direction that results from rotating the inflow through an angle of 2Φ. The streaks in the paint coincide with the theoretical jet directions, indicating that theory (equations 3.2a and 3.2b) correctly predicts the trajectory of re-entrant flow. Figure reproduced from *Harwood et al.* (2016c).

were taken of ventilated cavities in decelerating flows, immediately preceding the instant when the cavity became unstable. The cavity length was measured at three spanwise stations, as shown in figure 3.4a, through which was fitted an affine curve to get the value of $\bar{\Phi}$, measured from the horizontal plane after correcting for perspective distortion. $\bar{\Phi}$ is plotted as a function of α and AR_h in figure 3.4b. The results show the cavity angle at washout to be tightly clustered around a mean of $\bar{\Phi} \approx 41°$ for all values of α and AR_h, which is acceptably close to the proposed stability boundary at $\bar{\Phi} = 45°$.

Therefore, we posit that a ventilated cavity will be stable if $\bar{\Phi} < 45°$ and will be unstable if $\bar{\Phi} > 45°$. This stability criterion, along with other more-obvious aspects of the flow, will next be used to define the four characteristic flow regimes.

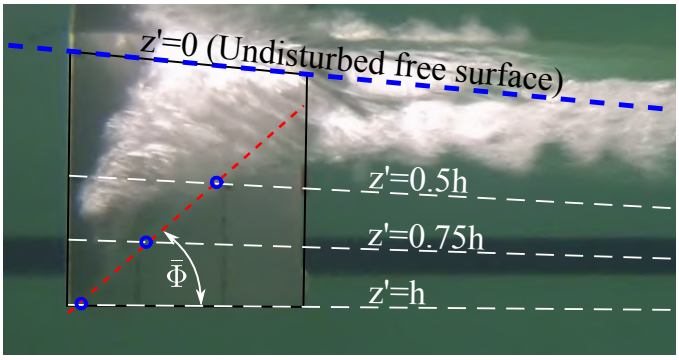

(a) Linearized fit of cavity closure-line used to determine the approximate cavity closure angle ($\bar{\Phi}$) at the time of cavity-instability.

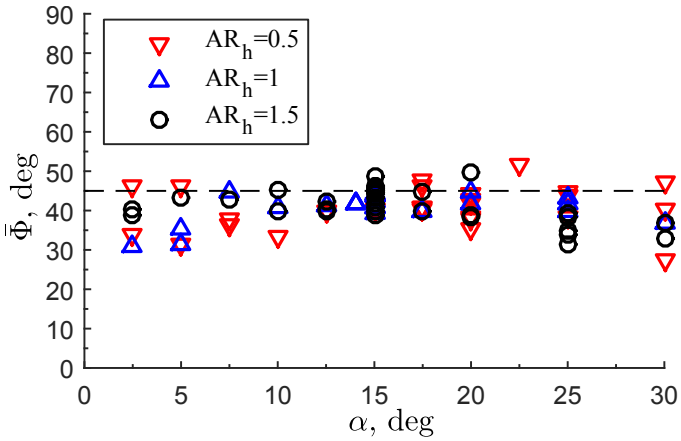

(b) Angles of cavity closure-lines as a function of α and AR_h.

Figure 3.4: Experimental quantification of cavity closure angles at the point of cavity instability *via* pinch-off for immersed aspect ratios of $AR_h = 0.5, 1, 1.5$. The example shown in (a) is at $Fn_h = 1.5; \alpha = 20°; AR_h = 1.0$. Cavity closure line profiles were linearly approximated to find $\bar{\Phi}$, shown in (b). The mean value of $\bar{\Phi}$ is 40.75°.

3.1.2 Fully Wetted Flow Regime

Fully Wetted (FW) flow is defined as the regime in which no pronounced entrainment of gas occurs. In the present experiments, a small aerated base cavity was typically observed in the separated wake of the blunt trailing edge. However the effects of the trailing edge were confined to a relatively small region immediately aft of the trailing edge; neither the flow separation nor the base cavity materially affected the hydrodynamic response of the hydrofoil (*Perry*, 1955). An example of FW flow is shown in figure 3.5. Flow is pictured moving from left to right. The nominal free surface indicates the initial calm water surface identified by the $z' = 0$ plane, where it intersects with the foil's suction surface. The free surface profile changes when subjected to the pressure distribution around the hydrofoil, and is termed the "deformed" free surface.

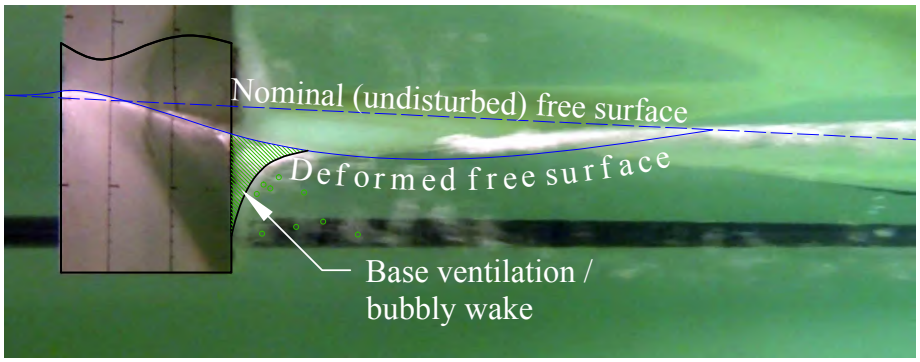

Figure 3.5: Fully wetted (FW) flow over the suction surface of model 0 at $\alpha = 10°; Fn_h = 2; AR_h = 1.0$. Flow is pictured from left to right. The FW regime shows no entrainment of air along the suction surface ($D = 0$, as measured from the nominal free surface). Some base ventilation occurs aft of the foil's blunt trailing edge. Figure reproduced from *Harwood et al.* (2016c).

3.1.3 Partially Ventilated Flow Regime

Partially ventilated (PV) flow is defined as the entrainment of a cavity either which does not span the entire immersed portion of the hydrofoil, or which does not meet the stability conditions to sustain fully ventilated flow (*e.g.* a destabilizing re-entrant jet exists). Figure 3.6 depicts two examples of partial ventilation. The flow in figure 3.6a is designated Partially Ventilated (PV) because the cavity does not reach the immersed tip of the hydrofoil ($0 \leq D < h$). In this case, the cavity depth and length are potentially unsteady. The flow pictured in figure 3.6b is so designated because the approximate cavity closure line, shown as a solid line fitted through the

cavity closure region, exceeds the $\bar{\Phi} = 45°$ stability condition, which is indicated by the dashed white line. As a result, a significant portion of the re-entrant jet is directed toward the foil's Leading Edge (LE). At small angles of attack, the resulting upstream flow may cause unsteady shedding of bubbly structures in a region confined to the trailing edge of the cavity, while at larger angles of attack, the jet destabilizes the entire cavity by impinging on the cavity interface and leading to pinch-off. In either case, the increased unsteadiness and decreased stability of the flow when $\bar{\Phi} \geq 45°$ serve to distinguish it from Fully Ventilated (FV) flow.

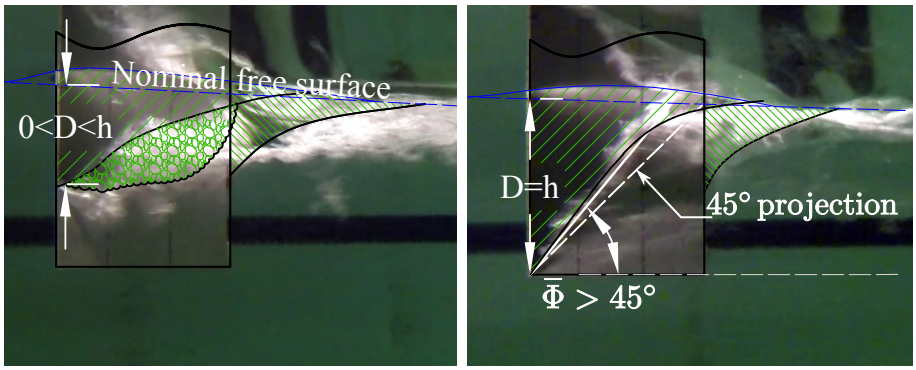

(a) $\alpha = 20°; Fn_h = 1.0; AR_h = 1.0$ (b) $\alpha = 7.5°; Fn_h = 1.54; AR_h = 1.0$

Figure 3.6: Partially Ventilated (PV) flow over the suction surface of model 2. (a) Shows the case where the cavity does not reach the free tip ($0 < D < h$). (b) Shows the case where the cavity reaches the free tip ($D = h$), but the angle of the solid line fitted through the cavity closure region is greater than the critical angle ($\bar{\Phi} = 45°$, shown as a dashed white line). Figure reproduced from *Harwood et al.* (2016c).

3.1.4 Fully Ventilated Flow Regime

Fully ventilated (FV) flow is defined as the case where a cavity is entrained along the entire immersed span of the hydrofoil's suction surface ($D = h$, where D is the maximum depth of the ventilated cavity beneath the nominal free surface), and where no inherently-destabilizing re-entrant jet occurs ($\bar{\Phi} < 45°$). Figure 3.7 shows an example of a fully ventilated cavity. The suction surface of the hydrofoil (pictured) is enveloped entirely inside of a ventilated cavity. The near wall of the cavity detaches from the LE of the hydrofoil. The pressure side of the hydrofoil is fully wetted, and flow detaches smoothly from the corner of the pressure-side and trailing edge to form the opposing cavity wall. Large spray sheets develop on both sides of the hydrofoil; the lower edge of the suction-side spray sheet is visible in figure 3.7. Note that the angle of the cavity closure-line is very shallow ($\bar{\Phi} << 45°$). As a result, the stream-

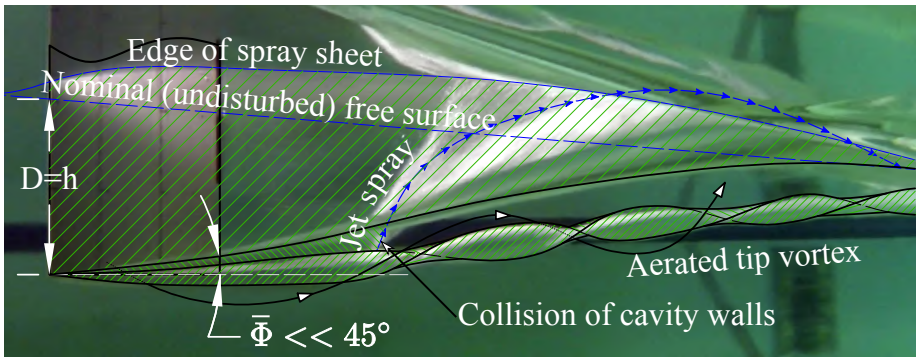

Figure 3.7: Fully Ventilated (FV) flow over the suction surface of model 0 at $\alpha = 15°; Fn_h = 3.0; AR_h = 1.0$. The suction surface (pictured) is contained entirely within the walls of the cavity. The cavity satisfies both FV flow criteria ($D = h$ and $\bar{\Phi} \leq 45°$). In the case pictured, a strong tip vortex is present, the core of which aerates by ingesting air from the cavity. Figure reproduced from *Harwood et al.* (2016c).

wise component of any re-entrant flow is directed toward the trailing edge of the hydrofoil, where it presents no detriment to the cavity's stability. In figure 3.7, a strong tip vortex is present, the core of which aerates by ingesting air from the cavity. When the flow is in a fully ventilated state, the blunt trailing edge is contained entirely within the cavity, so it does not interact with the liquid flow. In the case pictured, and in other cases with a sufficiently strong tip vortex, the circumferential flow around the vortex impinges on the near (as pictured) cavity wall, forcing a small jet horizontally across the cavity. The impact of this jet on the far cavity wall causes a vertical jet spray to develop in the ventilated wake, visible as a pronounced "rooster tail" projecting above the free surface.

3.1.5 Partially Cavitating Flow Regime

Partial cavitation, as described in chapter I, involves the development of a vapor-filled cavity on a hydrofoil surface at low values of the vaporous cavitation number σ_v. Low cavitation numbers were reached during testing at INSEAN by evacuating air from the test section. Figure 3.8 Partially Cavitating (PC) flow on Model 0. Note that flow is pictured from right to left. Note that near the LE, the cavity is vaporous (hence, $P_c \approx P_v$), while the base cavity at the Trailing Edge (TE) is ventilated ($P_c = P_0$). Thus, the case shown actually constitutes a three-phase flow.

As was also described in chapter I, partial leading edge cavities tend to be highly unsteady. Figure 3.8 by itself does not give a good sense of the unsteadiness of the flow topology, so figure 3.9 shows a time-averaged image of 500 frames, overlaid by contours of variance of pixel-intensity, increasing from blue to white. In other words,

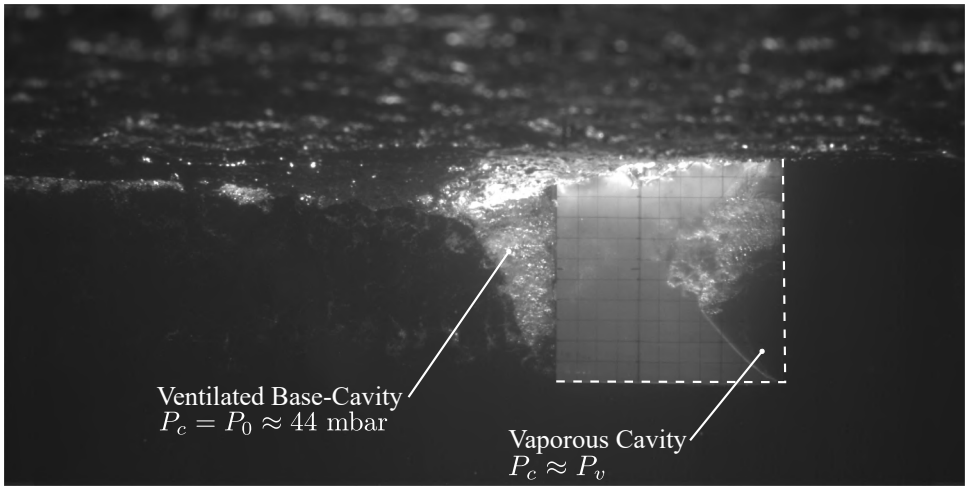

Figure 3.8: Snapshot of PC flow on the surface-piercing hydrofoil at INSEAN. The flow conditions are $\alpha = 5°$; $Fn_h = 2.25$; $AR_h = 1.0$; P_0 =44 mbar; σ_v =0.364.

the contours indicate increasingly unsteady regions, in a visual sense. It should not be surprising that it outlines the vaporous partial cavity, the aerated base cavity, and the free surface. Note, however, that the contour lines do not reach the LE of the hydrofoil. This is because, while the length of the vapor-filled cavity fluctuates significantly, it never sheds off of the hydrofoil in its entirety. Particularly near the tip of the hydrofoil and near the free surface, the local angle of the cavity closure directs the re-entrant jet back toward the middle of the immersed span, so the unsteadiness is concentrated around those sections where the mean cavity length is largest.

The criteria for the four flow regimes may be summarized as,

$D = 0$			Fully wetted (FW) flow
$D = h$	AND	$\bar{\Phi} < 45°$	Fully ventilated (FV) flow
$0 < D < h$	OR	$\bar{\Phi} \geq 45°$	Partially ventilated (PV) flow,
$D = 0$	AND	Water vapor present	Partially cavitating (PC) flow,

where D is the depth of a ventilated cavity, measured along the leading edge from the free surface and $\bar{\Phi}$ is the angle of an affine approximation to the cavity-closure line.

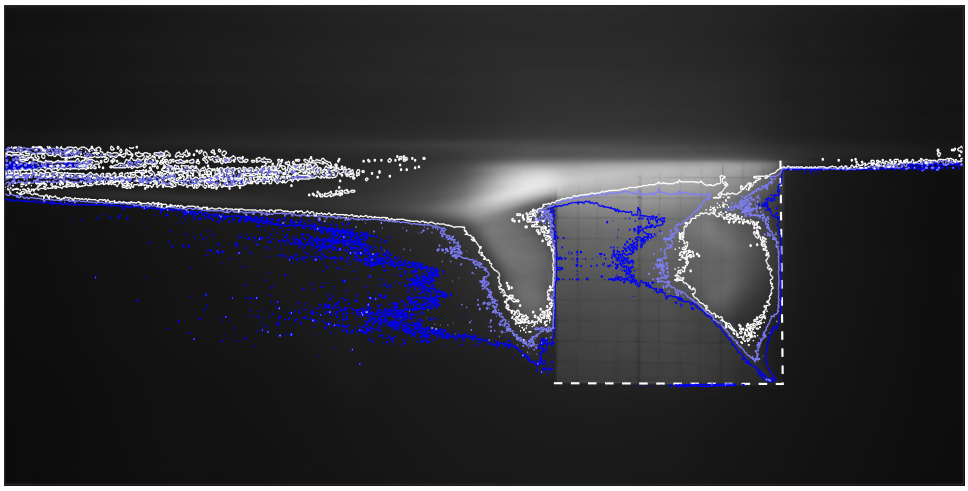

Figure 3.9: Time-average of 500 video frames (1 second of data), overlaid by contours of pixel intensity variance, increasing from blue to white. The variance serves as a metric for the unsteady component of the flow, and indicate the regions in which the base cavity and fluctuating partial cavity are most unsteady.

3.2 Flow Regime Stability

Recall from §1.4 that certain operating conditions are shared by numerous flow regimes, with the result that flow at these conditions can be hysteretic and unpredictable (figure 1.7 illustrates very effectively). The FW, PC, PV, and FV flow regimes are mapped as functions of α and Fn_h for an immersed aspect ratio of $AR_h = 0.5$ in figure 3.10, for $AR_h = 1.0$ in figure 3.11, and for $AR_h = 1.5$ in figure 3.12. Plotted in a parametric space, the collection of points for which a flow is stable will be referred to as that regime's stability region. Points indicate parameter values for which a flow was experimentally observed, and shaded/hatched regions indicate the inferred interior of each stability region. A flow regime is locally or globally stable inside of its stability region, locally stable on the edge of its stability region, and unstable outside of its stability region, so we term the edges of respective regions the stability boundaries. Three distinct stability regions are immediately evident, which overlap in zones 1, 2, and 3. Note that in figure 3.11, the PC region is also dependent upon a third variable σ_v, and so is a projection of a 3-D volume onto the 2-D plane shown rather than a uniquely-defined region in α–Fn_h space.

The overlapping areas in Zones 1, 2, and 3 correspond to the hysteretic conditions of flow referred to by *Fridsma* (1963) as "unstable" and by *Brizzolara and Young* (2012); *Young and Brizzolara* (2013) as "transitional". However, by framing the shaded regions as stability regions, we now understand zones 1, 2, and 3 to be

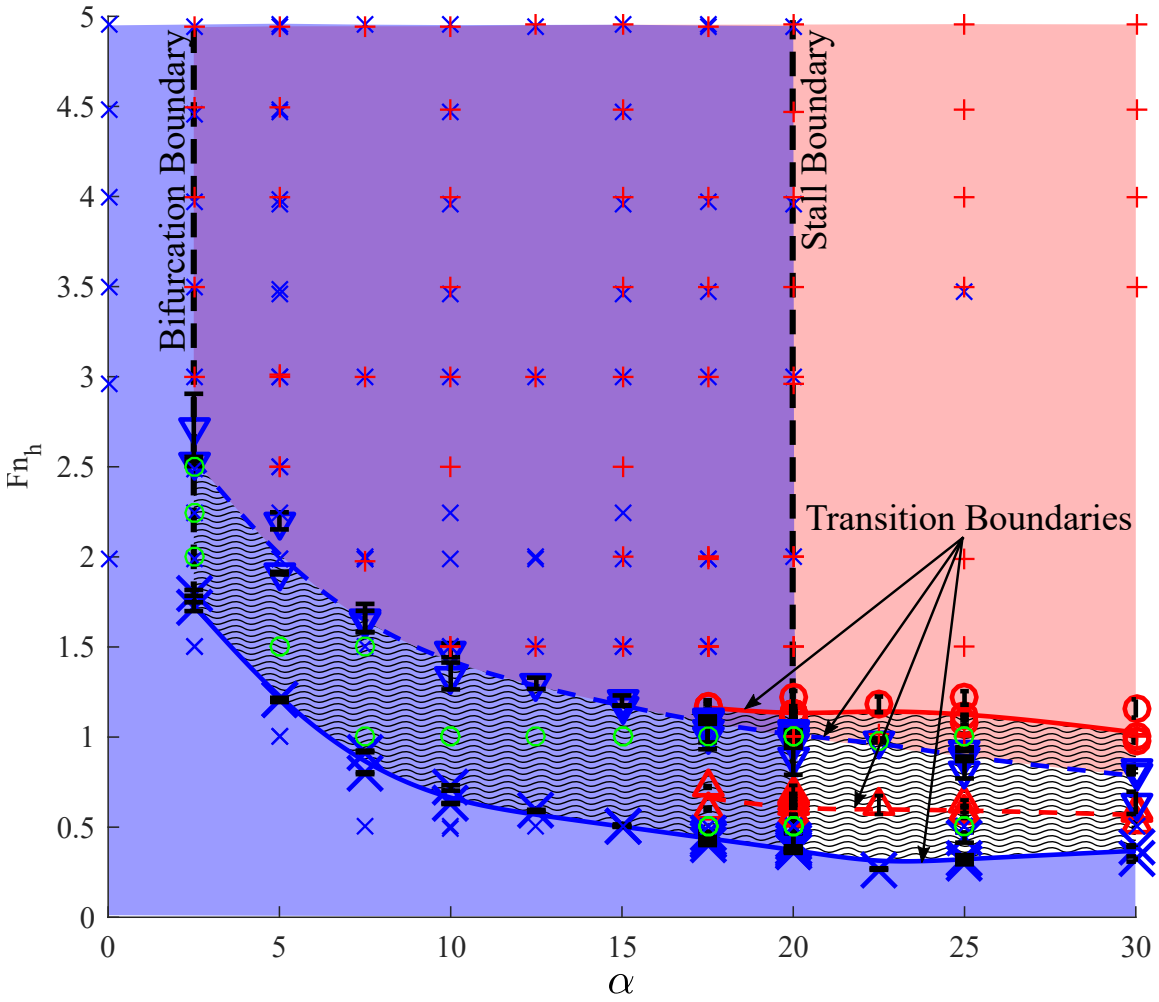

Figure 3.10: (See figure 3.11 for legend.) Stability regions for Aluminum hydrofoil (Model 0) at $AR_h = 0.5$. Data are from testing in the MHL towing tank.

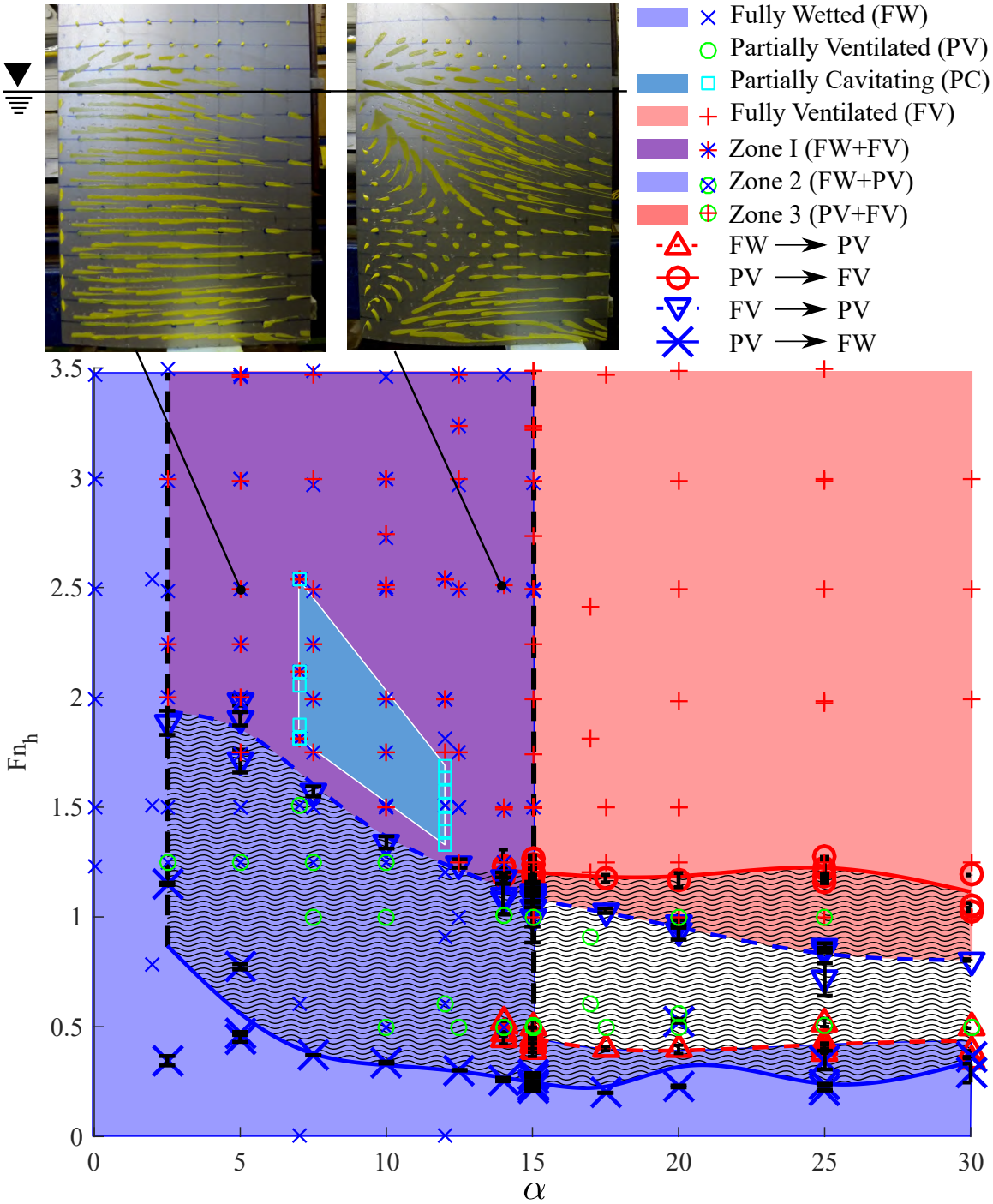

Figure 3.11: Stability regions for Aluminum hydrofoil (Model 0) at $AR_h = 1.0$ Data are aggregated from testing in the MHL towing tank and in the INSEAN cavitation tunnel. PC flow occupies a 3-D volume described by α, Fn_h, and σ_v ($0.37 \leq \sigma_v \leq 1.5$), and is shown projected onto the α–Fn_h plane. Surface flow visualizations at $\alpha = 5°; Fn_h = 2.5$ and $\alpha = 14°; Fn_h = 2.5$ illustrate the effect of α on suction-side flow separation.

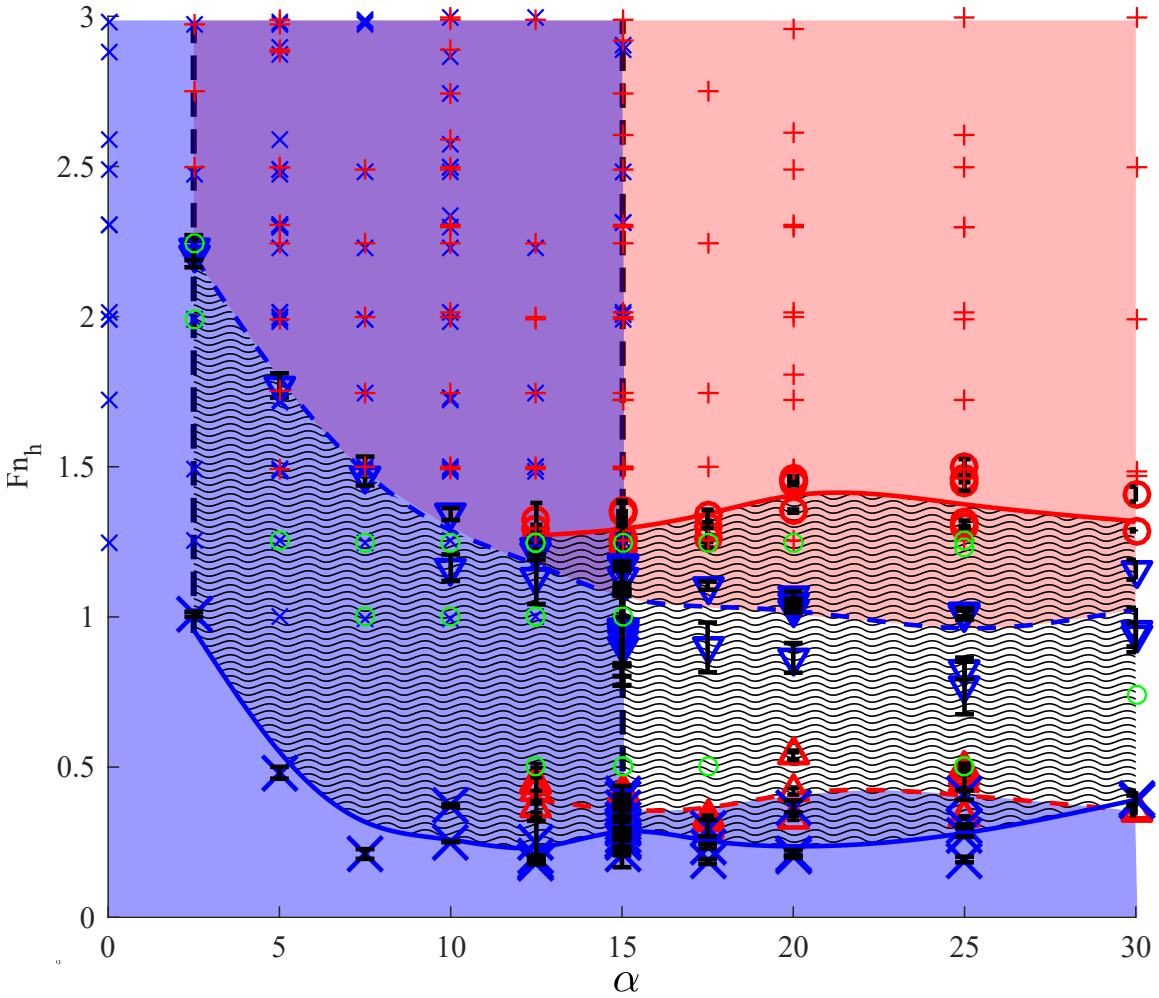

Figure 3.12: (See figure 3.11 for legend.) Stability regions for Aluminum hydrofoil (Model 0) at $AR_h = 1.5$. Data are from testing in the MHL towing tank.

multiply-stable regions. More specifically, they indicate bi-stability. Anywhere inside of Zones 1, 2, or 3, two alternative flow regimes can exist stably. In general, one will be locally stable and the other globally stable.

Three types of boundaries are present in each figure, and are labeled in figure 3.11 for clarity. Bold symbols and fitted curves indicate that some destabilization of one regime (and the stabilization of another) were experimentally observed (the type of destabilization is the topic of chapter IV). These curves are called transition boundaries, and they separate flow regime stability regions primarily along the Fn_h axis. The regimes divided by these curves are indicated in the legend.

The second boundary is the bifurcation boundary, defined as the vertical locus of points separating FW flow from the bi-stable regions and labeled in figure 3.10. In other words, for parameters to the left of the bifurcation boundary, FW flow alone was observed, and FW flow alone is assumed to be stable. To the right of the boundary, the stable flow bifurcates into two locally-stable branches (hence the choice of name). Note that the bifurcation boundary shifts to lower α as Fn_h increases, as shown conceptually in figure 1.7. This is not well-reflected in figures 3.10–3.12 because α was not finely-enough resolved during testing to precisely reconstruct the boundary from the experimental data. As will be shown in § 4.2, the sustain ventilation depends upon both flow separation and minimum pressures. For this reason, it is expected that the shape of the bifurcation boundary in a 2-D space defined by α and Fn_h will vary as a function of the geometry of the hydrofoil being tested.

The final boundary is the stall boundary, made up by the locus of maximum α contained in zone 1 for each value of Fn_h. It is so-named because during experiments, flow along this boundary was strongly separated, and ventilation was inherently tied to the process of stall. The stall boundary is meaningful because it forms a roughly-vertical demarcation between the right-most boundary of bi-stability in zone 1 and the exclusively-stable FV regime. It therefore also indicates the right-most boundary for which FW flow is stable at moderate and large Fn_h.

The bifurcation, stall, and transition boundaries collectively form the assorted *stability boundaries* of their respective regimes. Recall that the review in chapter I revealed that both low pressures and flow separation are required to initiate and sustain a naturally-ventilated cavity. The shapes of the stability boundaries are in perfect agreement with this conjecture. For a sharp-nosed geometry, separation is tied most closely to α (*Gault*, 1957; *Hecker and Ober*, 1974). Surface-flow visualizations (see figure 3.11) show that, in the FW flow regime, wetted flow separation was confined to a leading-edge separation bubble with a length of less than $0.5c$. Visual-

izations also indicate that for all flow conditions at which PV and FV flow occurred (*i.e.* to the right of the bifurcation boundary), ventilation was preceded by some wetted separation at the leading edge. Thus, the bifurcation and stall boundaries respectively indicate those conditions for which sufficient flow separation exists to permit ventilation, and those conditions for which too much flow separation exists to permit wetted flow.

The dynamic pressures on the hydrofoil's suction surface, on the other hand, are primarily dependent upon the flow speed, and we can interpret the approximately-horizontal stability boundaries as indicators of the minimum Fn_h to satisfy the requisite suction pressures. Both PV and FV flow regimes satisfy the condition of flow separation, so the boundary between PV and FV flow regimes is primarily a function of dynamic pressure (and hence Fn_h). Conversely, the boundary between FW flow and any other regime is primarily a function of flow separation (and hence α). An exception is made for very small Fn_h, where suction pressures are not sufficient to cause ventilation, even beyond the stall angle.

Compare the collective transition boundaries shown in figures 3.10, 3.11, and 3.12. Interestingly, the primarily-horizontal transition boundaries appear nearly insensitive to AR_h. Fn_h is proportional to the ratio of dynamic to hydrostatic pressures, so this is reasonable. The consistency of Fn_h along each stability region for different values of AR_h suggests that Fn_h dictates when the dynamic pressure drop along the suction surface is sufficient to negate hydrostatic pressure. Moreover, this allows a concise and intuitive summary to be made of the knowledge we glean from figures 3.10 – 3.12: Ventilation can occur under conditions of sufficient separation (governed primarily by α) and sufficiently low dynamic pressures (governed primarily by Fn_h). A flow to the right of the bifurcation boundary satisfies the first condition, while a flow above a transition boundary satisfies the second condition for the respective flow regime.

3.3 Steady Hydrodynamic Loads

3-D lift, drag, and yawing moment coefficients are defined as,

$$C_{L_{3D}} = \frac{F_Y}{1/2\rho U^2 hc}; \tag{3.3a}$$

$$C_{D_{3D}} = \frac{-F_X}{1/2\rho U^2 hc}; \tag{3.3b}$$

$$C_{M_{3D}} = \frac{M_Z}{1/2\rho U^2 hc^2}. \tag{3.3c}$$

F_X, F_Y, and M_Z are taken with respect to the coordinate system shown in figure 2.2. In the following paragraphs, we will explore how the hydrodynamic loading changes with α, Fn_h, AR_h, and of course, with flow regime. Alternatively, one may speak of how the hydrodynamic response changes with different trajectories through – and between – the domains of figures 3.10, 3.11, and 3.12.

3.3.1 The Effect of Angle of Attack and Flow Regime on Hydrodynamic Loading

When ventilation occurs, most or all of a lifting-surface's suction surface becomes encapsulated in the resulting cavity. The cavity pressure P_c is, by necessity, higher than the local absolute pressure in the prior wetted flow. Suction pressures along the portions of the hydrofoil within the cavity are thus strongly attenuated, with the result that hydrodynamic forces can vary widely from one flow regime to another. Consider a series of horizontal cuts taken through the parametric space defined by α and Fn_h, such as those shown in figure 3.13 at Froude numbers of $Fn_h = 1.5$, $Fn_h = 2.0$, $Fn_c = 2.5$, and $Fn_h = 3$. Steady-state values of $C_{L_{3D}}$, $C_{D_{3D}}$, and $C_{M_{3D}}$ along these cuts are plotted respectively in figure 3.14, figure 3.15, and figure 3.16 for an immersed aspect ratio of $AR_h = 1$. Data from towing tank tests and cavitation-tunnel testing at INSEAN have been aggregated together to populate the figures [1]. All four flow regimes described in the preceding section are present in the figures, though the FW and FV regimes clearly predominate. Note that the bifurcation angle α_b and stall angle α_s correspond to the points where the horizontal cuts cross the bifurcation and stall boundaries. The resulting bi-stability is immediately clear, where the FW and FV regimes occupy overlapping bands of the α axis.

Figure 3.14 shows a distinctive grouping of the lift coefficient $C_{L_{3D}}$ into FW and FV flow regimes. PV and PC data are also present, but are sparse enough that not much information can be inferred from them at this point. The FW and FV data are each fitted by an affine approximation for each angle of Fn_h. In general, lift in the FV regime is significantly lower than that in the FW regime. The slope of the FV data is also reduced, so the difference in lift between the two regimes tends to increase with increasing α. The lift for all four values of Fn_h are approximately co-linear in the FW regime, with the exception of FW and PC data at $Fn_h = 1.5$, where an augmentation of the lift probably results from leading edge wetted and cavitating separation bubbles, respectively. The line fitted to the FV data at each

[1] A misalignment of the flow of occurred in the cavitation tunnel, which caused a bias of $+2^\circ$ in measured data. All data collected in the cavitation tunnel have been shifted up by 2° as a correction.

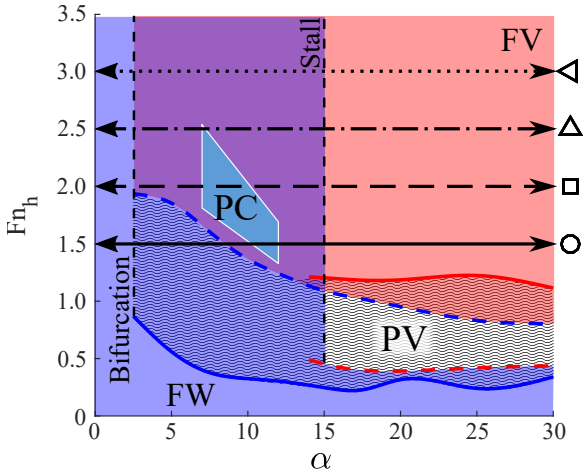

Figure 3.13: Horizontal cuts through α – Fn_h domain at $AR_h = 1.0$. The cuts are made at constant Froude numbers of $Fn_h = 1.5$, $Fn_h = 2.0$, $Fn_c = 2.5$, and $Fn_h = 3$. The line types and symbols correspond to the legend for figures 3.14 through 3.16.

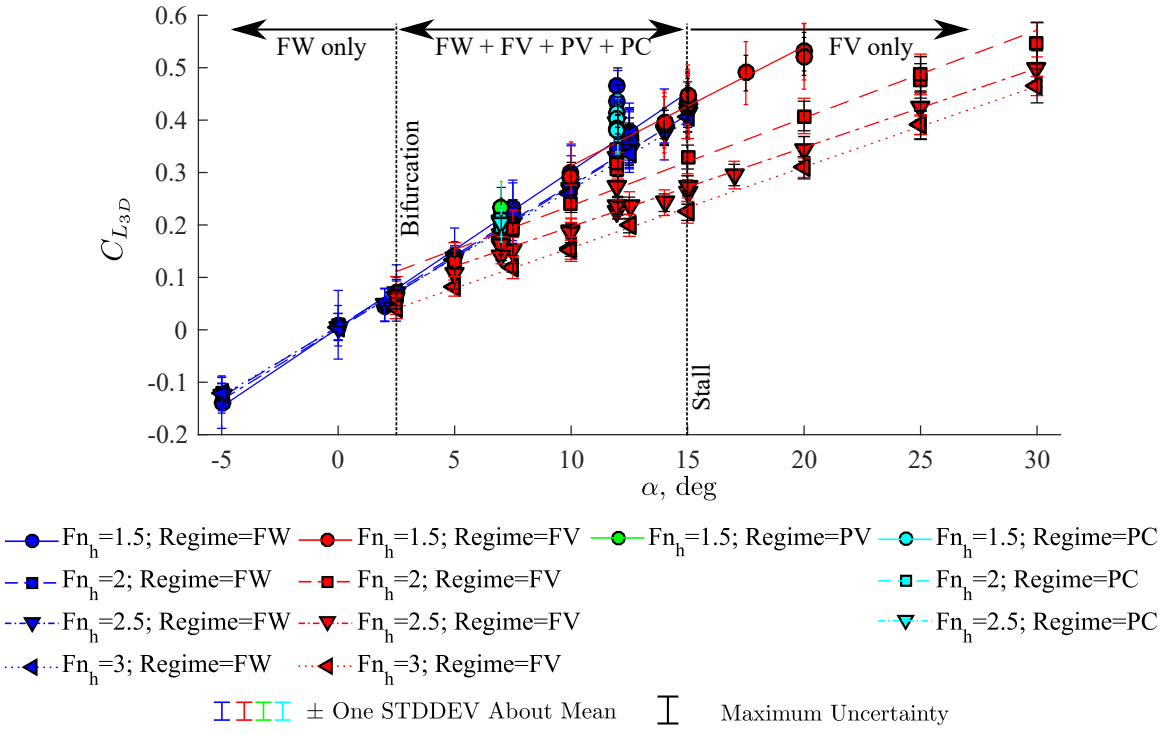

Figure 3.14: Steady $C_{L_{3D}}$ as a function of α for the Aluminum hydrofoil at $AR_h = 1$ and $Fn_h = 2.0$, 2.5, 3.0, and 3.5 (corresponding to the cuts across the stability plane shown in figure 3.13). The data are predominated by the FW and FV flow regimes, which occupy overlapping ranges of α.

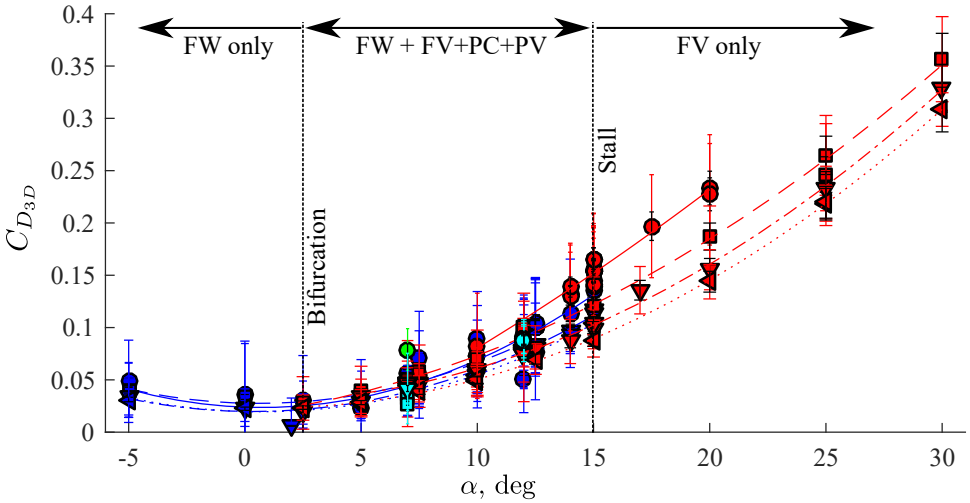

Figure 3.15: Steady $C_{D_{3D}}$ as a function of α for the Aluminum hydrofoil at $AR_h = 1$ and Fn_h = 2.0, 2.5, 3.0, and 3.5. The data are predominated by the FW and FV flow regimes, which occupy overlapping ranges of α. Refer to figure 3.14 for legend.

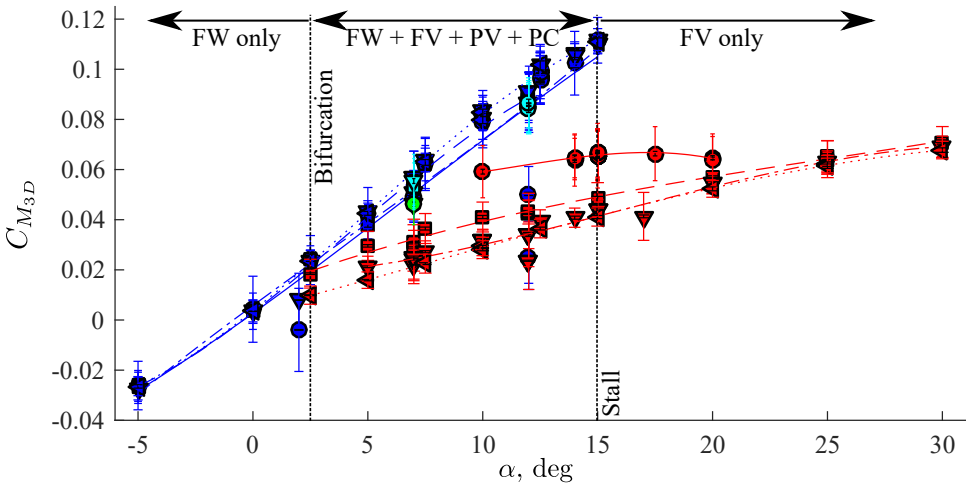

Figure 3.16: Steady $C_{M_{3D}}$ (measured about mid-chord) as a function of α for the Aluminum hydrofoil at $AR_h = 1$ and Fn_h = 2.0, 2.5, 3.0, and 3.5. The data are predominated by the FW and FV flow regimes, which occupy overlapping ranges of α. Refer to figure 3.14 for legend.

Froude number appears to have a non-zero intercept, which has been attributed to a camber-like curvature in the streamlines bounding the hydrofoil and the cavity. This effect will be discussed further in the following section. The FV lift coefficients decrease monotonically with increasing Fn_h. At $Fn_h = 1.5$, the FV data are not much different from the FW and PV data. As the value of Fn_h is increased, the slope of the FV lift coefficient with changing α is reduced and the data are shifted vertically down along the $C_{l_{2D}}$ axis. The change in slope appears to asymptote quickly, and the change in Y-intercept continues to decrease monotonically with increasing Froude number. If the non-zero intercept of the FV data are likened to the effect of camber, then the effect of increasing Fn_h appears to be a decrease in the effective camber.

The drag coefficient $C_{D_{3D}}$ is shown in figure 3.15 for the same set of conditions. All data follow the classic quadratic trend with α. Again, FW and FV results are dominant, while data in the PV and PC flow regimes are neither plentiful nor outstanding enough to merit discussion. Unlike $C_{L_{3D}}$, $C_{D_{3D}}$ is relatively insensitive to the flow regime. A similar observation was made by *Breslin and Skalak* (1959), who suggested that ventilation caused a simultaneous increase in the form drag of a strut and a decrease in the frictional drag. Adding to this assertion, it was observed in *Harwood et al.* (2016c) that the lift-induced component of drag decreases with ventilation as well, since the lift itself is so strongly reduced, while spray drag is probably increased by the generation of large suction-side spray sheets in the FV regime. The decrease in both $C_{L_{3D}}$ and $C_{D_{3D}}$ with increasing Fn_h demonstrates that the lift-induced drag is a dominant component of the total drag. The counteraction of these drag components causes, for the data shown, a minimal net change in total drag with flow regime. It is important to note, however, that because the form drag, induced drag, and frictional drag are all dependent upon the geometry of the lifting-surface in question, this result may not hold for hydrofoils with different section shapes and/or plan forms. Just as with the lift, there is a monotonic decrease in $C_{D_{3D}}$ with increasing Fn_h in the FV regime only.

The yawing moment coefficient, $C_{M_{3D}}$, measured about the mid-chord axis and defined positive "nose-up" (in the direction of positive α), is shown in figure 3.16. The FW data follow an approximately-linear relationship with respect to α. The FV data exhibit a significant reduction in $C_{M_{3D}}$, compared to the wetted data. This is partly due to the reduction in $C_{L_{3D}}$ shown in figure 3.14, and is compounded by the movement of the center of pressure towards the mid-chord. The result is a sub-linear trend in $C_{M_{3D}}$ with respect to changing α. Here, more than in the preceding two figures, data at $Fn_h = 1.5$ appears anomalous. Rather than grouping into the FV

data, it appears to bridge the FW and PV data at small values of α to the FV data at larger α. The FV lift coefficients in figure 3.14 at $Fn_h = 1.5$ are approximately collinear with the FW values, so the behavior of $C_{M_{3D}}$ is probably isolated to the movement in the pressure center from near the quarter-chord location in FW flow toward the mid-chord location in FV flow. There is a decreasing trend in $C_{M_{3D}}$ with increasing Fn_h in the bi-stable band only, but the different Froude numbers collapse together as α is increased.

Let us now focus on the behavior of $C_{L_{3D}}$ in an expanded parametric space. In figure 3.17, $C_{L_{3D}}$ is plotted as a function of α at values of Fn_h between 0.5 and 3.5, creating a response-surface representation of $C_{L_{3D}}$ in the FW and FV regimes. The figure can be thought of as a combination of figure 3.11 and figure 3.14, focusing on the two dominant flow regimes. PV data are also present in figure 3.17, however the $C_{L_{3D}}$ contours and surface-fit are omitted for the PV regime to avoid over-crowding. PC data have here been omitted because their projection onto the 3-D surfaces would confuse the figure further.

In the FW regime, the $C_{L_{3D}}$ contours are parallel to the Fn_h axis for $Fn_h > 1$, indicating that $C_{L_{3D}}$ is speed-dependent only at very low speeds. For $Fn_h \leq 1$, the Reynolds numbers are low ($Re_c \leq 5 \times 10^5$), resulting in leading-edge laminar separation, which in turn causes a characteristic increase in lift (*Breslin and Skalak*, 1959). In the FV regime, lift monotonically decreases with increasing Froude number at a fixed angle of attack, made apparent by the curvature of $C_{L_{3D}}$ contours in the FV regime, consistent with the observations from figure 3.14. Affine fits through the $C_{L_{3D}}$ values in the FW and FV flow regimes with respect to α are shown as dotted lines. As a result of the non-zero intercept of the FV affine fits, the fitted lines intersect with those of the FW regime. Cross-hatched circular markers indicate the intersection between the fully wetted and fully ventilated affine data fits at each respective value of Fn_h. Thus, they indicate where lift coefficients in the two overlapping flow regimes are approximately equal. The dependence of $C_{L_{3D}}$ upon Fn_h in the FV regime leads to intersection points at increasingly large angles of attack as the Froude number is decreased. Orthographic projections of this locus are made onto the α – Fn_h and Fn_h – $C_{L_{3D}}$ planes and are shown as black dashed lines in figure 3.17. These projections will be used later in chapter IV.

Recall that the bifurcation angle is defined for a given Froude number as the angle below which FW flow was the sole flow regime observed during experiments. In figure 3.17, the bifurcation boundary from figure 3.11 is shown as a solid black line, clearly demonstrating what the associated bifurcation of $C_{L_{3D}}$ looks like. The

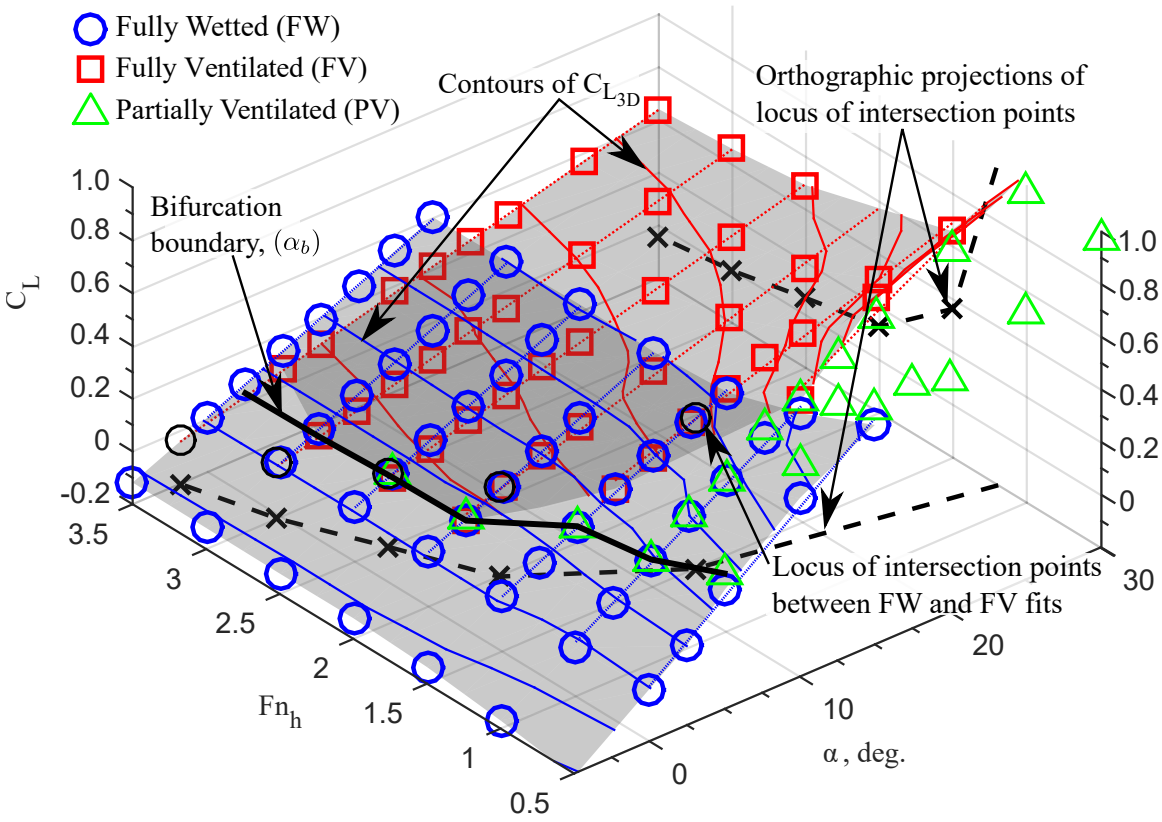

Figure 3.17: $C_{L_{3D}}$ surface as a function of α and Fn_h for $AR_h = 1$. Contours of constant $C_{L_{3D}}$ are shown as solid lines in the FW and FV regimes (the PV surface and contours are omitted for clarity). $C_{L_{3D}}$ is a strong function of Fn_h in the FV regime, where for a fixed α, $C_{L_{3D}}$ decreases as Fn_h increases. At low speeds ($Fn_h \leq 1$), laminar separation occurs at the accompanying low Reynolds numbers ($Re_c \leq 5 \times 10^5$), causing an increase in $C_{L_{3D}}$ in the FW regimes. Affine fits of $C_{L_{3D}}$ as a function of α are shown as dotted lines at each Fn_h, with the intersection between the FW and FV fits indicated by cross-hatched circles. The dashed lines are orthographic projections of the locus of intersection points onto the α - Fn_h plane and the Fn_h - $C_{L_{3D}}$ plane. A heavy solid line indicates the locus of bifurcation angles (α_b), forming a bifurcation boundary, below which only FW flow was observed. Figure reproduced from *Harwood et al.* (2016c).

bifurcation boundary takes on a value of $\alpha_b \approx 2.5^\circ$ at $Fn_h \geq 2$, and increases along the α-axis with decreasing values of Fn_h for $Fn_h < 2$. In the neighborhood of α_b, values of $C_{L_{3D}}$ in the FW, FV, and (where applicable) the PV regimes are nearly-coincident. This observation suggests that the suction surface pressures of the wetted flow near α_b are only mildly sub-atmospheric, so that ventilation formation does not materially affect the magnitude of suction surface pressures. Reinforcing this hypothesis, the intersection of the affine curve-fits approximates the bifurcation angle (α_b) at each value of Fn_h.

3.3.2 The Effects of Froude Number and Aspect Ratio Upon Hydrodynamic Loading

This section will continue to explore the ways in which altering the Fn_h affects the resultant load coefficients on the hydrofoil. Additionally, the effects of the immersed aspect ratio AR_h will be examined. A comprehensive collection of the lift, drag, and moment coefficients for most experimental combinations of Fn_h and AR_h follows in figures 3.18, 3.19, and 3.20. First, consider the locations of the stall boundaries. The stall angle is $\alpha_s = 20^\circ$ for $AR_h = 0.5$, and $\alpha_s = 15^\circ$ for $AR_h > 0.5$, supporting the observation made earlier regarding the stability regions. Within each value of AR_h, the stall boundary is independent of the Froude number. Second, the observation continues to hold that the lift, drag, and moment coefficients decrease monotonically with increasing values of Fn_h in the FV regime only. At the lowest values of Fn_h, FV and PV lift and drag coefficients are actually larger than those in the FW regime. At these same Froude numbers, $C_{M_{3D}}$ appears once again to smoothly bridge the FW and FV data. Increasing Fn_h causes the FV data to evolve toward what appears to be an asymptotic limit in each case. Finally, the difference in loading between the FW and FV regimes (especially $C_{L_{3D}}$ and $C_{M_{3D}}$) becomes more pronounced as the immersed aspect ratio increases. The change in lift-slope, in particular, appears to be very sensitive to AR_h. At $AR_h = 0.5$, the slope of the FW and FV lift coefficients are similar. For AR_h, the slope in the FV regime is substantially lower than that in the FW regime.

Let us first confront the question of why the hydrodynamic load coefficients decrease with increasing Fn_h in the FV regime only. Consider a surface piercing hydrofoil with an attached cavity. It has been demonstrated at this point that the cavity length changes along the submerged span as a function of spanwise variation in σ_c (due to the hydrostatic pressure gradient) and sectional angles of attack α_{eff}. Consider now a sectional cut taken through a representative section of the hydrofoil,

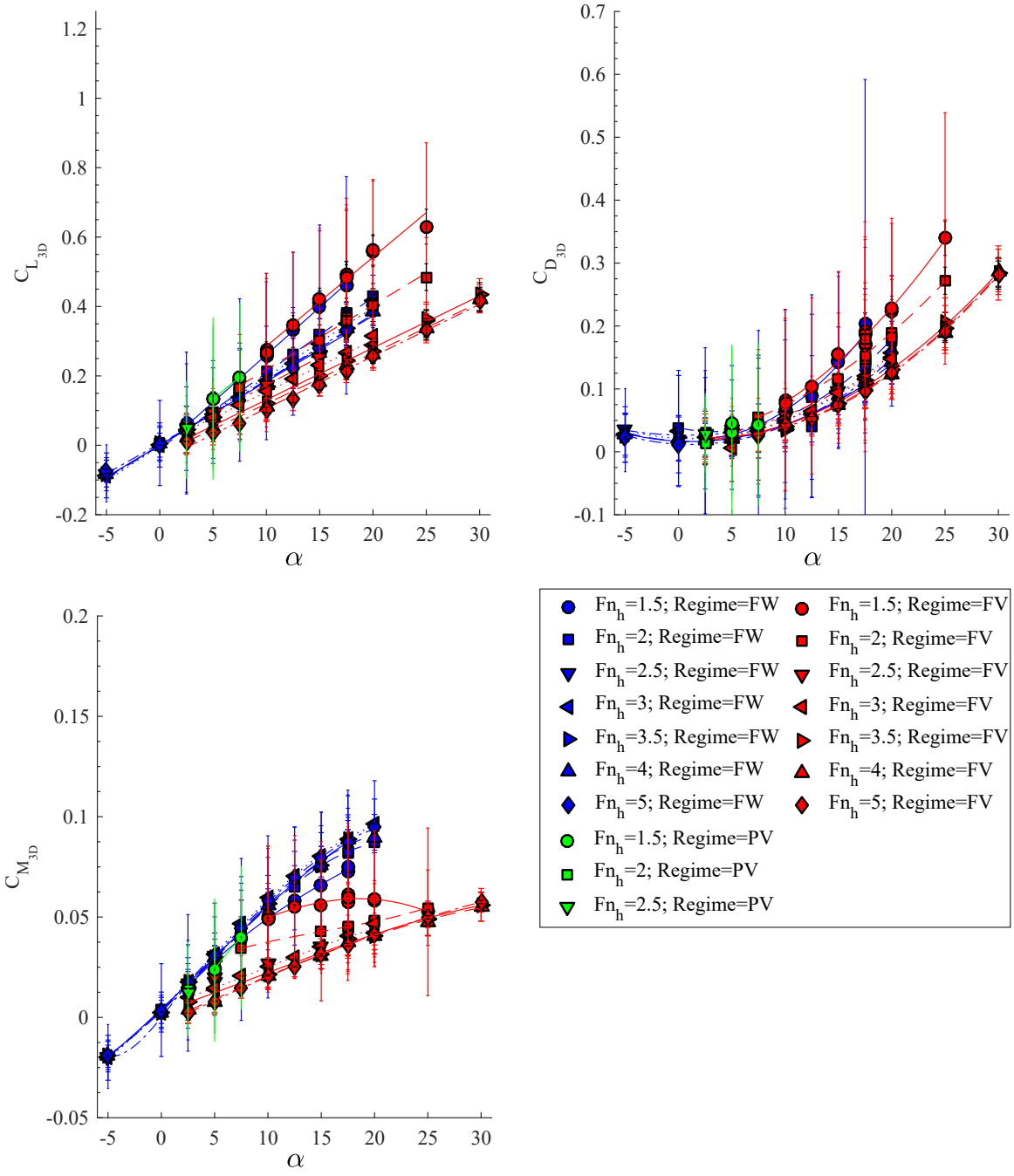

Figure 3.18: Hydrodynamic load coefficients as functions of α and Fn_h for $AR_h = 0.5$.

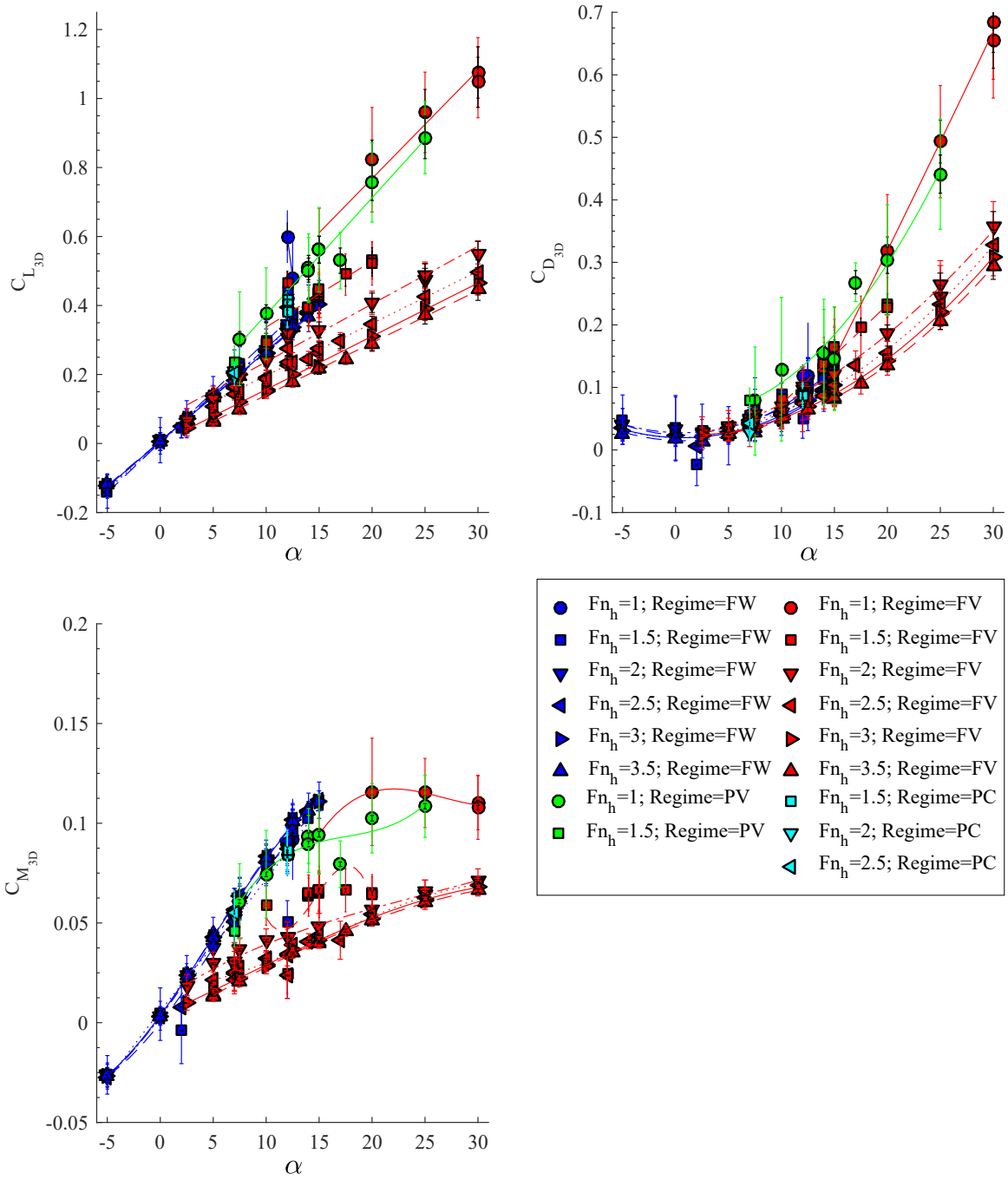

Figure 3.19: Hydrodynamic load coefficients as functions of α and Fn_h for $AR_h = 1$.

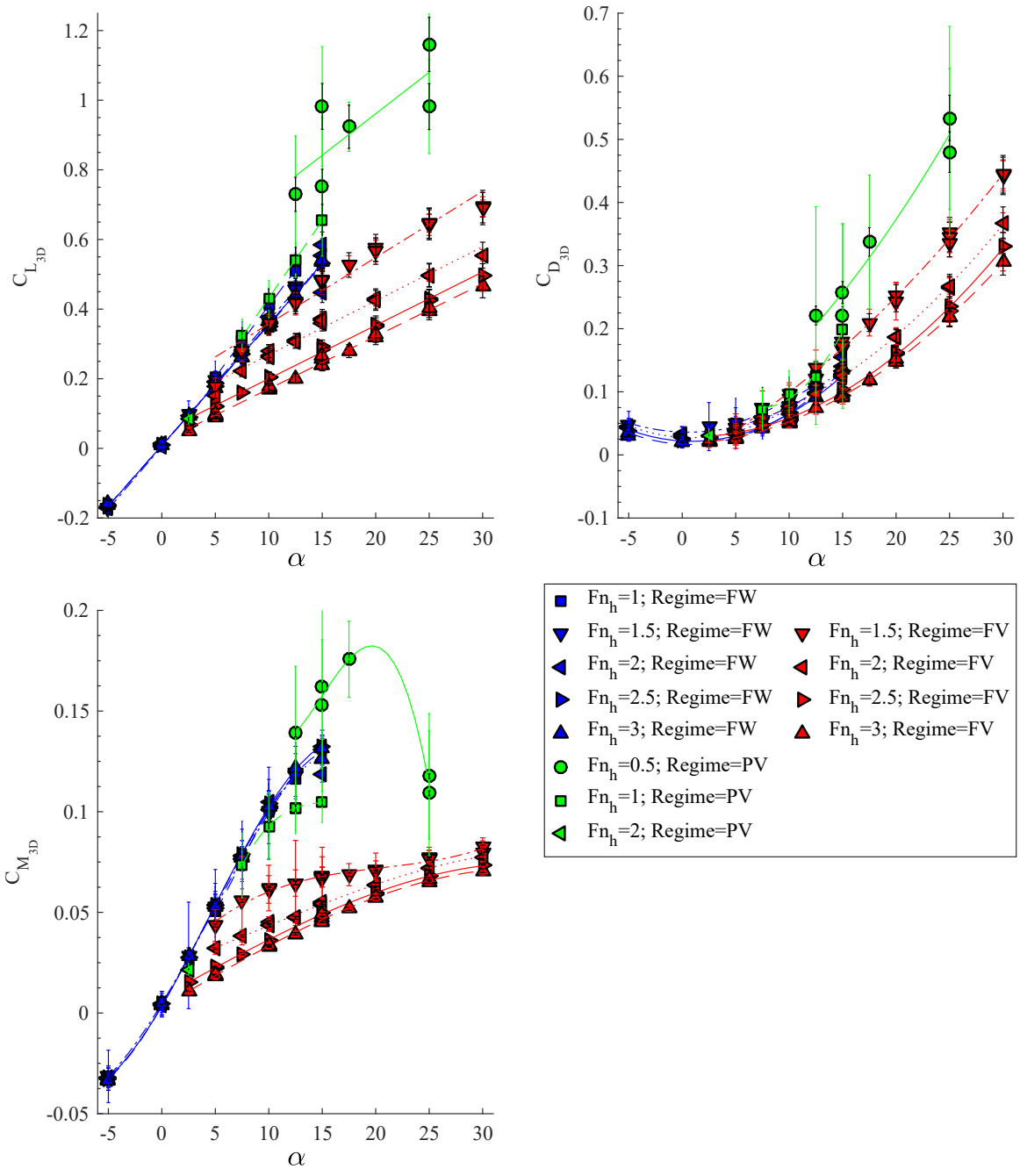

Figure 3.20: Hydrodynamic load coefficients as functions of α and Fn_h for $AR_h = 1.5$.

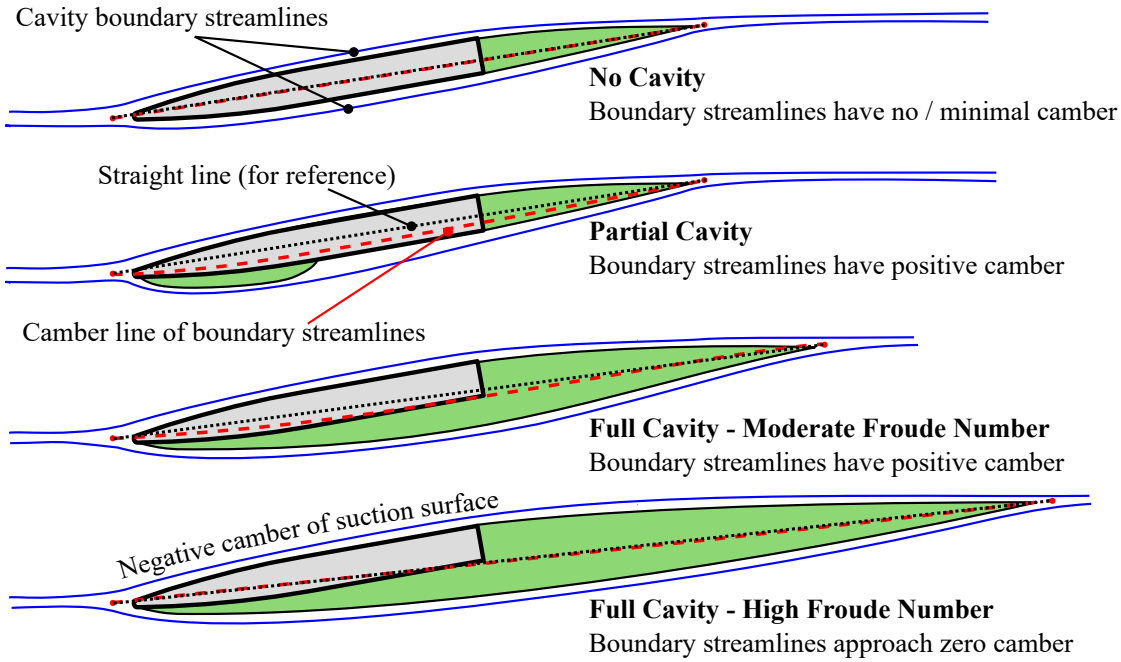

Figure 3.21: Illustration of effective camber of cavitating hydrofoil section with changing Froude number. The black dotted line is the effective nose-tail line of the hydrofoil section and cavity. The red dashed line is the camber line formed by the bounding streamlines.

depicted in figure 3.21 in 2-D regimes including fully wetted flow, partially cavitating flow, and two variations of supercavitation. Recall that the generalized cavitation number at a section σ_c varies with ${Fn_h}^{-2}$, so an increase in Froude number begets a longer cavity. In fully wetted flow, the geometric camber of the section is zero, *i.e.* the red dashed line and black dotted line in figure 3.21 are coincident. If some wetted flow separation exists (which occurs at low values of Re_c), then some positive effective camber may result in the boundary streamlines. It is a well-documented phenomenon that leading-edge laminar separation bubbles augment a section's lift by increasing the effective camber.

Now consider the lift on a hydrofoil suction as a leading edge partial cavity develops. The same augmentation of the lift applies to vapor cavities as to laminar separation, so the limited leading edge cavity will induce some positive camber on the hydrofoil, thus augmenting its lift. However, when a body with a finite thickness (such as the semi-ogival section in question) ventilates, the suction-side cavity effectively hides the curvature of the foil section's suction side, while exposing the convex curvature of the pressure side to the external flow. As a result, the suction-side flow increasingly resembles that of a cavitating flat plate as the sectional cavity lengths

increase and the suction force developed over its convex curvature is negated. The wetted pressure side may simultaneously develop significant suction force as a result of its convex curvature, the effect of which is to negate some of the positive lift developed by the positive incidence angle of the hydrofoil. In doing so, the pressure-surface can be thought to contribute some negative value toward the effective camber of the section. This phenomenon was noted first by *Breslin and Skalak* (1959), who likened it to the suction developed on the spoon-shaped bows of early seaplane hulls. Thus, there are two opposing factors in the effective camber of the section: the positive effective camber induced by the curvature of streamlines around the cavity, and the negative effective camber created by the convex curvature of the suction surface.

At large values of Fn_h, the representative section will become supercavitating. The locus of points midway between the bounding streamlines describes the effective camber line (the red dashed line in figure 3.21), the curvature of which will begin to approach zero. As the cavity's trailing edge extends further and further downstream, it becomes less and less sensitive to changes in the cavity length, and thus less sensitive to the value of Fn_h as the cavity becomes symmetric. The negation of lift by the convex suction surface, however, remains. Thus, the total effective camber of the section may actually become negative. At large Froude numbers and small positive yaw angles, the direction of lift may even become reversed – a case that was not observed in the present experiments, but which was reported by *Breslin and Skalak* (1959); *Rothblum et al.* (1969).

The amount of camber directly affects the developed lift. The moment, however, also depends upon the line of action of the lift, which occurs through the center of pressure. As a cavity grows in length, the location of the resultant lift will move aft from a location at approximately $0.25c$ aft of the LE to a location near mid-chord. As a result, we expect the yawing moment about the mid-chord of the hydrofoil to follow the same general trend as does the lift, but with some additional nonlinearity caused by the motion of the pressure center. The effect of the changing cavity shape upon the drag should be much less pronounced, since the projected area of the supercavity isn't much altered by the Froude number. Instead, the decrease in $C_{D_{3D}}$ with increasing Fn_h is attributed to a decrease in the lift-induced drag, and thus follows from the behavior of the hydrodynamic lift.

Consider two more cuts through the stability plane in figure 3.11, this time taken vertically at $\alpha = 10°$ and $\alpha = 25°$, as shown in figure 3.22. $C_{L_{3D}}$, $C_{D_{3D}}$, and $C_{M_{3D}}$ along these cuts are plotted in figure 3.23 for $AR_h = 1.0$. FW, FV, and PV data are present. Note that, although the $\alpha = 10°$ cut passes through the PC results, no

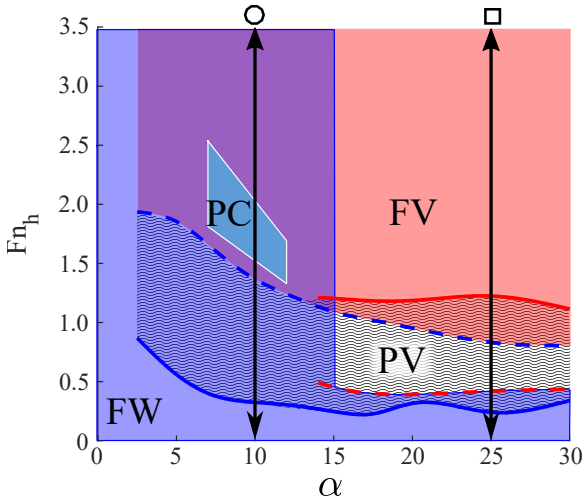

Figure 3.22: Horizontal cuts through α – Fn_h domain at $AR_h = 1.0$. The cuts are made at constant yaw angles of $\alpha = 10°$ and $\alpha = 25°$. The symbols at the end of the cuts correspond to the legend in figure 3.23.

steady-state data were collected at that angle of attack. Viewing the hydrodynamic loads as functions of Fn_h reinforces the conjectures made up to this point. All three hydrodynamic loads are well-separated between the two values of α. At very low values of Fn_h, the lift and moment are augmented by either wetted laminar separation (FW) or the development of a LE partial cavity (PV). Additionally, the lift and moment in the PV regime exceed those in the FW regime at small Froude numbers, though so much fluctuation was present that the measurement standard deviations are quite large. As Fn_h increases, $C_{L_{3D}}$, $C_{D_{3D}}$ and $C_{M_{3D}}$ in the FW regime approach a constant value; for $Fn_h \gtrsim 1.0$, hydrodynamic load coefficients in the FW regime are constant. In the FV regime, all hydrodynamic load coefficients monotonically decrease, but with at a decreasing rate, so they appear to be approaching an asymptotic limit.

One final set of plots will be useful to combine the preceding insights and highlight the effects of AR_h and Fn_h upon the hydrodynamic lift in particular. As described, affine fits were performed through all FW and FV lift coefficients (PV and PC data were too sparse to yield good-quality fits). The slopes of the affine fits ($\partial C_{L_{3D}}/\partial\alpha$) are plotted in figure 3.24 as functions of AR_h and Fn_h in both flow regimes. The intercepts of the affine fits of $C_{L_{3D}}$ (C_{L_0}) are similarly show in figure 3.25.

First, consider figure 3.24. The slope in the FW regime increases with AR_h, which follows logically from finite-aspect ratio effects described by *Prandtl* (1918); *Glauert* (1943); *Faltinsen* (2005), among others. Conversely, the slope in the FV regime is almost entirely independent of AR_h. This can be explained by considering the way

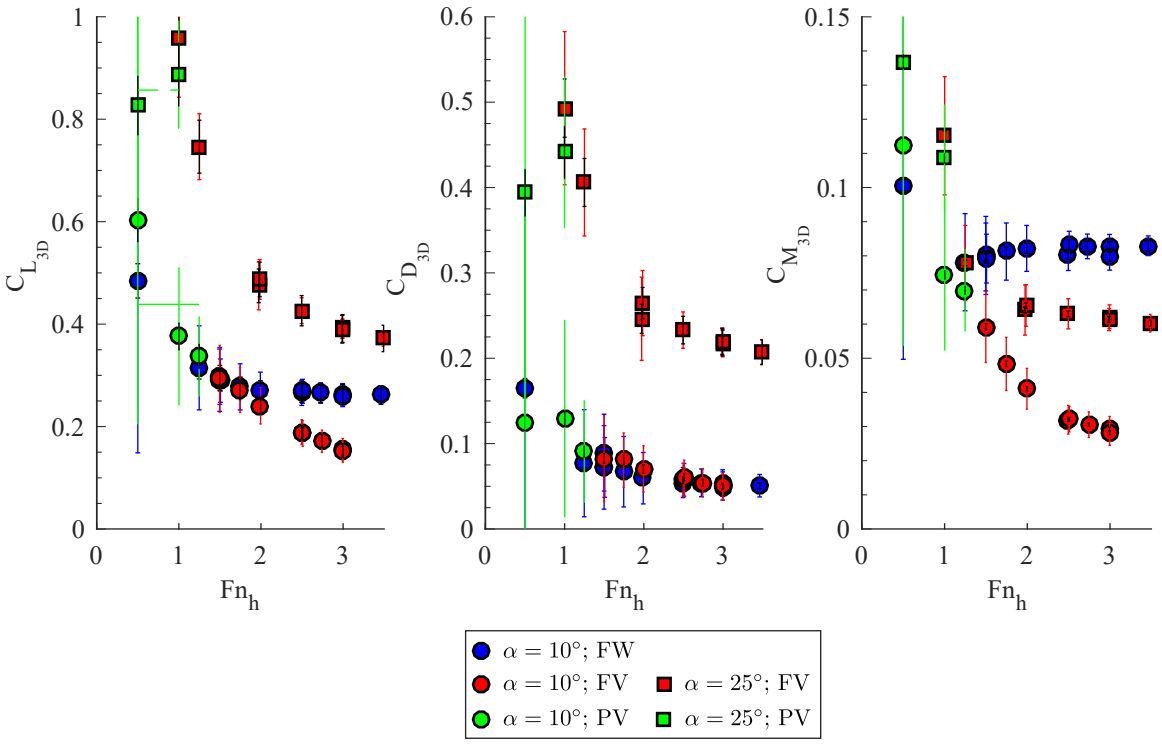

Figure 3.23: Froude number effect on steady hydrodynamic force coefficients

in which finite-aspect-ratio effects occur. FV flow brings with it reduced loading, compared to the FW regime. Thus, the induced downwash and cross-flow effects that underpin the attenuation of lift for wings and hydrofoils of finite aspect ratio are not so strong in FV flow as in FW flow, and the 3-D effects themselves are suppressed. It follows logically from these observations that the reduction in lift from FW to FV flow is more dramatic when the aspect ratio is higher – a fact that was earlier observed with reference to figures 3.18-3.20.

Next, consider the Y-intercept in figure 3.25. The Y-intercept of $C_{L_{3D}}$ is, in linear foil theory, indicative of the amount of effective camber. Naturally, we see that for FW flow, all of the data fall near zero because the hydrofoil model possesses no geometric camber, so $C_{L_0} = 0$. However, in the FV flow regime, the result is much different. The data for the three aspect ratios collapse together sufficiently well to envision a single curve passing through all three sets of data. The preceding conjectures hold once again. In the FV regime, the effective camber of the hydrofoil's bounding streamlines is positive at low and moderate values of Fn_h. As the Froude number is increased, the effective camber decreases monotonically. At the three highest values of Fn_h, the apparent camber becomes negative.

To summarize, the Froude number alters the length and symmetry of the cavity

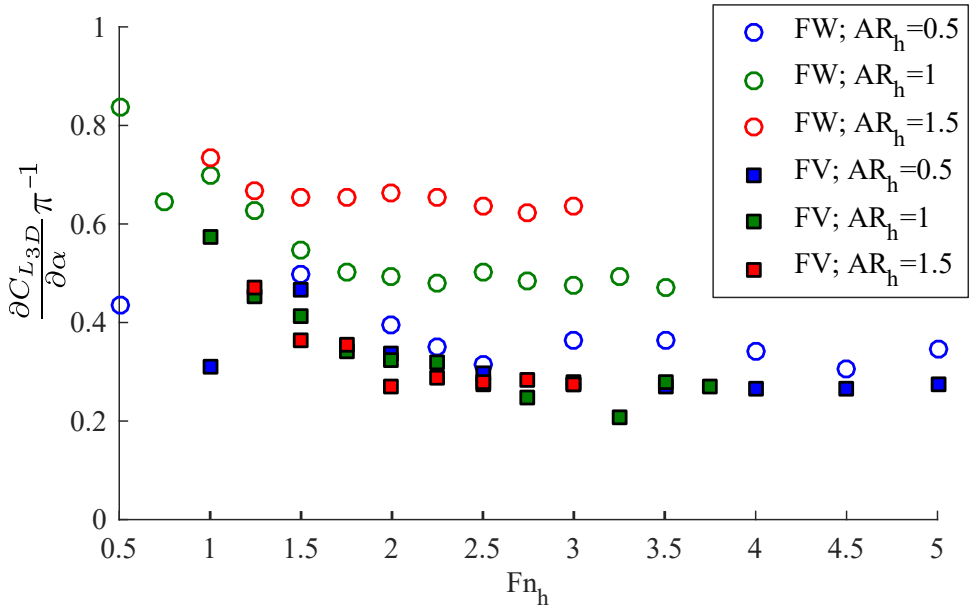

Figure 3.24: Lift-slope $\partial C_{L_{3D}}/\partial\alpha$ as a function of Fn_h for $AR_h = 0.5, 1.0, 1.5$. Slopes correspond to the affine fits to experimental data.

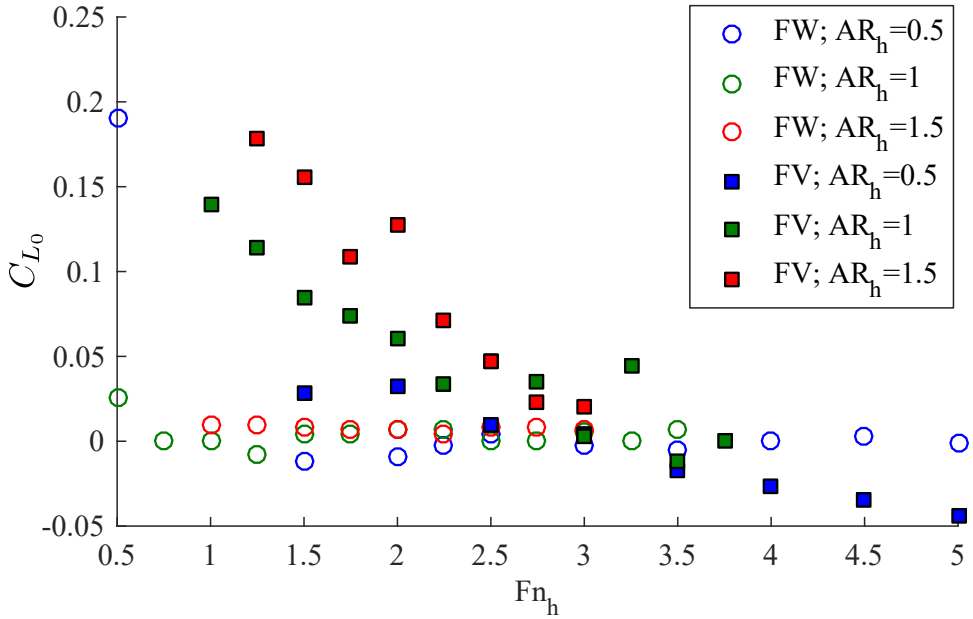

Figure 3.25: Y-intercept of fitted $C_{L_{3D}}$ as a function of Fn_h. The data demonstrate that for FV data only, an increase in Fn_h has an effect of reducing the apparent camber presented by the combined foil and camber.

to modify the effective camber of the hydrofoil in the FV regime. At large Froude numbers ($Fn_h \gtrsim 4$), the effective camber of the hydrofoil becomes negative. The effective camber scales approximately with Fn_h and is only mildly dependent upon the value of AR_h. The stall angle is larger and the effect of ventilation upon all of the hydrodynamic loads is less dramatic for $AR_h = 0.5$ than for $AR_h = 1$ and $AR_h = 1.5$. In the FV flow regime, the de-loading of the hydrofoil suppresses 3-D effects, so the slope of the lift coefficient becomes insensitive to the aspect ratio.

3.3.3 The Effect of General Cavitation Number Upon Hydrodynamic Loading

Figures 3.26, 3.27, and 3.28 show the values of $C_{L_{3D}}/(\pi\alpha)$, $C_{D_{3D}}/(\pi\alpha^2)$, and $C_{M_{3D}}/(\pi\alpha)$, respectively, plotted against σ_c/α. Note that the generalized cavitation number has been defined at the mid-span section, and the value P_c is specified as a function of the flow regime, as follows:

$$\sigma_c = \sigma_v + \frac{1}{{Fn_h}^2} \qquad \text{FW and PC flows}$$

$$\sigma_c = \frac{1}{{Fn_h}^2} \qquad \text{PV and FV flows.}$$

In figure 3.26, the data for all four flow regimes collapse along a curve reminiscent of the two-dimensional theory in chapter I, which demonstrates that the cavitation parameter is very effective at scaling the lift of cavity flows, regardless of the composition of the cavity. In the FV regime, there is some additional scatter caused by the apparent camber effect described in the preceding section. At the limit of small σ_c/α, the data approach a value of $C_{L_{3D}}/(\pi\alpha)$ equal to approximately 50% the value of that at the limit of large σ/α – a departure from the 2-D theory, which suggests that the lift in the supercavitating regime should approach one-quarter the value achieved in fully wetted flow. This departure from the 2-D result is consistent with the observation made in the preceding section that the effects of the finite aspect ratio are suppressed by the reduction of sectional $C_{l_{2D}}$ values in the FV flow regime. It is also interesting to note that data collected in the PC flow regime collapse along the same curve as the ventilated data, and occupy a region roughly coincident with that of PV flow, and there is very little overlap with the FV flow regime. These observations lead us to conclude that sufficiently-small values of σ_c/α cause a vaporous cavity to become unstable, leading to atmospheric ventilation and FV flow.

The scaling of $C_{D_{3D}}$ in figure 3.27 is more scattered, but we still see values grouped

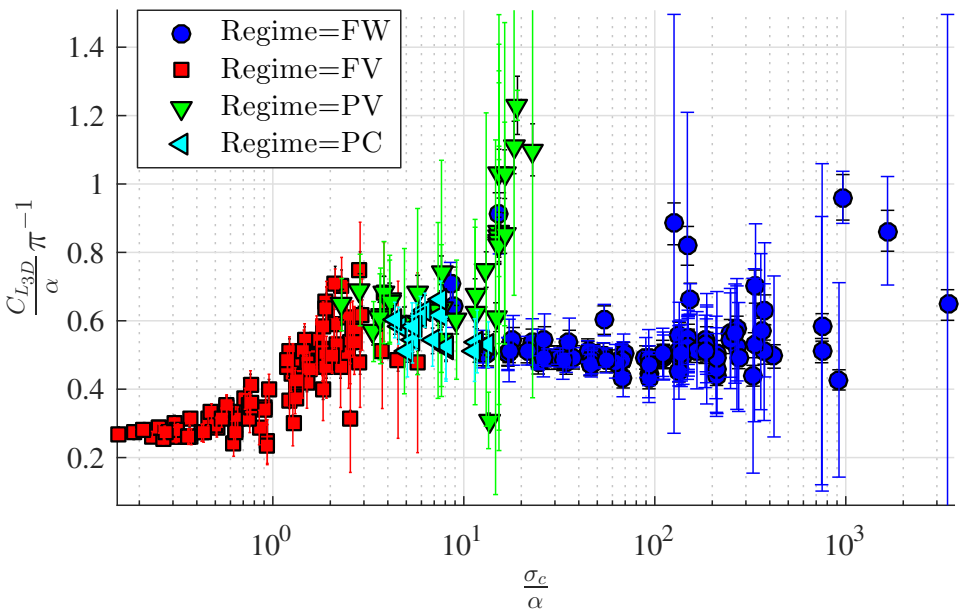

Figure 3.26: $C_{L_{3D}}/(\alpha\pi)$ plotted against σ_c/α for FW, PV, FV, and PC flow regimes on model 0 at $AR_h = 1.0$.

by flow regime. Significantly, we see that there is no obvious difference in the drag between the four flow regimes for values of $\sigma_c/\alpha \gtrsim 1$. As the cavitation parameter is reduced, however, a consistent decrease in the curvature of $C_{D_{3D}}$ is evident.

Figure 3.28 demonstrates another striking collapse of experimental data for all four flow regimes. Comparison of figures 3.26 and 3.28 reveals that the center of pressure must be moving toward the mid-chord position as the cavitation parameter decreases.

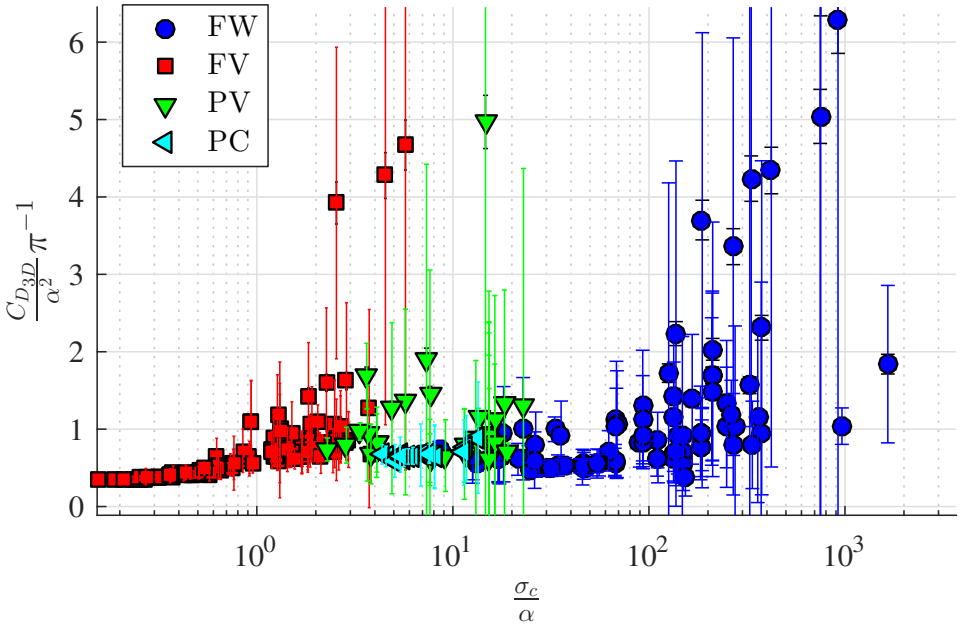

Figure 3.27: $C_{L_{3D}}/(\alpha\pi)$ plotted against σ_c/α for FW, PV, FV, and PC flow regimes on model 0 at $AR_h = 1.0$.

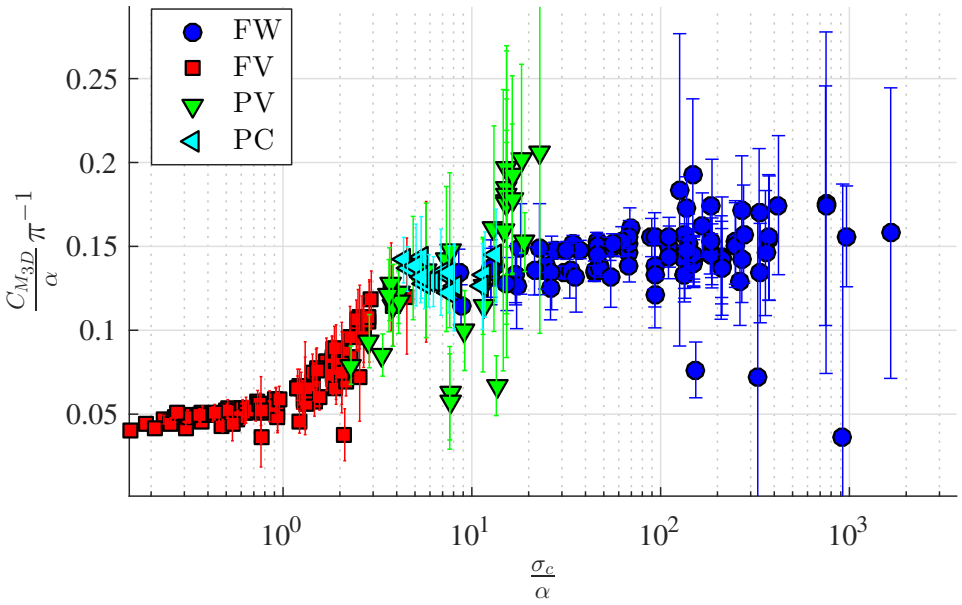

Figure 3.28: $C_{L_{3D}}/(\alpha\pi)$ plotted against σ_c/α for FW, PV, FV, and PC flow regimes on model 0 at $AR_h = 1.0$.

3.4 Modeling of the Cavity Flow

In this section, a simple model will be developed to describe the dominant features of wetted and ventilated flows on the surface piercing hydrofoil. The approach is based upon the classic lifting-line theory of *Prandtl* (1918); *Glauert* (1943).

3.4.1 Low-Fidelity Model: Linear Lifting Line Formulation

The Kutta-Joukowski theorem,

$$l(Z) = \Gamma(Z)U(Z)\rho \tag{3.4}$$

may be applied in a section-plane of a 3-D wing to yield the sectional lift-per-unit-span, $l(Z)$, as a function of the sectional bound vorticity strength, $\Gamma(Z)$, and inflow velocity component normal to the lift, $U(Z)$. Note that all quantities are here made a function of Z, which is the coordinate measured along the span of the hydrofoil. According to Helmholtz's second theorem, the change in bound vorticity from one section to the next must be accompanied by the shedding of a trailing vortex filament; the aggregate of the spanwise circulation gradient is a trailing vortex sheet, which in turn induces downwash in neighboring section-planes, reducing their effective angles of attack. This sets up the fundamental problem, wherein the interplay of circulation and downwash must be resolved.

3.4.1.1 Governing Equations

Glauert (1943) presents the following governing equations relating the induced downwash velocity, $v(Z)$, and bound circulation, $\Gamma(Z)$:

$$v(Z) = \int_0^S \frac{\frac{\partial\Gamma(\zeta)}{\partial\zeta}}{4\pi(\zeta - Z)}\partial\zeta, \tag{3.5}$$

and

$$\Gamma(Z) = \frac{c(Z)}{2}\left[a_0\left(U(Z)\alpha_{2D}(Z) - v(Z)\right) + C_{l_0}U(Z)\right], \tag{3.6}$$

where S is the span, a_0 is the slope of the 2-D lift curve, α_{2D} is the local (sectional) geometric angle of attack, U is the local velocity of the inflow (relative to which the angle of attack is measured), and C_{l_0} is the 2-D lift coefficient at $\alpha_{2D} = 0°$. Downwash is the name given to the induced component of velocity, v. Quantities are signed with respect to the coordinate system The two equations may be combined

into the fundamental integral equation for the circulation distribution, which must be satisfied at all points on the lifting-line:

$$\int_0^S \frac{\frac{\partial \Gamma(\zeta)}{\partial \zeta}}{4\pi(\zeta - Z)} \partial\zeta + \frac{2\Gamma(Z)}{a_0 c} = U(Z) \;\; \alpha_{2D}(Z) + \frac{C_{l_0}}{a_0} \quad . \tag{3.7}$$

Note that this is a linear form of the governing equation, *i.e.* it relies upon linear foil theory and an assumption of small angles. In this analysis, we re-cast equation (3.7) as a root-finding problem and remove the small-angle assumption, giving,

$$\frac{v(Z)}{U(Z)} + \sin(\alpha_{eff}(Z)) - \sin(\alpha_{2D}(Z)) = 0. \tag{3.8}$$

Equation 3.8 states that the effective angle of attack of a section (α_{eff}) is a sum of the geometric angle of attack (α_{2D}) and the dimensionless downwash induced at that section (v/U).

3.4.1.2 Numerical Solution Method

The first step in solving equation 3.8 numerically is to discretize the integral equation 3.5. The physical foil is first discretized into $N-1$ spanwise panels, with N nodes, as shown in Fig. 3.29. Equation 3.7 is satisfied at the panel-centers located at ζ_j. Vortex shedding is assumed to occur from the nodes located at Z_i, where,

$$\zeta_j = \frac{1}{2}(Z_j + Z_{j+1}). \qquad j = 1, 2, \ldots, N$$

By imposing equation 3.7 at the center of each panel, a second-order numerical algorithm can be created. Γ_j and v_j are the bound circulation strengths and induced downwash velocities at the panel centers, respectively, for $j = 1, 2, \ldots, N-1$. Γ_N is the circulation at the foil tip (node point Z_N), and is co-located with the N^{th} node.

The spanwise gradient of the circulation may be discretized using a second-order central-difference. A second-order backward-difference approximation is used to calculate the gradient at Z_N to accommodate the change in grid spacing at the tip. The discrete form of the integrand of equation 3.5 can be written as:

$$dv_{j_i} = \begin{cases} \frac{1}{4\pi} \frac{\Gamma_i - \Gamma_{i-1}}{ds\Delta_{j,i}} & , i = 1, 2, \ldots, N-1 \\ \frac{1}{4\pi} \frac{2(A\Gamma_N + B\Gamma_{N-1} + C\Gamma_{N-2})}{ds\Delta_{j,N}} & , i = N \end{cases} \quad j = 1, 2, \ldots, N \tag{3.9}$$

where the weights A, B, and C depend on the relative grid spacing at the tip, $ds =$

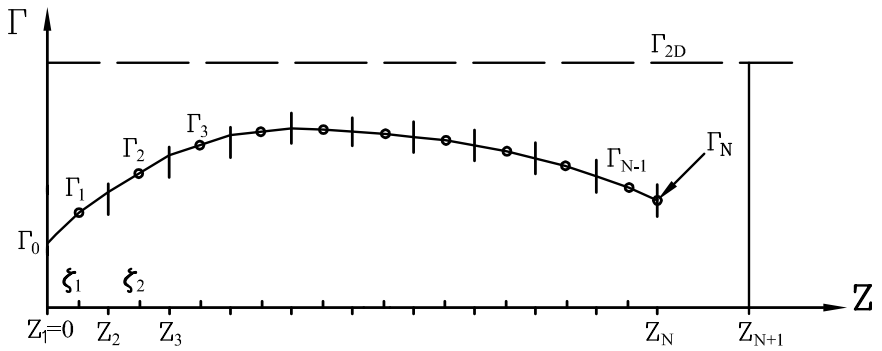

Figure 3.29: Discretization of hydrofoil in 1-D domain.

$S/(N-1)$ is the panel length on the foil, and

$$\Delta_{j,i} = Z_i - \zeta_j, \qquad \begin{matrix} i = 1, 2, \ldots, N+1 \\ j = 1, 2, \ldots, N \end{matrix}$$

is the "influence distance" from the collocation point at ζ_j to the node at Z_i.

Equation 3.5 may be replaced by a choice of closed Newton-Cotes quadrature rules and re-expressed as,

$$v_j = \sum_{i=1}^{N} dv_{j_i} W_i, \qquad j = 1, 2, \ldots, N \tag{3.10}$$

where the weights, W_i, are selected based on the desired order of accuracy of the integrator. With the values of dv_j substituted into equation 3.10, the summation expands into

$$\begin{aligned} v_j = & \frac{-1}{4\pi ds}\left[\Gamma_1 \frac{-W_2}{\Delta_{j,2}} + \Gamma_2 \quad \frac{W_2}{\Delta_{j,2}} - \frac{W_3}{\Delta_{j,3}} + \quad + \ldots \right. \\ & + \Gamma_{N-2} \quad \frac{W_{N-2}}{\Delta_{j,N-2}} - \frac{W_{N-1}}{\Delta_{j,N-1}} + \frac{2CW_N}{\Delta_{j,N}} \quad + \ldots \qquad j = 1, 2, \ldots, N \\ & \left. + \Gamma_{N-1} \quad \frac{W_{N-1}}{\Delta_{j,N-1}} + \frac{2BW_N}{\Delta_{j,N}} \quad + \Gamma_N \quad \frac{2AW_N}{\Delta_{j,N}} \right] . \end{aligned} \tag{3.11}$$

It is convenient to create modified vectors of quadrature and differencing weights.

$$W_i^* = \begin{cases} 0 & , i = 1 \\ W_i & , i = 2, 3, \ldots, N-1 \\ 0 & , i = N, N+1 \end{cases} \tag{3.12}$$

$$A_i^* = \begin{cases} 0 & , i = 1, 2, \ldots, N-3 \\ 2CW_N & , i = N-2 \\ 2BW_N & , i = N-1 \\ 2AW_N & , i = N \end{cases} \tag{3.13}$$

This allows summation 3.11 to be re-cast in a more-concise form,

$$v_j = \frac{1}{4\pi ds} \sum_{i=1}^{N} \Gamma_i \quad \frac{W_i^*}{\Delta_{j,i}} - \frac{W_{i+1}^*}{\Delta_{j,i+1}} + \frac{A_i^*}{\Delta_{j,N}} \quad . \quad j = 1, 2, \ldots, N \tag{3.14}$$

3.4.1.3 Physical Boundary Conditions

Often, lifting-line analysis is performed on only half of the domain, and a symmetric distribution of bound vorticity is assumed to exist on the other side of a center plane. This necessitates a reflected image of the vorticity distribution under consideration. Moreover, if the flow is being conducted in a flow channel (the case for which the lifting-line code was originally developed in *Harwood and Young* (2014)), then additional images are required to enforce symmetry not only at the root of the hydrofoil, but at the opposing wall of the tunnel. Thus, the combined foil and image must be repeated a sufficient number of times in each direction to effectively symmetrize the flow. A sample truncated domain is illustrated in Fig. 3.30.

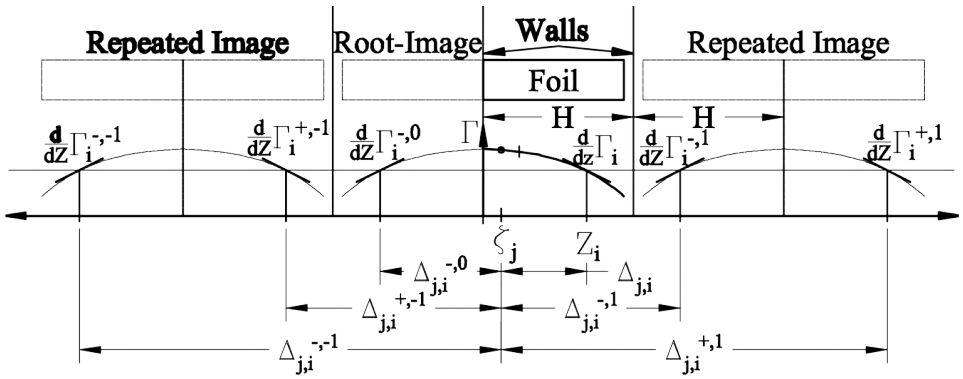

Figure 3.30: General arrangement of foil images to maintain symmetry about two planes in flow domain, as is required to simulate a flow channel. Figure reproduced from *Harwood and Young* (2014).

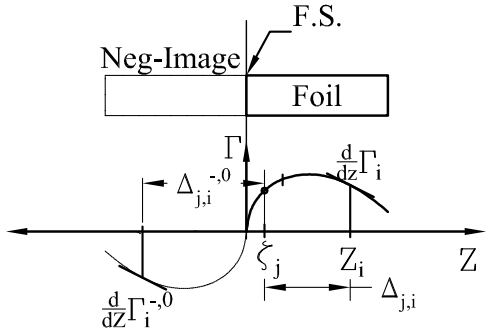

Figure 3.31: Single foil-and-image system, with a negative image used to enforce a zero-lift condition at the free-surface.

Equation 3.5 can be re-expressed as a piecewise integral to include the images:

$$v(Z) = \int_{Foil} \frac{\frac{\partial\Gamma}{\partial\zeta}}{4\pi(\zeta - Z)}\partial\zeta + \sum_{k=-n_{images}}^{n_{images}} \int_{Image_k} \frac{\frac{\partial\Gamma}{\partial\zeta}}{4\pi(\zeta - Z)}\partial\zeta. \tag{3.15}$$

For the case of a surface-piercing hydrofoil, the image arrangement is actually much simpler. There is no symmetry to maintain about walls of a flow channel. Instead, a choice must be made about how to model the free surface boundary. If the choice is made to model the free-surface as a constant-pressure boundary, then that constrains the lift – and hence, bound circulation – at the free surface to be zero. This leads naturally to what is often referred to as a "negative image," which enforces not the proper symmetry seen in symmetric flows, but an anti-symmetric distribution of vorticity on a virtual "image" foil. As a result, figure 3.30 simplifies to the arrangement in figure 3.31, where $n_{images} = 0$. Note that the negative image method can be derived by assuming $Fn_h = \infty$ and applying the linearized combined free-surface boundary conditions. As shown in Fig. 3.30, the circulation distribution on the negative image is (as the name implies) a negative of that on the physical hydrofoil, but by virtue of the anti-symmetry, $\frac{d\Gamma}{dZ}$ remains the same. The influence distances on the image are assigned as follows.

$$\Delta_{j,i}^{-,k} = -Z_i - \zeta_j \tag{3.16}$$

Note also that the coordinate Z corresponds to the distance measured along the submerged portion of the hydrofoil, downward from the free surface. In the coordinate system of the experiments, this is denoted z', so one should be careful not to confuse the local coordinate system of the lifting-line model with the experimental coordinate

system.

Combining equation 3.14 and equation 3.15 allows the terms containing Γ_i to be collected with identical weights, so that only the influence distances. The aggregate influence coefficients for the foil and its image may be written as,

$$\Omega_{j,i} = \frac{1}{4\pi ds}\left[W_i^*\left(\frac{1}{\Delta_{j,i}^{+,k}} - \frac{1}{\Delta_{j,i}^{-,k}}\right) + W_{i+1}^*\left(\frac{1}{\Delta_{j,i+1}^{+,k}} - \frac{1}{\Delta_{j,i+1}^{-,k}}\right) + A_i^*\left(\frac{1}{\Delta_{j,N}^{+,k}} - \frac{1}{\Delta_{j,N}^{-,k}}\right)\right]. \qquad \begin{matrix} i = 1, 2, \ldots, N \\ j = 1, 2, \ldots, N \end{matrix} \tag{3.17}$$

The other boundary condition to address is the value of Γ_N. In this work, where the foil tip is far from any physical boundaries, a classic boundary condition of $C_{l_{2D,N}} = \Gamma_N = 0$ is used, which allows the corresponding terms to be dropped from all subsequent summations.

3.4.2 Non-Linear Discrete Form of Lifting Line Equation

Equation 3.14 and equation 3.15 may be collectively re-cast in the compact form,

$$v_j = \sum_{i=1}^{N} \Gamma_i \Omega_{j,i}. \qquad j = 1, 2, \ldots, N-1 \tag{3.18}$$

Making dimensionless equation 3.4 and solving for $\Gamma(Z)$ yields,

$$\Gamma(Z) = C_{l_{2D}}(Z)\frac{U(Z)C(Z)}{2}. \tag{3.19}$$

Equation 3.19 may be substituted into equation 3.18. Dropping the summation form in favor of vector notation, we arrive at the compact discrete form of equation 3.5:

$$\{\boldsymbol{v}\} = [\boldsymbol{\Omega}]\{\boldsymbol{\Gamma}\} = \frac{1}{2}[\boldsymbol{U}]^D[\boldsymbol{c}]^D[\boldsymbol{\Omega}]\{\boldsymbol{C_{l_{2D}}}\}. \tag{3.20}$$

For a hydrofoil discretized with $N-1$ panels, $[\boldsymbol{\Omega}]$ is an $(N-1)\times(N-1)$ matrix operator containing the differencing and quadrature weights, $[\boldsymbol{c}]^D$ and $[\boldsymbol{U}]^D$ are diagonal $(N-1)\times(N-1)$ matrices with entries respectively corresponding to the chord and inflow velocities of each of the $N-1$ sections, and $\{\boldsymbol{C_{l_{2D}}}\}$ and $\{\boldsymbol{v}\}$ are each an $(N-1)\times 1$ column vector containing the sectional lift coefficients and induced downwash velocities of the sections, respectively.

By substituting equation 3.20 into equation 3.8, the following system is derived,

$$\frac{1}{2}\left[\boldsymbol{\Omega}\right]\left[\boldsymbol{c}\right]^{D}\left\{\boldsymbol{C_{l_{2D}}}\right\}+\sin(\left\{\boldsymbol{\alpha_{2D}}\right\})-\sin(\left\{\boldsymbol{\alpha}\right\})=\left\{\boldsymbol{0}\right\}. \tag{3.21}$$

Equation 3.21 is solved by iterating on $\{\boldsymbol{\alpha_{2D}}\}$ using a numerical root-finding algorithm. Once a solution is reached, integration of lift, drag, or any other quantity defined at the panel centers and tip node is performed in a piecewise manner by fitting cubic splines through the root and the tip ordinates, and integrating the polynomials exactly. The remainder of the foil has uniform spacing along the span, making it amenable to closed Newton-Cotes quadrature. The lift coefficient vector, $\{\boldsymbol{C_{l_{2D}}}\}$ is part of the converged solution. The induced drag component of $\{\boldsymbol{C_{d_{2D}}}\}$ (which does not include viscous or form drag) may be found by applying equation 3.20 to the resulting $\{\boldsymbol{C_{l_{2D}}}\}$ and using the Kutta-Joukowski law in equation 3.4 with $\{\boldsymbol{v}\}$ as the velocity, followed by the appropriate nondimensionalization. The moment may be computed by modeling the moment arm of the lift about the Z-axis and integrating the product of the moment arm and $\{\boldsymbol{C_{l_{2D}}}\}$ along the span.

What makes this form of the lifting-line model useful is the ability to "plug in" arbitrary models for section lift. In equations 3.20 and 3.21, the vector $\{\boldsymbol{C_{l_{2D}}}\}$ must be computed as some function of the known section parameters. In the linear lifting-line formulation, for example, this functional relationship is simply $\{\boldsymbol{C_{l_{2D}}}\}=2\pi\left\{\boldsymbol{\alpha_{eff}}\right\}$. However, the function need not be linear with the root-finding approach to solving equation 3.21. What follows is a brief description of how this modeling is performed for wetted and ventilated flows on the surface-piercing hydrofoil.

3.4.2.1 Modeling Boundary Layer Transition and Stall

To account for nonlinear effects in section lift, such as those caused by laminar separation or stall, the 2-D panel code XFOIL (*Drela*, 1989) was used to perform section-level computations. XFOIL is capable of handling arbitrary section shapes at varying Reynolds numbers. The code solves the 2-D boundary layer equations, coupled with a potential flow Boundary Element Method (BEM) code to predict pressure distributions, laminar-to-turbulent transition, laminar separation and reattachment, and turbulent stall. Direct coupling of XFOIL to the lifting-line model would require that XFOIL be called for every section during each iteration of the root-finding algorithm. A much-more expeditious approach was the generation of a response surface for $C_{l_{2D}}$ as a function of α_{2D} and Re_c, from which interpolation quickly yielded sectional lift coefficients during the iterative solution. Moreover, response surfaces

for $C_{m_{2D}}$ and $C_{f_{2D}}$ were easily used to estimate the sectional moment and frictional drag coefficient, which could be integrated over the length of span of the foil to yield 3-D values. The latter was, of course, complemented by the sectional induced drag coefficients (from lifting-line) to yield the total drag.

3.4.2.2 Modeling Cavitation and Ventilation

Following the 2-D cavitating-flow models in § 1.3, $C_{l_{2D}}$ is made a function of the respective sectional α_{2D} and σ_c. The derivations of the linear solutions in section 1.3 make no assumptions regarding the composition of gas inside the cavities, so both are judged to be applicable to ventilated cavities as long as the correct cavity pressure is used in equation 1.2 to compute σ_c. Recall the definition of σ_c for a ventilated flow beneath a free surface, given in equation 1.19, and reproduced here in the current coordinate system:

$$\sigma_c = \frac{2}{{Fn_h}^2}\frac{Z}{h}.$$

Which permits the sectional cavitation number to be calculated for any section. $\{\boldsymbol{\alpha_{eff}}\}$ is the input to the root-finding formulation in equation 3.21. For a given distribution of α_{eff} and with σ_c known at each spanwise section (*via* equation 1.2), the distribution of L_c/c is estimated by applying equation 1.8 to the calculated distributions of α_{2D} and σ_c. Equation 1.9 is then used to model the unscaled 2-D lift-coefficient vector, $\boldsymbol{C^*_{l_{2D}}}$. Proceeding in this manner, with the cavity lengths and $\boldsymbol{C^*_{l_{2D}}}$ updated at each step, a converged solution should be found for $\{\boldsymbol{\alpha_{eff}}\}$. However, it is wise to make one additional alteration to the model.

3.4.2.3 Modeling the Effects of Small Aspect Ratio

Lifting-line does not fully capture 3-D effects for very small aspect ratios because it neglects effect such as cross-flow. Small immersed aspect ratios are being considered in the present work, so a correction factor is used to re-scale the sectional distribution as a means of approximating the additional 3-D effects. *Helmbold* (1942) derived the expression for the total lift of rectangular wings of small aspect ratio ($AR < 4$) as,

$$C^H_{L_{3D}} = \left[\frac{a_0}{\frac{a_0}{\pi AR} + \sqrt{1 + \left(\frac{a_0}{\pi AR}\right)^2}}\right]\alpha. \tag{3.22}$$

Equation 3.22 is used to re-scale the computed $\boldsymbol{C^*_{l_{2D}}}$ for small aspect ratios, inside of the iterative solution of equation 3.21. At each iteration, the un-scaled 3-D lift coefficient ($C^*_{L_{3D}}$) is computed by integrating $C_{l_{2D}}$ along the span,

$$C^*_{L_{3D}} = \frac{1}{h} \int_0^h C_{l_{2D}}(z')dz'. \tag{3.23}$$

The lift-slope, a_0, also varies along the span. To find a single representative value for use in equation 3.22, a lift-weighted mean value (a^*_0) is estimated from the lifting-line results,

$$a^*_0 = \frac{1}{hC^*_{L_{3D}}} \int_0^h \frac{C^*_{l_{2D}}(z')^2}{\alpha^*_{2D}(z')}dz'. \tag{3.24}$$

Numerical quadrature is used to evaluate equations 3.23 and 3.24. a^*_0 is substituted into equation 3.22 with $AR = AR_h$ to yield the *scaled* 3-D lift coefficient (C^H_L). The Helmbold correction factor, H, is computed as the ratio,

$$H = \frac{C^H_{L_{3D}}}{C^*_{L_{3D}}}. \tag{3.25}$$

Finally, the 2-D lift distribution is re-scaled,

$$\{\boldsymbol{C_{l_{2D}}}\} = H \quad \boldsymbol{C^*_{l_{2D}}} \quad . \tag{3.26}$$

$\{\boldsymbol{C_{l_{2D}}}\}$ is then substituted into equation 3.21. By executing this procedure at each iteration, equation 3.21 may be iteratively solved for $\{\boldsymbol{\alpha_{eff}}\}$.

3.4.3 Cavity Topology and Hydrodynamic Loads Predicted by Lifting Line

The nondimensional distributions of α_{2D}/α, L_c/c, $a_0/(2\pi)$, σ_c, and $C_{l_{2D}}$ are shown in figure 3.32 for a case of $\alpha = 10°$, $Fn_h = 1.5$, and $AR_h = 1.0$. The planform of the ventilated cavity observed in experiments at the same flow conditions is shown for comparison. The lifting-line method is not proposed as a high-fidelity model, but the close agreement between the computed and observed cavity profiles suggests that the inclusion of gravitational effects (via σ_c), free surface (via the negative image), multi-phase flow effects (via the 2-D sectional cavity models), and 3-D effects (via the Helmbold correction and the lifting-line model itself) adequately captures the

dominant features of a 3-D ventilated cavity flow around a surface-piercing hydrofoil. Note the characteristic hump in the sectional angle of attack where the sections are supercavitating, which occurs because a_0 reduces sharply when $L_c/c > 1$, while $C_{l_{2D}}$ remains smooth and without major inflections. The shape of the a_0 distribution reflects that in figure 1.2, with a local maximum where sections are partially cavitating.

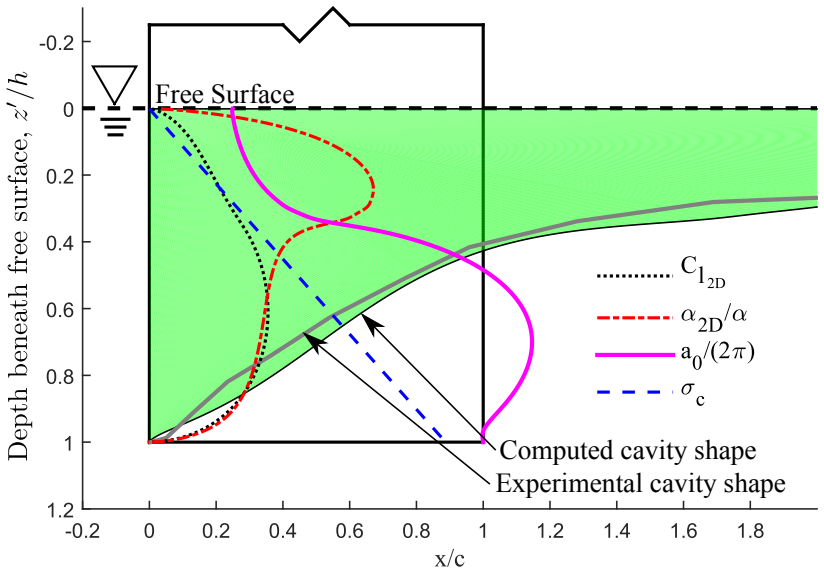

Figure 3.32: Nonlinear lifting-line model of a surface-piercing hydrofoil at $\alpha = 10°; Fn_h = 1.5; AR_h = 1.0$. The suction surface of the hydrofoil is shown. The effective angle of attack and cavitation number both vary along the span, leading to a spanwise non-uniform cavity. The agreement between computed and observed cavity shapes suggests that the simplistic model is suitable for capturing qualitative features of 3-D ventilated cavity flows. Figure reproduced from *Harwood et al.* (2016c).

With the modeled distribution of cavity lengths, equation 3.2 can be used to model the re-entrant jet trajectories. Figure 3.33 shows the cavity shape and re-entrant jet velocity vectors predicted by the nonlinear lifting-line model overlaid on an experimental photo.

A comparison of modeled and experimental values of $C_{L_{3D}}$ is shown in figure 3.34. In both regimes, the lifting-line model correctly captures the trends of the experimental measurements, though there is some over-prediction of the lift in the FV flow regime. In figure 3.35, dashed lines indicate the summed frictional and lift-induced drag coefficients from the lifting-line model. The skin friction coefficient was similarly estimated *via* the ITTC 1957 correlation line (*ITTC*, 2002) to be $C_{D_f} = 0.0047$. The skin friction was integrated over both surfaces of the foil in the FW regime and over the pressure surface only in the FV regime. Recall the hypothesis of *Breslin*

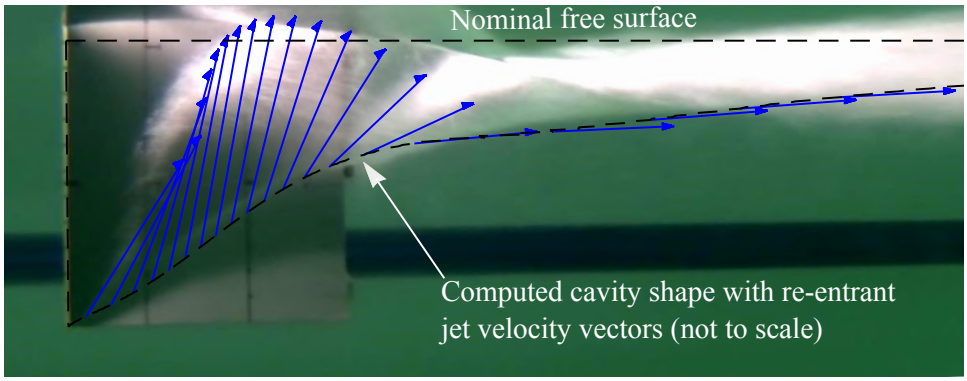

Figure 3.33: Cavity length distribution and velocity vectors of the re-entrant jet modeled with lifting-line for flow at $\alpha = 10°$, $Fn_h = 1.5$, and $AR_h = 1.0$.

and Skalak (1959) that, for certain geometries, a ventilated cavity yields an increased profile drag that roughly offsets the reduction in skin-friction and induced drag. The frictional drag represents only a very minor contribution to the total drag in both regimes, so the near-continuity of the total experimental drag between the FW and FV flow regimes implies that any changes in the remaining components of drag (induced drag, profile drag, spray drag, *etc.*) approximately counteract one another. The significant reduction in the induced drag predicted by the lifting-line model is caused by the previously-noted decrease in lift, and suggests that those drag components not captured by the lifting-line model – namely profile, wave, and spray drag – are substantially increased by the formation of a ventilated cavity.

Figure 3.36 shows $C_{M_{3D}}$ modeled by lifting-line theory and measured experimentally. The lifting-line code was used to approximate the yawing moment by integrating the product of the sectional lift and the moment arm of the lift. The dimensionless location of the center of pressure for fully wetted sections is estimated to be $e_{FW} = x_{cp}/c = 1/4$, where x_{cp} is the location of the center of pressure forward of mid-chord. For supercavitating sections, $e_{SC} = 3/16$ (*Akcabay and Young*, 2014). A sigmoid function was used to smoothly interpolate between the bounding values as a function of sectional cavity length,

$$e\left(L_c/c\right) = \frac{1}{2}\left\{e_{FW}\ \ 1 - \tanh\ \ \frac{L_c/c - 0.5}{0.25}\ \ + e_{SC}\ \ 1 + \tanh\ \ \frac{L_c/c - 0.5}{0.25}\ \right]\right\}\ . \tag{3.27}$$

The resulting estimates of $C_{M_{3D}}$ shown are good in the FW regime, but are slightly high in the FV regime. This is probably caused in part by the overprediction of $C_{L_{3D}}$ by the lifting-line model and further compounded by an overestimation of the distance of the lift-center from mid-chord.

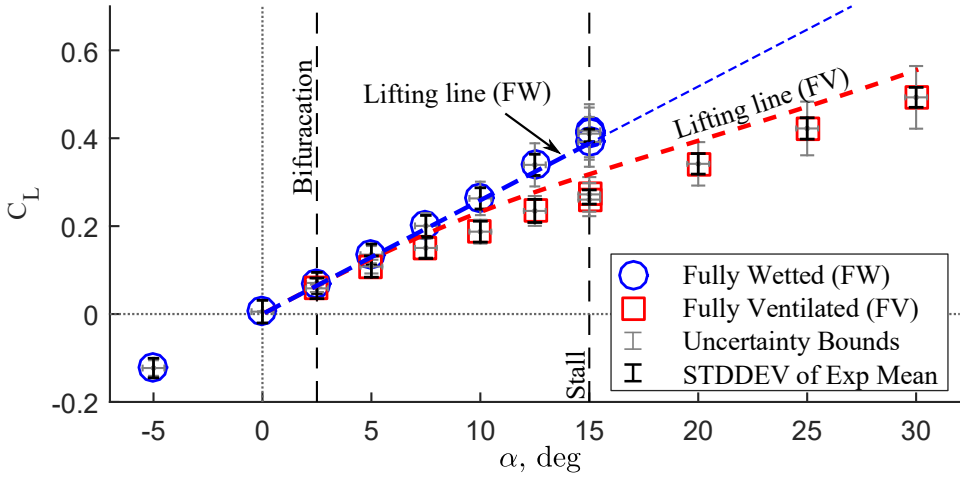

Figure 3.34: 3-D lift coefficient as a function of α at $Fn_h = 2.5$ and $AR_h = 1.0$. The nonlinear lifting-line model calculations are shown, with thin lines used to indicate predictions outside of the experimentally-observed ranges of α. Figure reproduced from *Harwood et al.* (2016c).

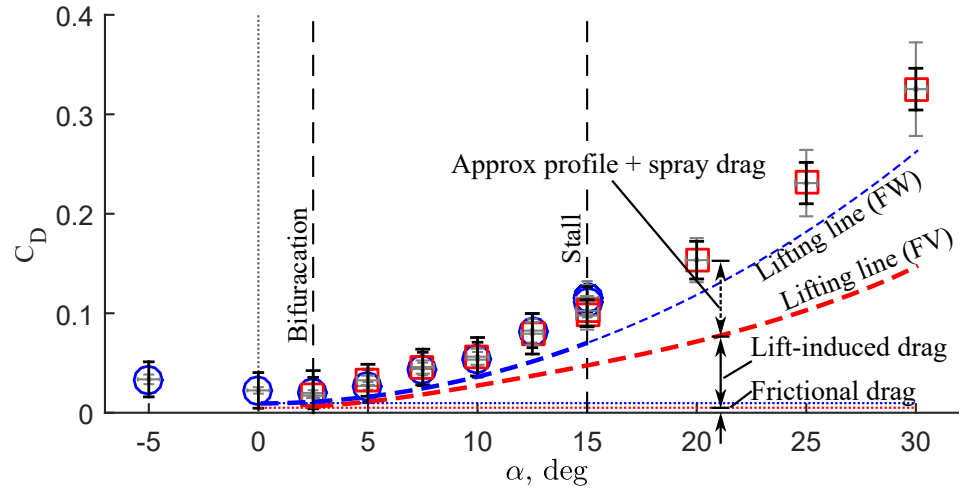

Figure 3.35: 3-D drag coefficient as a function of α at $Fn_h = 2.5$ and $AR_h = 1.0$. The results of the lifting-line model include induced and frictional drag only, suggesting that the increased profile drag and spray drag of the cavity roughly negate the reduction in frictional and induced drag. Figure reproduced from *Harwood et al.* (2016c).

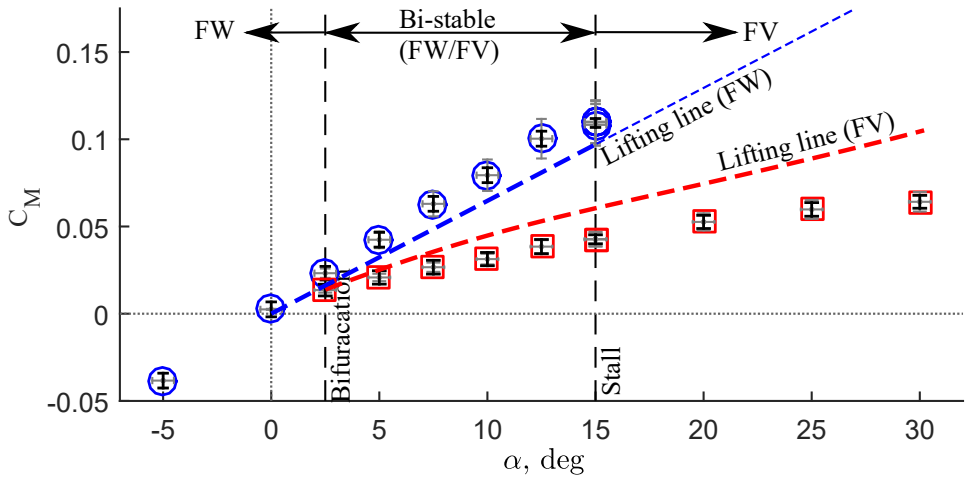

Figure 3.36: 3-D yawing moment coefficient as a function of α at $Fn_h = 2.5$ and $AR_h = 1.0$. Yawing moment is defined about mid-chord. The nonlinear lifting-line model calculations are shown, with thin lines used to indicate predictions outside of the experimentally-observed ranges of α. Figure reproduced from *Harwood et al.* (2016c).

Applications for such a fast model include early-stage design work, forecasting qualitative behaviors in parametric space, and real-time plant modeling for control applications (*Ward et al.*, 2016).

3.5 Summary and Discussion

3.5.1 Summary of Results

The major findings from this chapter are summarized below:

What are the characteristic steady flow regimes of surface-piercing lifting-surfaces and how are they formally defined?

Four flow regimes have identified: fully wetted (FW), partially ventilated (PV), fully ventilated (FV), and partially cavitating (PC) flows. Each possesses a unique visual topology, and definitions have been summarized for each.

What physical processes dictate the hydrodynamic response and stability of steady flow regimes?

The division between the three flow regimes has been made on the basis of the stability of the flow. Flows are categorized as either globally stable, locally stable, or unstable. Large-scale flow separation over more than half the chord length destabilizes FW flow, while a lack of separated flow permits no ventilation to occur. The stability

of flow in the FV regime, in particular, was tied to the development of upstream re-entrant flow at the cavity closure, where a cavity closure angle of $\bar{\Phi} < 45°$ indicates a stable FV cavity, and $\bar{\Phi} > 45°$ indicates an unstable cavity that will stabilize by taking on a PV flow topology. The experimental parameter space is populated with stability regions that overlap one another. Overlapping areas of these regions indicate multiply-stable flow conditions, where the flow may take on any one of the locally-stable regimes. Factors governing the regime of a given flow include hysteretic effects with movement through the parametric map (such as during flow acceleration and deceleration) or external perturbations to the flow.

How do hydrodynamic loads differ between flow regimes? How do the loads change with speed, immersion depth, and attack angle within each regime?

The hydrodynamic response of the surface piercing hydrofoil in lift, drag, and moment depends upon the flow regime, the dimensionless speed Fn_h, the yaw angle α, the generalized cavitation number σ_c, and the dimensionless immersion depth AR_h. Lift and moment coefficients decrease substantially with ventilation, while drag remains fairly continuous between wetted and ventilated regimes. At very low speeds, laminar separation, partial cavitation, and partial ventilation tend to augment the lift by inducing a positive effective camber. The drag and yawing moment are similarly affected. With increasing speed, the amount of apparent camber decreases as the cavity envelops the suction surface and extends far downstream. 3-D effects cause a typical reduction in hydrodynamic loads with AR_h in the FW regime, but flow in the FV regime attenuates sectional circulation so strongly that 3-D effects are suppressed in the FV regime. PC and PV flows occurred at the boundaries between FW and FV flow. The slope of $C_{L_{3D}}$ and $C_{M_{3D}}$ and the curvature of $C_{D_{3D}}$ with respect to α scales remarkably well with the cavitation parameter σ_c/α, as long as σ_c is carefully defined using appropriate cavity pressures for each regime.

What simple models can be derived to simulate the behavior of surface-piercing hydrofoils in multiphase flows?

A simple non-linear formulation and extension of classic lifting-line theory has been developed as a low-cost physics-based model. Including gravitational effects, free-surface effects, cavitation effects, and finite-aspect-ratio effects, the model produces a good qualitative approximation to experimental flow topologies and experimentally-measured loads.

3.5.2 Discussion

Callenaere et al. (2001) pointed out that viscosity probably slows the re-entrant jet down somewhat as it propagates along a solid boundary, especially when the cavities is very thin. Thin jets are more severely affected by wall friction than are thicker jets; the thinness of the cavities means that the jets often collide with – and become re-entrained in – the external flow. Thus, for small angles of attack ($\alpha \lesssim 5°$), the thin jet is not sufficient to perturb the flow away from its locally stable configuration, so the $\bar{\Phi} = 45°$ condition is not expected to reflect the stability of the flow at such small attack angles. However, when small cavities with closure angles of $\bar{\Phi} \approx 45°$ were subjected to external perturbations (air injections, small ripples, spray sheet, *etc.*), the flow often underwent a transition to PV flow, from which FV flow did not resume. At such small attack angles, $\bar{\Phi} = 45°$ is retained as the division between flow regimes – not because it necessarily signals instability caused by a re-entrant jet, but because it is a convenient and repeatable visual distinction which belies a tenuously stable flow configuration. Thick cavities, however, lead to thick re-entrant jets, which possess enough momentum that reductions in jet momentum by skin friction may be neglected. For the purposes of this discussion, it is assumed that the jet is sufficiently thick for $\alpha \geq 5°$ to preclude its stagnation by skin friction. Appendix D provides an order-of-magnitude analysis to support this assertion.

Data from the experiments were shared with computational researchers at Leidos Corp for preliminary validation of the Numerical Flow Analysis (NFA) code. NFA is an Implicit Large-Eddy Simulation (ILES) code that solves the Navier Stokes equations on a cartesian grid. The code simulates the flow of air and water domains using second-order Volume of Fluid (VOF) interface tracking, Quadratic Upwinded Interpolation for Convective Kinematics (QUICK) discretization of convective terms, and a multigrid Poisson solver for enforcement of fluid incompressibility. Details of the NFA solver may be found in *Dommermuth et al.* (2006, 2007); *O'Shea et al.* (2008); *Brucker et al.* (2010); *Dommermuth et al.* (2013). What distinguishes ILES from ordinary Large-Eddy Simulation (LES) is that subgrid-scale modeling is implicit in the QUICK scheme, rather than being provided by any explicit subgrid-scale model (*Leonard*, 1997; *Rottman et al.*, 2010). The simulation itself was carried out by Dr. Kyle Brucker, formerly of Leidos INC. More details may be found in the publication by *Harwood et al.* (2014). A single FV condition was simulated at $\alpha = 25°$; $Fn_h = 2.5$; $AR_h = 1.0$; P_0 =1 bar; σ_v =11. The cavity topology was captured extremely well by the solver, and all hydrodynamic loads were predicted with less than 4% error.

However, the NFA simulations required a discretized domain of 377 million ele-

ments and was distributed across 1,440 cores. The high-fidelity results are clearly more accurate than the lifting-line results, but the tradeoff is one of convenience. Modeling the lift, drag, and cavity-length distribution for both flow regimes across the entire range of α was faster than simulating the a single steady condition with NFA by six orders of magnitude. While the fidelity of NFA is striking (the lift, drag, and moment coefficients predicted by NFA were all within 3.8% of experimental values), one could make a convincing argument that the simpler model constitutes a worthwhile exchange of granularity for accessibility.

CHAPTER IV

Dynamic Flows with the Rigid Hydrofoil

Chapter III established four stable characteristic flow regimes that occurred on the rigid surface piercing hydrofoil: Fully Wetted (FW) flow, Partially Ventilated (PV) flow, Fully Ventilated (FV) flow, and Partially Cavitating (PC) flow. This chapter continues the discussion by exploring the unsteady mechanisms that cause movement or transition between the steady-state flow regimes. Referring again to the open research questions posed at the outset of the thesis, this chapter will address the following queries:

- How do flows transition between different regimes and how do transition mechanisms relate to the physics governing flow stability?
- What flow transition mechanisms occur on surface-piercing struts in subcavitating and cavitating flow?
- Can scaling relations be developed to describe the stability conditions of surface-piercing struts?

4.1 Unsteady Flow Regime Transition

Ventilation transition mechanisms collectively describe the processes by which the flow moves between stable flow regimes. Transition between stable flow regimes can occur wherever the stability regions of those respective regimes abut or overlap one another. In other words, transition signifies the flow leaving one stability region and entering another, whether that occurs by crossing a stability boundary or by jumping between locally-stable flows. A hierarchy of ventilation transition mechanisms is shown in figure 4.1, illustrating how each mechanism links the steady flow regimes defined in chapter III. The first distinction between transition mechanisms is made

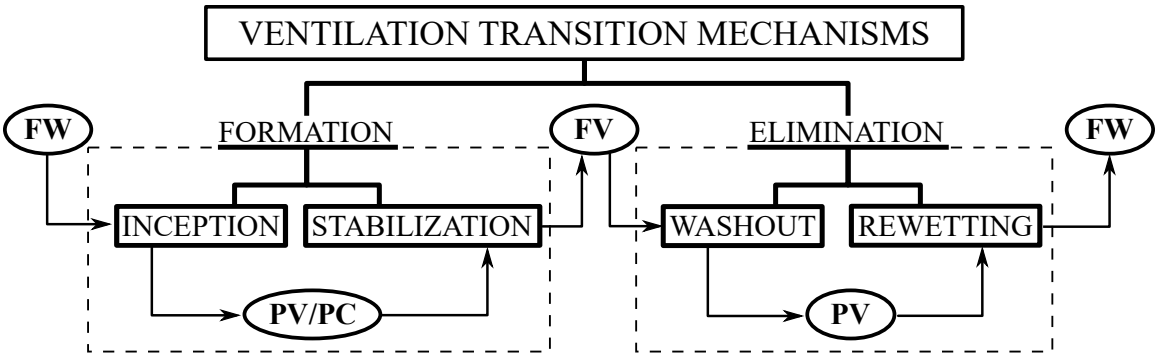

Figure 4.1: The hierarchy of ventilation transition mechanisms. The first level distinguishes the overall direction of transition. The second level identifies the individual stages of transition between the steady flow regimes established in chapter III. Figure reproduced with modifications from *Harwood et al.* (2016b).

on the basis of the overall direction of the transition, dividing ventilation transition into “formation" and “elimination" mechanisms. Formation mechanisms are classified as those which enhance the size or stability of a cavity, and are described in §4.2. Elimination mechanisms detract from the size or stability of a cavity, and are discussed in §4.3. As might be inferred from chapter III, the transition between the flow regimes can result in dramatic changes in hydrodynamic loading, which are described in §4.5.

To preface the following discussion, it is informative to consider the stability map introduced in chapter III. The stability map for $AR_h = 1.0$ is reproduced below with a few modifications. The transition boundaries have now been labeled according to the convention of figure 4.1, and example transition events are labeled. It can be helpful to visualize the stability map as being made up of overlapping planar regions in space, while the flow is described by a point moving around in this space. Transition between flow regimes occurs when the flow “falls off” the edge of one plane onto another or when something occurs to “push” the flow through one plane and onto another. Circular points in figure 4.2 indicate transition events occurring during an otherwise-steady flow. Since there is no “motion” through the parametric space, the implication is that transition for these points occurred because some process perturbed the flow away from a locally-stable regime and initiated a jump to another, globally-stable one. The black arrows describe trajectories through the parameter space, corresponding to acceleration and deceleration. Ventilation transition in these cases occurred as the flow crossed the transition boundaries.

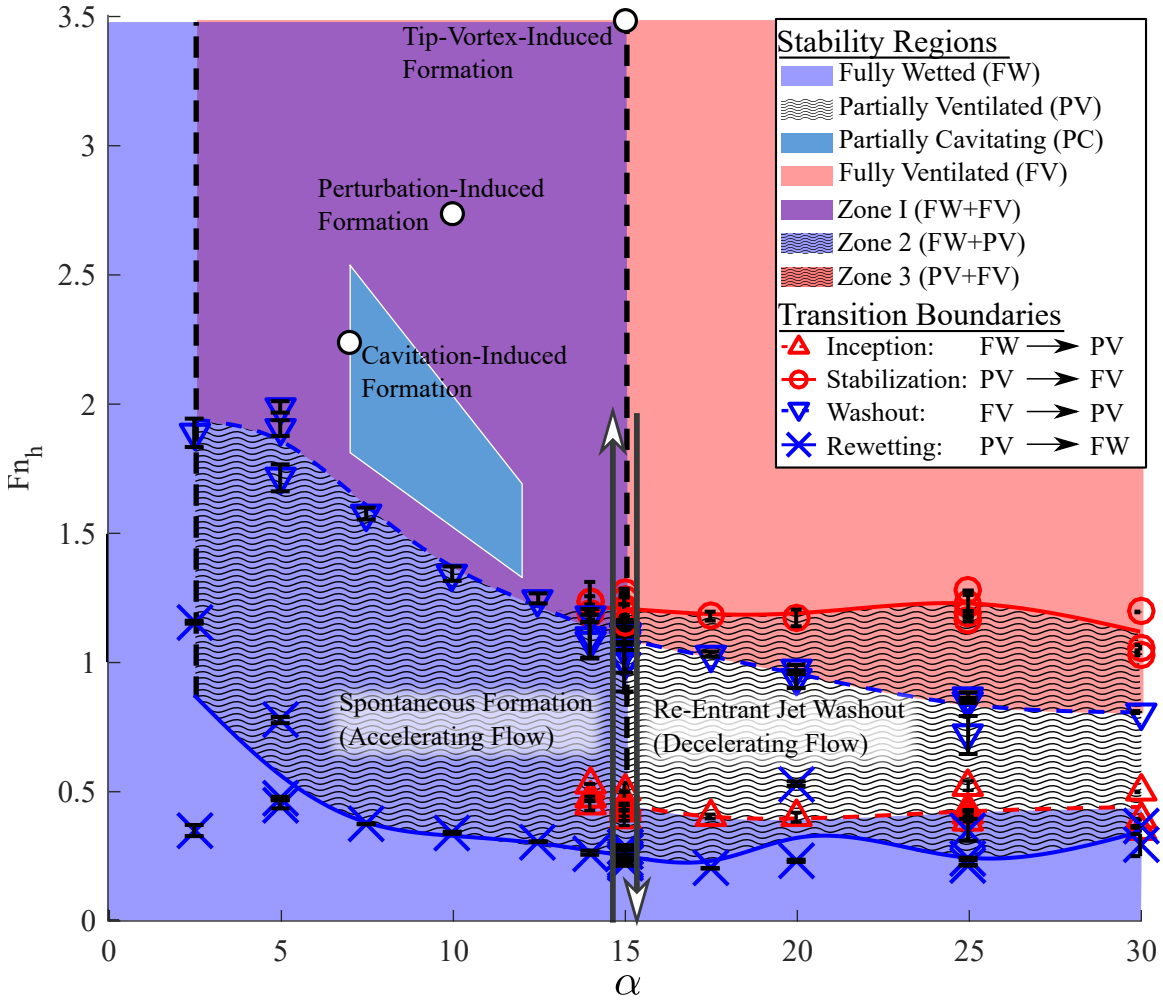

Figure 4.2: Stability map for $AR_h = 1.0$ with overlaid transition events.

4.2 Ventilation Formation

Formation mechanisms promote the growth and stability of a cavity, causing the flow to transition from a FW or a PV regime to a partially or FV regime, respectively (see figure 4.1). Additionally, the transitions from FW to PC flows or from PC to FV flows constitute formation processes, though the dependence of vaporous cavitation upon the additional variable σ_v makes it harder to generalize the progression. Since PC is a stable flow regime involving an entirely different multi-phase flow (vaporous cavitation as opposed to natural ventilation), let us define the transition processes that describe natural ventilation first and then describe the special case of vaporous cavitation, rather than trying to fit the PC flow regime into our generalized description of flow transition.

As shown in figure 4.1, formation mechanisms for a naturally-ventilated flow can be further decomposed into two sequential stages, as follows:

Inception is the transition from FW flow to PV flow, which marks the first stage in the formation of a ventilated cavity. The first visual evidence of persistent air-entrainment is sufficient to classify inception. Red triangular symbols along the upper boundary of the FW region for $\alpha \geq 14^\circ$ in figure 4.2 indicate spontaneous ventilation inception. Ventilation inception may also occur in zones 1 and 2 of figure 4.2, where the FW regime overlaps the FV and PV regimes, respectively (described in §4.2.5).

Stabilization is the transition from PV flow to FV flow, which completes ventilation formation. Stabilization is said to occur when the flow satisfies the criteria established for FV flow in §3.1. Red circles along the upper boundary of the PV region in figure 4.2 denote spontaneous stabilization events. Stabilization also immediately follows inception in zone 1 of figure 4.2. Under suitable conditions, stabilization can occur in zone 3 as well.

It has been established in the literature that the formation of a ventilated cavity occurs when some path of low-pressure (typically a vortex core) draws air into a region of flow with low pressures and some extent of flow separation (*Wadlin*, 1958; *Breslin and Skalak*, 1959; *Swales et al.*, 1974). The following formation mechanisms share one key thing in common: they provide a method for air to enter ventilation-ready flow. Mechanisms of generating the requisite vorticity through self-initiated features of the flow are collectively termed "spontaneous formation" mechanisms by *Harwood et al.* (2016c), and include stall-induced ventilation (*Kiceniuk*, 1954; *Wetzel*, 1957; *Breslin and Skalak*, 1959), tail ventilation caused by the amplification of free-surface disturbances (*Waid*, 1968; *Rothblum et al.*, 1969; *Swales et al.*, 1974), and tip-vortex-

induced ventilation (*Ramsen*, 1957; *Breslin and Skalak*, 1959; *Swales et al.*, 1974). These mechanisms may be enhanced or altered by the presence of vaporous cavities, leading to a number of cavitation-induced ventilation mechanisms (*Waid*, 1968; *Rothblum et al.*, 1969; *Swales et al.*, 1974; *Rothblum*, 1977b). The artificial introduction of vorticity into the flow (*Wadlin*, 1958; *Breslin and Skalak*, 1959; *Rothblum et al.*, 1969; *Swales et al.*, 1974) or the impingement upon the hydrofoil by disturbances in the incoming flow (*Rothblum et al.*, 1969; *Mcgregor et al.*, 1973; *Swales et al.*, 1974; *Rothblum*, 1977b) – in both cases, sufficient to cause ventilation – are referred to as cases of "perturbation-induced formation" mechanisms (*Harwood et al.*, 2016c).

4.2.1 Stall-Induced Formation

Stall-induced formation occurs when the angle of attack is set at or above the stall angle ($\alpha \geq \alpha_s$). An example of the stall-induced ventilation formation process is depicted in figure 4.3, along with experimental photos of the hydrofoil's suction surface. This case also corresponds to the vertical upward trajectory (acceleration) in figure 4.2. The flow begins in the FW regime. A large leading edge vortex creates a low-pressure, stagnant region of wetted separation, indicated by black hatching. In frame (a), the low pressures on the hydrofoil's surface create a steep depression of the free surface, forcing proximity between the free surface (an air source) and the separated flow (ventilation-prone flow). At the same time, small vortical disturbances develop near the toe of the free-surface depression. Such vorticity-development was noted in the waves generated by an un-yawed surface-piercing hydrofoil by *Pogozelski et al.* (1997). The vortical structures at the free surface can momentarily breach the surface seal, admitting air into the separated flow. If enough air is admitted, then it becomes stably entrained, constituting inception, shown in frame (b), and corresponding to a crossing of the inception boundary in figure 4.2. After inception, the flow is classified as PV. As the flow velocity increases, the suction-side dynamic pressure negates the hydrostatic pressure to increasing depths and the sectional values of σ_c decrease, causing the cavity to grow in both length and depth. As the cavity grows, it modifies the local chordwise pressure-gradients, causing the separated flow to propagate ahead of the cavity (*Tassin Leger and Ceccio*, 1998), creating a moving front of ventilation-prone flow. Frame (c) shows the instant when the cavity meets the conditions for FV flow given in §3.1 ($D = h$ and $\bar{\Phi} < 45°$). This constitutes stabilization, indicated in figure 4.2 by the trajectory crossing the stabilization boundary. Following stabilization, the flow is classified as FV. Stall-induced formation is a quasi-steady process, wherein the flow takes on an evolving state of equilibrium as the speed, and

hence the pressure distribution, changes. As a result, cavity formation takes place on a time-scale governed by the acceleration of the hydrofoil.

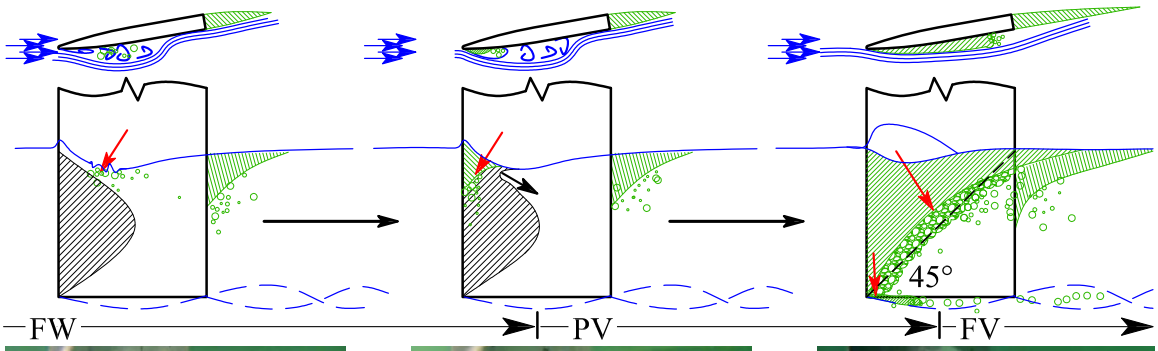

(*a*) $Fn_h = 0.44$ (*b*) $Fn_h = 0.6$ (*c*) $Fn_h = 1.16$

Figure 4.3: Spontaneous stall-induced ventilation formation occurring at $\alpha = 15° \approx \alpha_s; AR_h = 1$. Fn_h is given at the instant of each photograph. Blue lines denote streamlines, green lines and hatching indicate entrained air, black hatching indicates boundary layer separation, and red arrows indicate air ingress paths. Figure reproduced from *Harwood et al.* (2016b).

4.2.2 Tip-Vortex Induced Formation

Another case of spontaneous ventilation formation occurs when air enters the tip vortex at a downstream location and is transported upstream through the aerated vortex core. "Tip vortex inception" was observed by *Breslin and Skalak* (1959) and *Swales et al.* (1974) only at large angles of attack and small immersion depths (described in § 1.4). In the present experiments, air entered the tip vortex through the bubbly wake of the foil's blunt trailing edge. A process sketch and experimental photos are shown in figure 4.4. The corresponding circle at $\alpha = 15°; Fn_h = 3.5$ in figure 4.2 indicates that the flow speed does not change during the transition process. The flow begins in the FW regime, with a base-vented cavity attached to the blunt trailing edge. Eddies in the wake draw air bubbles into the low-pressure core of the tip vortex, where they coalesce into an aerated vortex core, shown in frame (*a*) of figure 4.4. The coalesced bubble migrates up the low-pressure core toward the foil's leading edge, where it encounters a favorable pressure gradient, as shown in frame (*b*).

In frame (c), the air reaches the region of separated flow and expands rapidly upwards and towards the foil trailing edge. FV flow is attained in a fraction of second, with no appreciable dwell in the PV regime. Tip-vortex-induced formation in the present experiments occurred only at $AR_h = 1.0$, at yaw angles very near the stall boundary ($\alpha \approx 15°$), and at $Fn_h \approx 3.5$. As a result of the rapid transition, hydrodynamic loads change violently during tip-vortex inception. The hysteretic loading during transition processes is discussed in §4.5.

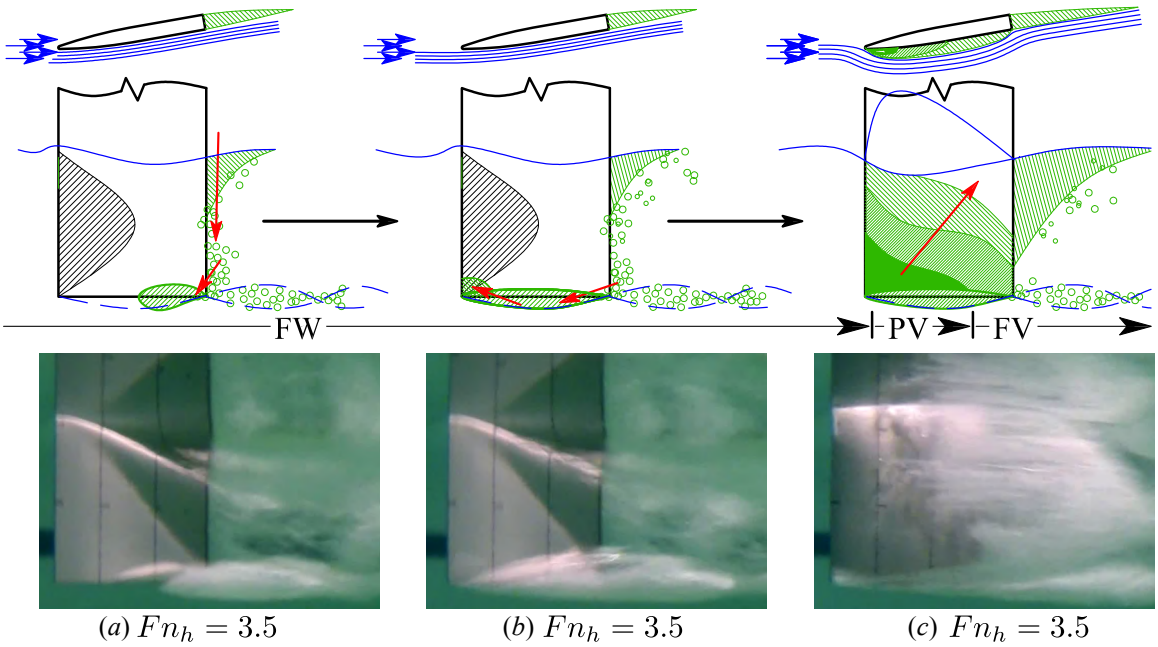

(*a*) $Fn_h = 3.5$ (*b*) $Fn_h = 3.5$ (*c*) $Fn_h = 3.5$

Figure 4.4: Tip vortex ventilation formation occurring at angles near stall, $\alpha = 15° \approx \alpha_s$; $AR_h = 1$. Fn_h is given at the instant of each photograph. Time is increasing from left to right at a constant Froude number for the case shown. Figure reproduced from *Harwood et al.* (2016b).

Figure 4.5 depicts a surface-flow visualization at $Fn_h = 2.5, \alpha = 14°, AR_h = 1.0$, corresponding to a location near the upper right corner of the FW stability region (in zone 1) in figure 4.2. A large separation bubble is clearly visible, indicated by the forward-swept paint streaks and black dashed outline. The separation bubble is conducive both to stall-induced formation and to tip-vortex-induced formation. In the former case, air ingress occurs through disturbances in the thin layer of liquid between the separation bubble and the free surface, indicated by the free surface profile and superimposed arrow in (a). In the latter case, air ingress occurs when a tip vortex develops of sufficient strength to transport air upstream to the separation bubble, shown in (b). Both stall-induced formation and tip-vortex-induced formation result when naturally-occurring air paths reach the nearest boundary of the region of

flow separation.

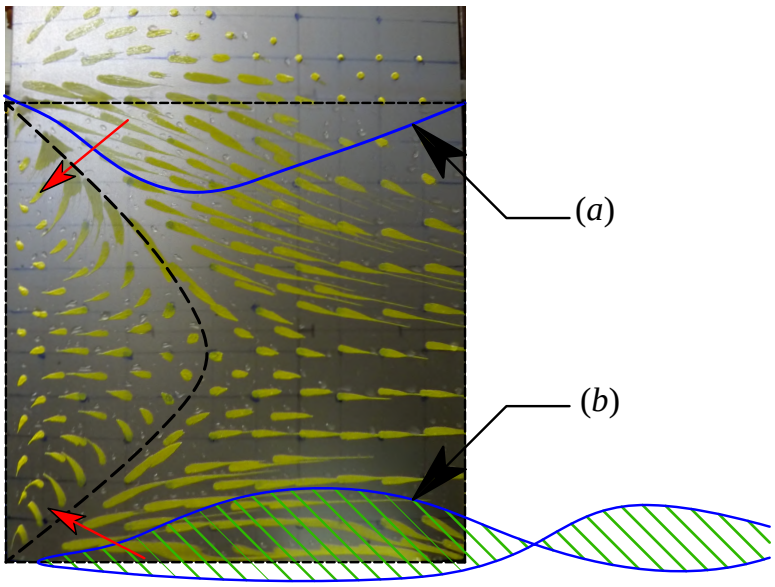

Figure 4.5: Surface flow visualization for $\alpha = 14°$, $Fn_h = 2.5$, $AR_h = 1.0$, showing two possible mechanisms of ventilation inception (the first stage of ventilation formation). Red arrows indicate the respective ingress-paths of air. (a) Depicts the free surface profile immediately preceding spontaneous stall-induced inception. (b) Depicts the aerated tip vortex immediately preceding tip-vortex-induced inception.Figure reproduced from *Harwood et al.* (2016b).

4.2.3 Tail Ventilation Formation

Another mode of spontaneous air entrainment is dubbed tail ventilation, which tends to occur at higher speeds and moderate angle of attack (*Rothblum et al.*, 1969; *Swales et al.*, 1974; *Rothblum*, 1977b). Tail ventilation, while similar to stall-induced ventilation, is a more-nuanced and complex mechanism of air-entrainment. Tail ventilation follows the development of Taylor instabilities on the free surface. This type of instability was first studied by *Taylor* (1950), who showed that surface waves on an inviscid fluid without surface tension became unstable and grew in time when the interface was accelerated downward in the direction of the dense fluid. It was shown both experimentally and analytically by *Emmons et al.* (1960) that the inclusion of viscosity decreased the rate of growth of surface waves, while the effect of surface tension was to limit the range of potentially-unstable wave numbers. A third-order potential-flow solution to the Laplace boundary value problem for a Two-Dimensional (2-D) domain, with surface-tension included in the dynamic free surface boundary condition and a linear sinusoidal initial wave elevation was derived. The

results showed a feedback mechanism from higher modes to the primary mode, which created instability when the wave number of the initial surface disturbances was below a critical value. The growth of unstable surface waves subjected to a downward acceleration develops into characteristic "spikes" (*Emmons et al.*, 1960) or jets, which develop additional Helmholtz-type instabilities along their surfaces.

In tail ventilation, the low pressure on the suction surface of the hydrofoil induces a downward acceleration of the free surface, forming the characteristic depression of the free-surface in FW flows. This effect can be particularly pronounced in the case of PC flow. Under sufficient downward acceleration, small perturbations on the free surface (ripples, capillary waves, or minute vortical structures) grow unstably, collapsing again as the low-pressure region passes and the downward acceleration ceases. The rapid growth, and subsequent collapse of these disturbances leave residual free-surface vortices, through which air enters the ventilation-prone flow. Tail ventilation in the present experiments was observed only when vaporous cavitation was present, so further discussion will be deferred until the following section.

4.2.4 Cavitation-Induced Formation

Cavitation may be regarded as a particular case of separation, since the cavity is bounded by wetted streamlines that have detached from the body. At very high speeds or low ambient pressures, the presence of vaporous cavitation may change the ventilation mechanisms significantly (*Waid*, 1968; *Rothblum et al.*, 1969; *Swales et al.*, 1974; *Rothblum*, 1977b). It was observed in figures 3.8 and 3.9 that the region of vaporous cavitation vanishes near the free tip and near the free surface. The resulting thin layer of subcavitating, attached flow between the vaporous cavity and the free surface is visual evidence of the free surface "seal" (*Wadlin*, 1958; *Breslin and Skalak*, 1959; *Rothblum et al.*, 1969; *Swales et al.*, 1974). Cavitation favors the ventilation process by providing an already-stable, separated region filled with vapor at low pressure ($P_v \approx 2-3$ kPa, which is much lower than $P_{atm} \approx 101$ kPa) (*Wadlin*, 1958). Cavitation can thus promote any of the inception mechanisms already described. Once the surface seal is breached by any of the preceding mechanisms, air will be entrained rapidly into the already-existent vaporous cavity because of the large difference in pressure between the atmosphere and the vaporous cavity. The increase in cavity pressure from vapor pressure to atmospheric pressure will cause a dramatic reduction in the cavitation number (i.e. $\sigma_c \to 2z'/(Fn_h{}^2 h)$ as $P_c \to P_{atm}$), which results in an explosive growth in the size of the cavity.

In the surface piercing hydrofoil experiments, cavitation in the PC flow regime

specifically favored the tail ventilation mechanism. A series of high-speed camera frames depicting ventilation transition from PC flow to FV flow is shown in figure 4.6. The frames are labeled (a) through (g), with the associate times relative to frame (a). To the right of each frame is a magnified view of the Taylor instability as it progresses along through the flow field. The conditions for the run were $\alpha = 5°$, $Fn_h = 2.25$, $AR_h = 1.0$, and $\sigma_v = 0.364$, indicated in figure 4.2 by the circle located where the PC, FW, and FV flow regimes overlap. In order to achieve the low vaporous cavitation number, the tunnel pressure at INSEAN was pulled down to $P_0 = 44$ mbar In frame (a), the thin free surface seal experiences a dramatic downward acceleration, induced by the low cavity pressures immediately below it. A ripple on the free surface is visible near the Leading Edge (LE) of the hydrofoil. In frame (b), that same ripple has convected downstream and grown in amplitude, indicating an incipient Taylor instability (*Taylor*, 1950). In frames (c), (d), and (e), the instability can be seen to make contact with the vaporous cavity, which begins to expand as air is admitted and the cavity pressure rises. In frames (f) and (g), the ventilated cavity develops rapidly, completing the transition from PC flow to FV flow in a total of approximately 0.08 seconds. The dimensional lift, drag, and moment before, during, and after the frame sequence is plotted in the lower right. It must be noted too, that the tip vortex ventilation mechanism is much more likely to occur if cavitation is present, since a vaporous cavitating vortex core will be more buoyant, and thus will connect with the free surface earlier than a subcavitating vortex.

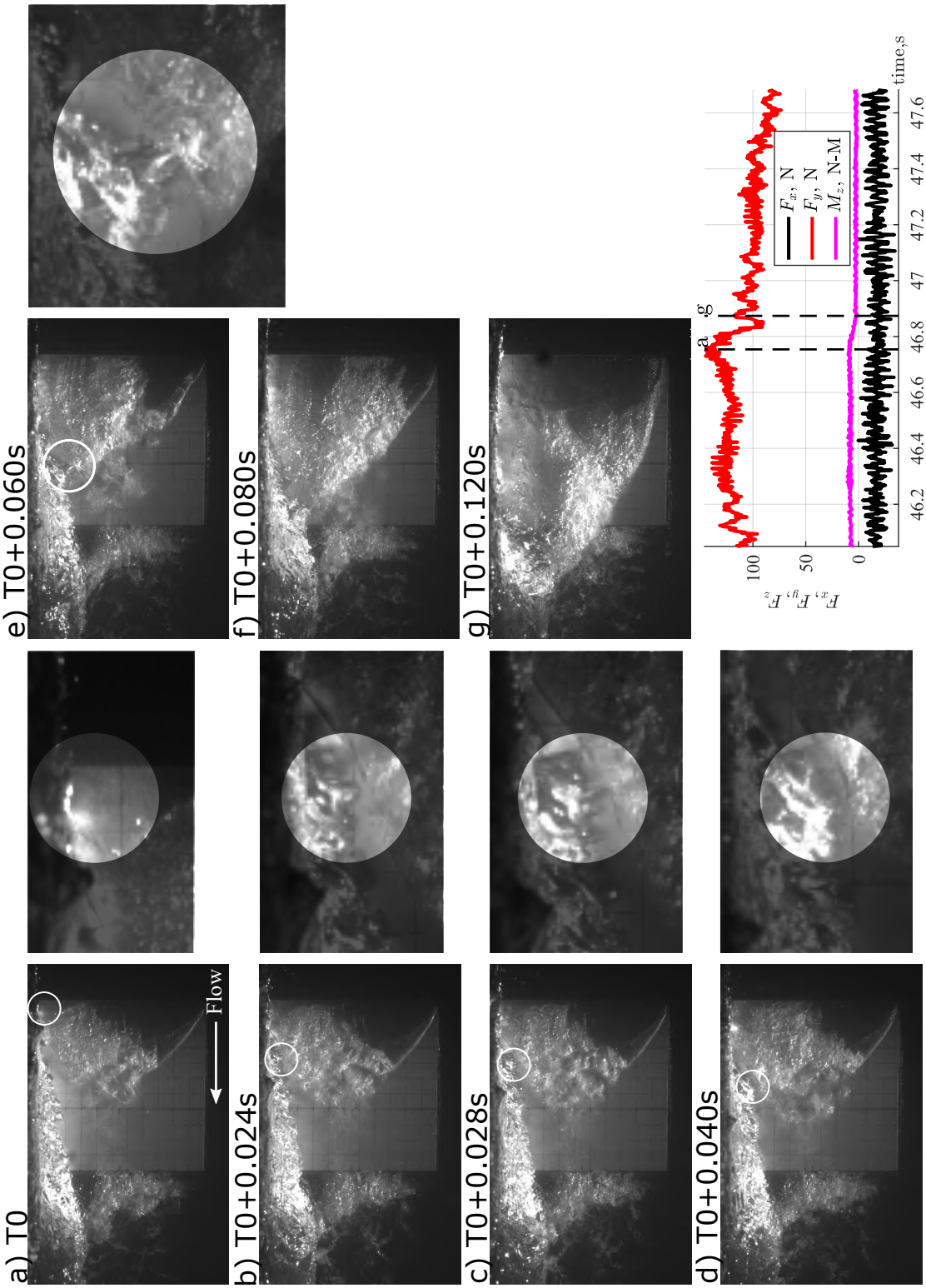

Figure 4.6: Tail ventilation on a partially cavitating flow at $\alpha = 7°$, $Fn_h = 2.25$, $AR_h = 1.0$, and $\sigma_v = 0.364$. The impingement of a Taylor-type instability, developed on the free surface, upon the cavity interface permits the rapid ingress of air as the cavity transitions from partial cavitation (vaporous) to full ventilation.

4.2.5 Perturbation-Induced Formation

When a source of sufficient vorticity does not inherently exist in the flow, then the FW flow regime can persist long after flow conditions on the submerged portions of a body are conducive to full ventilation. The delay is attributed to the thin layer of attached, high-momentum flow at the free surface (*Wadlin*, 1958; *Breslin and Skalak*, 1959; *Rothblum et al.*, 1969; *Swales et al.*, 1974; *Rothblum*, 1977a; *Harwood et al.*, 2016c), known as a "free surface seal". Ventilation caused by artificial disturbances is known as "perturbation-induced" ventilation formation. As noted in *Breslin and Skalak* (1959); *Swales et al.* (1974); *Harwood et al.* (2016c), air may be entrained by any local momentary flow separation mechanisms, or by natural and/or artificial free surface disturbances (e.g. waves, jet sprays, wake of an upstream body, thin wire intrusion, air injection at the foil leading edge, etc.). For lower speeds, these types of momentary surface seal breach mechanisms may be closed by additional disturbances, causing the cavity to be washed downstream. However, as speed or angle of attack increases and suction-side pressure becomes sub-atmospheric, the presence of transient air bubbles can perturb the chordwise pressure gradient and/or boundary layer sufficiently to initiate local flow separation and air entrainment. In turn, the entrained air forces the area of surrounding flow separation to grow (*Tassin Leger and Ceccio*, 1998; *Amromin*, 2007), and through a cascade-like process, results in massive flow separation and a FV cavity. Thus, initially attached flow can be destabilized and it may assume a new, stable, FV configuration. This disturbance, enacted in previous studies with a thin tripwire and in the present study with a high-pressure air-jet, constitutes a perturbation to the present stable flow by inducing flow separation, perturbing local pressure gradients, or otherwise violating the stability conditions of that flow regime in a very localized manner. When the parameters of a flow are inside one of the overlapping zones in figure 4.2, a suitable perturbation will destabilize the locally-stable flow state and initiate a jump to a lower-energy state (FW to FV *via* inception and stabilization in zone 1, FW to PV *via* inception in zone 2, PV to FV *via* stabilization in zone 3), or PC to FV *via* inception and stabilization inside of the PC stability region.

Figure 4.7 shows a sketch of a perturbation-induced ventilation formation process, indicated in figure 4.2 by a circular marker in Zone 1. In frame (a), the flow is FW. Compared to the case of stall-induced formation, the leading edge separation bubble is small and the large Froude number means that the free surface is not so steeply deformed, so the free surface never approaches the boundary of flow separation. As a result, a thin layer of attached flow exists just below the free surface (indicated by a

dashed line), sealing the ventilation-prone flow from the ingress of air. In frame (b), a high-pressure jet of air is injected at the junction of the leading edge and free surface, introducing vorticity and bubbles into the flow at the free surface to break the surface seal. In frame (c), a small cavity is entrained and grows rapidly from the point of inception toward the immersed trailing edge until it reaches the lower-energy, FV state. Entrainment and stabilization are nearly concurrent in this case, with little to no dwell in the PV regime. Fully ventilated flow can develop in approximately $1/10^{th}$ of a second following perturbation. For the case shown in figure 4.7 the lift force decreased by 38% between frames (a) and (c) (more details in §4.5).

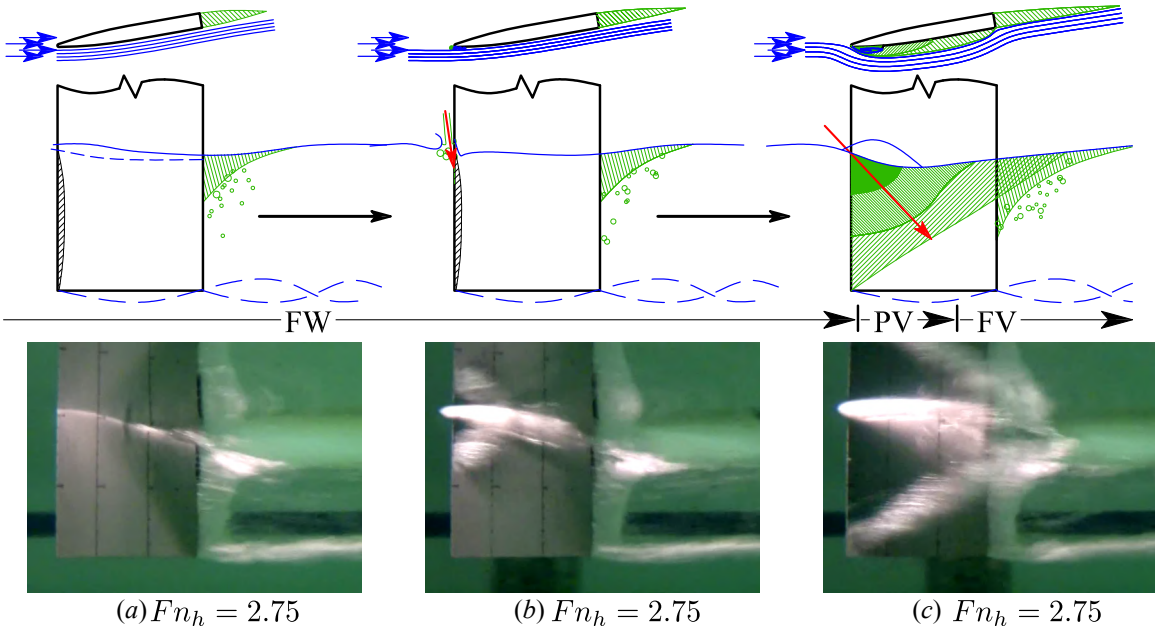

Figure 4.7: Perturbed ventilation formation occurring at sub-stall $\alpha = 10° < \alpha_s; AR_h = 1; Fn_h = 2.75$ (inside zone 1 of figure 4.2). Blue lines denote streamlines, green lines and hatching indicate entrained air, black hatching indicates boundary layer separation, the blue dashed line indicates the free surface seal, and red arrows indicate air ingress paths. Figure reproduced from *Harwood et al.* (2016b).

Figure 4.8 shows the surface-flow pattern at $\alpha = 10°, Fn_h = 2.5, AR_h = 1.0$. The small yaw angle creates a short leading edge separation bubble, where flow reversal has swept several of the forward-most columns of paint dots toward the leading edge. The free surface in the FW regime is superimposed as line (a). When air-injection is initiated, the depression of the free surface permits air to enter the small bubble and expand, shown by line (b). Again, experimental observations support the hypothesis that inception occurs when an air supply is made available to ventilation-prone flow.

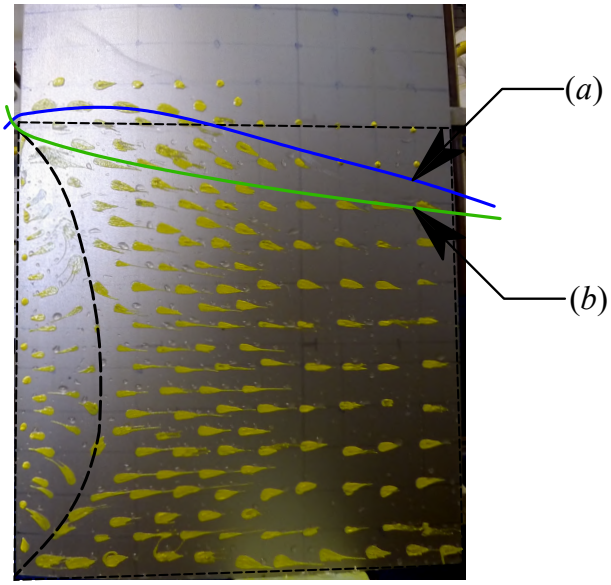

Figure 4.8: Surface flow visualization for $\alpha = 10°, Fn_h = 2.5, AR_h = 1.0$. The dashed line depicts the leading edge separation bubble caused by thin-airfoil stall. (a) indicates the free surface profile prior to ventilation inception and (b) indicates the air-filled depression created by the air-jet perturbation. Figure reproduced from *Harwood et al.* (2016b).

4.3 Ventilation Elimination

Elimination encompasses processes that detract from the size or stability of a ventilated cavity. They describe the movement from a fully or PV regime toward a PV or FW regime, respectively (see figure 4.1). As with formation mechanisms, elimination mechanisms can be broken down into two stages, given as follow:

Washout marks the transition from FV flow to PV flow. Washout is said to occur when the criteria for FV flow given in §3.1 are no longer satisfied. This typically corresponds to a large-scale shedding of the cavity, after which the cavity topology fluctuates visibly. Squares along the lower edge of the FV region in figure 4.2 denote the washout event.

Re-wetting marks the desinence of air-entrainment. It was observed that air was frequently ejected from the flow by laminar/turbulent reattachment of the flow at low speeds and angles of attack. It is said to occur when there ceases to be any visual evidence of air entrainment on the suction or pressure surfaces; there may still be bubbly flow entrained in the separated wake of the blunt trailing edge. Typically, the connection between the cavity and the free surface is terminated as the shallowly-immersed sections experience flow-reattachment. Isolated pockets of air cling to the leading edge of the hydrofoil until widespread reattachment of the flow sweeps the

bubbles away. "X" symbols at the lower edge of the PV region in figure 4.2 indicate observed re-wetting events. Ventilation elimination was investigated by starting from a FV state and decelerating the hydrofoil, describing a downward trajectory in figure 4.2, during which washout and re-wetting were recorded to form the stability boundaries.

4.3.1 Re-Entrant Jet Elimination

Cavity elimination by a re-entrant jet tends to occur at low speeds and moderate-to-large values of α, where a thick – but relatively short – cavity develops. When the cavity length on a lifting surface decreases (such as in decelerating flow) to the point where cavity closure occurs on the body, a re-entrant jet develops. When $\alpha \geq 5°$, the jet possesses enough momentum to impinge on the upstream cavity boundary (*Franc and Michel*, 2004; *Harwood et al.*, 2016c; *Callenaere et al.*, 2001; *Duttweiler and Brennen*, 1998).

A sketch of ventilation elimination caused by the re-entrant jet is shown in figure 4.9, corresponding to the downward (decelerating) trajectory in figure 4.2 drawn at $\alpha = 15°$. The flow begins in a FV condition. In frame (a), a re-entrant jet develops on the deeply-immersed hydrofoil section (shown by blue arrows). The cavity closure angle is shallow ($\bar{\Phi} < 45°$), so the jet flow does not impinge on the upstream flow. As the hydrofoil decelerates, the cavity remains attached to the immersed tip, but reduces in its length, causing the angle of the cavity closure line to increase. In frame (b), the mean cavity closure angle just exceeds 45°, imparting an upstream velocity component to the re-entrant jet, per equation 3.2. The jet pinches off a large portion of the cavity, causing it to be shed downstream (washout), leaving the flow in a PV state, from which FV flow does not resume. As the flow velocities decrease further in frame (c), the partial cavity is confined to a shrinking region near the foil's leading edge and the free surface. Eventually, the remaining air is ejected by laminar/turbulent reattachment of the flow, constituting re-wetting and the return to the FW regime. It is very interesting to observe that the washout boundary of figure 4.2 for $AR_h = 1.0$ and those for the other aspect ratios shown in chapter III approach values of approximately $Fn_h = 1.0$ at values of α sufficiently large to favor re-entrant jet washout. This highlights the interpretation of Fn_h as a ratio of spanwise to chordwise pressure gradients; when the two are approximately equal, the cavity's slope is approximately unity, and the flow is at a stability boundary.

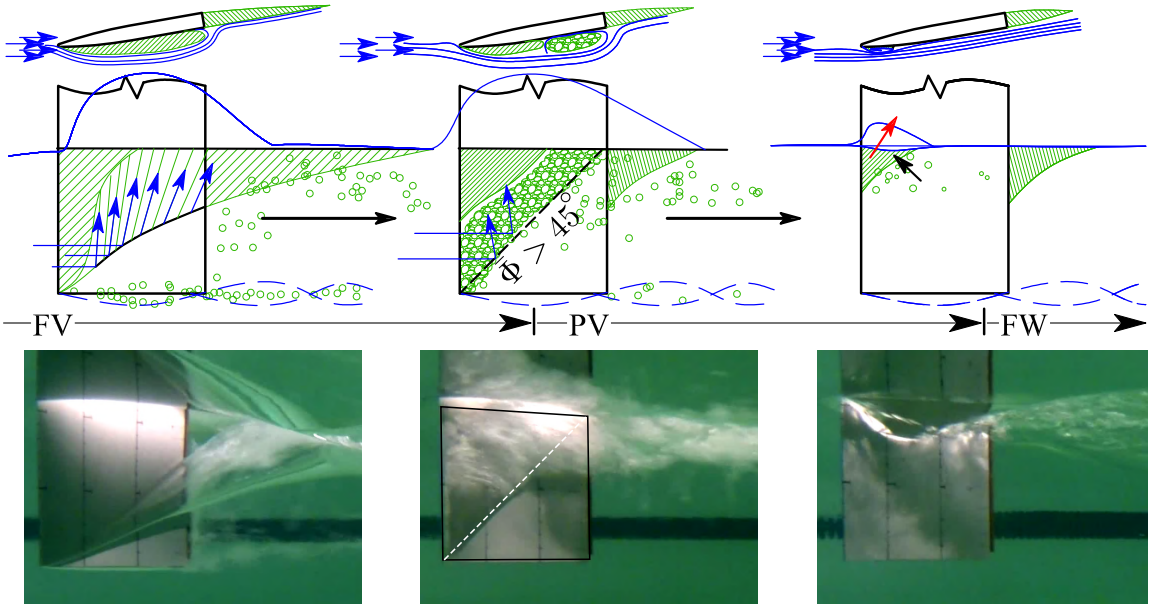

(*a*) $Fn_h = 1.59$ (*b*) $Fn_h = 1.1$ (*c*) $Fn_h = 0.49$

Figure 4.9: Ventilation elimination by re-entrant jet at $\alpha = 15°$ and $AR_h = 1.0$. Flow speed is decreasing from left to right. Fn_h is given at the instant of each photograph. Blue lines denote streamlines, green lines and hatching indicate entrained air, black hatching indicates boundary layer separation, and red arrows indicate air egress paths. Figure reproduced from *Harwood et al.* (2016b).

4.3.2 Turbulent Reattachment

At very small angles of attack ($\alpha \lesssim 5°$), the unsteadiness induced by the re-entrant jet is confined to the trailing edge of the cavity (*Franc and Michel*, 2004; *Harwood et al.*, 2016c). Instead of becoming unstable, the ventilated cavity shrinks to occupy only the locally-separated bubble on the suction surface of the hydrofoil (*Wadlin*, 1958; *Harwood et al.*, 2016c). In some cases, the supply of air from the free surface becomes cut off as the free-surface seal is re-established, leaving an orphaned leading-edge bubble that shrinks gradually as gas is ejected into the external flow without being replenished (*Wadlin*, 1958). A photographic sequence of turbulent reattachment is shown in figure 4.10. This mechanism is more gradual than re-entrant jet washout because no significant destabilizing event occurs. For the same reason, the mechanism is also less repeatable. As a result, there is significant scatter in the the washout and rewetting boundaries in figure 4.2 for small angles of attack.

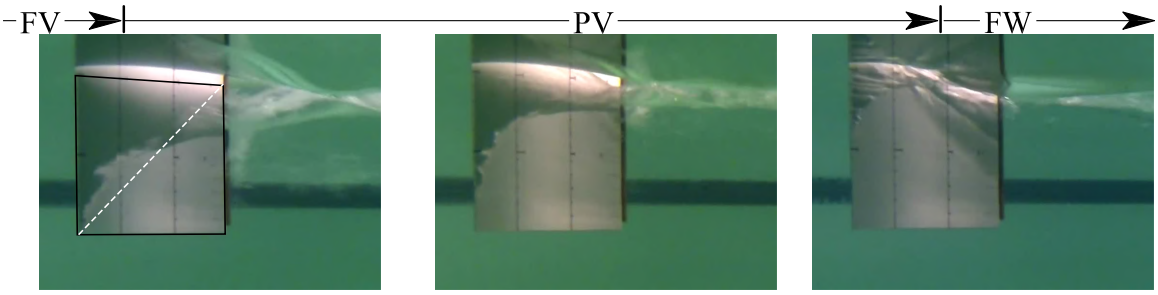

(*a*) $Fn_h = 1.72$ (*b*) $Fn_h = 1.34$ (*c*) $Fn_h = 0.96$

Figure 4.10: Ventilation elimination by turbulent reattachment at $\alpha = 5°$. Flow speed is decreasing from left to right. Fn_h is given at the instant of each photograph. Blue lines denote streamlines, green lines and hatching indicate entrained air, black hatching indicates boundary layer separation, and red arrows indicate air egress paths.

4.4 Taxonomy of Transition Mechanisms

To summarize the mechanisms described in the preceding sections, a taxonomy of ventilation formation and elimination mechanisms is shown in figure 4.11, depicting – in approximate terms – the evolution of the flow as it transitions between FW, PV, PC, and FV regimes in different regions of a parametric test space defined by α and Fn_h.

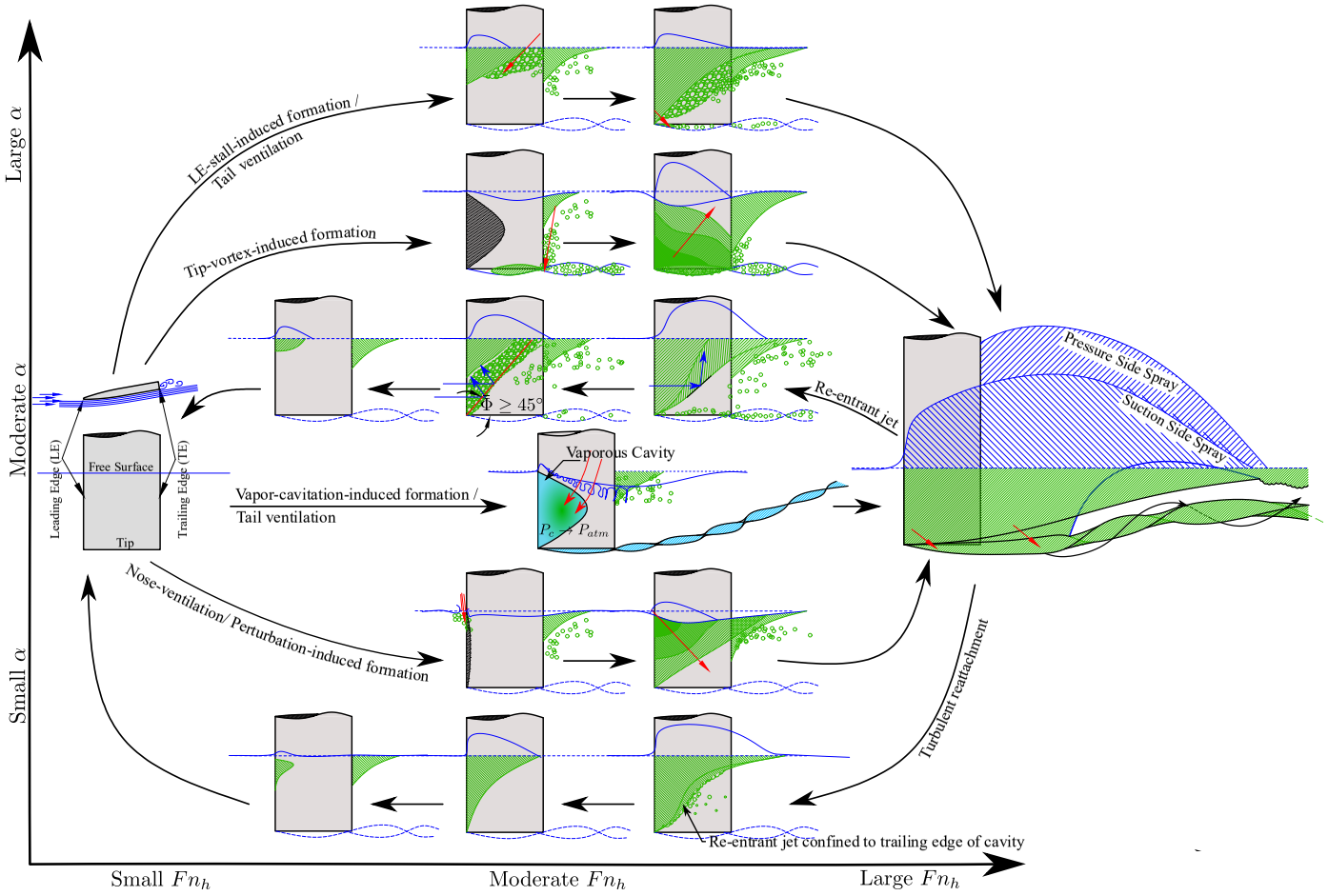

Figure 4.11: Taxonomy of ventilation formation and elimination mechanisms on a surface-piercing hydrofoil. The hydrofoil surface is shaded light grey. Blue lines indicate streamlines, free surface profiles, and spray. Green hatching and shading indicate air entrained below the initial free surface or disturbed free surface. Black stippling indicates wetted flow separation. Red arrows indicate paths of air ingress or egress. Light blue shading and hatching indicates water vapor created by cavitating flow. Figure reproduced with modifications from *Young et al.* (2016).

A schematic depiction of a surface-piercing hydrofoil, just prior to ventilation, is shown in figure 4.12 from *Young et al.* (2016). The figure conveys the various air paths that can lead to inception (initial air ingress) on a ventilated cavity. Zones of flow separation (if the flow is subcavitating) are indicated by hatching. In the case of vaporous cavitation, the shape of the vapor cavity is shown in blue shading. While ventilated supercavities were not observed in the present experiments, the same mechanism of Taylor instabilities applies for partial cavities. The various individual paths-of-ingress for air, corresponding to the mechanisms described above, and those arrayed in figure 4.11, are indicated by red arrows.

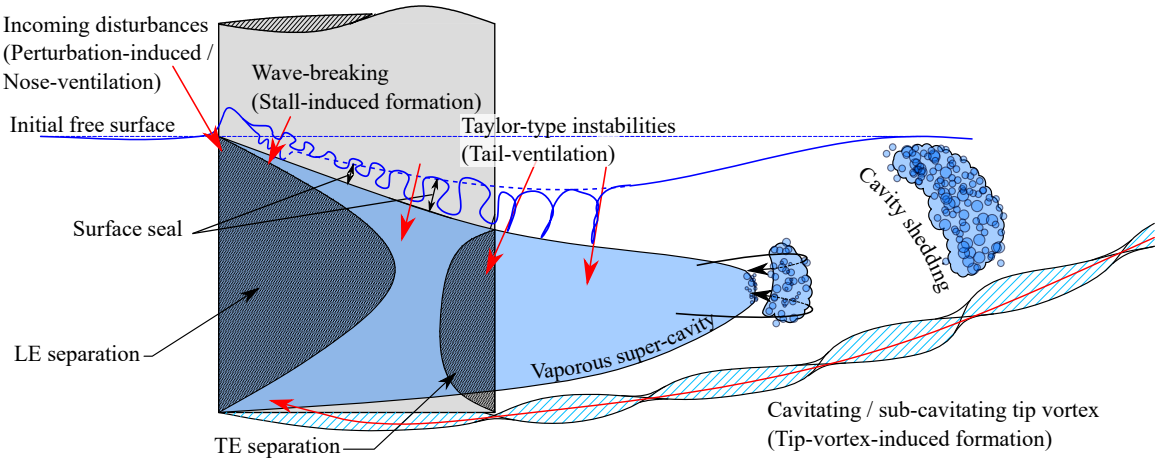

Figure 4.12: Sketch of a surface-piercing hydrofoil prior to the inception of a ventilated cavity. The suction side may be covered in a vaporous cavity, or may experience wetted separation at the leading or trailing edges. Initial air ingress (inception) occurs through any of the paths indicated by red arrows, including upstream disturbances, artificially-introduced perturbations, wave-breaking, Taylor-type instabilities, the tip vortex, or secondary interactions between the free-surface and vaporous cavity shedding. Figure reproduced from *Young et al.* (2016), and composited from sketches from *Rothblum et al.* (1969, 1974); *Rothblum* (1977b); *Waid* (1968); *Harwood et al.* (2016c)

4.5 Hysteresis of Ventilation Transition

The discussion thus far has concentrated on the topology of the flow as it moves through parametric space and transitions between flow regimes. However, as was hinted at in chapter III, the bi-stability of overlapping flow regimes, coupled with transition between flow regimes during changes in flow conditions, induces significant hysteresis in the hydrodynamic loads. The amount of hysteresis present depends upon the type of transition mechanism and the regimes through which the flow passes.

Time-histories of instantaneous lift, drag, and moment coefficients ($C_{L_{3D}}$, $C_{D_{3D}}$, and $C_{M_{3D}}$) are plotted against the instantaneous Froude number in figure 4.13 for stall-induced ventilation formation and tip-vortex-induced ventilation. The time traces correspond to the flows pictured in figures 4.3 and 4.4. It should be noted that at small Fn_h, the denominators of equations 3.3 vanish, and fluid inertial forces are large relative to the quasi-steady (velocity-dependent) load. As a result, $C_{L_{3D}}$, $C_{D_{3D}}$, and $C_{D_{3D}}$ may not be representative of steady-state results for $Fn_h \lesssim 1$. For $Fn_h \gtrsim 1.0$, however, the inertial terms are much smaller than the steady-state terms. Appendix E contains a scaling argument to support this assertion.

The grey and black traces describe two separate runs, each comprised of an acceleration-and-deceleration cycle. Dashed arrows indicate the direction of the traces with increasing time. Symbols indicate steady-state force and moment coefficients. Note that the steady-state data shown are projections of the same points shown in figures 3.14–3.17 in chapter III, plotted for a fixed α at different values of Fn_h. Lettered markers indicate the corresponding frames in figures 4.3 and 4.4. The trace corresponding to stall-induced formation (solid black line in figure 4.13) follows the PV and FV markers during acceleration and deceleration, with the forces passing gradually through the inception and stabilization events at increasing values of Fn_h. In the case of tip-vortex-induced formation (dashed grey line in figure 4.13), the loads pass through the FW points during the acceleration phase. At $Fn_h = 3.5$, inception and stabilization occur rapidly at a constant speed, indicated by a precipitous drop in $C_{L_{3D}}$ and $C_{M_{3D}}$. During deceleration, the measured forces and moment follow the FV and PV points, overlapping with the deceleration section of the stall-induced formation case.

For the case of vortex-induced ventilation, the result is a very large hysteresis loop, indicated by blue shading. In the case of stall-induced ventilation formation, the hysteresis is nearly nonexistent. These observations can once again be traced back to figure 4.2. Stall-induced ventilation formation involves crossing the stability boundaries of respective flow regimes, and the hysteresis between the boundaries is relatively small. Tip-vortex-induced ventilation, on the other hand, involves a perturbation to the FW flow that "pushes" the flow through the FW stability region onto the FV stability region, from which it does not return until the the flow is decelerated below the washout and rewetting boundaries – a much larger hysteretic range. The hysteresis is most pronounced in the lift and moment coefficients, which is unsurprising, since it was shown in chapter III that the drag is relatively insensitive to the flow regime. Time-histories of the lift, drag, and moment coefficients of the process

of perturbation-induced ventilation formation pictured in figure 4.7 are plotted against the instantaneous Froude number in figure 4.14. The resulting hysteresis loop is similar to that created by tip-vortex-induced formation in the sense that large changes in hydrodynamic loading occur on a short time-scale, and at otherwise-steady flow conditions.

For all of the cases shown, ventilation elimination occurred *via* re-entrant jet during the deceleration of the flow. During deceleration, there is also an increase in lift, most readily visible in figure 4.14. This augmented lift is a wake-memory effect, created by vorticity being shed into the wake of the hydrofoil during deceleration – a phenomenon easily modeled by indicial response functions such as the Wagner function (*Wagner*, 1925). As a result of the wake-memory and the increasing influence of inertial effects, it is hard to say how hysteretic the flow is at low Froude numbers, but the two figures here provide ample evidence that varying degrees of hysteresis can result from ventilation transition.

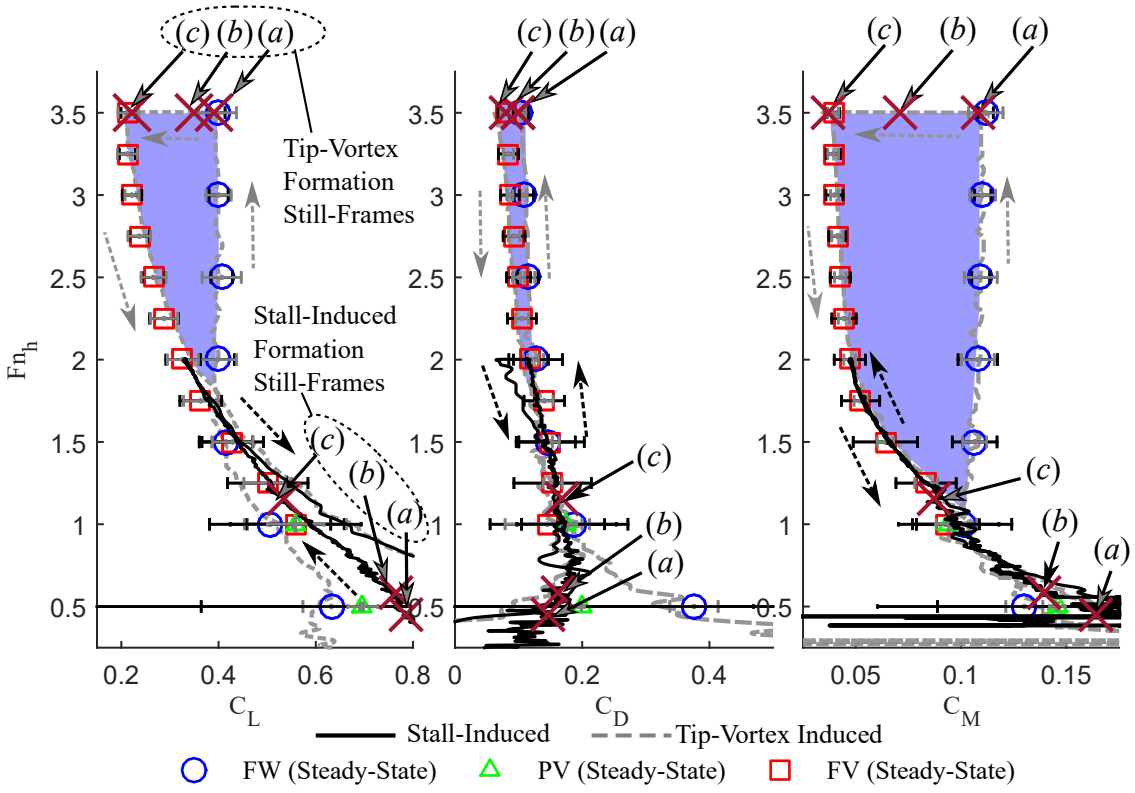

Figure 4.13: Hysteresis loops formed by lift, drag, and moment coefficients for stall-induced (as depicted in figure 4.3) and tip-vortex-induced (as depicted in figure 4.4) ventilation formation at $\alpha = 15°; AR_h = 1$. Ventilation elimination occurred as a result of re-entrant flow, as shown in figure 4.9. Dashed arrows indicate the acceleration and deceleration stages of the runs. Steady-state force/moment coefficients for all runs at $\alpha = 15°$ are plotted as open symbols, with measurement uncertainty and standard deviations indicated, respectively, by grey and black horizontal bars. Figure reproduced with modifications from *Harwood et al.* (2016b).

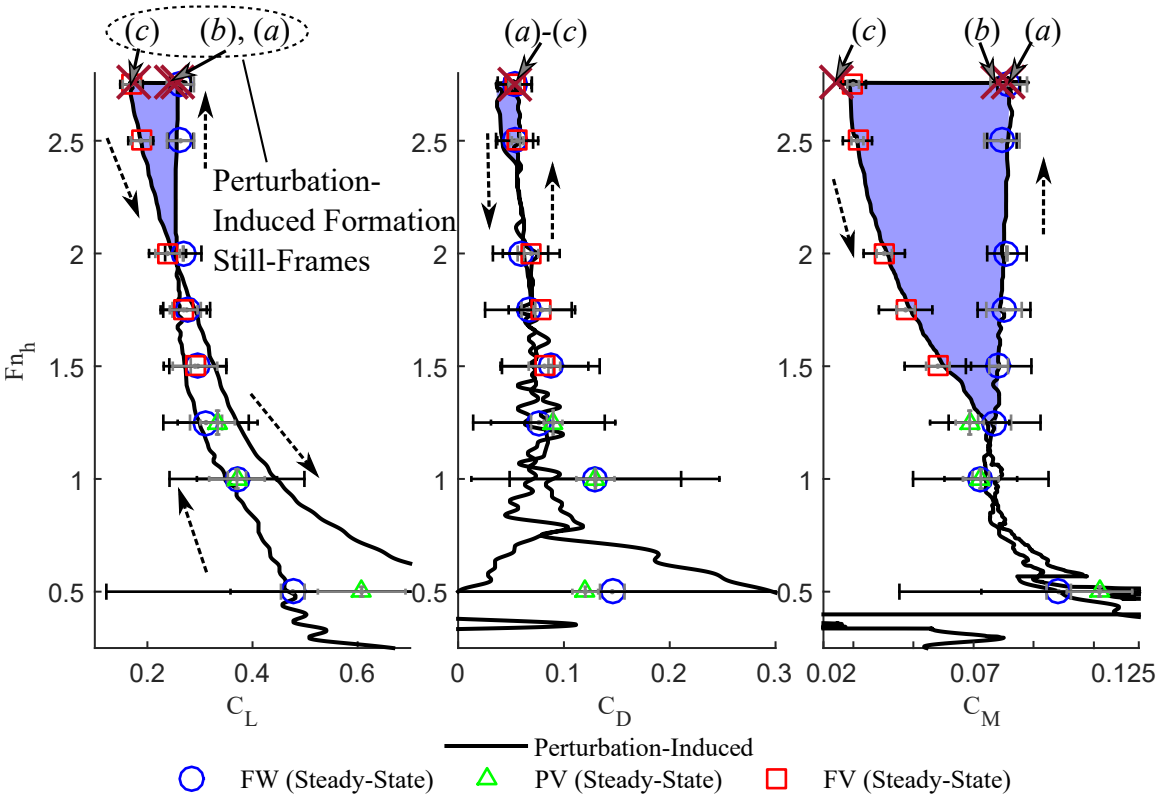

Figure 4.14: Hysteresis loops of lift, drag, and moment coefficients for perturbation-induced ventilation formation at $\alpha = 10°$; $AR_h = 1$. Ventilation elimination occurred as a result of re-entrant flow, as shown in figure 4.9. Lettered markers correspond to frames in the figure 4.7. Dashed arrows indicate the acceleration and deceleration stages. Steady-state force/moment coefficients for all runs at $\alpha = 10°$ are plotted as open symbols, with measurement uncertainty and standard deviations indicated, respectively, by grey and black horizontal bars. Figure reproduced with modifications from *Harwood et al.* (2016b).

4.6 Scaling of Washout Boundary

The experimentally-observed washout boundaries from the present experiment are plotted as open symbols in figure 4.15 as functions of instantaneous lift coefficient $C_{L_{3D}}$ and Fn_h for the three immersed aspect ratios ($AR_h = 0.5, 1, 1.5$). The plotted data denote the combination of Fn_h and $C_{L_{3D}}$ at the moment that washout was visually observed, *e.g.* in frame (*b*) of figure 4.9. Data from *Breslin and Skalak* (1959) for hydrofoils with circular-arc and cambered NACA sections at four immersed aspect ratios ($AR_h = 0.5, 1, 1.5, 2$) are plotted as filled symbols as well. The points indicate the boundary at which *Breslin and Skalak* (1959) observed the elimination of ventilated cavities; the specific stage of elimination was not specified in the original report, but is judged from context to be the cessation of FV flow, which has been defined as washout in the present work. Equation 1.22, shown as the black dashed line, represents the lower bound on stable FV flow proposed by *Breslin and Skalak* (1959).

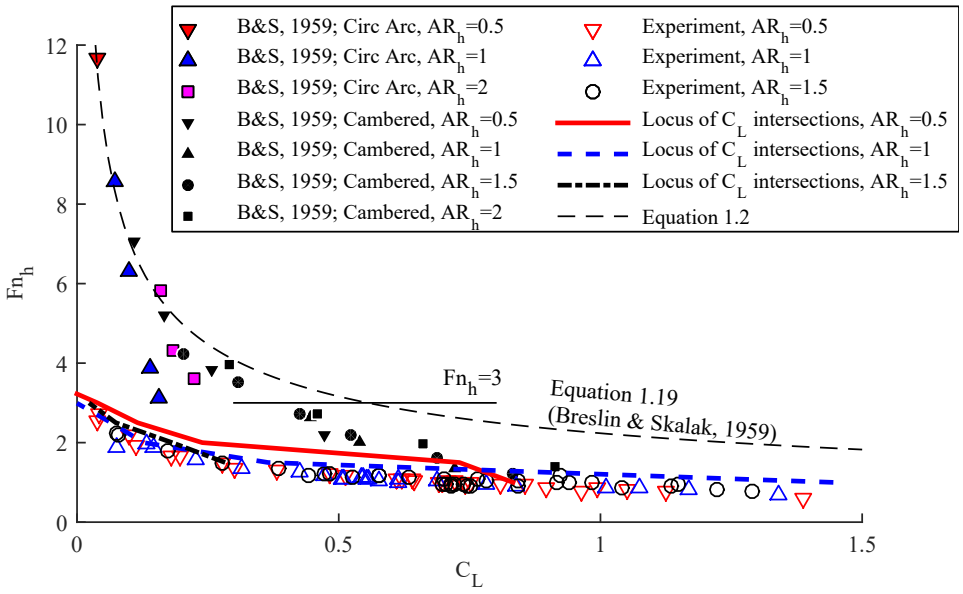

Figure 4.15: Scaled washout boundary in $C_{L_{3D}}, Fn_h$ space. Data from present experiments at three immersed aspect ratios and the experimentally observed boundary from *Breslin and Skalak* (1959) for cambered and circular-arc hydrofoils at four immersed aspect ratios are plotted in filled symbols are shown. Equation 1.22 overpredicts the washout Froude numbers from the present experiments. The projected loci of lift-intersection points closely match the washout boundaries, suggesting that the lift coefficient is similar between the three flow regimes at washout. Figure reproduced from *Harwood et al.* (2016b).

Note that the boundary given by equation 1.22 is valid only for $Fn_h \geq 3$ (*Breslin*,

1958), above the horizontal line in figure 4.15. This restricts usage of the boundary to relatively low values of $C_{L_{3D}}$. Recall also that *Breslin and Skalak* (1959) defined equation 1.22 such that C_{L_w} is the instantaneous lift coefficient, measured when the hydrofoil is in a FW flow at the conditions under which ventilation elimination occurred. This makes equation 1.22 difficult to apply directly, because the lift coefficient may be unknown for FW flows at the combination of α and Fn_h observed at the moment of washout. Recall that in figure 3.17, the approximated intersection points between affine fits through the FV and FW lift coefficients formed a locus of intersection points. In order to justify the application of equation 1.22 to lift coefficients measured in the FV regime, the orthographic projections of these loci are plotted as bold lines in figure 4.15, where the lines closely follow the experimentally-observed washout boundaries. This means that, at the conditions of washout, the lift coefficients in the FV, PV, and FW regimes are approximately equal, so the measured $C_{L_{3D}}$ at washout is a suitable approximation of C_{L_w}. As shown in figure 4.15, equation 1.22 over-predicts the washout-Fn_h for a given $C_{L_{3D}}$. In fact, it passes through only a few of the experimental points from *Breslin and Skalak* (1959), while washout was never observed at $Fn_h > 3$ in the present experiments.

There are several reasons why the experimentally-observed washout boundaries would differ between the present study and that of *Breslin and Skalak* (1959). The first is the difference in section profiles. The present model has a rectangular section aft of mid-chord, while both of the models used by *Breslin and Skalak* (1959) had sharp trailing edges and convex curvature on the suction surfaces aft of mid-chord. As a result, washout may have occurred at higher Froude numbers for the latter model because the re-entrant jet was enhanced by an adverse pressure gradient developed on the wetted portion of the suction surface. Another factor is the difference in size between the two models. The present model is approximately 4-5 times as large as those used by *Breslin and Skalak*; the smaller model would be more susceptible to surface-tension effects (*Wetzel*, 1957), where spray sheets close and cut off the supply of air to the cavity in a process called cavity "choking" (*Elata*, 1967). Equation 1.22 also over-predicts the washout boundary of *Breslin and Skalak* (1959) for $3 < Fn_h < 6$. This occurs because equation 1.22 was derived from a linearized fit at very large Fn_h and vanishingly small $C_{L_{3D}}$. Equation 1.22 does form an upper bound on all other presented experimental data, so it is appropriate to consider it a boundary above which FV flow is likely to be stable, but not a boundary below which full ventilation is necessarily unstable.

To develop an improved washout scaling relation, the kinematic stability boundary

on the cavity shape ($\bar{\Phi} = 45°$) can be used, along with models for the cavity length (L_c), lift coefficient ($C_{L_{3D}}$), Froude number (Fn_h), aspect ratio (AR_h), and angle of attack (α). Figure 4.16 schematically depicts a FV cavity. A sectional cut is taken

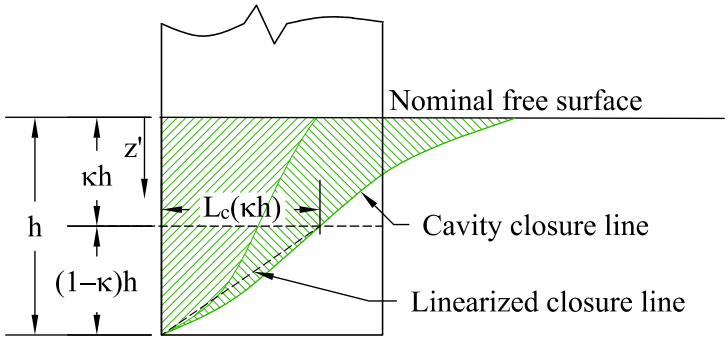

Figure 4.16: Sketch of cavity topology used to set up scaling of washout. The cavity stability criterion of §3.1 is expressed using a two-point linearization of the cavity closure line. When the slope of the linearized cavity closure line approaches unity ($\bar{\Phi} = 45°$), it is hypothesized that washout is imminent. Figure reproduced from *Harwood et al.* (2016c).

at a dimensionless depth of $\kappa = z'/h$ and a linear approximation of the cavity closure angle is made between this section and the immersed tip – a distance of $(1-\kappa)h$. The stability limit of $\bar{\Phi} = 45°$ is equivalent to a unity-slope condition on this linearization. Recall that the cavity length was modeled as a function of the local cavitation number σ_c and α in equation 1.8 and equation 1.9. While not shown in chapter I, *Harwood et al.* (2016c) found that a single-term polynomial also yielded an acceptable fit to the free-streamline theory solutions, given by,

$$\frac{L_c}{c} = 4.62\frac{\alpha_{eff}}{\sigma_c}. \tag{4.1}$$

Applying this at the sectional cut depicted in figure 4.16 yields the unity-slope condition in the form,

$$\frac{L_c(z' = \kappa h)}{c} = (1-\kappa)\frac{h}{c} = 4.62\frac{\alpha_{eff}(z' = \kappa h)}{\sigma_c(z' = \kappa h)}. \tag{4.2}$$

The next step is to infer the sectional lift coefficient at the representative section from the Three-Dimensional (3-D) lift coefficient, which requires *a priori* knowledge of the distribution of lift along the span. An elliptical shape-function may be applied to the lift-distribution as a simple approximation for rectangular wings (*Glauert*, 1943), and one which retains the salient features of the lift distribution shown in figure 3.32. The low aspect ratio is not a concern because the elliptical distribution

can be scaled such that integration along the span yields the experimentally-measured 3-D lift coefficient. Thus, the sectional lift coefficient at the representative section is taken to be,

$$C_{l_{2D}}(z' = \kappa h) = \frac{4}{\pi} C_{L_{3D}} \quad \overline{1 - (2\kappa - 1)^2}. \tag{4.3}$$

The effective angle of attack can be found by substituting $L_c/c = (1-\kappa)AR_h$ into equation 1.9 to find a_0, giving,

$$\begin{aligned}\alpha_{2D}(z' = \kappa h) &= \arcsin \quad \frac{C_{l_{2D}}(z' = \kappa h)}{a_0(z' = \kappa h)} \quad \approx \frac{C_{l_{2D}}(z' = \kappa h)}{a_0(z' = \kappa h)} \\ &= \frac{4C_{L_{3D}}\sqrt{\kappa - \kappa^2} \quad 4\pi\left[(1-\kappa)AR_h\right]^3 - 4\pi\left[(1-\kappa)AR_h\right]^2 + 3\pi\left[(1-\kappa)AR_h\right] + 2}{\pi \quad \pi^2\left[(1-\kappa)AR_h\right]^3 - 4\pi\left[(1-\kappa)AR_h\right]^2 + 9\pi(1-\kappa)AR_h + 2\pi}.\end{aligned} \tag{4.4}$$

It follows from equation 1.2 that,

$$\sigma_c = \frac{2}{Fn_h^2}\frac{z'}{h} = \frac{2}{Fn_h^2}\kappa, \tag{4.5}$$

which may be substituted into equation 4.2, along with equation 4.4. The representative section of the hydrofoil is taken at mid-span ($\kappa = 0.5$), with the reasoning that any re-entrant jet posing a threat of destabilization to the flow is anticipated to be reflected about the deeply-submerged portions of the cavity. Solving for Fn_h yields the semi-theoretical washout Froude number,

$$Fn_h = \frac{\pi}{4} \quad \overline{\frac{\frac{\pi}{2}AR_h^4 - 4AR_h^3 + 18AR_h^2 + 8AR_h}{2.31C_{L_{3D}}\left(\pi AR_h^3 - 2\pi AR_h^2 + 3\pi AR_h + 4\right)}}. \tag{4.6}$$

The boundaries given by equation 4.6 are shown in figure 4.17, again with the data of *Breslin and Skalak* (1959) and equation 1.22. The present experimental washout boundary is captured very well by equation 4.6. The data of *Breslin and Skalak* (1959) are reasonably-well approximated by the present theory for $Fn_h \leq 3$, while equation 1.22 better approximates the points at very small values of $C_{L_{3D}}$ and $Fn_h > 3$.

$C_{L_{3D}}$ is often not know *a priori*, requiring it to be inferred as well. Recall that equation 3.22 may be used to model $C_{L_{3D}}$ by assuming a representative value of a_0. Equation 3.24 can be used again to calculate the lift-weighted mean, a_0^*, but doing so requires that the cavity length and lift distributions are known. The distribution of

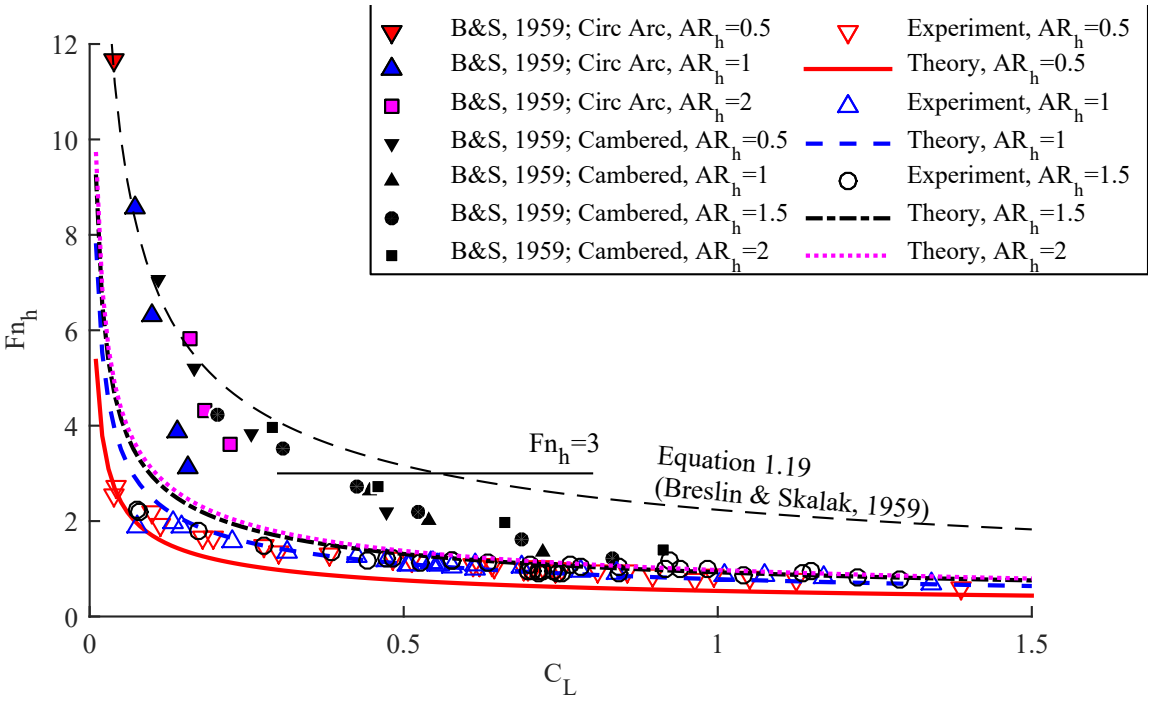

Figure 4.17: Scaled washout boundary in $C_{L_{3D}} - Fn_h$ space. Data from present experiments and data from *Breslin and Skalak* (1959) are plotted. The stability boundary of *Breslin and Skalak* (1959) (equation 1.22) over-predicts the washout Froude numbers, while the present semi-theoretical boundary (equation 4.6) captures the present experimental data across the range of $C_{L_{3D}}$, and captures the data of *Breslin and Skalak* (1959) for $C_{L_{3D}} \gtrsim 0.6$.

cavity lengths is constrained by the assumption of $\bar{\Phi} = 45^\circ$ to be,

$$\frac{L_c(\kappa)}{c} = AR_h(1-\kappa). \tag{4.7}$$

Equation 4.7 may be substituted into equation 1.9 to get $a_0(\kappa)$. The assumed elliptical lift distribution is scaled to yield an integral of one, giving the shape function,

$$E(\kappa) = \frac{4}{\pi} \sqrt{1-(2\kappa-1)^2}. \tag{4.8}$$

By weighting $a_0(\kappa)$ with $E(\kappa)$, equation 3.24 becomes, under a change-of-variables,

$$a_0^* = \int_0^1 a_0(\kappa)E(\kappa)d\kappa, \tag{4.9}$$

which is evaluated using numerical integration. a_0^* is substituted into equation 3.22, and the predicted $C_{L_{3D}}$ is in turn substituted into equation 4.6. Doing so yields a function of Fn_h, α, and AR_h. As before, solving for Fn_h results in a washout Froude number, plotted in figure 4.18 as a boundary in α – Fn_h space. A value of $\kappa = 0.5$ is again assumed. The boundaries from present experiments at three aspect ratios ($AR_h = 0.5, 1, 1.5$) are shown as open symbols. Experimental points from *Breslin and Skalak* (1959) (circular-arc hydrofoil at AR_h = 0.5, 1, 1.5, and 2) and *Swales et al.* (1974) (biogival hydrofoil at $AR_h = 2$) are shown for comparison. The two sets of data shown for *Swales et al.* (1974) are from tests conducted in a towing tank at atmospheric pressure and tests in a variable-pressure water tunnel under reduced ambient pressure. The experimental data represent a very diverse range of operating conditions, model sizes, and model geometries, which are in good general agreement with the semi-theoretical washout boundary.

At this point, one might wonder why so much trouble has been undertaken by assuming elliptical load distributions and a simplified cavity length relationship, when these quantities are all computed by the lifting-line model presented in §3.4. We certainly could use the lifting line mode. Doing so would eliminate the assumptions made in the preceding derivation, including the elliptical load distribution and the simplified functional relationship between σ_c, α, and L_c/c. The resulting boundaries, shown in figure 4.19, also approximate the experimental boundaries. However, doing so also sacrifices the ability to write a closed-form scaling expression like that in equation 4.6. Moreover, the improvement upon the preceding semi-theoretical derivation. While the lifting-line model produces good results, so does the simplified scaling

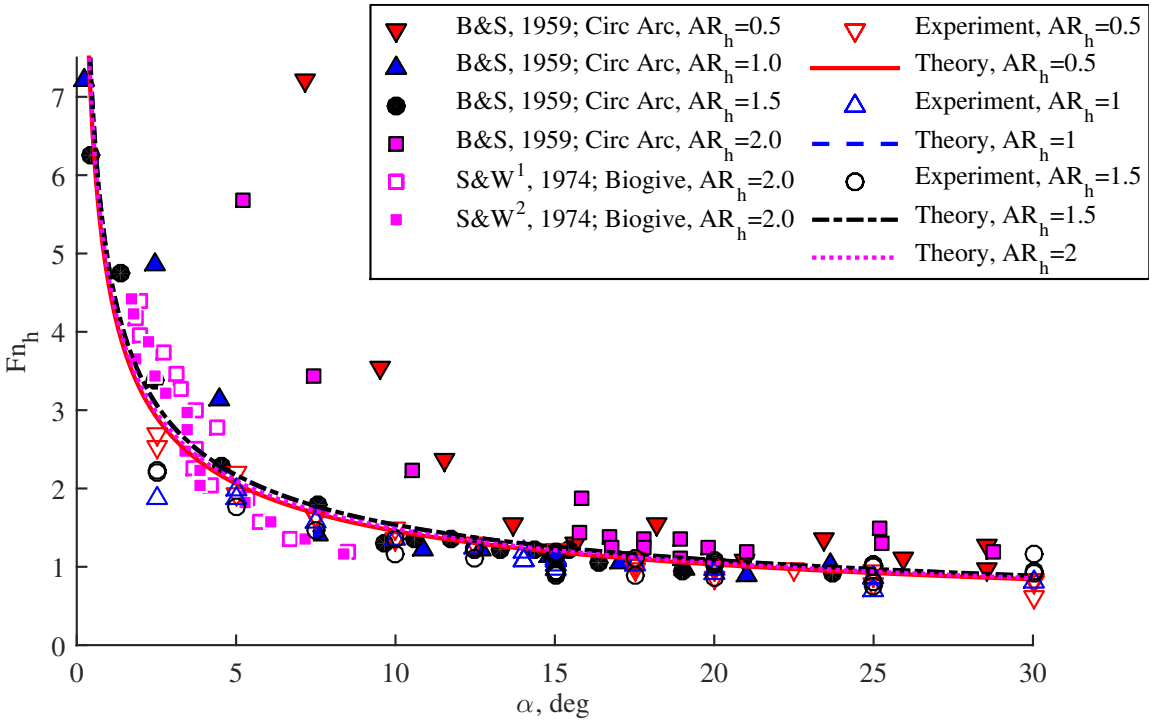

Figure 4.18: Scaled washout boundary in $\alpha - Fn_h$ space. Data from present experiments and previous experiments are plotted as symbols.; B&S: *Breslin and Skalak* (1959); S&W: *Swales et al.* (1974) experiments in variable-pressure water tunnel. [1]Tests conducted at atmospheric pressure. [2]Tests conducted at reduced pressure of 4.67 kPa.

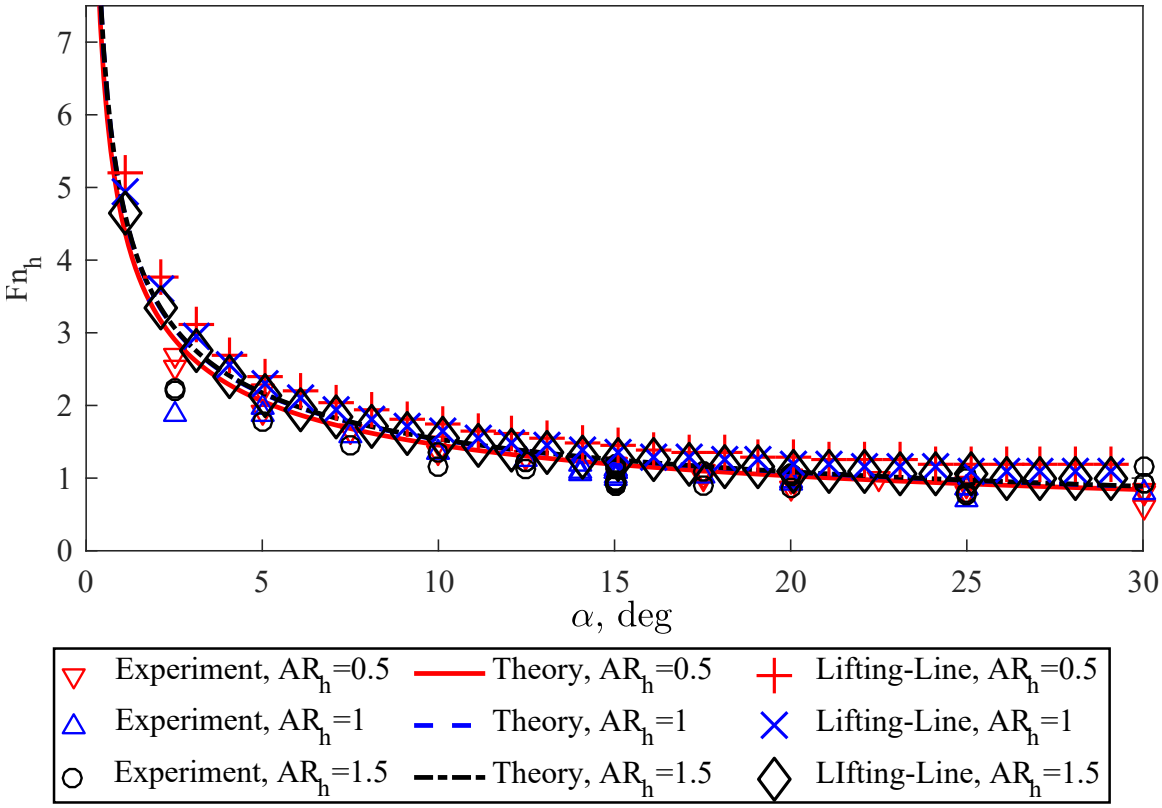

Figure 4.19: Comparison of washout boundaries observed experimentally, those from the semi-theoretical scaling relationship, and those predicted using the nonlinear lifting-line model from §3.4. The agreement between all three methods is very close, suggesting that the added fidelity of usign the lifting-line model is not worth losing the ability to write out a closed-form scaling expression.

approach.

4.7 Summary and Discussion

4.7.1 Summary of Results

The findings of this chapter are summarized below:

How do flows transition between different regimes and how do transition mechanisms relate to the physics governing flow stability?

We've shown in this chapter that transition mechanisms produce motion between stable flow regimes when some aspect of the flow violates the stability conditions of the flow regime. Visually, this corresponds to a movement of the flow across the stability boundaries in figure 4.2 or a movement between overlapping stability regions. The destabilizing influence of the flow takes the form of vorticity and eddying flow in

the case of formation mechanisms, and it takes the form of an upstream re-entrant jet in the case of elimination mechanisms. Ventilation transition mechanisms have been subdivided into formation stages, which include inception and stabilization, and elimination stages, which include washout and rewetting. The four sub-stages describe the boundaries between the FW, PV, FV, and PC flow regimes.

Ventilation inception is the first stage of formation, and it requires that air enters low-pressure and locally-separated flow. Stabilization occurs when the air entrainment satisfies the stability conditions established in chapter III for FV flow.

Washout is the reverse of stabilization, and occurs when a cavity becomes destabilized by the re-entrant jet or its closure line forms an angle steeper than the $\bar{\Phi} = 45°$ criterion established for stable FV flow. Rewetting occurs when all entrained air is expelled from the suction-side flow.

What flow transition mechanisms occur on surface-piercing struts in subcavitating and cavitating flow?

In subcavitating flows, a number of ventilation elimination formation and elimination mechanisms were described. The distinction between the mechanisms is made on the basis of how air is first entrained into the flow (inception). Spontaneous inception occurs when some self-induced process of the flow admits air from a natural source, and includes stall-induced, tip-vortex-induced, and Taylor-instability-induced mechanisms. Perturbation-induced inception requires that an external source of air be provided, an example being the air jet used in the present study. Air can only become stably entrained where low pressure permits its ingress and separated flow permits its residence. Ventilation formation follows from wetted flow separation or eddying flow. When vaporous cavitation is present, such as in the PC regime, it enhances the formation mechanisms already present by providing a stationary region of ventilation-prone flow in which air can reside. In the present work, wetted ventilation formation usually occurred through leading-edge stall. In cavitating flows, the formation mechanism shifted to tail ventilation, where Taylor instabilities developed on the free surface transport air to the vaporous cavity.

Can scaling relations be developed to describe the stability conditions of surface-piercing struts?

A scaling relationship was derived to describe the washout boundary of ventilated flow. By expressing a kinematic condition for destabilization of FV flow, a series of semi-theoretical models were used to predict the boundaries in the $C_{L_{3D}} - Fn_h$ and in the $\alpha - Fn_h$ domain. The scaled boundaries agree well with the present experimental

data, and with data from *Swales et al.* (1974) and *Breslin and Skalak* (1959) (for $Fn_h \lesssim 3$). At large Froude numbers ($Fn_h > 3$) and vanishingly small angles of attack, the relationship proposed by *Breslin and Skalak* (1959) yielded a better fit to the data.

4.7.2 Discussion:

It was hypothesized in this chapter that the entrained air modifies the local pressure gradients, inducing further flow separation, as observed in vaporous cavitating flows by *Tassin Leger and Ceccio* (1998). This suggests that large-scale separation need not precede ventilation if the injected air induces its own region of separation. If an air supply is continuously available, this will result in a cavity that expands by propagating flow separation ahead of it, and then occupying the newly separated flow in a continuous evolution. Equilibrium will be reached when the increasing hydrostatic pressures – and not the extent of flow separation – arrests the growth of the cavity. It is thought that this evolution of separation and propagation occurs very suddenly for short-timescale formation processes, and very gradually for stall-induced formation. Such a hypothesis requires further validation, but if verified, it would be consistent with the idea that destabilization of a steady FW flow leads to the formation of a FV flow as a second stable flow state.

To relate the present work to the literature, stall-induced ventilation formation is consistent with the description by *Wetzel* (1957) of "creeping" ventilation, occurring at post-stall yaw angles. Both tip-vortex-induced ventilation formation and perturbation-induced ventilation formation are consistent with *Wetzel*'s description of "flash ventilation," occurring at sub-stall yaw angles.

Previous studies have also noted an effect of Weber number and Reynolds number on ventilation formation boundaries, as most were conducted with small-scale models at lower Weber numbers and Reynolds numbers than the present tests. These effects influence the rupture of the free surface seal and boundary layer separation, respectively (*Wetzel*, 1957; *Breslin and Skalak*, 1959). However, the data of *Wetzel* (1957) showed that the effect of Weber number was significant only when $We \lesssim 250$, so surface tension becomes negligible at the present model scale, where $We \gtrsim 10^4$. Moreover, the separation bubble indicated by the surface flow visualizations is not thought to be a strong function of Reynolds number. The works of *Gault* (1957); *Chang* (1960, 1961); *Hecker and Ober* (1974) indicate that, for the sharp-nosed geometry used, separation is of the thin-airfoil type, and is primarily a function of the angle of attack. If a streamlined foil section were to be used, the size of the separation

bubble would likely be more susceptible to Reynolds number effects.

Ventilation elimination appears to be strongly tied to the re-entrant jet's potential for destabilization of the flow. The derived scaling relationship approximates the present data much better than does equation 1.22 for $Fn_h \leq 3$. When $Fn_h > 3$, washout appears to occur at vanishingly small angles of attack. The scaling relation is not expected to yield satisfactory results at such small angles of attack because the re-entrant jet may be too thin at such angles to destabilize the cavity (*Callenaere et al.*, 2001; *Franc and Michel*, 2004). Additionally, washout may occur at higher Froude numbers than those predicted by the derived scaling relation for streamlined sections as a result of adverse pressure gradients developed over the after-body of sections with zero trailing-edge thickness. It is also possible that the data from *Breslin and Skalak* (1959) shown in figure 4.15 and figure 4.17 do not represent washout as it has been defined in this work; if the data denote a stage of elimination other than washout, the scaling approach can not be expected to adequately capture the respective boundary.

It is also worth noting that the experimental washout boundary of *Breslin and Skalak* (1959) in figures 4.15, 4.17, and 4.18 deviates from the present semi-theoretical and experimental boundaries quite severely at immersed aspect ratios of $AR_h = 0.5$ and 2.0. This is a result of a distinct bucket-shape in the minimum ventilated yaw angle plotted against AR_h in the results from *Breslin and Skalak* (1959). The reasons for the non-monotonic behavior are not discussed in the original report, but may be a result of surface-tension effects, given the smaller model-scale used.

CHAPTER V

The Hydrodynamic Response of the Flexible Hydrofoils

In this chapter, we will examine the steady and unsteady passive hydroelastic response of the flexible hydrofoils (model 1, constructed of PVC only, and model 2, constructed of PVC with an aluminum reinforcement strip at the trailing edge). The concepts of wetted, ventilated, and cavitating flows have been introduced in chapters III and IV. Thus, the discussion will first address the altered hydrodynamic response of the hydrofoil in each flow regime when the hydrofoil is flexible, followed by the hydroelastic response of the flexible hydrofoil to differing flow regimes. Additionally, some investigations will be made into scaling into scaling of the hydroelastic response. This chapter will address the following questions posed in §1.6:

- What effect does hydrofoil flexibility have upon the hydrodynamic response, stability, and flow regimes of the flexible hydrofoils?
- How does multi-phase flow affect the static and dynamic hydroelastic response and stability of the hydrofoil?
- Can scaling relations be used to describe the static and dynamic loads and structural responses of the surface-piercing hydrofoils?

5.1 Representative 2-Dimensional, 2-Degree of Freedom Model

Let us revisit the Two-Dimensional (2-D), Two-Degree of Freedom (DOF) model originally presented in chapter I, which is shown in figure 5.1 with the semi-ogival section and is assumed to be chordwise rigid. The equations of motion are re-stated as well.

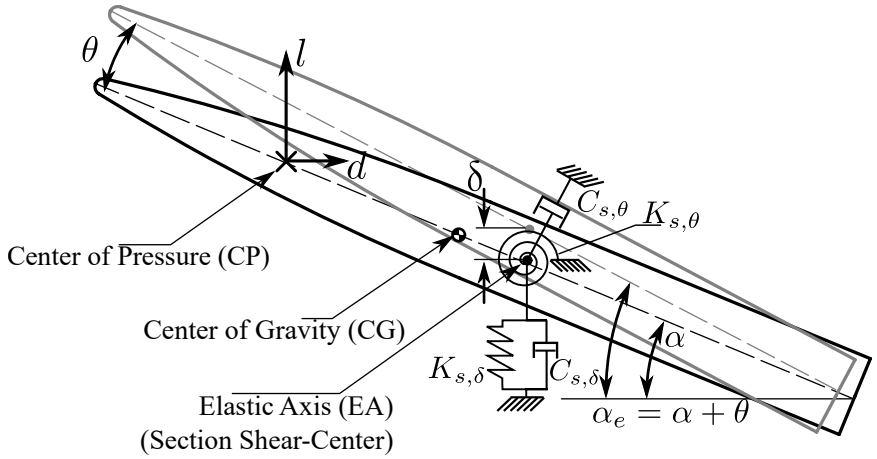

Figure 5.1: A 2-degree-of-freedom model of a sectional cut through model 1 or 2.

$$[\boldsymbol{M_s}] \quad \ddot{\boldsymbol{X}} \quad + [\boldsymbol{C_s}] \quad \dot{\boldsymbol{X}} \quad + [\boldsymbol{K_s}] \{\boldsymbol{X}\} = \{\boldsymbol{F_{EX}}\} + \{\boldsymbol{F_{fl}}\} \qquad \text{(1.24 revisited)}$$

The section is assumed to have two degrees of freedom, δ and θ, which are defined at the Elastic Axis (EA):

$$\{\boldsymbol{X}\} = \left\{ \begin{array}{c} \delta \\ \theta \end{array} \right\}$$

$\{\boldsymbol{F_{EX}}\}$ contains external forces on the system, and $\{\boldsymbol{F_{fl}}\}$ describes the hydrodynamic loading (lift and moment) per unit span.

The matrices are given by,

$$[\boldsymbol{M_s}] = \left[\begin{array}{cc} m & S_\theta \\ S_\theta & I_\theta \end{array} \right]; \quad [\boldsymbol{C_s}] = \left[\begin{array}{cc} C_{s,\delta} & 0 \\ 0 & C_{s,\theta} \end{array} \right]; \quad [\boldsymbol{K_s}] = \left[\begin{array}{cc} K_{s,\delta} & 0 \\ 0 & K_{s,\theta} \end{array} \right], \qquad \text{(1.27 revisited)}$$

where $K_{s,\delta}$ and $K_{s,\theta}$ are structural stiffness parameters of the section in bending and twisting, $C_{s,\delta}$ and $C_{s,\theta}$ are structural damping values in bending and twisting, m is the structural mass per unit span, I_θ is the polar mass moment of inertia per unit span, and S_θ is the static unbalance.

In this chapter, we will consider the case where $\{\boldsymbol{F_{EX}}\} = \{\boldsymbol{0}\}$. Let the steady and unsteady sectional force induced by the fluid be represented by,

$$\{\boldsymbol{F_{fl}}\} = \left\{ \begin{array}{c} l \\ m \end{array} \right\},$$

where, by the definitions in equation 1.1,

$$l = C_{l_{2D}} qc$$
$$m = C_{m_{2D}} qc^2.$$

Here, $q = \rho_f U^2/2$ is the dynamic pressure. $C_{l_{2D}}$ and $C_{m_{2D}}$ come from the application of hydrodynamic theory, as described in §1.5.

5.2 Steady-State Flow Regimes

The definitions of flow regimes established in chapter III hold for the flexible hydrofoils as well. Fully Wetted (FW) flow is shown in figure 5.2, Partially Ventilated (PV) flow is shown in figure 5.3, Fully Ventilated (FV) flow is shown in figure 5.5, and Partially Cavitating (PC) flow is shown in figure 5.4. The images were captured at the INSEAN cavitation tunnel with model 2 – the hydrofoil with the reinforced Trailing Edge (TE). There were no significant differences in the flow regimes between the flexible hydrofoils (model 1 and model 2) and the rigid hydrofoil (model 0).

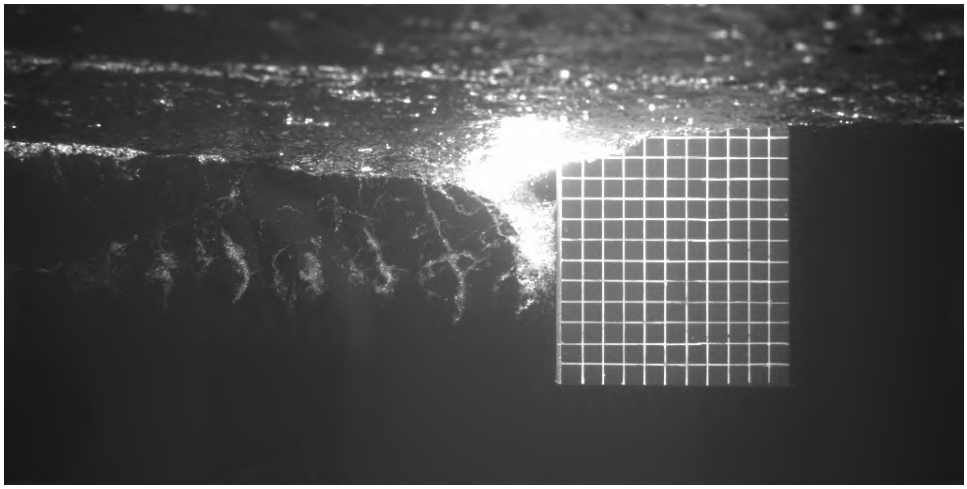

Figure 5.2: Photo of FW flow over the suction surface of the PVC foil (model 2) from INSEAN. Run conditions: $\alpha = 5°$; $Fn_h = 2$; $AR_h = 1$; P_0 =1 bar; σ_v =18

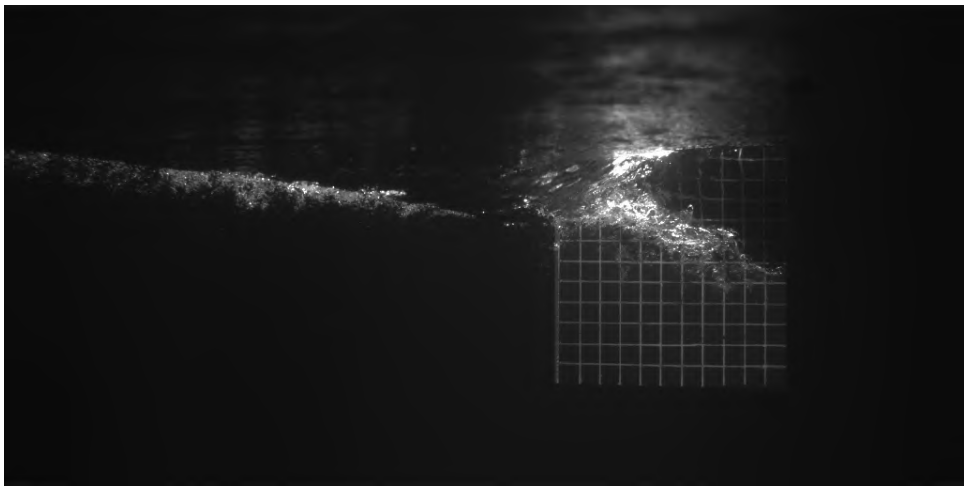

Figure 5.3: Photo of PV flow over the suction surface of the PVC foil (model 2) from INSEAN. Run conditions: $\alpha = 15°$; $Fn_h = 1$; $AR_h = 1$; P_0 =1 bar; σ_v =77

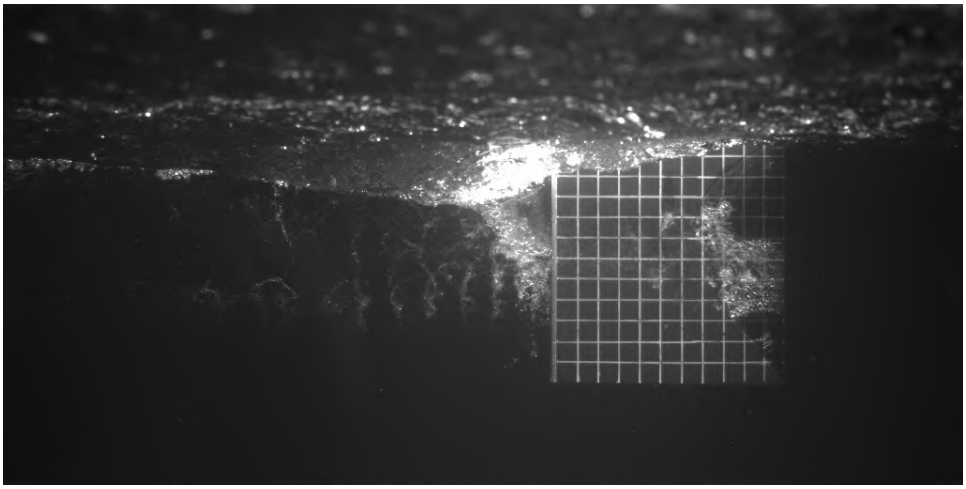

Figure 5.4: Photo of PC flow over the suction surface of the PVC foil (model 2) from INSEAN. Run conditions: $\alpha = 5°$; $Fn_h = 2.17$; $AR_h = 1$; P_0 =47 mbar; σ_v =0.35

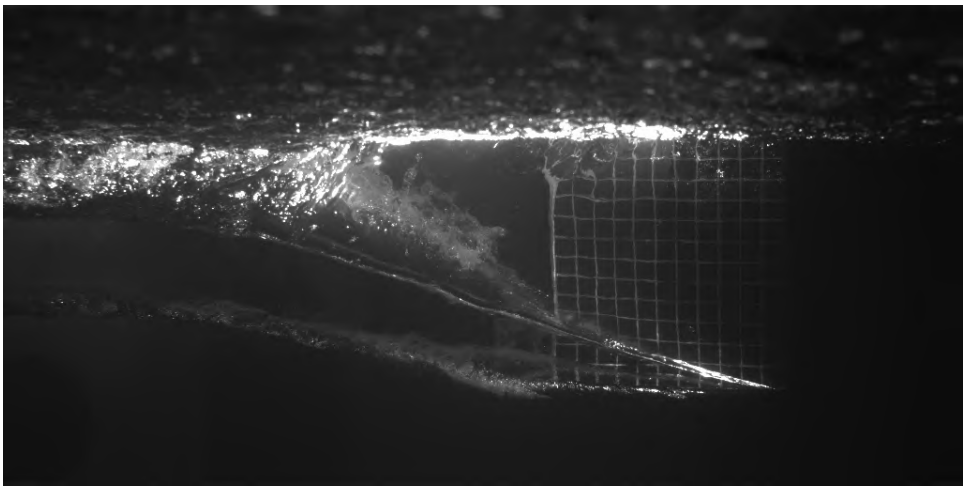

Figure 5.5: Photo of FV flow over the suction surface of the PVC foil (model 2) from INSEAN. Run conditions: $\alpha = 15°$; $Fn_h = 2$; $AR_h = 1$; P_0 =1 bar; σ_v =18

5.3 Flow Regime Stability

5.3.1 Stability Condition for Re-Entrant Jet

Several trials at INSEAN were dedicated to testing near the stability boundary between PV and FV flow. The washout Froude number was taken from the respective boundary in figure 4.18 for $\alpha = 12°$ and $AR_h = 1$. Froude numbers of $Fn_h = 1.2$ and $Fn_h = 1.33$ were tested. The resulting photos demonstrate especially well the reflection of flow about the trailing edge of the cavity, as well as the tenuous stability of the cavity when its closure angle $\bar{\Phi}$ is very near the stability limit of $\bar{\Phi} = 45°$. Figure 5.6 shows the flow on the transition boundary between PV and FV flows, while figure 5.7 shows the flow slightly above the boundary (in the FV stability region). In both cases, 200 frames were averaged, and the time-averaged images were overlaid with contour plots of pixel-intensity variance. Pixel-intensity variance is used as an indicator of visually-unsteady regions of the image, and contours from blue to white in color denote increasing variance. In both cases, a red dashed line is also overlaid to indicate the $\bar{\Phi} = 45°$ stability criterion for FV flow, established in chapter IV.

The cavity closure angle $\bar{\Phi}$ is noticeably steeper in figure 5.6, falling approximately on the line denoting the stability boundary. As a result of the upstream re-entrant flow, the cavity's stability is tenuous, indicated by the unsteadiness contours near the leading edge at the free tip of the hydrofoil. Conversely, in figure 5.7, $\bar{\Phi} < 45°$, suggesting a more-stable cavity. This is corroborated by the observation that the unsteadiness contours do not extend to the leading edge, indicating that the re-entrant jet did not propagate far enough forward to destabilize the FV flow.

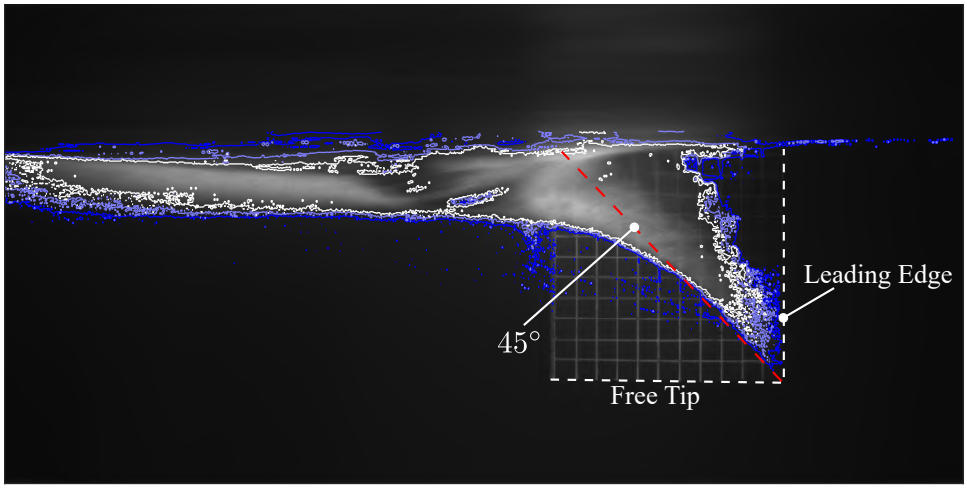

Figure 5.6: Flow on model 2 at the stability boundary between PV and FV flow. Average of 200 frames, overlaid with contours of pixel intensity variance. Pixel variance increases from the blue contours to white. Run conditions: $\alpha = 10°$; $AR_h = 1.0$; $Fn_h = 1.2$; $P_{atm} = 1$ bar

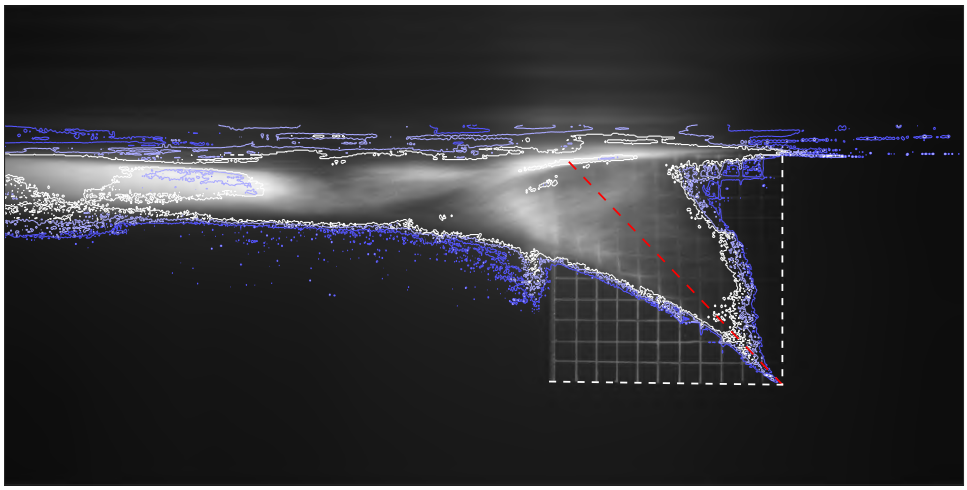

Figure 5.7: FV flow on model 2 just above the stabilization boundary (inside the FV stability region). Average of 200 frames, overlaid with contours of pixel intensity variance. Pixel variance increases from the blue contours to white. Run conditions: $\alpha = 10°$; $AR_h = 1.0$; $Fn_h = 1.33$; $P_{atm} = 1$ bar

5.3.2 Stability Regions of Model 1

Figure 5.8 depicts the experimental stability regions for model 1, collected in the towing tank at $AR_h = 1.0$. Model 1 was not tested in the cavitation tunnel, so PC data were unavailable for the homogeneous PVC model. Model 2, on the other hand, was tested primarily at steady-state conditions in the INSEAN cavitation tunnel, and the associated transition boundaries were not well-resolved. Nevertheless, the stability map closely mirrors that in figure 3.11, with the exception that the stall boundary is located along $\alpha_s = 13°$, suggesting that stall is advanced with model 1, relative to the rigid hydrofoil (for which $\alpha_s = 15°$). Note that the test matrix did not include runs at $\alpha = 2.5°$ for model 1, so the bifurcation boundary (α_b) was not resolved experimentally. Instead, the bifurcation boundary shown in figure 5.8 has been inferred from figure 3.11, and the stability regimes in the range of $2.5° \leq \alpha \leq 5°$ have been extrapolated, indicated by hatching.

Below the bifurcation and rewetting boundaries, FW flow is exclusively and globally stable. To the right of the bifurcation boundary, sufficient flow separation exists to permit air entrainment, and the amount of entrainment becomes a function of the balance between dynamic and hydrostatic pressure. Below the rewetting boundary, dynamic pressures are not sufficient to retain any entrained air in the presence of hydrostatic pressures, so FW flow remains exclusively stable. The washout boundary demarcates the PV and FV flow regimes

As shown in §3.2, the stability of the steady-state flow regimes depends strongly upon α, particularly near the stall angle. The static hydroelastic coupling of the flexible hydrofoil, which results in an additive (nose-up) twisting deformation, has the effect of advancing the stall angle slightly. Repeatability of measurements along the stall boundary were challenging however, presumably because the imminently-stalled flow is sensitive to small variations in water properties (fluctuations in the water temperature throughout the year caused changes in the Reynolds number (Re_c) as large as 15%). Thus, we cannot ascribe with complete certainty the shift in the stall boundary to the hydrofoil flexibility.

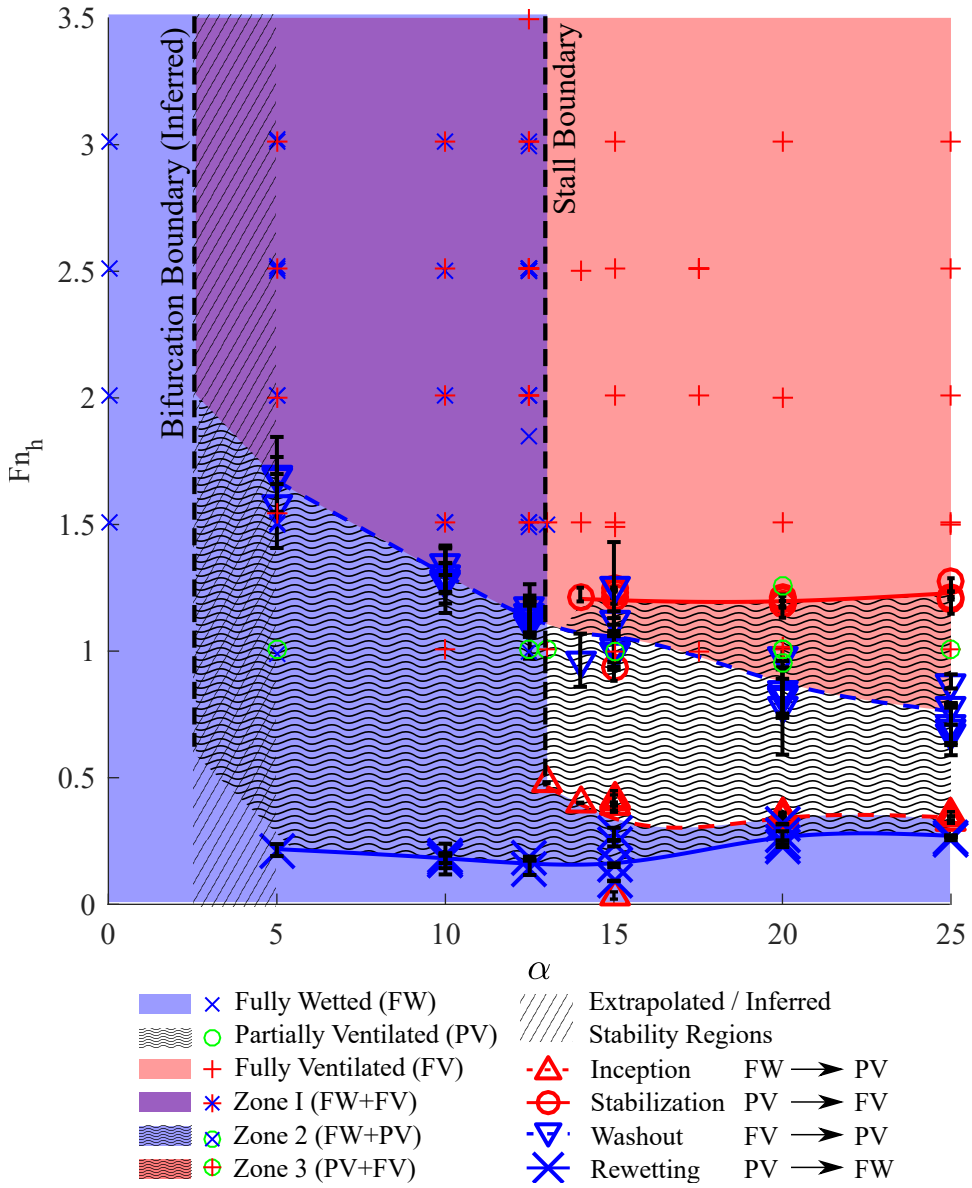

Figure 5.8: Stability regions for PVC hydrofoil (model 1) at $AR_h = 1.0$ Data are from testing in the MHL towing tank.

5.4 Static Hydroelasticity

Consider equation 1.24. Let $\{\boldsymbol{F_{fl}}\}$ be the 2-D steady hydrodynamic lift and moment per unit span. Recall that for a symmetric foil section, linear foil theory gives,

$$C_{l_{2D}} = a_0 \alpha_e$$
$$C_{m_{2D}} = a_0 \alpha_e \frac{e}{2},$$

where $\alpha_e = \alpha_{2D} + \theta$ is the effective angle of attack.

Thus, $\{\boldsymbol{F_{fl}}\}$ may be written,

$$\{\boldsymbol{F_{fl}}\} = \begin{Bmatrix} C_{l_{2D}} qc \\ C_{m_{2D}} qc^2 \end{Bmatrix} \tag{5.1}$$

$$= \begin{Bmatrix} a_0 qc \\ a_0 qc^2 \frac{e}{2} \end{Bmatrix} (\alpha_{2D} + \theta) \tag{5.2}$$

Dropping all first and second derivatives from equation 1.24 and substituting equation 5.2 allows us to write,

$$\begin{bmatrix} K_{s,\delta} & 0 \\ 0 & K_{s,\theta} \end{bmatrix} \begin{Bmatrix} \delta \\ \theta \end{Bmatrix} = \begin{Bmatrix} 1 \\ \frac{e}{2}c \end{Bmatrix} a_0(\alpha_{2D}) qc + \begin{bmatrix} 0 & a_0 qc \\ 0 & a_0 qec^2/2 \end{bmatrix} \begin{Bmatrix} \delta \\ \theta \end{Bmatrix}; \tag{5.3a}$$

$$= \begin{Bmatrix} l_{rigid} \\ m_{rigid} \end{Bmatrix} - \begin{bmatrix} 0 & K_{fl,\delta\theta} \\ 0 & K_{fl,\theta\theta} \end{bmatrix} \begin{Bmatrix} \delta \\ \theta \end{Bmatrix}; \tag{5.3b}$$

$$= \{\boldsymbol{F_{r,steady}}\} - [\boldsymbol{K_{fl}}] \{\boldsymbol{X}\}. \tag{5.3c}$$

where $[\boldsymbol{K_{fl}}]$ is the fluid stiffness matrix and $\{\boldsymbol{F_{r,steady}}\}$ is the steady fluid force vector on an equivalent rigid section set at α_{2D}.

Subtraction of $[\boldsymbol{K_{fl}}]$ yields the equation of static hydroelastic equilibrium for the 2-D section.

$$\begin{bmatrix} K_{s,\delta} & -a_0 qc \\ 0 & K_{s,\theta} - a_0 qec^2/2 \end{bmatrix} \begin{Bmatrix} \delta \\ \theta \end{Bmatrix} = \begin{Bmatrix} a_0 qc \\ a_0 qc^2 \frac{e}{2} \end{Bmatrix} \alpha_{2D}, \tag{5.4}$$

from which the expressions in chapter I were derived:

$$\delta = \frac{a_0 \alpha q c}{K_{s,\delta}} \quad 1 + \frac{a_0 \frac{e}{2} q c^2}{K_{s,\theta} - a_0 \frac{e}{2} q c^2} \tag{1.30a revisited}$$

$$\theta = \frac{a_0 \alpha \frac{e}{2} q c^2}{K_{s,\theta} - a_0 \frac{e}{2} q c^2}. \tag{1.30b revisited}$$

While the above equations were derived for a 2-D, 2-DOF model, they're demonstrative of the behavior of many-DOF elastic systems. We can generalize equation 5.4 to an arbitrarily large model,

$$\left([\boldsymbol{K_s}] + [\boldsymbol{K_{fl}}] \right) \{\boldsymbol{X}\} = \{\boldsymbol{F_{r,steady}}\}. \tag{5.5}$$

The fluid stiffness matrix, $[\boldsymbol{K_{fl}}]$, is determined by the choice of Three-Dimensional (3-D) hydrodynamic theory, but we may expect that equation 5.5 will behave in substantially the same manner as equation 5.4, *i.e.* when the Center of Pressure (CP) is located upstream of the EA, there should be a reduction in the effective stiffness at non-zero speeds. The reduction should become more substantial as e, q, and/or a_0 increase. As alluded to in chapter I, when

$$K_{s,\theta} + K_{fl,\theta\theta} = K_{s,\theta} - a_0 q c^2 \frac{e}{2} = 0,$$

static divergence instability occurs. Note, however, that all conditions tested in this work were well below the divergence dynamic pressure q_D.

5.4.1 Steady Hydrodynamic Loads

Figure 5.9 shows the measured values of $C_{L_{3D}}$ as a function of α for models 0, 1, and 2 at $Fn_h = 3$, $AR_h = 1.0$. In chapter I, we asserted that when the center of pressure is located forward of the elastic axis, the resulting nose-up twisting moment will increase the effective angle of attack α_e. Thus, the lift at each spanwise station on the hydrofoil will be increased. Figure 5.9 supports this conjecture. The measured values of $C_{L_{3D}}$ are larger on models 1 and 2 than on model 0. In the FW regime, the difference is small – in some cases less than the experimental uncertainty. However, the difference is consistent for every angle of attack. This, along with the reduction in the stall angle from $\alpha_s = 15°$ (model 0) to $\alpha_s = 13°$ (model 1, model 2), lends some confidence to the observation. In the FV regime, the effect difference between models 0, 1, and 2 become statistically insignificant. In light of equations 5.4 and 5.4, this is

a reasonable result. In the FV regime, both a_0 and e are reduced, as demonstrated in chapter III. As a result, the hydroelastic coupling becomes less pronounced when ventilation is present.

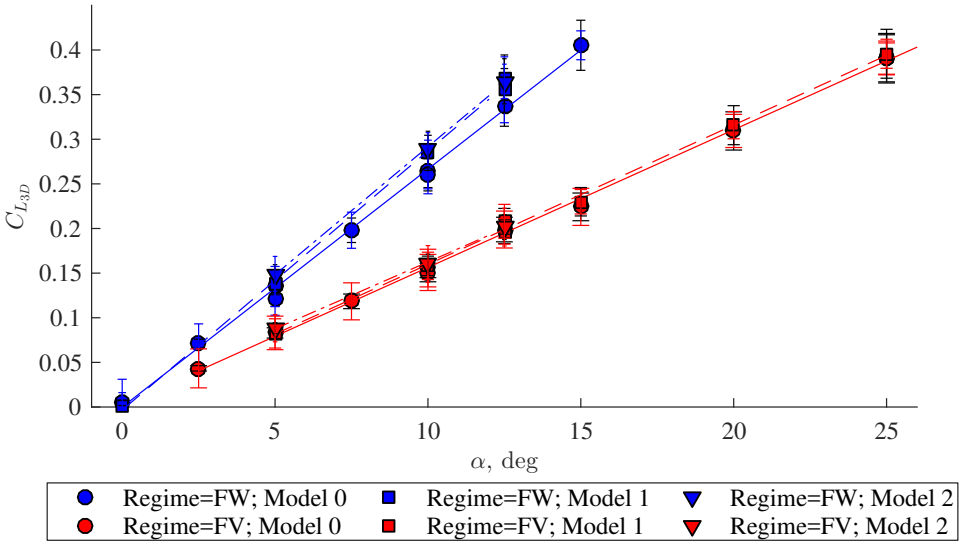

Figure 5.9: $C_{L_{3D}}$ as a function of α for models 0, 1, and 2 at $Fn_h = 3$, $AR_h = 1.0$

Figure 5.10 shows a comparison across hydrofoil models of the measured drag coefficient, $C_{D_{3D}}$. The drag coefficient is insensitive to the effect of foil flexibility. As discussed chapter III, the drag coefficient is a sum of profile, spray, and lift-induced components. Only the lift-induced drag has a significant known dependence upon α_e. As a result, small changes in the distribution of sectional α_e are not expected to have a significant effect on the aggregate values of $C_{D_{3D}}$.

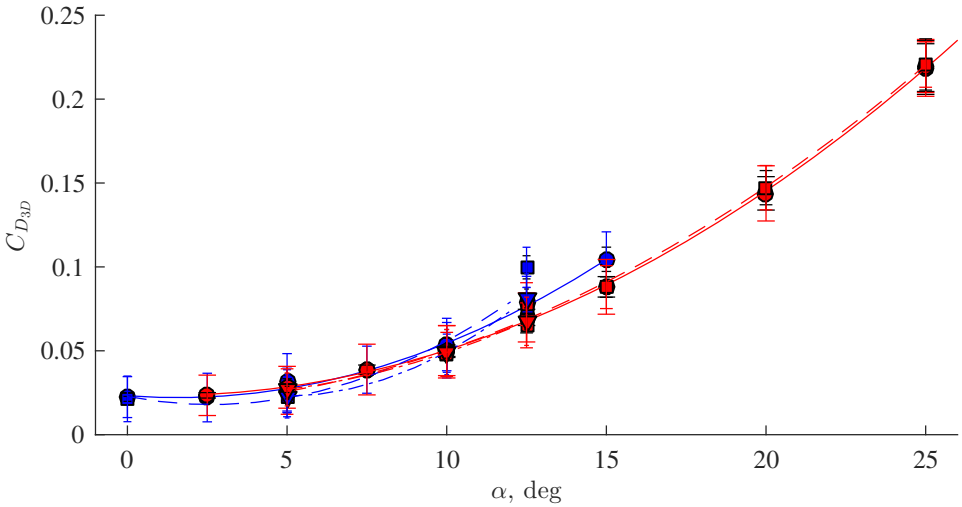

Figure 5.10: $C_{D_{3D}}$ as a function of α for models 0, 1, and 2 at $Fn_h = 3$, $AR_h = 1.0$

Finally, the yawing moment coefficient $C_{M_{3D}}$ measured about mid-chord, is plotted in figure 5.11. As in the case of the lift coefficient, there is a measurable increase in $C_{M_{3D}}$ measured for on the flexible hydrofoils, relative to that measured on the rigid hydrofoil. Once again, the difference is most pronounced in the FW regime, where the elements of the fluid stiffness matrix in equation 5.5 are maximized.

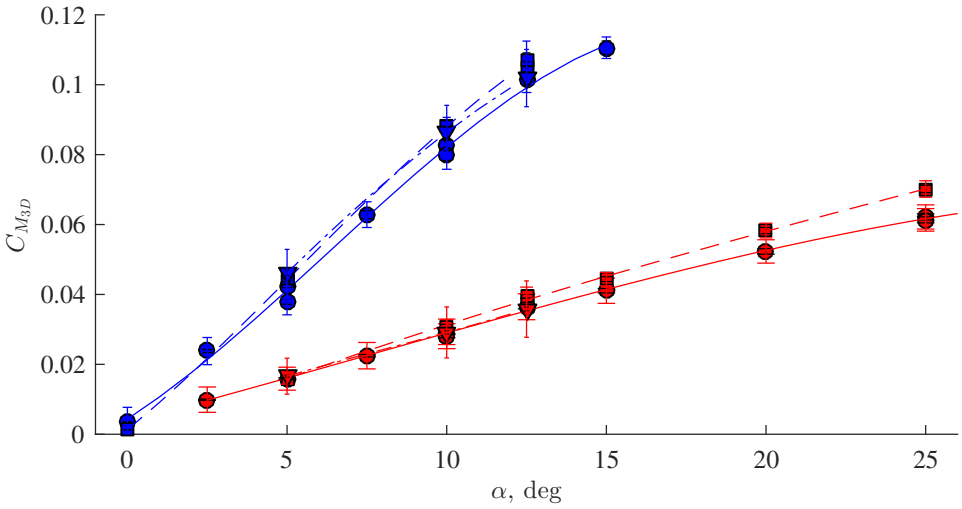

Figure 5.11: $C_{M_{3D}}$ as a function of α for models 0, 1, and 2 at $Fn_h = 3$, $AR_h = 1.0$

To summarize, the changes in hydrodynamic loading between flow regimes are exactly like those shown in chapter III. $C_{L_{3D}}$ and $C_{M_{3D}}$ are measurably larger for the flexible hydrofoils (models 1 and 2) than for the rigid model 0. With reference to equation 5.5, we see that the increased hydroelastic coupling is introduced through the change in $K_{s,\theta}$ (and hence in the total effective stiffness). The difference between model 1 and 2, however, is less than the experimental uncertainty. We expect models 1 and 2 to have roughly equivalent values of a_0. Therefore, only changes in e (caused by movement of the elastic axis, while the center of pressure remains fixed for a given flow condition), and $K_{s,\theta}$ would introduce variation into $[\boldsymbol{K_{fl}}]$ between model 1 and model 2. Taking the section properties from table 2.2, we find that the moment arm of the lift about the EA is 43% larger on model 2 than on model 1 – a result of aft-ward movement of the EA with the addition of the reinforcement strip. However, the torsional rigidity GJ of model 2 is increased by 36%, relative to that of model 1. As a result, the ratios of GJ to e vary by less than 5% between model 1 and model 2 (with model 2 having a smaller value). Therefore, it is unsurprising that the static hydroelastic coupling is essentially equal between the two flexible models.

5.4.2 Static Hydroelastic Coupling

Contours of the 3-D lift and moment coefficients, $C_{L_{3D}}$, $C_{M_{3D}}$, δ, and θ are shown as functions of α and Fn_h in figure 5.12 for model 1 and figure 5.13 for model 2. δ and θ are measured at the free tip of the hydrofoil, using the shape-sensing spars described in §2.5. Blue, red and green "X" symbols indicate experimentally-observed FW, FV, and PV flows, respectively.

The FW and FV flow regimes are respectively represented by the blue and red contour lines. In general, the lift (shown in figures 5.12(a) and 5.13(a)) is reduced. The ingestion of air along the suction surface of the strut limits the development of low-pressures, which are instrumental in generating large forces. The moment coefficient (figures 5.12(b) and 5.13(b)) is attenuated both because the lift is reduced and because the center of pressure translates from its location of approximately 0.25 chord-lengths forward of mid-chord in FW flow towards a position at mid-chord in FV flow, causing both the lift and its moment arm to be reduced. As was observed on model 0 in chapter III, $C_{L_{3D}}$ and $C_{M_{3D}}$ in the FV regime decrease monotonically with increasing Fn_h. At the upper limits of the Fn_h axis, the curvature of the $C_{L_{3D}}$ and $C_{M_{3D}}$ contours indicate that they are approaching parallel with the Fn_h axis, suggesting that the dependence is reduced at high Froude numbers. With transition from FW to FV flow, the value of $C_{L_{3D}}$ doesn't change significantly at low values of Fn_h while at large value of Fn_h reductions are as large as 40%. The same is true of $C_{M_{3D}}$ but with reductions as large as 60% at large Fn_h. Note that along the stall boundary of figure 5.12(d), tip-twisting angles approach a maximum of $\theta \approx 1^\circ$ in the FW regime. Thus, the conjecture drawn in 5.3.2 that elastic twist advances the stall angle is reasonable, but the effect is small.

The changes in tip bending and twisting deflections (figures 5.12(c,d) and 5.13(c,d)) with the transition to FV flow are commensurate with the changes in $C_{L_{3D}}$ and $C_{M_{3D}}$. However, the deflections are proportional to the dimensional hydrodynamic loads, which results in the bending and twisting deflections increasing along both the α and Fn_h axes. Considering equations 1.30a and 1.30b for the 2-D model, we see that there is no way in which to remove all speed-dependence from δ and θ. However, if we divide each by ${Fn_h}^2$ (which is proportional to q), we are left with,

$$\frac{\delta}{{Fn_h}^2} = \frac{a_0 \alpha \rho_f g h c/2}{K_{s,\delta}} \quad 1 + \frac{a_0 \frac{e}{2} q c^2}{K_{s,\theta} - a_0 \frac{e}{2} q c^2} \qquad \propto C_{l_{2D}}; \tag{5.6a}$$

$$\frac{\theta}{{Fn_h}^2} = \frac{a_0 \alpha \rho_f g h c^2 e/4}{K_{s,\theta} - a_0 \frac{e}{2} q c^2} \qquad \propto C_{m_{2D}}. \tag{5.6b}$$

Thus, if we assume the same functional behavior to apply to the 3-D hydrofoil, the contours of equations 5.6 should parallel the contours of $C_{L_{3D}}$ and $C_{M_{3D}}$. These contours are shown in figures 5.12(e,f) and 5.13(e,f). In general, the scaled bending and twisting deflections appear proportional to $C_{L_{3D}}$ and $C_{M_{3D}}$ respectively. There is some deviation of the $\theta/Fn_h{}^2$ contours from those of $C_{M_{3D}}$ but the contour spacing in the former is less than the experimental uncertainty. Therefore, not much can be inferred from the minor inconsistency.

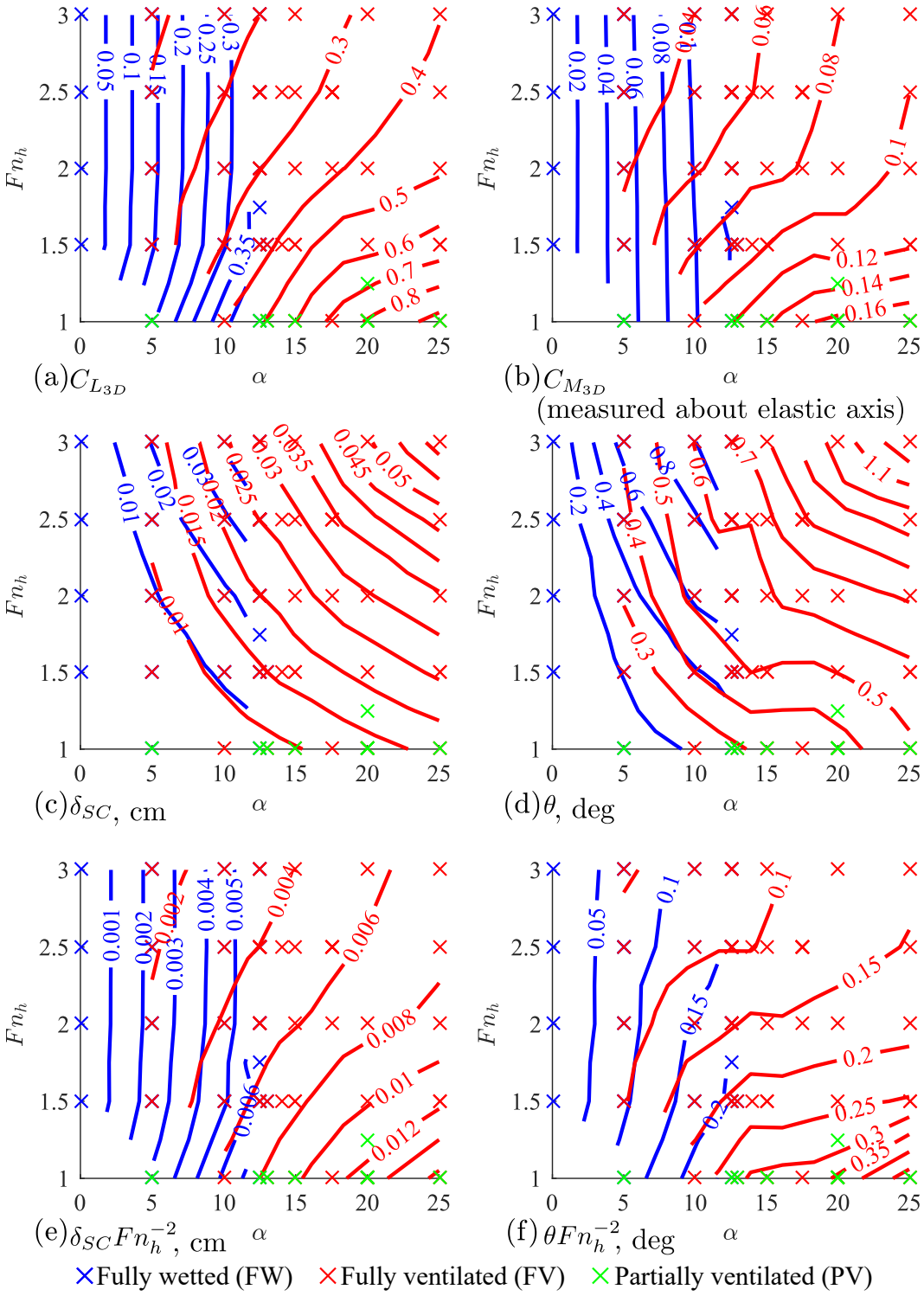

Figure 5.12: Model 1: contours of (a)$C_{L_{3D}}$ (b)$C_{M_{3D}}$ (about the elastic axis), (c) δ measured at the hydrofoil tip, (d)θ measured at the hydrofoil tip, (e) $\delta {Fn_h}^{-2}$, (d) $\theta {Fn_h}^{-2}$. Blue and red contours indicate FW and FV flow, respectively. The dimensional hydrofoil deflections can be made proportional to $C_{L_{3D}}$ and $C_{M_{3D}}$ by factoring out ${Fn_h}^2$.

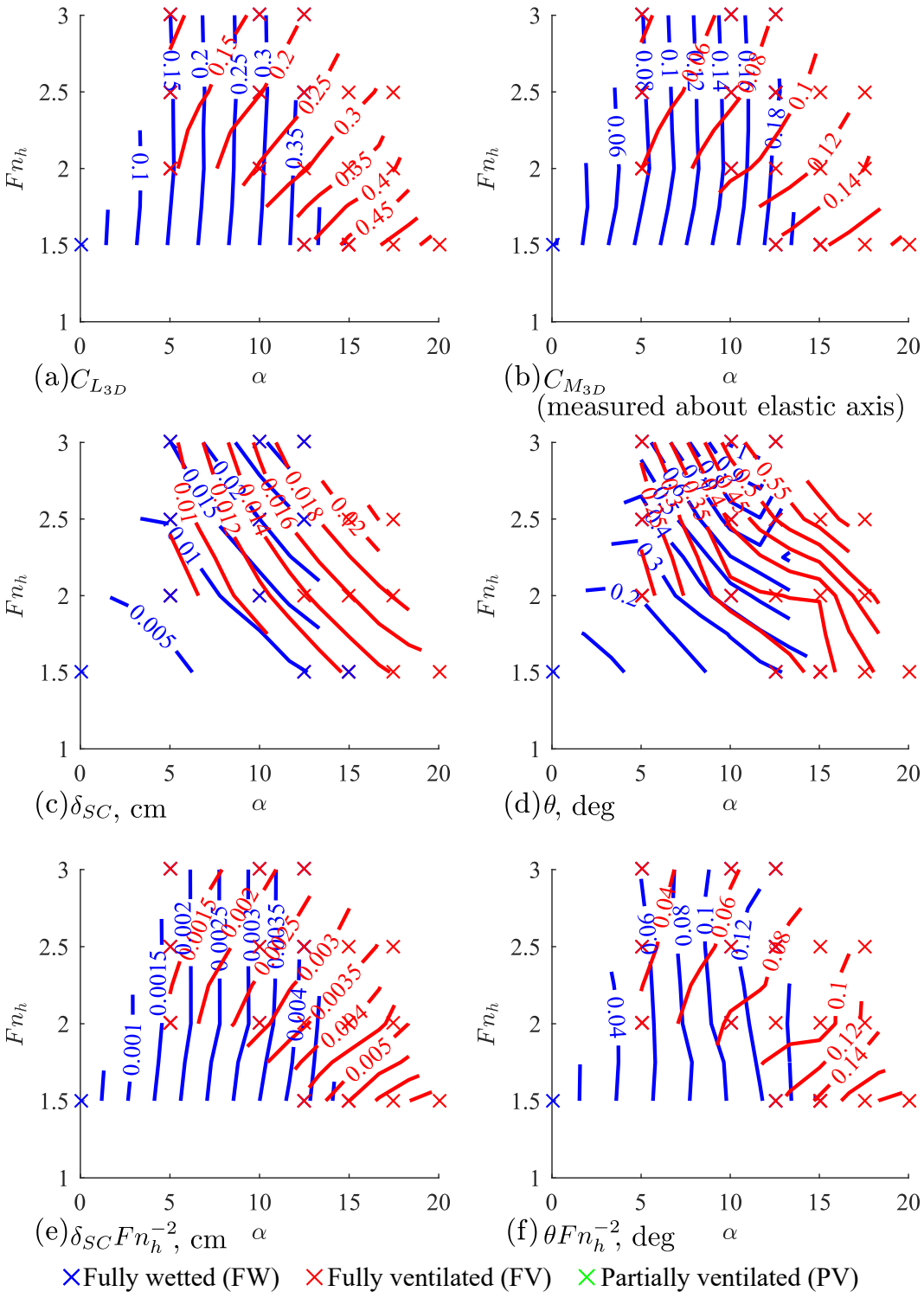

Figure 5.13: Model 1: contours of (a)$C_{L_{3D}}$ (b)$C_{M_{3D}}$ (about the elastic axis), (c) δ measured at the hydrofoil tip, (d)θ measured at the hydrofoil tip, (e) $\delta {Fn_h}^{-2}$, (d) $\theta {Fn_h}^{-2}$. Blue and red contours indicate FW and FV flow, respectively. The dimensional hydrofoil deflections can be made proportional to $C_{L_{3D}}$ and $C_{M_{3D}}$ by factoring out ${Fn_h}^2$.

5.4.3 Scaled Static Hydroelastic Response

Manipulating equation 1.30b yields the dimensionless scaling expression,

$$\frac{\theta}{\theta+\alpha} = \frac{\theta}{\alpha_e} = \frac{c}{2K_{s,\theta}} e a_0 q$$
$$\propto e a_0 {Fn_h}^2. \tag{5.7}$$

For a given lift-slope (constant a_0), and a fixed center of pressure (constant e), equation 5.7 predicts a linear relationship between the squared Froude number and dimensionless ratio of elastic twist to effective angle of attack for the 2-D model. We again generalize this to a representative section of the 3-D hydrofoil. The dimensionless ratio is plotted as a function of ${Fn_h}^2$ in figure 5.14 for model 1 and in figure 5.15 for model 2. The data in all three flow regimes (FW, PV, and FV) are bounded above by the FW data, which lie along a line, and bounded below by the FV data at $\alpha = 25°$. It was shown in chapter III that, as α and Fn_h increase, the mean cavity length increases, causing both a_0 and e to decrease. As a result, PV data and FV data at small values of α and Fn_h are roughly coincident with data in the FW regime. As α and/or Fn_h increase, the data in the FV regime approach a lower asymptotic limit. At high speeds and yaw angles, all sections along the hydrofoil span are in the supercavitating regime. Thus, the upper bound is fixed by the values of e and a_0 in FW flow, the lower limit is fixed by the values of e and a_0 for supercavitating sections, and flows at low and moderate values of Fn_h (where variation in the cavity length along the span is significant), will fall inside of the triangular regions between the upper and lower bounds. Note that a_0 is neither 2π in FW flow nor $\pi/2$ in FV flow (as it would be for a 2-D section) because the finite aspect ratio, free tip, and free surface introduce 3-D effects,

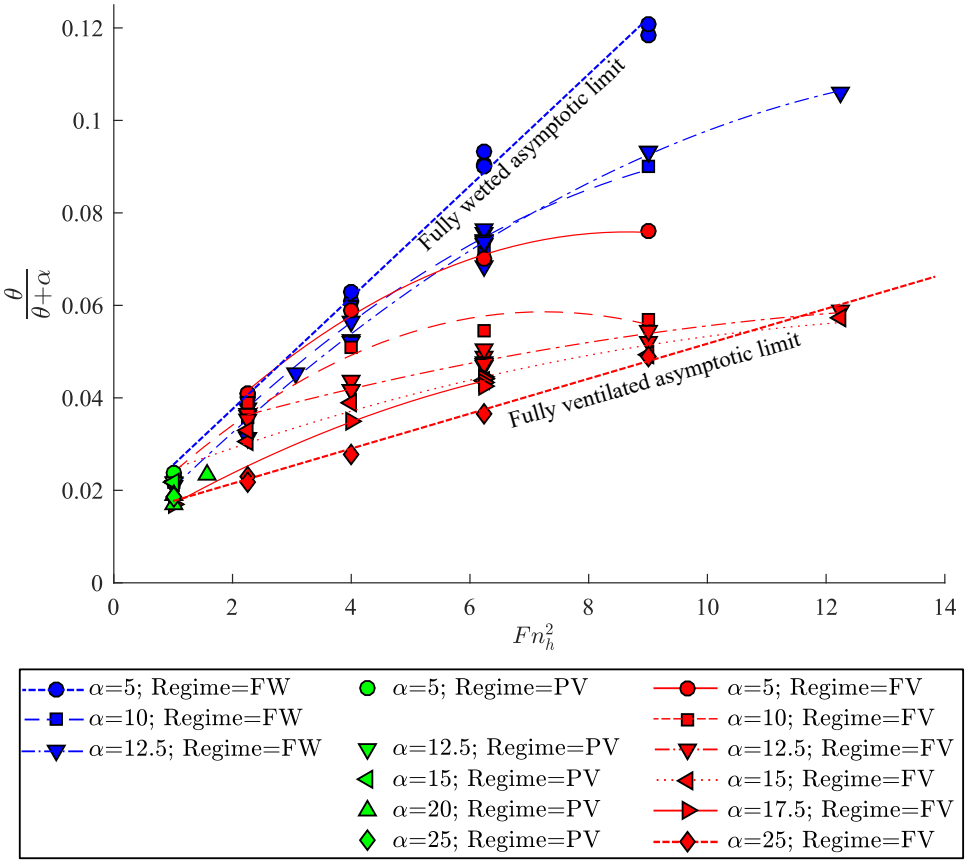

Figure 5.14: Model 1: Dimensionless twisting deformations at hydrofoil tip, scaled by total effective angle of attack. The data in the FW and FV flow regimes approach asymptotically-linear bounds, presumably corresponding to the limiting cases of fully wetted sections and supercavitating sections everywhere along the span.

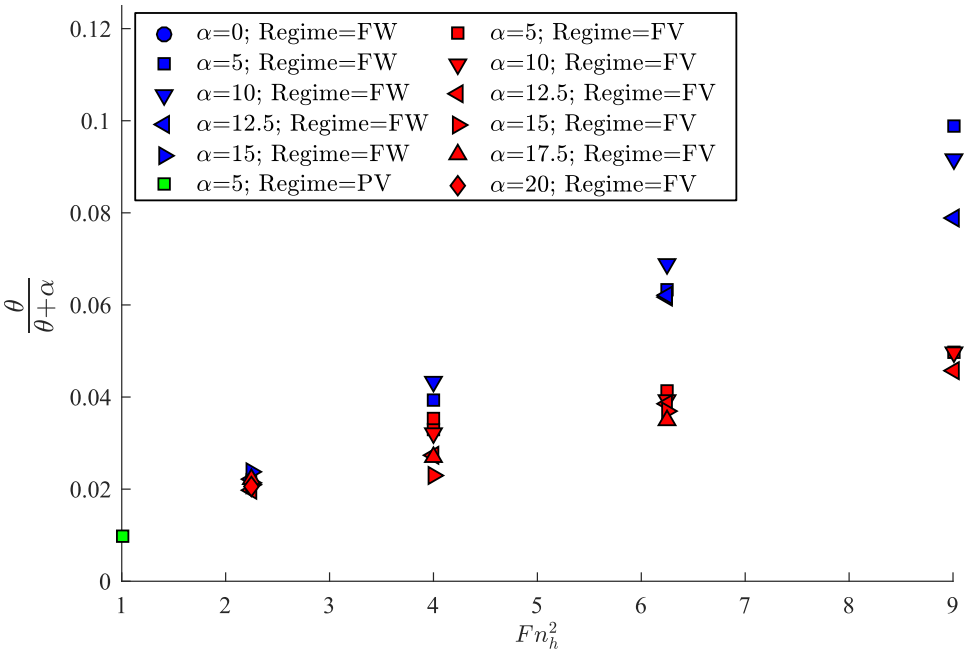

Figure 5.15: Model 2: Dimensionless twisting deformations at hydrofoil tip, scaled by total effective angle of attack. The data in the FW and FV flow regimes approach asymptotically-linear bounds, presumably corresponding to the limiting cases of fully wetted sections and supercavitating sections everywhere along the span.

5.5 Dynamic Hydroelastic Response

For unsteady flows, we once again consider all of the terms in equation 1.24. The loads contained in the vector $\{\boldsymbol{F_{fl}}\}$ are no longer so simple to model as in the case of steady flow, even for a 2-D hydrofoil. As described in chapter I, there exist a wide range of theories for modeling the unsteady hydrodynamic loads. However, the various theoretic methods are not within the scope of this thesis. Instead, we'll consider unsteady flows in a phenomenological manner and offer some general inferences regarding the unsteady forces and moments.

Two sources of unsteadiness exist in the present experiments: changes in the flow conditions (*e.g.* ventilation transition, acceleration, or deceleration), and structural motions excited either by an external source or by flow-induced vibrations. In this section, we will briefly examine the response of the hydrofoil to dynamic flows in the form of ventilation formation and vortex shedding.

5.5.1 Hydroelastic Response to Perturbation-Induced Ventilation

Figure 5.16 shows time histories of measured loads, bending and twisting of the hydrofoil tip, and forward speed for model 1 during a towing-tank trial. At a time

of approximately 48.8 s, the air jet was used to perturb the formation of a cavity, prompting rapid transition from FW flow to FV flow. Photos of the flow before and after formation are shown in figure 5.17(a) and (b). Figure 5.17(c) depicts the deflected shape of the hydrofoil before and after ventilation formation, as reconstructed from the shape-sensing beams. Consider the highlighted region of the time histories in figure 5.16. During the times shown, the flow is steady but for the transition event. When FV flow is triggered, the measured lift and yawing moment are reduced by nearly 50%. The bending deflection at the foil tip is reduced by a similar percentage. Twisting motion at the foil tip appears almost unaffected by transition. The reasons for this aren't entirely clear; it may be that the large bending deflection results in a spurious reduction in the inferred twist angle, as discussed in §2.5.

Transition appears as a step-change in the flow conditions. The flexible hydrofoil responds by assuming a new equilibrium condition with only a small transient oscillation about the new equilibrium point. The limited overshoot and short settling time of the hydrofoil's deflections indicate that the system is highly damped. The lack of a time-lag between the hydrofoil's motion and the instantaneous loads indicates that, at least for the step response, unsteady terms in the hydrodynamic force vector $\{\boldsymbol{F_{fl}}\}$ are unimportant. Even the quasi-steady response of the system, however, is quite dramatic. Figure 5.17 gives a good impression of the magnitude of the hydrofoil's deflections. Bending at the tip was approximately 30% of the chord length in the FW flow regime and approximately 20% in the FV flow regime – a relaxation of the hydrofoil's structural deflections of nearly 40% in less than 0.1 second. While the system in this case is highly damped, such a dramatic step-change in loading and structural response could trigger instability in a lightly damped system.

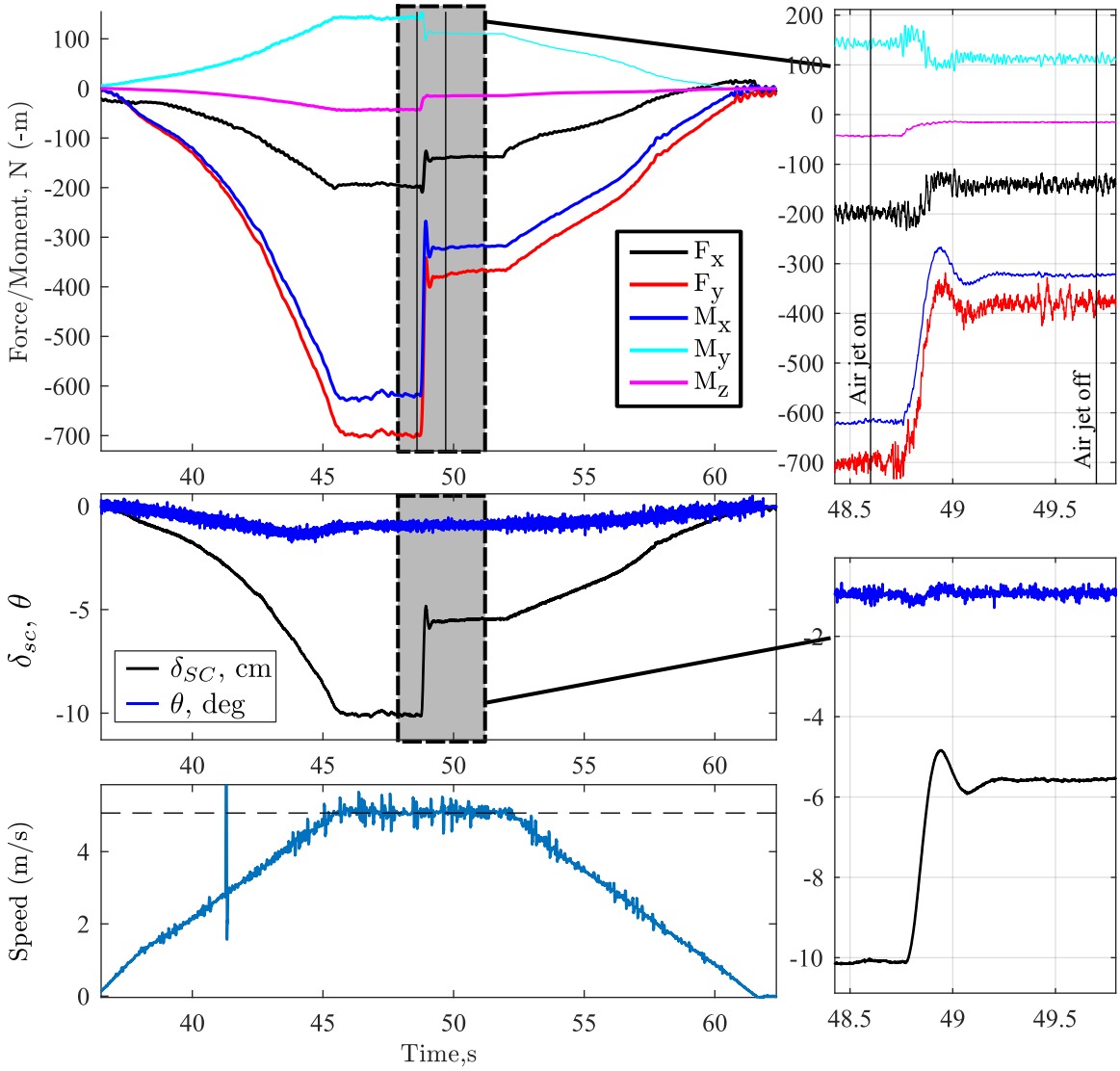

Figure 5.16: Time histories of measured forces and moments, foil tip deflections, and flow speed for model 1 at $\alpha = -12.5°$, $AR_h = 1.5$, and a steady-state Froude number of $Fn_h = 2.5$. Ventilation was triggered by perturbation with the air jet in otherwise-steady flow. Loads and deflections are both substantially reduced (figure 5.17 shows photos and 3-D hydrofoil deformations preceding and following ventilation). A small period of transience following the step-change in loading indicates high, but sub-critical, damping.

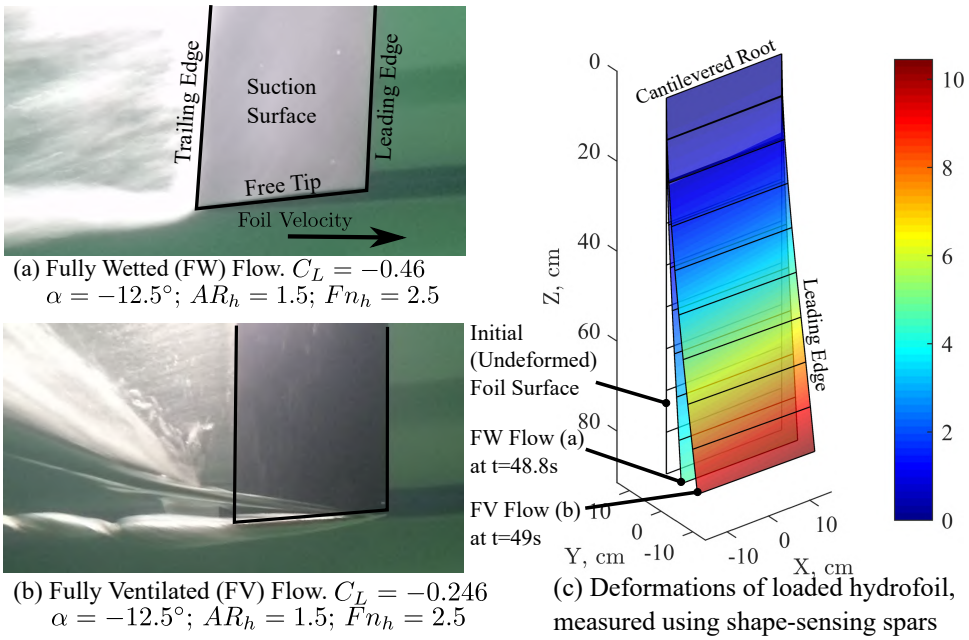

(a) Fully Wetted (FW) Flow. $C_L = -0.46$
$\alpha = -12.5°$; $AR_h = 1.5$; $Fn_h = 2.5$

(b) Fully Ventilated (FV) Flow. $C_L = -0.246$
$\alpha = -12.5°$; $AR_h = 1.5$; $Fn_h = 2.5$

(c) Deformations of loaded hydrofoil, measured using shape-sensing spars

Figure 5.17: Photos of the hydrofoil's suction surface and the deflected shape of the hydrofoil (inferred by shape-sensing spars) immediately preceding and following ventilation formation in figure 5.16. The development of the ventilated cavity causes a reduction in lift of approximately 40%, with a commensurate reduction in the bending deflections.

5.5.2 Hydroelastic Response to Coherent Vortex Shedding

As described in chapter I, flow-induced vibration can result from unsteady components of $\{\boldsymbol{F_{fl}}\}$ resulting from cavity or vortex shedding. The blunt trailing edge of the hydrofoil models provided extremely reliable points of flow detachment, such that parallel Von Kármán vortex streets were observed in the wake even at high speeds and Reynolds numbers approaching $Re_c \approx 10^6$. Figure 5.18 shows vortex shedding in the wake of model 2 in the INSEAN cavitation tunnel. The hydrofoil is set at $\alpha = 7°$– a yaw angle small enough that flow detachment still occurs from the sharp corners at the TE. Vortices shed into the wake contain air entrained from the free surface and the ventilated base cavity, making them clearly visible as regular striations. Detail views are shown on the right hand side of figure 5.18, with red dashed lines drawn through the vortex cores – note that the circulation of alternating vortices will change sign. The longitudinal distance between counter-rotating vortex pairs was found to be 1.5 times the trailing edge thickness. *Bearman* (1967); *Sallet* (1969) found that the longitudinal spacing of co-rotating vortices (along the same shear layer) was approximately,

$$\beta \approx 3h', \tag{5.8}$$

where β is the longitudinal vortex spacing and h' is the lateral distance between shear layers – taken here to be the thickness of the blunt TE. *Bearman* (1967) also showed that the longitudinal vortex spacing remained approximately the same when air was bled into the vortex street *via* a base cavity. Thus, we can conclude that the striations in figure 5.18 are indeed formed by a von Kármán vortex street, and that it remains remarkably coherent at high speeds. The corresponding Strouhal number was found to be,

$$St_t = f\frac{t}{U} = 0.275, \tag{5.9}$$

where f is the frequency of vortex shedding and t is the thickness across the TE of the hydrofoil. The shedding frequency $f_{shedding}$ was determined by using the SR830 lock-in amplifiers and accelerometers at the the hydrofoil tip to isolate coherent frequency content.

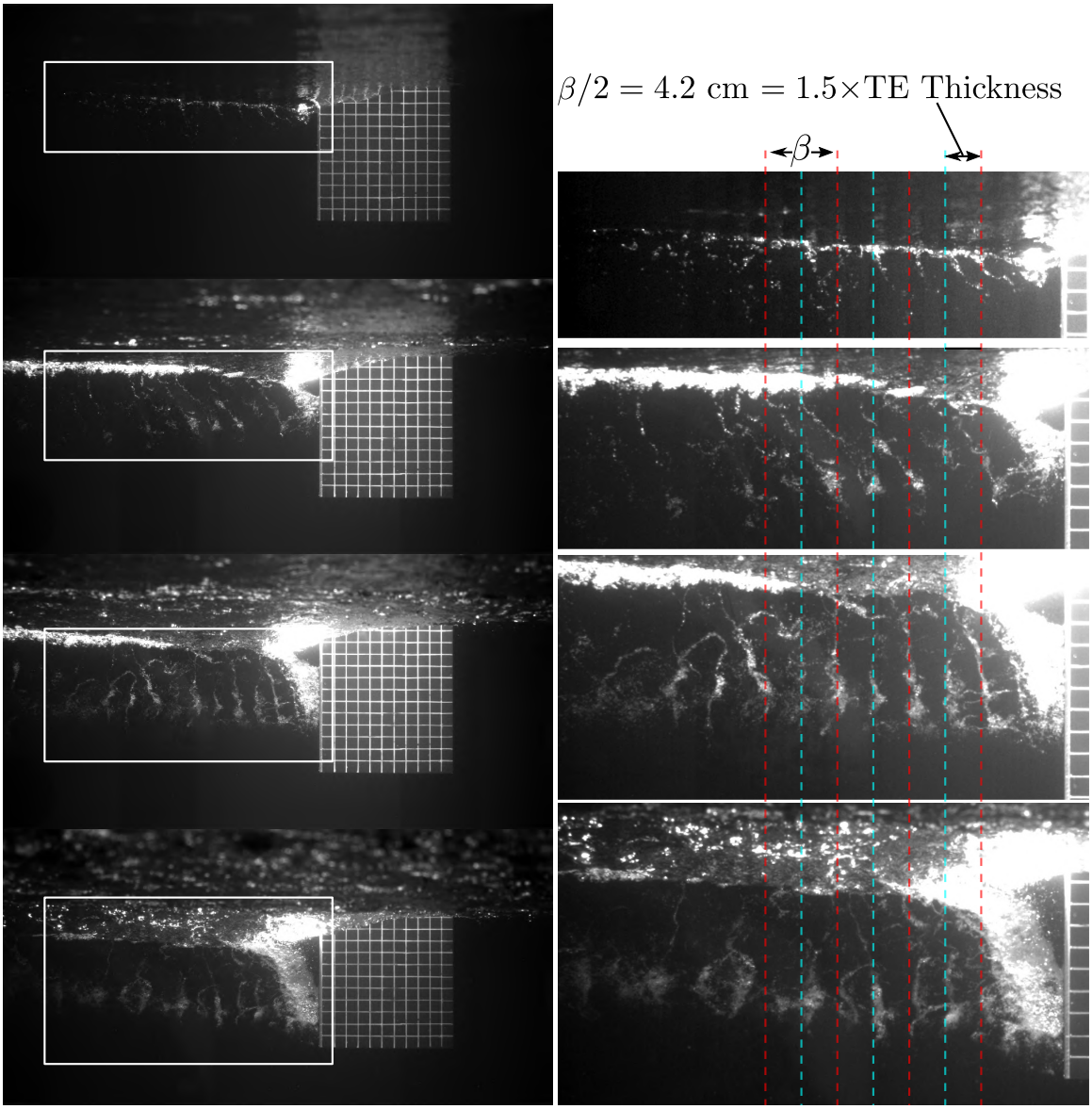

Figure 5.18: Coherent vortex shedding from model 2 in the INSEAN cavitation tunnel. The hydrofoil was set at $\alpha = 7°$. From top to bottom: $Fn_h = 1$, $Fn_h = 1.5$,$Fn_h = 2$,$Fn_h = 2.5$. Details on the right show that the longitudinal distance between counter-rotating vortex pairs is equal to 1.5 times the thickness of the trailing edge, in agreement with *Bearman* (1967); *Sallet* (1969). The Strouhal number of vortex shedding (based on TE thickness t) was found to be $St_t = \frac{f_{shedding}t}{U} = 0.275$.

5.5.3 Flow-Induced Vibration, Lock-In, and Lock-Off

Figure 5.19 shows smoothed auto-power spectra of the measured lift (F_y) and bending deflections (δ) at the tip of model 2, plotted for Froude numbers of $0.3 \leq Fn_h \leq 2.5$. The yawing moment (M_z) and twisting deflections (θ) are shown in figure 5.20. All cases shown are FW flow with a yaw angle of $\alpha = 7^\circ$ and $AR_h = 1.0$. The loads and deflections have all been multiplied by ${Fn_h}^{-2}$ to keep the spectra approximately constant along the Fn_h axis. Vortex shedding frequencies ($f_{shedding}$) corresponding to Strouhal numbers of $St_t = 0.275 \pm 0.025$ are indicated by red dashed lines on the f–Fn_h plane, and by red highlighted portions of the spectra. The wetted resonant frequencies of the first three modes of model 2 at an immersed aspect ratio of $AR_h = 1.0$ are shown as dotted black lines on the f–Fn_h plane. The method used to find the natural frequencies will be described in chapter VI. Note that regular sharp peaks appear in the spectra as a result of AC line noise at 50 Hz, its harmonics, and what is thought to be a beat frequency resulting from a non-integer division of the line frequency into the 500 Hz sample-clock frequency.

Flow induced vibration is evident at all values of Fn_h. Peaks in the force and moment spectra indicate vortex shedding, while peaks in the bending and twisting spectra indicate flow-induced vibration. The spectra of M_z and θ, in particular, show clearly-defined vibration occurring close to the constant Strouhal number of $St_t = 0.25$. The exceptions are at $Fn_h = 0.3$, $Fn_h = 2$, and $Fn_h = 2.5$, where the vortex-shedding frequencies match the first, second, and third wetted modal frequencies of the hydrofoil, respectively.

Lock-in occurs where when the vortex-shedding frequency is near one of the hydrofoil's wetted modal frequencies, such that the vortices begin to shed at the frequency of the structural motions, causing a flow-induced resonance. Three cases of potential lock-in are apparent. At $Fn_h = 0.3$, a sharp peak in both figure 5.19 and figure 5.20 where the vortex shedding meets the first modal frequency indicates a lock-in condition. Lock-in with mode 1 was visually obvious during the experiments because the hydrofoil underwent visible cyclic bending motion, while a coherent vortex street was shed from the trailing edge. Thus, it is also most prominent in the bending spectrum in figure 5.19b. A peak is also visible where the vortex shedding frequency intersects the second modal frequency at $Fn_h = 2$, though it is not as distinct as first-mode lock-in. The same is true at $Fn_h = 2.5$, where a peak is evident at the crossing of the vortex shedding frequency with the third wetted modal frequency. While regular vortex shedding was observed at higher speeds, the coherence of the vortices undeniably decreases with increasing flow speed (see figure 5.18), so it is possible that the vortex

shedding at $Fn_h = 2$ and $Fn_h = 2.5$ are not sufficiently regular to cause flow-induced resonance.

The occurrence of lock in at $Fn_h = 0.3$ is emphasized by plotting the spectra with a linear Z-scale. Figure 5.21 shows the scaled bending spectra for model 2 at $\alpha = 2°$, this time with a linear vertical scale. The flow-induced vibrations contain too little energy to be visible with the linear scale, but lock-in with the first bending mode is clearly visible.

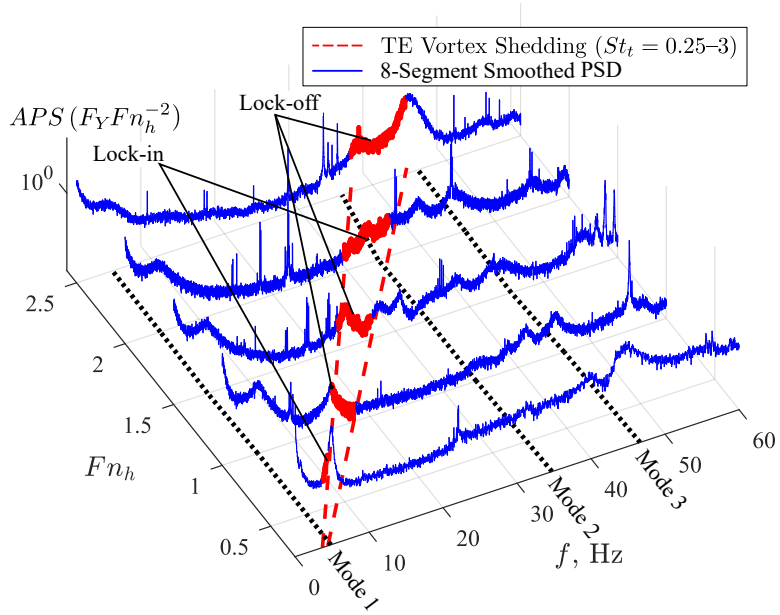

(a) Cascade of lift auto-power spectra.

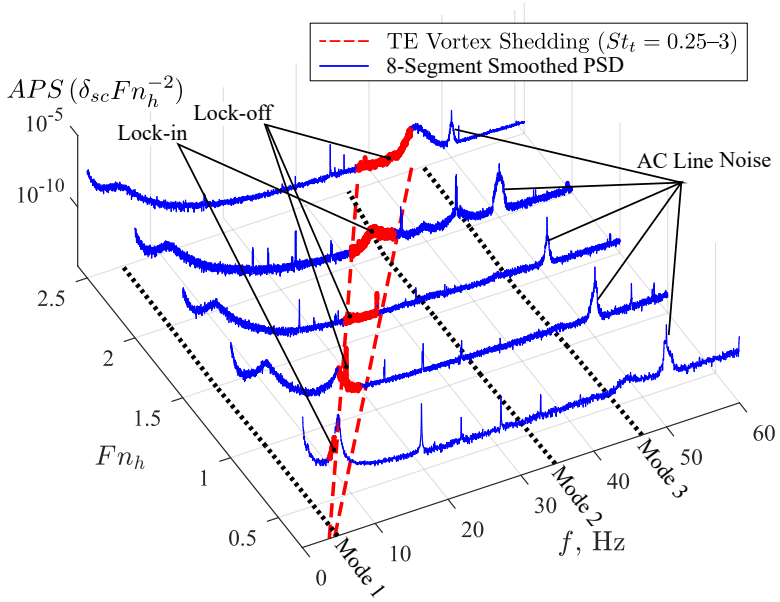

(b) Cascade bending auto-power spectra.

Figure 5.19: Smoothed auto-power spectra of lift F_y and bending deflections at the shear center δ, each scaled by ${Fn_h}^{-2}$. Flow-induced vibrations are apparent at each Froude number, but lock-in with the first mode is especially apparent. Model 2 at $\alpha = 7°$, $AR_h = 1.0$.

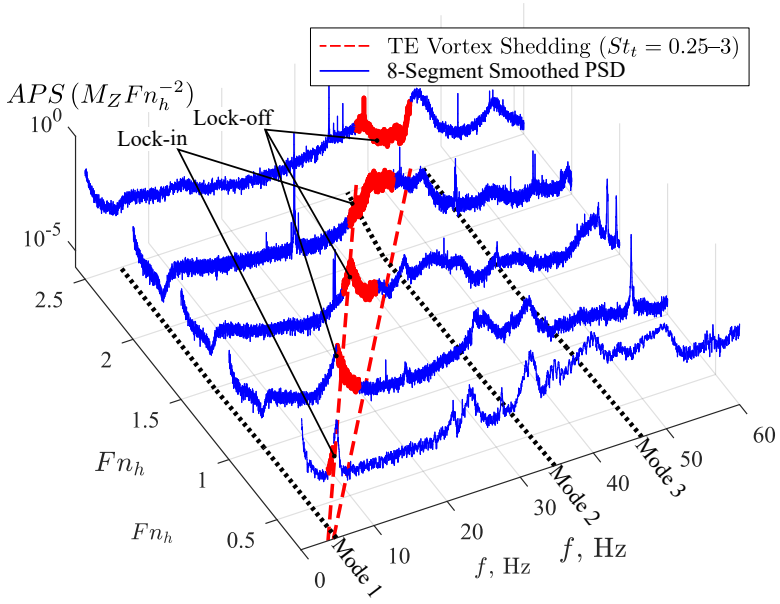

(a) Cascade of yawing moment auto-power spectra.

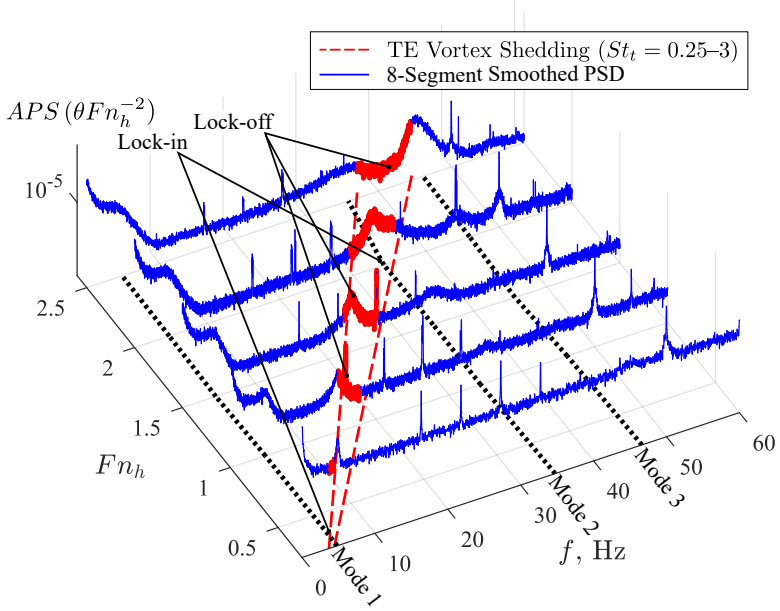

(b) Cascade twisting auto-power spectra.

Figure 5.20: Smoothed auto-power spectra of yawing moment M_z and twisting deflections at the EA θ, each scaled by ${Fn_h}^{-2}$. Model 2 at $\alpha = 7°$, $AR_h = 1.0$.

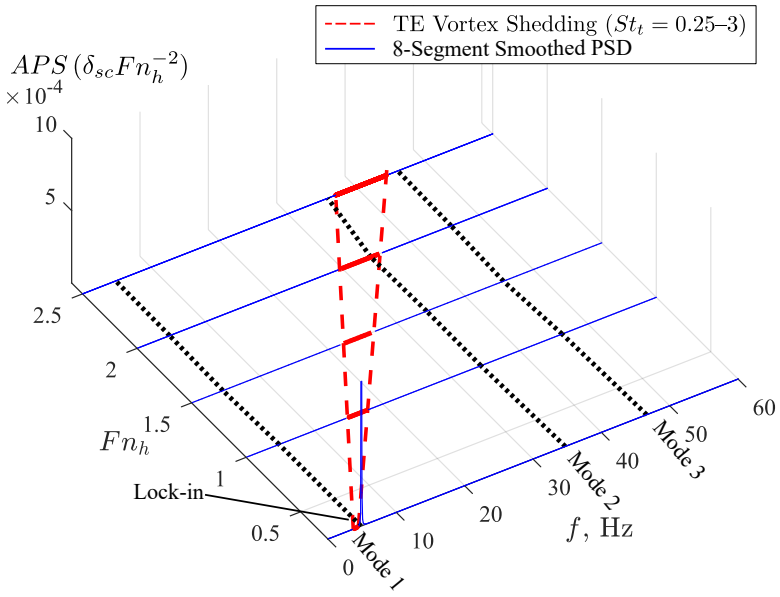

Figure 5.21: Smoothed auto-power spectra deflections at the shear center δ, scaled by ${Fn_h}^{-2}$. The linear vertical scale emphasizes the lock-in between vortex shedding and the first bending mode at $Fn_h = 0.3$. Model 2 at $\alpha = 2°$, $AR_h = 1.0$.

5.6 Effect of Foil Flexibility on Ventilation Transition

There were no observed changes to the ventilation transition mechanisms described in § IV as a result of foil flexibility. The taxonomy of figure 4.11 is still applicable, with the same mechanisms predominating.

5.6.1 Effects of Passive Hydrofoil Deformations

The transition boundaries of model 1 are next compared with those of the model 0. The formation boundaries (inception and stabilization) are shown in figure 5.22a, and the elimination boundaries (washout and rewetting) are shown in figure 5.22b. All four boundaries (inception, stabilization, washout, and re-wetting) for model 1 fall slightly below and/or to the left of the boundaries for model 0. This indicates that for a given initial angle of attack, α, the deformation of model 1 causes ventilation transition mechanisms to occur at somewhat smaller values of Fn_h than in the case of model 0, with the potential for slightly greater hysteresis in the transition between regimes. The change in boundary locations, however, is most significant for the inception and rewetting boundaries. Changes in the location of the stabilization and washout boundaries are within the uncertainty bounds, indicated by vertical bars for each transition event.

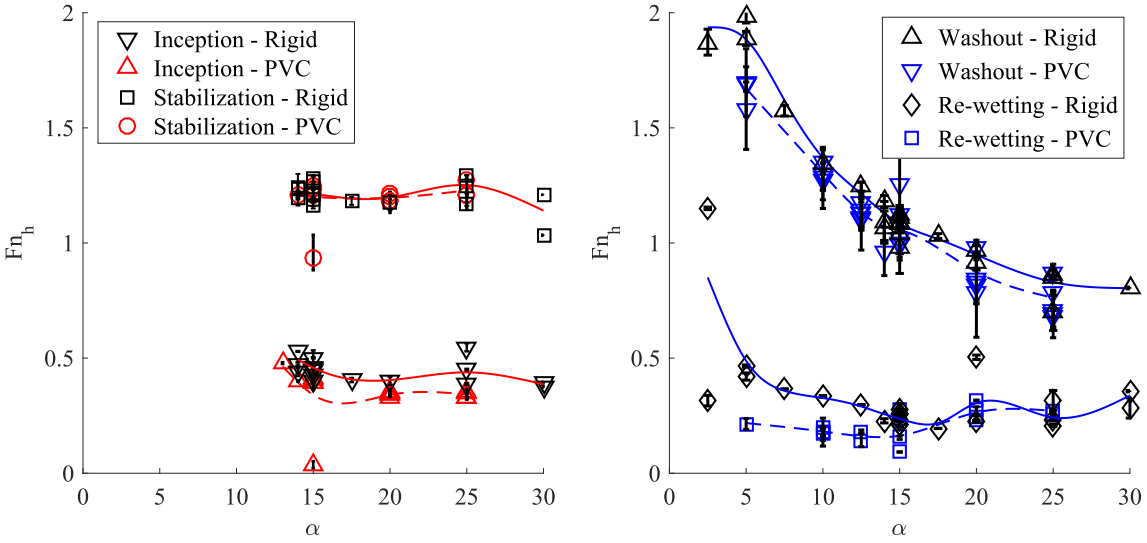

(a) Formation boundaries for rigid and PVC hydrofoils (model 0 and model 1).

(b) Washout boundaries for rigid and PVC hydrofoils (model 0 and model 1).

Figure 5.22: Ventilation formation and washout boundaries for model 1, compared to those for model 0. The model 1 boundaries are located below and to the left of the boundaries of model 0, indicating that the flexible hydrofoil crosses the transition boundaries at slightly lower values of α and/or Fn_h. The effect is most pronounced in the inception and re-wetting boundaries, while differences in the stabilization and washout boundaries are within the uncertainty bounds shown.

5.6.2 Changes Caused by Active External Excitation

As described in chapter II, an electrodynamic shaker motor was attached to model 2 as a means to provide harmonic excitation to the hydrofoil. The response of the hydrofoil to forced harmonic motion is the topic of chapter VI, but one ancillary aspect of the forced-excitation is applicable here. It was discovered that by exciting the hydrofoil in different modes, the frequencies and mode shapes of which were determined *a priori*, some control could be affected on the formation and elimination of ventilated cavities. Figure 5.23 shows an example from the towing-tank. Time histories of the measured lift, drag, and yawing moment are shown on the top axes, and a time-history of the commanded excitation frequency is shown on the lower axes, overlaid by the modal frequencies of model 1. Still-frames from the underwater camera depict the flow at different times during the run, which occurred at a constant $Fn_h = 0.75$, $\alpha = 15°$, $AR_h = 1$. Excitation of mode 1 appeared to promote the inception of a ventilated cavity, while excitation at modes 2, 3, and 4 caused rewetting of the hydrofoil. Figure 5.24 depicts a similar process on model 2 at the INSEAN cavitation tunnel at conditions of $\alpha = 5°$, $Fn_h = 1.5$, $AR_h = 1$. High-speed video frames provide a better time-resolved impression of the rewetting process during shaker excitation, which appears to occur by reattachment of the flow near the free surface. Moreover, control over the flow is affected with a shaker force amplitude of

$$F_{shaker} \approx 0.06 F_y.$$

It appears that the motion of the hydrofoil in higher-order and/or coupled twisting and bending modes encourages reattachment of flow near the leading edge. It has been established in literature (*McCroskey et al.*, 1976, 1981, 1982) that pitching (twisting) motion of airfoil sections can delay flow separation by attenuating the adverse pressure gradient along the chord of 2-D foil sections. It is possible that a similar effect is occurring here, where the pressure gradient is suppressed, encouraging reattachment of the flow. It is also possible that the hydrofoil motion at high frequencies imparts additional energy to the wetted flow in the form of turbulence, which disrupts the region of flow separation occupied by the cavity. This is a preliminary finding, and one that merits further investigation in the future.

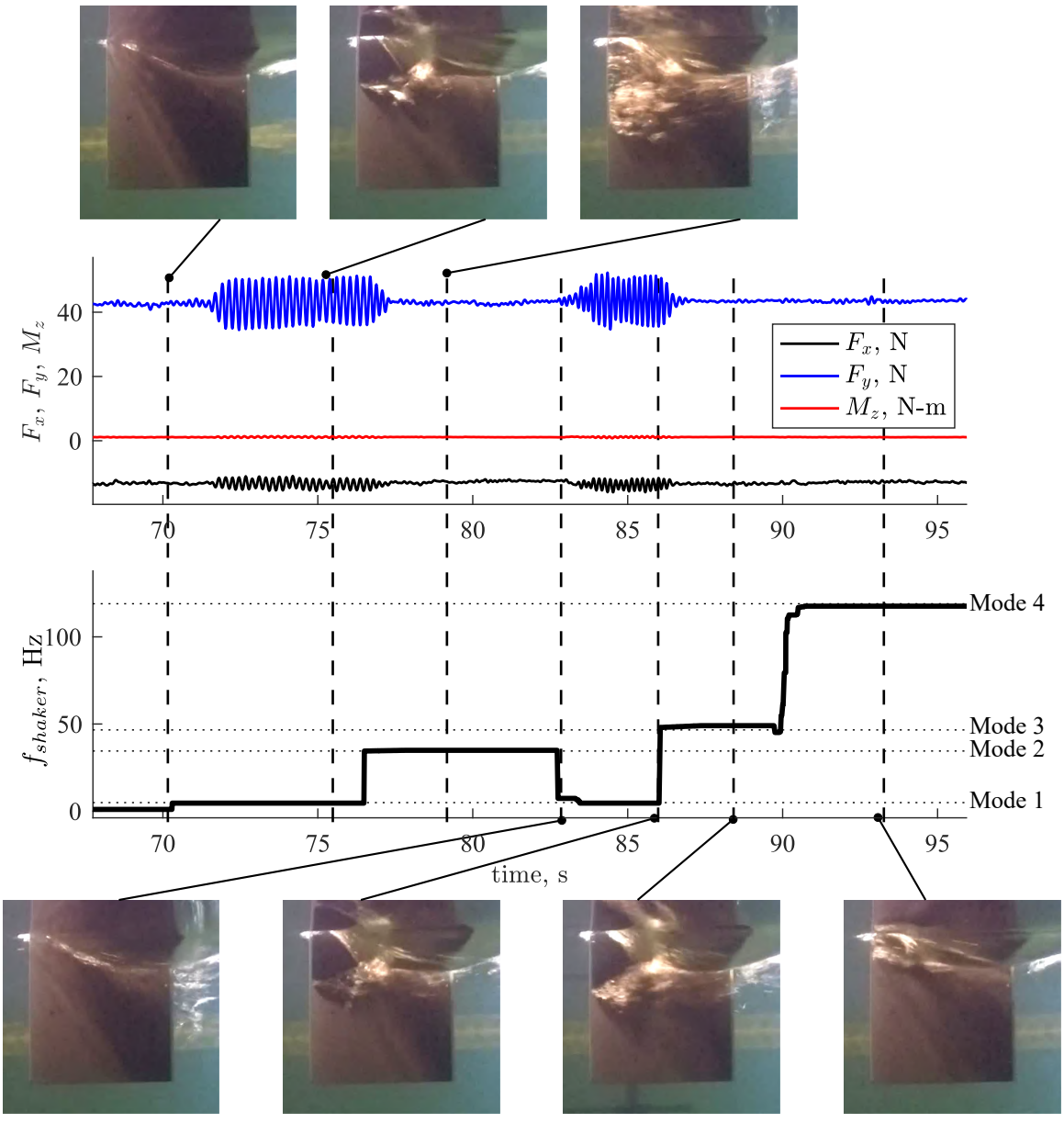

Figure 5.23: The effect of active excitation of model 2 at $\alpha = 15°$, $Fn_h = 0.75$, and $AR_h = 1.0$ in the towing tank. Excitation at the first modal frequency promoted ventilation, while excitation at higher modal frequencies induced re-wetting of the flow.

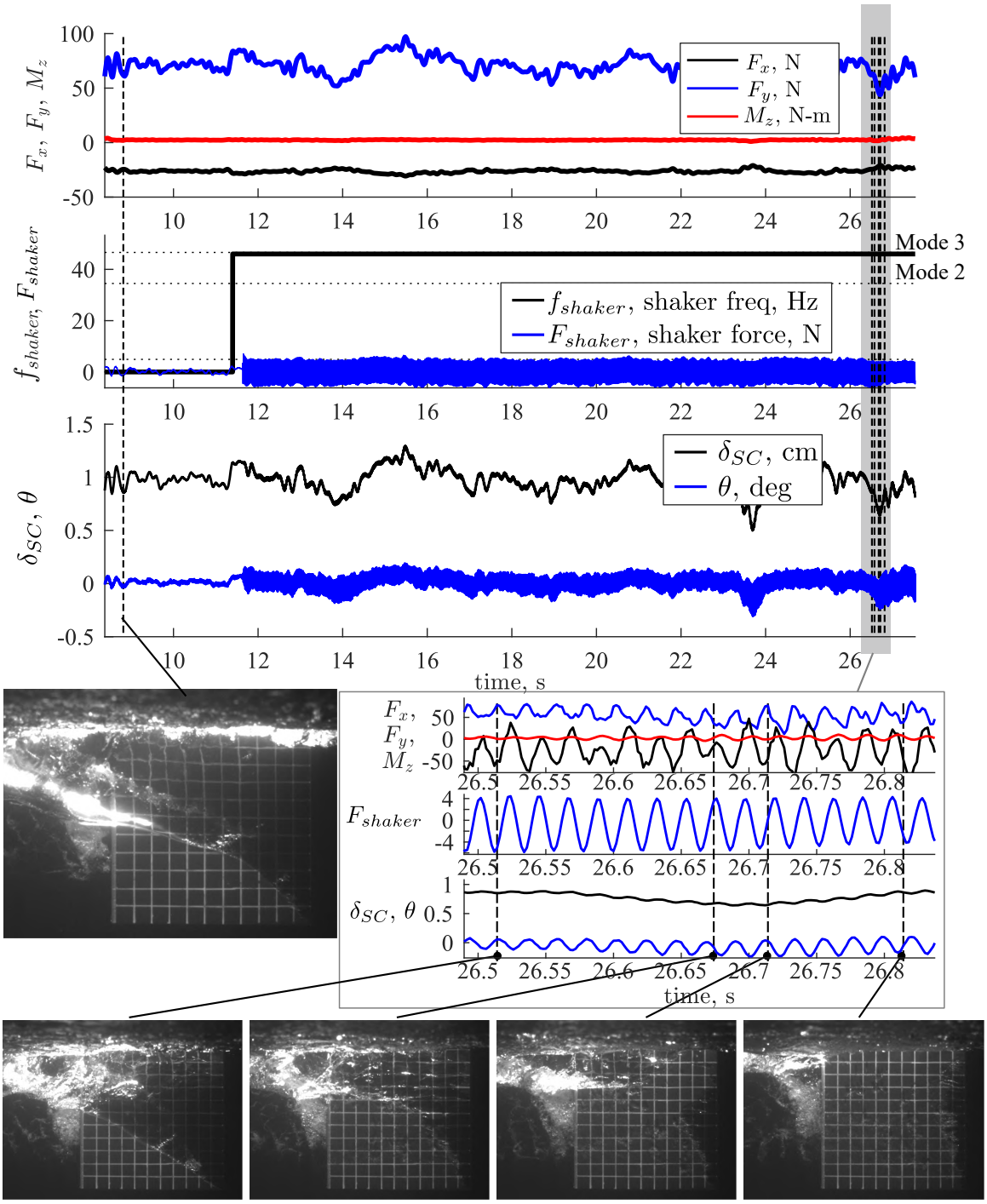

Figure 5.24: The effect of active excitation of model 2 at $\alpha = 5°$, $Fn_h = 1.5$, and $AR_h = 1.0$ in the cavitation tunnel. Excitation at the third modal frequency caused washout and re-wetting by promoting reattachment of the flow near the free-surface, thereby cutting off the supply of air to the cavity. Note that the amplitude of the shaker motor force (F_{shaker}) was approximately 5% the mean lift, F_y.

5.7 Summary and Discussion

5.7.1 Summary of Results

The results of the chapter are summarized below:

What effect does hydrofoil flexibility have upon the hydrodynamic response, stability, and flow regimes of the flexible hydrofoils?

The same flow regimes and transition mechanisms are present on the flexible hydrofoil models as on the rigid hydrofoil model, and the physics dictating flow stability are unchanged. The stability regimes of model 1 show a reduction in the stall angle from $\alpha_s = 15°$ to $\alpha_s = 13°$ as a result of the hydrofoil flexibility. Hydroelastic coupling causes the steady lift and yawing moment coefficients to be larger for the flexible hydrofoils (models 1 and 2) than for the rigid model 0, while the differences between models 1 and 2 are within the experimental uncertainty bounds. The drag coefficient is relatively unaffected by hydrofoil flexibility.

Passive deformations of model 1 are shown to shift the transition boundaries (inception, stabilization, washout, and rewetting) slightly downward and/or to the right, relative to the boundaries of model 0. The differences are small, however, and in the cases of the stabilization and washout boundaries, the rigid and flexible boundaries are within the experimental uncertainty. Active excitation of model 2 at its resonant modes was found to modify the local/global stability of overlapping flow regimes in the bi-stable regions of parameter space. Excitation of the first bending mode encouraged ventilation inception, while excitation of twisting modes and higher-order bending modes caused washout and rewetting.

How does multi-phase flow affect the static and dynamic hydroelastic response and stability of the hydrofoil?

Bending and twisting deflections are proportional to the lift and yawing moment in each flow regime. As a result, structural deflections are much smaller in the FV regime than in the FW regime. The maximum twist angle induced by hydrodynamic loading on either model 1 or model 2 is approximately $\theta = 1°$, measured at the foil tip. Thus, it is conceivable that the stall angle is advanced, though the test matrix resolution is too course to resolve the stall angle precisely.

When the flow regime changes suddenly, such as during perturbation-induced ventilation formation, the structural deflections and unsteady hydrodynamic forces exhibit mimic the step response of a highly, but sub-critically damped dynamical system. At small yaw angles, coherent vortex shedding (into a von Kármán street)

from the blunt TE of model 2 was shown to excite flow-induced vibrations at Froude numbers of $0.3 \leq Fn_h \leq 2.5$. Lock-in was observed where the frequency of vortex shedding crossed resonant frequencies of the the hydrofoil. Peaks elsewhere in the spectra of hydrodynamic force and hydrofoil tip motions indicate flow-induced vibration.

Can scaling relations be used to describe the static and dynamic loads and structural responses of the surface-piercing hydrofoils?

The bending and twisting deflections measured at the tips of models 1 and 2, and scaled by the dynamic pressure, are proportional to $C_{L_{3D}}$ and $C_{M_{3D}}$ respectively. Additionally, the ratio of elastic twist angle to total effective angle of attack, measured at the foil tip, is shown to scale with ${Fn_h}^2$ for constant a_0 and e. Thus, attached flow in the FW flow regime form one asymptotic boundary, while FV flow at large α and Fn_h form another. These results are consistent with the numerical study of *Akcabay and Young* (2014). Intermediate yaw angles and Froude numbers, for which spanwise variations in cavity length cause both a_0 and e to vary along the span, fall between these established limits. Finally, the distance between vortices shed from the trailing edge was found to remain constant at all speeds, so the vortex shedding frequency scales linearly with forward speed.

5.7.2 Discussion

It was observed in §5.3 that the experimentally-observed stall angle of model 1 is lower than that of model 0. The results shown in this chapter (particularly those in figure 5.12), suggest that this is due at least in part to an increase in the effective yaw angle by twisting deflections. However, we cannot say with certainty that the advancement of the stall angle is due solely to flexibility of models 1 and 2. Variations in the water temperature of approximately 5C were measured between summer and winter testing. Thus, testing during the winter resulted in a chord-based Reynolds number Re_c as much as 15% smaller than that at the same conditions tested during the summer. The sharp Leading Edge (LE) geometry was expected to fix the separation point regardless of small variations in Re_c, but it appears that near the stall boundary, there was still some influence of viscosity. yielded a greater impact upon the stability boundaries of the flow regimes than did the flexibility of the hydrofoil.

CHAPTER VI

Preliminary Modal Analysis of Flexible Hydrofoil

This chapter presents recent work on the dynamic hydroelastic behavior of the flexible hydrofoils undergoing vibration. The chapter will address the following research question, posed in chapter I:

- How are the system resonant frequencies, mode shapes, and damping coefficients altered by flow speed and multi-phase flow?
- Can ventilation and/or cavitation cause hydroelastic instability?

Additionally, we will touch upon dynamical modeling and system identification. We begin by presenting a general dynamical system model for a hydroelastic system like the hydrofoils under consideration.

6.1 The Equations of Motion of a Hydroelastic System

In this chapter, we depart from the simplified Two-Dimensional (2-D), Two-Degree of Freedom (DOF) model previously used to demonstrate hydroelastic interactions. Instead, the surface piercing hydrofoil is modeled as a generic dynamical system like that described by equation 1.24, which is reproduced below:

$$[\boldsymbol{M_s}] \ \ddot{\boldsymbol{X}} \ + [\boldsymbol{C_s}] \ \dot{\boldsymbol{X}} \ + [\boldsymbol{K_s}] \{\boldsymbol{X}\} = \{\boldsymbol{F_{EX}}\} + \{\boldsymbol{F_{fl}}\} . \qquad \text{(1.24 revisited)}$$

It is useful to add a hysteretic damping term, $[\boldsymbol{G_s}]$, to equation 1.24, which is commonly used to represent dissipation of energy into bolted connections and into thermal losses in the material itself. Doing so yields,

$$[\boldsymbol{M_s}] \ \ddot{\boldsymbol{X}} \ + [\boldsymbol{C_s}] \ \dot{\boldsymbol{X}} \ + [\boldsymbol{G_s}] [\boldsymbol{S}]^D \ \dot{\boldsymbol{X}} \ + [\boldsymbol{K_s}] \{\boldsymbol{X}\} = \{\boldsymbol{F_{EX}}\} + \{\boldsymbol{F_{fl}}\} , \qquad (6.1)$$

$[\boldsymbol{S}]^D$ is a scale matrix, defined such that,

$$S_{ij} = \delta_{ij} \frac{|X_i|}{|\dot{X}_i|}, \tag{6.2}$$

where δ_{ij} is the Kronecker delta. Equation 6.2 causes the structural hysteretic damping force to be proportional to displacement, while in phase with the velocity (*Soroka*, 1949). This structural damping model the causes the proportion of energy dissipated per unit cycle – otherwise known as the hysteretic loss factor – to be independent of frequency. As a result, the model is non-causal, and not strictly physical. However, as described by *Crandall* (1970); *Bert* (1973), the spurious non-causal behavior is negligible. More importantly, the proportional energy dissipation per cycle of real solid materials is approximately constant over a sufficient range of frequencies that the linear structural damping model does relatively well over the frequency range of interest in this study.

Finally, we are not concerned with the static equilibrium deflections of the model, which were discussed in chapter V. Thus, let equation 6.1 be written with the linear steady-state hydroelastic response

$$\{\boldsymbol{X_{steady}}\} = \left([\boldsymbol{K_s}] + [\boldsymbol{K_{fl}}]\right)^{-1} \{\boldsymbol{F_{r,steady}}\},$$

subtracted from the response, such that $\{\boldsymbol{X}\}$ describes the displacement about the static equilibrium deflections.

In this chapter, we consider the case where $\{\boldsymbol{F_{fl}}\} = 0$ and $\{\boldsymbol{F_{EX}}\} = 0$. Let the fluid force vector contain components proportional to the structural motions (*Theodorsen*, 1935; *Münch et al.*, 2010; *Akcabay et al.*, 2014a). This assumption yields added mass, damping, and stiffness matrices, allowing us to write,

$$\{\boldsymbol{F_{fl}}\} = - \ [\boldsymbol{M_{fl}}] \ \ddot{\boldsymbol{X}} \ + [\boldsymbol{C_{fl}}] \ \dot{\boldsymbol{X}} \ + [\boldsymbol{K_{fl}}]\{\boldsymbol{X}\} \ + \{\boldsymbol{F_{other}}\}. \tag{6.3}$$

$\{\boldsymbol{F_{other}}\}$ represents complex non-linear forces or those caused by hydrodynamic phenomena not inherently related to structural motions, such as unsteady cavity shedding, vortex shedding, or boundary layer instability (*Ducoin et al.*, 2012a; *Akcabay et al.*, 2014a; *Akcabay and Young*, 2015; *Caverly et al.*, 2016).

Thus, we have, as general equations of motion for a hydroelastic lifting surface,

$$([\boldsymbol{M_s}] + [\boldsymbol{M_{fl}}]) \quad \ddot{\boldsymbol{X}} \quad + ([\boldsymbol{C_s}] + [\boldsymbol{C_{fl}}]) \quad \dot{\boldsymbol{X}} \quad + [\boldsymbol{G_s}] [\boldsymbol{S}]^D \quad \dot{\boldsymbol{X}} \quad + \ldots$$
$$([\boldsymbol{K_s}] + [\boldsymbol{K_{fl}}]) \{\boldsymbol{X}\} = \{\boldsymbol{F_{EX}}\} + \{\boldsymbol{F_{other}}\} . \quad (6.4)$$

Equation 6.4 forms the basis for modeling in this chapter, and we will revisit it in §6.4, when the model is applied to the interpretation of experimental data.

6.2 Finite Element Method Predictions of Modal Characteristics of Flexible Hydrofoils

Finite Element Method (FEM) modeling was performed in ANSYS Mechanical® for both flexible hydrofoil models (model 1 and model 2) to predict the approximate modal frequencies and mode shapes in dry conditions. Models were assigned the properties in table 2.1 and table 2.2. In each case, the nodes on the surface of the foil tang were constrained in all degrees of freedom to simulate the physical clamp, and the shape sensing spars were omitted from both models. Figure 6.1 depicts the meshed FEM model of model 2, which differs from model 1 only in the aluminum strip at the Trailing Edge (TE). Each model was meshed with 160,000 to 180,000 elements.

The resonant frequencies and descriptions of each mode shape are given in table 6.1. The mode shapes themselves are shown later in §6.3 for model 1, and §6.5.2 for model 2.

Additional FEM modeling was performed by collaborators, using ABAQUS® to simulate model 1 in a partially-immersed condition in both Fully Wetted (FW) and Fully Ventilated (FV) flows. The liquid domain was modeled with zero-shear and zero-stiffness acoustic elements, which retains only the inertial effect of water. Ventilation was simulated by specifying the assigning the properties of air to the acoustic elements within a prismatic wedge of fluid (see figure 6.2). Further details of the simulation may be found in *Harwood et al.* (2016a), and results will be briefly discussed in §6.3.

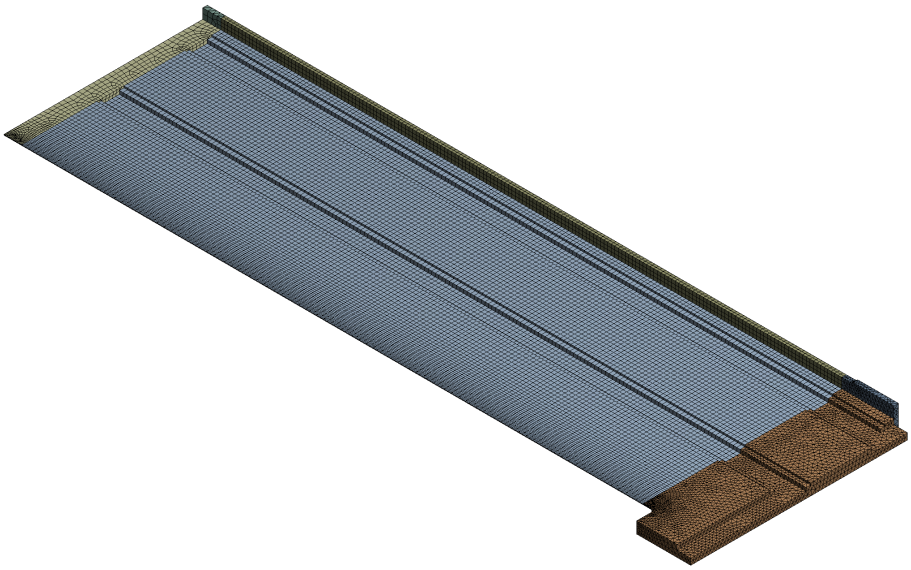

Figure 6.1: FEM model of flexible hydrofoil. Model 2 is shown. Model 1 was simulated by removing the aluminum strip at the TE.

Table 6.1: Undamped *in-vacuo* normal modes of model 1 and model 2 predicted by FEM model.

Mode		Model 1	Model 2
Mode 1	Name	X-Bend 1	X-Bend 1
	Frequency	8.0 Hz	9.9 Hz
	Mode Shape	First bending mode	First bending mode
Mode 2	Name	X-Bend 2	Z-Twist 1
	Frequency	48.9 Hz	51.6 Hz
	Mode Shape	Second bending mode with secondary twisting	First twisting mode with secondary bending
Mode 3	Name	Z-Twist 1	X-Bend 2
	Frequency	54.5 Hz	63.0 Hz
	Mode Shape	First twisting mode	Second bending mode with secondary twisting
Mode 4	Name	Y-Bend 1	Y-Bend 1
	Frequency	68.6 Hz	93.3 Hz
	Mode Shape	First lead-lag mode	First lead-lag mode
Mode 5	Name	X-Bend 3	X-Bend 3
	Frequency	134.8 Hz	148.1 Hz
	Mode Shape	Third bending mode	Third bending mode
Mode 6	Name	Z-Twist 2	Z-Twist 2
	Frequency	166.3 Hz	182.7 Hz
	Mode Shape	Second Twisting mode	Second Twisting mode

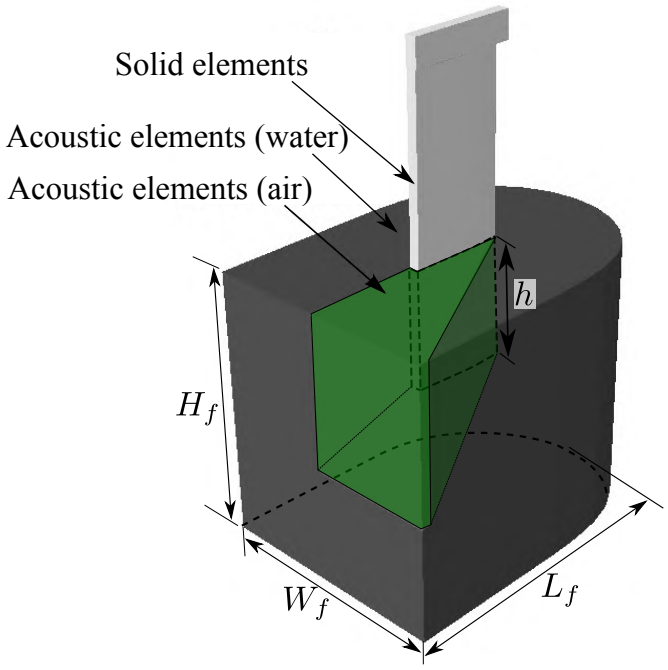

Figure 6.2: FEM domain for the surface-piercing strut simulated in FV flow. A wedge-shaped volume of acoustic elements are switched from water to air to approximate the effect of ventilation on the modal response of the strut. Reproduced from *Harwood et al.* (2016a).

6.3 Output-Only Operational Analysis of Model 0 and Model 1

An output-only analysis of the free vibrations of the aluminum (model 0) and PVC (model 1) struts was performed by *Harwood et al.* (2016a). The study was performed by striking the struts with an un-instrumented hammer while measuring the outputs from a suite of accelerometers, strain-gauges, and a single-point Laser Doppler Velocimetry (LDV). Such an analysis, performed without knowledge of the spectral energy of the input, is known as an *operational* analysis, as opposed to a modal analysis, since the former can only provide insight into the spectral content of the system's output while the system is operating, and cannot characterize the way the system responds to inputs not present in the system's measured operation.

Most of the analyses were later improved and expanded upon with the shaker-motor testing of model 2 (with TE reinforcement). While the model-1-specific results should be found in *Harwood et al.* (2016a), the salient points will be herein summarized to frame the discussion of modal coalescence and to form the foundation for the modal analysis that follows.

To collect vibration data, each strut was suspended from the steel dry-land frame

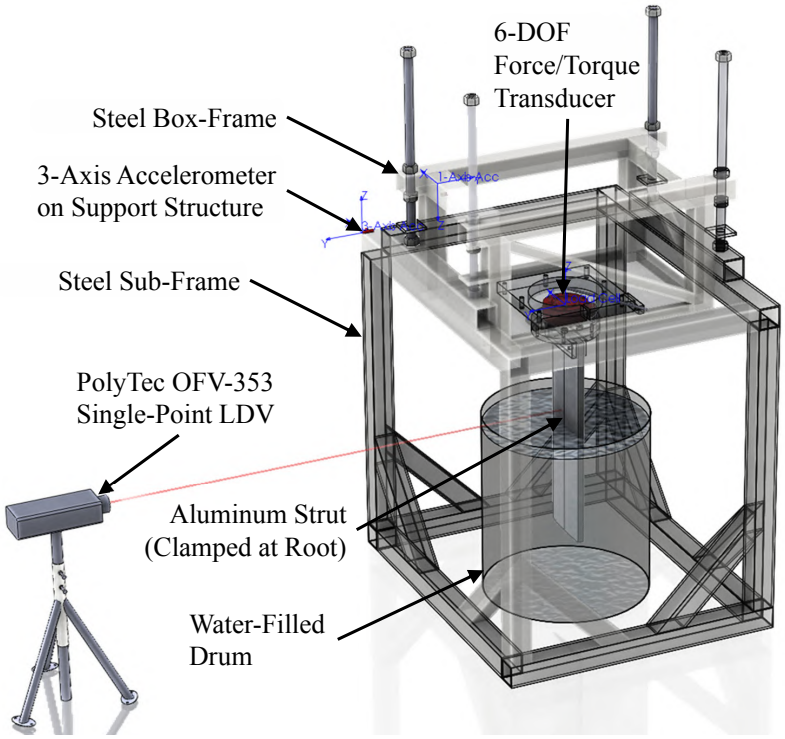

Figure 6.3: Experimental setup used to measure vibratory response of struts. A large steel structure holds the surface-piercing strut in a vertically-cantilevered configuration, suspended either in air or in a 65-gallon (246 liter) drum with the free tip immersed to depth h. Reproduced from *Harwood et al.* (2016a).

(described in § 2.2.1) in a vertically cantilevered configuration. The root of the strut was clamped to the box frame in exactly the same manner as during towing-tank testing. The free tip of the strut was lowered into a 250 liter (65-gallon) drum, which was filled with freshwater until the desired depth of immersion (h) was achieved. Immersed aspect ratios ($AR_h = h/c$) of 0, 0.5, 1.0, and 1.5 were assessed, with $AR_h = 0$ corresponding to the dry configuration. The motions of the hydrofoils were measured via a Polytec OFV-353 single-point LDV, and the internal shape-sensing spars were used to measure the deflections of model 1 only. The strut was excited by hammer strikes, after which the decaying free-vibration response was recorded as a time-series of length M. Sampling rates of $F_s = 1$ kHz and 5 kHz were used for the aluminum and PVC struts, respectively. The experimental setup is illustrated in figure 6.3.

The Discrete Fourier Transform (DFT) was used to generate frequency spectra for each recorded channel,

$$\left[\tilde{\boldsymbol{X}}\right] = \mathcal{D}([\boldsymbol{X}]), \tag{6.5}$$

where X_{jm} is a sample on channel j collected at time t_m and $\tilde{X}_{jm}$ is the complex-valued number corresponding to channel j at frequency f_m, where $m = 1, 2, \ldots, M$. The magnitudes of the frequency response $\left| \tilde{\boldsymbol{X}} \right|$ were plotted for each collected data channel, denoted by index j, and the collective frequency distributions were used to locate peaks in the frequency spectra corresponding to resonant modes. The location of a peak on each channel was taken as the j^{th} estimate of the resonant frequency of mode n, denoted as $f_{0,(n,j)}$.

Taking the imaginary part of row m from $\tilde{\boldsymbol{X}}$ yields the operating deflection shape (ODS) for frequency f_m. When the sampled strain-gauge signals are considered, the ODS represents the strain distribution that oscillates sinusoidally at that frequency:

$$\{\tilde{\boldsymbol{\epsilon}}_{\boldsymbol{z}}\} = \mathbb{I}\text{m} \quad \tilde{\boldsymbol{X}}_{\ m} \quad . \tag{6.6}$$

The ODS strains for each resonant condition were translated into a surface ODS, $\tilde{\boldsymbol{Y}}$, *via* equations 2.3-2.6. For resonant peaks that are well-separated from one another, the ODS at the peak of mode n is dominated by the underlying normal mode shape, $\{\boldsymbol{\Theta}\}_n$ (*Schwarz and Richardson*, 1999).

6.3.1 Operating Deflection Shapes

The measured operating deflection shapes (ODSs) and corresponding resonant frequencies (f_0) of model 1 are shown in figure 6.4. The rows are ordered by increasing immersed aspect ratio AR_h, and the columns are ordered from left to right by ascending resonant frequencies within each row. Note that the Y-Bend-1 mode (also known as the "lead-lag" mode) is not captured in the experiments because the half-bridges used fo the shape-sensing spars reject axial strains. The X-Bend-1 and X-Bend-3 modes are clearly represented in the ODS. As the immersion depth is increased, these modes appear to change only slightly (some induced twist appears in the X-Bend-3 mode), but remain recognizable. The X-Bend-2 and Z-Twist-1 modes, however, are located relatively close to one another in the frequency domain, and both underlying normal modes contribute to the ODS at nearby frequencies. As a result, the underlying modes cannot be extricated from the ODS; rather, the ODS must be regarded as weighted superposition of the underlying modes. As the immersion depth is increased to $AR_h = 0.5$, the second and third resonant modes become so closely-coupled (less than 2 Hz of separation), that the ODSs are almost indistinguishable. At $AR_h = 1.0$, the second and third resonant ODSs are re-ordered, relative to the dry ordering, such that Z-Twist-1 actually occurs at a slightly lower frequency than

does X-Bend-2. At $AR_h = 1.5$, the original order is restored. Resonant mode shapes predicted by FEM for the cases where re-ordering occurs are shown at the bottom of the figure, corroborating the result of mode re-ordering.

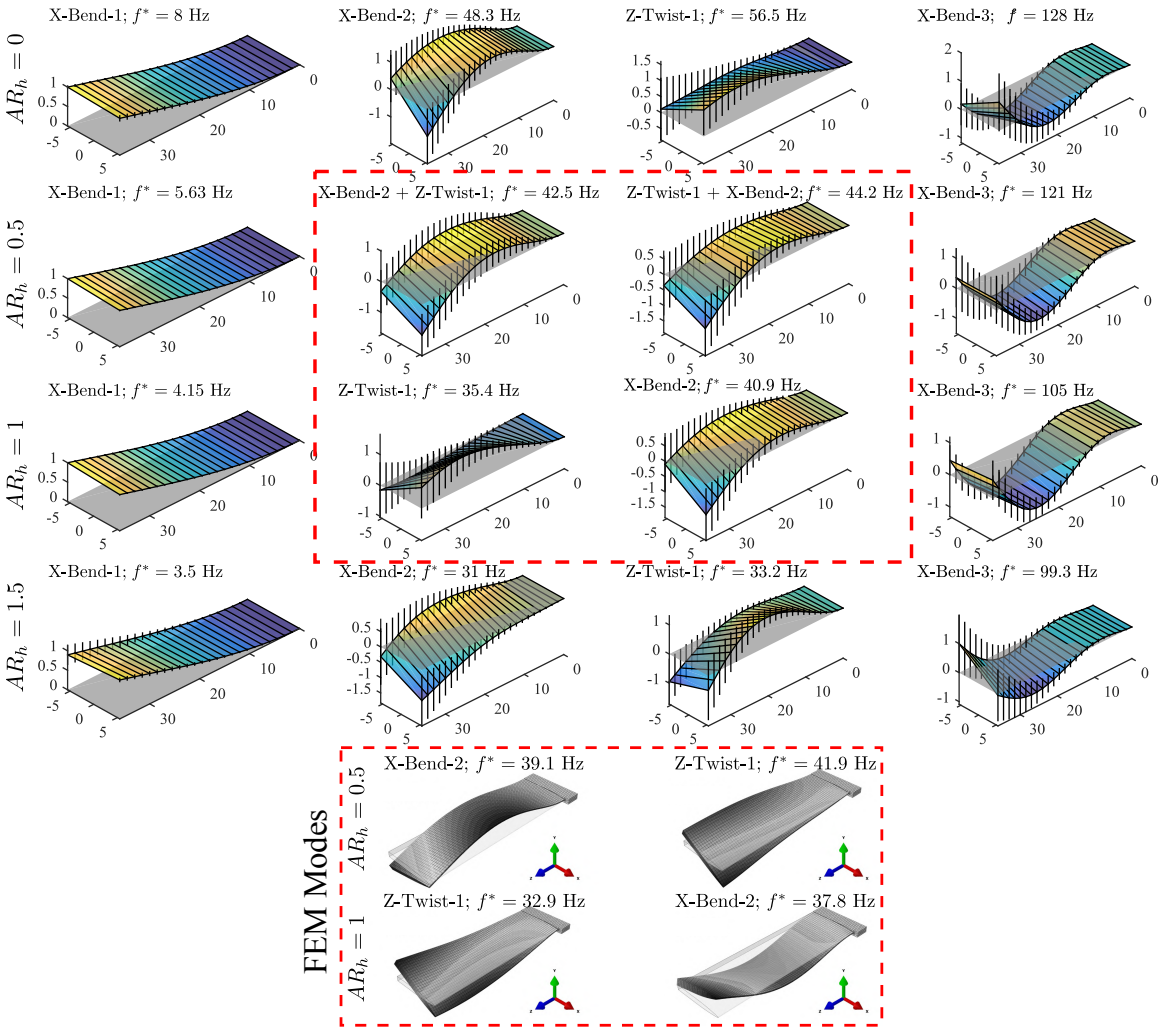

Figure 6.4: Resonant Operating Deflection Shapes (ODSs) measured in experiments for model 1. The undeformed surface is indicated by the grey patch. Vertical bars indicate ± one standard deviation in the ODS. The second and third resonant modes coalesce and reverse order between $AR_h = 0.5$ and $AR_h = 1.0$, and return to the original order at $AR_h = 1.5$. Modes predicted by FEM, shown at the bottom of the figure, also indicate a re-ordering of the second and third modes between $AR_h = 0.5$ and $AR_h = 1.0$. Reproduced from *Harwood et al.* (2016a).

6.3.2 Effects of Partial-Immersion on Resonant Frequencies

The resonant frequencies of the aluminum (model 0) and PVC (model 1) struts are respectively shown in figure 6.5a and figure 6.5b. The resonance frequencies, nondimensionalized by the corresponding dry modal frequencies for each mode, $f_{0,n}/f_{0,n}^{DRY}$ are shown for both models in figure 6.5c and figure 6.5d, respectively.

The agreement between the FEM results and the experimental results are good in most cases. A notable exception is the X-Bend-2 mode of the aluminum strut, where the FEM-predicted frequencies are consistently higher than the experimentally-observed ones. A likely explanation for the discrepancy is the root boundary condition. In the FEM model, the root of the strut was perfectly clamped, while the experimental setup may have been influenced by the compliance of the load cell, reducing the stiffness of the system.

In general, with increasing AR_h, the resonant frequencies in figure 6.5a and figure 6.5b decrease, with the exception of the Y-Bend-1 mode. As figure 6.5c and figure 6.5d demonstrate, the reduction is more severe for the PVC strut than the aluminum strut. Both effects are attributed to the inertial resistance of the water to the strut's motion. Added mass is the integrated inertial resistance to the local accelerations of the body, which as the name implies, may be modeled by additional mass distributed on the structure. The distribution of the added mass is purely a function of the body's motion (if free-surface waves are neglected). For similar mode shapes, the fluid added mass will be nearly identical for the two struts, but will make up a greater percentage of the total system mass in the case of the PVC strut. As a result, the lighter structure is influenced to a much greater degree by the immersion into a dense fluid – a result shown both analytically and numerically by *Motley et al.* (2013) and *Kramer et al.* (2013).

Mode shapes where deflection occurs in a direction with a large projected area (e.g. X-Bend-1) are necessarily more-strongly affected by the surrounding fluid's added mass than are mode shapes that present minimal projected area in the direction of primary motion (Y-Bend-1). This is demonstrated in figure 6.5c and figure 6.5d by the fact that, as the struts are immersed, the reductions to the resonant frequencies are not uniform. Namely, the first-order resonant modes (X-Bend-1 and Z-Twist-1) are affected more-severely than the higher-order modes. Moreover, note that inflections occur in the resonant frequencies of the higher-order modes. This occurs when a nodal line of the respective resonant mode is submerged. Motion along the node lines is identically zero, and so induces very little acceleration in the surrounding fluid; the result is a near-zero change in the hydrodynamic added mass.

As observed in the preceding section, the second and third modes approach one another (frequency coalescence) between $AR_h = 0.5$ and $AR_h = 1.5$. This occurs because the node line of the X-Bend-2 becomes submerged at approximately $AR_h = 1$, causing the added mass component to plateau. The added mass effect is proportionally severe enough to cause a re-ordering of modes at AR_h only in the case of the PVC strut.

6.3.3 FEM Prediction of the Effects of Ventilation on Resonant Frequencies

The hydrofoils remained in the stationary drum during testing, so no experimental data were available to assess the effect of ventilation on modal frequencies or ODSs. Data were limited instead to the FEM predictions. The dashed lines in figs 6.5 denote the numerical resonant frequencies when the air-filled cavity was included in the fluid domain. In all cases, the resonance frequencies increase from their fully-wetted values. In the fully-ventilated configuration, nearly half of the previously-wetted area is surrounded by air, which presents a negligible inertial opposition to motion, thus reducing the added mass. As a result, the resonant frequencies increase to a value somewhere between those in the corresponding fully-wetted condition and the dry condition.

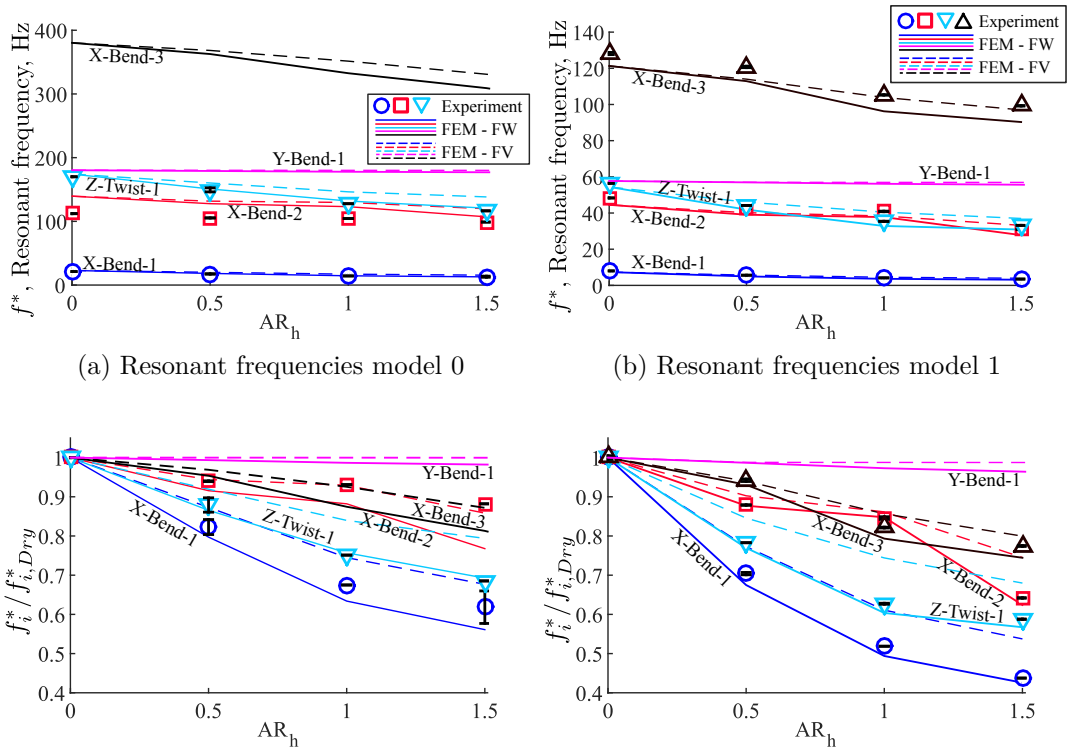

(a) Resonant frequencies model 0

(b) Resonant frequencies model 1

(c) Wet-dry frequency ratios of model 0

(d) Wet-dry frequency ratios of model 1

Figure 6.5: Dimensional resonant frequencies of **(a)** aluminum (model 0) and **(b)** PVC (model 1) struts and the wet-to-dry frequency ratios of **(c)** model 0 and **(d)** model 1 struts with varying immersed aspect ratio. Symbols denote mean experimental resonant frequencies, with bars indicating ± one standard deviation. Solid lines indicate the FEM results with a fully-wetted fluid domain and dashed lines indicate the FEM results with a simulated fully-ventilated cavity. Reproduced from *Harwood et al.* (2016a).

6.3.4 Insights gained from Output-Only Analysis

Partial immersion in water causes the resonant frequencies of both struts to decrease, though the effect is more pronounced for the PVC strut because hydrodynamic added mass makes up a greater proportion of the effective system mass. The modal-dependence of the fluid added mass causes the second bending and first twisting frequencies to approach one another for the aluminum strut and to change order for the PVC strut. The re-ordering of modes has been shown by the numerical mode shapes and by the operating deflection shapes (ODSs) measured in the experiments. Frequency coalescence is significant because it can be a precursor to dynamic modes of hydroelastic instability. It signifies the sharing of energy between two modes; in extreme cases, one mode can feed energy into another in an unbounded fashion. The formation of a FV cavity causes the resonant frequencies to increase again, as air replaces some of the water surrounding the strut, reducing the fluid added-mass. Damping coefficients were not obtained successfully because output-only damping estimates (*e.g.* the fractional-power-bandwidth method (*Bert*, 1973; *Reese*, 2010; *Chae et al.*, 2016)) do not perform well in the vicinity of closely-coupled modes. In the following section, a method will be presented by which a more-rigorous analysis of the modal behavior of a flexible hydrofoil may be performed.

6.4 Input-Output Modal Analysis of Model 2

This section introduces the concepts and tools used to analyze the vibrations of the hydrofoils. The concept of a frequency response function will be presented first, followed by a derivation of the frequency response function and complex transfer function representations for a general vibratory system with multiple degrees of freedom. The application of the derived relationships to experimentally-collected data will then be outlined, and the methods validated with a simple demonstration problem.

6.4.1 Frequency Response Function of an MDOF Dynamical System

Central to operational and modal vibration analysis is the Frequency Response Function (FRF), which is a complex-valued representation of a system's response to a given input,

$$H(\omega) = \frac{\text{Output}(\omega)}{\text{Input}(\omega)}. \tag{6.7}$$

Table 6.2: Common names of frequency response functions with input measurements X and output measurements Y

X	Y	Y/X	X/Y
Force	Displacement	Compliance	Dynamic Stiffness
Force	Velocity	Mobility	Impedance
Force	Acceleration	Inertance / Receptance	Dynamic Mass

.

For a vibratory system with only one degree of freedom, the FRF describes the response of the entire system. For multiple-degree-of-freedom (MDOF) systems with N degrees of freedom, the FRF takes the form of an $N \times N$ matrix, each containing a complex valued function $H_{ij}(\omega)$, that maps an input at the j^{th} degree of freedom to an output at the i^{th} degree of freedom of a system excited at an angular frequency of *omega*.

The name given to an FRF matrix depends upon the quantities defined as inputs and outputs. Table 6.2 gives a summary of common FRF types. If one assumes a linear system with time-invariant parameters, then reciprocity of the system may be assumed, such that the FRF matrix is symmetric. As a result, only one row or column of the FRF matrix is needed to completely characterize the response of the system. A single column might be measured by exciting the system at a single point and measuring the response at distributed points on the structure, while a row may be measured by measuring the response at a single location while moving the point of excitation to different locations on the model (an example being a roving-hammer test).

6.4.2 Dynamical-System Model for Surface-Piercing Hydrofoil

In this section, the equations of motion of a general hydroelastic system (equation 6.4) will be developed into a modally-decomposed reduced-order model. Consider equation 6.4. Let the structural and fluid mass, damping, and stiffness matrices be summed together:

$$\begin{aligned} [\boldsymbol{M}] &= [\boldsymbol{M_s}] + [\boldsymbol{M_{fl}}] \\ [\boldsymbol{C}] &= [\boldsymbol{C_s}] + [\boldsymbol{C_{fl}}] \\ [\boldsymbol{K}] &= [\boldsymbol{K_s}] + [\boldsymbol{K_{fl}}] \,. \end{aligned} \tag{6.8}$$

Listed below are the assumptions under which the following derivation is per-

formed:

- The fluid added mass, added damping, and added stiffness matrices are, in general, dependent upon ω. We will assume that the frequency-dependency in these matrices may be neglected relatively narrow bands of the frequency domain, *i.e.* the matrices are assumed frequency-independent in the immediate neighborhood of modal peaks.

- The same assumption is made regarding the structural damping matrix $[\boldsymbol{G_s}]$. The frequency dependency is neglected in the immediate neighborhood of modal peaks.

- Fluid added mass, damping, and stiffness matrices are assumed to be linear with respect to $\{\ddot{\boldsymbol{X}}\}$, $\{\dot{\boldsymbol{X}}\}$, and $\{\boldsymbol{X}\}$, respectively.

- The structural and fluid damping matrices, $[\boldsymbol{C_s}]$, $[\boldsymbol{G_s}]$, and $[\boldsymbol{C_{fl}}]$ are assumed to reside within the matrix space defined by the bases $[\boldsymbol{M}]$ and $[\boldsymbol{K}]$, such that each may be written as a linear combination of the mass and stiffness matrices. This is a form of damping known as proportional Rayleigh damping. Rayleigh damping is the classic example of general proportional damping (*Rayleigh*). Recently, formulations have also been proposed for more-general forms of proportional damping, based on Caughey series (*Adhikari*, 2006).

- The matrices $[\boldsymbol{M}]$, $[\boldsymbol{C}]$, $[\boldsymbol{G_s}]$, and $[\boldsymbol{K}]$ are assumed to be symmetric, such that they may be diagonalized by a matrix of real eigenvectors.

Together, the above assumptions mean that we may assume the system under consideration to behave as a *sufficiently* linear, time-invariant, and frequency-independent system within a small band of frequencies surrounding each resonant mode.

Let $\{\boldsymbol{f_{other}}\} = 0$ and assume the external force to be harmonic with an angular frequency ω, *i.e.* $\{\boldsymbol{F_{EX}}\} = \tilde{\boldsymbol{f_{ex}}}\ e^{i\omega t}$, with an associated harmonic response $\{\boldsymbol{X}\} = \tilde{\boldsymbol{X_0}}\ e^{i\omega t}$, where the tilde ($\tilde{}$) indicates a complex number. Under such assumptions, equation 6.4 reduces to,

$$-\omega^2 [\boldsymbol{M}] + i\omega [\boldsymbol{C}] + [\boldsymbol{K}] + i [\boldsymbol{G_s}] \quad \tilde{\boldsymbol{X_0}} \quad = \quad \tilde{\boldsymbol{f_{ex}}} \quad , \tag{6.9}$$

The frequency response function is defined as the complex-valued mapping from a forcing vector $\{\boldsymbol{f}\}$ to a selected response vector (in this case the deflections $\tilde{\boldsymbol{X_0}}$),

$$\tilde{\boldsymbol{H}}(\boldsymbol{\omega}) \quad \tilde{\boldsymbol{f_{ex}}} \quad = \quad \tilde{\boldsymbol{X_0}} \quad . \tag{6.10}$$

By inspection, equation 6.9 yields that,

$$\tilde{\boldsymbol{H}}(\boldsymbol{\omega})^{-1} = -\omega^2 [\boldsymbol{M}] + i\omega [\boldsymbol{C}] + [\boldsymbol{K}] + i [\boldsymbol{G_s}]. \tag{6.11}$$

6.4.3 Modal Decomposition of Equations of Motion

Let $[\boldsymbol{\Theta}]$ and $\boldsymbol{\omega_0^2}^D$ be, respectively, the mass-orthonormalized eigenvectors (in columns) and corresponding eigenvalues (in the form of a diagonal matrix) that span the solutions to the homogeneous, undamped equation of motions,

$$[\boldsymbol{K}] - \omega^2 [\boldsymbol{M}] = \{\boldsymbol{0}\}. \tag{6.12}$$

$[\boldsymbol{\Theta}]$ and $[\boldsymbol{\omega_0}]^D$ are thus respectively referred to as the undamped mode shapes and undamped natural frequencies. Under the assumption of proportional damping, the undamped mode shapes and eigenvalues can be used to modally-decompose equation 6.11 to give,

$$\begin{aligned}[\boldsymbol{\Theta}]^T \tilde{\boldsymbol{H}}(\boldsymbol{\omega})^{-1} [\boldsymbol{\Theta}] &= [\boldsymbol{\Theta}]^T \left(-\omega^2 [\boldsymbol{M}] + i\omega [\boldsymbol{C}] + [\boldsymbol{K}] + i [\boldsymbol{G_s}]\right) [\boldsymbol{\Theta}] \\ &= -\omega^2 [\boldsymbol{I}] + i\omega [\boldsymbol{C_m}]^D + \boldsymbol{\omega_0^2}^D + i [\boldsymbol{\eta_m}]^D. \end{aligned} \tag{6.13}$$

$[\boldsymbol{C_m}]^D$ denotes the diagonal matrix of viscous damping coefficients (combined structural and fluid). η is the structural hysteretic loss-factor, defined as the proportion of energy dissipated during each cycle to hysteretic losses within the material. The degrees of freedom have been transformed into modal participation factors $\tilde{P}_n$, which describe the contribution of each mode shape $\{\boldsymbol{\Theta_n}\}$ to the system response, where n is the mode number. Note that there is no loss of generality in the solution, since $\{\boldsymbol{P}\}$ and $\tilde{\boldsymbol{X}}_{\boldsymbol{0}}$ are related by the change-of-basis transformation,

$$\tilde{\boldsymbol{X}}_{\boldsymbol{0}} = [\boldsymbol{\Theta}] \tilde{\boldsymbol{P}}. \tag{6.14}$$

Inverting both sides of equation 6.13 produces a representation of the FRF in terms of modal parameters,

$$[\boldsymbol{\Theta}]^{-1} \tilde{\boldsymbol{H}}(\boldsymbol{\omega}) [\boldsymbol{\Theta}]^{-T} = \left(-\omega^2 [\boldsymbol{I}] + i\omega [\boldsymbol{C_m}]^D + \boldsymbol{\omega_0^2}^D + i [\boldsymbol{\eta_m}]^D\right)^{-1} \tag{6.15}$$

$$\tilde{\boldsymbol{H}}(\boldsymbol{\omega}) = [\boldsymbol{\Theta}] \left(-\omega^2 [\boldsymbol{I}] + i\omega [\boldsymbol{C_m}]^D + \boldsymbol{\omega_0^2}^D + i [\boldsymbol{\eta_m}]^D\right)^{-1} [\boldsymbol{\Theta}]^T. \tag{6.16}$$

Each individual FRF in the FRF matrix $\tilde{\boldsymbol{H}}$ may be written as

$$H_{jk}(\omega) = \sum_{n=1}^{N_{DOF}} \frac{\Theta_{nj}\Theta_{nk}}{\omega_{0,n}^2 - \omega^2 + i(\eta_n + 2\omega\omega_{0,n}\xi_n)}, \tag{6.17}$$

where j and k are the indices of the excitation and response degrees of freedom. N_{DOF} denotes the number of instrumented degrees of freedom, and hence the number of modes that can be resolved. Alternatively, the summation may be performed over some truncated number of modes, $N < N_{DOF}$, rendering equation 6.17 a reduced-order model.

6.4.4 Equivalent Viscous Damping

There is no practicable way to extricate the two forms of damping contained in the denominator of equation 6.17. As a final simplification of the model, we'll assume that in the immediate vicinity of each mode n ($\omega \approx \omega_{0,n}$), the damping terms may be combined to yield,

$$H_{jk}(\omega) = \sum_{n=1}^{N} \frac{\Theta_{nj}\Theta_{nk}}{\omega_{0,n}^2 - \omega^2 + i\omega\omega_{0,n}\xi_{e,n}}. \tag{6.18}$$

Note that equation 6.18 is summed over N modes, where N describes the order of the resulting reduced order model. $\xi_{e,n}$ is an equivalent viscous damping ratio that approximates, by a linear dashpot, the total damping of mode n due to structural, fluid, hysteretic and other sources. Other researchers (*Blake*, 1972; *Reese*, 2010) have instead grouped all damping components into an equivalent loss factor, η_T. The choice is a purely semantic one, and the viscous model is chosen in this work. In what follows, an attempt will be made to separate the total damping into three constituent parts: the structural damping, the quiescent fluid damping, and the hydrodynamic damping. Thus, the linear summation is proposed,

$$\xi_{e,n} = \xi_{s,n} + \xi_{q,n} + \xi_{hd,n}, \tag{6.19}$$

where the damping components are described in table 6.3. Note that this superposition is proposed to separate the dissipative effects of the hydrofoil structure, the effects of the dense fluid (water), and the effects of fluid motion. Individual sources of damping will contribute to each of the three components in table 6.3, including both linear and nonlinear effects. The components in equation 6.19 and table 6.3

Table 6.3: Description of damping components that make up total equivalent damping ratio ξ_e.

Notation	Description	Physical Mechanisms
ξ_s	Structural damping	Viscoelastic, coulomb, and hysteretic damping in the material and at bolted interfaces.
ξ_q	Quiescent fluid damping	Viscous dissipation of eddies, wave radiation damping, and acoustic radiation. Assumed to be independent of fluid velocity.
ξ_{hd}	Hydrodynamic damping	Circulatory damping, nonlinear wave generation, spray, and other velocity-dependent components.

are therefore linearizations of the marginal damping ratios in the *in-vacuo*, quiescent fluid, and moving fluid regimes.

6.4.5 Transfer Function Representation

Note that equation 6.17 takes the form of a transfer function. Transfer functions are frequently represented in terms of the Laplace variable $s = \sigma + i\omega$, where σ is the damping coefficient in the complex s plane. The frequency response function can be viewed as a transfer function evaluated only along the frequency axis of the s domain, or under the substitution of $s = i\omega$. This is illustrated in figure 6.6, where the FRF is shown to be a slice through the complex transfer function along the frequency axis of the s plane.

For undamped vibratory systems, the poles of the transfer function are located on the frequency axis, such that the FRF becomes singular at the undamped resonant frequency ω_0, of each mode. The introduction of damping rotates the location of the pole in the complex s plane, moving it off of the frequency axis such that the frequency response function never becomes singular and the damped resonant frequency is slightly reduced.

Expanding the FRF and consolidating it into a single rational polynomial function of s gives the transfer function representation, referred to by *Richardson and Formenti* (1982) as the Rational Fraction Polynomial (RFP) model,

$$\tilde{\boldsymbol{H}}(\boldsymbol{s}) = \frac{\sum_{m=0}^{M_n} b_m s^m}{\sum_{n=0}^{N_d} a_n s^n}, \tag{6.20}$$

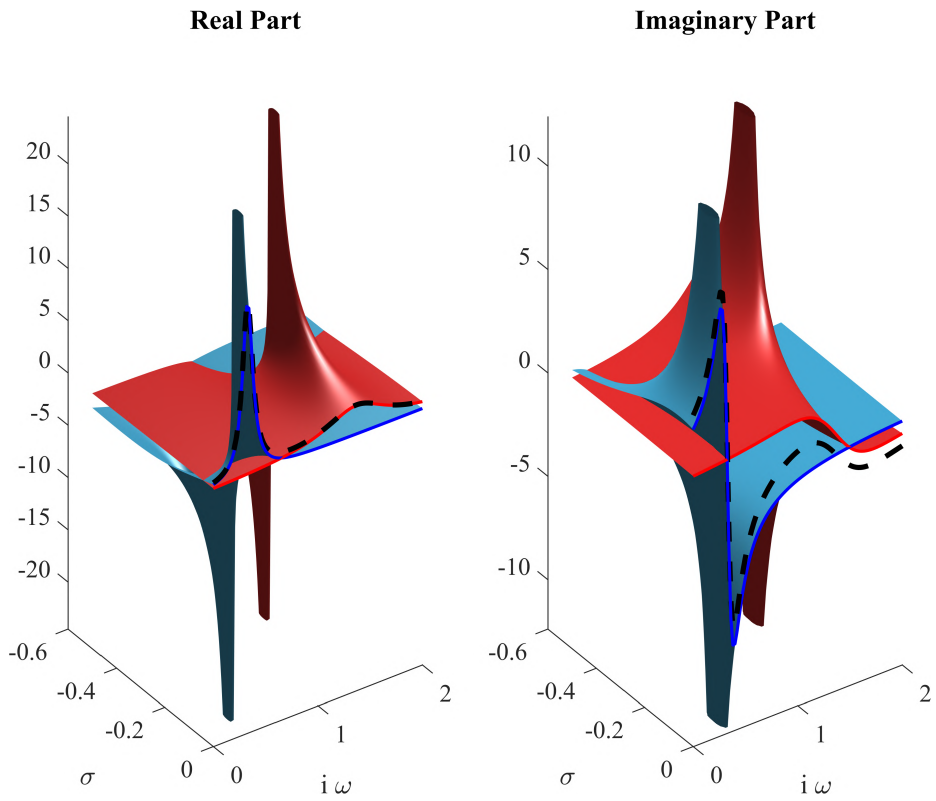

Figure 6.6: A sample 2-DOF system, represented by its transfer function of the variable $s = \sigma + i\omega$. The frequency response function is formed by taking a slice through the resulting surfaces along the frequency axis. The individual modal responses are shown in red and blue, while the sum of the modal FRF contributions is shown as a dashed black line. The poles of the system are moved off of the frequency axis by the introduction of damping.

where the degrees of the numerator and denominator polynomials are independent of one another, and respectively dictate the number of zeros and poles of the transfer function. A detailed description of the types and natures of poles is beyond the scope of this work. For the purposes of this discussion, we may assume that the denominator of the transfer function is the characteristic polynomial of the vibratory system it describes, such that it has N_d roots, corresponding to the N_d poles of the transfer function.

For a linear, time-invariant system, the transfer function will possess Hermitian symmetry, such that its poles exist in complex conjugate pairs. Leveraging this fact permits a partial-fraction expansion of equation 6.20 to yield,

$$\tilde{\boldsymbol{H}}(\boldsymbol{s}) \;= \sum_{n=1}^{N_d/2} \left(\frac{\tilde{\boldsymbol{R}}_{\boldsymbol{n}}}{s - \tilde{p}_n} + \frac{\tilde{\boldsymbol{R}}_{\boldsymbol{n}}{}^*}{s - \tilde{p}_n^*} \right). \tag{6.21}$$

Here, $\tilde{\boldsymbol{R}}_{\boldsymbol{n}}$ and $\tilde{\boldsymbol{R}}_{\boldsymbol{n}}{}^*$ are the residue matrix and its complex conjugate, respectively, of the n^{th} mode. Similarly, $\tilde{p}_n$ and $\tilde{p}_n^*$ are the n^{th} complex pole and its conjugate. Transfer function coefficients, poles, residues, and direct terms were found by sequential application of MATLAB® functions invfreqs and residue. Hermitian symmetry was ensured by reflecting the experimentally-measured $\tilde{\boldsymbol{H}}$ about the origin and imposing anti-symmetry on the imaginary component, thus ensuring that poles and residues were returned as conjugate pairs.

6.4.6 Parameter Estimation and System Identification using Rational Fraction Polynomial

For a system of N_{DOF} degrees of freedom, $N_d = 2N_{DOF}$, signifying that the partial-fraction expansion of the transfer function represents a sum of modal contributions from each of the N_{DOF} modes of the vibratory system, along with the complex conjugate of each. Recalling that $s = \sigma + i\omega$, each pole yields,

$$\begin{aligned} \tilde{p}_n &= \sigma_n + i\omega_n \\ &= \omega_{0,n}\xi_n + i\omega_{0,n} \quad \sqrt{1 - \xi_n^2}. \end{aligned} \tag{6.22}$$

The undamped resonant frequency, damped resonant frequency, and damping

ratio are then given by,

$$\omega_{0,n} = ||\tilde{p}_n|| \qquad \text{Undamped Natural Frequency} \tag{6.23}$$

$$\omega_n = \mathbb{I}\text{m}\left\{\tilde{p}_n\right\} \qquad \text{Damped Natural Frequency} \tag{6.24}$$

$$\xi_{e,n} = \frac{\mathbb{R}\text{e}\left\{\tilde{p}_n\right\}}{||\tilde{p}_n||} \qquad \text{Modal Damping Ratio} \tag{6.25}$$

It is important to note that, while the FRF (and its transfer function representation) is an $N_{DOF} \times N_{DOF}$ matrix of residues (related to the N_{DOF} degrees of freedom of the system), the denominator of each modal contribution is a complex scalar. The interpretation of this fact is important: the resonant frequency and damping (respectively $\omega_{0,n}$ and $\xi_{e,n}$) of each mode n is a global parameter. It does not vary with the location of the input or output and, as a result, each FRF measurement in the FRF matrix should contain identical modal parameters. Let N denote the number of modes in some portion of the frequency axis on which we wish to perform an identification. Note that N can be less than the number of physical poles of the system because it represents the number of poles residing along the portion of the frequency axis spanned by the FRF. For each of the N identified poles of the transfer function, a vector of resonant frequencies and viscous damping ratios can be obtained, respectively, $\{\boldsymbol{\omega_0}\} \in \mathbb{R}^{N_{DOF}\times 1}$ and $\{\boldsymbol{\xi_e}\} \in \mathbb{R}^{N_{DOF}\times 1}$. From these samples, means and standard deviations were computed for each identified pole.

Comparison of equation 6.17 and equation 6.21 reveals that the residue matrix of the n^{th} mode is related to the outer product of the n^{th} mode shape. Without going into too much detail, this relationship can be expressed as,

$$\tilde{\boldsymbol{R}}_{\boldsymbol{n}} = \tilde{q}_n \left\{\boldsymbol{\Theta_n}\right\} \left\{\boldsymbol{\Theta_n}\right\}^T, \tag{6.26}$$

where q_n is an undetermined scaling factor. As a result, any row or column of the residue matrix contains a re-scaled mode shape. If a single modal contribution is considered (mode n), then when $\omega = \omega_{0,n}$, the real part of equation 6.13 becomes zero, leaving the imaginary part only. Another way to interpret this is that when the excitation occurs at the undamped resonant frequency of a given mode, that respective mode's temporal term is 90° out of phase with the excitation. Finally, a straightforward (but laborious) expansion of the n^{th} term of equation 6.21 shows that, if equation 6.21 is to satisfy the same condition at the undamped resonant frequency, then the real part of the Residue matrix $\tilde{\boldsymbol{R}}_{\boldsymbol{n}}$ must be zero.

From these considerations, an unscaled mode shape – or more precisely, a mode

shape with an unknown scaling factor – denoted $\hat{\boldsymbol{\Theta}}_{\boldsymbol{n}}$, may be obtained from any row or column of the residue matrix (depending upon whether the data were collected in a SIMO, MIMO, or MISO fashion) as,

$$\hat{\boldsymbol{\Theta}}_{\boldsymbol{n}} = \mathbb{I}\mathrm{m}\left\{\{\boldsymbol{R_n}\}\right\}, \tag{6.27}$$

where $\{\boldsymbol{R_n}\}$ is any column or row of $\tilde{\boldsymbol{R}}_{\boldsymbol{n}}$, recast as a column-vector.

6.4.7 Validation Study: System Identification of a Proportionally-Damped MDOF System

A 6-by-6 model was created with known resonant frequencies, mode shapes, and viscous and structural damping ratios. FRF matrices were synthesized from the known values and used to test the system-ID approach described in the preceding sections. The undamped resonant frequencies may be found in table 6.4.
Three test cases were considered:

1. $\xi_v = 0.025$ viscous damping for all modes; $\eta_s = 0$ structural damping for all modes; no noise added to spectrum.

2. $\xi_v = 0.025$ viscous damping for all modes; $\eta_s = 0.025/(2\omega_{0,n}^2)$ structural damping for all modes; no noise added to spectrum.

3. $\xi_v = 0.025$ viscous damping for all modes; $\eta_s = 0.025/(2\omega_{0,n}^2)$ structural damping for all modes; random noise added to spectrum.

A single row of the FRF matrix was retained at each frequency, simulating the case of a multiply-instrumented test specimen with a single excitation point. For all cases, the modal viscous damping ratio was set to a constant $\xi_v = 2.5\%$. For case #2, the structural damping was defined as $\eta_s = \xi_s/(2\omega_{0,n}^2)$, so that the equivalent viscous damping ratio ξ_s would be constant for all modes. The notation of the damping ratio components is unimportant, but note that the system ID will attempt to recover the total equivalent damping,

$$\xi_e = \xi_v + \xi_s.$$

Finally, for case #3, uniformly distributed random error $\epsilon \in [0, 1]$ was added to the real and imaginary parts of the FRF. The random signal was generated with an Root Mean Square (RMS) proportional to the RMS of the FRF. Mode shapes were defined as

$$[\boldsymbol{\Theta}] = [\sin\{\boldsymbol{\phi}\} \quad \cos\{\boldsymbol{\phi}\} \quad \tan\{\boldsymbol{\phi}\} \quad \sinh\{\boldsymbol{\phi}\} \quad \cosh\{\boldsymbol{\phi}\} \quad \tanh\{\boldsymbol{\phi}\}],$$

where $\{\phi\} = [0.1\pi \ldots 0.9\pi]^T$.

Case # 1 is presented below, while test cases 2 and 3 are contained in appendix F.

A litmus test of any system identification procedure is whether or not the algorithm can recover prescribed system parameters under perfectly ideal conditions, *i.e.* no noise or nonlinearities. The first test of the RFP modal used only the linear viscous damping coefficient. The entire simulated frequency range was used to perform identification with $N = 6$ (all modes being identified). The resulting synthesized FRF magnitude, fitted FRF, and contribution of each identified mode are shown in figure 6.7. As shown in table 6.4 and figure 6.7, the quantitative identification is excellent.

ξ_v	ξ_s	$\frac{RMS_{noise}}{RMS_{FRF}}$
0.025	0	0

	ω_n, rad/s			ξ_e		
	Truth	ID	% Error	Truth	ID	% Error
Mode 1	1.2	'1.2±1.16e-06'	-3.8E-07	0.03	'0.025±7.78e-07'	-1.2E-05
Mode 2	2.24	'2.24±1.95e-07'	-4.2E-08	0.03	'0.025±1.23e-08'	-2.3E-07
Mode 3	7.2	'7.2±3.73e-05'	-2.0E-06	0.03	'0.025±3.43e-07'	-3.2E-06
Mode 4	8	'8±1.46e-06'	6.9E-08	0.03	'0.025±1.05e-07'	-2.0E-06
Mode 5	10	'10±1.33e-08'	5.0E-11	0.03	'0.025±3.42e-10'	8.4E-09
Mode 6	12.3	'12.3±7.48e-09'	-1.5E-10	0.03	'0.025±1.21e-09'	1.3E-08

Table 6.4: Summary of results for test case 1 with viscous damping only.

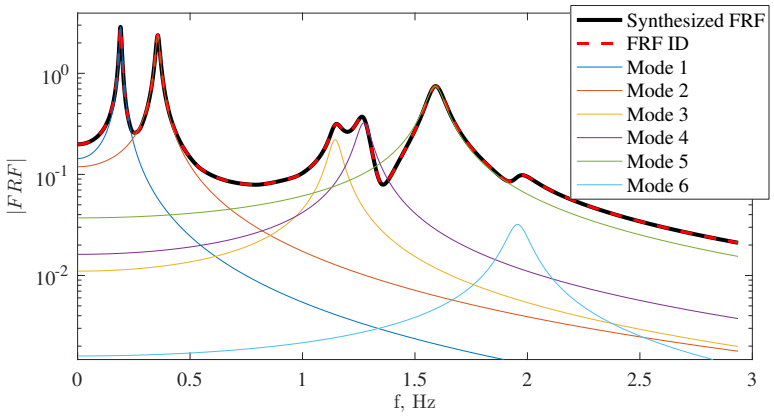

Figure 6.7: Test case #1: FRF Reconstruction with $\xi_v = 2.5\%; \xi_s = 0\%$

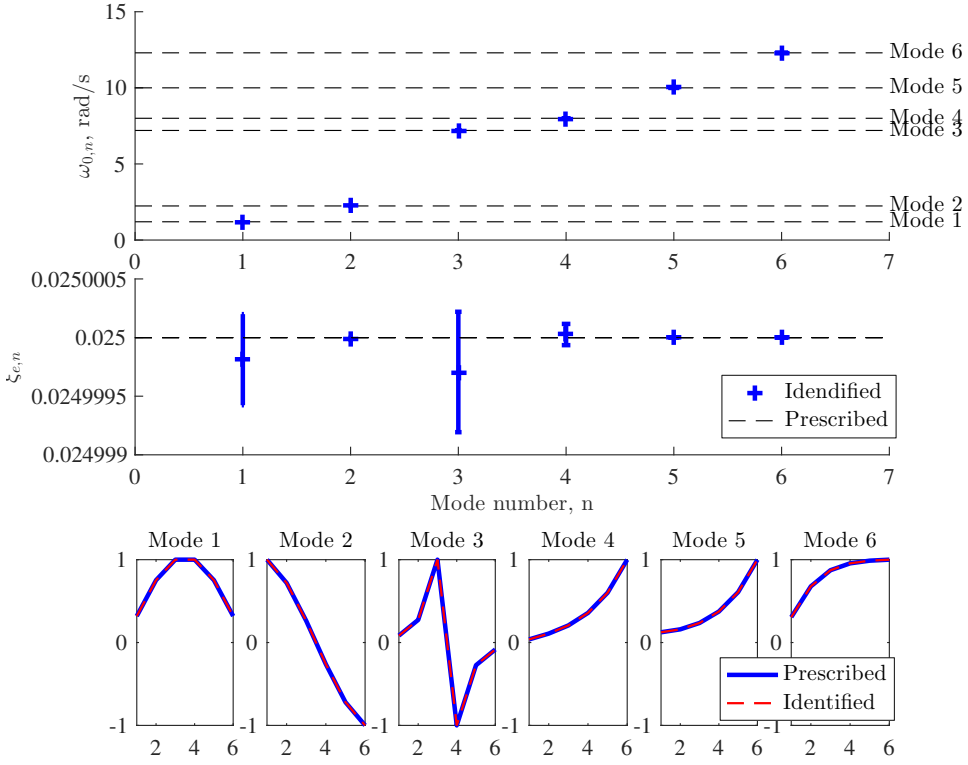

Figure 6.8: Test case #1: Parameter ID with $\xi_v = 2.5\%; \xi_s = 0\%$. Blue markers indicate means and standard deviations of identified values. Grey dashed lines indicate the "true" prescribed values. Mode shapes along the bottom of the figure are plotted with the degree of freedom on the X-axis and the unscaled modal participation factor on the Y-axis.

6.5 Vibratory Behavior of the Flexible Hydrofoil With Reinforced TE

In this section, the system identification approach described above will be applied to the input-output data collected on model 2. The work presented herein are preliminary, and further refinements to both the identification method and the interpretation of results are planned for future work, as described in chapter VII.

6.5.1 Modal Analysis Procedure

All modal analyses were performed on model 2, using the shaker motor force as the input. As mentioned in chapter II, the excitation signal was a sinusoid, the frequency of which was swept across a commanded range. During early tests, the sweep rate was linear. During later tests, a discrete logarithmic sweep was used, such that the excitation was held at a constant frequency for a specified integer number of periods before stepping to the next frequency (an example time-history of excitation frequency is shown in figure 6.9). The linear sweep is convenient because it produces a flat input power spectrum, but the logarithmic sweep is ultimately preferable because it minimizes the amount of spectral leakage and improves the confidence of measurements at each frequency. All data was recorded with a sample rate of $f_s = 500$ Hz.

FRF matrices were estimated by the H_1 estimator, defined as,

$$\tilde{H}_{1,ij} = \frac{XPS(F_i, X_j)}{APS(F_i)}, \tag{6.28}$$

where F_i is an input at degree of freedom i and X_j is the output at degree of freedom j. For all cases, smoothed auto-power spectra (APS) and cross-power spectra (XPS) were used to reject noise. Between 8 and 32 hanning-windowed segments with 75% overlap were used for smoothing. Note that in the following text, the subscripted 1 will be dropped. The compliance FRF $\tilde{\boldsymbol{H}}^{\boldsymbol{comp}}$ was determined by using inferred deflections as the system output. The structural deflections of the hydrofoil were reconstructed at ten uniformly-distributed spanwise locations along both the Leading Edge (LE) and TE. Excluding the root, at which point motion is identically zero, this yields a row of the compliance FRF matrix, $\tilde{\boldsymbol{H}}^{\boldsymbol{comp}} \in \mathbb{C}^{1\times 18}$, at each frequency. Note that eight strain gauges were installed, so RANK $\tilde{\boldsymbol{H}}^{\boldsymbol{comp}} = 8$, yielding only eight independent estimates of the modal parameters for each mode. However, interpolation at additional points ensures that if a reconstruction point falls on or near a

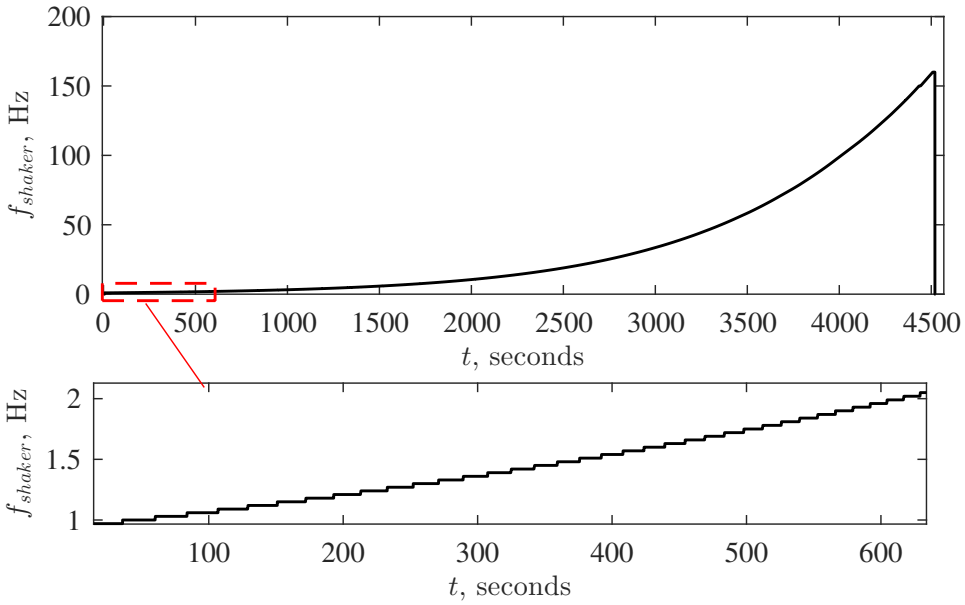

Figure 6.9: Time history of excitation frequency during a logarithmic sweep from 1 Hz to 160 Hz with a step size of $\delta_f = 0.03$ Hz. At each step, the frequency was held constant for 25 periods before stepping to the next frequency.

node line – and consequently produces a spurious identification – it can be rejected as an outlier while retaining eight independent estimates. The inertance FRF was obtained by taking the accelerations measured at the tip of each spar as outputs, yielding a row of the inertance matrix, $\tilde{\boldsymbol{H}}^{\boldsymbol{inert}} \in \mathbb{R}^{1\times 2}$.

Spectra were analyzed in an interactive manner. Regions of the spectra were selected, numerator and denominator orders were specified for the RFP model, and the resulting modes were identified by the extracted mode shape. Estimates of global parameters ξ_e and ω_0 for each mode were aggregated from the inertance and compliance FRFs. Anomalous parameter estimates for each mode were first removed manually, and the remaining estimates were subjected to an iterative Grubb's test (*Grubbs*, 1969) with a 95% confidence interval to remove statistical outliers. Outlier-rejection was performed with the MATLAB script deleteouliers (*Shoelson*, 2011).

Means and standard deviations were computed for $\omega_{0,n}$, $\xi_{e,n}$ from the remaining estimates. For each fitted mode, the pole P_n is a global quantity, common to every FRF in the FRF matrix. To improve the estimates of mode shapes, new residue matrices were fitted with the pole locations fixed, thus ensuring that the modal constants of all FRF components correspond to the same frequency.

6.5.2 Vibration Spectra and Normal Mode Shapes in Various Flow Regimes

To examine the ways in which the vibratory response of the hydrofoil changes as a function of flow conditions, we consider five example trials, conducted at the INSEAN cavitation tunnel. A brief discussion of each is offered in this section. FRFs and mode shapes for each may also be found in appendix G. The cases are as follows:

1. Dry conditions
2. Partial immersion ($AR_h = 1.0$) in still-water
3. Partial immersion ($AR_h = 1.0$) at forward speed ($Fn_h = 1.5$) in FW flow at $\alpha = 0°$
4. Partial immersion ($AR_h = 1.0$) at forward speed ($Fn_h = 1.5$) in FV flow at $\alpha = 10°$
5. Partial immersion ($AR_h = 1.0$) at forward speed ($Fn_h = 1.5$) in Partially Cavitating (PC) flow at $\alpha = 10°$; $\sigma_v = 0.85$

The hydrofoil response in dry conditions presents an opportunity to compare the experiments with the FEM simulations described in §6.2. Figure 6.10 shows a comparison between the simulated mode shapes and the experimentally-determined mode shapes in dry conditions. All mode shapes are oriented with the clamped root on the right hand side and the LE toward the viewer. The undeformed shapes of the hydrofoil are depicted in translucent grey. In the case of the experimental mode shapes, nodal lines are also shown as bold black lines. The agreement is quite good and most mode shapes are qualitatively similar. The location of the nodal line, however, does differ between simulation and experiment in the case of the X-Bend 2 mode. Otherwise, the number of nodal lines and the general character of the deflection (primary bending with secondary twist) are shared.

The compliance FRF, decomposed into the contributions from each mode (modal participation factors) is shown in figure 6.11. The 18 individual FRF components in the measured row of the compliance matrix were averaged together, and the magnitude of the mean FRF was plotted. The modal frequencies predicted with the FEM model are overlaid and labeled as vertical lines. Note that the discrepancy between the predicted and measured locations of the X-Bend 2 mode is probably due in part to compliance of the load cell. At some frequencies, components of the mounting structure or facility would begin to resonate, creating an artificial peak in the measured

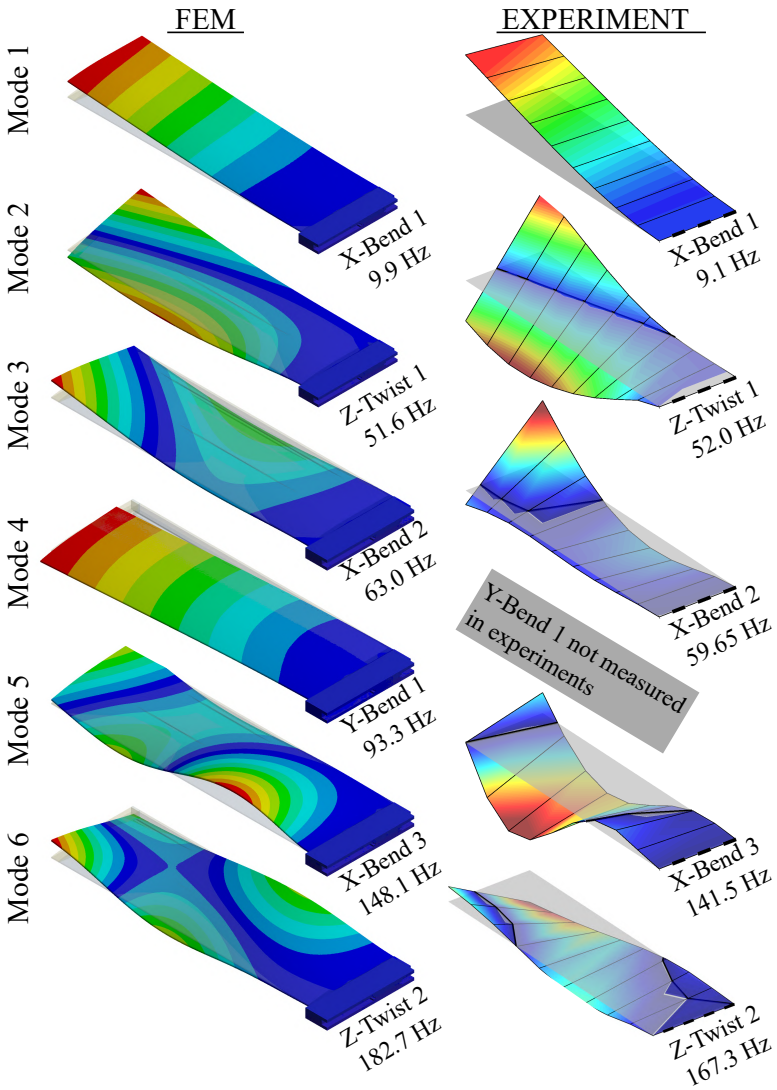

Figure 6.10: Comparison of mode shapes (model 2) predicted by FEM model and measured experimentally. The experimental mode shapes have been placed in the same orientation as the FEM figures. Qualitative agreements are good, though the nodal line of the X-Bend 2 mode does not match between the experiment and the simulation.

FRF. These are designated in the figure as "contaminants." The primary contaminant is thought to be resonance of the bracket used to attach the shaker motor to the hydrofoil, which occurs between 50 Hz and 55 Hz. Over the course of testing, some loosening of the braces on the mount caused a slow migration of the bracket's resonant frequencies. A second significant source of contamination occurred with vibration of the transverse rails, to which the hydrofoil setup was attached (see the transverse members in figure 2.16b). The rail (which acted as a simply-supported beam) began vibrating in a fundamental vertical mode at 38 Hz. The thick grey line plotted over the measured FRF indicates the spectral response reconstructed from only the identified modes of interest, and so represents a type of principal-component reconstruction of the compliance FRF.

Figure 6.12 depicts a detailed view of the *inertance* FRF components in the neighborhood of the closely-coupled modes near 50 Hz for the dry vibration case. On the top axes are plotted the magnitudes of the two inertance FRF components, with separated modes and the cumulative fit overlaid. The left-hand plots correspond to the accelerometer at the tip of spar "A" (near the trailing edge), while the right-hand plots correspond to the accelerometer on spar "B," near the leading edge. The real and imaginary parts of the FRF are shown, indicating that the RFP method successfully fits the complex-valued FRF across the nearby peaks, and the real and imaginary components are shown in Argand planes in the bottom set of axes. Note that each of the identified modes independently passes through the origin of the Argand plane, indicating that each behaves as a Single-degree-of-freedom (SDOF) mode.

The measured, fitted, and decomposed spectra are plotted below for the remaining four demonstration cases. In figure 6.13, the resonant frequencies of all modes decrease as a result of fluid added mass, which presents inertial resistance to the motion of the hydrofoil. The contaminating modes, however, remain fixed (one of the ways in which the contaminants were identified and separated from the modes of interest). Some additional contamination of the spectrum near $f = 100$ Hz is due to another resonant mode of the cavitation tunnel structure, and is compounded by the second harmonic of the AC line-noise at 50 Hz. Modes as high as the sixth mode (Z-Twist 2) were successfully extracted from the FRF, and a tentative identification of mode 7 was made, though it is possibly the case that mode 7 is actually a contaminant. The widths of the individual fitted modal peaks are not visibly different from those in the dry case, suggesting that the damping is not strongly affected by immersion in the quiescent fluid, and thus that the associated component of damping ξ_q is very small.

In FW flow with forward speed, additional flow-induced motion and facility vibra-

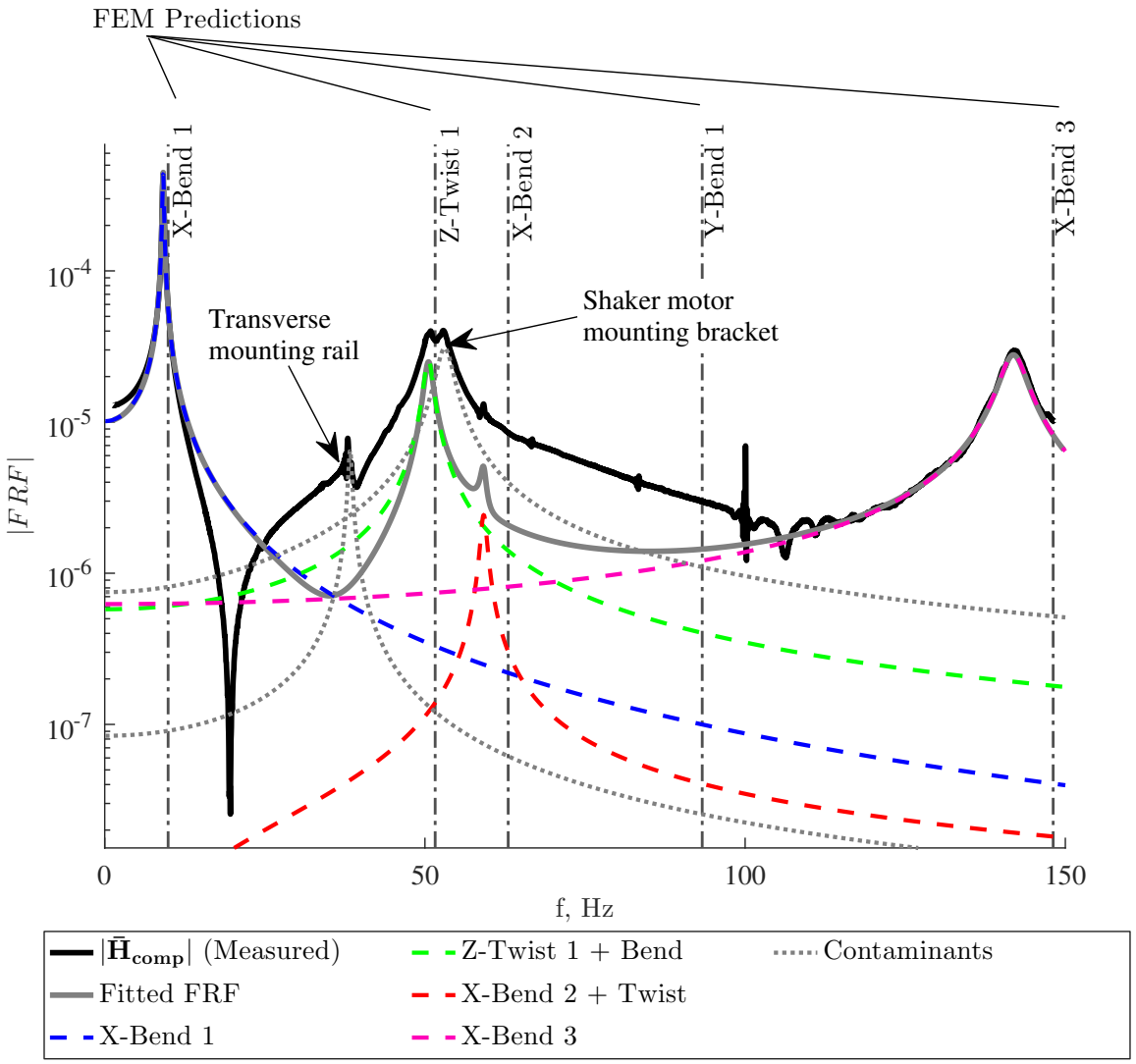

Figure 6.11: FRF decomposition for model 2 in dry conditions. The vertical grey lines indicate modal frequencies predicted by the FEM model. Data collected for 1,660 seconds at 500 Hz.

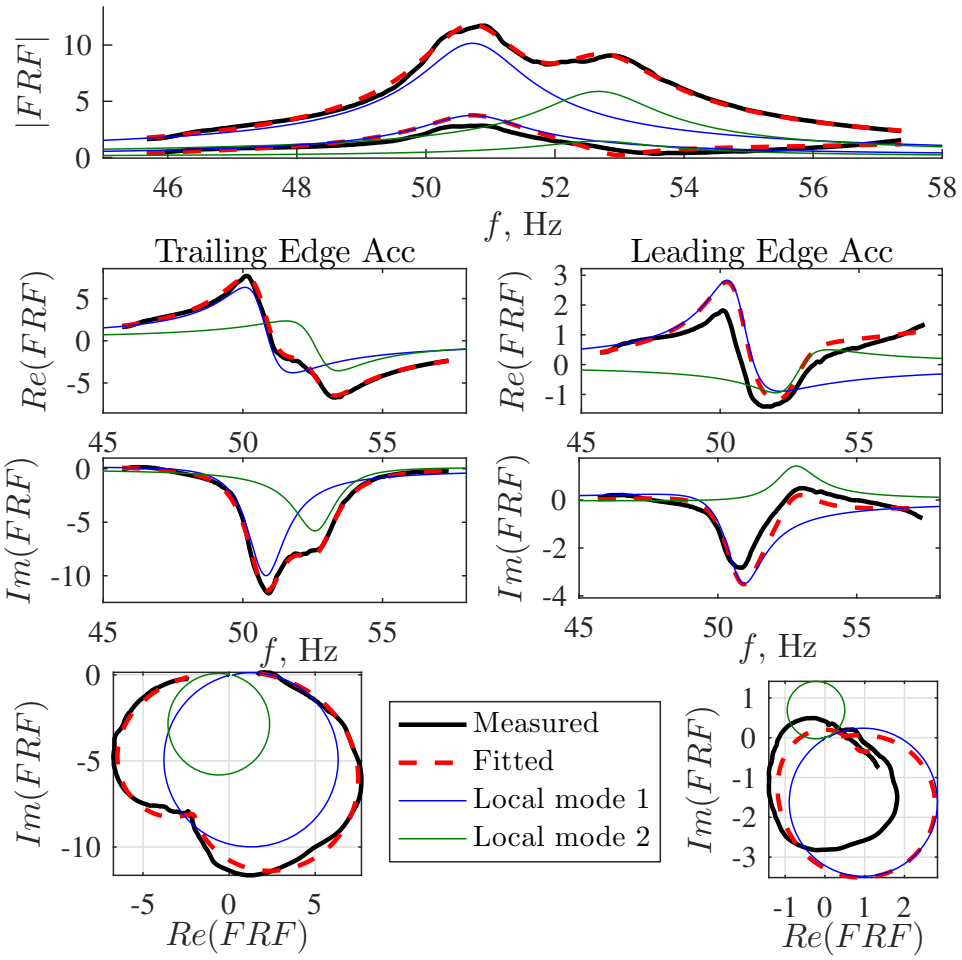

Figure 6.12: Detail view of the FRF in the neighborhood of closely-coupled modes of model 2 in dry conditions. The RFP identification is successfully used to decouple the modes and relegate each to a SDOF representation. The resulting FRF is thus seen to be made up of two circles in the Argand plane, each of which pass through the origin.

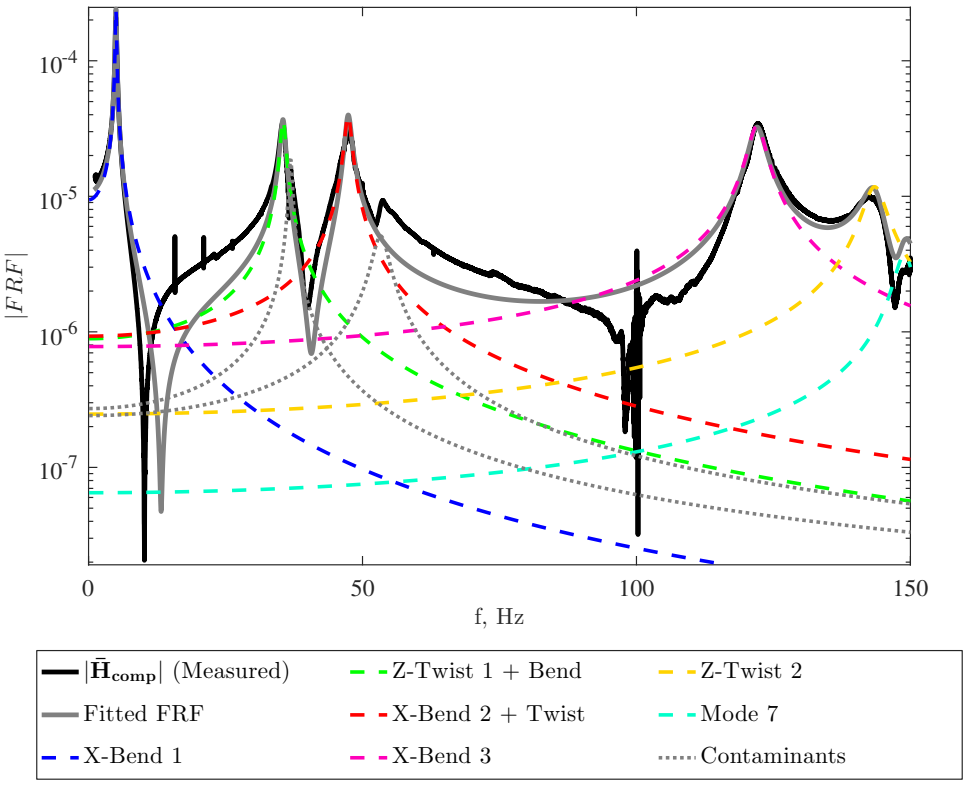

Figure 6.13: FRF decomposition for model 2 in still water $\alpha = 10°$; $Fn_h = 0$; $AR_h = 1.0$. Data collected for 4,500 seconds at 500 Hz.

tions are present in the collected time series, resulting in a noisier spectrum, depicted in figure 6.14. Modal peaks are still successfully extracted, and some visible broadening of the individual peaks suggests that some additional damping may be introduced by the hydrodynamic ξ_{hd} term.

In FV flow at the same Fn_h and AR_h, depicted in figure 6.15, the spectrum appears noisier than in the FW case, though this is due in part to a longer run-duration and resulting finer frequency resolution. The contaminant modes are no longer very clear, and no attempt was made to identify them. Note that the non-zero angle of attack causes steady deflections in bending and twisting, which introduce a DC component in the frequency domain.

Finally, figure 6.16 depicts the spectrum in PC flow. The noise level is similar to that in the FV flow regime, but the peaks are somewhat less distinct. We theorize that the unsteadiness of the vaporous cavity at the LE causes periodic modulations of the fluid mass, damping, and stiffness matrices (*Akcabay et al.*, 2014a; *Akcabay and Young*, 2015). As shown in the photos on the right hand side of figure 6.16, the vaporous cavity at the leading edge is highly unsteady. The resulting vibrations would

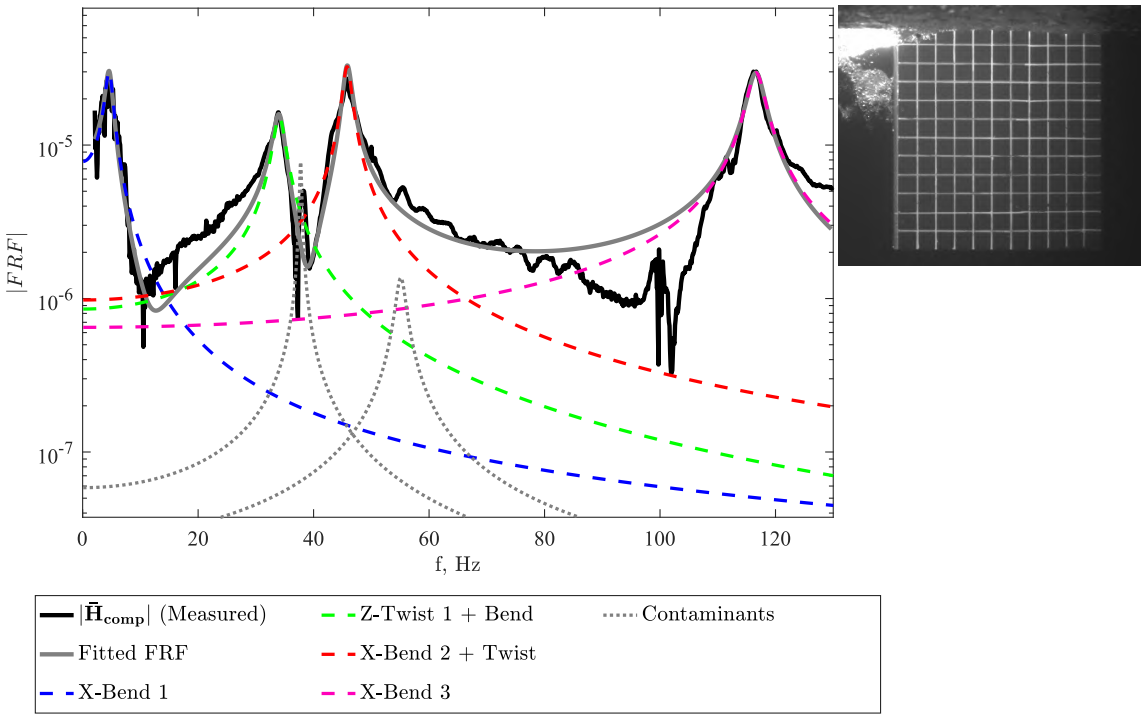

Figure 6.14: FRF decomposition for model 2 in fully wetted (FW) flow at $\alpha = 0°$; $Fn_h = 1.5$; $AR_h = 1.0$. Data collected for 520 seconds at 500 Hz.

be non-stationary, and the spectrum in figure 6.16 would represent an average of the time-varying spectra. Joint time-frequency analysis was not undertaken in this work, however, so this conjecture remains unconfirmed for the time. Note that coherent cavitation shedding was not observed at any point during testing, probably because vaporous cavities were observed to be quite short (as in the case of figure 6.16), and because significant spanwise variation in the cavity length caused incoherent Three-Dimensional (3-D) cavity shedding to predominate.

Additional low-frequency unsteadiness in the cavitation tunnel, caused by sloshing, eddying inlet flow, and a periodic (but small) velocity surge, cause increased spectral content at low, but non-zero frequencies. It will be demonstrated in following sections that, particularly at higher speeds, the low-frequency flow-induced vibrations are extremely difficult to separate from the first bending mode.

The mode shapes, resonant frequencies, and estimated effective damping ratios for each identified mode are shown in figure 6.17. Columns correspond to modes and rows correspond to flow regimes. The colored surfaces indicate the mid-plane of the hydrofoil, oriented with the trailing edge nearest the viewer and the clamped

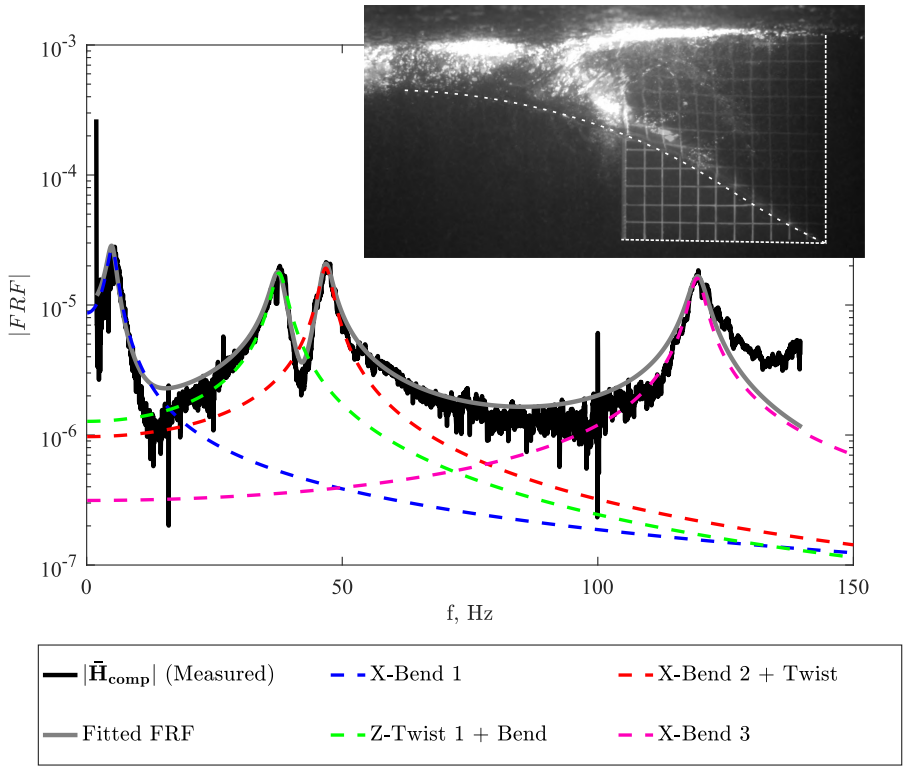

Figure 6.15: FRF decomposition for model 2 in fully ventilated (FV) flow at $\alpha = 10°$; $Fn_h = 1.5$; $AR_h = 1.0$. Data collected for 1,900 seconds at 500 Hz.

root on the right. Arrows at the tip of the hydrofoil indicate the mode shapes of the accelerometers at the tip of the hydrofoil, estimated from the inertance FRF. The grey translucent plane indicates the undeformed shape of the hydrofoil, and bold black contours indicate nodal lines. Finally, the translucent blue surface in the x-y plane indicates the still free surface (for cases of partial immersion). The mode shapes in each case have been re-scaled to maximum value of ± 1. The mode shapes remain quite consistent across all of the operating conditions. As the condition changes from dry to partial immersion in quiescent water, the nodal line of the Z-Twist 1 mode moves toward the trailing edge, and a minor reduction in curvature below the free surface is evident in the X-Bend 3 mode. The curvature in X-Bend 3 increases again in the FW and PC flow regimes, probably due to the reduction in fluid mass near the points of maximum deflection just beneath the free surface.

The resonant frequencies and damping coefficients in figure 6.17 certainly indicate changes with different flow conditions. For example, the modal frequency of the X-Bend 1 mode is approximately halved, and the damping ratio grows by a factor of twelve in FW flow, compared to dry conditions. The resonant frequencies and

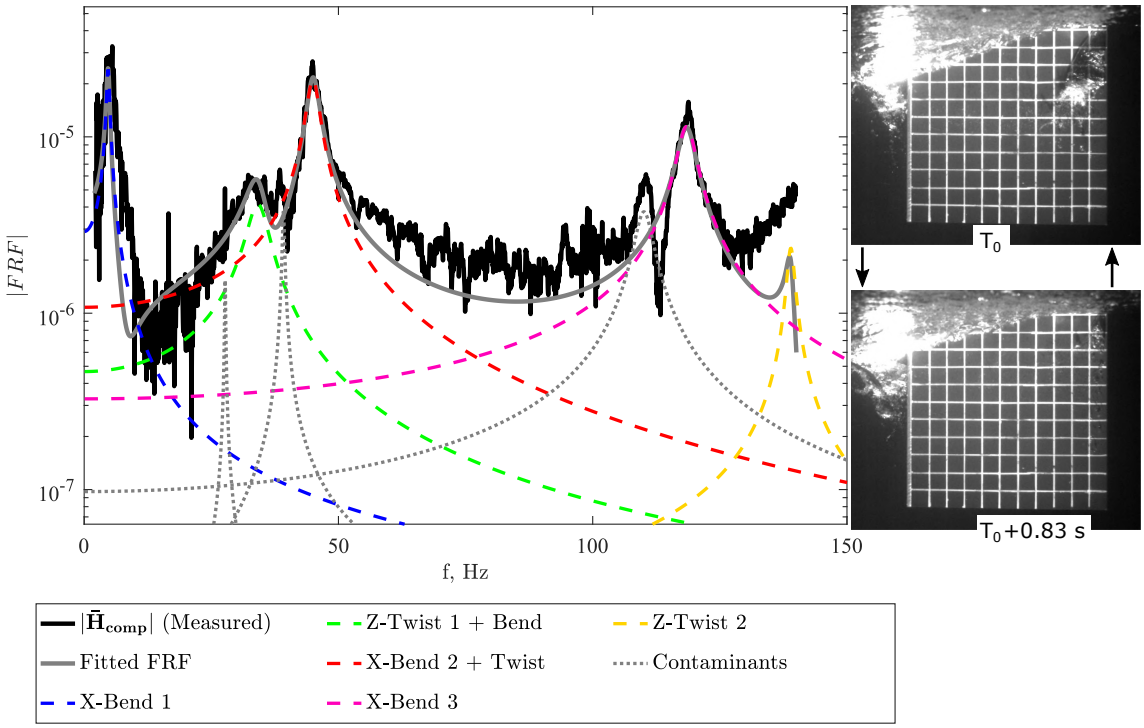

Figure 6.16: FRF decomposition for model 2 in partially cavitating (PC) flow at $\alpha = 10°$; $Fn_h = 1.5$; $AR_h = 1.0$; $\sigma_v = 0.85$. Data collected for 930 seconds at 500 Hz. The photos to the right show the size of the cavity at two instants 0.83 seconds apart.

damping ratios are addressed in greater detail in the following two sections.

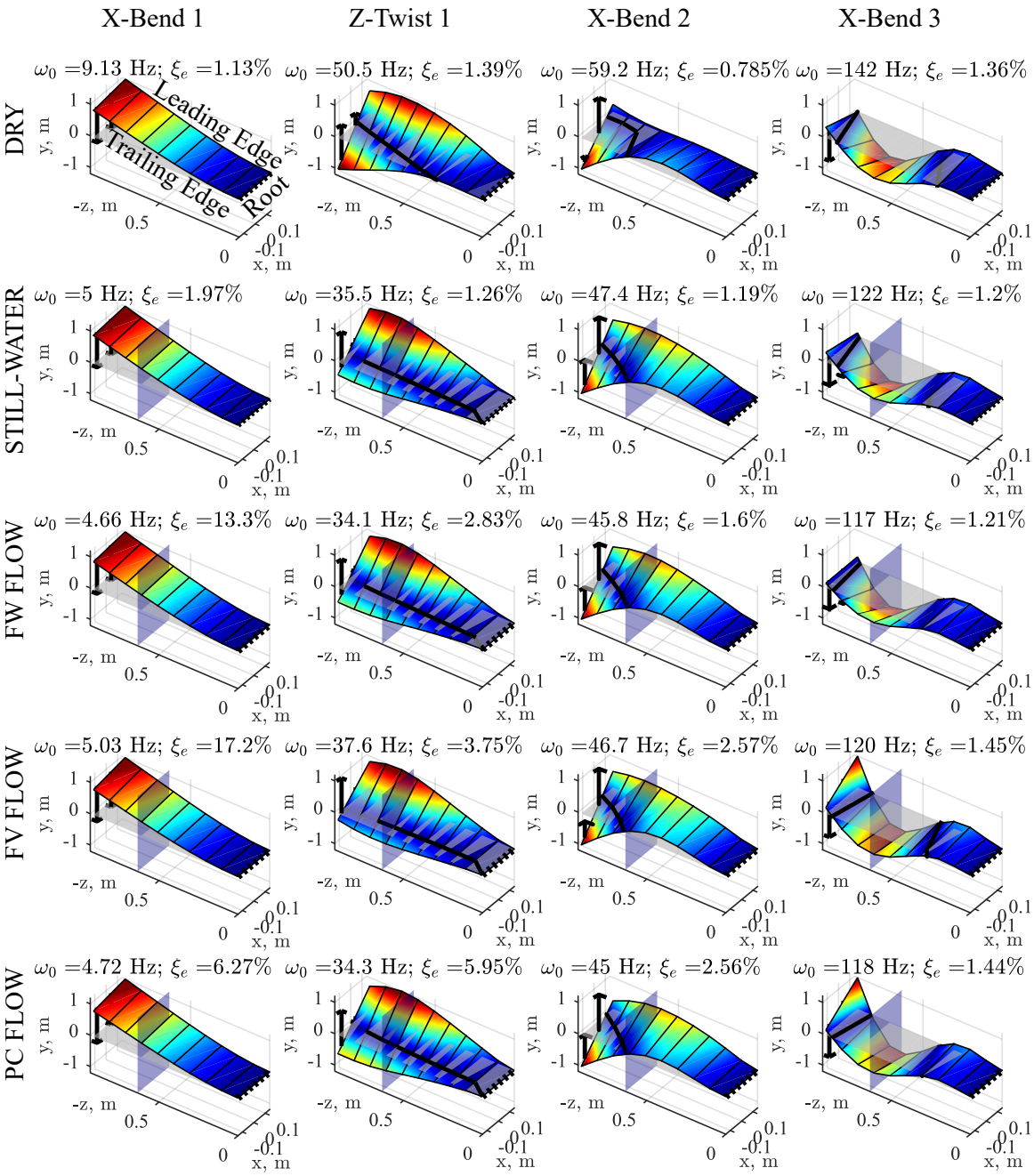

Figure 6.17: Table of mode shapes, resonant frequencies, and equivalent viscous damping ratios of modes 1, 2, 3 and 5 for model 2 in the following conditions, from top to bottom: Dry conditions, partial immersion in quiescent water at $AR_h = 1.0$, FW flow at $\alpha = 0°; Fn_h = 1.5; AR_h = 1.0$, FV flow at $\alpha = 10°; Fn_h = 1.5; AR_h = 1.0$, and PC flow at $\alpha = 10°; Fn_h = 1.5; AR_h = 1.0$. The grey translucent plane indicates the undeformed hydrofoil. The blue translucent plane indicates the still free surface. Arrows at the tip of the foil indicate the corresponding mode shapes of the accelerometers installed at the end of the shape-sensing spars.

6.5.3 Natural Frequencies of Hydrofoil

Modal frequencies for modes 1, 2, 3, 5, and 6 of model 2 (see figure 6.10 for mode shapes) are shown in figure 6.18 as functions of Fn_h. Note that mode 4, alternatively known as Y-Bend 1 or the lead-lag mode, was not measured during experiments. Axes to the right contain the same data, but with the each mode plotted on magnified axes. At each condition, an aggregate sample was formed from all channels across all repeated trials. Filled symbols indicate the mean at each conditions (average of all signals across all trial repetitions). Open symbols indicate the mean across all channels for each individual trial. Vertical bars indicate ± one standard deviation of the aggregate sample. Note that the line types in the detail plots on the right have been changed to solid to improve readability.

The resonant frequencies of all modes in partially-immersed conditions (quiescent water, FW, FV, and PC flows) are substantially lower than those in the dry conditions. As described in chapter I, the dense liquid presents an inertial resistance to the foil's motion, which is expressed in equation 6.4 as the fluid added-mass matrix $[\boldsymbol{M_{fl}}]$. Assuming approximate decoupling of the equations of motion by the modal decomposition (or at least diagonally-dominant system matrices), we can infer that the added mass of each mode increases substantially. In the case of mode 1 (X-Bend 1), there is no fluid stiffness term present in the quiescent water, so the change in modal frequency is attributable only to a change in the modal mass. Again assuming diagonal modal matrices, we can write for mode n,

$$\begin{aligned}\left(\frac{\omega_{0,n}^{dry}}{\omega_{0,n}^{wet}}\right)^2 =& \frac{M_{s_{m,n}} + M_{fl_{m,n}}}{K_{s_{m,n}}} \frac{K_{s_{m,n}}}{M_{s_{m,n}}} \\ &= 1 + m_{fl,m,n}, \end{aligned} \tag{6.29}$$

where $m_{fl,m,n} = M_{fl_{m,n}}/M_{s_{m,n}}$ is the dimensionless fluid added mass coefficient for mode n, plotted in figure 6.19 for modes 1, 2, 3, 5, and 6. By inspection, we can see that mode 1 has the largest added mass coefficient, which is substantially. The added mass coefficient decreases monotonically with increasing mode numbers. This is likely due to the fact that vibration amplitudes decrease with increasing frequency. Additionally, fluid inertial forces most strongly oppose motion normal to faces with large projected areas. Thus, mode 1, which is typified by large-amplitude motion normal to the pressure and suction surfaces of the foil, is affected most substantially by the fluid added mass. The same conclusion was reached for model 1 by *Harwood et al.* (2016a). By extension, it is no surprise that the modal frequencies are higher

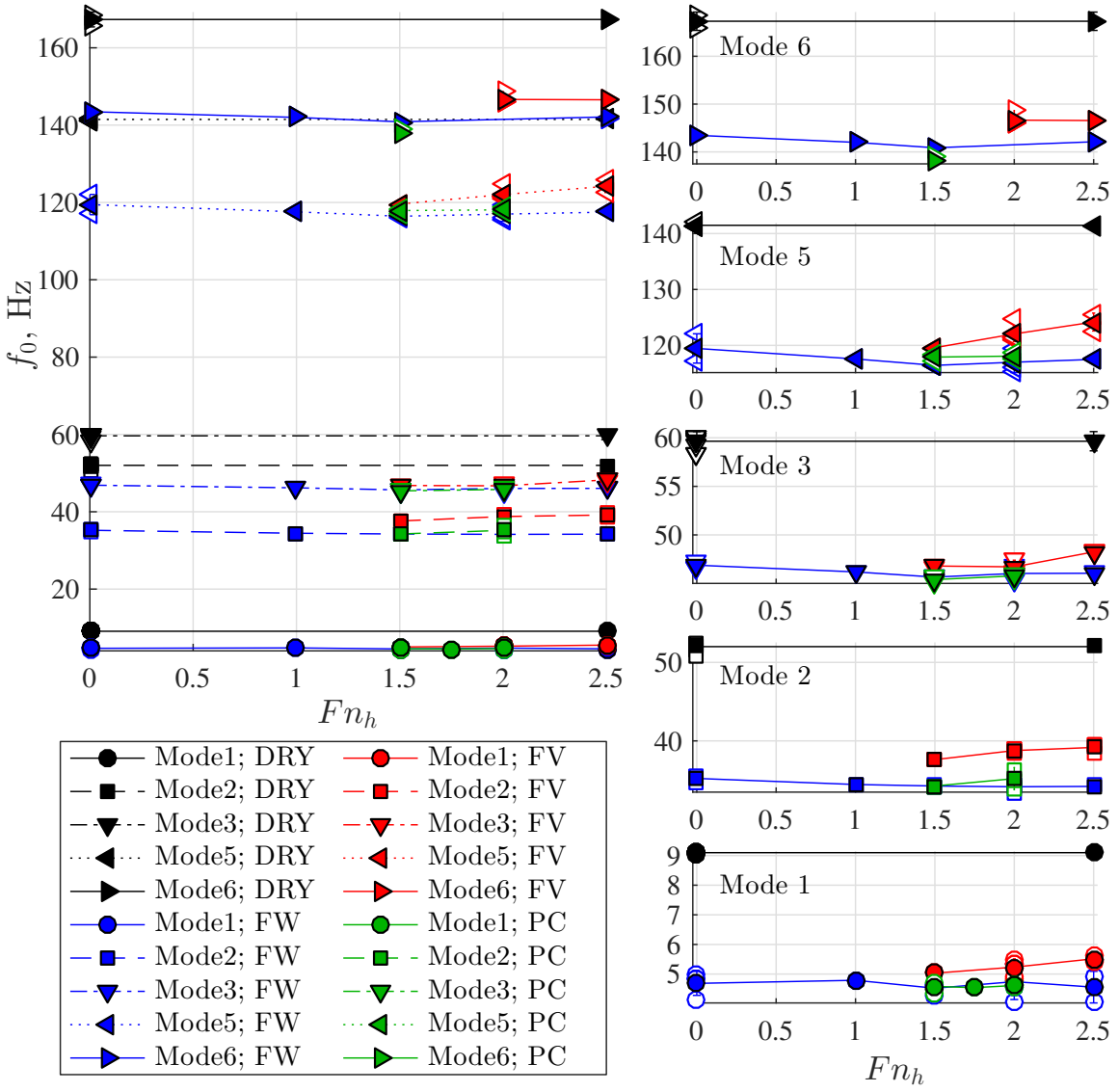

Figure 6.18: Dimensional modal frequencies of model 2 as functions of Froude number in FW flow ($0° \leq \alpha \leq 12°$), FV flow ($7° \leq \alpha \leq 12°$), and PC flow ($\alpha = 7°, 12°$ and $0.42 \leq \sigma_v \leq 0.85$). All data (except dry conditions) are for $AR_h = 1.0$.

in FV flow than in FW flow in figure 6.18 for all modes. A substantial portion of the dense fluid (water) is displaced by air (the precise proportion is a function of the cavity's size, and thus depends upon all the attending physics). As a result, the fluid inertial forces, which are proportional to the fluid density, are reduced significantly. The frequencies in the PC flow regime fall within the experimental scatter of the FW data points. Despite the fact that water vapor is lighter than liquid water by five orders of magnitude, the maximum length of the cavity at the mid-span was less than 40% of the chord length in all tested conditions. Thus, the density field was modified only over a small portion of the hydrofoil surface.

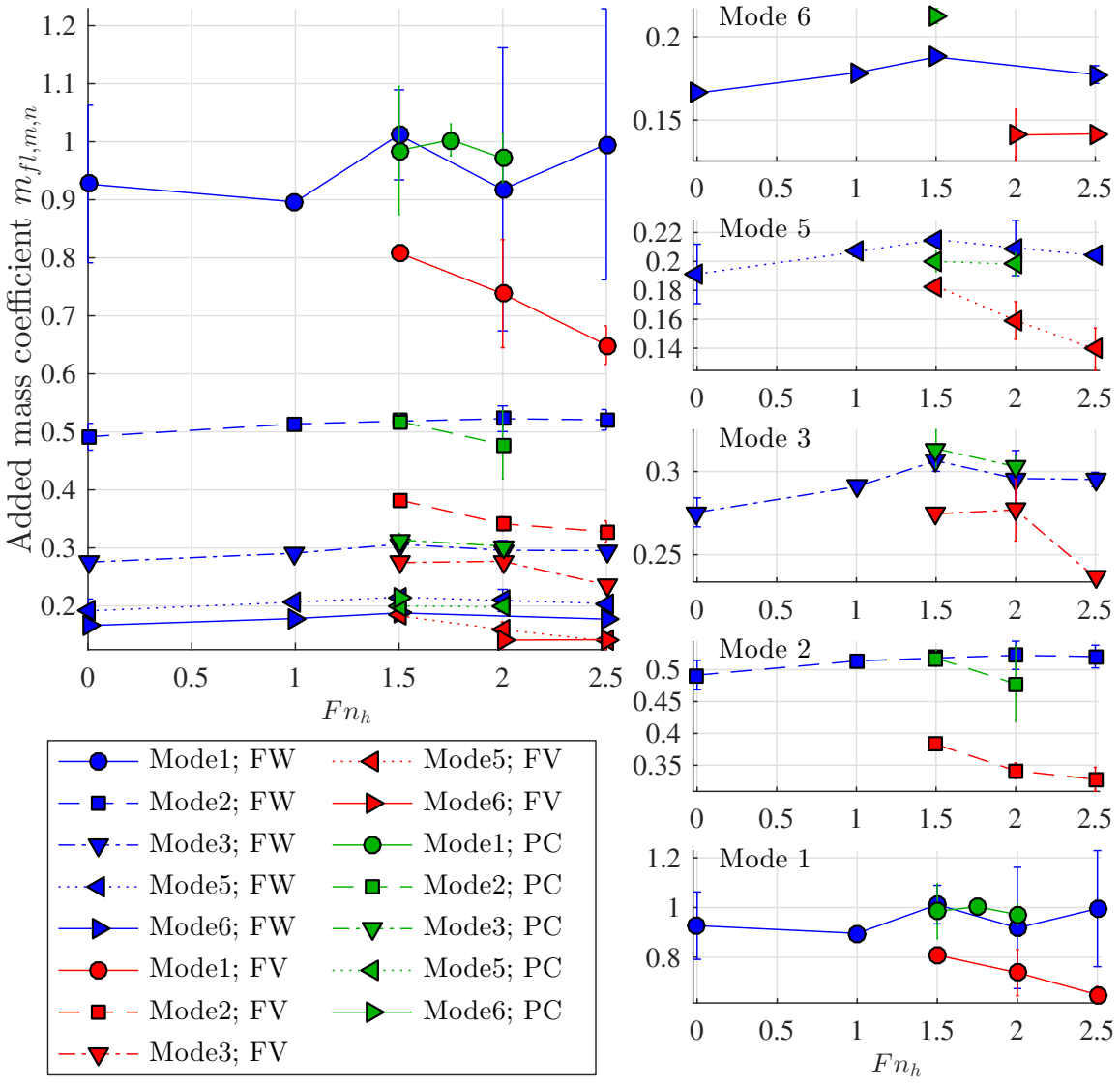

Figure 6.19: Dimensionless added mass coefficients of model 2 as functions of Froude number in FW flow ($0° \leq \alpha \leq 12°$), FV flow ($7° \leq \alpha \leq 12°$), and PC flow ($\alpha = 7°, 12°$ and $0.42 \leq \sigma_v \leq 0.85$). All data (except dry conditions) are for $AR_h = 1.0$.

There appears to be only a minor effect of forward speed upon natural frequency in the FW regime. There is a small decreasing trend in the FW resonant frequencies with increasing Froude number, but the trend is non-monotonic. Results from *Besch and Liu* (1973) demonstrated a similar behavior, with a weak initial decrease in modal frequencies, followed by an increase at higher speeds. Note, also, that the results shown are the *undamped* resonant frequencies identified with the modally-decomposed model, so changes caused by damping are not reflected. Thus, we may conjecture that in the speed range tested, that the fluid stiffness is weakly negative. On the other hand, frequencies corresponding to FV flow increase measurably with increasing speed in figure 6.18 and the added mass coefficients in figure 6.19 decrease monotonically with increasing speed. Recall that the length of a ventilated cavity increases with the forward speed of the hydrofoil, so we may conclude that as Fn_h increases, the growing cavity displaces water over an increasingly-large area of the hydrofoil's suction surface. The decrease in local fluid densities leads to an increase in the modal frequencies and a reduction in the fluid inertial loading.

6.5.4 Equivalent Damping Ratios

The equivalent viscous damping ratio (ξ_e) is plotted for all conditions in figure 6.20. The marker styles and arrangement of axes follows the conventions of figure 6.18. The estimates of damping exhibit significantly more scatter than those of modal frequencies. Damping values are extremely sensitive to small changes in the FRF, and are notoriously difficult measure consistently (*Soroka*, 1949; *Bert*, 1973; *Reese*, 2010).

Modal damping in dry conditions (where $\xi_e \approx \xi_s$) is between 1.2% and 1.7% for each mode, which agrees well with published data for PVC. Additionally, the near-constancy of the damping across all modes suggests frequency-independence – a feature of structural hysteretic damping. ξ_e is approximately equal in dry conditions and immersion in the quiescent fluid. This is a surprising result since it suggests that those components that make up the quiescent fluid damping (viscous dissipation, acoustic radiation, wave radiation, etc.), are either very small, or that they counteract one another.

Modes 2, 3, 5, and 6 exhibit increasing damping with forward speed – though in the case of modes 3 and 5, the increase is non-monotonic. The damping of mode 1 initially increases, but between $Fn_h = 1.5$ and $Fn_h = 2.5$, the damping decreases to an apparently-negative value. This result is certainly non-physical, since it would ordinarily indicate a destructive dynamic instability – which did not occur during

testing. Instead, it is proposed that the spuriously-low damping is a result of low-frequency flow-induced vibrations. It was mentioned previously that eddying flow, in particular, caused unsteady motions of the hydrofoil at frequencies of $f \lesssim 5Hz$. As a result, there is spectral energy in the neighborhood of mode 1 that is not accounted for by taking the shaker motor force as the system input. It is believed that the RFP method erroneously infers negative damping from the excess energy density. For example, motion of the hydrofoil without any excitation by the shaker motor would appear, from a system input-output perspective, to indicate an undamped or negatively-damped system.

Damping in the FV and PC flow regimes are approximately equal to those in the FW flow regime for mode 1, though the preceding discussion suggests that damping estimates for mode 1 are suspect. In modes 2, 3, and 6, the damping in the FV flow regime is initially higher than that in the FW flow regime, but becomes smaller with increasing speed. For mode 5, damping in the FV regime remains higher at all speeds than that in the FW regime. The predominant increase in damping from FW flow to FV flow suggests that the ventilated cavity presents an additional mechanism for energy dissipation in the form of the cavity wall. The cavity's wall is an additional free surface on which radiated waves may develop with motion of the body. Damping values in the PC flow regime follow the same trends as do the FV data. In the case of PC flow, condensation and evaporation may play a role as energy dissipation mechanisms.

The results in figure 6.20 correspond to the aggregate effective damping ratio,

$$\xi_e = \xi_s + \xi_q + \xi_{hd}.$$

The structural damping (ξ_s) was obtained from measurements in the dry condition, the quiescent fluid component (ξ_q) was obtained from testing in the quiescent body of water and subtracting the structural component, and the hydrodynamic component was inferred from the linear superposition of the two known components:

$\xi_s = \xi_e$	Dry conditions
$\xi_q = \xi_e - \xi_s$	Quiescent water
$\xi_{hd} = \xi_e - (\xi_q + \xi_s)$	At each forward-speed condition

The damping ratios of the three constituent elements are presented in table 6.5. The mean and standard deviations of estimates are given for each. The quantitative results

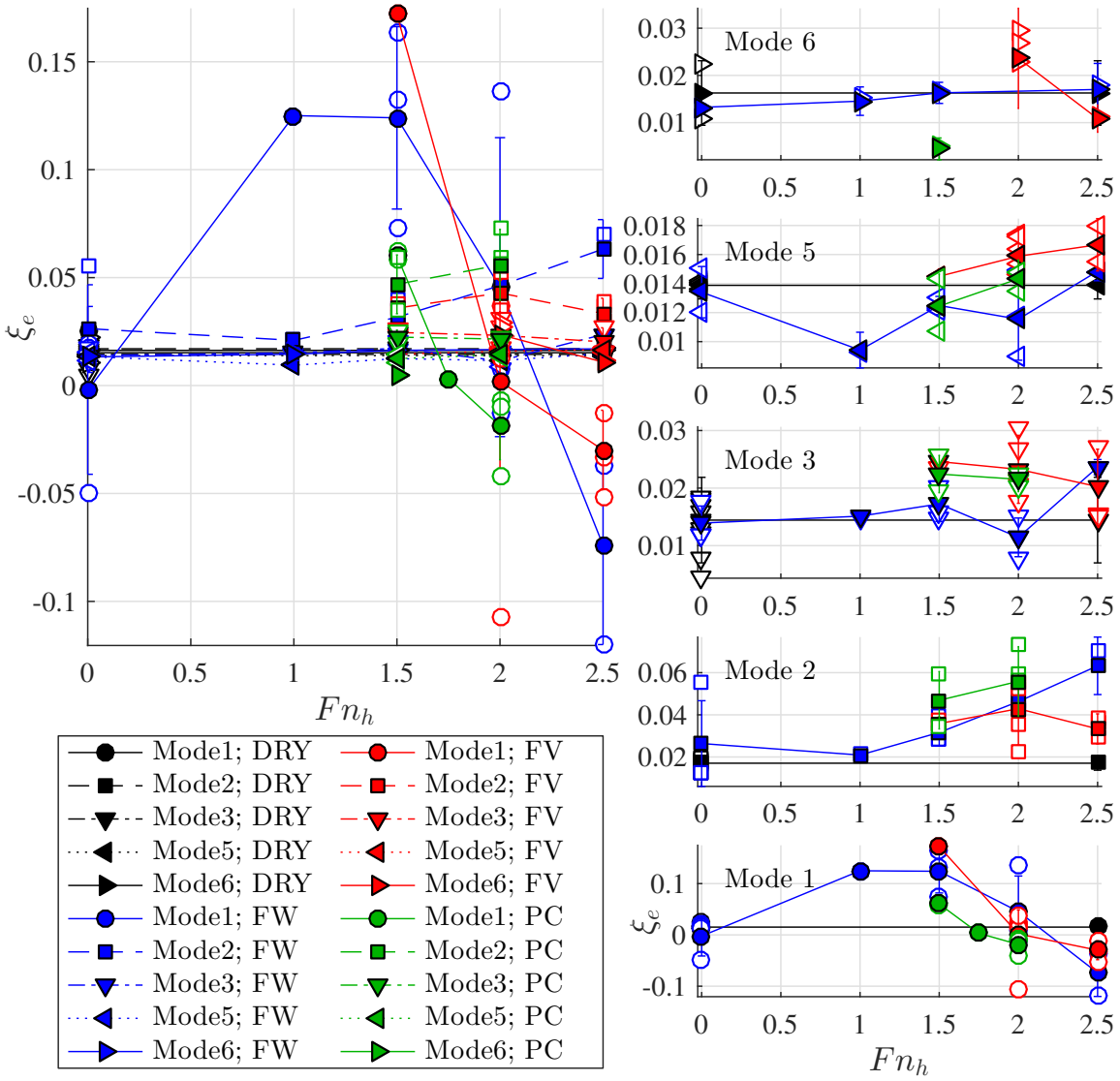

Figure 6.20: Equivalent total damping ratios of model 2 as functions of Froude number in FW flow ($0° \leq \alpha \leq 12°$), FV flow ($7° \leq \alpha \leq 12°$), and PC flow ($\alpha = 7°, 12°$ and $0.42 \leq \sigma_v \leq 0.85$). All data (except dry conditions) are for $AR_h = 1.0$.

reinforce the observations made regarding figure 6.20. First, the structural damping is approximately constant for all modes. Second, the quiescent fluid component of damping is negligible for all modes. Third, the hydrodynamic damping is significant, and it exhibits a general increase with forward speed.

Table 6.5: Tabulations of equivalent total damping ratios of PVC hydrofoil (model 2), decomposed into structural (ξ_s), quiescent (ξ_q), and hydrodynamic (ξ_{hd}) components. Data were collected in FW flow ($0° \leq \alpha \leq 12°$), FV flow ($7° \leq \alpha \leq 12°$), and PC flow ($\alpha = 7°, 12°$ and $0.42 \leq \sigma_v \leq 0.85$). All data (except dry conditions) are for $AR_h = 1.0$.

		ξ_s Dry	ξ_q Still Water	ξ_{hd} $Fn_h = 1.0$	$Fn_h = 1.5$	$Fn_h = 2.0$	$Fn_h = 2.5$
Mode 1	DRY	0.015±0.0048	N/A	N/A	N/A	N/A	N/A
	FW		0.004±0.0056	0.091±0.0204	0.101±0.06	0.027±0.0981	-0.093±0.0652
	FV			N/A	0.151±0.0063	-0.0171±0.0664	-0.049±0.0265
	PC			N/A	0.041±0.0061	-0.038±0.0227	-0.019±0.0048
Mode 2	DRY	0.017±0.0033	N/A	N/A	N/A	N/A	N/A
	FW		0.003±0.0161	0.±0.0039	0.012±0.0096	0.026±0.0066	0.043±0.0195
	FV			N/A	0.016±0.0055	0.023±0.0247	0.013±0.0106
	PC			N/A	0.027±0.0195	0.036±0.0234	N/A
Mode 3	DRY	0.014±0.0074	N/A	N/A	N/A	N/A	N/A
	FW		0.±0.0079	0.±0.0076	0.003±0.0086	-0.003±0.0088	0.01±0.0077
	FV			N/A	0.011±0.0077	0.009±0.0112	0.006±0.0118
	PC			N/A	0.008±0.0087	0.008±0.008	N/A
Mode 5	DRY	0.014±0.0009	N/A	N/A	N/A	N/A	N/A
	FW		0.±0.0022	-0.003±0.0034	-0.002±0.0013	-0.002±0.0041	0.001±0.0013
	FV			N/A	0.±0.0012	0.002±0.003	0.003±0.0027
	PC			N/A	-0.002±0.0033	N/A	N/A
Mode 6	DRY	0.016±0.0068	N/A	N/A	N/A	N/A	N/A
	FW		-0.003±0.0069	0.002±0.008	0.003±0.0075	N/A	0.004±0.0104
	FV			N/A	N/A	0.011±0.0165	-0.002±0.0079
	PC			N/A	-0.0086±0.0076	0.001±0.0071	N/A

6.5.5 Frequency Spectra Cascades

A more holistic view of the vibratory behavior of the flexible hydrofoil may be achieved by adding a third axis to the frequency response functions for speed – or, more specifically, Fn_h. Recall that an analogous representation of the output-only frequency response was shown in §5.5.2 to show the coherence of vortex shedding and the occurrence of flow-induced vibration. Figure 6.21 shows the measured mean compliance FRF as a function of flow regime and Fn_h. The low-frequency energy content is particularly apparent in the figure; the peak corresponding to mode 1 becomes indistinct amongst the flow-induced vibrations.

By truncating the transfer function to a finite number of modal contributions via the RFP form, it becomes a reduced-order model. The reduction is not unlike principal component analyses such as Proper Orthogonal Decomposition (POD) or Dynamic Mode Decomposition (DMD). POD or DMD are commonly used as de-noising tools by discarding – via truncation – the less-coherent dynamics in the data. FRFs of identified modes can be linearly summed (as demonstrated in § 6.4.7) to yield a similarly de-noised FRF of the hydrofoil. These de-noised FRFs can be arranged to form another pseudo-map of the frequency response, shown in figure 6.22. The spectra are much cleaner, but we can immediately see that the reconstructions in the neighborhood of mode 1 are un-physically "peaky," which in turn leads to the negative inferred damping.

The spectra in figure 6.21 and figure 6.22 do not suggest any impending instability, but there are signs that it could occur at certain operating conditions. Modes 2 and 3 (respectively first twisting and second bending) are the two nearest one another along the frequency axis, and are therefore the most obvious candidates for coupled flutter instability. The FW damping for both increases with speed, and the FW resonant frequencies show no sign of coalescing together. However, in the FV flow regime, the damping of both modes is found to be decreasing with increasing speed, and the modal frequency of mode 2 is increasing more quickly than the modal frequency of mode 3. Additionally, at deeper immersion depths, we expect the added mass to make up a greater proportion of the total system mass (*Harwood et al.*, 2016a), so the increase in frequency with the onset of FV flow is also expected to be more significant. Thus, it is conceivable that at high-speeds and deeper immersion depths (*e.g.* $AR_h > 1.0$), there might arise a dynamic instability involving the first twisting and second bending modes of model 2.

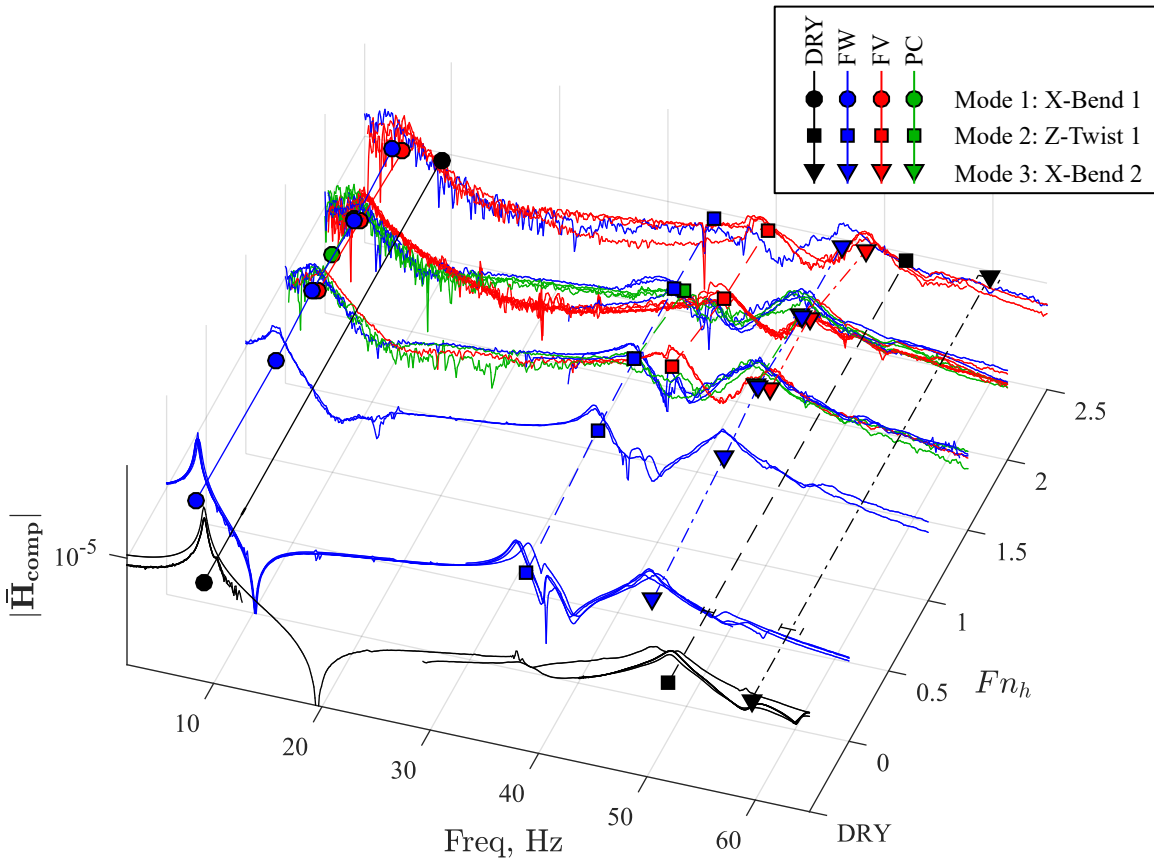

Figure 6.21: Cascade of mean compliance magnitudes for model 2 at different Froude numbers in FW flow ($0° \leq \alpha \leq 12°$), FV flow ($7° \leq \alpha \leq 12°$), and PC flow ($\alpha = 7°, 12°$ and $0.42 \leq \sigma_v \leq 0.85$). All data (except dry conditions) are for $AR_h = 1.0$. Markers and lines indicate the undamped modal frequency at each condition.

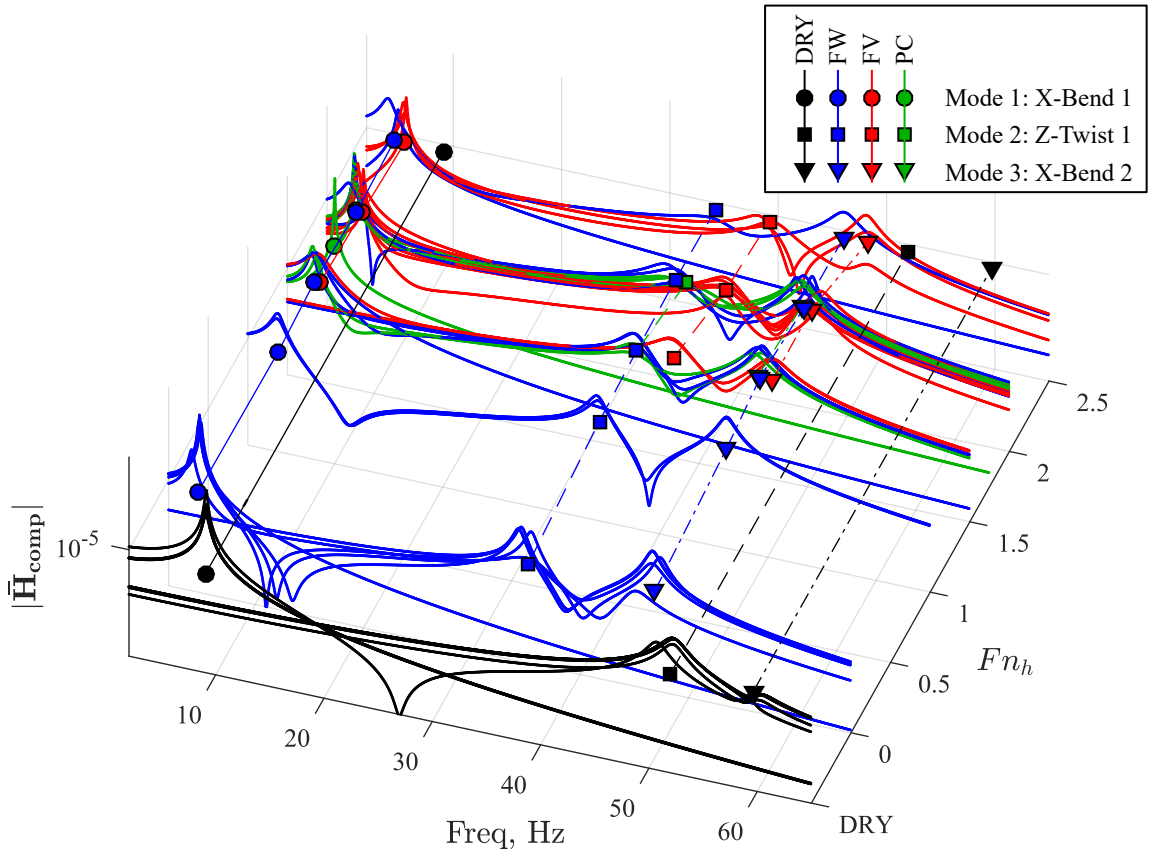

Figure 6.22: Cascade of de-noised mean compliance magnitudes for model 2 at different Froude numbers in FW flow ($0° \leq \alpha \leq 12°$), FV flow ($7° \leq \alpha \leq 12°$), and PC flow ($\alpha = 7°, 12°$ and $0.42 \leq \sigma_v \leq 0.85$). All data (except dry conditions) are for $AR_h = 1.0$. Spectra are reconstructed from reduced-order transfer-function representations. Markers and lines indicate the undamped modal frequency at each condition.

6.6 Summary and Discussion

6.6.1 Summary of Results

In this chapter, experimental modal analyses of model 2 (PVC with a reinforced trailing edge) were conducted in varying flow regimes. The major findings are summarized below:

How are the system resonant frequencies, mode shapes, and damping coefficients altered by flow speed and multi-phase flow?

Natural frequencies decrease substantially with immersion of the hydrofoil as a result of increasing fluid added mass. The added mass coefficient is approximately $m_{fl_{m,1}} \approx 0.9$ for mode 1 and is shown to decrease monotonically with increasing mode number. Forward speed has only a minimal effect on resonant frequencies in the FW flow regime, which we conjecture to be caused by a weakening of the effective system stiffness with forward speed. FV flow reduces fluid added mass, causing resonant frequencies to increase to a value somewhere between the dry and FW values. Increasing cavity sizes in the FV flow regime further reduce the added mass, causing resonant frequencies to increase with increasing speed. PC flow was not observed to affect the resonant frequencies.

All damping values were expressed in by total damping ratios, modeled by an equivalent linear dashpot. The structural damping, ξ_s was found to be $\xi_s \approx 1.5\%$ for all modes. Immersion in quiescent body of water caused changes of less than 1% from the dry values, indicating that quiescent fluid damping is negligible, possibly due to the small immersion ratio of $AR_h = 1.0$. Hydrodynamic damping was highly variable, but in general, damping in the FW regime increased slightly with forward speed. FV damping values are higher than FW values at low speeds – suggesting that energy is being dissipated into waves on the cavity interface – and tend to decrease with forward speed. Damping in the PC flow regime was typically larger than in the FW regime, suggesting that energy was being dissipated *via* condensation and vaporization at the cavity interface. Low-frequency flow-induced vibration are conjectured to add energy to the hydrofoil motions at frequencies near the first-bending mode, for which the RFP model does not account. This leads to spurious negative modal damping ratios being inferred for mode 1 at large Fn_h.

Mode shapes were quite insensitive to the operating conditions and flow regimes. There was evidence that the maximum deformations of the third bending mode (mode 5) are decreased in the still-water and FW cases (relative to dry testing), and increased

again in the FV and PC flow regimes. In both multi-phase flow regimes, cavities are located near the point of maximum deformation of mode 5, which reduces the fluid's inertial resistance to motion in that locale.

Can ventilation and/or cavitation cause hydroelastic instability?

None of the tested conditions resulted in hydroelastic instability. There is no evidence in the FW flow regime of approaching instability. However, in the FV flow regime (which is likely to be the operating regime at speeds high enough to present a risk of flutter), the resonant frequency of mode 2 (first twisting mode) is approaching that of mode 3 (second bending mode) while the hydrodynamic damping ratios of both modes are decreasing. It is conceivable that at significantly higher speeds or different submergence depths than those tested, flutter might be a concern. It should be noted that the center of gravity of model 2 is located forward of the elastic axis, which is suggested by linear aeroelastic flutter analysis to mean that flutter will probably not occur at any speed.

6.6.2 Discussion

The results of this chapter are a significant departure from the preceding chapters, and are preliminary in nature. Many areas exist in which improvements or alternative analyses could be used, a few of which will be highlighted below.

The RFP method of curve-fitting FRFs appears very robust. However, algorithmic improvements could be made to its implementation by, for example, using an iterative scheme to improve initial estimates of pole locations, or by projecting the transfer function onto a set of orthogonal polynomials, as proposed by *Richardson and Formenti* (1982). Additionally, it would be beneficial to assess the effect of spectral smoothing on the resulting modal parameter estimates. Quantitative estimates of modal mass could be obtained using drive-point inertance measurements, yielded by the combination acceleration-and-force transducer used to couple the shaker motor to the model. Different drive points and an improved mounting design for the shaker motor could yield less contamination by unwanted vibrations.

The periodic modulation of added mass, damping, and stiffness components during vaporous cavity shedding is an interesting effect, but one that did not become wholly apparent in this research. As mentioned in the chapter, the non-stationary vibrations resulting from cavity shedding may have broadened the modal peaks, resulting in erroneously large estimates of damping. Without a detailed joint time-frequency analysis, however, it is difficult to say with any surety whether this was the case.

Cavity shedding was not very coherent during testing because the vaporous cavities observed were thin and short – longer, thicker cavities were not stable and immediately transitioned to FV flow.

Operating conditions in the cavitation tunnel were limited to $AR_h = 1.0$ and $Fn_h \leq 2.5$ by facility constraints. Future studies should investigate other values of AR_h, and should extend the testing matrix to higher values of Fn_h to investigate the possibility of flutter in different flow regimes.

CHAPTER VII

Conclusions, Contributions, and Future Work

7.1 Conclusions

A series of experiments have been performed to investigate the hydrodynamic and hydroelastic response and stability of one rigid and two flexible surface piercing hydrofoils in multi-phase flow. Experiments were performed in a towing tank at atmospheric pressure and in a free-surface cavitation tunnel at both atmospheric and reduced pressures. Chapter I summarized previous research in the atmospheric ventilation of surface-piercing bodies, and the basics of hydroelasticity were reviewed before establishing a number of open questions, which have been addressed throughout the thesis. In chapter II, the details of the experimental program were described. Chapter III explored flow stability and steady hydrodynamic loads on the rigid hydrofoil. In chapter IV, the concept of flow stability was used to describe the mechanisms by which unsteady transition between flow regimes occurred. In chapter V, the ramifications of hydrofoil flexibility and hydroelastic coupling upon both steady and unsteady multi-phase flows were explored. Chapter VI explored the response of a flexible hydrofoil to external harmonic excitation in addition to natural flow-induced excitation, using experimental modal analysis techniques. The flexible hydrofoils were instrumented with custom-designed shape-sensing spars, the design and characterization of which were described in chapter II. The major conclusions from each chapter are summarized below.

What are the characteristic steady flow regimes of surface-piercing lifting-surfaces and how are they formally defined?

Four flow regimes have identified: Fully Wetted (FW), Partially Ventilated (PV), Fully Ventilated (FV), and Partially Cavitating (PC) flow regimes. FW flow is single-phase, with the exception of base cavitation or base ventilation in the wake. PV flow

is a transitional flow regime in which air entrainment occurs along an incomplete portion of the submerged span. FV flow is characterized by the stable entrainment of air along the entire submerged span. PC flow is marked by the vaporization and condensation of water along the suction surface, leading to an unsteady vapor-filled cavity. A flow is said to be globally stable if, when subjected to a perturbation, it returns unerringly to its pre-perturbation configuration, locally stable if a sufficiently-large perturbation causes the flow to alter its configuration without returning, and unstable if the flow spontaneously changes its configuration absent any perturbation.

What physical processes dictate the hydrodynamic response and stability of steady flow regimes?

At yaw angles below the bifurcation boundary α_b, the attached flow satisfies stability conditions only for the FW regime. Above the bifurcation boundary, limited flow separation exists, and FW flow is locally stable. FW flow is destabilized by large-scale flow separation over more than half the chord length, which occurs along the stall boundary α_s. The stability of flow in the FV regime is tied to the development of upstream re-entrant flow at the cavity closure. For stable FV flow to occur, the cavity must reach the immersed tip of the hydrofoil and the slope of the cavity closure line ($\bar{\Phi}$) must satisfy the condition,

$$\bar{\Phi} < 45^{\circ}.$$

Flow that does not satisfy this condition will stabilize by changing to a PV flow topology. In the PV and FV flow regimes, the cavity lengths vary along the submerged span, due in part to the hydrostatic pressure gradient. As a result, the stability boundary between PV and FV flow is primarily a function of Fn_h. The experimental parameter space is populated with stability regions that overlap one another. Overlapping areas of these regions indicate multiply-stable flow conditions, where the flow may take on any one of the locally-stable regimes. Factors governing the regime of a given flow include hysteretic effects with movement through the parametric map (such as during flow acceleration and deceleration) or external perturbations to the flow.

How do hydrodynamic loads differ between flow regimes? How do the loads change with speed, immersion depth, and attack angle within each regime?

The hydrodynamic response of the surface piercing hydrofoil in lift, drag, and

moment depends upon the flow regime, the dimensionless speed Fn_h, the yaw angle α, general cavitation number σ_c, and the dimensionless immersion depth AR_h. Lift and moment coefficients decrease substantially with ventilation, while drag remains fairly continuous between wetted and ventilated regimes. At very low speeds, laminar separation, partial ventilation, and partial cavitation augment the lift by inducing a positive effective camber. The drag and yawing moment are similarly affected. With increasing speed, the amount of apparent camber decreases as the cavity envelops the suction surface and extends far downstream. Three-Dimensional (3-D) effects cause a typical reduction in hydrodynamic loads with AR_h in the FW regime, but flow in the FV regime attenuates sectional circulation so strongly that 3-D effects are suppressed in the FV regime. The cavitation parameter σ_c/α was used to scale the slope of $C_{L_{3D}}$ and $C_{M_{3D}}$ and the curvature of $C_{D_{3D}}$ with respect to α for all experimental data at an immersed aspect ratio of $AR_h = 1$. The resulting curvs share salient features with Two-Dimensional (2-D) cavity flow theory, but are complicated by the effects of the finite aspect ratio.

What simple models can be derived to simulate the behavior of surface-piercing hydrofoils in multiphase flows?

A simple nonlinearization and extension of classic lifting-line theory was developed as a low-cost physics-based model. The model produces a good qualitative approximation to experimental flow topologies and experimentally-measured loads by including gravitational effects, free-suraface effects, cavitation effects, and finite-aspect-ratio effects.

How do flows transition between different regimes, and how do transition mechanisms relate to the physics governing flow stability?

Transition mechanisms are responsible for moving the flow between stable configurations when some aspect of the flow violates the stability conditions of the flow regime. The destabilizing influence of the flow takes the form of vorticity and eddying flow in the cases of formation mechanisms, and it takes the form of an upstream reentrant jet, gradual flow reattachment, and increasing local pressures in cases of elimination mechanisms. Ventilation transition mechanisms have been subdivided into formation stages, which include inception and stabilization, and elimination stages, which include washout and rewetting. The four sub-stages describe the boundaries between the FW, PV, FV, and PC flow regimes.

Ventilation inception is the first stage of formation, and it requires that air enters low-pressure and locally-separated flow. Stabilization occurs when the air entrainment

satisfies the stability conditions established in chapter III for FV flow. Washout is the reverse of stabilization, and occurs when a cavity becomes destabilized by the re-entrant jet or its closure line forms an angle steeper than the $\bar{\Phi} = 45°$ criterion established for stable FV flow. Rewetting occurs when all entrained air is expelled from the suction-side flow.

Spontaneous transition mechanisms occur where when changing flow conditions cross the stability boundary separating one flow regime from another. In the multiply-stable zones of parameteric space, where flow stability regions overlap one another, external perturbations to the flow are responsible for initializing transition.

What flow transition mechanisms occur on surface-piercing struts in subcavitating and cavitating flow?

In subcavitating flows, a number of ventilation formation and elimination mechanisms were described. The distinction between the mechanisms is made on the basis of how air is first entrained into the flow (inception). Spontaneous inception occurs when some self-induced process of the flow admits air from a natural source, and includes stall-induced, tip-vortex-induced, and Taylor-instability-induced mechanisms. Perturbation-induced inception requires that an external source of air be provided, an example being the air jet used in the present study. Air can only become stably entrained where low pressure permits its ingress and separated flow permits its residence – criteria that invoke the stability conditions of each respective flow regime. When vaporous cavitation is present, such as in the PC regime, it enhances the formation mechanisms already present by providing a stationary region of ventilation-prone flow into which air is readily admitted. In the present work, wetted ventilation formation usually occurred through leading-edge stall. In cavitating flows, the formation mechanism shifted to tail ventilation, where Taylor instabilities (*Taylor*, 1950; *Emmons et al.*, 1960; *Swales et al.*, 1974) developed on the free surface and transported air to the trailing edge of the vaporous cavity.

Can scaling relations be developed to describe the stability conditions of surface-piercing struts?

A scaling relationship was derived to describe the washout boundary of ventilated flow. By expressing a kinematic condition for destabilization of FV flow, a series of semi-theoretical models were used to predict the boundaries in the $C_{L_{3D}}$– Fn_h plane.

The stability boundary is sufficiently described by the relation,

$$Fn_h = \frac{\pi}{4} \sqrt{\frac{\frac{\pi}{2}AR_h^4 - 4AR_h^3 + 18AR_h^2 + 8AR_h}{2.31C_{L_{3D}}\left(\pi AR_h^3 - 2\pi AR_h^2 + 3\pi AR_h + 4\right)}}. \qquad \text{(4.6 revisited)}$$

Further modeling of $C_{L_{3D}}$ produced stability curves in the $\alpha - Fn_h$ plane. An assumed elliptical lift distribution and application of the Helmbold correction (*Helmbold*, 1942) both yielded curves that captured the present experimental data and data from *Breslin and Skalak* (1959) and *Swales et al.* (1974) very well (for $Fnh \lesssim 3$). At large Froude numbers and small angles of attack, the relationship proposed by *Breslin and Skalak* (1959) yielded a better fit to the data.

What effect does hydrofoil flexibility have upon the hydrodynamic response, stability, and flow regimes of the flexible hydrofoils?

The same flow regimes and transition mechanisms are present on the flexible hydrofoil models as on the rigid hydrofoil model, and the physics dictating flow stability are unchanged. The stability regimes of model 1 show a reduction in the stall angle from $\alpha_s = 15°$ to $\alpha_s = 13°$ as a result of the hydrofoil flexibility. Hydroelastic coupling causes the steady lift and yawing moment coefficients to be larger for the flexible hydrofoils (models 1 and 2) than for the rigid model 0, while the differences between models 1 and 2 are within the experimental uncertainty bounds. The drag coefficient is relatively unaffected by hydrofoil flexibility.

Passive deformations of model 1 are shown to shift the transition boundaries (inception, stabilization, washout, and rewetting) slightly downward and/or to the right, relative to the boundaries of model 0. The differences are small, however, and in the cases of the stabilization and washout boundaries, the rigid and flexible boundaries are within the experimental uncertainty. Active excitation of model 2 at its resonant modes was found to modify the local/global stability of overlapping flow regimes in the bi-stable regions of parameter space. Excitation of the first bending mode encouraged ventilation inception, while excitation of twisting modes and higher-order coupled bending-twisting modes caused washout and rewetting.

How does multi-phase flow affect the static and dynamic hydroelastic response and stability of the hydrofoil?

Bending and twisting deflections are proportional to the lift and yawing moment in each flow regime. As a result, structural deflections are much smaller in the FV regime than in the FW regime. The maximum twist angle induced by hydrodynamic

loading on either model 1 or model 2 is approximately $\theta = 1°$, measured at the foil tip. Thus, it is conceivable that the stall angle is advanced, though the test matrix resolution is too coarse to resolve the stall angle precisely.

When the flow regime changes suddenly, such as during perturbation-induced ventilation formation, the structural deflections and unsteady hydrodynamic forces mimic the step response of a highly, but sub-critically damped dynamical system. At small yaw angles, coherent vortex shedding (into a von Kármán street) from the blunt Trailing Edge (TE) of model 2 was shown to excite flow-induced vibrations at Froude numbers of $0.3 \leq Fn_h \leq 2.5$. Lock-in was observed where the frequency of vortex shedding crossed resonant frequencies of the the hydrofoil; elsewhere, peaks in the spectra of hydrodynamic force and hydrofoil tip motions indicate flow-induced vibration.

Can scaling relations be used to describe the static and dynamic loads and structural responses of the surface-piercing hydrofoils?

The flow-induced bending and twisting deflections measured at the free tips of models 1 and 2, and scaled by the dynamic pressure, are proportional to $C_{L_{3D}}$ and $C_{M_{3D}}$ respectively. Additionally, the ratio of elastic twist angle to total effective angle of attack, measured at the foil tip, is shown to scale with ${Fn_h}^2$ for constant a_0 and e. Thus, attached flow in the FW flow regime form one asymptotic boundary, while FV flow at large α and Fn_h form another. These results are consistent with the numerical study of *Akcabay and Young* (2014). Intermediate yaw angles and Froude numbers, for which spanwise variations in cavity length cause both a_0 and e to vary along the span, fall between these established limits. Finally, the distance between vortices shed from the trailing edge was found to remain constant at all speeds (a result of the constancy of the Strouhal number St_t), so the vortex shedding frequency scales linearly with forward speed.

How are the system resonant frequencies, mode shapes, and damping coefficients altered by flow speed and multi-phase flow?

The natural frequencies decrease substantially with immersion of the hydrofoil as a result of fluid added mass. The added mass is variable between modes, and generally decreases in proportion to the solid mass with increasing mode numbers. Forward speed has only a minimal effect on resonant frequencies in the FW flow regime for the models and flow speeds investigated. FV flow reduces fluid added mass, causing resonant frequencies to increase to a value somewhere between the dry and FW values. Increasing cavity sizes in the FV flow regime further reduce the added mass, causing

resonant frequencies to increase with increasing speed. PC flow was not observed to affect the resonant frequencies because, for the cases tested, only small vaporous cavities existed stably, which did modify the density field very substantially.

All damping was cumulatively modeled by an equivalent viscous dashpot, described by the effective damping ratio, ξ_e. The structural damping, ξ_s, was found to be $\xi_s \approx 1.5\%$ for all modes. Immersion in still water caused changes of less than 0.5% from the dry values, indicating that quiescent fluid damping, ξ_q, is negligible at $AR_h = 1.0$ (though this result may not hold at other immersion depths). Hydrodynamic damping, ξ_{hd}, was highly variable, but in general, damping in the FW regime increased slightly with forward speed. In general, FV damping values are higher than FW values at low speeds – suggesting that energy is being dissipated into waves on the cavity interface – and tend to decrease with forward speed. Damping in the PC flow regime was typically larger than in the FW regime, suggesting that energy was being dissipated *via* condensation and vaporization at the cavity interface and *via* unsteady cavity shedding. Low-frequency flow-induced vibration are conjectured to add energy to the hydrofoil motions at frequencies near the first-bending mode, for which the Rational Fraction Polynomial (RFP) model does not account. This leads to spurious negative damping values being inferred.

Mode shapes were quite insensitive to the operating conditions and flow regimes. There was evidence that the maximum deformations of the third bending mode (mode 5) are decreased in the still-water and FW cases (relative to dry testing), and increased again in the FV and PC flow regimes. In both multi-phase flow regimes, cavities are located near the point of maximum deformation of mode 5, which reduces the fluid's inertial resistance to motion in that locale.

Can ventilation and/or cavitation cause hydroelastic instability?

None of the tested conditions posed any risk of hydroelastic instability in the FW flow regime. In the FV flow regime (which is likely to be the operating regime at speeds high enough to present a risk of flutter), the resonant frequency of mode 2 (first twisting mode) was found to approach that of mode 3 (second bending mode) while the hydrodynamic damping ratios of both modes are decreasing. It is conceivable that at significantly higher speeds than those tested, or at different submergence depths, flutter might be a concern. However, the center of gravity of model 2 is located forward of the elastic axis, which is suggested by linear aeroelastic theory to mean that flutter will probably not occur at any speed.

7.2 Major Contributions

The methodology and results presented in this thesis, which are summarized in the preceding section, represent a significant advancement in our understanding of hydroelasticity and multi-phase flows. Ventilation, cavitation, and hydroelasticity are complicated disciplines on their own, and the intersection of these topics presents a flow of such complexity that it confounds classical theory, exceeds the capabilities of present numerical models, and makes experimental study extremely challenging. A number of specific contributions to the field have been made, which are summarized below:

- A unified concept of flow regimes, flow stability, and transition mechanisms has been established that enables researchers and designers to consider multi-phase flows more holistically than in the past. This thesis defines in precise terms the characteristic flow regimes, the individual stage of unsteady transitional flow, and the taxonomy of transition mechanisms on surface-piercing hydrofoils. In doing so, it puts forward a much-needed standardization of the terminology, criteria, and definitions, which was not present in the literature. This enables researchers to disseminate results of future studies with minimal ambiguity.

- This work has demonstrated the feasibility of performing a meaningful experimental study of highly complex flows involving multiple phases and Fluid Structure Interaction (FSI). A methodology has been proposed for the experimental collection and analysis data for multi-phase FSI problems. As part of this process, a versatile experimental setup has been constructed. Both the procedure and the physical setup may be expanded or modified to accommodate a wide variety of models in various experimental facilities, thus benefiting experimentalists studying similarly-complex flows in the future.

- Shape-sensing spars were designed, built, and benchmarked with promising results. The spars require no visual access to the test specimen in order to operate, and they are shown to be competitive with optical methods in spatial resolution and accuracy. Combined with the modal analysis of chapter VI, the spars permit robust inferences of mode shapes to be made off-line, or approximate mode shapes to be inferred on-line. Thus, they have demonstrated value as research tools. Moreover, they are low-cost, field-replaceable, and easily constructed, which gives them potential as robust and deployable tools for the collection of full-scale operating data in the field.

- Future research efforts will benefit from the outlined methodology and the results that have been presented. Practitioners of marine design can also benefit from the quantitative characterization of hydrodynamic loads and hydroelastic responses, as well as the various scaling relations that have been developed. Finally, this work has yielded a rich dataset with uniquely-available measurements. These data are useful for future analysis and for the validation of next-generation numerical tools used to simulate multi-phase FSI problems.

As a whole, this work has led to a deeper understanding of the characteristics of natural ventilation and vaporous cavitation, and of the interactions of multi-phase flows with structural dynamics. The methods that have been outlined, the results that have been presented, and the knowledge inferred from such results are all important contributions toward a field of study that will enable the design of safe, fast, controllable, stable, and efficient lifting surfaces with a wide range of marine applications.

7.3 Future Work

The work presented in this thesis suggest a number of avenues for fruitful research in the future. Future works fall into three general categories: future experimental studies, development of sensors, and model development.

7.3.1 Future Experimental Studies

What is the effect of viscosity on the suction side flow, and how does it affect the transition to ventilated flow?

The relatively sharp leading edge of the semi-ogival model used in this work was designed to serve as a fixed separation point, thus removing any primary dependence of the suction-side flow upon the Reynolds number, Re_c. Numerous observations have been made throughout the thesis, however, that suggest an influence of the Reynolds number on experimental results. The lift generated in wetted flow at low speeds showed a characteristic increase at moderate, sub-stalled angles of attack, for example – a hallmark feature of laminar separation. Additionally, flow visualizations demonstrated that thin-airfoil stall preceded most cases of ventilation inception, and the stall boundary was observed to vary with the water temperature, which suggests that the imminently-stalled flow is sensitive to small changes in the fluid viscosity at Reynolds numbers on the order of $Re_c = \mathrm{O}\left(10^5\right)$ to $\mathrm{O}\left(10^6\right)$. The preceding observations beg the question: what is the precise character of the boundary layer on the

suction surface of a sharp-nosed section, and how does it change with variations in Re_c?

A suggested approach for answering this question is to perform experiments with a two additional geometrically-similar models of differing scales. Particle Image Velocimetry (PIV) measurements should be made of the suction-side flow in stable fully wetted flows and in flows preceding ventilation inception. By comparing the separation patterns of flows that vary only in Re_c, the role of the boundary layer and flow separation in dictating flow stability may be more fully understood. Flow near the stall boundary, in particular, was characterized by eddying flow at the free surface along the suction side. Similar observations have been made by *Pogozelski et al.* (1997), who characterized the near-surface turbulent flow structures around an unyawed surface-piercing strut possessing an airfoil section with a thickness-to-chord ratio of $T/c = 0.33$. PIV visualization of the near-surface flow demonstrated that the wave crest at the leading edge of the strut generated significant vorticity, and that flow separation occurred at the ensuing wave trough at certain values of the chord-based Froude number.

Qualitative observations of the flows in this thesis suggest that air entrainment occurs through this separated wave trough for stall-induced ventilation formation. However, neither the effect of the pressure gradient on a yawed body, nor the effect of the Reynolds number are known. Thus, PIV surveys of the near-surface flows along the stall boundary for several model scales would illuminate a number of interesting physical processes, and would allow us to better understand how and when air entrainment occurs. This understanding might, in turn, lead to improved methodologies for the suppression of ventilation in full-scale marine systems.

How does unsteady hydrofoil motion affect the dynamics of cavity formation and elimination?

Ventilated flows depend upon the extent of flow separation and the magnitude of local suction pressures. Work by *McCroskey et al.* (1976, 1981); *McCroskey* (1982) have shown that unsteady pitching motion of airfoils both delay flow separation and reduce peak suction pressures. Moreover, the results of chapter V demonstrated that forced vibration of the hydrofoil had a measurable impact upon the stability of ventilated cavities. Thus, a natural extension of this work is to study the case when the yawing motion of the hydrofoil is made unsteady.

By varying the reduced frequency of the yawing motions,

$$k = \frac{\pi f_\alpha c}{U}, \tag{7.1}$$

where f_α is the frequency of yaw oscillations in Hz, the effects of separation-suppression could be studied. Marine lifting-surfaces are typically actuated by changing the attack-angle, rather than by changing the flow speed. Thus, the resulting hysteresis loops of ventilation as functions of α would be also be more useful in the design of marine controllers. By using harmonic yawing motion, comparisons could also be made with classical fluid dynamics theories, such as the Theodorsen equation (*Theodorsen*, 1935), and would enable reduced-order models of unsteady hydrodynamic loads to be developed as functions of k, as shown in *Kennedy* (2015) and *Caverly et al.* (2016).

How can we better understand the bi-stability of wetted and ventilated flow?

This thesis has concluded that flow conditions exist at which there exist two or more stable configurations of the flow, but the nature of the stable states are not explored mathematically. Work by *Tassin Leger and Ceccio* (1998) has demonstrated that vaporous cavitation on a body causes the point of separation to move upstream as the cavity and flow field arrive at a stable configuration. In this thesis, it has been conjectured that air entrainment drives a similar alteration of flow separation-patterns, but that because the pressure of a naturally ventilated cavity is larger than that of a vaporous cavity in most cases, the process of cavity stabilization is changed. Ventilation does not occur until noncondensible is introduced from some external source, so it is possible to sustain a wetted, but ventilation-ready flow almost indefinitely. The region of flow separation may be very limited, as indicated by surface-flow visualizations in this thesis, and upon the introduction of air, the cavity quickly grows beyond the extents of the prior wetted flow separation.

A suggested study would involve studying a limited leading-edge separation bubble on a sharp-nosed 2-D flat plate. Time-resolved PIV measurements of the suction surface flow should be made while an air-path is made available to a small region of leading. The objective would be to measure how the separation pattern is modified by the initial ingress of air (and the associated rise in local pressures), and to explore the unsteady stabilization of the flow. Does the point of flow reattachment move downstream ahead of the growing cavity, or does the initial ingress of air lead to complete flow detachment from the suction surface?

7.3.2 Sensor Development

The shape-sensing spars developed in this thesis show significant promise. However, the spars used to collect data were the first versions of the sensors, and there is room for significant improvement. The resolution of twisting motions, in particular, should be a focus of future developments. Two proposed improvements follow:

Use strain rosettes to measure bending strain and shear strain.

Doing so would improve estimates of twisting motions because twist angles would no longer be inferred from the small difference between large bending deflections. Doing so may also eliminate the need for two separate spars, as a single spar could be instrumented to measure both strain components.

Develop smaller spars, instrumented with semi-conductor strain gauges.

The spars used in this test are relatively large, and the strain gauges used were resistive-type metallic elements. Silicone strain gauges are much smaller than resistive gauges, which would permit the entire spar design to be miniaturized, and which would better approximate ideal point-measurements of surface strains. Additionally, silicone gauges have gauge factors one to two orders of magnitude higher than those of metallic gauges, which improves the signal-to-noise ratio of the instrument as a whole.

7.3.3 Modeling Development

Work is ongoing in the reduced-order modeling and physics-based modeling of the surface piercing hydrofoils in wetted and ventilated flows, which are briefly described below.

Reduced-Order Modeling: Modal Analysis

The modal analysis of chapter VI is based on a reduced-order model of the hydrofoil equations of motion in terms of vibratory modes and their transfer functions. Refinements of the model and the system identification technique are expected to yield additional insight into the hydrofoil's modal response. For example, the impedence head of the shaker motor, which measures both forces and accelerations, can be used to estimate the drive-point inertance Frequency Response Function (FRF). Drive point measurements permit estimates to be made of the modal mass, which in turn allow the dimensional fluid mass components to be estimated for each mode. Moreover, knowledge of the modal mass allows the calculation of properly-scaled

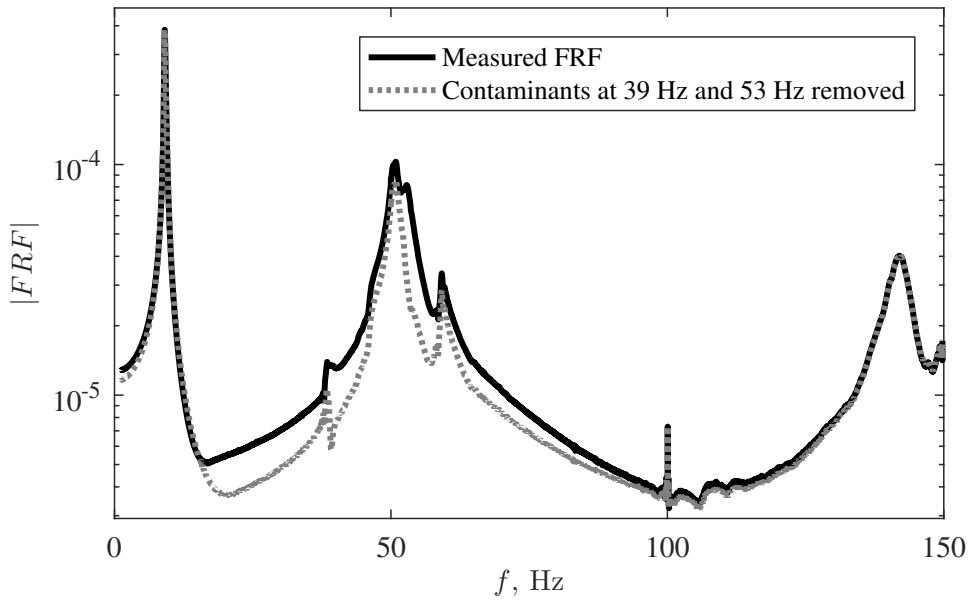

Figure 7.1: Mean compliance FRFs for model 2 in dry conditions. Measured data and measured data with fitted contaminant modes removed are shown.

mode shapes.

An effort should be made to remove some unwanted spectral content from the measured data for mode 2. For example, the shaker-motor housing and the transverse support rails in the cavitation tunnel (the two greatest sources of spectral contamination) were each instrumented with accelerometers. The cross-power spectra of these measured signals with signals of interest (those composing the compliance and inertance FRF vectors) may be used to reduce the prominence of the undesired spectral peaks. Alternatively, the RFP method used in chapter VI may used to identify modes that are not of interest, and the individual modal contributions can be removed from the measured spectra. Figure 7.1 shows a preliminary result of the latter approach. The RFP model was used to fit the modal contributions of the transverse support rails and shaker-motor bracket at 38 Hz and 53 Hz, respectively. The Single-degree-of-freedom (SDOF) representation of each contaminant was then subtracted from the experimentally-measured FRF.

The transfer function summation is also a linear system representation, and one that requires diagonalizable mass, damping, and stiffness matrices. Thus, system identification performed in chapter VI does not capture nonlinear, non-stationary, or frequency-dependent effects. In the case of the flexible surface-piercing hydrofoil, the presence of the free surface introduces frequency dependence into the wave radiation damping and fluid added mass. The structural hysteretic damping coefficient is, by

its definition, frequency dependent. Nonlinearities are introduced by fluid viscosity, mechanical losses at bolted joints, and multi-phase flows. Non-stationary vibrations occur when ventilation or cavitation shedding cause periodic modulation of the system parameters *Akcabay and Young* (2015); *Caverly et al.* (2016). Plans to address these concerns include performing a nonlinear system identification on the time-domain signals to investigate the importance of nonlinearities and frequency-dependent parameters. Joint time-frequency analysis, including wavelet analysis and short-time Fourier transforms will be used to gain insight into non-stationary vibrations in time-varying flow conditions. The field of hydroacoustics is rich with methods for analyzing complex dynamical systems, and a more-complete survey of available analysis techniques is planned. Results from chapter VI are planned for future publication.

Physics-Based Modeling: Hydroelastic Lifting Line Model

The lifting line model developed in chapter III has been incorporated into a coupled hydroelastic model, which uses a beam-element Finite Element Method (FEM) model to simulate the hydrofoil's structural response (*Ward et al.*, 2016). The coupled models have been found to accurately predict the steady-state lift, moment, spanwise bending, and spanwise twisting response of hydrofoil models 1 and 2. Current developments include implementing unsteady hydrodynamic forces into the model in the form of a Theodorsen function for harmonic motion (*Theodorsen*, 1935), and a Wagner function convolution for arbitrary motion (*Wagner*, 1925).

By developing an unsteady hydroelastic model that produces qualitatively-correct predictions with a computational cost, inverse models can be developed, with which the operating conditions, load distributions, and motion history of the hydrofoil can be inferred from the deflections measured by shape-sensing spars. Load reconstruction using FEM models is ordinarily an ill-posed problem because only a few strain measurements are available to reconstruct the load distribution at a much larger number of nodes. However, the physics-based hydroelastic model is used in this case to constrain the search space to only those load distributions that are physically-realistic. Thus, the search space is reduced to the size of the vector defining the inputs to the physics-based model. Preliminary results by *Ward et al.* (2016) have demonstrated that for steady flow conditions, the measured deflections can successfully be used to infer the yaw angle α and immersed aspect ratio AR_h within 5% of experimental values.

APPENDICES

APPENDIX A

Construction Drawings

A.1 Construction Drawings

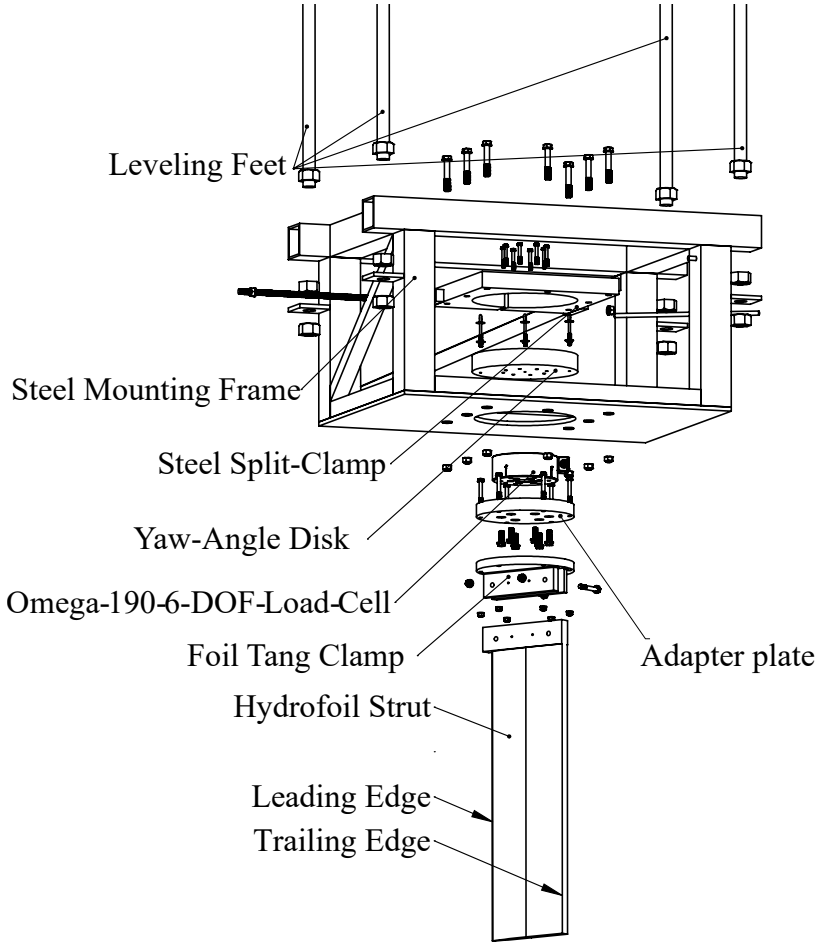

Figure A.1: Exploded view of experimental setup. Dimensions are in inches.

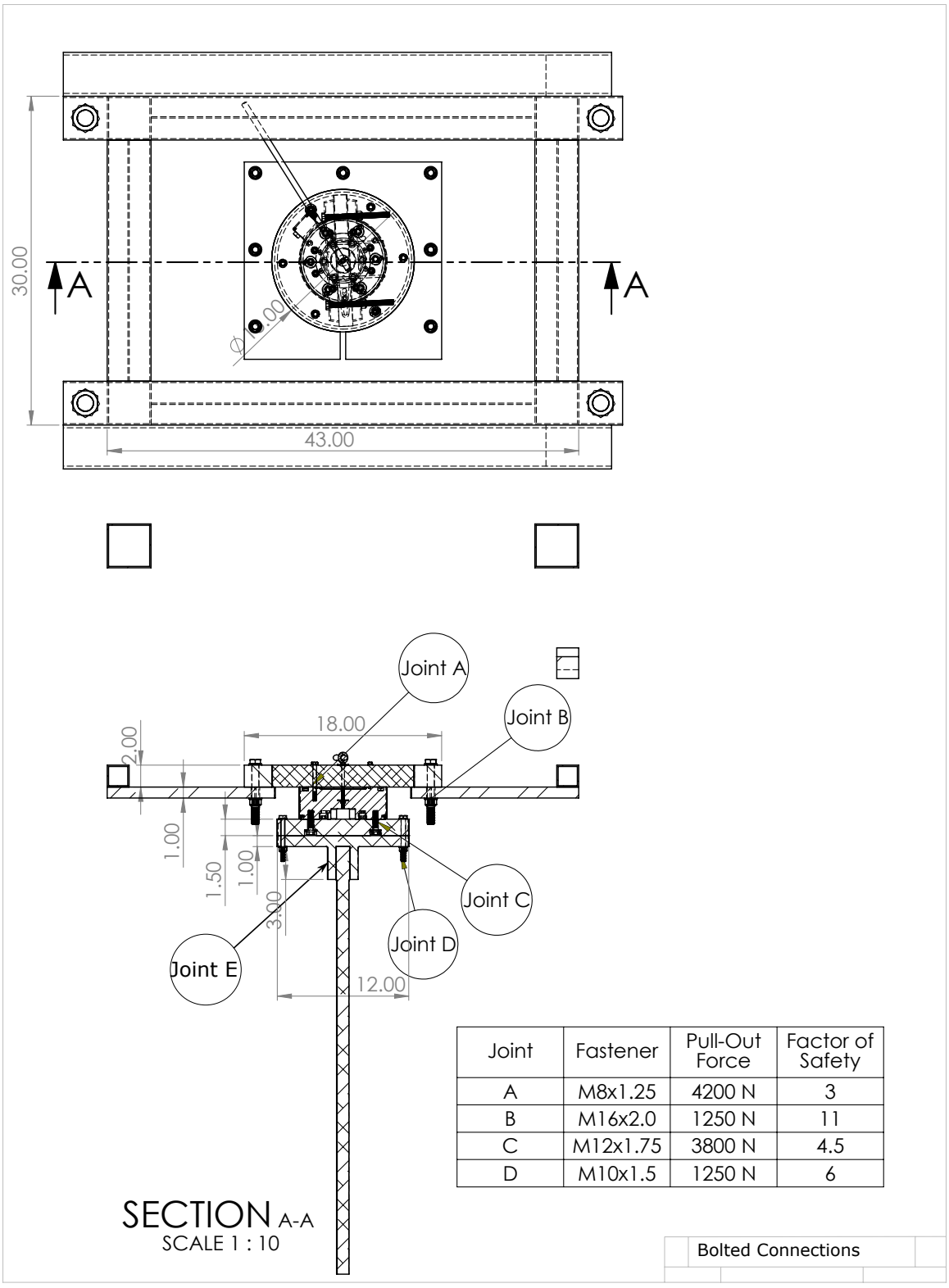

Joint	Fastener	Pull-Out Force	Factor of Safety
A	M8x1.25	4200 N	3
B	M16x2.0	1250 N	11
C	M12x1.75	3800 N	4.5
D	M10x1.5	1250 N	6

Figure A.2: Labeling of bolted non-permanent joints. Dimensions are in inches.

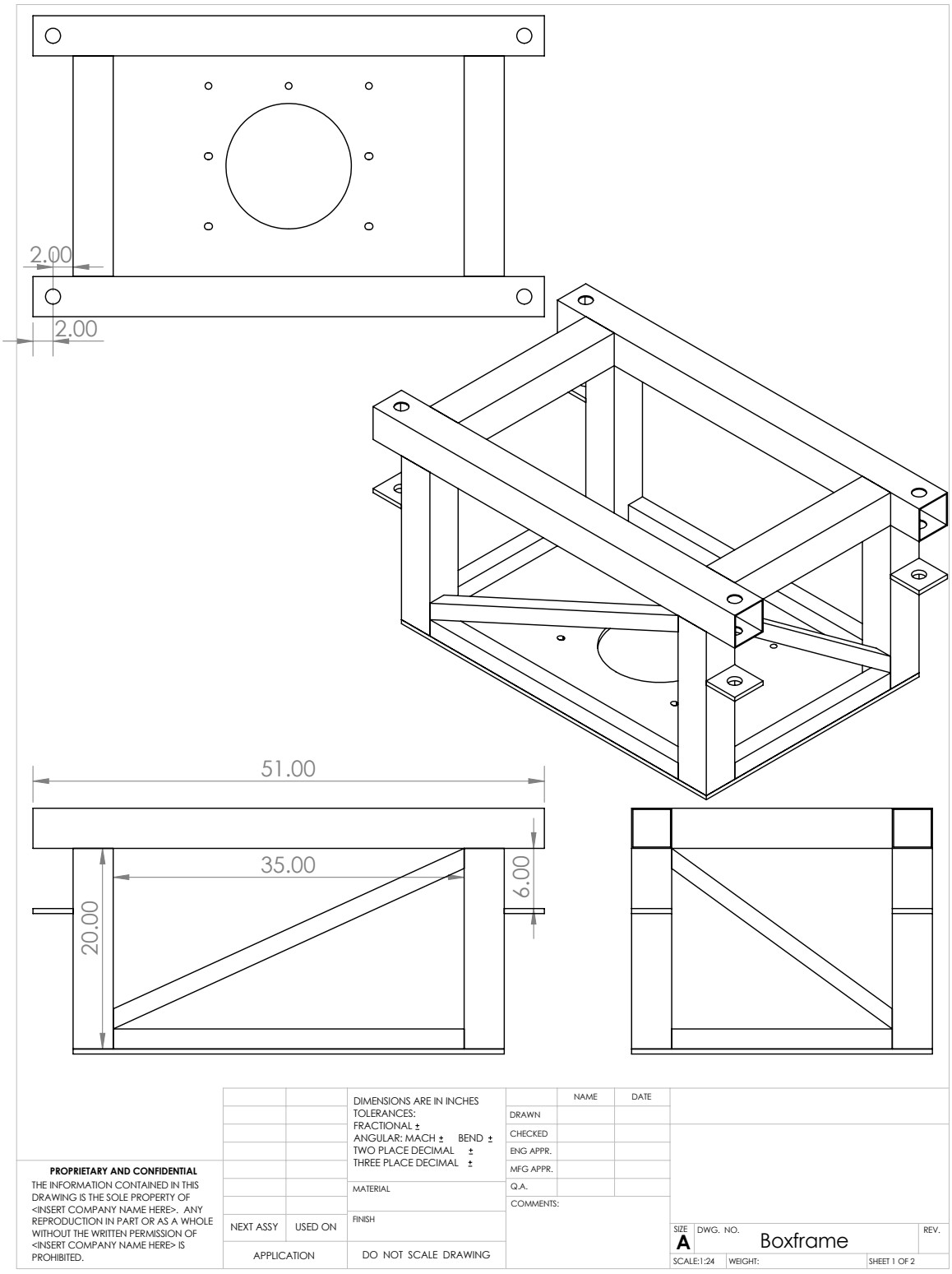

Figure A.3: Steel box frame used to mount hydrofoil onto towing-tank carriage. Dimensions are in inches.

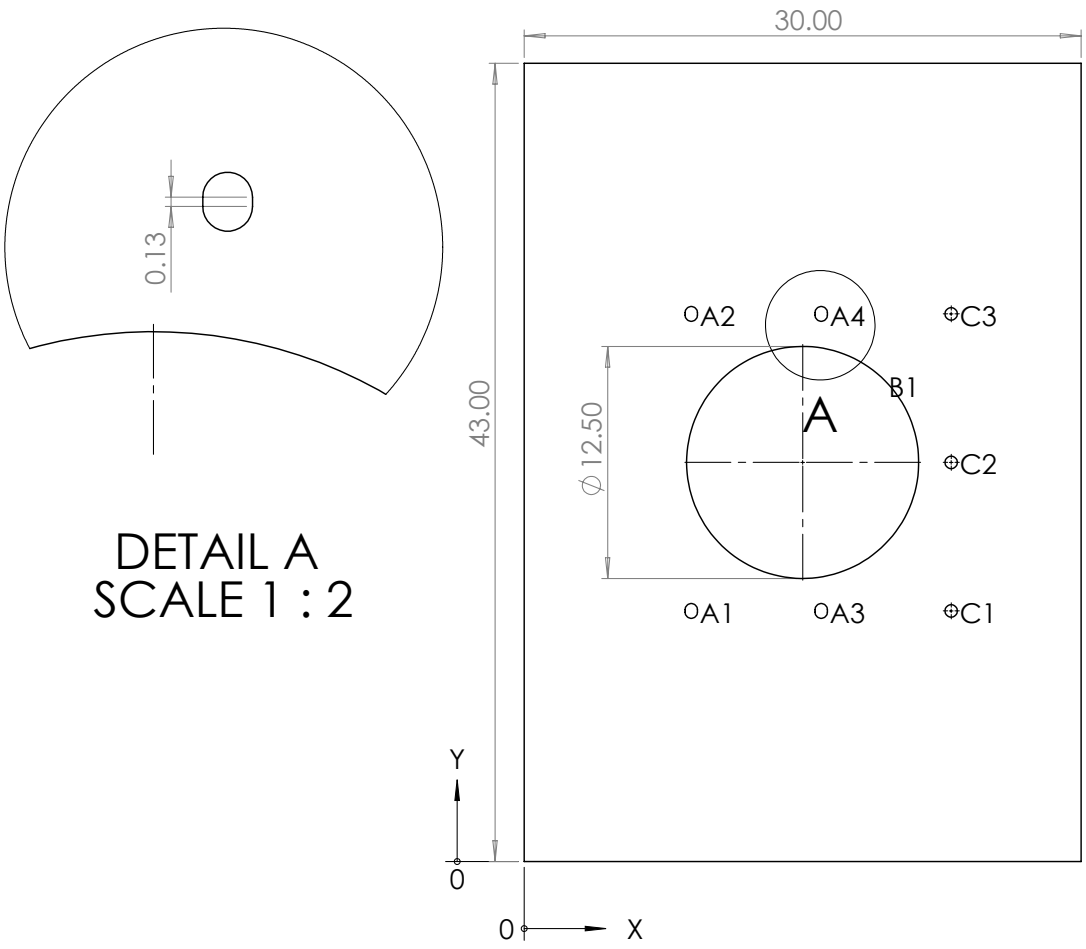

TAG	X LOC	Y LOC	Size
A1	9.00	13.50	Elongated M16
A2	9.00	29.50	Elongated M16
A3	16.00	13.50	Elongated M16
A4	16.00	29.50	Elongated M16
B1	15.00	21.50	12.5"
C1	23.00	13.50	M16 Clearance
C2	23.00	21.50	M16 Clearance
C3	23.00	29.50	M16 Clearance

Note: 48x48x0.5" steel plate will be provided. Waterjet cut desired. Bolt-up pattern should match steel collar (split-clamp).

SIZE	DWG. NO.	REV.
A	Baseplate	
SCALE:1:20	WEIGHT: 164.07	SHEET 1 OF 1

Figure A.4: Hole pattern in base plate of box frame. Dimensions are in inches.

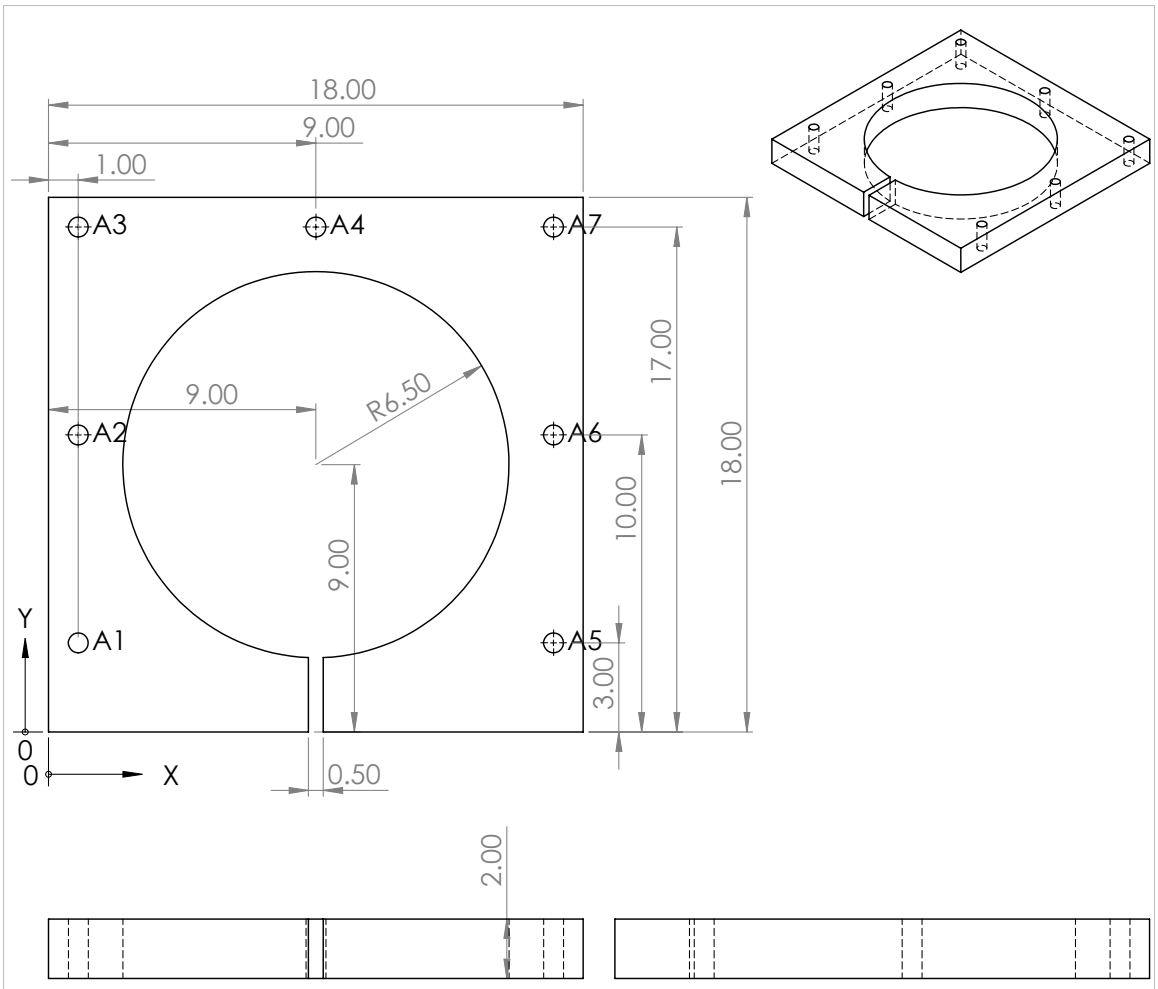

TAG	X LOC	Y LOC
A1	1.00	3.00
A2	1.00	10.00
A3	1.00	17.00
A4	9.00	17.00
A5	17.00	3.00
A6	17.00	10.00
A7	17.00	17.00

Note: All holes are M16 clearance

24x24x2" steel billet will be provided

Bolt-up pattern matches steel base-plate

13" dia center hole should fit aluminum drum

MATERIAL Plain Carbon Steel

FINISH

DO NOT SCALE DRAWING

SIZE A | DWG. NO. Collar Clamp | REV.

SCALE:1:10 | WEIGHT: 105.70 | SHEET 1 OF 1

Figure A.5: Steel collar clamp used to set yaw angle. Dimensions are in inches.

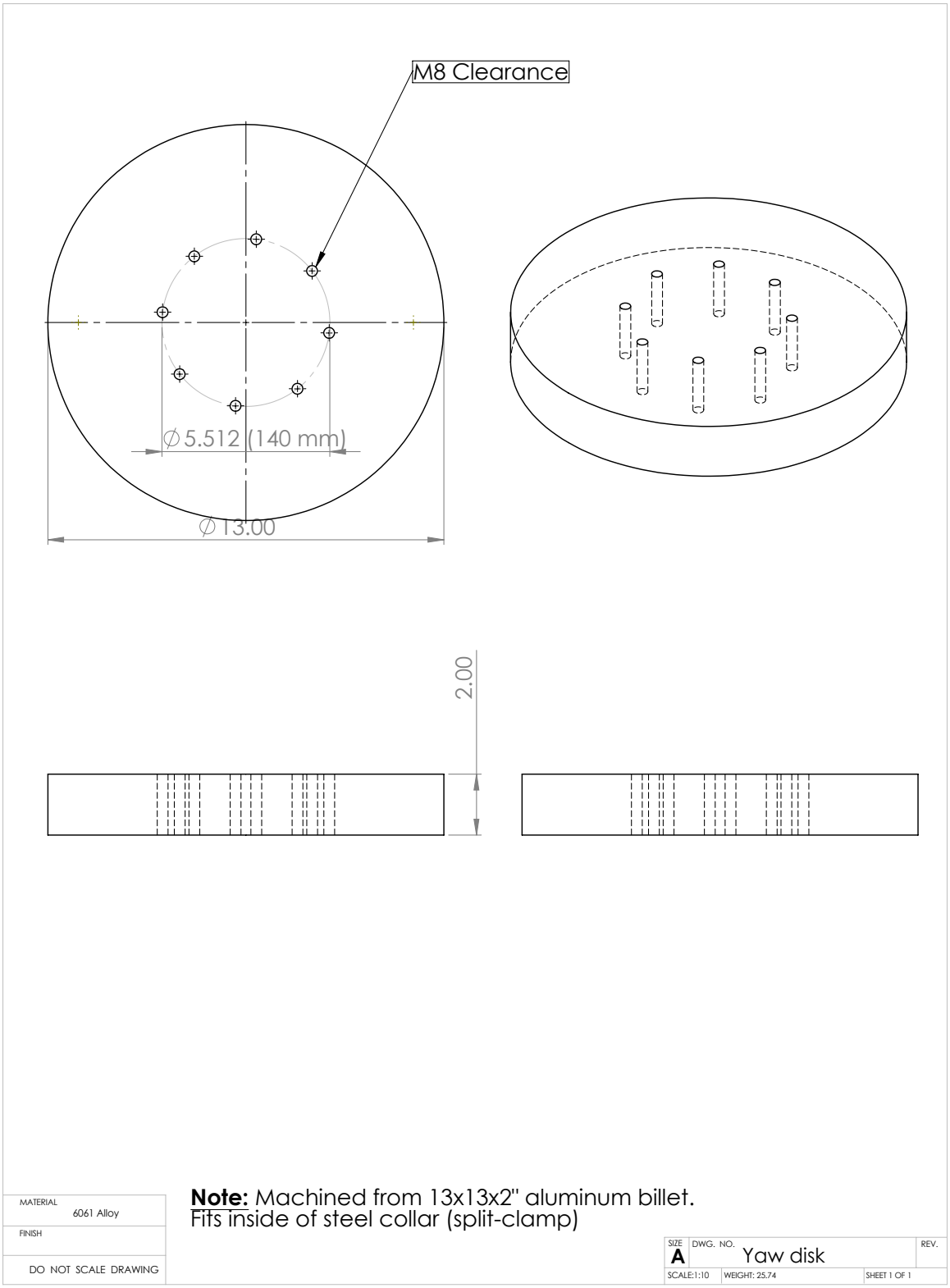

Figure A.6: Yaw-angle disk. Dimensions are in inches.

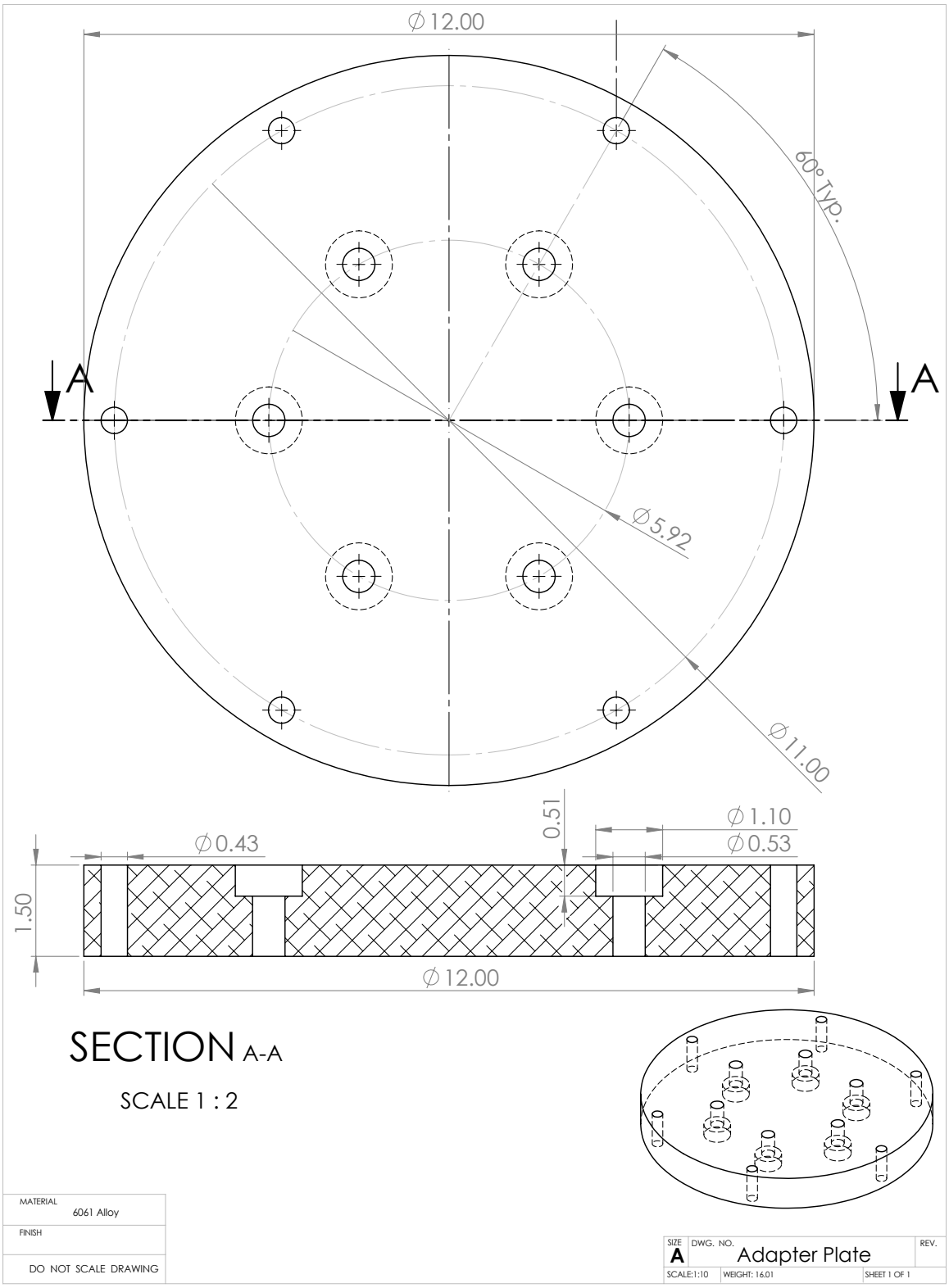

Figure A.7: Adapter plate between load cell and foil tang clamp. Dimensions are in inches.

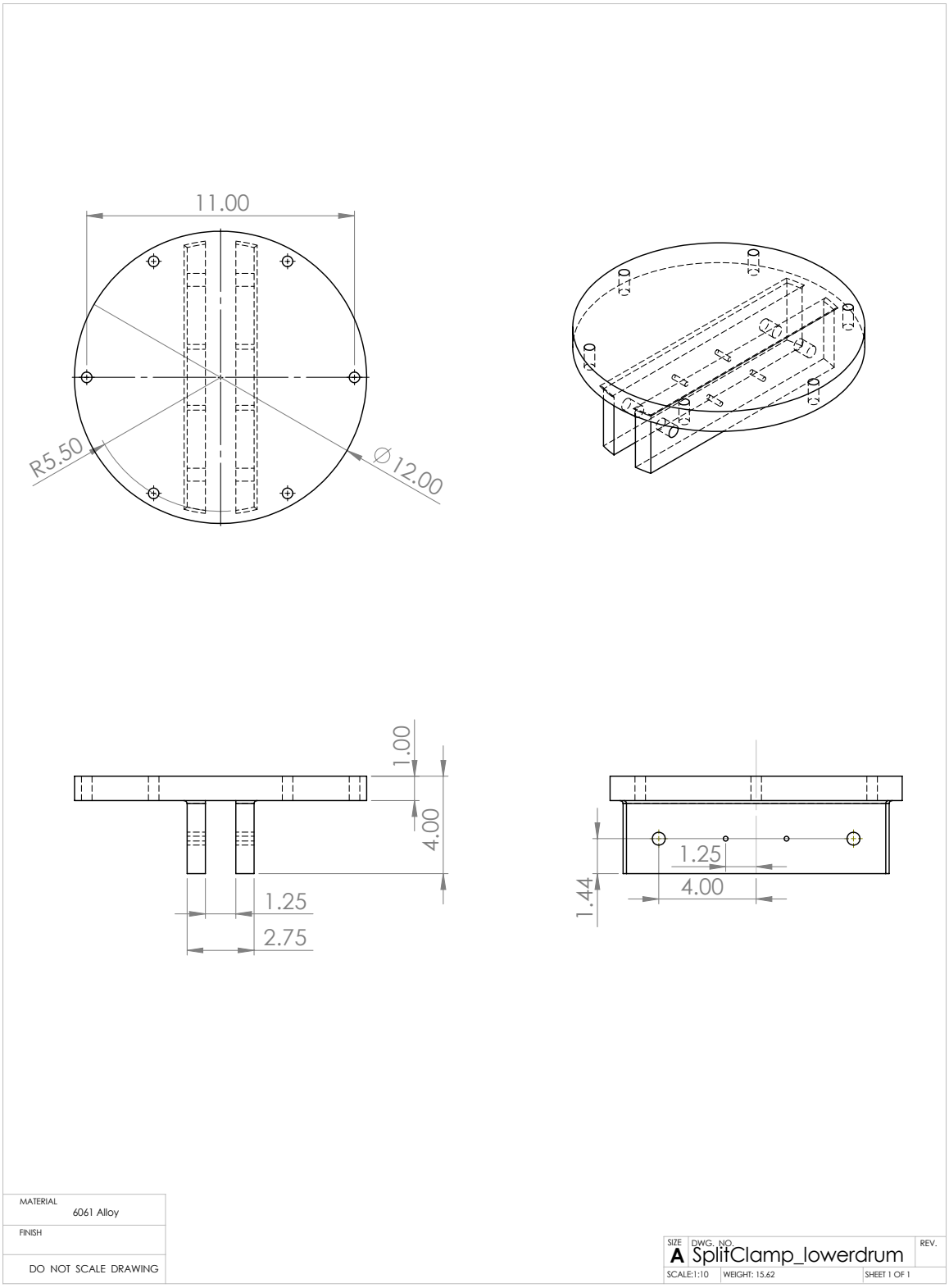

Figure A.8: Foil tang clamp. Dimensions are in inches.

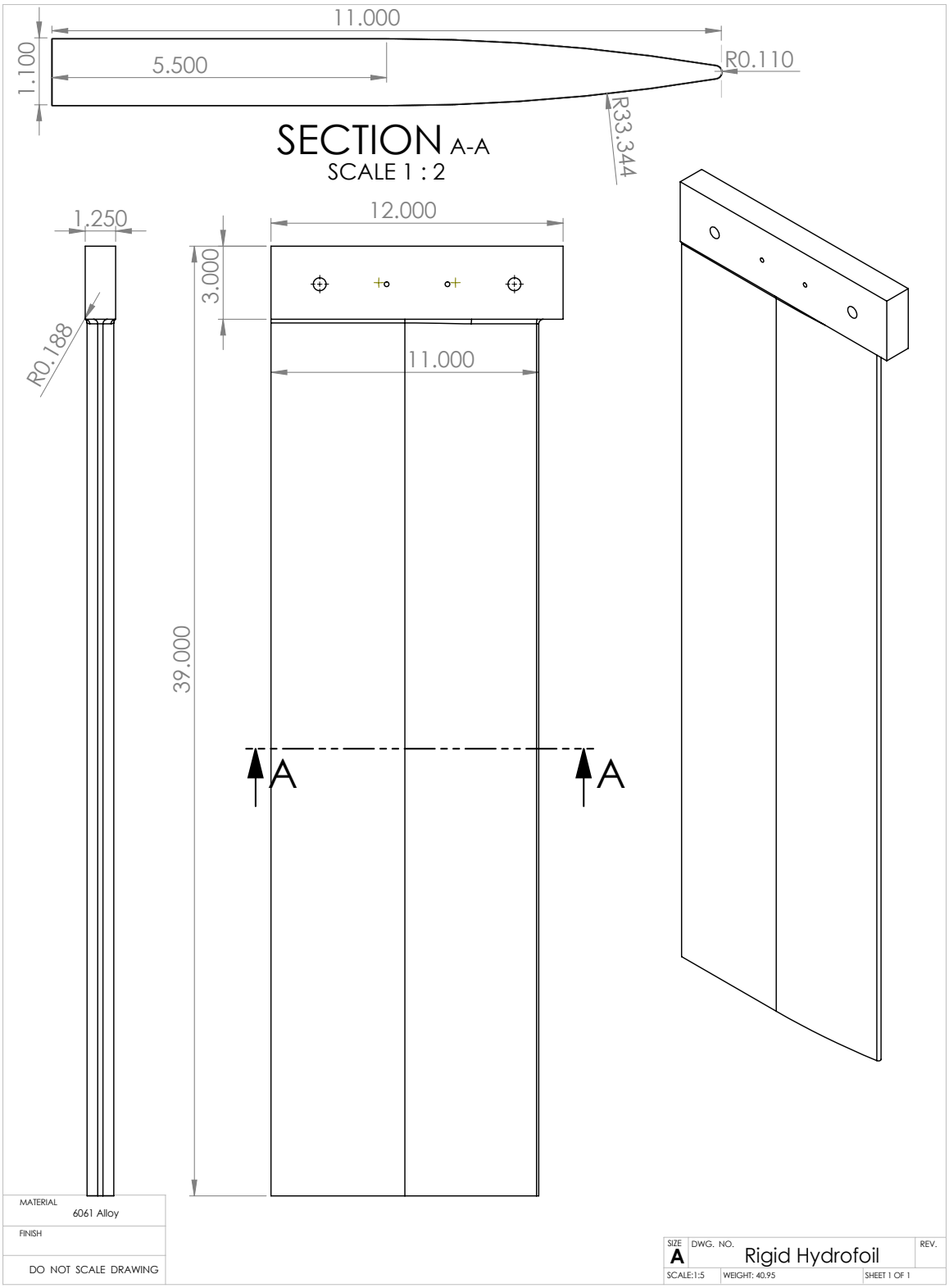

Figure A.9: Rigid model 0. Dimensions are in inches.

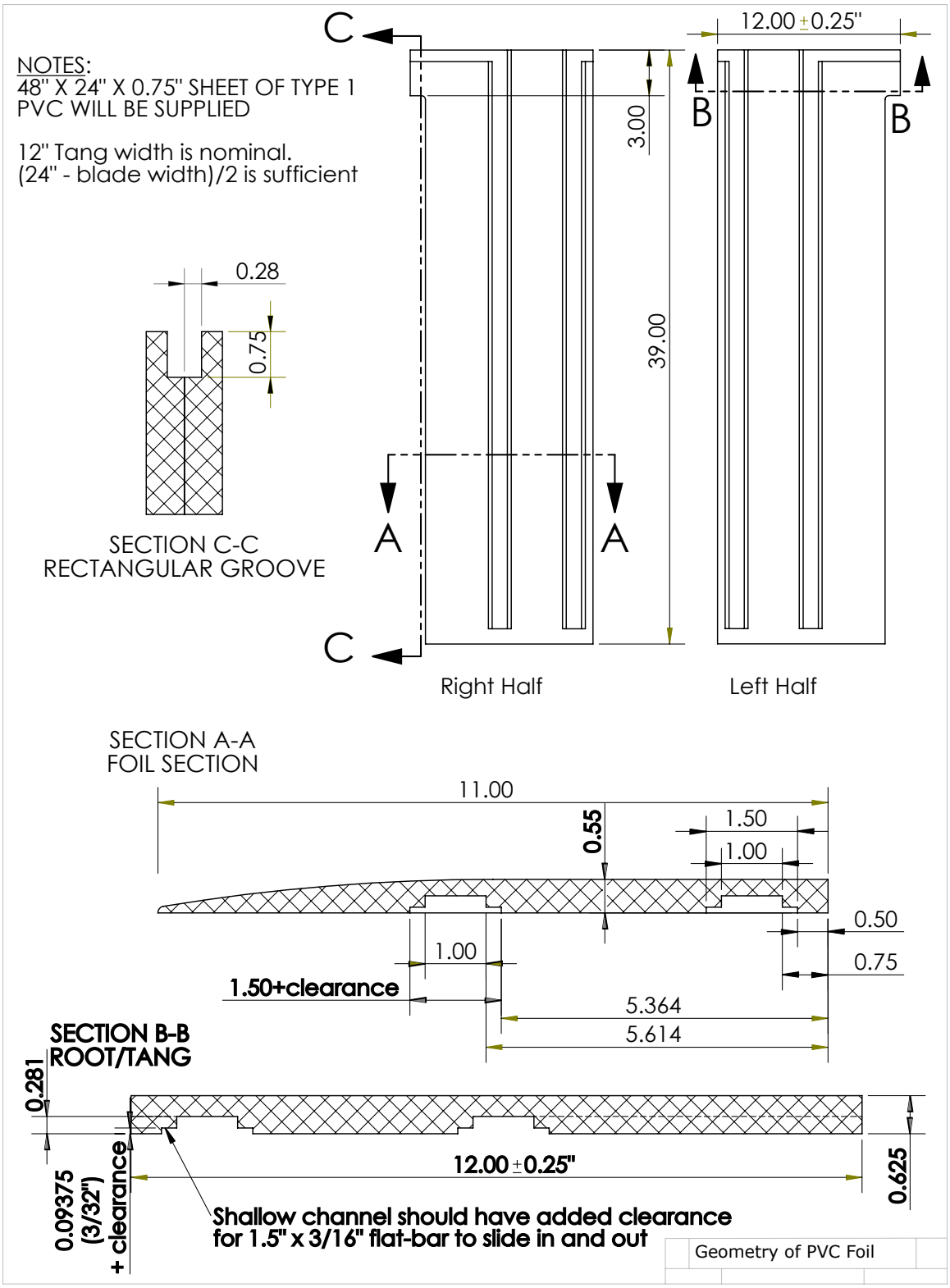

Figure A.10: Flexible model 1. Dimensions are in inches.

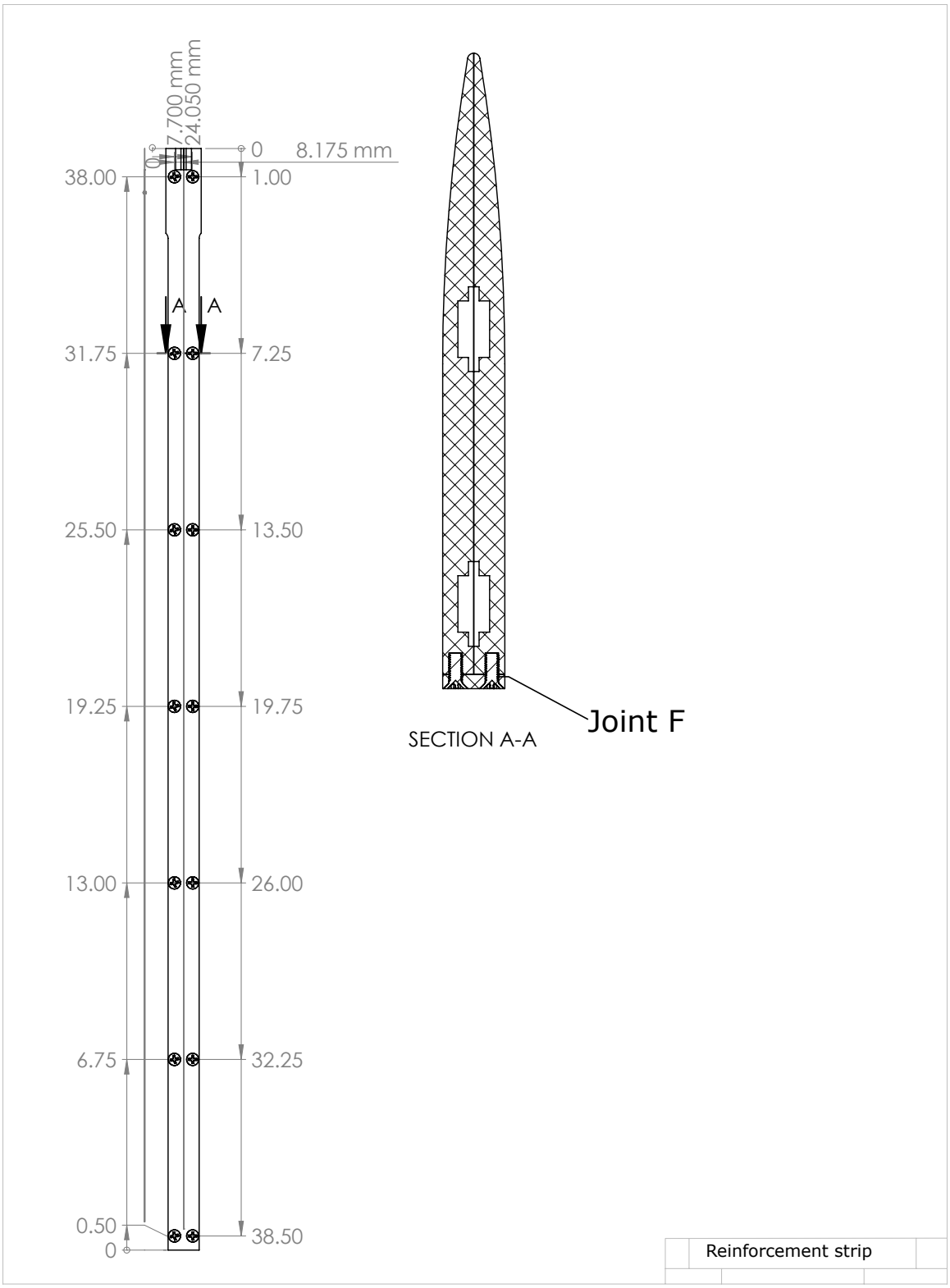

Figure A.11: Flexible model 2: addition of aluminum strip to trailing edge of model 1

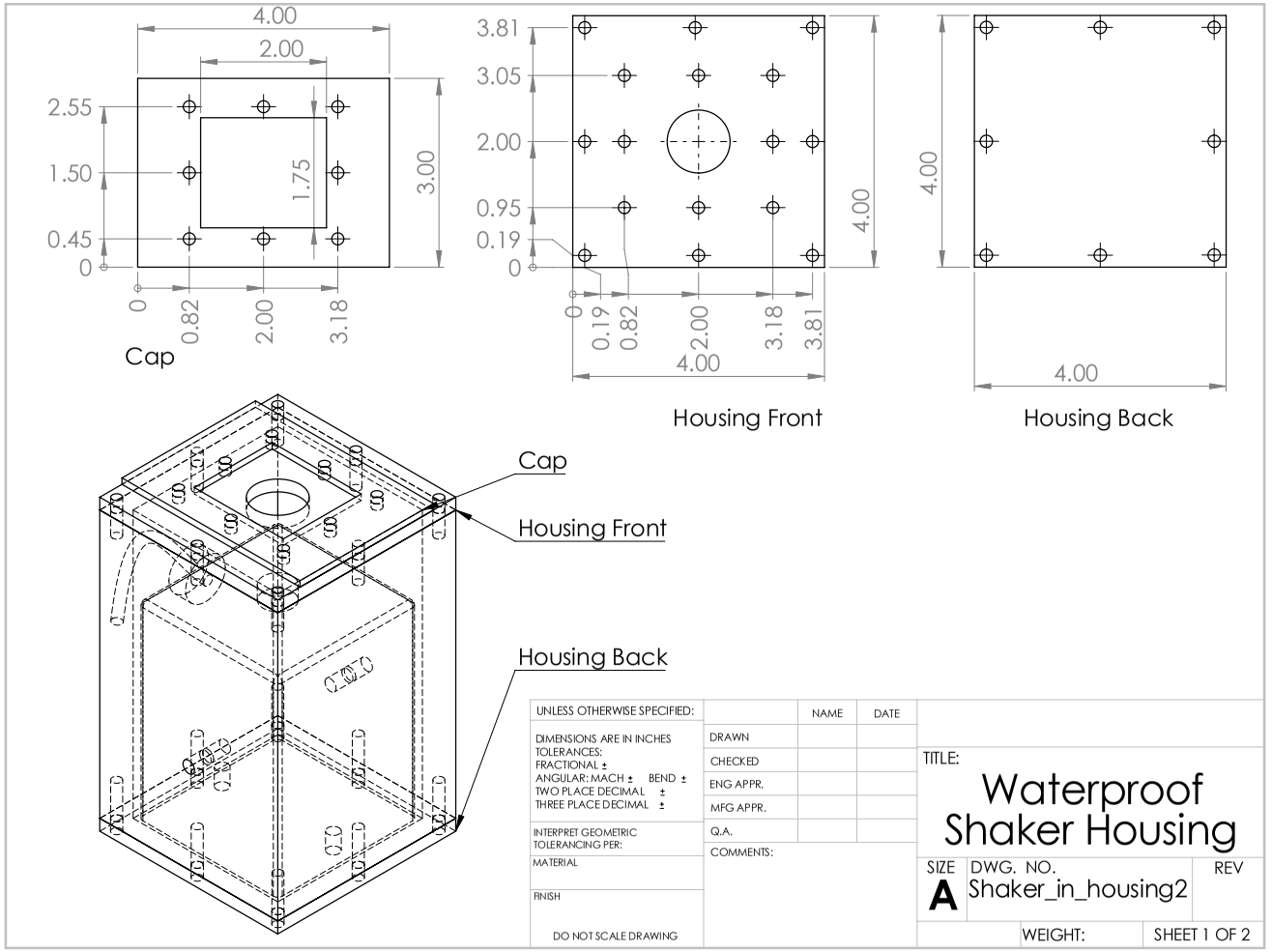

Figure A.12: Waterproof housing for shaker motor - hole patterns

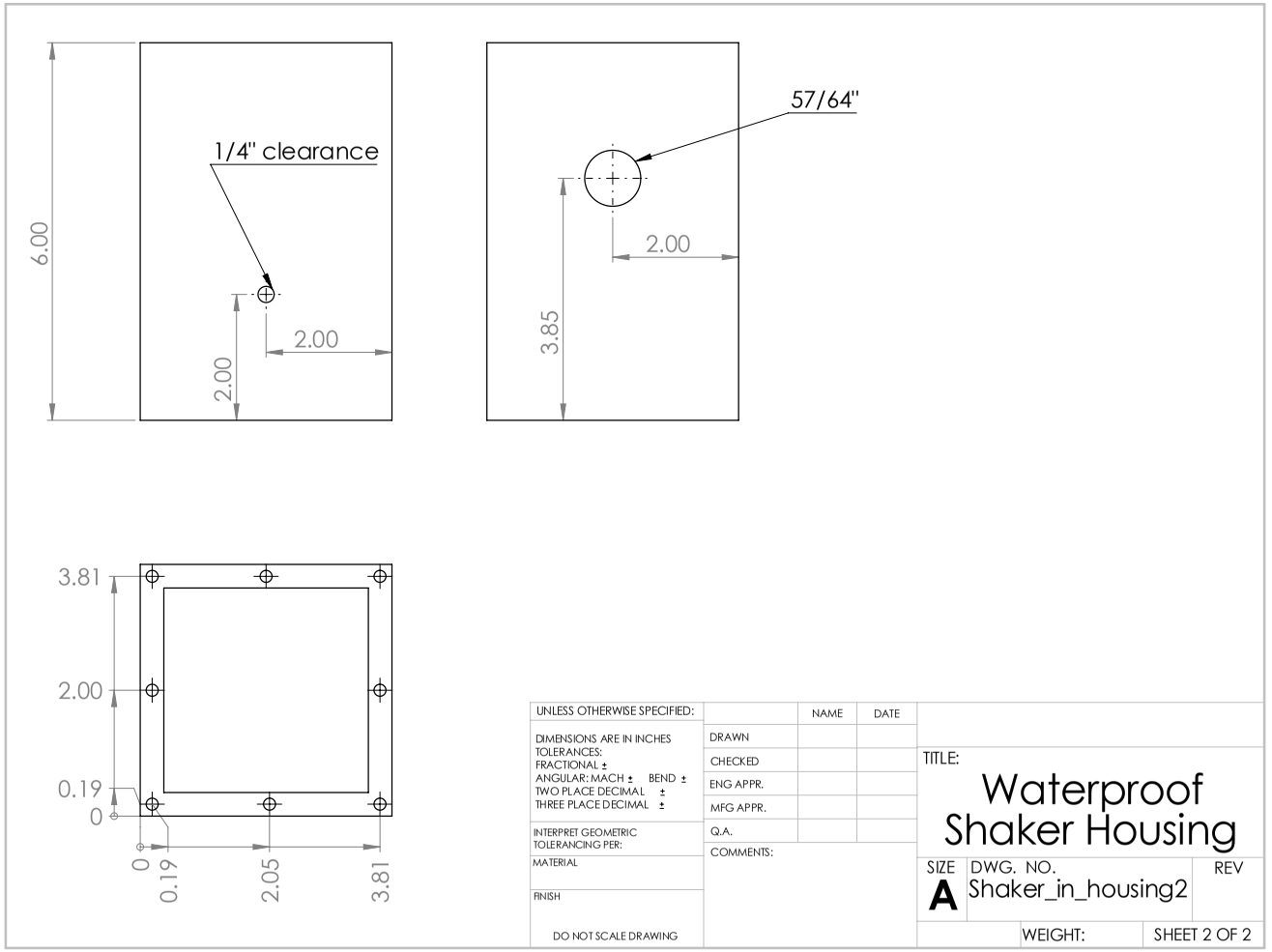

Figure A.13: Exploded view of experimental setup.

A.2 Bolted Joint Calculations

The following are the joint-strength calculations used to determine the torque specifications, pull-out strengths, and factors of safety for the primary load-bearing joints of the experimental rig. All calculations follow the methods of *Budynas et al.* (2011).

Non-Permanent Joint Calculations: Joint "A" - Yaw Disk to Load Cell

								Input Field
								Result / Guideline
Screwed Joint								
Fastener Designation		M	8	x	1.25			
Screw dimensions								
Nominal Diameter	D	8.00	mm	=	8.00E-03	m		
Minor Diameter	D_M	6.46	mm	=	6.46E-03	m		
Mean Diameter	d_m	7.23	mm	=	7.23E-03	m		
Min Length	L(min)	64.20	mm	=	6.42E-02	m	**If min>max, use Max value as limit**	
Max Length	L(max)	64.70	mm	=	6.47E-02	m		
Length	L	60	mm	=	6.00E-02	m		
Minor Area	A_M	32.8	mm^2	=	3.28E-05	m^2	Shigley, p. 398	
Tensile Area	A_T	36.6	mm^2	=	3.66E-05	m^2		
Thread half-cone angle	α	30	deg	=	5.24E-01	rad		
Bolt Properties								
Young's Modulus	E_b	208	Gpa	=	2.08E+11	Pa		
Washer-Shoulder Diameter	D_W	12	mm	=	1.20E-02	m		
Req'd Proof Strength	S_p(min)	301	Mpa	=	3.01E+08	Pa		
Proof Strength	S_p	830	Mpa	=	8.30E+08	Pa		
Yield Strength	S_y	850	Mpa	=	8.50E+08	Pa	Shigley, p. 420	
Ultimate Strength	S_Ut	1040	Mpa	=	1.04E+09	Pa		
Nut and Washer								
Washer Thickness	T_W	1.4	mm	=	1.40E-03	m		
Washer Modulus	E_W	210	Gpa	=	2.10E+11	Pa		
Material properties								
Collar Friction Coeff	f_c	0.15					hardened steel	
Thread-pair Friction Coeff	f	0.2					(steel-steel; dry)	
Frustrum Angle	alpha	30	deg	=	5.24E-01	rad		
Bolted Members								
Member 1								
Thickness	T_m1	50.8	mm	=	5.08E-02	m		
Young's Modulus	E_m1	70	Gpa	=	7.00E+10	Pa		
Member 2 (Female Threaded)								
Female Threaded Depth	T_m2	12.5	mm	=	1.25E-02	m		
Young's Modulus	E_m2	208	Gpa	=	2.08E+11	Pa		
Joint Loading								
Joint Separation Force	F_e	4169	N	=	9.37E+02	lbf	From load calculations	
Minimum Pre-tension	F_i(min)	3150	N	=	7.08E+02	lbf	Iterate on pre-tension	
Spec'd Pre-Load Tension	F_i	10000	N	=	2.25E+03	lbf		
Results								
Total Member Stiffness	K_Eff	5.13E+08	N/m	=	5.13E+05	N/mm		
Fastener Spring Const	K_b	1.66E+08	N/m	=	1.66E+05	N/mm		
Joint Stiffness Constant	C	2.45E-01						
Torque Coefficient	K_torque	0.225						
Req'd Nut Torque	T	17.97	N-m	=	5.53E+00	lbf-ft		
Member Force	F_m	-6.85E+03	N	=	-1.54E+03	lbf	Negative indicates compressive force	
Bolt Force	F_b	1.10E+04	N	=	2.48E+03	lbf		
Proof-Strength	F_p	3.04E+04	N					
Load Factor	**n**	**20.0**					Proof stress safety factor (excl. pre-tension)	
Total safety factor	**N**	**2.8**					Proof stress safety factor (incl. pre-tension)	
Separation Factor	n_0	3.2					Safety factor on external load by **joint separation criterion**	

Non-Permanent Joint Calculations: Joint "B" - Collar Clamp to Steel Base-Plate

Input Field
Result / Guideline

Thru-Bolted Connection								
Bolt Designation		M	16	x	2			
Bolt Dimensions								
Nominal Diameter	D	16.00	mm	=	0.0160	m		
Minor Diameter	D_M	13.55	mm	=	0.0135	m		
Mean Diameter	d_m	14.77	mm	=	0.0148	m		
Min Length	L(min)	82.50	mm	=	0.0825	m		
Target Length	L(ideal)	88.50	mm	=	0.0885	m		
Length	L	100	mm	=	1.00E-01	m		
Minor Area	A_M	144.1	mm^2	=	1.44E-04	m^2		
Req'd Tensile Area (based on N=2 proof stress criterion)	A_T(min)	25	mm^2		2.47E-05		Shigley, p. 398 (Geometry Table)	
Tensile Area	A_T	157	mm^2	=	1.57E-04	m^2		
Thread half-cone angle	α	30	deg	=	0.52359878	rad		
Bolt Properties								
Bolt Young's Modulus	E_b	208	Gpa	=	2.08E+11	Pa		
Washer-Shoulder Diameter	D_W	24	mm	=	2.40E-02	m		
Req'd Proof Strength	S_p(min)	65	Mpa	=	6.52E+07	Pa		
Proof Strength	S_p	830	Mpa	=	8.30E+08	Pa	Shigley, p. 420 (Functions of bolt grade)	
Yield Strength	S_y	850	Mpa	=	8.50E+08	Pa		
Ultimate Strength	S_Ut	1040	Mpa	=	1.04E+09	Pa		
Nut and Washer								
Washer Thickness	T_W	3	mm	=	3.00E-03	m		
Washer Young's Modulus	E_W	207	Gpa	=	2.07E+11	Pa		
Nut Thickness	T_N	13	mm	=	1.30E-02	m		
Material properties								
Collar-Friction Coefficient	f_c	0.15					hardened steel	
Thread-pair Friction Coeff	f	0.2					(steel-steel; dry)	
Frustrum Angle	alpha	30	deg	=	5.24E-01	rad		
Bolted Members								
Member 1								
Thickness	T_m1	12.7	mm	=	0.0127	m		
Young's Modulus	E_m1	208	Gpa	=	2.08E+11	Pa		
Member 2								
Thickness	T_m2	50.8	mm	=	0.0508	m		
Young's Modulus	E_m2	208	Gpa	=	2.08E+11	Pa		
Joint Loading								
Joint Separation Force	F_e	1149	N	=	258.26	lbf	From load calculations	
Minimum Pre-tension	F_i(min)	910	N	=	204.62	lbf	Iterate on pre-tension	
Spec'd Pre-Load Tension	F_i	10000	N	=	2248.20	lbf		
Results								
Total Member Stiffness	K_Eff	2.50E+09	N/m	=	2.50E+06	N/mm		
Fastener Spring Const	K_b	6.54E+08	N/m	=	6.54E+05	N/mm		
Joint Stiffness Constant	C	2.08E-01						
Torque Coefficient	K_torque	0.222						
Req'd Nut Torque	T	35.44	N-m	=	26.16	lbf-ft	Use whichever measurement is most convenient	
Req'd Bolt Elongation	dL	0.015	mm	=	1.5E-05	m	Use whichever measurement is most convenient	
Member Force	F_m	########	N	=	-2043.58	lbf	Negative indicates compressive force	
Bolt Force	F_b	1.02E+04	N	=	2301.84	lbf		
Proof-Strength	F_p	1.30E+05	N					
Load Factor	**n**	**504.2**					Proof stress safety factor (excl. pre-tension)	
Total safety factor	**N**	**12.7**					Proof stress safety factor (incl. pre-tension)	
Separation Factor	n_0	11.0					Safety factor on external load by **joint separation criterion**	

Non-Permanent Joint Calculations: Joint "C" - Adapter Plate to Load Cell

								Input Field
Screwed Joint								**Result / Guideline**
Fastener Designation		M	12	x	1.75			
Screw dimensions								
Nominal Diameter	D	12.00	mm	=	1.20E-02	m		
Minor Diameter	D_M	9.86	mm	=	9.86E-03	m		
Mean Diameter	d_m	10.93	mm	=	1.09E-02	m		
Min Length	L(min)	47.95	mm	=	4.79E-02	m	**If min>max, use Max value as limit**	
Max Length	L(max)	41.95	mm	=	4.19E-02	m		
Length	L	40	mm	=	4.00E-02	m		
Minor Area	A_M	76.3	mm^2	=	7.63E-05	m^2	Shigley, p. 398	
Tensile Area	A_T	84.3	mm^2	=	8.43E-05	m^2		
Thread half-cone angle	α	30	deg	=	5.24E-01	rad		
Bolt Properties								
Young's Modulus	E_b	208	Gpa	=	2.08E+11	Pa		
Washer-Shoulder Diameter	D_W	18	mm	=	1.80E-02	m		
Req'd Proof Strength	S_p(min)	190	Mpa	=	1.90E+08	Pa		
Proof Strength	S_p	830	Mpa	=	8.30E+08	Pa		
Yield Strength	S_y	850	Mpa	=	8.50E+08	Pa	Shigley, p. 420	
Ultimate Strength	S_Ut	1040	Mpa	=	1.04E+09	Pa		
Nut and Washer								
Washer Thickness	T_W	4.8	mm	=	4.80E-03	m		
Washer Modulus	E_W	210	Gpa	=	2.10E+11	Pa		
Material properties								
Collar Friction Coeff	f_c	0.15					hardened steel	
Thread-pair Friction Coeff	f	0.2					(steel-steel; dry)	
Frustrum Angle	alpha	30	deg	=	5.24E-01	rad		
Bolted Members								
Member 1								
Thickness	T_m1	25.146	mm	=	2.51E-02	m		
Young's Modulus	E_m1	70	Gpa	=	7.00E+10	Pa		
Member 2 (Female Threaded)								
Female Threaded Depth	T_m2	12	mm	=	1.20E-02	m		
Young's Modulus	E_m2	208	Gpa	=	2.08E+11	Pa		
Joint Loading								
Joint Separation Force	F_e	3809	N	=	8.56E+02	lbf	From load calculations	
Minimum Pre-tension	F_i(min)	2771	N	=	6.23E+02	lbf	Iterate on pre-tension	
Spec'd Pre-Load Tension	F_i	15000	N	=	3.37E+03	lbf		
Results								
Total Member Stiffness	K_Eff	1.40E+09	N/m	=	1.40E+06	N/mm		
Fastener Spring Const	K_b	5.25E+08	N/m	=	5.25E+05	N/mm		
Joint Stiffness Constant	C	2.72E-01						
Torque Coefficient	K_torque	0.224						
Req'd Nut Torque	T	40.26	N-m	=	29.7	lbf-ft		
Member Force	F_m	-1.22E+04	N	=	-2.75E+03	lbf	Negative indicates compressive force	
Bolt Force	F_b	1.60E+04	N	=	3.61E+03	lbf		
Proof-Strength	F_p	7.00E+04	N					
Load Factor	**n**	**53.0**					Proof stress safety factor (excl. pre-tension)	
Total safety factor	**N**	**4.4**					Proof stress safety factor (incl. pre-tension)	
Separation Factor	n_0	5.4					Safety factor on external load by **joint separation criterion**	

Non-Permanent Joint Calculations: Joint "D" - Load Cell Adapter Plate to Tang Clamp

Input Field
Result / Guideline

Thru-Bolted Connection								
Bolt Designation		M	10	x	1.5			
Bolt Dimensions								
Nominal Diameter	D	10.00	mm	=	0.0100	m		
Minor Diameter	D_M	8.16	mm	=	0.0082	m		
Mean Diameter	d_m	9.08	mm	=	0.0091	m		
Min Length	L(min)	77.50	mm	=	0.0775	m		
Target Length	L(ideal)	82.00	mm	=	0.0820	m		
Length	L	110	mm	=	1.10E-01	m		
Minor Area	A_M	52.3	mm^2	=	5.23E-05	m^2		
Req'd Tensile Area (based on N=2 proof stress criterion)	A_T(min)	21	mm^2		2.05E-05		Shigley, p. 398 (Geometry Table)	
Tensile Area	A_T	58	mm^2	=	5.80E-05	m^2		
Thread half-cone angle	α	30	deg	=	0.52359878	rad		
Bolt Properties								
Bolt Young's Modulus	E_b	208	Gpa	=	2.08E+11	Pa		
Washer-Shoulder Diameter	D_W	15	mm	=	1.50E-02	m		
Req'd Proof Strength	S_p(min)	147	Mpa	=	1.47E+08	Pa		
Proof Strength	S_p	830	Mpa	=	8.30E+08	Pa	Shigley, p. 420 (Functions of bolt grade)	
Yield Strength	S_y	850	Mpa	=	8.50E+08	Pa		
Ultimate Strength	S_Ut	1040	Mpa	=	1.04E+09	Pa		
Nut and Washer								
Washer Thickness	T_W	2	mm	=	2.00E-03	m		
Washer Young's Modulus	E_W	210	Gpa	=	2.10E+11	Pa		
Nut Thickness	T_N	10	mm	=	1.00E-02	m		
Material properties								
Collar-Friction Coefficient	f_c	0.15					hardened steel	
Thread-pair Friction Coeff	f	0.2					(steel-steel; dry)	
Frustrum Angle	alpha	30	deg	=	5.24E-01	rad		
Bolted Members								
Member 1								
Thickness	T_m1	38.1	mm	=	0.0381	m		
Young's Modulus	E_m1	70	Gpa	=	7E+10	Pa		
Member 2								
Thickness	T_m2	25.4	mm	=	0.0254	m		
Young's Modulus	E_m2	70	Gpa	=	7E+10	Pa		
Joint Loading								
Joint Separation Force	F_e	1522	N	=	342.10	lbf	From load calculations	
Minimum Pre-tension	F_i(min)	1008	N	=	226.68	lbf	Iterate on pre-tension	
Spec'd Pre-Load Tension	F_i	8000	N	=	1798.56	lbf		
Results								
Total Member Stiffness	K_Eff	5.70E+08	N/m	=	5.70E+05	N/mm		
Fastener Spring Const	K_b	2.90E+08	N/m	=	2.90E+05	N/mm		
Joint Stiffness Constant	C	3.37E-01						
Torque Coefficient	K_torque	0.224						
Req'd Nut Torque	T	17.92	N-m	=	2.51	lbf-ft	Use whichever measurement is most convenient	
Req'd Bolt Elongation	dL	0.028	mm	=	2.8E-05	m	Use whichever measurement is most convenient	
Member Force	F_m	########	N	=	-1571.88	lbf	Negative indicates compressive force	
Bolt Force	F_b	8.51E+03	N	=	1913.99	lbf		
Proof-Strength	F_p	4.81E+04	N					
Load Factor	**n**	**78.2**					Proof stress safety factor (excl. pre-tension)	
Total safety factor	**N**	**5.7**					Proof stress safety factor (incl. pre-tension)	
Separation Factor	n_0	7.9					Safety factor on external load by **joint separation criterion**	

Non-Permanent Joint Calculations: Joint "E" - Foil Tang Clamp

							Input Field
							Result / Guideline
Thru-Bolted Connection							
Bolt Designation		M	12	x	1.75		
Bolt Dimensions							
Nominal Diameter	D	12.00	mm	=	0.0120	m	
Minor Diameter	D_M	13.55	mm	=	0.0135	m	
Mean Diameter	d_m	12.77	mm	=	0.0128	m	
Min Length	L(min)	86.85	mm	=	0.0869	m	
Target Length	L(ideal)	92.10	mm	=	0.0921	m	
Length	L	140	mm	=	1.40E-01	m	
Minor Area	A_M	144.1	mm^2	=	1.44E-04	m^2	
Req'd Tensile Area (based on N=2 proof stress criterion)	A_T(min)	25	mm^2		2.49E-05		Shigley, p. 398 (Geometry Table)
Tensile Area	A_T	157	mm^2	=	1.57E-04	m^2	
Thread half-cone angle	α	30	deg	=	0.523598776	rad	
Bolt Properties							
Bolt Young's Modulus	E_b	208	Gpa	=	2.08E+11	Pa	
Washer-Shoulder Diameter	D_W	18	mm	=	1.80E-02	m	
Req'd Proof Strength	S_p(min)	66	Mpa	=	6.59E+07	Pa	
Proof Strength	S_p	830	Mpa	=	8.30E+08	Pa	Shigley, p. 420 (Functions of bolt grade)
Yield Strength	S_y	850	Mpa	=	8.50E+08	Pa	
Ultimate Strength	S_Ut	1040	Mpa	=	1.04E+09	Pa	
Nut and Washer							
Washer Thickness	T_W	2.5	mm	=	2.50E-03	m	
Washer Young's Modulus	E_W	207	Gpa	=	2.07E+11	Pa	
Nut Thickness	T_N	12	mm	=	1.20E-02	m	
Material properties							
Collar-Friction Coefficient	f_c	0.15					hardened steel
Thread-pair Friction Coeff	f	0.2					(steel-steel; dry)
Frustrum Angle	alpha	30	deg	=	5.24E-01	rad	
Bolted Members							
Member 1							
Thickness	T_m1	38.1	mm	=	0.0381	m	
Young's Modulus	E_m1	71	Gpa	=	71000000000	Pa	
Member 2							
Thickness	T_m2	31.75	mm	=	0.03175	m	
Young's Modulus	E_m2	71	Gpa	=	71000000000	Pa	
Joint Loading							
Joint Separation Force	F_e	1149	N	=	258.26	lbf	From load calculations
Minimum Pre-tension	F_i(min)	809	N	=	181.95	lbf	Iterate on pre-tension
Spec'd Pre-Load Tension	F_i	10000	N	=	2248.20	lbf	
Results							
Total Member Stiffness	K_Eff	6.92E+08	N/m	=	6.92E+05	N/mm	
Fastener Spring Const	K_b	2.90E+08	N/m	=	2.90E+05	N/mm	
Joint Stiffness Constant	C	2.95E-01					
Torque Coefficient	K_torque	0.241					
Req'd Nut Torque	T	28.96	N-m	=	2.45	lbf-ft	Use whichever measurement is most convenient
Req'd Bolt Elongation	dL	0.034	mm	=	3.4E-05	m	Use whichever measurement is most convenient
Member Force	F_m	-9.19E+03	N	=	-2066.25	lbf	Negative indicates compressive force
Bolt Force	F_b	1.03E+04	N	=	2324.51	lbf	
Proof-Strength	F_p	1.30E+05	N				
Load Factor	**n**	**354.5**					Proof stress safety factor (excl. pre-tension)
Total safety factor	**N**	**12.6**					Proof stress safety factor (incl. pre-tension)
Separation Factor	n_0	12.4					Safety factor on external load by **joint separation criterion**

Non-Permanent Joint Calculations: Joint F- Trailing Edge Reinforcement for Model 2

								Input Field
Screwed Joint								**Result / Guideline**
Fastener Designation		M	6	x	1			
Screw dimensions								
Nominal Diameter	D	6.00	mm	=	6.00E-03	m		
Minor Diameter	D_M	4.92	mm	=	4.92E-03	m		
Mean Diameter	d_m	5.46	mm	=	5.46E-03	m		
Min Length	L(min)	15.45	mm	=	1.55E-02	m	**If min>max, use Max value as limit**	
Max Length	L(max)	18.95	mm	=	1.90E-02	m		
Length	L	16	mm	=	1.60E-02	m		
Minor Area	A_M	19	mm^2	=	1.90E-05	m^2	Shigley, p. 398	
Tensile Area	A_T	21.1	mm^2	=	2.11E-05	m^2		
Thread half-cone angle	α	30	deg	=	5.24E-01	rad		
Bolt Properties								
Young's Modulus	E_b	208	Gpa	=	2.08E+11	Pa		
Washer-Shoulder Diameter	D_W	9	mm	=	9.00E-03	m		
Req'd Proof Strength	S_p(min)	26	Mpa	=	2.60E+07	Pa		
Proof Strength	S_p	830	Mpa	=	8.30E+08	Pa		
Yield Strength	S_y	850	Mpa	=	8.50E+08	Pa	Shigley, p. 420	
Ultimate Strength	S_Ut	1040	Mpa	=	1.04E+09	Pa		
Nut and Washer								
Washer Thickness	T_W	0.1	mm	=	1.00E-04	m		
Washer Modulus	E_W	210	Gpa	=	2.10E+11	Pa		
Material properties								
Collar Friction Coeff	f_c	0.15					hardened steel	
Thread-pair Friction Coeff	f	0.5					(steel-steel; dry)	
Frustrum Angle	alpha	30	deg	=	5.24E-01	rad		
Bolted Members								
Member 1								
Thickness	T_m1	6.35	mm	=	6.35E-03	m		
Young's Modulus	E_m1	70	Gpa	=	7.00E+10	Pa		
Member 2 (Female Threaded)								
Female Threaded Depth	T_m2	12.5	mm	=	1.25E-02	m		
Young's Modulus	E_m2	3.36	Gpa	=	3.36E+09	Pa		
Joint Loading								
Joint Separation Force	F_e	100	N	=	2.25E+01	lbf	From load calculations	
Minimum Pre-tension	F_i(min)	51	N	=	1.15E+01	lbf	Iterate on pre-tension	
Spec'd Pre-Load Tension	F_i	500	N	=	1.12E+02	lbf		
Results								
Total Member Stiffness	K_Eff	4.61E+08	N/m	=	4.61E+05	N/mm		
Fastener Spring Const	K_b	4.41E+08	N/m	=	4.41E+05	N/mm		
Joint Stiffness Constant	C	4.89E-01						
Torque Coefficient	K_torque	0.393						
Req'd Nut Torque	T	1.18	N-m	=	1.74E-01	lbf-ft		
Member Force	F_m	-4.49E+02	N	=	-1.01E+02	lbf	Negative indicates compressive force	
Bolt Force	F_b	5.49E+02	N	=	1.23E+02	lbf		
Proof-Strength	F_p	1.75E+04	N					
Load Factor	**n**	**347.9**					Proof stress safety factor (excl. pre-tension)	
Total safety factor	**N**	**31.9**					Proof stress safety factor (incl. pre-tension)	
Separation Factor	n_0	9.8					Safety factor on external load by **joint separation criterion**	

APPENDIX B

Experimental Run Log

#	Date	Run Name	Facility	Model	AR_h	α, deg	Speed, m/s	Fn_h	P_0, mbar	Water Temp, C	Comment	Shaker
1	12/17/2013	Run316	MHL	Model 0	0.5	0	0.00	1.50	1000	15.6	Hammer test; mid chord excitations except for the last strike at TE	OFF
2	7/30/2013	Run116	MHL	Model 0	0.5	0	3.51	1.50	1000	20.5	Ramp up	OFF
3	12/17/2013	Run317	MHL	Model 0	0.5	-5	3.51	1.73	1000	15.6	calibration run	OFF
4	7/30/2013	Run117	MHL	Model 0	0.5	-5	4.10	2.02	1000	20.5	0.5in h2o	OFF
5	7/30/2013	Run118	MHL	Model 0	0.5	-5	4.68	2.31	1000	20.5	0in h2o	OFF
6	7/30/2013	Run119	MHL	Model 0	0.5	0	5.27	1.73	1000	20.5	0in h2o	OFF
7	12/17/2013	Run318	MHL	Model 0	0.5	0	5.85	2.02	1000	15.6	High speed calibration run	OFF
8	12/17/2013	Run319	MHL	Model 0	0.5	0	2.34	2.31	1000	15.6	Ramped calibration run 60s ramp up;	OFF
9	7/30/2013	Run120	MHL	Model 0	0.5	5	3.51	1.73	1000	20.5	ramp up; 0in h2o at speed	OFF
10	7/30/2013	Run121	MHL	Model 0	0.5	5	4.10	2.02	1000	20.5	0in h2o; fully base ventilated	OFF
11	12/19/2013	Run389	MHL	Model 0	0.5	5	4.10	2.31	1000	15.6	FW hammer test	OFF
12	7/30/2013	Run122	MHL	Model 0	0.5	10	4.68	1.73	1000	20.5	0in h2o	OFF
13	7/30/2013	Run123	MHL	Model 0	0.5	10	5.27	2.02	1000	20.5	0in h2o	OFF
14	12/17/2013	Run320	MHL	Model 0	0.5	10	5.85	2.31	1000	15.6	High speed calibration	OFF
15	12/17/2013	Run321	MHL	Model 0	0.5	10	2.34	2.02	1000	15.6	60s ram up	OFF
16	12/17/2013	Run322	MHL	Model 0	0.5	10	2.34	2.31	1000	15.6	60s ramp down	OFF
17	12/17/2013	Run324	MHL	Model 0	0.5	10	2.63	2.31	1000	15.6	Small LE bubble forced	OFF
18	12/17/2013	Run323	MHL	Model 0	0.5	10	2.93	1.73	1000	15.6	Nice triggered cavity. Clearly laminar separation	OFF
19	12/17/2013	Run330	MHL	Model 0	0.5	10	3.22	1.73	1000	15.6	45s ramp down Interesting washout; appears laminar	OFF
20	12/17/2013	Run325	MHL	Model 0	0.5	15	3.51	1.73	1000	15.6	Tripped cavity. Blower worked	OFF
21	12/17/2013	Run326	MHL	Model 0	0.5	15	4.10	1.73	1000	15.6	Nice cavity tripped by blower. Laminar washout	OFF
22	12/17/2013	Run327	MHL	Model 0	0.5	15	4.68	2.02	1000	15.6	Blower tripped cavity. Interesting "texture" to the cavity wall.	OFF
23	12/17/2013	Run328	MHL	Model 0	0.5	15	5.27	2.02	1000	15.6	Triggered FV cavity	OFF
24	12/17/2013	Run329	MHL	Model 0	0.5	15	5.85	2.31	1000	15.6	FA run. hi-speed	OFF
25	12/17/2013	Run329b	MHL	Model 0	0.5	15	5.85	1.73	1000	15.6	Tripped cavity	OFF
26	12/17/2013	Run331	MHL	Model 0	0.5	20	2.34	1.73	1000	15.6	60s ramp up; wetted	OFF
27	12/17/2013	Run332	MHL	Model 0	0.5	20	2.34	2.02	1000	15.6	60s ramp down. FW	OFF
28	12/17/2013	Run336	MHL	Model 0	0.5	20	2.34	2.31	1000	15.6	60 s ramp down. Laminar washout. Don't think camera got it.	OFF
29	12/17/2013	Run336b	MHL	Model 0	0.5	20	2.34	1.73	1000	15.6	Repeat of 60s ramp down. Manually triggered	OFF
30	12/17/2013	Run333	MHL	Model 0	0.5	25	2.93	1.73	1000	15.6	Blower didn't trigger cavity; manual inception	OFF
31	7/30/2013	Run124	MHL	Model 0	0.5	25	3.51	2.02	1000	20.5	Ramp up; Manual inception at >10fps; appears PV; Actually 5deg; correct L,D accordingly	OFF
32	7/30/2013	Run128	MHL	Model 0	0.5	25	3.51	2.31	1000	20.5	Ramp down; manual inception; PV at speed	OFF
33	7/30/2013	Run128b	MHL	Model 0	0.5	25	3.51	2.31	1000	20.5	ramp down; repeat w video	OFF
34	12/17/2013	Run334	MHL	Model 0	0.5	25	3.51	1.73	1000	15.6	Triggered with blower	OFF
35	7/30/2013	Run125	MHL	Model 0	0.5	5	4.10	2.60	1000	20.5	blower failed, Manual inception; 0in h2o ; appears PV	OFF
36	7/30/2013	Run126	MHL	Model 0	0.5	5	4.68	2.60	1000	20.5	0in h2o; blower failed; manual inception on 2nd attempt ; appears PV	OFF
37	7/30/2013	Run127	MHL	Model 0	0.5	5	5.27	2.60	1000	20.5	0in h2o; blower failed; manual inception ; appears PV	OFF
38	12/17/2013	Run335	MHL	Model 0	0.5	5	5.85	2.31	1000	15.6	Untripped high-speed	OFF
39	12/17/2013	Run335b	MHL	Model 0	0.5	5	5.85	2.31	1000	15.6	Blower aimed wrong. Triggered manually	OFF
40	12/18/2013	Run339	MHL	Model 0	0.5	5	1.76	2.31	1000	15.6	Cavity was triggered by blower, washed out by rod, and re-triggered	OFF

#	Date	Run Name	Facility	Model	AR_h	α, deg	Speed, m/s	Fn_h	P_0, mbar	Water Temp, C	Comment	Shaker
41	12/17/2013	Run337	MHL	Model 0	0.5	-5	2.34	2.31	1000	15.6	60s ramp up	OFF
42	12/17/2013	Run338	MHL	Model 0	0.5	0	2.34	2.31	1000	15.6	60s ramp down.	OFF
43	12/18/2013	Run338b	MHL	Model 0	0.5	10	2.34	2.31	1000	15.6	60s ramp down. Repeated last run from yesterday	OFF
44	12/18/2013	Run342	MHL	Model 0	0.5	15	2.34	2.31	1000	15.6	Laminar washout. Nice looking. Some bumps on acceleration, but gone by the time target speed was reached	OFF
45	12/18/2013	Run340	MHL	Model 0	0.5	15	3.51	2.60	1000	15.6	blower triggered cavity	OFF
46	12/18/2013	Run341	MHL	Model 0	0.5	15	5.85	2.89	1000	15.6	FW run at high speed	OFF
47	12/18/2013	Run341b	MHL	Model 0	0.5	15	5.85	2.89	1000	15.6	Blower did not trigger cavity; manually triggered	OFF
48	12/18/2013	Run345	MHL	Model 0	0.5	20	1.76	2.31	1000	15.6	Cavity forced by rod	OFF
49	12/18/2013	Run343	MHL	Model 0	0.5	20	2.34	2.60	1000	15.6	60s ramp up	OFF
50	12/18/2013	Run344	MHL	Model 0	0.5	20	2.34	2.89	1000	15.6	60s ramp down	OFF
51	12/18/2013	Run348	MHL	Model 0	0.5	25	2.34	2.60	1000	15.6	60s ramp down.	OFF
52	7/30/2013	Run152	MHL	Model 0	0.5	25	3.51	2.89	1000	20.5	ramp up; 2in h2o; base ventilated	OFF
53	7/30/2013	Run153	MHL	Model 0	0.5	-5	3.51	2.60	1000	20.5	ramp down; carriage moving before daq starts	OFF
54	12/18/2013	Run346	MHL	Model 0	0.5	-5	3.51	2.89	1000	15.6	thumpthumpthumpsomething in the wheel	OFF
55	12/18/2013	Run346b	MHL	Model 0	0.5	0	3.51	2.60	1000	15.6	Forced by blower. Three "bumps" shortly after triggering where something was in the wheel.	OFF
56	7/30/2013	Run129	MHL	Model 0	0.5	0	4.10	2.89	1000	20.5	0in h2o; manual inception; blower failed	OFF
57	7/30/2013	Run130	MHL	Model 0	0.5	5	4.68	2.89	1000	20.5	Manual inception; 0in h2o	OFF
58	7/30/2013	Run131	MHL	Model 0	0.5	10	5.27	2.60	1000	20.5	0in h2o; blower failed; manual inception	OFF
59	12/18/2013	Run347	MHL	Model 0	0.5	10	5.85	2.89	1000	15.6	Untripped run.	OFF
60	12/18/2013	Run347b	MHL	Model 0	0.5	25	5.85	1.95	1000	15.6	Blower didn't trigger cavity. Wind resistance pushed it a little too far to the side. Manualy triggered.	OFF
61	12/18/2013	Run351	MHL	Model 0	0.5	-5	1.76	1.50	1000	15.6	Low speed; blower triggered	OFF
62	12/18/2013	Run349	MHL	Model 0	0.5	-5	2.34	2.00	1000	15.6	60s ramp up. untriggered	OFF
63	12/18/2013	Run350	MHL	Model 0	0.5	-5	2.34	2.50	1000	15.6	60s ramp down; untripped	OFF
64	12/18/2013	Run354	MHL	Model 0	0.5	-5	2.34	3.00	1000	15.6	60s ramp down. Blower triggered	OFF
65	12/18/2013	Run352	MHL	Model 0	0.5	0	3.51	1.50	1000	15.6	Blower triggered	OFF
66	12/18/2013	Run353	MHL	Model 0	0.5	0	5.85	2.00	1000	15.6	FW high speed run	OFF
67	12/18/2013	Run353b	MHL	Model 0	0.5	0	5.85	2.50	1000	15.6	Blower triggered cavity	OFF
68	12/18/2013	Run357	MHL	Model 0	0.5	0	1.76	3.00	1000	15.6	Blower triggered	OFF
69	12/18/2013	Run355	MHL	Model 0	0.5	5	2.34	1.50	1000	15.6	60s ramp up Untriggered	OFF
70	12/18/2013	Run356	MHL	Model 0	0.5	5	2.34	2.00	1000	15.6	60s ramp down. Untriggered	OFF
71	12/18/2013	Run360	MHL	Model 0	0.5	5	2.34	2.50	1000	15.6	60s ramp down; blower triggered	OFF
72	7/30/2013	Run150	MHL	Model 0	0.5	5	3.51	2.50	1000	20.5	ramp up; 0in h2o at speed; base ventilation only; Actually 15 deg, correct L D accordingly	OFF
73	7/30/2013	Run151	MHL	Model 0	0.5	5	3.51	3.00	1000	20.5	ramp down; blower failed; manual inception	OFF
74	12/18/2013	Run358	MHL	Model 0	0.5	10	3.51	1.50	1000	15.6	blower triggered	OFF
75	7/30/2013	Run132	MHL	Model 0	0.5	10	4.10	2.00	1000	20.5	0in h2o; blower failed; manual inception	OFF
76	12/19/2013	Run388	MHL	Model 0	0.5	10	4.10	2.50	1000	15.6	hammer test underway in FA; 2PS; 2SS	OFF
77	12/19/2013	Run388b	MHL	Model 0	0.5	10	4.10	2.50	1000	15.6	FW hammer test; see video	OFF
78	7/30/2013	Run133	MHL	Model 0	0.5	10	4.68	2.50	1000	20.5	0in h2o; blower failed; manual inception	OFF

#	Date	Run Name	Facility	Model	AR_h	α, deg	Speed, m/s	Fn_h	P_0, mbar	Water Temp, C	Comment	Shaker
79	7/30/2013	Run134	MHL	Model 0	0.5	10	5.27	3.00	1000	20.5	0in h2o; blower failed; manual inception	OFF
80	12/18/2013	Run359	MHL	Model 0	0.5	10	5.85	1.50	1000	15.6	No vortex; untripped	OFF
81	12/18/2013	Run359b	MHL	Model 0	0.5	15	5.85	1.50	1000	15.6	Blower triggered	OFF
82	12/19/2013	Run366	MHL	Model 0	0.5	15	1.76	2.00	1000	15.6	blower triggered	OFF
83	12/18/2013	Run361	MHL	Model 0	0.5	15	2.34	2.00	1000	15.6	60s ramp up; spontaneous	OFF
84	12/18/2013	Run362	MHL	Model 0	0.5	15	2.34	2.50	1000	15.6	45s up 15 down	OFF
85	12/19/2013	Run362b	MHL	Model 0	0.5	15	2.34	3.00	1000	15.6	repeat of last run; 45s up 15s down	OFF
86	12/19/2013	Run363	MHL	Model 0	0.5	15	2.34	3.00	1000	15.6	30s up; 30 down. Forced incptn this time	OFF
87	12/19/2013	Run364	MHL	Model 0	0.5	15	2.34	1.50	1000	15.6	15s up; 45s down; forced incptn	OFF
88	12/19/2013	Run365	MHL	Model 0	0.5	20	2.34	1.50	1000	15.6	5s up; 60s down; forced by blower	OFF
89	12/19/2013	Run367	MHL	Model 0	0.5	20	3.51	2.00	1000	15.6	blower triggered	OFF
90	12/19/2013	Run369	MHL	Model 0	0.5	20	4.10	2.50	1000	15.6	Forced ventilation	OFF
91	12/19/2013	Run370	MHL	Model 0	0.5	20	4.68	3.00	1000	15.6	Blower triggered	OFF
92	12/19/2013	Run368	MHL	Model 0	0.5	20	5.85	1.50	1000	15.6	No vortex inception	OFF
93	12/19/2013	Run368b	MHL	Model 0	0.5	25	5.85	0.75	1000	15.6	no inception; forgot to turn on vvs	OFF
94	12/19/2013	Run368c	MHL	Model 0	0.5	25	5.85	2.00	1000	15.6	blower triggered	OFF
95	12/19/2013	Run377	MHL	Model 0	0.5	25	1.76	2.50	1000	15.6	spontaneous	OFF
96	12/19/2013	Run371	MHL	Model 0	0.5	25	2.34	3.00	1000	15.6	60s up	OFF
97	12/19/2013	Run372	MHL	Model 0	0.5	25	2.34	1.50	1000	15.6	5s up; 60s down; no incptn	OFF
98	12/19/2013	Run373	MHL	Model 0	0.5	30	2.34	0.75	1000	15.6	45s up; 15s down	OFF
99	12/19/2013	Run374	MHL	Model 0	0.5	30	2.34	2.00	1000	15.6	30s up; 30s down	OFF
100	12/19/2013	Run375	MHL	Model 0	0.5	30	2.34	2.50	1000	15.6	15s up; 45 down	OFF
101	12/19/2013	Run376	MHL	Model 0	0.5	30	2.34	3.00	1000	15.6	5s up; 60s down; forced	OFF
102	7/30/2013	Run148	MHL	Model 0	0.5	30	3.51	1.50	1000	20.5	0in h2o at speed	OFF
103	7/30/2013	Run149	MHL	Model 0	0.5	-5	3.51	2.50	1000	20.5	Ramp Down	OFF
104	12/19/2013	Run378	MHL	Model 0	0.5	-5	3.51	3.00	1000	15.6	blower set late. Tripped manually	OFF
105	7/30/2013	Run135	MHL	Model 0	0.5	-5	4.10	3.50	1000	20.5	0in h2o; blower blew after FV reached; spontaneous cavity appeared very early during acceleration (starting vortex?)	OFF
106	7/30/2013	Run136	MHL	Model 0	0.5	0	4.68	2.50	1000	20.5	0in h2o; blower worked; tripping required this time	OFF
107	7/30/2013	Run137	MHL	Model 0	0.5	0	5.27	3.00	1000	20.5	0in h2o; spontaneous cavity at very low speed;	OFF
108	12/19/2013	Run379	MHL	Model 0	0.5	0	5.85	3.50	1000	15.6	no vortex inception	OFF
109	12/19/2013	Run379b	MHL	Model 0	0.5	5	5.85	2.50	1000	15.6	Triggered	OFF
110	12/19/2013	Run380	MHL	Model 0	0.5	5	2.34	3.00	1000	15.6	spontaneous. Past the inception angle	OFF
111	12/19/2013	Run381	MHL	Model 0	0.5	5	2.34	3.50	1000	15.6	60s ramp up	OFF
112	12/19/2013	Run382	MHL	Model 0	0.5	10	2.34	2.50	1000	15.6	5s up; 60s ramp down	OFF
113	7/30/2013	Run146	MHL	Model 0	0.5	10	3.51	2.50	1000	20.5	0in h2o at speed	OFF
114	7/30/2013	Run147	MHL	Model 0	0.5	10	3.51	3.00	1000	20.5	Ramp Down	OFF
115	7/30/2013	Run138	MHL	Model 0	0.5	10	4.10	3.00	1000	20.5	0in h2o; Vortex-induced?	OFF
116	7/30/2013	Run138b	MHL	Model 0	0.5	10	4.10	3.50	1000	20.5	0in h2o; spontaneous incpt early in acceleration this time; no vortex induced mech evident.	OFF
117	12/19/2013	Run387	MHL	Model 0	0.5	15	4.10	2.00	1000	15.6	Hammer test underway; two strikes on SS, one on PS; video	OFF
118	7/30/2013	Run139	MHL	Model 0	0.5	15	4.68	2.50	1000	20.5	Inception very early during acceleration	OFF

#	Date	Run Name	Facility	Model	AR_h	α, deg	Speed, m/s	Fn_h	P_0, mbar	Water Temp, C	Comment	Shaker
119	7/30/2013	Run140	MHL	Model 0	0.5	15	5.27	2.50	1000	20.5	0in h2o; Spontaneous ventilation early in acceleration; LE vortex appears to draw air.	OFF
120	12/19/2013	Run383	MHL	Model 0	0.5	15	5.85	3.00	1000	15.6	high speed. Nozzle caught in PS spraysheet and dragged against foil.	OFF
121	12/19/2013	Run383b	MHL	Model 0	0.5	15	5.85	3.50	1000	15.6	High speed	OFF
122	12/19/2013	Run384	MHL	Model 0	0.5	15	2.34	3.50	1000	15.6	60s ramp up	OFF
123	12/19/2013	Run385	MHL	Model 0	0.5	15	2.34	2.00	1000	15.6	5s up; 60s down	OFF
124	7/30/2013	Run144	MHL	Model 0	0.5	20	3.51	2.00	1000	20.5	Inception early in acceleration; Ramp UP	OFF
125	7/30/2013	Run145	MHL	Model 0	0.5	20	3.51	2.50	1000	20.5	0in h2o at speed	OFF
126	7/30/2013	Run141	MHL	Model 0	0.5	20	4.10	3.00	1000	20.5	0in h2o; early spontaneous inception; LE vortex again	OFF
127	7/30/2013	Run142	MHL	Model 0	0.5	20	4.68	3.50	1000	20.5	use 2nd LED signal in videos; first run with all cams working in long time	OFF
128	7/30/2013	Run143	MHL	Model 0	0.5	20	5.27	2.00	1000	20.5	0in h2o; large spray sheet	OFF
129	12/19/2013	Run386	MHL	Model 0	0.5	25	5.85	2.00	1000	15.6	High speed	OFF
130	7/30/2013	Run110	MHL	Model 0	1	25	3.31	2.50	1000	20.5	Ramp up	OFF
131	12/4/2013	Run224	MHL	Model 0	1	25	3.31	3.00	1000	16	Pressure not measured, valve did not trigger	OFF
132	12/5/2013	Run224b	MHL	Model 0	1	25	3.31	3.00	1000	16		OFF
133	7/29/2013	Run078	MHL	Model 0	1	25	4.14	3.50	1000	20.5	1.5 in H20; Ramp up	OFF
134	7/29/2013	Run079	MHL	Model 0	1	25	4.97	1.95	1000	20.5	-1 in H20	OFF
135	7/29/2013	Run080	MHL	Model 0	1	30	5.79	2.00	1000	20.5	1in H20	OFF
136	12/16/2013	Run314	MHL	Model 0	1	30	0.00	2.50	1000	15.6	zero speed hammer test	OFF
137	7/30/2013	Run111	MHL	Model 0	1	30	3.31	3.00	1000	20.5	Ramp Up	OFF
138	12/5/2013	Run225	MHL	Model 0	1	30	3.31	3.50	1000	16	Pressure transduced didn't trigger	OFF
139	7/29/2013	Run081	MHL	Model 0	1	30	4.14	2.00	1000	20.5	-2in H20	OFF
140	12/16/2013	Run315	MHL	Model 0	1	-5	4.14	2.00	1000	15.6	13.58fps hammer test	OFF
141	7/29/2013	Run082	MHL	Model 0	1	0	4.97	2.00	1000	20.5	-2in h20	OFF
142	12/5/2013	Run226	MHL	Model 0	1	5	4.97	2.00	1000	16		OFF
143	7/29/2013	Run083	MHL	Model 0	1	5	5.79	2.50	1000	20.5	-0.75in h20	OFF
144	12/5/2013	Run227	MHL	Model 0	1	5	2.48	3.00	1000	16	ramp up	OFF
145	12/5/2013	Run228	MHL	Model 0	1	5	2.48	3.50	1000	16	ramp down	OFF
146	12/5/2013	Run229	MHL	Model 0	1	5	3.31	2.00	1000	16	forces with rod.	OFF
147	12/5/2013	Run234	MHL	Model 0	1	5	3.31	2.00	1000	16	ramp down	OFF
148	12/5/2013	Run230	MHL	Model 0	1	10	3.72	2.00	1000	16	forced with rod.	OFF
149	12/5/2013	Run230b	MHL	Model 0	1	10	3.72	2.00	1000	16	rod forced. Cavity chokes???	OFF
150	12/5/2013	Run230c	MHL	Model 0	1	-5	3.72	3.00	1000	16	forced with rod before using blower	OFF
151	12/5/2013	Run231	MHL	Model 0	1	-5	4.14	3.50	1000	16	rod inception	OFF
152	12/5/2013	Run232	MHL	Model 0	1	-5	4.97	4.00	1000	16	valves off	OFF
153	12/5/2013	Run232b	MHL	Model 0	1	-5	4.97	4.50	1000	16	rod forced	OFF
154	12/5/2013	Run233	MHL	Model 0	1	0	5.79	3.00	1000	16	rod forced	OFF
155	12/5/2013	Run233b	MHL	Model 0	1	0	5.79	3.50	1000	16	rod inception for full ventilation this time	OFF
156	12/5/2013	Run235	MHL	Model 0	1	0	2.48	4.00	1000	16	ramp up	OFF
157	12/5/2013	Run236	MHL	Model 0	1	0	2.48	4.50	1000	16	ramp down	OFF
158	7/31/2014	Run396	MHL	Model 0	1	5	2.48	3.00	1000	18.5	8-8-1; good streaking	OFF

#	Date	Run Name	Facility	Model	AR_h	α, deg	Speed, m/s	Fn_h	P_0, mbar	Water Temp, C	Comment	Shaker
159	12/5/2013	Run237	MHL	Model 0	1	5	2.90	3.50	1000	16	rod forced ventilation.	OFF
160	7/30/2013	Run112	MHL	Model 0	1	5	3.31	4.00	1000	20.5	2.75in h2o; ramp up	OFF
161	7/30/2013	Run113	MHL	Model 0	1	5	3.31	4.50	1000	20.5	Partial cavity ; ramp down	OFF
162	7/30/2013	Run113b	MHL	Model 0	1	5	3.31	3.00	1000	20.5	Repeated with gopros; partial cavity	OFF
163	12/6/2013	Run240	MHL	Model 0	1	10	3.31	3.50	1000	16	Ramp down from rod forced FV	OFF
164	12/5/2013	Run238	MHL	Model 0	1	10	3.72	4.00	1000	16	forced with rod.	OFF
165	7/29/2013	Run084	MHL	Model 0	1	10	4.14	4.50	1000	20.5	-1.75in; failed forced inception	OFF
166	7/30/2013	Run084b	MHL	Model 0	1	15	4.14	3.50	1000	20.5	-2.5in h2o; manually forced inception	OFF
167	7/31/2014	Run397	MHL	Model 0	1	15	4.14	4.00	1000	18.5	8-5-1; 8-7-1 at LE only; excellent streaking with a separation bubble	OFF
168	7/31/2014	Run398	MHL	Model 0	1	15	4.14	4.50	1000	18.5	8-5-1; tripped with rod	OFF
169	7/29/2013	Run085	MHL	Model 0	1	20	4.97	3.50	1000	20.5	-1.75 in H20; Failed forced incptn	OFF
170	7/30/2013	Run085b	MHL	Model 0	1	20	4.97	4.00	1000	20.5	-0.5in h2o; blower worked this time	OFF
171	7/29/2013	Run086	MHL	Model 0	1	20	5.79	4.50	1000	20.5	-1in H20; failed forced incptn	OFF
172	7/30/2013	Run086b	MHL	Model 0	1	25	5.79	3.50	1000	20.5	0in h2o; blower worked this time	OFF
173	12/5/2013	Run239	MHL	Model 0	1	25	5.79	4.00	1000	16	No Forcing	OFF
174	12/6/2013	Run239b	MHL	Model 0	1	25	5.79	4.50	1000	16	forced with rod.	OFF
175	12/6/2013	Run243	MHL	Model 0	1	30	2.07	3.50	1000	16	Forced with rod, PV	OFF
176	12/6/2013	Run241	MHL	Model 0	1	30	2.48	4.00	1000	16	ramp up. no inception, FA	OFF
177	12/6/2013	Run242	MHL	Model 0	1	30	2.48	4.50	1000	16	Ramp down, FA	OFF
178	12/6/2013	Run244	MHL	Model 0	1	30	2.90	3.00	1000	16	Rod forced FV, valves open late.	OFF
179	12/6/2013	Run250	MHL	Model 0	1	30	2.90	3.00	1000	16	forced FV. Ramp down	OFF
180	12/6/2013	Run245	MHL	Model 0	1	25	3.31	3.00	1000	16	Forced FV	OFF
181	12/6/2013	Run246	MHL	Model 0	1	25	3.72	3.50	1000	16	Force FV	OFF
182	12/6/2013	Run247	MHL	Model 0	1	25	4.14	3.00	1000	16	Forced FV.	OFF
183	12/6/2013	Run248	MHL	Model 0	1	20	4.97	3.00	1000	16	forced FV	OFF
184	12/6/2013	Run249	MHL	Model 0	1	20	5.79	3.00	1000	16	forced FV	OFF
185	12/6/2013	Run253	MHL	Model 0	1	15	2.07	3.00	1000	16	Low speed run. PV cavity triggered with rod (blower didn't work)	OFF
186	12/6/2013	Run251	MHL	Model 0	1	15	2.48	3.00	1000	16	Ramp Up. No anomolies. Did not trigger	OFF
187	12/6/2013	Run252	MHL	Model 0	1	10	2.48	3.00	1000	16	Ramp down. No ventilation.	OFF
188	12/6/2013	Run259	MHL	Model 0	1	10	2.48	3.00	1000	16	Very slow ramp down.	OFF
189	8/1/2014	Run407	MHL	Model 0	1	5	2.48	3.00	1000	18.5	8-8-1; good LSB	OFF
190	12/6/2013	Run254	MHL	Model 0	1	-5	2.90	2.00	1000	16	Blower didn't cause inception. Forced with rod	OFF
191	12/6/2013	Run255	MHL	Model 0	1	0	3.22	2.00	1000	16	Blower still not forcing inception. Rod-forced	OFF
192	7/30/2013	Run114	MHL	Model 0	1	2.5	3.31	2.00	1000	20.5	Ramp up corrected from 5-> 10 deg	OFF
193	7/30/2013	Run115	MHL	Model 0	1	2.5	3.31	1.50	1000	20.5	Ramp down corrected from 5-> 10deg	OFF
194	7/29/2013	Run087	MHL	Model 0	1	2.5	4.14	2.00	1000	20.5	0.25 in h20; failed forced incpn	OFF
195	7/29/2013	Run087b	MHL	Model 0	1	2.5	4.14	2.25	1000	20.5	0 in h20; successfully forced	OFF
196	7/31/2014	Run399	MHL	Model 0	1	2.5	4.14	2.50	1000	18.5		OFF
197	7/31/2014	Run400	MHL	Model 0	1	2.5	4.14	3.00	1000	18.5	8-5-1; trigger failed	OFF
198	7/31/2014	Run401	MHL	Model 0	1	2.5	4.14	3.00	1000	18.5	8-5-1; blower worked this time	OFF
199	12/6/2013	Run256	MHL	Model 0	1	2.5	4.55	2.00	1000	16	Blower worked this time	OFF

#	Date	Run Name	Facility	Model	AR_h	α, deg	Speed, m/s	Fn_h	P_0, mbar	Water Temp, C	Comment	Shaker
200	7/29/2013	Run088	MHL	Model 0	1	5	4.97	1.50	1000	20.5	Forgot Vvs	OFF
201	7/29/2013	Run088b	MHL	Model 0	1	5	4.97	1.50	1000	20.5	0 in h20 in FV	OFF
202	12/6/2013	Run257	MHL	Model 0	1	5	4.97	2.00	1000	16	Waited for vortex inception, but none occurred.	OFF
203	12/6/2013	Run257b	MHL	Model 0	1	5	4.97	2.25	1000	16	Repeat with blower. Inception triggered successfully this time.	OFF
204	7/29/2013	Run089	MHL	Model 0	1	5	5.79	2.50	1000	20.5	0 in h20	OFF
205	12/6/2013	Run258	MHL	Model 0	1	5	5.79	3.00	1000	16	Waited for vortex inception, but none occurred	OFF
206	12/11/2013	Run266	MHL	Model 0	1	5	1.66	1.50	1000	15.6	Blower didn't trigger cavity. Rod used.	OFF
207	12/6/2013	Run260	MHL	Model 0	1	5	2.48	2.00	1000	16	Very slow ramp (45s ramp up)	OFF
208	12/6/2013	Run261	MHL	Model 0	1	7.5	2.48	1.50	1000	16	Slow ramp (35 s)	OFF
209	12/6/2013	Run262	MHL	Model 0	1	7.5	2.48	1.50	1000	16	Med ramp 25s. No cavity	OFF
210	12/6/2013	Run263	MHL	Model 0	1	7.5	2.48	1.00	1000	16	Med ramp 15s. Still no ventilation	OFF
211	12/11/2013	Run264	MHL	Model 0	1	7.5	2.48	1.25	1000	15.6	Faster ramp (10s). No ventilation noted	OFF
212	12/11/2013	Run265	MHL	Model 0	1	7.5	2.48	1.50	1000	15.6	ramp down (25s) No ventilation.	OFF
213	12/11/2013	Run272	MHL	Model 0	1	7.5	2.48	1.75	1000	15.6	Ramp down	OFF
214	12/11/2013	Run267	MHL	Model 0	1	7.5	2.90	2.00	1000	15.6	Blower didn't cause cavity. Rod used	OFF
215	12/11/2013	Run268	MHL	Model 0	1	7.5	4.14	2.25	1000	15.6	Blower tip was dragging in water slightly. Blower forced cavity	OFF
216	12/11/2013	Run269	MHL	Model 0	1	7.5	4.97	2.50	1000	15.6	Blower worked this time	OFF
217	12/11/2013	Run270	MHL	Model 0	1	7.5	5.38	2.00	1000	15.6	Waited for vortex. No inception.	OFF
218	12/11/2013	Run270b	MHL	Model 0	1	7.5	5.38	2.50	1000	15.6	Blower tripped cavity this time	OFF
219	12/11/2013	Run271	MHL	Model 0	1	7.5	5.79	3.00	1000	15.6	No inception? Paint chip in wheel.	OFF
220	12/11/2013	Run271b	MHL	Model 0	1	7.5	5.79	3.00	1000	15.6	Triggered high speed run this time	OFF
221	7/31/2014	Run404	MHL	Model 0	1	7.5	4.14	3.00	1000	18.5	8-5-1; still spontaneous; strange	OFF
222	8/1/2014	Run406	MHL	Model 0	1	10	1.66	1.00	1000	18.5	8-12-1;	OFF
223	12/16/2013	Run307	MHL	Model 0	1	10	2.48	1.50	1000	15.6	Spontaneous. 45s ramp up	OFF
224	12/16/2013	Run308	MHL	Model 0	1	10	2.48	1.50	1000	15.6	5 s up; 45s ramp down. Forced inception to FV	OFF
225	12/16/2013	Run309	MHL	Model 0	1	10	2.48	1.50	1000	15.6	35 s up; 15s ramp down. Forced inception to FV	OFF
226	12/16/2013	Run310	MHL	Model 0	1	10	2.48	1.75	1000	15.6	60s ramp up; Spontaneous inception	OFF
227	12/16/2013	Run312	MHL	Model 0	1	10	4.14	2.00	1000	15.6	Hammer test at 13.58 fps;	OFF
228	12/16/2013	Run313	MHL	Model 0	1	10	4.14	2.25	1000	15.6	Hamemr test in FV condition	OFF
229	7/31/2014	Run402	MHL	Model 0	1	10	4.14	2.50	1000	18.5	8-5-1	OFF
230	7/31/2014	Run403	MHL	Model 0	1	10	4.14	2.75	1000	18.5	8-5-1; spontaneous	OFF
231	8/1/2014	Run405	MHL	Model 0	1	10	4.14	3.00	1000	18.5	8-5-1; blower failed	OFF
232	12/16/2013	Run311	MHL	Model 0	1	10	5.79	3.00	1000	15.6	No tripping; waited for vortex inception, but none occurred.	OFF
233	12/12/2013	Run278	MHL	Model 0	1	10	1.66	1.50	1000	15.6	Sponaneous PV case	OFF
234	12/11/2013	Run273	MHL	Model 0	1	12.5	2.48	1.50	1000	15.6	Spontaneous. 45 s ramp up. Cameras were dead	OFF
235	12/11/2013	Run273b	MHL	Model 0	1	12.5	2.48	1.50	1000	15.6	Spontaneous. Repeated last run for video. 45 s ramp up	OFF
236	12/11/2013	Run274	MHL	Model 0	1	12.5	2.48	1.00	1000	15.6	Spontaneous (35s ramp)	OFF
237	12/11/2013	Run275	MHL	Model 0	1	12.5	2.48	1.00	1000	15.6	Spontaneous	OFF
238	12/12/2013	Run276	MHL	Model 0	1	12.5	2.48	1.25	1000	15.6	Spontaneous ventilation (15s ramp.) Careful; LED may have turned on before data collection started.	OFF
239	12/12/2013	Run276b	MHL	Model 0	1	12.5	2.48	1.25	1000	15.6	Repeated run to make sure video was synced. (15s) Spontaneous.	OFF

#	Date	Run Name	Facility	Model	AR_h	α, deg	Speed, m/s	Fn_h	P_0, mbar	Water Temp, C	Comment	Shaker
240	12/12/2013	Run277	MHL	Model 0	1	12.5	2.48	1.25	1000	15.6	Fast ramp (5s) Spontaneous	OFF
241	12/12/2013	Run288	MHL	Model 0	1	12.5	2.48	1.50	1000	15.6	Spontaneous inception. 45s ramp down	OFF
242	12/12/2013	Run289	MHL	Model 0	1	12.5	2.48	1.75	1000	15.6	Spontaneous inception; 35 s ramp down	OFF
243	12/12/2013	Run290	MHL	Model 0	1	12.5	2.48	2.00	1000	15.6	25 s ramp. Spontaneous	OFF
244	12/12/2013	Run291	MHL	Model 0	1	12.5	2.48	2.00	1000	15.6	Spontaneous. 15s ramp down	OFF
245	12/12/2013	Run279	MHL	Model 0	1	12.5	2.90	2.25	1000	15.6	Spontaneous inception still.	OFF
246	7/29/2013	Run090	MHL	Model 0	1	12.5	3.31	3.00	1000	20.5	Ramp Up; 1 in h20	OFF
247	7/29/2013	Run094	MHL	Model 0	1	12.5	3.31	3.00	1000	20.5	Ramp Down; Started at 0in h20 and gradually transitioned to hydrostatic	OFF
248	12/12/2013	Run280	MHL	Model 0	1	12.5	3.31	1.50	1000	15.6	Still getting spontaneous inception. Checked dihedral; 0.00 degrees found	OFF
249	12/12/2013	Run281	MHL	Model 0	1	12.5	3.72	1.50	1000	15.6	Spontaneous. Inception originates near mid-chord, where depression in free surface is greatest.	OFF
250	7/29/2013	Run091	MHL	Model 0	1	15	4.14	1.25	1000	20.5	0.5in h20; failed forced	OFF
251	7/29/2013	Run091b	MHL	Model 0	1	15	4.14	1.50	1000	20.5	0in h20 Higher blower pressure; successful triggering	OFF
252	12/12/2013	Run282	MHL	Model 0	1	15	4.14	1.50	1000	15.6	Spontaneous inception	OFF
253	12/12/2013	Run283	MHL	Model 0	1	15	4.55	1.50	1000	15.6	There is a particle on the LE causing a streak pattern in the cavity. Perhaps it's promoting spontaneous inception?	OFF
254	7/29/2013	Run092	MHL	Model 0	1	15	4.97	1.00	1000	20.5	0 in h20 at FV	OFF
255	12/12/2013	Run284	MHL	Model 0	1	15	4.97	1.75	1000	15.6	Cleaning LE did not change the spontaneous behavior	OFF
256	12/12/2013	Run285	MHL	Model 0	1	15	5.38	2.25	1000	15.6		OFF
257	12/12/2013	Run285b	MHL	Model 0	1	15	5.38	2.75	1000	15.6	Repeated to try and get vortex inception. Spontaneous again	OFF
258	12/12/2013	Run285c	MHL	Model 0	1	15	5.38	3.00	1000	15.6	Shortened wait time to see if that impacted inceptiom mech. Nope	OFF
259	7/29/2013	Run093	MHL	Model 0	1	15	5.79	1.50	1000	20.5	0 in h20 ;blower touched water	OFF
260	7/29/2013	Run093b	MHL	Model 0	1	17.5	5.79	1.25	1000	20.5	-0.25in h20; Blower touched water briefly after triggering	OFF
261	12/12/2013	Run286	MHL	Model 0	1	17.5	5.79	1.50	1000	15.6	VORTEX INCEPTION	OFF
262	12/12/2013	Run287	MHL	Model 0	1	17.5	6.10	1.00	1000	15.6	Vortex inceptin again. Baffling why only the highest speed runs don't show spontaneous inception early during acceleration.	OFF
263	12/12/2013	Run292	MHL	Model 0	1	17.5	2.48	1.75	1000	15.6	35 s ramp up. Spontaneous	OFF
264	12/12/2013	Run293	MHL	Model 0	1	17.5	2.48	2.25	1000	15.6	35 s ramp down	OFF
265	12/12/2013	Run294	MHL	Model 0	1	17.5	5.79	2.75	1000	15.6	High speed run to see if inception was delayed. Spontaneous inception still occured Actually 17.5 deg (entered 19.01deg); correct L/D accordingly	OFF
266	12/16/2013	Run305	MHL	Model 0	1	17.5	0.00	3.00	1000	15.6	LE, Mid, TE at 0.5s; mid at WL; zero-speed hammer test	OFF
267	8/1/2014	Run408	MHL	Model 0	1	17.5	0.83	1.25	1000	18.5	8-12-1; very slight streaking	OFF
268	8/1/2014	Run409	MHL	Model 0	1	20	0.91	1.50	1000	18.5	8-15-1	OFF
269	12/16/2013	Run298	MHL	Model 0	1	20	1.66	1.50	1000	15.6	PV run at low speed	OFF
270	12/16/2013	Run297	MHL	Model 0	1	25	2.07	1.50	1000	15.6	Low speed run. Ended up FV	OFF
271	12/16/2013	Run295	MHL	Model 0	1	25	2.48	1.50	1000	15.6	Nice separated flow. 45 s ramp up. Spontaneous	OFF
272	12/16/2013	Run296	MHL	Model 0	1	-5	2.48	2.00	1000	15.6	45 s ramp down. Forgot to turn on vvs	OFF
273	7/30/2013	Run095	MHL	Model 0	1	-5	3.31	2.00	1000	20.5	-0.25in h20; ACC GAINS Changed from 2 to 10 on controller; Ramp up; lift/drag need to be corrected 15->20deg	OFF
274	7/30/2013	Run099	MHL	Model 0	1	0	3.31	2.00	1000	20.5	Ramp down	OFF
275	12/16/2013	Run306	MHL	Model 0	1	0	3.31	3.00	1000	15.6	Underway hammer test; Excited at LE and midchord at about 0.3s	OFF
276	7/30/2013	Run096	MHL	Model 0	1	2.5	4.14	1.50	1000	20.5	0in h20	OFF
277	7/30/2013	Run097	MHL	Model 0	1	2.5	4.97	1.50	1000	20.5	0 in h2o	OFF

#	Date	Run Name	Facility	Model	AR_h	α, deg	Speed, m/s	Fn_h	P_0, mbar	Water Temp, C	Comment	Shaker
278	7/30/2013	Run098	MHL	Model 0	1	2.5	5.79	2.00	1000	20.5	0in h2o	OFF
279	12/16/2013	Run301	MHL	Model 0	1	2.5	1.66	2.25	1000	15.6	Nice recirculating flow. PV	OFF
280	12/16/2013	Run299	MHL	Model 0	1	2.5	2.48	2.25	1000	15.6	45 s ramp up; nice bubbly flow in separated region near LE	OFF
281	12/16/2013	Run300	MHL	Model 0	1	2.5	2.48	2.25	1000	15.6	Nice washout. 45 s ramp down	OFF
282	7/30/2013	Run104	MHL	Model 0	1	2.5	3.22	2.50	1000	20.5	ramp down; re-entry jet is very obvious from observation	OFF
283	7/30/2013	Run100	MHL	Model 0	1	2.5	3.31	3.00	1000	20.5	ramp up; actually 25 deg- adjust L,D accordingly	OFF
284	7/30/2013	Run101	MHL	Model 0	1	2.5	4.14	3.00	1000	20.5	0in h2o	OFF
285	7/30/2013	Run102	MHL	Model 0	1	2.5	4.97	3.50	1000	20.5	blower draggin in water; needs to be repeated	OFF
286	7/30/2013	Run102b	MHL	Model 0	1	2.5	4.97	3.50	1000	20.5	0in h2o	OFF
287	7/30/2013	Run103	MHL	Model 0	1	2.5	5.79	2.00	1000	20.5	0 in h2o	OFF
288	12/16/2013	Run304	MHL	Model 0	1	5	1.66	1.50	1000	15.6	Started PV then went FV	OFF
289	12/16/2013	Run302	MHL	Model 0	1	5	2.48	1.50	1000	15.6	FV flow/ 45 s ramp up	OFF
290	12/16/2013	Run303	MHL	Model 0	1	5	2.48	1.75	1000	15.6	FV flow. 45 s ramp down	OFF
291	7/30/2013	Run105	MHL	Model 0	1	5	3.31	2.25	1000	20.5	Ramp up	OFF
292	7/30/2013	Run109	MHL	Model 0	1	5	3.31	3.50	1000	20.5	ramp down	OFF
293	7/30/2013	Run106	MHL	Model 0	1	5	4.14	3.50	1000	20.5	0in h2o; Huge spray sheet	OFF
294	7/30/2013	Run107	MHL	Model 0	1	5	4.97	2.00	1000	20.5	0in h2o	OFF
295	7/30/2013	Run108	MHL	Model 0	1	7.5	5.79	1.50	1000	20.5	0in h2o	OFF
296	7/26/2013	Run041	MHL	Model 0	1.5	7.5	3.04	1.50	1000	20.5	Ramp up	OFF
297	7/17/2013	Run001	MHL	Model 0	1.5	7.5	3.51	1.25	1000	20.5	Neg 5 deg for alignment	OFF
298	7/26/2013	Run042	MHL	Model 0	1.5	7.5	4.05	1.75	1000	20.5	Manometer reads 4 inch H2O	OFF
299	9/18/2013	Run154	MHL	Model 0	1.5	7.5	4.05	2.00	1000	20	Oops. Shoulda been 154	OFF
300	7/17/2013	Run002	MHL	Model 0	1.5	7.5	4.10	2.25	1000	20.5		OFF
301	7/17/2013	Run003	MHL	Model 0	1.5	7.5	4.68	2.50	1000	20.5		OFF
302	7/18/2013	Run003b	MHL	Model 0	1.5	7.5	4.68	3.00	1000	20.5		OFF
303	7/26/2013	Run043	MHL	Model 0	1.5	7.5	5.07	3.50	1000	20.5	Manometer reads 0 inch H2O	OFF
304	7/18/2013	Run034	MHL	Model 0	1.5	7.5	5.27	1.75	1000	20.5		OFF
305	7/18/2013	Run035	MHL	Model 0	1.5	10	5.85	1.50	1000	20.5		OFF
306	7/26/2013	Run044	MHL	Model 0	1.5	10	6.08	1.50	1000	20.5	Manometer reads -2in H2O	OFF
307	7/29/2014	Run006s	MHL	Model 0	1.5	10	1.83	1.25	1000	18.5	8-8-1 actually -3deg; some streaking	OFF
308	7/26/2013	Run045	MHL	Model 0	1.5	10	3.04	1.75	1000	20.5	Ramp up	OFF
309	7/17/2013	ZeroingRun1	MHL	Model 0	1.5	10	3.05	1.94	1000	20.5	zeroing run	OFF
310	7/17/2013	ZeroingRun2	MHL	Model 0	1.5	10	3.05	2.75	1000	20.5	zeroing run	OFF
311	7/17/2013	Run004	MHL	Model 0	1.5	10	3.51	3.00	1000	20.5	Ramp	OFF
312	7/26/2013	Run046	MHL	Model 0	1.5	10	4.05	3.00	1000	20.5		OFF
313	9/18/2013	Run155	MHL	Model 0	1.5	10	4.05	3.50	1000	20	3 way valve didn't open	OFF
314	7/17/2013	Run005	MHL	Model 0	1.5	10	4.10	1.50	1000	20.5		OFF
315	7/17/2013	Run006	MHL	Model 0	1.5	12.5	4.68	1.50	1000	20.5		OFF
316	7/18/2013	Run006b	MHL	Model 0	1.5	12.5	4.68	1.50	1000	20.5		OFF
317	7/26/2013	Run047	MHL	Model 0	1.5	12.5	5.07	1.50	1000	20.5		OFF
318	7/18/2013	Run036	MHL	Model 0	1.5	12.5	5.27	1.50	1000	20.5	No UW video	OFF

#	Date	Run Name	Facility	Model	AR_h	α, deg	Speed, m/s	Fn_h	P_0, mbar	Water Temp, C	Comment	Shaker
319	7/18/2013	Run037	MHL	Model 0	1.5	12.5	5.85	1.50	1000	20.5	No UW video	OFF
320	7/26/2013	Run048	MHL	Model 0	1.5	12.5	6.08	1.50	1000	20.5	Manometer reads -1.5in H2O	OFF
321	9/18/2013	Run157	MHL	Model 0	1.5	12.5	3.04	1.00	1000	20	Ramp down	OFF
322	9/18/2013	Run156	MHL	Model 0	1.5	12.5	4.05	1.75	1000	20	RUN SPEED 9.98 (Correct during post-proc) Ramp up	OFF
323	9/18/2013	Run158	MHL	Model 0	1.5	12.5	4.05	2.50	1000	20	forces by rod, after the blower failed. Partial cavity.	OFF
324	9/18/2013	Run162	MHL	Model 0	1.5	12.5	4.05	3.00	1000	20	manual inception ramp down	OFF
325	9/18/2013	Run159	MHL	Model 0	1.5	12.5	4.56	3.25	1000	20	Manual rod inception again. partial cavity....	OFF
326	9/18/2013	Run160	MHL	Model 0	1.5	12.5	5.07	3.25	1000	20	manual inception	OFF
327	9/18/2013	Run161	MHL	Model 0	1.5	12.5	6.08	3.50	1000	20		OFF
328	9/18/2013	Run161b	MHL	Model 0	1.5	12.5	6.08	3.50	1000	20	manual inception	OFF
329	7/30/2014	Run390	MHL	Model 0	1.5	12.5	2.03	1.50	1000	18.5	8-10-1; untripped; minimal streaking	OFF
330	7/30/2014	Run391	MHL	Model 0	1.5	15	2.03	1.50	1000	18.5	8-12-1; tripped with rod	OFF
331	7/26/2013	Run049	MHL	Model 0	1.5	15	3.04	1.50	1000	20.5	Ramp up	OFF
332	9/18/2013	Run163	MHL	Model 0	1.5	15	3.04	1.50	1000	20	ramp up. manometer valve opened late, no usable data	OFF
333	9/18/2013	Run164	MHL	Model 0	1.5	15	3.04	1.50	1000	20	ramp down	OFF
334	9/18/2013	Run169	MHL	Model 0	1.5	15	3.04	1.50	1000	20	Ramp down. manual inception	OFF
335	7/28/2014	Run001s	MHL	Model 0	1.5	15	3.35	1.50	1000	18.5		OFF
336	7/17/2013	Run007	MHL	Model 0	1.5	15	3.51	1.50	1000	20.5	Ramp	OFF
337	7/26/2013	Run050	MHL	Model 0	1.5	15	4.05	1.00	1000	20.5	Failed forced ventilation. Manometer reads 2 inch H2O	OFF
338	9/18/2013	Run165	MHL	Model 0	1.5	15	4.05	1.75	1000	20		OFF
339	9/18/2013	Run169b	MHL	Model 0	1.5	15	4.05	2.00	1000	20	Repeat 169 ramping down from 13.3. manual inception	OFF
340	7/17/2013	Run009	MHL	Model 0	1.5	15	4.10	2.25	1000	20.5	Failed forced inception	OFF
341	9/18/2013	Run166	MHL	Model 0	1.5	15	4.56	2.50	1000	20	manual inception	OFF
342	7/17/2013	Run010	MHL	Model 0	1.5	15	4.68	2.75	1000	20.5	Failed forced inception	OFF
343	7/18/2013	Run010b	MHL	Model 0	1.5	15	4.68	3.00	1000	20.5	failed forced inception	OFF
344	7/18/2013	Run010c	MHL	Model 0	1.5	15	4.68	3.25	1000	20.5		OFF
345	7/18/2013	Run010d	MHL	Model 0	1.5	15	4.68	3.50	1000	20.5		OFF
346	7/26/2013	Run051	MHL	Model 0	1.5	15	5.07	3.25	1000	20.5	Failed forced inception. Manometer reads -1.5in H2O	OFF
347	7/26/2013	Run051b	MHL	Model 0	1.5	15	5.07	3.25	1000	20.5	Ventilation forced by rod. Manometer reads 0 in H2O after SV flow regime	OFF
348	9/18/2013	Run167	MHL	Model 0	1.5	15	5.07	3.68	1000	20		OFF
349	7/18/2013	Run027	MHL	Model 0	1.5	15	5.27	1.50	1000	20.5		OFF
350	7/18/2013	Run027b	MHL	Model 0	1.5	15	5.27	1.50	1000	20.5	no forced inception.	OFF
351	7/18/2013	Run027c	MHL	Model 0	1.5	15	5.27	1.50	1000	20.5	no inception	OFF
352	7/18/2013	Run038	MHL	Model 0	1.5	15	5.85	1.50	1000	20.5		OFF
353	7/26/2013	Run052	MHL	Model 0	1.5	17.5	6.08	1.50	1000	20.5	Manometer reads -0.75in H2O at SV regime	OFF
354	9/18/2013	Run168	MHL	Model 0	1.5	17.5	6.08	1.50	1000	20		OFF
355	9/18/2013	Run172	MHL	Model 0	1.5	17.5	2.03	3.50	1000	20		OFF
356	9/18/2013	Run173	MHL	Model 0	1.5	20	2.53	1.50	1000	20		OFF
357	9/18/2013	Run170	MHL	Model 0	1.5	20	3.04	1.50	1000	20	ramp up. pressure valve closed prematurely	OFF
358	9/18/2013	Run171	MHL	Model 0	1.5	20	3.04	1.25	1000	20	ramp down	OFF
359	9/18/2013	Run174	MHL	Model 0	1.5	20	3.04	1.00	1000	20		OFF

#	Date	Run Name	Facility	Model	AR_h	α, deg	Speed, m/s	Fn_h	P_0, mbar	Water Temp, C	Comment	Shaker
360	9/18/2013	Run175	MHL	Model 0	1.5	25	3.55	1.50	1000	20		OFF
361	9/18/2013	Run176	MHL	Model 0	1.5	25	4.05	1.50	1000	20	manual inception	OFF
362	9/18/2013	Run176b	MHL	Model 0	1.5	25	4.05	1.00	1000	20	failed forced inception	OFF
363	9/18/2013	Run177	MHL	Model 0	1.5	30	4.56	1.50	1000	20	manual inception	OFF
364	9/18/2013	Run178	MHL	Model 0	1.5	30	5.07	1.50	1000	20		OFF
365	9/19/2013	Run178b	MHL	Model 0	1.5	30	5.07	1.00	1000	20	Repeat of previous days last run for exp error; blower worked	OFF
366	9/19/2013	Run179	MHL	Model 0	1.5	20	6.08	0.00	1000	20	Blower went too late; FW at SS	OFF
367	9/19/2013	Run179b	MHL	Model 0	1.5	20	6.08	2.00	1000	20	Blower failed	OFF
368	9/19/2013	Run179c	MHL	Model 0	1.5	14	6.08	1.50	1000	20	Blower still didn't work	OFF
369	7/29/2014	Run004s	MHL	Model 0	1.5	14	1.83	1.50	1000	18.5	8-12-1 streaking	OFF
370	7/29/2014	Run005s	MHL	Model 0	1.5	14	1.83	1.50	1000	18.5	8-10-1 streaking	OFF
371	7/29/2014	Run006bs	MHL	Model 0	1.5	14	1.83	1.50	1000	18.5	8-8-1 Some streaking from 006	OFF
372	7/29/2014	Run007s	MHL	Model 0	1.5	14	1.83	3.50	1000	18.5	8-8-1; Some streaking on SS	OFF
373	7/29/2014	Run008s	MHL	Model 0	1.5	14	1.83	2.50	1000	18.5	8-7-1 minimal shearing at speed	OFF
374	9/19/2013	Run181	MHL	Model 0	1.5	14	2.03	2.50	1000	20	manual inception, partial cavity. VERY slow ramp	OFF
375	7/30/2014	Run392	MHL	Model 0	1.5	0	2.03	0.00	1000	18.5	8-12-1; tripped with rod	OFF
376	7/29/2014	Run009s	MHL	Model 0	1.5	0	2.44	2.50	1000	18.5	8-7-1 More strwaking occurred. Reused previous paint	OFF
377	7/26/2013	Run053	MHL	Model 0	1.5	-5	3.04	0.00	1000	20.5	ramp up	OFF
378	7/26/2013	Run057	MHL	Model 0	1.5	-5	3.04	3.00	1000	20.5	ramp down. no GP video	OFF
379	9/19/2013	Run182	MHL	Model 0	1.5	-5	3.04	5.00	1000	20	Pres valve did not trigger	OFF
380	9/19/2013	Run183	MHL	Model 0	1.5	0	3.04	2.00	1000	20		OFF
381	9/19/2013	Run184	MHL	Model 0	1.5	0	3.04	5.00	1000	20	ramp down	OFF
382	9/19/2013	Run191	MHL	Model 0	1.5	2.5	3.04	2.00	1000	20	ramp down	OFF
383	7/28/2014	Run002s	MHL	Model 0	1.5	2.5	3.05	2.00	1000	18.5	8-10-1 mix trial 1	OFF
384	7/28/2014	Run003s	MHL	Model 0	1.5	2.5	3.05	2.50	1000	18.5	8-12-1 mix	OFF
385	7/29/2014	Run010s	MHL	Model 0	1.5	2.5	3.05	2.25	1000	18.5	8-7-1 with fresh paint at higher speed. Good streaking	OFF
386	7/29/2014	Run011s	MHL	Model 0	1.5	2.5	3.05	3.00	1000	18.5	8-5-1; moderate streaking only	OFF
387	7/17/2013	Run011	MHL	Model 0	1.5	2.5	3.51	3.50	1000	20.5	Ramp	OFF
388	7/17/2013	Run014	MHL	Model 0	1.5	2.5	3.51	4.00	1000	20.5	Rod forced inception. Ramp down	OFF
389	7/17/2013	Run014b	MHL	Model 0	1.5	2.5	3.51	4.50	1000	20.5	Repeat 14 because inception mechanism touched the free surface in run 14	OFF
390	9/19/2013	Run185	MHL	Model 0	1.5	2.5	3.55	5.00	1000	20		OFF
391	7/26/2013	Run054	MHL	Model 0	1.5	2.5	4.05	5.00	1000	20.5	Man. reads 0in H2O in SV regime	OFF
392	9/19/2013	Run186	MHL	Model 0	1.5	2.5	4.05	2.75	1000	20		OFF
393	7/17/2013	Run012	MHL	Model 0	1.5	5	4.10	2.00	1000	20.5	Failed forced inception	OFF
394	7/17/2013	Run012b	MHL	Model 0	1.5	5	4.10	2.00	1000	20.5	REpeat 12, this time inception works	OFF
395	9/19/2013	Run187	MHL	Model 0	1.5	5	4.56	2.50	1000	20		OFF
396	7/17/2013	Run013	MHL	Model 0	1.5	5	4.68	3.00	1000	20.5	Failed forced inception	OFF
397	7/17/2013	Run013b	MHL	Model 0	1.5	5	4.68	5.00	1000	20.5	froces with rod after automatic inception failed	OFF
398	7/17/2013	Run013c	MHL	Model 0	1.5	5	4.68	5.00	1000	20.5	Air inceptor hit the free surface	OFF
399	7/18/2013	Run013d	MHL	Model 0	1.5	5	4.68	2.00	1000	20.5		OFF

#	Date	Run Name	Facility	Model	AR_h	α, deg	Speed, m/s	Fn_h	P_0, mbar	Water Temp, C	Comment	Shaker
400	7/26/2013	Run055	MHL	Model 0	1.5	5	5.07	2.00	1000	20.5	Failed foreced inception. Repeat. NO GoPro VIDEO (not in 54 either) -1 in H2O in base ventilated regime	OFF
401	7/26/2013	Run055b	MHL	Model 0	1.5	7.5	5.07	2.00	1000	20.5	Failed forced inception, no GP video.	OFF
402	7/26/2013	Run055c	MHL	Model 0	1.5	7.5	5.07	2.00	1000	20.5	Manometer reads -0.25in H2O. No gopro video	OFF
403	9/19/2013	Run188	MHL	Model 0	1.5	7.5	5.07	2.00	1000	20		OFF
404	7/18/2013	Run039	MHL	Model 0	1.5	7.5	5.27	1.50	1000	20.5	LEDS turn on twice. If both are seen in video, use second	OFF
405	9/19/2013	Run189	MHL	Model 0	1.5	7.5	5.57	3.00	1000	20		OFF
406	7/18/2013	Run040	MHL	Model 0	1.5	7.5	5.85	5.00	1000	20.5		OFF
407	7/26/2013	Run056	MHL	Model 0	1.5	7.5	6.08	5.00	1000	20.5	-2.5in H2O	OFF
408	9/19/2013	Run190	MHL	Model 0	1.5	7.5	6.08	2.00	1000	20		OFF
409	9/19/2013	Run190b	MHL	Model 0	1.5	10	6.08	2.00	1000	20		OFF
410	9/19/2013	Run194b	MHL	Model 0	1.5	10	2.02	2.00	1000	20	repeated for video, incepted naturally during acceleration	OFF
411	9/19/2013	Run194	MHL	Model 0	1.5	10	2.03	1.50	1000	20		OFF
412	7/30/2014	Run393	MHL	Model 0	1.5	10	2.03	3.00	1000	18.5	8-12-1; tripped with rod; great PV visual	OFF
413	9/19/2013	Run195	MHL	Model 0	1.5	10	2.53	3.00	1000	20		OFF
414	9/20/2013	Run195b	MHL	Model 0	1.5	10	2.53	5.00	1000	20	spontaneous inception at acel. Not properly clamped, probably some dihedral.	OFF
415	9/20/2013	Run195c	MHL	Model 0	1.5	10	2.53	5.00	1000	20		OFF
416	9/19/2013	Run192	MHL	Model 0	1.5	10	3.04	2.00	1000	20	ramp up	OFF
417	9/19/2013	Run193	MHL	Model 0	1.5	12.5	3.04	2.00	1000	20	ramp down	OFF
418	9/20/2013	Run196	MHL	Model 0	1.5	12.5	3.04	2.00	1000	20		OFF
419	9/20/2013	Run201	MHL	Model 0	1.5	12.5	3.04	1.50	1000	20	Ramp down. 0.25deg measured dihedral, repeat run	OFF
420	9/20/2013	Run201b	MHL	Model 0	1.5	12.5	3.04	3.00	1000	20	RAMP DOWN	OFF
421	9/20/2013	Run197	MHL	Model 0	1.5	12.5	3.55	5.00	1000	20		OFF
422	9/20/2013	Run198	MHL	Model 0	1.5	12.5	4.05	5.00	1000	20		OFF
423	9/20/2013	Run198b	MHL	Model 0	1.5	12.5	4.05	2.00	1000	20		OFF
424	9/20/2013	Run199	MHL	Model 0	1.5	15	4.56	2.00	1000	20		OFF
425	9/20/2013	Run200	MHL	Model 0	1.5	15	6.08	2.00	1000	20		OFF
426	9/20/2013	Run200b	MHL	Model 0	1.5	15	6.08	1.50	1000	20		OFF
427	9/20/2013	Run206	MHL	Model 0	1.5	15	2.03	3.00	1000	20		OFF
428	7/30/2014	Run394	MHL	Model 0	1.5	15	2.03	5.00	1000	18.5	8-12-1;	OFF
429	9/20/2013	Run202	MHL	Model 0	1.5	15	2.53	5.00	1000	20	ramp up	OFF
430	7/26/2013	Run058	MHL	Model 0	1.5	15	3.04	2.00	1000	20.5	4 inch H2O at 9.98 SV	OFF
431	7/26/2013	Run062	MHL	Model 0	1.5	17.5	3.04	2.00	1000	20.5	ramp down	OFF
432	9/20/2013	Run203	MHL	Model 0	1.5	17.5	3.04	2.00	1000	20	Ramp up. Noticed prssure tube was vibrting so moved up from this test on. New P-tube location is 11in submergence.	OFF
433	9/20/2013	Run204	MHL	Model 0	1.5	17.5	3.04	2.00	1000	20	ramp up	OFF
434	9/20/2013	Run205	MHL	Model 0	1.5	17.5	3.04	2.00	1000	20	Turned up TE air injection	OFF
435	9/20/2013	Run211	MHL	Model 0	1.5	17.5	3.04	2.00	1000	20	ramp down	OFF
436	7/17/2013	Run015	MHL	Model 0	1.5	17.5	3.51	2.00	1000	20.5	artificial inception system toched the free surface	OFF
437	7/17/2013	Run015b	MHL	Model 0	1.5	17.5	3.51	1.50	1000	20.5		OFF
438	7/17/2013	Run018	MHL	Model 0	1.5	17.5	3.51	3.00	1000	20.5	Ramp down	OFF
439	9/20/2013	Run207	MHL	Model 0	1.5	17.5	3.55	5.00	1000	20		OFF

#	Date	Run Name	Facility	Model	AR_h	α, deg	Speed, m/s	Fn_h	P_0, mbar	Water Temp, C	Comment	Shaker
440	7/26/2013	Run059	MHL	Model 0	1.5	17.5	4.05	3.50	1000	20.5	-6 in H2O	OFF
441	7/26/2013	Run059b	MHL	Model 0	1.5	17.5	4.05	4.00	1000	20.5	-1 in H2O, in SV condition	OFF
442	7/30/2014	Run395	MHL	Model 0	1.5	17.5	4.05	5.00	1000	18.5	8-5-1; FW flow; very nice streaking	OFF
443	7/17/2013	Run016	MHL	Model 0	1.5	17.5	4.10	5.00	1000	20.5	No inception ???	OFF
444	7/17/2013	Run016b	MHL	Model 0	1.5	20	4.10	2.00	1000	20.5		OFF
445	9/20/2013	Run208	MHL	Model 0	1.5	20	4.56	2.00	1000	20	Carriage cams need to be trimmed. Dead leading time.	OFF
446	7/17/2013	Run017	MHL	Model 0	1.5	20	4.68	2.00	1000	20.5		OFF
447	7/18/2013	Run017b	MHL	Model 0	1.5	20	4.68	2.00	1000	20.5		OFF
448	7/26/2013	Run060	MHL	Model 0	1.5	20	5.07	2.00	1000	20.5	-3in H2O in SV regime	OFF
449	7/18/2013	Run028	MHL	Model 0	1.5	20	5.27	2.00	1000	20.5		OFF
450	9/20/2013	Run209	MHL	Model 0	1.5	20	5.57	1.50	1000	20		OFF
451	7/18/2013	Run029	MHL	Model 0	1.5	20	5.85	3.00	1000	20.5		OFF
452	7/18/2013	Run029b	MHL	Model 0	1.5	20	5.85	5.00	1000	20.5		OFF
453	7/26/2013	Run061	MHL	Model 0	1.5	20	6.08	5.00	1000	20.5	-3 in H2O	OFF
454	7/26/2013	Run061b	MHL	Model 0	1.5	22.5	6.08	2.00	1000	20.5	-3 in H2O	OFF
455	9/20/2013	Run210	MHL	Model 0	1.5	25	6.08	2.00	1000	20		OFF
456	9/20/2013	Run214	MHL	Model 0	1.5	25	2.03	2.00	1000	20		OFF
457	9/20/2013	Run212	MHL	Model 0	1.5	25	2.53	5.00	1000	20	ramp up	OFF
458	9/20/2013	Run219	MHL	Model 0	1.5	25	2.53	5.00	1000	20		OFF
459	9/20/2013	Run213	MHL	Model 0	1.5	30	3.04	2.00	1000	20	ramp up	OFF
460	9/20/2013	Run215	MHL	Model 0	1.5	30	3.55	2.00	1000	20		OFF
461	9/20/2013	Run216	MHL	Model 0	1.5	30	4.56	5.00	1000	20		OFF
462	9/20/2013	Run217	MHL	Model 0	1.5	25	5.57	3.50	1000	20		OFF
463	9/20/2013	Run218	MHL	Model 0	1.5	15	6.08	3.50	1000	20		OFF
464	7/26/2013	Run063	MHL	Model 0	1.5	15	3.04	3.50	1000	20.5	ramp up	OFF
465	7/26/2013	Run067	MHL	Model 0	1.5	0	3.04	3.50	1000	20.5	ramp down	OFF
466	9/20/2013	Run220	MHL	Model 0	1.5	5	3.04	1.65	1000	20	ramp up	OFF
467	9/20/2013	Run221	MHL	Model 0	1.5	10	3.04	1.50	1000	20	ramp down	OFF
468	7/17/2013	Run019	MHL	Model 0	1.5	10	3.51	1.50	1000	20.5	Ramp up	OFF
469	7/17/2013	Run022	MHL	Model 0	1.5	10	3.51	0.90	1000	20.5	ramp down	OFF
470	7/26/2013	Run064	MHL	Model 0	1.5	10	4.05	0.90	1000	20.5	-1in H2O	OFF
471	7/17/2013	Run020	MHL	Model 0	1.5	-3	4.10	0.90	1000	20.5		OFF
472	7/17/2013	Run021	MHL	Model 0	1.5	10	4.68	0.90	1000	20.5		OFF
473	7/18/2013	Run021b	MHL	Model 0	1.5	10	4.68	0.90	1000	20.5		OFF
474	7/26/2013	Run065	MHL	Model 0	1.5	10	5.07	0.90	1000	20.5	0 in H2O	OFF
475	7/18/2013	Run030	MHL	Model 0	1.5	10	5.27	1.20	1000	20.5		OFF
476	7/18/2013	Run031	MHL	Model 0	1.5	10	5.85	1.50	1000	20.5		OFF
477	7/26/2013	Run066	MHL	Model 0	1.5	10	6.08	1.50	1000	20.5	0 in H2O	OFF
478	7/26/2013	Run068	MHL	Model 0	1.5	5	1.52	1.00	1000	20.5	ramp up	OFF
479	7/26/2013	Run072	MHL	Model 0	1.5	5	3.04	1.00	1000	20.5	ramp down	OFF
480	9/20/2013	Run222	MHL	Model 0	1.5	10	3.04	1.00	1000	20	ramp up	OFF

#	Date	Run Name	Facility	Model	AR_h	α, deg	Speed, m/s	Fn_h	P_0, mbar	Water Temp, C	Comment	Shaker
481	9/20/2013	Run223	MHL	Model 0	1.5	12.5	3.04	1.00	1000	20	ramp down	OFF
482	7/17/2013	Run023	MHL	Model 0	1.5	15	3.51	1.00	1000	20.5	ramp up	OFF
483	7/18/2013	Run026	MHL	Model 0	1.5	15	3.51	2.00	1000	20.5	Ramp down	OFF
484	7/25/2013	Test002	MHL	Model 0	1.5	5	3.96	1.50	1000	20.5	Runing Mid Tank Camera- ATM Pressure	OFF
485	7/26/2013	Run069	MHL	Model 0	1.5	5	4.05	2.50	1000	20.5	0inH2O	OFF
486	7/17/2013	Run024	MHL	Model 0	1.5	5	4.10	2.50	1000	20.5		OFF
487	7/17/2013	Run025	MHL	Model 0	1.5	10	4.68	2.50	1000	20.5		OFF
488	7/18/2013	Run025b	MHL	Model 0	1.5	10	4.68	2.50	1000	20.5		OFF
489	7/26/2013	Run070	MHL	Model 0	1.5	10	5.07	2.50	1000	20.5	0 in H2O	OFF
490	7/18/2013	Run032	MHL	Model 0	1.5	14	5.27	2.50	1000	20.5		OFF
491	7/18/2013	Run033	MHL	Model 0	1.5	14	5.85	2.50	1000	20.5		OFF
492	7/26/2013	Run071	MHL	Model 0	1.5	13	6.08	2.50	1000	20.5	0 in H2O	OFF
493	7/26/2013	Run073	MHL	Model 0	1.5	14	1.52	2.50	1000	20.5	ramp up	OFF
494	7/26/2013	Run077	MHL	Model 0	1.5	14	3.04	1.00	1000	20.5	ramp down	OFF
495	7/26/2013	Run074	MHL	Model 0	1.5	10	4.05	1.50	1000	20.5	0 inch H2O	OFF
496	7/26/2013	Run075	MHL	Model 0	1.5	20	5.07	0.50	1000	20.5	0 in h2o	OFF
497	7/26/2013	Run076	MHL	Model 0	1.5	20	6.08	0.55	1000	20.5	0 in h2o	OFF
498	9/4/2015	FC001	MHL	Model 1	0	0	0.00	1.50	1000	18		OFF
499	8/27/2015	F100	MHL	Model 1	0.5	-5	1.76	1.23	1000	17.77	No video	OFF
500	8/27/2015	F101	MHL	Model 1	0.5	-5	2.34	1.23	1000	17.77	No camera	OFF
501	8/27/2015	F102	MHL	Model 1	0.5	-5	2.93	1.63	1000	17.77	No Camera	OFF
502	8/27/2015	F103	MHL	Model 1	0.5	-5	3.51	2.04	1000	17.77	no camera	OFF
503	8/27/2015	F104	MHL	Model 1	0.5	-5	4.68	2.45	1000	17.77	no camera	OFF
504	8/27/2015	F105	MHL	Model 1	0.5	0	5.85	1.23	1000	17.77	No camera	OFF
505	8/27/2015	F106	MHL	Model 1	0.5	0	1.76	1.63	1000	17.77	No camera	OFF
506	8/27/2015	F107	MHL	Model 1	0.5	0	2.34	2.04	1000	17.77	no camera	OFF
507	8/27/2015	F108	MHL	Model 1	0.5	0	3.51	2.45	1000	17.77	No camera	OFF
508	8/27/2015	F109	MHL	Model 1	0.5	5	4.68	1.63	1000	17.77	no camera	OFF
509	8/27/2015	F110	MHL	Model 1	0.5	5	5.85	1.63	1000	17.77	no camera	OFF
510	8/27/2015	F111	MHL	Model 1	0.5	10	1.76	1.63	1000	17.77	Unable to trigger cavity	OFF
511	8/27/2015	F112	MHL	Model 1	0.5	5	2.34	1.23	1000	17.77	Cavity formed, was not sustained	OFF
512	8/27/2015	F116	MHL	Model 1	0.5	5	2.34	1.23	1000	17.77	Cavity was formed by blower, was not sustained	OFF
513	8/27/2015	F113	MHL	Model 1	0.5	5	3.51	1.23	1000	17.77	10 up, 10 down	OFF
514	8/27/2015	F117	MHL	Model 1	0.5	5	3.51	1.63	1000	17.77	Blower worked, 40s ramp down	OFF
515	8/27/2015	F114	MHL	Model 1	0.5	5	4.68	2.04	1000	17.77	Cavity induced with rod	OFF
516	8/27/2015	F115	MHL	Model 1	0.5	5	5.85	2.04	1000	17.77	Cavity induced with rod	OFF
517	8/27/2015	F118	MHL	Model 1	0.5	5	1.76	2.45	1000	17.77	60 up, 15 down. Rod used to induce cavity	OFF
518	8/27/2015	F119	MHL	Model 1	0.5	5	2.34	1.63	1000	17.77	Ventilation forced with rod	OFF
519	8/27/2015	F123	MHL	Model 1	0.5	5	2.34	1.63	1000	17.77	Both blower and rod failed to produce a cavity	OFF
520	8/27/2015	F124	MHL	Model 1	0.5	10	2.93	1.23	1000	17.77	Valve control was not on, used rod	OFF
521	8/27/2015	F124A	MHL	Model 1	0.5	10	2.93	1.63	1000	17.77	Blower worked	OFF

#	Date	Run Name	Facility	Model	AR_h	α, deg	Speed, m/s	Fn_h	P_0, mbar	Water Temp, C	Comment	Shaker
522	8/27/2015	F120	MHL	Model 1	0.5	10	3.51	2.04	1000	17.77	Blower worked	OFF
523	8/27/2015	F121	MHL	Model 1	0.5	10	4.68	2.45	1000	17.77	Blower worked	OFF
524	8/27/2015	F122	MHL	Model 1	0.5	10	5.85	1.23	1000	17.77	Blower worked	OFF
525	8/27/2015	F125	MHL	Model 1	0.5	12.5	1.76	1.23	1000	17.77	Blower worked	OFF
526	8/27/2015	F130	MHL	Model 1	0.5	12.5	1.76	1.63	1000	17.77	Blower worked, ramp down	OFF
527	8/27/2015	F126	MHL	Model 1	0.5	12.5	2.34	2.04	1000	17.77	Blower Worked	OFF
528	8/27/2015	F127	MHL	Model 1	0.5	12.5	3.51	1.00	1000	17.77	Blower worked	OFF
529	8/27/2015	F128	MHL	Model 1	0.5	12.5	4.68	1.50	1000	17.77	Blower didn't work, used rod	OFF
530	8/27/2015	F129	MHL	Model 1	0.5	12.5	5.85	2.00	1000	17.77	Blower failed, used rod	OFF
531	8/27/2015	F129A	MHL	Model 1	0.5	15	5.85	1.00	1000	17.77	Blower worked	OFF
532	8/28/2015	F131	MHL	Model 1	0.5	12.5	1.76	1.00	1000	18		OFF
533	8/28/2015	F136	MHL	Model 1	0.5	12.5	1.76	1.50	1000	18		OFF
534	8/28/2015	F132	MHL	Model 1	0.5	15	2.34	1.00	1000	18		OFF
535	8/28/2015	F133	MHL	Model 1	0.5	15	3.51	1.00	1000	18		OFF
536	8/28/2015	F134	MHL	Model 1	0.5	15	4.68	1.50	1000	18	Cavity did not form spontaneously, used rod	OFF
537	8/28/2015	F134A	MHL	Model 1	0.5	15	4.68	2.00	1000	18	Blower worked	OFF
538	8/28/2015	F135	MHL	Model 1	0.5	15	5.85	2.50	1000	18	Blower Worked	OFF
539	8/28/2015	F137	MHL	Model 1	0.5	15	1.76	1.50	1000	18		OFF
540	8/28/2015	F142	MHL	Model 1	0.5	20	1.76	1.00	1000	18		OFF
541	8/28/2015	F138	MHL	Model 1	0.5	20	2.34	1.50	1000	18		OFF
542	8/28/2015	F139	MHL	Model 1	0.5	20	3.51	2.00	1000	18		OFF
543	8/28/2015	F140	MHL	Model 1	0.5	20	4.68	1.50	1000	18	Blower worked	OFF
544	8/28/2015	F141	MHL	Model 1	0.5	25	5.85	1.00	1000	18	Blower tip may have dragged in water	OFF
545	8/28/2015	F143	MHL	Model 1	0.5	25	1.76	1.50	1000	18		OFF
546	8/28/2015	F148	MHL	Model 1	0.5	25	1.76	2.00	1000	18		OFF
547	8/28/2015	F144	MHL	Model 1	0.5	25	2.34	1.50	1000	18		OFF
548	8/28/2015	F145	MHL	Model 1	0.5	5	3.51	1.50	1000	18		OFF
549	8/28/2015	F146	MHL	Model 1	0.5	5	4.68	1.50	1000	18	Nozzle caught in spray	OFF
550	8/28/2015	F147	MHL	Model 1	0.5	5	5.85	2.00	1000	18		OFF
551	9/4/2015	FC014	MHL	Model 1	1	5	-2.48	2.00	1000	18	Reverse Run	OFF
552	9/4/2015	FC012	MHL	Model 1	1	5	1.66	2.50	1000	18	PV run past camera	OFF
553	9/4/2015	FC013	MHL	Model 1	1	10	2.07	1.50	1000	18	PV Run past camera	OFF
554	9/4/2015	FC011	MHL	Model 1	1	10	2.44	2.00	1000	18		OFF
555	9/4/2015	FC011A	MHL	Model 1	1	10	2.44	2.50	1000	18	Slow ramp past camera	OFF
556	9/4/2015	FC011B	MHL	Model 1	1	10	2.44	1.50	1000	18	Ramp past camera	OFF
557	9/4/2015	FC011C	MHL	Model 1	1	-5	2.44	1.50	1000	18	Ram0p past camera	OFF
558	9/4/2015	FC011D	MHL	Model 1	1	-5	2.44	2.00	1000	18	Ramp past camera	OFF
559	9/4/2015	FC007	MHL	Model 1	1	-5	3.31	2.50	1000	18	Spontaneous; Repeat 1	OFF
560	9/4/2015	FC008E	MHL	Model 1	1	-5	3.31	2.50	1000	18		OFF
561	9/4/2015	FC008	MHL	Model 1	1	-5	4.14	3.00	1000	18		OFF
562	9/4/2015	FC008A	MHL	Model 1	1	0	4.14	1.50	1000	18	Repeat 2	OFF

#	Date	Run Name	Facility	Model	AR_h	α, deg	Speed, m/s	Fn_h	P_0, mbar	Water Temp, C	Comment	Shaker
563	9/4/2015	FC008B	MHL	Model 1	1	0	4.14	2.00	1000	18	Repeat3	OFF
564	9/4/2015	FC008C	MHL	Model 1	1	0	4.14	2.50	1000	18	repeat4	OFF
565	9/4/2015	FC008D	MHL	Model 1	1	0	4.14	3.00	1000	18		OFF
566	9/4/2015	FC006	MHL	Model 1	1	5	2.48	1.00	1000	18	Blower didn't trigger cavity	OFF
567	9/4/2015	FC002	MHL	Model 1	1	5	3.05	1.50	1000	18	Air didn't work	OFF
568	9/4/2015	FC003	MHL	Model 1	1	5	3.31	2.00	1000	18	Cavity triggered	OFF
569	9/4/2015	FC004	MHL	Model 1	1	5	4.14	2.50	1000	18	Blower worked; dragged in water somewhat	OFF
570	9/4/2015	FC009	MHL	Model 1	1	5	4.14	2.50	1000	18		OFF
571	9/4/2015	FC009A	MHL	Model 1	1	5	4.14	2.50	1000	18	Blower aimed straight down at water ahead of foil LE. Worked nicely with a nice HS video	OFF
572	9/4/2015	FC009B	MHL	Model 1	1	5	4.14	3.00	1000	18	Forgot to turn on valve	OFF
573	9/4/2015	FC009C	MHL	Model 1	1	5	4.14	1.50	1000	18	Blower worked this time	OFF
574	9/4/2015	FC009D	MHL	Model 1	1	5	4.14	2.00	1000	18	Final repeat	OFF
575	9/4/2015	FC005	MHL	Model 1	1	10	4.97	1.00	1000	18	Blower worked	OFF
576	9/4/2015	FC010	MHL	Model 1	1	10	5.79	1.50	1000	18	High speed	OFF
577	8/25/2015	F049	MHL	Model 1	1	10	2.48	2.00	1000	17.89		OFF
578	8/25/2015	F050	MHL	Model 1	1	10	3.31	2.50	1000	17.89	FW throughout	OFF
579	8/25/2015	F051TEST	MHL	Model 1	1	10	4.14	3.00	1000	17.89	Test	OFF
580	8/25/2015	F051	MHL	Model 1	1	10	4.14	1.50	1000	17.89	FW throughout	OFF
581	8/25/2015	F052	MHL	Model 1	1	12.5	4.97	1.00	1000	17.89	FW throughout	OFF
582	8/25/2015	F053	MHL	Model 1	1	12.5	2.48	1.50	1000	17.89	Zeroing run	OFF
583	8/25/2015	F054	MHL	Model 1	1	12.5	3.31	2.00	1000	17.89	zeroing run; speed output looks really noisy	OFF
584	8/25/2015	F055	MHL	Model 1	1	12.5	4.14	2.00	1000	17.89	zeroing run; speed output looks really noisy	OFF
585	8/25/2015	F056	MHL	Model 1	1	12.5	4.97	2.50	1000	17.89		OFF
586	8/25/2015	F057	MHL	Model 1	1	12.5	1.66	3.00	1000	17.89	Partial isolated cavity	OFF
587	8/25/2015	F058	MHL	Model 1	1	12.5	2.48	1.50	1000	17.89	Blower didn't work	OFF
588	8/25/2015	F062	MHL	Model 1	1	15	2.48	1.00	1000	17.89	Blower failed; was unable to trip cavity until during ramp-down	OFF
589	8/25/2015	F059	MHL	Model 1	1	15	3.31	1.50	1000	17.89	Blower worked	OFF
590	8/25/2015	F063	MHL	Model 1	1	15	3.31	2.00	1000	17.89	Blower worked; 5up 40 down	OFF
591	8/25/2015	F060	MHL	Model 1	1	15	4.14	2.50	1000	17.89	Blower failed	OFF
592	8/25/2015	F060A	MHL	Model 1	1	15	4.14	3.00	1000	17.89		OFF
593	8/25/2015	F060B	MHL	Model 1	1	15	4.14	3.50	1000	17.89	Re-run; blower worked	OFF
594	8/25/2015	F061	MHL	Model 1	1	15	4.97	1.50	1000	17.89	Blower worked	OFF
595	8/25/2015	F064	MHL	Model 1	1	20	1.66	1.00	1000	17.89	Really bad test; blower failed and couldn't get a cavity to open cleanly at low speed	OFF
596	8/25/2015	F065	MHL	Model 1	1	20	2.48	1.50	1000	17.89	Blower worked; Air compressor turned on after trigger	OFF
597	8/25/2015	F069	MHL	Model 1	1	20	2.48	2.00	1000	17.89	5up 50 down; washout ramp; blower worked	OFF
598	8/25/2015	F066	MHL	Model 1	1	20	3.31	2.50	1000	17.89	10 up 10 down; Blower worked	OFF
599	8/25/2015	F067	MHL	Model 1	1	20	4.14	3.00	1000	17.89	5 up 5 down;	OFF
600	8/25/2015	F068	MHL	Model 1	1	20	4.97	1.50	1000	17.89	5 up 5 down; blower worked	OFF
601	8/25/2015	F070	MHL	Model 1	1	25	1.66	1.00	1000	17.89	60up 15down; PV run; blower worked	OFF
602	8/25/2015	F071	MHL	Model 1	1	25	2.48	1.50	1000	17.89	30up 10 down; blower worked	OFF

#	Date	Run Name	Facility	Model	AR_h	α, deg	Speed, m/s	Fn_h	P_0, mbar	Water Temp, C	Comment	Shaker
603	8/26/2015	F075	MHL	Model 1	1	25	2.48	2.00	1000	17.84	5UP 50 DOWN; WASHOUT; BLOWER WORKED	OFF
604	8/25/2015	F072	MHL	Model 1	1	25	3.31	2.50	1000	17.89	10up 10 down; blower failed; used rod	OFF
605	8/26/2015	F072A	MHL	Model 1	1	25	3.31	3.00	1000	17.84	10 up 10 down; Blower worked ; Tank filter left on	OFF
606	8/26/2015	F073	MHL	Model 1	1	25	4.14	1.50	1000	17.84	5up 5 down; blower worked ; Tank filter left on	OFF
607	8/26/2015	F074	MHL	Model 1	1	14	4.97	1.50	1000	17.84	5up 5 down; blower worked	OFF
608	8/26/2015	F099	MHL	Model 1	1	14	1.66	3.00	1000	17.84	60s up 15 down. SPontaneous this time	OFF
609	8/26/2015	F098	MHL	Model 1	1	13	2.48	1.50	1000	17.84	Triggered with rod	OFF
610	8/26/2015	F096	MHL	Model 1	1	13	2.48	1.00	1000	17.84	50s ramp up; 5down	OFF
611	8/26/2015	F097	MHL	Model 1	1	-5	4.97	1.50	1000	17.84	Still spontaneous	OFF
612	8/26/2015	F076	MHL	Model 1	1	-5	1.66	2.00	1000	17.84	60S UP; 15 DOWN;	OFF
613	8/26/2015	F077	MHL	Model 1	1	-5	2.48	2.50	1000	17.84	30up 10 down	OFF
614	8/26/2015	F082	MHL	Model 1	1	-5	2.48	3.00	1000	17.84	5up 50 down; nice washout	OFF
615	8/26/2015	F078	MHL	Model 1	1	-5	3.31	4.00	1000	17.84	10 up 10 down;	OFF
616	8/26/2015	F079	MHL	Model 1	1	-5	4.14	5.00	1000	17.84	10up 5 down	OFF
617	8/26/2015	F080	MHL	Model 1	1	0	4.97	1.50	1000	17.84	5up 5 down	OFF
618	8/26/2015	F081	MHL	Model 1	1	0	5.79	2.00	1000	17.84	High speed attempt for vortex inception; Nope	OFF
619	8/26/2015	F083	MHL	Model 1	1	0	1.66	3.00	1000	17.84	60 up 15 down; appeared to have negative twist; AOA recorded as 15; actually 20.	OFF
620	8/26/2015	F084	MHL	Model 1	1	0	2.48	4.00	1000	17.84	30 up 10 down. Negative twist again	OFF
621	8/26/2015	F088	MHL	Model 1	1	0	2.48	5.00	1000	17.84	5 up 50 down; negative twist again	OFF
622	8/26/2015	F085	MHL	Model 1	1	5	3.31	1.50	1000	17.84	10up 10 down	OFF
623	8/26/2015	F086	MHL	Model 1	1	5	4.14	2.00	1000	17.84	10 up 5 down; positive twist this time	OFF
624	8/26/2015	F087	MHL	Model 1	1	5	4.97	3.00	1000	17.84	Blower activated for some reason	OFF
625	8/26/2015	F089	MHL	Model 1	1	5	1.66	4.00	1000	17.84	60s up 15 down;	OFF
626	8/26/2015	F090	MHL	Model 1	1	5	2.48	5.00	1000	17.84	30 up 10 down; back to positive twist	OFF
627	8/26/2015	F094	MHL	Model 1	1	5	2.48	2.00	1000	17.84	5up 50 down; SG seems correct now	OFF
628	8/26/2015	F091	MHL	Model 1	1	5	3.31	3.00	1000	17.84	10UP 10 DOWN;	OFF
629	8/26/2015	F092	MHL	Model 1	1	10	4.14	1.50	1000	17.84	10up 15 down; nice spray sheet	OFF
630	8/26/2015	F093	MHL	Model 1	1	10	4.97	2.00	1000	17.84	Strange behavior from the strain gauges	OFF
631	9/6/2015	FC150	MHL	Model 1	1.5	10	2.03	3.00	1000	18	PV run past camera	OFF
632	9/6/2015	FC153	MHL	Model 1	1.5	10	5.07	4.00	1000	18	HIGH load. Large deflection. Triggering worked	OFF
633	9/6/2015	FC151	MHL	Model 1	1.5	10	2.03	5.00	1000	18	Blower didn't trigger	OFF
634	9/6/2015	FC151A	MHL	Model 1	1.5	10	2.03	2.00	1000	18	Blower worked	OFF
635	8/20/2015	F001	MHL	Model 1	1.5	10	2.48	2.50	1000	18	Strain Gauge Test; FW; looks good	OFF
636	8/20/2015	F001A	MHL	Model 1	1.5	10	2.48	2.50	1000	18	Second run for F001	OFF
637	8/20/2015	F002	MHL	Model 1	1.5	15	3.31	1.50	1000	18	N/A	OFF
638	8/20/2015	F003	MHL	Model 1	1.5	15	4.14	2.00	1000	18	N/A	OFF
639	8/20/2015	F004	MHL	Model 1	1.5	15	4.97	3.00	1000	18		OFF
640	9/6/2015	FC152	MHL	Model 1	1.5	15	6.08	4.00	1000	18	High speed trigger. Blower worked	OFF
641	8/20/2015	F005	MHL	Model 1	1.5	15	2.48	5.00	1000	18		OFF
642	8/20/2015	F000	MHL	Model 1	1.5	15	3.05	5.00	1000	18	Zero-angle calibration	OFF
643	8/20/2015	F006	MHL	Model 1	1.5	15	3.31	1.50	1000	18		OFF

#	Date	Run Name	Facility	Model	AR_h	α, deg	Speed, m/s	Fn_h	P_0, mbar	Water Temp, C	Comment	Shaker
644	8/20/2015	F007	MHL	Model 1	1.5	17.5	4.14	1.50	1000	18		OFF
645	8/20/2015	F008	MHL	Model 1	1.5	17.5	4.97	2.00	1000	18		OFF
646	8/21/2015	F010	MHL	Model 1	1.5	17.5	2.48	3.00	1000	18		OFF
647	8/21/2015	F010A	MHL	Model 1	1.5	17.5	2.48	4.00	1000	18	Blower didn't work. Forced with rod	OFF
648	8/21/2015	FTEST	MHL	Model 1	1.5	17.5	2.48	4.00	1000	18	Data reset test	OFF
649	8/24/2015	F041	MHL	Model 1	1.5	17.5	3.04	5.00	1000	17.9	20 up 15 down; blower failed; rod used	OFF
650	8/24/2015	F041A	MHL	Model 1	1.5	17.5	3.04	1.50	1000	17.9	5 up, 5 down, blower worked	OFF
651	8/20/2015	F009	MHL	Model 1	1.5	20	3.31	1.50	1000	18		OFF
652	8/20/2015	F009A	MHL	Model 1	1.5	20	3.31	2.00	1000	18	Manually intoduced ventilation, did not sustain	OFF
653	8/21/2015	F011	MHL	Model 1	1.5	20	3.31	3.00	1000	18	15s ramp up. Blower failed. Triggered with rod.	OFF
654	8/21/2015	F014	MHL	Model 1	1.5	20	3.31	4.00	1000	18	Blower failed; used rod; 40s ramp down	OFF
655	8/21/2015	F014_TEST	MHL	Model 1	1.5	20	3.31	5.00	1000	18	Data reset test	OFF
656	8/24/2015	F042	MHL	Model 1	1.5	20	4.05	1.50	1000	17.9	5 up, 5 down, blower failed	OFF
657	8/24/2015	F042A	MHL	Model 1	1.5	25	4.05	1.50	1000	17.9	5up 5down; rod used during acceleration	OFF
658	8/21/2015	F012	MHL	Model 1	1.5	25	4.14	2.00	1000	18	Tip of water jet slightly in the water	OFF
659	8/21/2015	F012A	MHL	Model 1	1.5	25	4.14	3.00	1000	18	Butterworth filter on speed. Blower failed; used rod to trigger	OFF
660	8/21/2015	F013	MHL	Model 1	1.5	25	4.97	4.00	1000	18	Blower worked	OFF
661	8/24/2015	F043	MHL	Model 1	1.5	25	5.07	5.00	1000	17.9	5 up, 5 down, blower worked	OFF
662	8/21/2015	F015	MHL	Model 1	1.5	25	2.48	1.50	1000	18	Blower failed. Air compressor kicked in. AOA reported as 5; actually 10.	OFF
663	8/21/2015	F019	MHL	Model 1	1.5	0	2.48	0.00	1000	18	blower failed. used rod, 45s ramp down	OFF
664	8/24/2015	F044	MHL	Model 1	1.5	-12.5	3.04	1.84	1000	17.9	30 up, 5 down. Blower failed - used rod	OFF
665	8/24/2015	F047	MHL	Model 1	1.5	-12.5	3.04	2.00	1000	17.9	5 up, 45 down. Blower did not work, used rod	OFF
666	8/20/2015	F009B	MHL	Model 1	1.5	-12.5	3.31	2.50	1000	18	Manually forced ventilation, was not sustained	OFF
667	8/21/2015	F016	MHL	Model 1	1.5	-12.5	3.31	3.00	1000	18	Blower worked	OFF
668	8/24/2015	F045	MHL	Model 1	1.5	-12.5	4.05	1.50	1000	17.9	5 up, 5 down. Blower worked but nozzle may have dragged	OFF
669	8/21/2015	F017	MHL	Model 1	1.5	-17.5	4.14	2.00	1000	18	Blower worked	OFF
670	8/21/2015	F018	MHL	Model 1	1.5	-17.5	4.97	2.50	1000	18	Blower worked; really jumped back toward straight during inception	OFF
671	8/24/2015	F046	MHL	Model 1	1.5	-17.5	5.07	2.50	1000	17.9	5 up, 5 down. Blower worked	OFF
672	8/21/2015	F023	MHL	Model 1	1.5	-17.5	2.03	2.50	1000	18	Spontaneous development of cavity.	OFF
673	8/21/2015	F027	MHL	Model 1	1.5	-17.5	2.03	2.50	1000	18	Rod used to trigger cavity; Blower activated during deceleration. 45s ramp down. Mistakenly reported as 15deg; actually 12.5	OFF
674	8/21/2015	F020	MHL	Model 1	1.5	-17.5	2.48	2.50	1000	18	45s ramp up; rod used to force inception	OFF
675	8/21/2015	F024	MHL	Model 1	1.5	-17.5	3.04	2.00	1000	18	blower successful	OFF
676	8/24/2015	F027A	MHL	Model 1	1.5	-12.5	3.04	2.50	1000	17.9	Blower worked 45s ramp down	OFF
677	8/21/2015	F021	MHL	Model 1	1.5	-12.5	3.31	2.50	1000	18	Blower worked; 15s ramp up	OFF
678	8/21/2015	F025	MHL	Model 1	1.5	-12.5	4.05	2.50	1000	18	Blower worked;	OFF
679	8/21/2015	F022	MHL	Model 1	1.5	-12.5	4.14	2.50	1000	18	Blower worked. Really distinct relaxation of foil during inception.	OFF
680	8/21/2015	F026	MHL	Model 1	1.5	-12.5	2.03	2.50	1000	18		OFF
681	8/24/2015	ZEROTEST	MHL	Model 1	1.5	-12.5	2.03	3.50	1000	17.9	Noise floor test	OFF
682	8/24/2015	F028	MHL	Model 1	1.5	-20	2.03	1.47	1000	17.9	45s ramp up; spontaneous	OFF
683	8/24/2015	F029	MHL	Model 1	1.5	-20	3.04	1.47	1000	17.9	45s ramp up	OFF

#	Date	Run Name	Facility	Model	AR_h	α, deg	Speed, m/s	Fn_h	P_0, mbar	Water Temp, C	Comment	Shaker
684	8/24/2015	F032	MHL	Model 1	1.5	-20	3.04	1.47	1000	17.9	5up 45 down	OFF
685	8/24/2015	F030	MHL	Model 1	1.5	-20	4.05	1.47	1000	17.9	10 up 10 down	OFF
686	8/24/2015	F031	MHL	Model 1	1.5	-20	5.07	1.47	1000	17.9	5 up 5 down	OFF
687	8/24/2015	F033	MHL	Model 1	1.5	-20	2.03	1.00	1000	17.9	60 ramp up	OFF
688	8/24/2015	F034	MHL	Model 1	1.5	-20	3.04	1.25	1000	17.9	45s up 5 down	OFF
689	8/24/2015	F036	MHL	Model 1	1.5	-20	3.04	-1.50	1000	17.9	5 up 45 down	OFF
690	8/24/2015	F035DEMO	MHL	Model 1	1.5	-15	4.05	1.00	1000	17.9	10s up 10 down	OFF
691	8/24/2015	F037	MHL	Model 1	1.5	-10	2.03	1.00	1000	17.9	60s up	OFF
692	8/24/2015	F038	MHL	Model 1	1.5	-10	3.04	1.00	1000	17.9	45s up	OFF
693	8/24/2015	F040	MHL	Model 1	1.5	-5	3.04	3.00	1000	17.9	5 up, 45 down	OFF
694	8/24/2015	F039	MHL	Model 1	1.5	-12.5	4.05	2.50	1000	17.9	10 up, 10 down ramp	OFF
695	3/9/2016	D006	MHL	Model 2	0	7.5	0.00	1.50	1000	18	Static Load test for elastic axis	OFF
696	3/5/2016	S025	MHL	Model 2	0	0	0.00	1.50	1000	18.6	Stillwater	ON
697	3/5/2016	S025A	MHL	Model 2	0	0	0.00	1.50	1000	18.6		ON
698	3/5/2016	S031	MHL	Model 2	0	0	0.00	0.00	1000	18.6	Still Water Sweep	ON
699	3/9/2016	D000	MHL	Model 2	0	10	0.00	1.50	1000	18	Dry modal sweep	ON
700	3/9/2016	D001	MHL	Model 2	0	10	0.00	1.50	1000	18	Dry modal sweep	ON
701	3/9/2016	D002	MHL	Model 2	0	10	0.00	2.00	1000	18	Dry modal sweep	ON
702	3/9/2016	D003	MHL	Model 2	0	0	0.00	0.00	1000	18	Dry modal sweep	ON
703	3/9/2016	D004	MHL	Model 2	0	10	0.00	2.00	1000	18	Dry modal sweep	ON
704	3/9/2016	D005	MHL	Model 2	0	10	0.00	0.00	1000	18	Dry modal sweep	ON
705	3/3/2016	S000	MHL	Model 2	1	10	0.00	0.00	1000	18.7	FW Sweep in still water; zero-speed	ON
706	3/3/2016	S000A	MHL	Model 2	1	10	0.00	0.00	1000	18.7	Long sweep at zero speed; ar = 1	ON
707	3/4/2016	S017	MHL	Model 2	1	10	1.66	0.00	1000	18.5	Modes 2-3 zero angle	ON
708	3/5/2016	S026	MHL	Model 2	1	10	1.66	1.50	1000	18.6	Turned on excitation late	ON
709	3/5/2016	S026A	MHL	Model 2	1	10	1.66	1.50	1000	18.6	Repeat FW modes 2-3	ON
710	3/3/2016	S002	MHL	Model 2	1	10	2.48	1.50	1000	18.7	Fully wetted Mode 1	ON
711	3/3/2016	S003	MHL	Model 2	1	10	2.48	0.00	1000	18.7	Mode 2 FW	ON
712	3/4/2016	S011	MHL	Model 2	1	10	2.48	1.50	1000	18.5	Zero angle mode 1 FW	ON
713	3/4/2016	S016	MHL	Model 2	1	0	2.48	1.50	1000	18.5	Mode 2 Zero angle	ON
714	3/4/2016	S018	MHL	Model 2	1	0	2.48	2.00	1000	18.5	Higher modes sweep at zero angle	ON
715	3/5/2016	S027	MHL	Model 2	1	0	2.48	2.00	1000	18.6	modes 2 3 FW	ON
716	3/4/2016	S012	MHL	Model 2	1	0	3.31	2.50	1000	18.5	Zero-angle Mode 1	ON
717	3/4/2016	S011B	MHL	Model 2	1	0	3.31	2.50	1000	18.5	zero speed	ON
718	3/4/2016	S015	MHL	Model 2	1	0	3.31	2.50	1000	18.5	Zero angle mode 2	ON
719	3/5/2016	S028	MHL	Model 2	1	0	3.31	2.00	1000	18.6	Speed didn't work.	ON
720	3/6/2016	S046	MHL	Model 2	1	0	4.14	1.50	1000	18.7	Zeroing Run	OFF
721	3/4/2016	S013	MHL	Model 2	1	0	4.14	1.00	1000	18.5	Mode 1; Blower dragged	ON
722	3/4/2016	S013A	MHL	Model 2	1	0	4.14	1.50	1000	18.5	Mode 1 Zero angle	ON
723	3/4/2016	S014	MHL	Model 2	1	10	4.14	1.00	1000	18.5	Mode 2 Zero angle	ON
724	3/5/2016	S029	MHL	Model 2	1	10	4.14	1.50	1000	18.6	Modes 2-3 FW	ON

#	Date	Run Name	Facility	Model	AR_h	α, deg	Speed, m/s	Fn_h	P_0, mbar	Water Temp, C	Comment	Shaker
725	3/5/2016	S030	MHL	Model 2	1	10	4.97	1.50	1000	18.6	Mode 2 FW	ON
726	3/6/2016	S047	MHL	Model 2	1	10	3.31	1.50	1000	18.7	Blower worked	OFF
727	3/6/2016	S050	MHL	Model 2	1	10	3.31	1.50	1000	18.7	5 up; 40 down	OFF
728	3/6/2016	S048	MHL	Model 2	1	10	4.14	1.50	1000	18.7	Blower Worked	OFF
729	3/6/2016	S049	MHL	Model 2	1	10	4.97	2.00	1000	18.7	Blower didn't work	OFF
730	3/6/2016	S049A	MHL	Model 2	1	10	4.97	2.00	1000	18.7	Blower Worked	OFF
731	3/3/2016	S001	MHL	Model 2	1	10	2.48	2.50	1000	18.7	Mode 1 excitation	ON
732	3/4/2016	S007	MHL	Model 2	1	10	0.00	2.50	1000	18.5	Mode 1 Sweep	ON
733	3/4/2016	S008	MHL	Model 2	1	10	0.00	0.00	1000	18.5		ON
734	3/4/2016	S009	MHL	Model 2	1	0	0.00	0.00	1000	18.5	Modes 2-3 FV	ON
735	3/4/2016	S010	MHL	Model 2	1	0	0.00	0.00	1000	18.5		ON
736	3/4/2016	S000C	MHL	Model 2	1	0	0.00	1.00	1000	18.5	Sweep with lower gain; still saturated; zero speed	ON
737	3/4/2016	S024	MHL	Model 2	1	0	0.00	1.00	1000	18.5	Zero-speed sweep	ON
738	3/4/2016	S019	MHL	Model 2	1	0	1.66	1.50	1000	18.5	FW Mode 1	ON
739	3/3/2016	S004	MHL	Model 2	1	0	2.48	2.00	1000	18.7		ON
740	3/3/2016	S004A	MHL	Model 2	1	0	2.48	2.50	1000	18.7	FV Mode 1	ON
741	3/4/2016	S009A	MHL	Model 2	1	0	2.48	3.00	1000	18.5	Modes 2-3 FV	ON
742	3/4/2016	S010A	MHL	Model 2	1	0	2.48	0.00	1000	18.5	Modes 2-3 FW	ON
743	3/4/2016	S000B	MHL	Model 2	1	10	2.48	1.50	1000	18.5		ON
744	3/4/2016	S000D	MHL	Model 2	1	10	2.48	1.50	1000	18.5		ON
745	3/4/2016	S020	MHL	Model 2	1	10	2.48	2.00	1000	18.5	FV Mode 1	ON
746	3/4/2016	S020A	MHL	Model 2	1	10	2.48	2.00	1000	18.5	FW Mode 1	ON
747	3/4/2016	S020Z	MHL	Model 2	1	13	2.48	2.00	1000	18.5	Zero Speed	ON
748	3/4/2016	S021	MHL	Model 2	1	13	2.48	2.50	1000	18.5	FV Modes 2-3	ON
749	3/4/2016	S021A	MHL	Model 2	1	13	2.48	2.50	1000	18.5	fw mODES 2-3	ON
750	3/5/2016	S032	MHL	Model 2	1	13	2.48	3.00	1000	18.6	Modes 2-3 FV; AOA SUSPECT	ON
751	3/5/2016	S032A	MHL	Model 2	1	13	2.48	3.00	1000	18.6	FW Modes 2-3 AOA SUSPECT	ON
752	3/6/2016	S051	MHL	Model 2	1	15	3.31	1.50	1000	18.7	Blower Worked; 5up 5 down	OFF
753	3/6/2016	S054	MHL	Model 2	1	15	3.31	1.50	1000	18.7	5up 40down Washout Ramp	OFF
754	3/3/2016	S005	MHL	Model 2	1	15	3.31	1.50	1000	18.7	FV Mode 1	ON
755	3/4/2016	S006	MHL	Model 2	1	15	3.31	1.00	1000	18.5	FW Mode 1	ON
756	3/4/2016	S022	MHL	Model 2	1	16	3.31	1.00	1000	18.5	Modes 2-3 FV	ON
757	3/4/2016	S022A	MHL	Model 2	1	16	3.31	0.75	1000	18.5	FW Modes 2-3	ON
758	3/5/2016	S033	MHL	Model 2	1	15	3.31	0.75	1000	18.6	Modes 2-3, FV AOA SUSPECT	ON
759	3/5/2016	S033A	MHL	Model 2	1	15	3.31	1.25	1000	18.6	Modes 2-3, FW AOA SUSPECT	ON
760	3/6/2016	S054A	MHL	Model 2	1	15	3.31	0.00	1000	18.7	5up 40down. Shaker Mode 1	ON
761	3/6/2016	S054B	MHL	Model 2	1	0	3.31	2.50	1000	18.7	5up 40 down; Mode 2	ON
762	3/6/2016	S054C	MHL	Model 2	1	5	3.31	2.00	1000	18.7	5up 40 down; Mode 3 washout	ON
763	3/6/2016	S054D	MHL	Model 2	1	5	3.31	2.50	1000	18.7	5up 40 down; washout mode 4	ON
764	3/6/2016	S052	MHL	Model 2	1	5	4.14	3.00	1000	18.7	Blower worked; 5up 5 down	OFF
765	3/4/2016	S023	MHL	Model 2	1	5	4.14	3.00	1000	18.5	Modes 2,3 FV	ON

#	Date	Run Name	Facility	Model	AR_h	α, deg	Speed, m/s	Fn_h	P_0, mbar	Water Temp, C	Comment	Shaker
766	3/4/2016	S023A	MHL	Model 2	1	5	4.14	2.00	1000	18.5	FW Modes 1,2	ON
767	3/6/2016	S053	MHL	Model 2	1	10	4.97	2.00	1000	18.7	Blower worked; 5up 5down	OFF
768	3/6/2016	S055	MHL	Model 2	1	10	3.31	2.50	1000	18.7	5up 5down; blower worked	OFF
769	3/6/2016	S058	MHL	Model 2	1	10	3.31	3.00	1000	18.7	5up 40down; unexcited washout	OFF
770	3/6/2016	S058A	MHL	Model 2	1	10	3.31	2.00	1000	18.7	5up 40 down; mode 1 washout	ON
771	3/6/2016	S056	MHL	Model 2	1	10	4.14	2.00	1000	18.7	Forgot to turn on valve control	OFF
772	3/6/2016	S056A	MHL	Model 2	1	10	4.14	2.00	1000	18.7	Blower worked; 5up 5down	OFF
773	3/6/2016	S057	MHL	Model 2	1	10	4.97	2.00	1000	18.7	5up 5down; Blower worked	OFF
774	3/5/2016	S033B	MHL	Model 2	1	10	3.31	2.00	1000	18.6	Modes 2-3, FW AOA SUSPECT	ON
775	3/5/2016	S034	MHL	Model 2	1	12.5	4.14	2.00	1000	18.6	Modes 2-3, FV AOA SUSPECT	ON
776	3/5/2016	S034A	MHL	Model 2	1	12.5	4.14	2.50	1000	18.6	Modes 2-3, FV AOA SUSPECT	ON
777	3/5/2016	S035	MHL	Model 2	1	12.5	4.97	2.50	1000	18.6	Modes 2-3 FW AOA SUSPECT	ON
778	3/5/2016	S035A	MHL	Model 2	1	12.5	4.97	3.00	1000	18.6	FV Mode 2 AOA SUSPECT	ON
779	3/6/2016	S058B	MHL	Model 2	1	12.5	3.31	2.00	1000	18.7	5up 40 down; washout mode 2. Torsional vibration moved AOA to 14 deg- data unreliable.	ON
780	3/5/2016	S045	MHL	Model 2	1	12.5	0.00	2.00	1000	18.6	Still Water Sweep - End of day	ON
781	3/5/2016	S043	MHL	Model 2	1	13.5	1.24	2.00	1000	18.6	Higher modes seem to do a better job eliminating the cavity	ON
782	3/5/2016	S040	MHL	Model 2	1	15	1.66	2.00	1000	18.6	Alternate inception and rewetting via shaker excitation	ON
783	3/5/2016	S044	MHL	Model 2	1	15	2.07	2.50	1000	18.6	Bubble Responded interestingly to excitation	ON
784	3/5/2016	S036	MHL	Model 2	1	15	2.48	3.00	1000	18.6	Shook foil near stall boundary. No spontaneous 15 deg	ON
785	3/5/2016	S037	MHL	Model 2	1	15	2.48	2.00	1000	18.6	Mode 1 during acceleration; spontaneous formation	ON
786	3/5/2016	S039	MHL	Model 2	1	15	2.48	2.00	1000	18.6	12	ON
787	3/6/2016	S059	MHL	Model 2	1	15	3.31	2.00	1000	18.7	40up 5down	OFF
788	3/6/2016	S062	MHL	Model 2	1	15	3.31	2.00	1000	18.7	5up 40 down; no excitation	OFF
789	3/6/2016	S062A	MHL	Model 2	1	17.5	3.31	2.00	1000	18.7	5up 40down washout mode 1	ON
790	3/6/2016	S062B	MHL	Model 2	1	17.5	3.31	2.00	1000	18.7	5up 40 down; washout mode 3	ON
791	3/6/2016	S062C	MHL	Model 2	1	17.5	3.31	2.00	1000	18.7	5up 40 down; washout mode 2	ON
792	3/6/2016	S060	MHL	Model 2	1	17.5	4.14	2.00	1000	18.7	5up 5down	OFF
793	3/6/2016	S061	MHL	Model 2	1	17.5	4.97	2.50	1000	18.7	No spontaneous cavity. Weird	OFF
794	3/5/2016	S042	MHL	Model 2	1	17.5	1.24	2.00	1000	18.6	High degree of control over cavity using frequency	ON
795	3/5/2016	S041	MHL	Model 2	1	17.5	1.66	2.00	1000	18.6	Inception Delayed by Torsional vibration	ON
796	3/6/2016	S063	MHL	Model 2	1	17.5	3.31	2.00	1000	18.7	40 up 5 down; AOA was logged as 0 instead of 17.5 - adjust lift accordingly	OFF
797	3/6/2016	S065	MHL	Model 2	1	17.5	3.31	2.00	1000	18.7	5up 50 down no excitation	OFF
798	3/6/2016	S063A	MHL	Model 2	1	20	3.31	2.00	1000	18.7	40up; 5down; 1st mode excitation on ramp up	ON
799	3/6/2016	S063B	MHL	Model 2	1	0	3.31	0.00	1000	18.7	40s up; shaker mode 2	ON
800	3/6/2016	S063C	MHL	Model 2	1	0	3.31	0.00	1000	18.7	40s up; mode 3 excitation	ON
801	3/6/2016	S065A	MHL	Model 2	1	0	3.31	0.00	1000	18.7	5up 40 down; mode 1 exc	ON
802	3/6/2016	S065B	MHL	Model 2	1	0	3.31	0.00	1000	18.7	5up 40 down; mode 2 excitation	ON
803	3/6/2016	S065C	MHL	Model 2	1	0	3.31	0.00	1000	18.7	5 up 40 down mode 3 excitation; forgot to turn off recporting	ON
804	3/6/2016	S064	MHL	Model 2	1	0	4.14	0.00	1000	18.7	5up 5down	OFF
805	3/6/2016	S066	MHL	Model 2	1	0	3.31	0.00	1000	18.7	20up 20 down; LAST MHL TEST	OFF

#	Date	Run Name	Facility	Model	AR_h	α, deg	Speed, m/s	Fn_h	P_0, mbar	Water Temp, C	Comment	Shaker
806	5/11/2016	AL_SWEEP_001	INSEAN	Model 0	0	0	0.00	0.00	1000	17	Dry Sweep Aluminum	ON
807	5/11/2016	AL_SWEEP_002	INSEAN	Model 0	0	0	0.00	0.00	1000	17	Dry Sweep2 Aluminum	ON
808	5/11/2016	AL_SWEEP_003	INSEAN	Model 0	0	0	0.00	0.00	1000	17	Dry Sweep Aluminum 3	ON
809	5/11/2016	AL_SWEEP_004	INSEAN	Model 0	0	0	0.00	0.00	1000	17	3 Sweeps while filling aluminum	ON
810	5/17/2016	A10_U0P0_DRY_AL_S_ON_023	INSEAN	Model 0	0	0	0.00	0.30	1000	17.5	Dry Sweep with top on; 5-200Hz; 8 cycles	ON
811	5/17/2016	A10_U0P0_DRY_AL_S_ON_024	INSEAN	Model 0	0	0	0.00	0.30	1000	17.5	Dry sweep with top on; two pieces of wood; 5-200; 8 cycles	ON
812	5/11/2016	AL_SWEEP_005	INSEAN	Model 0	1	0	0.50	0.30	1000	17	Wetted Sweep	ON
813	5/11/2016	AL_SWEEP_006	INSEAN	Model 0	1	0	0.50	1.51	1000	17		ON
814	5/11/2016	AL_SWEEP_007	INSEAN	Model 0	1	0	0.50	1.51	1000	17	FW Still Water Aluminum	ON
815	5/13/2016	A00_U1P3_FW_AL_S_OFF_006	INSEAN	Model 0	1	0	1.30	1.51	1000	17.4	VK Vortex shedding; 17.4C, 1bar, no excitation	OFF
816	5/13/2016	A00_U1P3_FW_AL_S_ON_007	INSEAN	Model 0	1	0	1.30	2.54	1000	17.4	Excited at 13.67 after VK vortices stationary; seemed to amplify; 17.4C; 1bar; long video	ON
817	5/13/2016	A00_U2P5_FW_AL_S_OFF_002	INSEAN	Model 0	1	0	2.50	2.54	1000	17	Steady State, No Excitation	OFF
818	5/12/2016	A00_U2P5_FW_AL_S_ON_001	INSEAN	Model 0	1	0	2.50	0.79	1000	17	8-25Hz Sweep FW	ON
819	5/13/2016	A00_U2P5_FW_AL_S_ON_003	INSEAN	Model 0	1	0	2.50	0.79	1000	17	5-200Hz; 8cycles; 16.6C; 1.086bar	ON
820	5/13/2016	A00_U4P2_FW_AL_S_OFF_004	INSEAN	Model 0	1	10	4.20	0.60	1000	16	No excitation; ; 15.8C; 1Bar; GoProdid not record	OFF
821	5/13/2016	A00_U4P2_FW_AL_S_ON_005	INSEAN	Model 0	1	10	4.20	1.51	1000	17.4	5-200Hz 8 cycles, 17.4; 1bar;	ON
822	5/17/2016	A05_U0P0_FW_AL_S_OFF_029	INSEAN	Model 0	1	10	0.00	1.51	1000	17.5	Still water; no excitation; reference; 17.5C; 1 bar; short video	OFF
823	5/18/2016	A05_U0P0_FW_AL_S_OFF_P250_042	INSEAN	Model 0	1	10	0.00	2.54	250	18	Zero speed; FW; no excitation; 18C; 250mbar; HS video	OFF
824	5/17/2016	A05_U1P0_FW_AL_S_OFF_030	INSEAN	Model 0	1	10	1.00	2.54	1000	17.5	Steady state with video. No excitation; 17.5 C; 1bar	OFF
825	5/17/2016	A05_U1P0_FW_AL_S_ON_031	INSEAN	Model 0	1	10	1.00	2.54	1000	17.5	Shaker test; 5-200Hz; 8cycles; 17.5C; 1bar	ON
826	5/17/2016	A05_U1P0_FWPV_AL_S_ON_041	INSEAN	Model 0	1	10	1.00	2.54	1000	17.5	FW Shaker sweep; 5-200hz; 8cycles; 17.5C; 1bar	ON
827	5/17/2016	A05_U2P5_FW_AL_S_OFF_032	INSEAN	Model 0	1	10	2.50	1.51	1000	17.5	Steady state with video; no excitation; 17.5C; 1bar	OFF
828	5/17/2016	A05_U2P5_FWPV_AL_S_OFF_039	INSEAN	Model 0	1	10	2.50	1.51	1000	17.5	Forced formation during video	OFF
829	5/17/2016	A05_U2P5_FWPV_AL_S_OFF_040	INSEAN	Model 0	1	15	2.50	0.60	1000	17.5	Shook cavity off with 1st torsion mode; no HS video; 17.5C; 1bar	OFF
830	5/17/2016	A05_U2P5_FW_AL_S_ON_033	INSEAN	Model 0	1	15	2.50	0.91	1000	17.5	Shaker; 5-200Hz; 8cycles; 17.5C; 1bar	ON
831	5/18/2016	A05_U3P0_FWFV_AL_S_OFF_P200_051	INSEAN	Model 0	1	15	3.00	1.21	200	18	Triggered FV cavity during HS video; Cavity then vanished at end of run. GoPro videos with strobe. 18C; 200bar	OFF
832	5/18/2016	A05_U3P0_FWFV_AL_S_OFF_P150_052	INSEAN	Model 0	1	15	3.00	1.81	150	18	FW to FV triggering on video; 18C; 150mbar	OFF

#	Date	Run Name	Facility	Model	AR_h	α, deg	Speed, m/s	Fn_h	P_0, mbar	Water Temp, C	Comment	Shaker
833	5/18/2016	A05_U3P0_FV_AL_S_ON_P150_053	INSEAN	Model 0	1	15	3.00	2.42	150	18	Shook cavity during HS video; 18C; 150mbar	ON
834	5/18/2016	A05_U3P0_FWPC_AL_S_OFF_P100_055	INSEAN	Model 0	1	15	3.00	2.42	100	18		OFF
835	5/18/2016	A05_U3P0_FW_AL_S_ON_P100_054	INSEAN	Model 0	1	10	3.00	0.00	100	18	FW Sweep; 18C; 100mbar	ON
836	5/18/2016	A05_U3P0_FWPC_AL_S_OFF_P70_056	INSEAN	Model 0	1	10	3.00	0.00	70	18		OFF
837	5/18/2016	A05_U3P0_FWPC_AL_S_ON_P70_057	INSEAN	Model 0	1	10	3.00	0.00	70	18	Sweep with incipient cavitation; 5-200; 4cycles; 18C; approx 70 mbar	ON
838	5/18/2016	A05_U3P0_FWPC_AL_S_ON_P70_058	INSEAN	Model 0	1	10	3.00	0.00	70	18	Played with 1st torsion and bending and incipient cavitation	ON
839	5/18/2016	A05_U3P0_PC_AL_S_OFF_P68_059	INSEAN	Model 0	1	10	3.00	0.60	68	18	nose PC; long acquisition; only last video was saved; pressure swept from 68-53 mbar; 18C Video taken at 53 mbar.	OFF
840	5/18/2016	A05_U3P0_PC_AL_S_OFF_P50_060	INSEAN	Model 0	1	10	3.00	0.60	50	18	LE partial cavity at 50mbar; Long video;	OFF
841	5/18/2016	A05_U3P0_PC_AL_S_OFF_P50_061	INSEAN	Model 0	1	5	3.00	0.00	50	18	Sweep from 49-47 mbar; PC; no HS video	OFF
842	5/18/2016	A05_U3P0US_PC_AL_S_OFF_P46_062	INSEAN	Model 0	1	5	3.00	0.60	46	18	Velocity increased form 3 to 3.1.	OFF
843	5/18/2016	A05_U3P1_PC_AL_S_OFF_P45_063	INSEAN	Model 0	1	5	3.10	0.60	45	18	PC steady state; no HS video. 1 gopro; 45mbar; 18C	OFF
844	5/18/2016	A05_U3P1US_PC_AL_S_OFF_P45_064	INSEAN	Model 0	1	5	3.10	1.51	45	18	Ramp from 3.1 to 3.2 at 45 mbar	OFF
845	5/18/2016	A05_U3P2_PC_AL_S_ON_P45_065	INSEAN	Model 0	1	5	3.20	1.51	45	18	Sweep 5-180; 8cycles; PC; 44-45mbar; 18C	ON
846	5/18/2016	A05_U3P2US_PC_AL_S_OFF_P44_067	INSEAN	Model 0	1	5	3.20	2.54	44	18	Ramp from 3.2-3.4 at 44mbar; PC; 18C	OFF
847	5/18/2016	A05_U3P2_PC_AL_S_ON_P44_066	INSEAN	Model 0	1	5	3.20	2.54	44	18	Two local sweeps; PC; turned up shaker excitation amplitude; 44 mbar; 18C	ON
848	5/18/2016	A05_U3P6_PC_AL_S_OFF_P44_073	INSEAN	Model 0	1	5	3.60	2.54	44	18		OFF
849	5/18/2016	A05_U3P6US_PCFV_AL_S_OFF_P44_074	INSEAN	Model 0	1	5	3.60	2.54	44	18	Ramped from 3.6 to 3.77m/s; PC to FV transition- caught on HS camera; 18C; 44mbar	OFF
850	5/17/2016	A05_U4P2_FW_AL_S_OF_034	INSEAN	Model 0	1	5	4.20	2.54	1000	17.5	Steady state; no shaker; video; 17.5C; 1 bar	OFF
851	5/17/2016	A05_U4P2_FWFV_AL_S_OFF_036	INSEAN	Model 0	1	5	4.20	1.51	1000	17.5	Tripped to FV while recording video; no shaker excitation	OFF
852	5/17/2016	A05_U4P2_FW_AL_S_ON_035	INSEAN	Model 0	1	5	4.20	1.51	1000	17.5	Sweep 5-200Hz; 8 cycles; 17.5C; 1bar	ON
853	5/17/2016	A05_U4P2_FW_AL_S_ON_037	INSEAN	Model 0	1	5	4.20	0.60	1000	17.5	Sweep; 5-200Hz; 8cycles; FW; 17.5C; 1bar	ON
854	5/17/2016	A05_U4P2_FWFV_AL_S_ON_038	INSEAN	Model 0	1	5	4.20	0.00	1000	17.5	Played with excitation to try to remove cavity after inception; 17.5C; 1bar	ON
855	5/18/2016	A05_U4P2_FW_AL_S_OF_P250_044	INSEAN	Model 0	1	7	4.20	2.11	250	18	FW; steady state; HS video; no strobe; 18C; 250mbar	OFF
856	5/18/2016	A05_U4P2_FW_AL_S_OF_P200_045	INSEAN	Model 0	1	5	4.20	2.54	200	18	FW; steady state with HS video; strobe worked; 18C; 200mbar	OFF

#	Date	Run Name	Facility	Model	AR_h	α, deg	Speed, m/s	Fn_h	P_0, mbar	Water Temp, C	Comment	Shaker
857	5/18/2016	A05_U4P2_FW_AL_S_OFF_P150_046	INSEAN	Model 0	1	5	4.20	2.54	150	18	Vaporous inception; Spontaneous FV formation; pressure swept from 150 to 147mbar	OFF
858	5/18/2016	A05_U4P2_FV_AL_S_OFF_P150_047	INSEAN	Model 0	1	5	4.20	2.54	150	18	FV Steady state; 18C 150mbar	OFF
859	5/18/2016	A05_U4P2_FV_AL_S_ON_P150_048	INSEAN	Model 0	1	5	4.20	2.54	150	18	FV shaker sweep; 5-200Hz; 8 cycles;	ON
860	5/18/2016	A05_U3P4_PC_AL_S_OFF_P44_068	INSEAN	Model 0	1	5	3.40	2.54	44	18	PC Steady state with HS video; 18C; 44mbar	OFF
861	5/18/2016	A05_U3P4US_PC_AL_S_OFF_P44_070	INSEAN	Model 0	1	7	3.40	2.11	44	18	Sweep from 3.4 to 3.5m/s; 18C; 44mbar	OFF
862	5/18/2016	A05_U3P4_PC_AL_S_ON_P44_069	INSEAN	Model 0	1	7	3.40	2.11	44	18	Sweep; 5-180hz; 20cycles; 44mbar; 18C; PC	ON
863	5/18/2016	A05_U3P5_FW_AL_S_OFF_P250_043	INSEAN	Model 0	1	5	3.50	1.81	250	18	FW steady state; no excitation; HS video; strobe didn't work; 18C; 250mbar	OFF
864	5/18/2016	A05_U3P5_FV_AL_S_OFF_P200_049	INSEAN	Model 0	1	5	3.50	1.81	200	18	FV steady state; no shaker; 18; 200mbar; long HS video	OFF
865	5/18/2016	A05_U3P5_FVFW_AL_S_ON_P200_050	INSEAN	Model 0	1	5	3.50	1.81	200	18	Shaker sweep; Cavity washed out; Gopro video; no HS video; 5-20Hz; 8cycles	ON
866	5/18/2016	A05_U3P5_FV_AL_S_OFF_P44_071	INSEAN	Model 0	1	5	3.50	1.81	44	18	Steady state FV; 18C; 44mbar; accidentally triggered cavity; HS video	OFF
867	5/18/2016	A05_U3P5_PC_AL_S_OFF_P43_072	INSEAN	Model 0	1	5	3.50	1.81	43	18	Ramp up to 3.65m/s; cavity ventilated spontaneously; 18C; 43mbar	OFF
868	5/17/2016	A10_U0P0_FW_AL_S_OFF_025	INSEAN	Model 0	1	5	0.00	1.81	1000	17.5	FW; still-water; 17.5C; 1bar; no excitation	OFF
869	5/17/2016	A10_U0P0_FW_AL_S_ON_026	INSEAN	Model 0	1	5	0.00	1.81	1000	17.5	FW Sweep; Zero speed ; 5-200Hz; 8cycles; 19 C; 1bar	ON
870	5/19/2016	A10_U0P0_FW_AL_S_OFF_P250_075	INSEAN	Model 0	1	5	0.00	1.81	250	18.5	Zero_run; still water; reference HS video; collected; 18.5C; 250mbar	OFF
871	5/19/2016	A10_U0P0_FW_AL_S_OFF_P190_111	INSEAN	Model 0	1	5	0.00	1.81	190	18.5	Zero run at 190mbar at end of day	OFF
872	5/17/2016	A10_U1P0_FW_AL_S_OFF_027	INSEAN	Model 0	1	5	1.00	1.81	1000	17.5	FW; No excitation; Small LE bubble developed mid-run, but was shed; 17.5C; 1bar	OFF
873	5/13/2016	A10_U1P0_PV_AL_S_ON_008	INSEAN	Model 0	1	5	1.00	1.81	1000	17.4	Torsional vibration for flow control in PV conditions successful. Video should show effect of excitation.	ON
874	5/17/2016	A10_U1P0_FW_AL_S_ON_028	INSEAN	Model 0	1	5	1.00	1.81	1000	17.5	FW/PV Sweep; 5-200; 8cycles; 17.5C; 1bar	ON
875	5/19/2016	A10_U1P0_FWPV_AL_S_OFF_P050_087	INSEAN	Model 0	1	5	1.00	1.87	49	18.5	PV flow; Steady state; 18.5C; 49mbar	OFF
876	5/19/2016	A10_U1P5_FW_AL_S_OFF_P050_088	INSEAN	Model 0	1	5	1.50	1.87	46	18.5	FW steady state; 18C; 46mbar	OFF
877	5/19/2016	A10_U2P0_FW_AL_S_OFF_P045_089	INSEAN	Model 0	1	5	2.00	1.93	45	18.5	FW steady state; 18.5c; 45MBAR	OFF
878	5/19/2016	A10_U2P0US_PC_AL_S_OFF_P045_090	INSEAN	Model 0	1	5	2.00	1.93	44	18.5	Ramped to 2.2m/s; PC; 18.5C; 44mbar	OFF
879	5/19/2016	A10_U2P2_PC_AL_S_OFF_P044_091	INSEAN	Model 0	1	5	2.20	1.93	44	18.5	PC steady state with short video; 18.5C: 44mbar	OFF
880	5/19/2016	A10_U2P2US_PC_AL_S_OFF_P044_092	INSEAN	Model 0	1	7	2.20	2.05	44	18.5	Ramp from 2.2 to 2.3; PC; 18.5C; 44mbar;	OFF

#	Date	Run Name	Facility	Model	AR_h	α, deg	Speed, m/s	Fn_h	P_0, mbar	Water Temp, C	Comment	Shaker
881	5/19/2016	A10_U2P3_PC_AL_S_OFF_P044_093	INSEAN	Model 0	1	7	2.30	2.05	44	18.5	steady state PC; 18.5C; 44mbar	OFF
882	5/19/2016	A10_U2P3US_PC_AL_S_OFF_P044_094	INSEAN	Model 0	1	7	2.30	2.05	44	18.5	Ramp to 2.4; pc; 18.5C 44mbar	OFF
883	5/19/2016	A10_U2P4_PC_AL_S_OFF_P044_095	INSEAN	Model 0	1	7	2.40	2.11	44	18.5	Steady PC with video; 18.5C; 44mbar	OFF
884	5/19/2016	A10_U2P4US_PC_AL_S_OFF_P044_096	INSEAN	Model 0	1	7	2.40	2.11	44	18.5	Ramp to 2.5; PC; 18.5C; 44mbar	OFF
885	5/13/2016	A10_U2P5_FW_AL_S_OFF_009	INSEAN	Model 0	1	5	2.50	2.17	1000	17.4	FW; No excitation; Long video; overwrote previous to correct for ACC_A sensitivity	OFF
886	5/13/2016	A10_U2P5_FV_AL_S_OFF_015	INSEAN	Model 0	1	5	2.50	2.17	1000	17.5	Steady state with video; FV; 17.5C; 1bar; no excitation	OFF
887	5/13/2016	A10_U2P5_FW_AL_S_ON_010	INSEAN	Model 0	1	10	2.50	0.00	1000	17.5	Shaker sweep; FW; 5-200; 8cycles; 17.5C; 1bar	ON
888	5/13/2016	A10_U2P5_FV_AL_S_ON_016	INSEAN	Model 0	1	10	2.50	1.81	1000	17.5	Sweep 5-200; 8cycles; FV; 17.5C; 1bar	ON
889	5/19/2016	A10_U2P5_PC_AL_S_OFF_P044_097	INSEAN	Model 0	1	12	2.50	1.99	44	18.5	PC steady with video; 18.5C; 44mbar	OFF
890	5/19/2016	A10_U2P5US_PC_AL_S_OFF_P044_098	INSEAN	Model 0	1	12	2.50	1.99	44	18.5	Ramp to 2.6; PC; 18.5; 44mbar	OFF
891	5/19/2016	A10_U2P6_PC_AL_S_OFF_P044_099	INSEAN	Model 0	1	10	2.60	2.54	44	18.5	PC steady state with video; 18.5; 44mbar	OFF
892	5/19/2016	A10_U2P6US_PC_AL_S_OFF_P044_100	INSEAN	Model 0	1	10	2.60	2.54	44	18.5	Ramp to 2.7; 18.5; 44mbar	OFF
893	5/19/2016	A10_U2P7_PC_AL_S_OFF_P044_101	INSEAN	Model 0	1	10	2.70	2.54	44	18.5	PC steady state with video; 18.5C; 44mbar	OFF
894	5/19/2016	A10_U2P7US_PC_AL_S_OFF_P044_102	INSEAN	Model 0	1	12	2.70	1.99	44	18.5	Ramp to 2.8; 18c; 44mbar	OFF
895	5/19/2016	A10_U2P8_PC_AL_S_OFF_P044_103	INSEAN	Model 0	1	12	2.80	1.99	44	18.5	PC steady state with video; 18.5; 44mbar	OFF
896	5/19/2016	A10_U2P8US_PC_AL_S_OFF_P044_104	INSEAN	Model 0	1	12	2.80	1.99	44	18.5	Ramp to 2.9; Transition to FV; 18.5C; 44mbar	OFF
897	5/19/2016	A10_U2P9_FV_AL_S_OFF_P044_105	INSEAN	Model 0	1	12	2.90	1.99	44	18.5	Steady FV with video; 18.5; 44mbar; some tip vortex cavitation	OFF
898	5/19/2016	A10_U3P0_FW_AL_S_OFF_P250_076	INSEAN	Model 0	1	12	3.00	1.99	250	18.4	FW; steady state with video; 18.4C; 250mbar	OFF
899	5/13/2016	A10_U4P2_FW_AL_S_OFF_011	INSEAN	Model 0	1	10	4.20	0.60	1000	17.5	FW; Steady state with video; 17.5C; 1bar	OFF
900	5/13/2016	A10_U4P2_FV_AL_S_OFF_013	INSEAN	Model 0	1	10	4.20	0.91	1000	17.5	FW Steady state with video; 17.5C; 1bar	OFF
901	5/13/2016	A10_U4P2_FW_AL_S_ON_012	INSEAN	Model 0	1	10	4.20	1.21	1000	17.5	Spontaneously ventilated; 17.5C	ON
902	5/13/2016	A10_U4P2_FV_AL_S_ON_014	INSEAN	Model 0	1	10	4.20	1.21	1000	17.5	Sweep; 5-200; 8 cycles; FV; no video; 17.5C; 1bar	ON
903	5/19/2016	A10_U4P2_FW_AL_S_OFF_P250_079	INSEAN	Model 0	1	10	4.20	1.33	250	18.4	FW steady state; Video; 18.4C; 250mbar	OFF
904	5/19/2016	A10_U4P2_FV_AL_S_OFF_P250_080	INSEAN	Model 0	1	10	4.20	1.33	250	18.4	FV steady state with video;	OFF

#	Date	Run Name	Facility	Model	AR_h	α, deg	Speed, m/s	Fn_h	P_0, mbar	Water Temp, C	Comment	Shaker
905	5/19/2016	A10_U4P2_FV_AL_S_ON_P250_081	INSEAN	Model 0	1	10	4.20	1.39	250	18.5	FV Shaker test; 5-180; 8cycles; 18.5C; 250mbar	ON
906	5/19/2016	A10_U4P2_FV_AL_S_OFF_P044_109	INSEAN	Model 0	1	10	4.20	1.39	44	18.5	FV steady state; 18.5C; 44mbar	OFF
907	5/19/2016	A10_U4P2_FV_AL_S_ON_P044_110	INSEAN	Model 0	1	10	4.20	1.45	44	18.5	FV; local sweeps: mode 1- 12-20; mode 2- 100-160; 20cycles; 18C; 44mbar	ON
908	5/19/2016	A10_U3P3_FW_AL_S_OFF_P250_077	INSEAN	Model 0	1	10	3.30	1.45	250	18.4	FW; steady state; shaker off; 18.4C; 250mbar	OFF
909	5/19/2016	A10_U3P3_FW_AL_S_ON_P250_078	INSEAN	Model 0	1	10	3.30	1.51	250	18.4	FW; Shaker; 5-180; 8cycles; 18.4C; 250mbar	ON
910	5/19/2016	A10_U3P3_FW_AL_S_OFF_P200_082	INSEAN	Model 0	1	10	3.30	1.51	200	18.5	FW steady state with video; 18.5; 200mbar	OFF
911	5/19/2016	A10_U3P3_FW_AL_S_OFF_P200US_083	INSEAN	Model 0	1	10	3.30	1.57	200	18.5		OFF
912	5/19/2016	A10_U3P3_FW_AL_S_OFF_P150_084	INSEAN	Model 0	1	10	3.30	1.57	150	18.4	FW steady state with video; 18.4C; 150mbar	OFF
913	5/19/2016	A10_U3P3_FW_AL_S_OFF_P150US_085	INSEAN	Model 0	1	10	3.30	1.63	150	18.4	Transition to FV flow occurred spontaneously; 18C; 132mbar at end	OFF
914	5/19/2016	A10_U3P3_FV_AL_S_OFF_P132_086	INSEAN	Model 0	1	10	3.30	1.63	132	18.4	FV steady state with video; no shaker; 18.4C; 132mbar	OFF
915	5/19/2016	A10_U3P3_FV_AL_S_OFF_P044_108	INSEAN	Model 0	1	10	3.30	1.69	44	18.5	Steady state FV	OFF
916	5/19/2016	A10_U3P3_FV_AL_S_ON_P044_106	INSEAN	Model 0	1	10	3.30	1.69	44	18.5	Long sweep; 5-180Hz; 20cycles; FV; 18.5C; 44mbar	ON
917	5/19/2016	A10_U3P3_FV_AL_S_ON_P044_107	INSEAN	Model 0	1	10	3.30	1.75	44	18.5	Long detailed sweeps over mode 1 - 10-20hz; 20cycles; and mode 2 -100-150 20cycles;	ON
918	5/16/2016	A15_U1P0_PV_AL_S_OFF_017	INSEAN	Model 0	1	12	1.00	1.99	1000	17.6	17.6C; 1bar; PV steady state without excitation	OFF
919	5/16/2016	A15_U1P5_PV_AL_S_OFF_018	INSEAN	Model 0	1	12	1.50	1.99	1000	17.5	PV Steady state; No excitation; 17.5C; 1bar	OFF
920	5/16/2016	A15_U2P0_FV_AL_S_OFF_019	INSEAN	Model 0	1	12	2.00	1.99	1000	17.5	FV Steady state; no excitation; 17.5C; 1bar	OFF
921	5/16/2016	A15_U3P0_FV_AL_S_OFF_020	INSEAN	Model 0	1	10	3.00	2.54	1000	17.5	Steady state FV; no excitation; 17.5C; 1bar	OFF
922	5/16/2016	A15_U4P0_FV_AL_S_OFF_021	INSEAN	Model 0	1	10	4.00	2.54	1000	17.5	FV Steady state; no excitation; 17.5C; 1bar	OFF
923	5/16/2016	A15_U4P0_FV_AL_S_ON_022	INSEAN	Model 0	1	10	4.00	0.00	1000	17.5	5-200Hz; 8cycles; 17.5C; 1bar	ON
924	5/2/2016	Shaker001	INSEAN	Model 2	0	10	0.00		1000	0	f0=8 f1=10 5cycles df=0.01 12.000000	ON
925	5/2/2016	Shaker002	INSEAN	Model 2	0	0	0.00		1000	0	f0=8 f1=10 10cycles df=0.01 12.000000	ON
926	5/2/2016	Shaker003	INSEAN	Model 2	0	0	0.00		1000	0	f0=8 f1=10 15cycles df=0.01 12.000000	ON
927	5/2/2016	Shaker004	INSEAN	Model 2	0	0	0.00		1000	0	f0=8 f1=10 20cycles df=0.01 12.000000	ON
928	5/2/2016	Shaker005	INSEAN	Model 2	0	0	0.00		1000	0	f0=30 f1=70 5cycles df=0.01 12.000000	ON
929	5/2/2016	Shaker006	INSEAN	Model 2	0	0	0.00		1000	0	f0=45 f1=70 10cycles df=0.01 12.000000	ON
930	5/2/2016	Shaker007	INSEAN	Model 2	0	0	0.00		1000	0	f0=45 f1=70 15cycles df=0.01 12.000000	ON
931	5/2/2016	Shaker008	INSEAN	Model 2	0	0	0.00		1000	0	f0=45 f1=70 20cycles df=0.01 12.000000	ON
932	5/2/2016	Shaker009	INSEAN	Model 2	0	0	0.00		1000	0	f0=45 f1=70 5cycles df=0.01 12.000000	ON

#	Date	Run Name	Facility	Model	AR_h	α, deg	Speed, m/s	Fn_h	P_0, mbar	Water Temp, C	Comment	Shaker
933	5/3/2016	Impulse	INSEAN	Model 2	0	0	0.00		1000	0	impulsive loading	ON
934	5/20/2016	A10_U0P0_DRY_PVC_S_ON_P1000_112	INSEAN	Model 2	0	0	0.00	0.97	1000	18.5	Dry Sweep of PVC foil	ON
935	5/31/2016	AN05_U1P6_FW_PVC_S_OFF_P1000_135	INSEAN	Model 2	1	0	1.60	0.97	1000	20.7	FW steady state; 20.7C; 1bar; negative AOA	OFF
936	5/31/2016	AN05_U2P5_FW_PVC_S_OFF_P1000_136	INSEAN	Model 2	1	0	2.50	1.51	1000	20.7	FW steady state; negative AOA; 20.7C; 1bar	OFF
937	5/31/2016	AN05_U4P2_FW_PVC_S_OFF_P1000_138	INSEAN	Model 2	1	0	4.20	1.51	1000	20.7	Negative AOA; FW steady state; 20.7C; 1bar	OFF
938	5/31/2016	AN05_U4P2_FWFV_PVC_S_OFF_P1000_139	INSEAN	Model 2	1	2	4.20	1.99	1000	20.7	Cavity was triggered, but it did not stay. Effective AOA probably too small to be stable	OFF
939	5/31/2016	AN05_U3P3_FW_PVC_S_OFF_P1000_137	INSEAN	Model 2	1	2	3.30	1.99	1000	20.7	negative AOA; steady state; FW; 20.7C; 1bar	OFF
940	5/20/2016	A00_U0P0_FW_PVC_S_OFF_P1000_000	INSEAN	Model 2	1	2	0.00	1.99	1000	18.5	Zero; Still-water reference;	OFF
941	5/30/2016	A00_U0P0_FW_PVC_S_OFF_P1000_121	INSEAN	Model 2	1	2	0.00	1.99	1000	20	Zero-speed reference run at beginning of day. FW	OFF
942	5/30/2016	A00_U0P0_FW_PVC_S_OFF_P1000_122	INSEAN	Model 2	1	2	0.00	1.99	1000	20	Another zero; SG gains increased to 4000	OFF
943	5/31/2016	A00_U0P0_FW_PVC_S_OFF_P1000_127	INSEAN	Model 2	1	2	0.00	1.99	1000	20	Zero-reference run at start of day; Yesterday ended with a power failure and a wave washing over the experiment; be wary of electrical shorts causing weird signals today.	OFF
944	5/31/2016	A00_U0P0_FW_PVC_S_OFF_P1000_128	INSEAN	Model 2	1	2	0.00	2.11	1000	20	Pre-run zero; strain gauges re-trimmed; forgot to unbias load cell; re-running	OFF
945	5/31/2016	A00_U0P0_FW_PVC_S_OFF_P1000_129	INSEAN	Model 2	1	5	0.00	0.00	1000	20	re-running zero reference; SG re-trimmed and load cell unbiased	OFF
946	5/20/2016	A00_U0P0_FW_PVC_S_ON_P1000_001	INSEAN	Model 2	1	5	0.00	0.97	1000	18.5	Long sweep; 1-120 with slight pause at 100; 15cycles; still water; 18.5C; 1bar	ON
947	5/20/2016	A00_U0P0_FW_PVC_S_ON_P1000_002	INSEAN	Model 2	1	5	0.00	0.00	1000	18.5	Mode 1 with video; still water; FW; 18.5C; 1bar	ON
948	5/20/2016	A00_U0P0_FW_PVC_S_ON_P1000_003	INSEAN	Model 2	1	5	0.00	0.00	1000	18.5	Mode 2 (twisting primary) with video; FW; still water; 18.5C; 1000mbar	ON
949	5/20/2016	A00_U0P0_FW_PVC_S_ON_P1000_004	INSEAN	Model 2	1	5	0.00	0.00	1000	18.5	Mode 3 (Primary 2noded bending) with video; FW: still water; 18.5C; 1000mbar	ON
950	5/20/2016	A00_U0P0_FW_PVC_S_ON_P1000_005	INSEAN	Model 2	1	5	0.00	0.00	1000	18.5	Mode4; 3noded bending with video; still water; 18.5C; 1000mbar	ON
951	5/30/2016	A00_U0P0_FW_PVC_S_ON_P1000_123	INSEAN	Model 2	1	5	0.00	1.51	1000	20	Long segmented sweep over modes 1, 2-3, 4; 0.02Hz step; 50 cycles; still-water	ON
952	5/20/2016	A00_U0P5_FW_PVC_S_OFF_P1000_006	INSEAN	Model 2	1	7	0.50	1.99	1000	18.5	Passive VK vortices with video; then excited at bending freq with motor;	OFF
953	5/20/2016	A00_U0P5_FW_PVC_S_ON_P1000_007	INSEAN	Model 2	1	5	0.50	2.54	1000	18.5	FW; VK vortices locked into bending mode with shaker. Video after shaker turned on; 18.5C; 1000mbar	ON
954	5/20/2016	A00_U1P6_FW_PVC_S_OFF_P1000_008	INSEAN	Model 2	1	5	1.60	2.54	1000	18.5	FW steady state with video; no shaker; 18.5C: 1000mbar	OFF
955	5/20/2016	A00_U1P6_FW_PVC_S_ON_P1000_009	INSEAN	Model 2	1	5	1.60	2.54	1000	18.5	FW steady state; VK frequency excited with motor; 18.5C; 1000mbar	ON
956	5/20/2016	A00_U1P6_FW_PVC_S_ON_P1000_010	INSEAN	Model 2	1	5	1.60	2.54	1000	18.5	Sweep; FW; 2-120Hz; 10cycles; 18.5C; 1000mbar	ON

#	Date	Run Name	Facility	Model	AR_h	α, deg	Speed, m/s	Fn_h	P_0, mbar	Water Temp, C	Comment	Shaker
957	5/20/2016	A00_U2P5_FW_PVC_S_OFF_P1000_011	INSEAN	Model 2	1	5	2.50	2.54	1000	18.5	FW; steady state; video; 18.5C; 1bar	OFF
958	5/20/2016	A00_U2P5_FW_PVC_S_ON_P1000_012	INSEAN	Model 2	1	5	2.50	2.54	1000	18.5	FW sweep; 2-130Hz; 10cycles; 18.5C; 1bar	ON
959	5/30/2016	A00_U2P5_FW_PVC_S_ON_P1000_124	INSEAN	Model 2	1	5	2.50	2.54	1000	20	Mode 1 at 0.02-0.03Hz spacing; FW; 1bar	ON
960	5/30/2016	A00_U2P5_FW_PVC_S_ON_P1000_125	INSEAN	Model 2	1	5	2.50	2.54	1000	20	Modes 2-4 at 0.02-0.0Hz spacing; FW; 1bar	ON
961	5/31/2016	A00_U4P2_FW_PVC_S_OFF_P1000_130	INSEAN	Model 2	1	5	4.20	2.54	1000	20.7	FW Steady state; 20.7C; 1bar; SG A3 appears a bit wonky. Look out for odd twit-angles as a result	OFF
962	5/20/2016	A00_U3P3_FW_PVC_S_OFF_P1000_013	INSEAN	Model 2	1	7	3.30	1.99	1000	18.5	FW steady state with video; 18.5C 1bar	OFF
963	5/20/2016	A00_U3P3_FW_PVC_S_ON_P1000_014	INSEAN	Model 2	1	7	3.30	1.99	1000	18.5	FW sweep; 2-130; 10 cycles; 18.5C; 1bar	ON
964	5/20/2016	A00_U3P3_FW_PVC_S_ON_P1000_015	INSEAN	Model 2	1	5	3.30	1.51	1000	18.5	Mode 1; bending FW with video; 18.5C; 1bar	ON
965	5/20/2016	A00_U3P3_FW_PVC_S_ON_P1000_016	INSEAN	Model 2	1	5	3.30	1.51	1000	18.5	Mode 2 FW with video; 18.5C; 1bar	ON
966	5/20/2016	A00_U3P3_FW_PVC_S_ON_P1000_017	INSEAN	Model 2	1	5	3.30	1.51	1000	18.5	FW mode 3 with video; 18.5C; 1bar	ON
967	5/20/2016	A00_U3P3_FW_PVC_S_ON_P1000_018	INSEAN	Model 2	1	5	3.30	0.30	1000	18.5	Mode 4 fw with video; 18.5C; 1bar	ON
968	5/30/2016	A00_U3P3_FW_PVC_S_ON_P1000_126	INSEAN	Model 2	1	5	3.30	0.30	1000	20	LONG segmented sweep; FW; 0.02hz steps; 50 cycles; modes 1, 2-3, 4	ON
969	5/20/2016	A00_U3P5_FW_PVC_S_OFF_P1000_019	INSEAN	Model 2	1	5	3.50	0.30	1000	18.5	FW steady state; VK freq should be close to torsion; 18.5C 1bar	OFF
970	5/23/2016	A05_U0P0_FW_PVC_S_OFF_P1000_020	INSEAN	Model 2	1	5	0.00	0.00	1000	19	Zero-speed reference run	OFF
971	5/23/2016	A05_U0P0_FW_PVC_S_OFF_P1000_024	INSEAN	Model 2	1	5	0.00	0.00	1000	19	Still water; reference	OFF
972	5/23/2016	A05_U0P0_FW_PVC_S_OFF_P1000_044	INSEAN	Model 2	1	5	0.00	0.00	1000	19	Reference zero run at end of day	OFF
973	5/23/2016	A05_U0P0_FW_PVC_S_ON_P1000_022	INSEAN	Model 2	1	5	0.00	0.97	1000	19	Sweep from 1-27hz; 40 cycles; FW; zero speed	ON
974	5/23/2016	A05_U0P0_FW_PVC_S_ON_P1000_023	INSEAN	Model 2	1	5	0.00	0.97	1000	19	Sweep from 20-70Hz; 30cycles	ON
975	5/23/2016	A05_U0P0_FW_PVC_S_ON_P1000_025	INSEAN	Model 2	1	5	0.00	0.97	1000	19	Sweep 10Hz-30Hz; 30cycles	ON
976	5/24/2016	A05_U0P0_FW_PVC_S_OFF_P117_066	INSEAN	Model 2	1	5	0.00	1.51	100	19.5	zero at end of day; 117mbar ; was not captured on Mario's DAQ	OFF
977	5/24/2016	A05_U0P0_FW_PVC_S_OFF_P050_045	INSEAN	Model 2	1	5	0.00	1.51	50	19.3	Morning-zero ref	OFF
978	5/24/2016	A05_U0P0_FW_PVC_S_OFF_P1000_044_SWEEP	INSEAN	Model 2	1	5	0.00	1.51	50			ON
979	5/23/2016	A05_U0P5_FW_PVC_S_OFF_P1000_041	INSEAN	Model 2	1	7	0.50	1.99	1000	19	Passive VK shedding apears to be locked into 1st mode	OFF

#	Date	Run Name	Facility	Model	AR_h	α, deg	Speed, m/s	Fn_h	P_0, mbar	Water Temp, C	Comment	Shaker
980	5/23/2016	A05_U0P5_FW_PVC_S_ON_P1000_042	INSEAN	Model 2	1	7	0.50	1.99	1000	19	FW; turned shaker on and off. 180 deg and 0 deg initial phase	ON
981	5/23/2016	A05_U0P5_FW_PVC_S_ON_P1000_043	INSEAN	Model 2	1	7	0.50	1.99	1000	19	FW shaking at 1st torsional mode	ON
982	5/23/2016	A05_U1P6_FW_PVC_S_OFF_P1000_021	INSEAN	Model 2	1	7	1.60	2.11	1000	19	Long steady-state acquisition for statistics convergence; FW; 1bar; 18.9C; FOrgot to use most-recent load-cell bias. Used bias vector from 5/20	OFF
983	5/24/2016	A05_U1P6_FW_PVC_S_OFF_P050_046	INSEAN	Model 2	1	7	1.60	2.11	50	19.3	FW steady state with short video; 19.3C; 50mbar;	OFF
984	5/24/2016	A05_U1P6_FW_PVC_S_ON_P050US_047	INSEAN	Model 2	1	5	1.60	2.17	50	19.3	Long sweep; 1.5-150; 20cycles; FW; 19.2C 48-45mbar	ON
985	5/24/2016	A05_U1P6_FW_PVC_S_OFF_P045_048	INSEAN	Model 2	1	5	1.60	2.17	45	19.3	FW steady state with video; 19.3C; 44mbar	OFF
986	5/23/2016	A05_U2P5_FW_PVC_S_OFF_P1000_026	INSEAN	Model 2	1	5	2.50	2.30	1000	19	Long data acquisition. steady state FW; 19C; 1bar	OFF
987	5/23/2016	A05_U2P5_FV_PVC_S_ON_P1000_038	INSEAN	Model 2	1	5	2.50	2.30	1000	19	FV Mode 1 sweep; washed out toward end	ON
988	5/23/2016	A05_U2P5_FVFW_PVC_S_ON_P1000_039	INSEAN	Model 2	1	5	2.50	2.54	1000	19	Tried to make it through modes 2-3 in FV; washed out at end; 19C; 1bar	ON
989	5/23/2016	A05_U2P5_FWFV_PVC_S_ON_P1000_040	INSEAN	Model 2	1	7	2.50	1.99	1000	19	Triggered cavity on-camera and caused washout via shaker motor; long video (40s); 19C; 1bar	ON
990	5/24/2016	A05_U2P5_PC_PVC_S_OFF_P044_049	INSEAN	Model 2	1	7	2.50	1.99	45	19.3	PC steady state with video; 19.3C; 46mbar	OFF
991	5/24/2016	A05_U2P5US_PC_PVC_S_OFF_P046_051	INSEAN	Model 2	1	7	2.50	1.99	45	19.4	PC flow; increased from 2.5 to 3.3 m/s with gopros; 19.4C: 48mbar	OFF
992	5/24/2016	A05_U2P5_PC_PVC_S_ON_P046_050	INSEAN	Model 2	1	7	2.50	1.99	45	19.4	PC shaker sweep; 2-140; 15 cycles; 19.4C; 46mbar	ON
993	5/24/2016	A05_U3P6US_PC_PVC_S_OFF_P047_058	INSEAN	Model 2	1	5	3.60	0.00	48	19.4		OFF
994	5/24/2016	A05_U3P6_PC_PVC_S_OFF_P047_057	INSEAN	Model 2	1	8	3.60	0.00	47	19.4	PC; steady state with long video; no shaker; 19.4C; 47mbar	OFF
995	5/24/2016	A05_U3P8_PCFV_PVC_S_OFF_P047_059	INSEAN	Model 2	1	8	3.80	0.00	48	19.5	Transition from PC to FV caught on HS camera; Water level changed mid-run; careful about using mean loads. 19.4C; 47mbar;	OFF
996	5/24/2016	A05_U3P8_FV_PVC_S_OFF_P047_060	INSEAN	Model 2	1	8	3.80	0.97	48	19.5	FV steady state post-formation; no video; no shaker; 19.5c; 47mbar	OFF
997	5/23/2016	A05_U4P2_FW_PVC_S_OFF_P1000_028	INSEAN	Model 2	1	10	4.20	1.99	1000	19	Steady state FW; no excitation; long acquisition; 19C; 1bar	OFF
998	5/23/2016	A05_U4P2_FWFV_PVC_S_OFF_P1000_030	INSEAN	Model 2	1	10	4.20	1.99	1000	19	FV inception triggered on-camera by blower; 19C; 1bar	OFF
999	5/23/2016	A05_U4P2_FWFV_PVC_S_OFF_P1000_033	INSEAN	Model 2	1	10	4.20	1.99	1000	19	Triggered ventilation on camera; 19C; 1bar	OFF
1000	5/23/2016	A05_U4P2_FW_PVC_S_ON_P1000_029	INSEAN	Model 2	1	10	4.20	1.99	1000	19	Sweep 2-150; 10cycles; 19C; 1bar	ON
1001	5/23/2016	A05_U4P2_FV_PVC_S_ON_P1000_031	INSEAN	Model 2	1	8	4.20	0.00	1000	19	FV; Sweep 2-150; 10 cycles; 19C 1bar	ON
1002	5/23/2016	A05_U4P2_FV_PVC_S_ON_P1000_032	INSEAN	Model 2	1	10	4.20	0.00	1000	19	Foil rewetted early in sweep; 10 cycles;	ON
1003	5/23/2016	A05_U4P2_FV_PVC_S_ON_P1000_033_SWEEP	INSEAN	Model 2	1	10	4.20	0.00	1000		Quick sweep; null for data; fw	ON

#	Date	Run Name	Facility	Model	AR_h	α, deg	Speed, m/s	Fn_h	P_0, mbar	Water Temp, C	Comment	Shaker
1004	5/23/2016	A05_U4P2_FV_PVC_S_ON_P1000_034	INSEAN	Model 2	1	10	4.20	0.00	1000	19	Cavity washed out at 2.2 hz	ON
1005	5/23/2016	A05_U4P2_FV_PVC_S_ON_P1000_035	INSEAN	Model 2	1	10	4.20	0.00	1000	19	Longer sweep; 2-56Hz; 20cycles; re-wetted at end	ON
1006	5/24/2016	A05_U4P2_FV_PVC_S_OFF_P048_061	INSEAN	Model 2	1	10	4.20	0.00	48	19.5	FV steady state; no shaker; no HS video; 19.5C; 48mbar	OFF
1007	5/23/2016	A05_U3P3_FW_PVC_S_OFF_P1000_027	INSEAN	Model 2	1	10	3.30	0.97	1000	19	FW steady state; no excitation ; 19C; 1bar	OFF
1008	5/23/2016	A05_U3P3_FV_PVC_S_OFF_P1000_036	INSEAN	Model 2	1	10	3.30	1.51	1000	19	FV steady state; Re-wetted at end; 19C; 1bar	OFF
1009	5/23/2016	A05_U3P3_FW_PVC_S_OFF_P1000_037	INSEAN	Model 2	1	10	3.30	1.51	1000	19	Long acquisition for stat convergence. FW flow; 19C; 1bar	OFF
1010	5/24/2016	A05_U3P3_PC_PVC_S_OFF_P061_063	INSEAN	Model 2	1	12	3.30	1.99	61	19.5	PC steady state; no shaker; 19.5C; 61mbar	OFF
1011	5/24/2016	A05_U3P3_PCFV_PVC_S_OFF_P061_065	INSEAN	Model 2	1	12	3.30	1.99	61	19.5	Triggered PC to FV cavity with air jet; on HS camera; 19.5C 65 mbar	OFF
1012	5/24/2016	A05_U3P3_PC_PVC_S_ON_P061_062	INSEAN	Model 2	1	10	3.30	2.54	61	19.5	PC; sweep 2-140hz; 15cycles; no HS video; 19.5C 61 mbar	ON
1013	5/24/2016	A05_U3P3_PC_PVC_S_ON_P061_064	INSEAN	Model 2	1	10	3.30	2.54	61	19.5	quick sweep; 2-60hz; 10cycles; PC; 19.5C; 61mbar	ON
1014	5/24/2016	A05_U3P3_PC_PVC_S_OFF_P048_052	INSEAN	Model 2	1	10	3.30	2.54	45	19.4	PC steady state; 19.4C; 48mbar	OFF
1015	5/24/2016	A05_U3P3US_PC_PVC_S_OFF_P048_054	INSEAN	Model 2	1	10	3.30	2.54	45	19.4	PC flow; speed swept from 3.3 to 3.5m/s; 19.4c; 48mbar	OFF
1016	5/24/2016	A05_U3P3_PC_PVC_S_ON_P048_053	INSEAN	Model 2	1	12	3.30	1.99	45	19.4	sweep 2-140; 15cycles; PC; 19.4C; 48mbar	ON
1017	5/24/2016	A05_U3P5US_PC_PVC_S_OFF_P048_056	INSEAN	Model 2	1	12	3.50	1.99	46	19.4	PC sweep from 3.5-3.6; 19.4C; 47mbar	OFF
1018	5/24/2016	A05_U3P5_PC_PVC_S_OFF_P048_055	INSEAN	Model 2	1	10	3.50	0.00	45	19.4	PC steady state with short video at 3.5; 19.4C; 48mbar	OFF
1019	5/25/2016	A08_U0P0_FW_PVC_S_OFF_P1000_067	INSEAN	Model 2	1	10	0.00	0.00	1000	19.5	Zero run at start of day	OFF
1020	5/25/2016	A08_U0P0_FW_PVC_S_OFF_P1000_068	INSEAN	Model 2	1	10	0.00	1.51	1000	19.5	shorter zero-run	OFF
1021	5/25/2016	A08_U0P0_FW_PVC_S_OFF_P1000_074	INSEAN	Model 2	1	10	0.00	1.51	1000	19.5	zero reference run; 19.5C; 1bar	OFF
1022	5/25/2016	A08_U1P6_FW_PVC_S_OFF_P1000_069	INSEAN	Model 2	1	10	1.60	1.51	1000	19.5	FW steady state; 19.5C; 1bar	OFF
1023	5/25/2016	A10_U0P0_FW_PVC_S_OFF_P1000_076	INSEAN	Model 2	1	10	0.00	0.97	1000	19.6	Zero-ref; long run;	OFF
1024	5/25/2016	A10_U0P0_FW_PVC_S_OFF_P1000_077	INSEAN	Model 2	1	10	0.00	0.00	1000	19.6	Zero ref with video;	OFF
1025	5/25/2016	A10_U0P0_FW_PVC_S_OFF_P1000_078Z	INSEAN	Model 2	1	10	0.00	0.00	1000		re-zero strain gages; seem to drifting because of thermal effects (lights)	OFF
1026	5/25/2016	A10_U0P0_FW_PVC_S_OFF_P1000_078	INSEAN	Model 2	1	10	0.00	1.21	1000	19.6	Zero-run	OFF
1027	5/25/2016	A10_U0P0_FW_PVC_S_OFF_P1000_090	INSEAN	Model 2	1	10	0.00	1.33	1000	19.6	end-of-day zero	OFF

#	Date	Run Name	Facility	Model	AR_h	α, deg	Speed, m/s	Fn_h	P_0, mbar	Water Temp, C	Comment	Shaker
1028	5/31/2016	A10_U0P0_FW_PVC_S_OFF_P1000_131	INSEAN	Model 2	1	12	0.00	1.99	1000	20.7	Post-run zero to catch drift/hysteresis;	OFF
1029	5/31/2016	A10_U0P0_FW_PVC_S_OFF_P1000_132	INSEAN	Model 2	1	12	0.00	1.99	1000	20.7	Another zero-run with SG trimmed; 20.7C; 1bar	OFF
1030	5/31/2016	A10_U0P0_FW_PVC_S_OFF_P1000_140	INSEAN	Model 2	1	12	0.00	1.99	1000	20.7	Post-run zero; AOA changed to 10 beforehand	OFF
1031	5/31/2016	A10_U0P0_FW_PVC_S_OFF_P1000_141	INSEAN	Model 2	1	12	0.00	1.99	1000	20.7	Pre-run zero at 10deg; 20.7C; 1bar	OFF
1032	5/25/2016	A10_U0P0_FW_PVC_S_ON_P1000_075	INSEAN	Model 2	1	12	0.00	1.99	1000	19.6	LONG still-water sweep; 1-160hz; 25 cycles	ON
1033	5/26/2016	A10_U0P0_FW_PVC_S_OFF_P254_091	INSEAN	Model 2	1	12	0.00	1.99	254	20	FW zero-reference run while pressure decreased from 254 to 236 mbar; 20C	OFF
1034	5/27/2016	A10_U0P0_FW_PVC_S_OFF_P150_107	INSEAN	Model 2	1	10	0.00	0.00	150	20.1	Zero run at start of testing; 20.1; 150mbar	OFF
1035	5/27/2016	A10_U0P0_FW_PVC_S_OFF_P100_120	INSEAN	Model 2	1	10	0.00	0.00	100	20.3	end-of-day zero	OFF
1036	5/26/2016	A10_U0P0_FW_PVC_S_OFF_P053US_096	INSEAN	Model 2	1	10	0.00	1.51	53	19.7	Reference run; strain gauge A2 drifted way out, so we are re-zeroing; 19.7C; 53mbar	OFF
1037	5/26/2016	A10_U0P0_FW_PVC_S_OFF_P053US_097	INSEAN	Model 2	1	12	0.00	1.99	51	19.7	FW zero reference at 52-51mbar; 19.7C	OFF
1038	5/26/2016	A10_U0P0_FW_PVC_S_OFF_P050_106	INSEAN	Model 2	1	12	0.00	1.99	50	19.7	end-of-day zero; 50mbar	OFF
1039	5/27/2016	A10_U0P0_FW_PVC_S_OFF_P050_117	INSEAN	Model 2	1	10	0.00	1.51	50	20.3	post-run zero to quantify strain gauge drift; 20.3C; 50mbar;	OFF
1040	5/27/2016	A10_U0P0_FW_PVC_S_OFF_P050_118	INSEAN	Model 2	1	10	0.00	1.51	50	20.3	Pre-run zero with SG trimmed out; 20.3c; 50mbar	OFF
1041	5/25/2016	A10_U1P6_FW_PVC_S_OFF_P1000_079	INSEAN	Model 2	1	10	1.60	1.51	1000	19.6	FW steady state with video; 19.6c; 1bar	OFF
1042	5/31/2016	A10_U1P6_PV_PVC_S_OFF_P1000_134	INSEAN	Model 2	1	10	1.60	1.81	1000	20.7	PV Steady state; 20.7C; 1bar	OFF
1043	5/26/2016	A10_U1P6_PC_PVC_S_ON_P067US_095	INSEAN	Model 2	1	10	1.60	1.81	67	19.7	long video of modal excitation at each frequency; PC; 19.7 67mbar	ON
1044	5/26/2016	A10_U2P0_PVFV_PVC_S_OFF_P047_098	INSEAN	Model 2	1	12	2.00	1.99	47	19.7	Steady state at washout boundary with nice long video; 19.7C 47mbar	OFF
1045	5/26/2016	A10_U2P2_FV_PVC_S_OFF_P047_099	INSEAN	Model 2	1	10	2.20	0.00	47	19.7	FV steady state with long video; right above washout boundary; 19.7C; 47mbar	OFF
1046	5/25/2016	A10_U2P5_FW_PVC_S_OFF_P1000_080	INSEAN	Model 2	1	10	2.50	0.00	1000	19.6	FW steady state; 19.6c; 1bar	OFF
1047	5/25/2016	A10_U2P5_FW_PVC_S_ON_P1000_081	INSEAN	Model 2	1	12	2.50	1.99	1000	19.6	Long segmented sweeps over modes 1,2,3,4,5	ON
1048	5/26/2016	A10_U2P5_FV_PVC_S_OFF_P212_092	INSEAN	Model 2	1	10	2.50	0.00	250	19.8	FV steady state with video; 19.8; pressure from 212 to 185;	OFF
1049	5/26/2016	A10_U2P5_FV_PVC_S_ON_P185US_093	INSEAN	Model 2	1	0	2.50	0.00	250	19.7	long sweep; FV; 2-140; 20 cycles; marios daq stopped early; 19.7; pressure dropped from 185 to 149mbar	ON
1050	5/27/2016	A10_U2P5_FW_PVC_S_OFF_P150_108	INSEAN	Model 2	1	0	2.50	0.00	150	20.1	FW steady state with video; 20.1c; 150mbar	OFF
1051	5/26/2016	A10_U2P5_FV_PVC_S_ON_P142US_094	INSEAN	Model 2	1	0	2.50	0.00	142	19.7	Detailed sweep over modes 2-3; 30-50hz; FV 100cycles; 19.7C; pressure from 142-127mbar	ON

#	Date	Run Name	Facility	Model	AR_h	α, deg	Speed, m/s	Fn_h	P_0, mbar	Water Temp, C	Comment	Shaker
1052	5/27/2016	A10_U2P5_PC_PVC_S_OFF_P050_111	INSEAN	Model 2	1	0	2.50	1.51	50	20.2	PC steady state with video; 20.2C; 50mbar	OFF
1053	5/27/2016	A10_U2P5US_PC_PVC_S_OFF_P050_113	INSEAN	Model 2	1	0	2.50	1.51	50	20.2	Ramp up from 2.5 to 3m/s; 21.2C; 50mbar; PC	OFF
1054	5/27/2016	A10_U2P5_PC_PVC_S_ON_P050_112	INSEAN	Model 2	1	2	2.50	1.99	50	20.2	Sweep; 2-140; 10cycles; PC; 20.1; 50mbar	ON
1055	5/27/2016	A10_U3P0_PC_PVC_S_OFF_P050_114	INSEAN	Model 2	1	0	3.00	0.00	50	20.2	PC steady state with video; 20.1C; 50mbar	OFF
1056	5/27/2016	A10_U3P0_PCFV_PVC_S_ON_P050_115	INSEAN	Model 2	1	0	3.00	0.00	50	20.2	Spontaneously ventilated around 25hz; 20.1C; 50mbar	ON
1057	5/25/2016	A08_U3P3_FW_PVC_S_OFF_P1000_070	INSEAN	Model 2	1	0	3.30	0.00	1000	19.5	FW steady state with video UW gopro died halfway through; 19.5C; 1bar	OFF
1058	5/25/2016	A08_U3P3_FWFV_PVC_S_OFF_P1000_071	INSEAN	Model 2	1	0	3.30	2.54	1000	19.5	Triggered on-camera; 19.5c; 1bar	OFF
1059	5/25/2016	A08_U3P3_FV_PVC_S_OFF_P1000_072	INSEAN	Model 2	1	10	3.30	0.00	1000	19.5	FV steady state WITHOUT video; 19.5 C 1bar	OFF
1060	5/25/2016	A08_U3P3_FV_PVC_S_OFF_P1000_073	INSEAN	Model 2	1	10	3.30	0.00	1000	19.5	FV steady state with video; 19.5c; 1bar	OFF
1061	5/25/2016	A10_U4P2_FW_PVC_S_OFF_P1000_084	INSEAN	Model 2	1	12	4.20	1.99	1000	19.6	FW steady state with video; 19..7; 1bar	OFF
1062	5/25/2016	A10_U4P2_FV_PVC_S_OFF_P1000_086	INSEAN	Model 2	1	10	4.20	0.97	1000	19.6	FV steady state with video; 19.6c; 1bar	OFF
1063	5/25/2016	A10_U4P2_FW_PVC_S_ON_P1000_085	INSEAN	Model 2	1	-5	4.20	0.97	1000	19.6	Transition occurred spontaneously; 19.6c; 1bar	ON
1064	5/25/2016	A10_U4P2_FV_PVC_S_ON_P1000_087	INSEAN	Model 2	1	-5	4.20	1.51	1000	19.6	FV Sweep; 2-140hz; 10cycles; Mario's DAQ ran out of HDD space, so did not record; 19.6C; 1bar	ON
1065	5/25/2016	A10_U3P3_FW_PVC_S_OFF_P1000_082	INSEAN	Model 2	1	-3	3.30	1.99	1000	19.6	FW steady state with video; 19.6C; 1bar	OFF
1066	5/25/2016	A10_U3P3_FV_PVC_S_OFF_P1000_088	INSEAN	Model 2	1	-5	3.30	2.54	1000	19.6	FV steady state with video; 19.6C; 1bar	OFF
1067	5/31/2016	A10_U3P3_FV_PVC_S_OFF_P1000_133	INSEAN	Model 2	1	-5	3.30	2.54	1000	20.7	FV Steady state; 20.7C; 1bar	OFF
1068	5/31/2016	A10_U3P3_FV_PVC_S_OFF_P1000_142	INSEAN	Model 2	1	10	3.30	0.00	1000	20.7	FV steady state; long acquisition; 20.7C; 1bar	OFF
1069	5/25/2016	A10_U3P3_FW_PVC_S_ON_P1000_083	INSEAN	Model 2	1	10	3.30	0.00	1000	19.6	Long sweep; FW; 19.6C; 1bar	ON
1070	5/25/2016	A10_U3P3_FV_PVC_S_ON_P1000_089	INSEAN	Model 2	1	12	3.30	1.99	1000	19.6	FV sweep; 2-160; 10 cycles; 19.6; 1bar	ON
1071	5/27/2016	A10_U3P3_FW_PVC_S_OFF_P150_109	INSEAN	Model 2	1	15	3.30	0.00	150	20.1	FW steady state; watch the previous gopro video (around 1330 hours) to see the interaction of waves and varying immersion depth	OFF
1072	5/27/2016	A10_U3P3_FWPC_PVC_S_OFF_P134US_110	INSEAN	Model 2	1	15	3.30	0.97	134	20.2	Pressure swept from 110 to 61 mbar at 3.3m/s; 20.2; finished at 61 mbar	OFF
1073	5/27/2016	A10_U3P3_PC_PVC_S_OFF_P070_119	INSEAN	Model 2	1	15	3.30	1.51	70	20.3	PC steady state with video; 20.3c; 70 mbar	OFF
1074	5/26/2016	A10_U3P3_FV_PVC_S_OFF_P050_100	INSEAN	Model 2	1	17	3.30	1.99	51	19.7	FV steady state with video; 19.9C; 51mbar	OFF
1075	5/27/2016	A10_U3P3_FV_PVC_S_OFF_P050_116	INSEAN	Model 2	1	15	3.30	2.54	50	20.3	FV steady state; standardization run; 20.3; 50mbar	OFF

#	Date	Run Name	Facility	Model	AR_h	α, deg	Speed, m/s	Fn_h	P_0, mbar	Water Temp, C	Comment	Shaker
1076	5/26/2016	A10_U3P3_FV_PVC_S_ON_P050_102	INSEAN	Model 2	1	15	3.30	1.51	50	19.7	FV sweep; 2-140; 10cycles; 19.9c; 50mbar	ON
1077	5/26/2016	A10_U3P3_FV_PVC_S_ON_P050_103	INSEAN	Model 2	1	15	3.30	0.00	50	19.7	FV sweep; 2-140; 15cycles; 19.9c; 51mbar	ON
1078	5/26/2016	A10_U3P3_FV_PVC_S_ON_P050_104	INSEAN	Model 2	1	0	3.30	0.00	50	19.7	Sweep FV; 2-140; 20 cycles; 19.7C; 49 mbar	ON
1079	5/26/2016	A10_U3P3_FV_PVC_S_ON_P050_105	INSEAN	Model 2	1	0	3.30	0.00	50	19.7	Long FV sweep; 2-150 at 0.05step; 10cycles; 19.9c; 49 mbar	ON
1080	5/26/2016	A10_U3P3_FV_PVC_S_ON_P050_101	INSEAN	Model 2	1	0	3.30	0.00	49	19.7	FV sweep; 2-140; 5cycles	ON
1081	5/31/2016	A15_U0P0_FW_PVC_S_OFF_P1000_143	INSEAN	Model 2	1	0	0.00	0.00	1000	21.2	Zero-speed ref at 15deg with HS video; DAQ weirdness preceding run; forced me to restart computer and fight with hardware; 21.2C; 1bar	OFF
1082	5/31/2016	A15_U0P0_FW_PVC_S_OFF_P1000_149	INSEAN	Model 2	1	0	0.00	0.00	1000	21.2	Final zero-run; done testing	OFF
1083	5/31/2016	A15_U1P6_PV_PVC_S_OFF_P1000_144	INSEAN	Model 2	1	0	1.60	0.00	1000	21.2	PV steady state with video; 21.2C; 1bar	OFF
1084	5/31/2016	A15_U2P5_FV_PVC_S_OFF_P1000_145	INSEAN	Model 2	1	0	2.50	0.00	1000	21.2	FV steady state with video	OFF
1085	5/31/2016	A15_U2P5_FV_PVC_S_OFF_P1000_148	INSEAN	Model 2	1	0	2.50	0.00	1000	21.2	FV steady state; hyseresis run, ramped down from higher speed	OFF
1086	5/31/2016	A15_U4P2_FV_PVC_S_OFF_P1000_147	INSEAN	Model 2	1	0	4.20	0.00	1000	21.2	FV steady state with video	OFF
1087	5/31/2016	A15_U3P3_FV_PVC_S_OFF_P1000_146	INSEAN	Model 2	1	0	3.30	0.00	1000	21.2	FV Steady state with video	OFF

APPENDIX C

Tabulated Steady-State Data

The following list is a tabulation of the run parameters and steady-state forces and structural deflections for all steady-state results shown in the thesis. This is not a one-to-one match with the tabulated list of runs, as more than one set of steady-state data were sometimes processed from a single trial.

#	Run Name	Facility	Model	AR_h	Flow Regime	α, deg	Speed, m/s	Fn_h	Facility Pressure, bar	σ_v	Re_c	δ_{SC} at tip, m		θ at tip, deg		$C_{L,3D}$		$C_{D,3D}$		$C_{M,3D}$ (about 0.5c)	
												Mean	Std	Mean	Std	Mean	Std	Mean	Std	Mean	Std
1	Run116	MHL	Model 0	0.5	FW	-5	2.93	2.5	1.000	16.00	8.24E+05	0.000	0.000	0.000	0.000	-0.081	0.0822	0.03	0.0660	-0.027	0.0159
2	Run317	MHL	Model 0	0.5	FW	-5	3.51	3	1.000	16.11	8.74E+05	0.000	0.000	0.000	0.000	-0.087	0.0647	0.03	0.0442	-0.028	0.0112
3	Run117	MHL	Model 0	0.5	FW	-5	4.09	3.5	1.000	11.76	1.15E+06	0.000	0.000	0.000	0.000	-0.083	0.0477	0.03	0.0337	-0.027	0.0079
4	Run118	MHL	Model 0	0.5	FW	-5	4.66	4	1.000	9.00	1.31E+06	0.000	0.000	0.000	0.000	-0.081	0.0388	0.03	0.0335	-0.027	0.0070
5	Run119	MHL	Model 0	0.5	FW	-5	5.24	4.5	1.000	7.11	1.48E+06	0.000	0.000	0.000	0.000	-0.077	0.0377	0.02	0.0309	-0.027	0.0068
6	Run318	MHL	Model 0	0.5	FW	-5	5.79	5	1.000	5.80	1.44E+06	0.000	0.000	0.000	0.000	-0.075	0.0315	0.02	0.0385	-0.026	0.0055
7	Run319	MHL	Model 0	0.5	FW	0	2.33	2	1.000	36.25	5.82E+05	0.000	0.000	0.000	0.000	0.007	0.1228	0.04	0.0925	0.004	0.0231
8	Run120	MHL	Model 0	0.5	FW	0	3.47	3	1.000	16.00	9.77E+05	0.000	0.000	0.000	0.000	0.001	0.0637	0.03	0.0875	0.003	0.0100
9	Run121	MHL	Model 0	0.5	FW	0	4.09	3.5	1.000	11.76	1.15E+06	0.000	0.000	0.000	0.000	0.005	0.0511	0.02	0.0354	0.003	0.0084
10	Run122	MHL	Model 0	0.5	FW	0	4.67	4	1.000	9.00	1.32E+06	0.000	0.000	0.000	0.000	0.005	0.0468	0.02	0.0350	0.002	0.0075
11	Run123	MHL	Model 0	0.5	FW	0	5.24	4.5	1.000	7.11	1.48E+06	0.000	0.000	0.000	0.000	0.004	0.0390	0.02	0.0265	0.003	0.0071
12	Run320	MHL	Model 0	0.5	FW	0	5.79	5	1.000	5.80	1.44E+06	0.000	0.000	0.000	0.000	0.000	0.0346	0.01	0.0454	0.003	0.0058
13	Run322	MHL	Model 0	0.5	FW	2.5	1.76	1.5	1.000	36.25	4.38E+05	0.000	0.000	0.000	0.000	0.064	0.2044	0.03	0.1372	0.017	0.0340
14	Run330	MHL	Model 0	0.5	FW	2.5	1.76	1.5	1.000	19.17	4.38E+05	0.000	0.000	0.000	0.000	0.050	0.1852	0.02	0.1138	0.014	0.0248
15	Run321	MHL	Model 0	0.5	FW	2.5	2.33	2	1.000	36.25	5.82E+05	0.000	0.000	0.000	0.000	0.048	0.1205	0.03	0.0885	0.015	0.0208
16	Run324	MHL	Model 0	0.5	FW	2.5	2.63	2.25	1.000	28.64	6.56E+05	0.000	0.000	0.000	0.000	0.046	0.1244	0.03	0.0785	0.017	0.0233
17	Run323	MHL	Model 0	0.5	FW	2.5	2.92	2.5	1.000	23.20	7.27E+05	0.000	0.000	0.000	0.000	0.046	0.0962	0.03	0.0718	0.017	0.0185
18	Run325	MHL	Model 0	0.5	FW	2.5	3.51	3	1.000	16.11	8.74E+05	0.000	0.000	0.000	0.000	0.045	0.0679	0.02	0.0425	0.018	0.0118
19	Run326	MHL	Model 0	0.5	FW	2.5	4.09	3.5	1.000	11.84	1.02E+06	0.000	0.000	0.000	0.000	0.045	0.0480	0.02	0.0355	0.018	0.0088
20	Run327	MHL	Model 0	0.5	FW	2.5	4.64	4	1.000	9.06	1.16E+06	0.000	0.000	0.000	0.000	0.044	0.0399	0.02	0.0279	0.017	0.0071
21	Run328	MHL	Model 0	0.5	FW	2.5	5.21	4.5	1.000	7.16	1.30E+06	0.000	0.000	0.000	0.000	0.044	0.0383	0.02	0.0258	0.017	0.0065
22	Run329	MHL	Model 0	0.5	FW	2.5	5.79	5	1.000	5.80	1.44E+06	0.000	0.000	0.000	0.000	0.044	0.0335	0.02	0.0252	0.017	0.0059
23	Run128b	MHL	Model 0	0.5	FW	5	1.17	1	1.000	16.00	3.31E+05	0.000	0.000	0.000	0.000	0.175	0.3458	0.03	0.1821	0.026	0.0500
24	Run336b	MHL	Model 0	0.5	FW	5	1.17	1	1.000	36.25	2.92E+05	0.000	0.000	0.000	0.000	0.188	0.4118	0.07	0.2027	0.024	0.0528
25	Run331	MHL	Model 0	0.5	FW	5	2.33	2	1.000	36.25	5.82E+05	0.000	0.000	0.000	0.000	0.093	0.1304	0.03	0.0808	0.028	0.0221
26	Run332	MHL	Model 0	0.5	FW	5	2.33	2	1.000	36.25	5.81E+05	0.000	0.000	0.000	0.000	0.096	0.1482	0.04	0.0984	0.029	0.0280
27	Run124	MHL	Model 0	0.5	FW	5	2.62	2.25	1.000	16.00	7.38E+05	0.000	0.000	0.000	0.000	0.093	0.0936	0.03	0.0752	0.029	0.0165
28	Run333	MHL	Model 0	0.5	FW	5	2.92	2.5	1.000	23.20	7.29E+05	0.000	0.000	0.000	0.000	0.091	0.1000	0.03	0.0535	0.031	0.0169
29	Run334	MHL	Model 0	0.5	FW	5	3.51	3	1.000	16.11	8.74E+05	0.000	0.000	0.000	0.000	0.090	0.0644	0.03	0.0358	0.031	0.0108
30	Run125	MHL	Model 0	0.5	FW	5	4.05	3.5	1.000	11.76	1.14E+06	0.000	0.000	0.000	0.000	0.081	0.0552	0.02	0.0336	0.030	0.0092
31	Run126	MHL	Model 0	0.5	FW	5	4.63	4	1.000	9.00	1.30E+06	0.000	0.000	0.000	0.000	0.082	0.0380	0.02	0.0283	0.030	0.0058
32	Run127	MHL	Model 0	0.5	FW	5	5.23	4.5	1.000	7.11	1.47E+06	0.000	0.000	0.000	0.000	0.079	0.0323	0.02	0.0219	0.029	0.0056
33	Run335	MHL	Model 0	0.5	FW	5	5.81	5	1.000	5.80	1.45E+06	0.000	0.000	0.000	0.000	0.084	0.0329	0.02	0.0287	0.031	0.0052
34	Run342	MHL	Model 0	0.5	FW	7.5	0.59	0.5	1.000	36.25	1.46E+05	0.000	0.000	0.000	0.000	0.379	1.1654	0.16	0.6870	0.090	0.1626
35	Run339	MHL	Model 0	0.5	FW	7.5	1.75	1.5	1.000	64.44	4.37E+05	0.000	0.000	0.000	0.000	0.188	0.2340	0.04	0.1535	0.039	0.0403
36	Run337	MHL	Model 0	0.5	FW	7.5	2.33	2	1.000	36.25	5.82E+05	0.000	0.000	0.000	0.000	0.154	0.1209	0.04	0.0889	0.042	0.0218
37	Run338	MHL	Model 0	0.5	FW	7.5	2.33	2	1.000	36.25	5.81E+05	0.000	0.000	0.000	0.000	0.149	0.1307	0.04	0.1092	0.042	0.0246
38	Run338b	MHL	Model 0	0.5	FW	7.5	2.34	2	1.000	36.25	5.82E+05	0.000	0.000	0.000	0.000	0.156	0.1386	0.04	0.1130	0.044	0.0258

#	Run Name	Facility	Model	AR_h	Flow Regime	α, deg	Speed, m/s	Fn_h	Facility Pressure, bar	σ_v	Re_c	δ_{SC} at tip, m		θ at tip, deg		$C_{L,3D}$		$C_{D,3D}$		$C_{M,3D}$ (about 0.5c)	
												Mean	Std	Mean	Std	Mean	Std	Mean	Std	Mean	Std
39	Run340	MHL	Model 0	0.5	FW	7.5	3.51	3	1.000	16.11	8.74E+05	0.000	0.000	0.000	0.000	0.137	0.0675	0.03	0.0431	0.046	0.0121
40	Run341	MHL	Model 0	0.5	FW	7.5	5.80	5	1.000	5.80	1.45E+06	0.000	0.000	0.000	0.000	0.130	0.0319	0.03	0.0276	0.045	0.0054
41	Run153	MHL	Model 0	0.5	FW	10	0.58	0.5	1.000	16.00	1.64E+05	0.000	0.000	0.000	0.000	0.519	1.4371	0.11	0.7733	0.093	0.1762
42	Run348	MHL	Model 0	0.5	FW	10	0.58	0.5	1.000	36.25	1.46E+05	0.000	0.000	0.000	0.000	0.380	1.2822	0.07	0.8225	0.130	0.1799
43	Run344	MHL	Model 0	0.5	FW	10	1.76	1.5	1.000	36.25	4.38E+05	0.000	0.000	0.000	0.000	0.262	0.2093	0.07	0.1419	0.049	0.0348
44	Run345	MHL	Model 0	0.5	FW	10	1.75	1.5	1.000	64.44	4.37E+05	0.000	0.000	0.000	0.000	0.256	0.2396	0.07	0.1582	0.050	0.0404
45	Run343	MHL	Model 0	0.5	FW	10	2.33	2	1.000	36.25	5.81E+05	0.000	0.000	0.000	0.000	0.212	0.1314	0.06	0.1134	0.057	0.0230
46	Run152	MHL	Model 0	0.5	FW	10	2.62	2.25	1.000	16.00	7.38E+05	0.000	0.000	0.000	0.000	0.188	0.0971	0.05	0.0720	0.054	0.0162
47	Run346b	MHL	Model 0	0.5	FW	10	3.51	3	1.000	16.11	8.74E+05	0.000	0.000	0.000	0.000	0.187	0.0677	0.05	0.0412	0.060	0.0110
48	Run129	MHL	Model 0	0.5	FW	10	4.05	3.5	1.000	11.76	1.14E+06	0.000	0.000	0.000	0.000	0.170	0.0570	0.04	0.0363	0.057	0.0100
49	Run130	MHL	Model 0	0.5	FW	10	4.64	4	1.000	9.00	1.31E+06	0.000	0.000	0.000	0.000	0.173	0.0381	0.04	0.0316	0.056	0.0062
50	Run131	MHL	Model 0	0.5	FW	10	5.24	4.5	1.000	7.11	1.47E+06	0.000	0.000	0.000	0.000	0.172	0.0262	0.04	0.0203	0.056	0.0051
51	Run347	MHL	Model 0	0.5	FW	10	5.80	5	1.000	5.80	1.44E+06	0.000	0.000	0.000	0.000	0.177	0.0353	0.04	0.0265	0.058	0.0061
52	Run354	MHL	Model 0	0.5	FW	12.5	0.59	0.5	1.000	36.25	1.46E+05	0.000	0.000	0.000	0.000	0.450	1.1346	0.08	0.6996	0.140	0.1636
53	Run351	MHL	Model 0	0.5	FW	12.5	1.75	1.5	1.000	64.44	4.37E+05	0.000	0.000	0.000	0.000	0.332	0.2236	0.09	0.1606	0.058	0.0368
54	Run349	MHL	Model 0	0.5	FW	12.5	2.33	2	1.000	36.25	5.82E+05	0.000	0.000	0.000	0.000	0.261	0.1358	0.09	0.1313	0.066	0.0223
55	Run350	MHL	Model 0	0.5	FW	12.5	2.34	2	1.000	36.25	5.83E+05	0.000	0.000	0.000	0.000	0.234	0.1473	0.04	0.1128	0.065	0.0294
56	Run352	MHL	Model 0	0.5	FW	12.5	3.51	3	1.000	16.11	8.74E+05	0.000	0.000	0.000	0.000	0.236	0.0730	0.06	0.0452	0.070	0.0123
57	Run353	MHL	Model 0	0.5	FW	12.5	5.79	5	1.000	5.80	1.44E+06	0.000	0.000	0.000	0.000	0.221	0.0362	0.06	0.0272	0.070	0.0059
58	Run360	MHL	Model 0	0.5	FW	15	0.59	0.5	1.000	36.25	1.46E+05	0.000	0.000	0.000	0.000	0.544	1.1683	0.13	0.6991	0.147	0.1580
59	Run356	MHL	Model 0	0.5	FW	15	1.76	1.5	1.000	36.25	4.38E+05	0.000	0.000	0.000	0.000	0.411	0.2235	0.15	0.1402	0.066	0.0363
60	Run357	MHL	Model 0	0.5	FW	15	1.75	1.5	1.000	64.44	4.37E+05	0.000	0.000	0.000	0.000	0.398	0.2201	0.14	0.1357	0.066	0.0360
61	Run355	MHL	Model 0	0.5	FW	15	2.33	2	1.000	36.25	5.82E+05	0.000	0.000	0.000	0.000	0.321	0.1238	0.11	0.0844	0.075	0.0204
62	Run150	MHL	Model 0	0.5	FW	15	2.62	2.25	1.000	16.00	7.39E+05	0.000	0.000	0.000	0.000	0.288	0.0824	0.10	0.0704	0.073	0.0144
63	Run358	MHL	Model 0	0.5	FW	15	3.51	3	1.000	16.11	8.74E+05	0.000	0.000	0.000	0.000	0.293	0.0714	0.10	0.0439	0.080	0.0116
64	Run132	MHL	Model 0	0.5	FW	15	4.05	3.5	1.000	11.76	1.14E+06	0.000	0.000	0.000	0.000	0.271	0.0552	0.08	0.0414	0.076	0.0094
65	Run133	MHL	Model 0	0.5	FW	15	4.63	4	1.000	9.00	1.30E+06	0.000	0.000	0.000	0.000	0.267	0.0376	0.08	0.0311	0.076	0.0060
66	Run134	MHL	Model 0	0.5	FW	15	5.24	4.5	1.000	7.11	1.48E+06	0.000	0.000	0.000	0.000	0.261	0.0306	0.07	0.0257	0.075	0.0051
67	Run359	MHL	Model 0	0.5	FW	15	5.80	5	1.000	5.80	1.45E+06	0.000	0.000	0.000	0.000	0.282	0.0338	0.08	0.0242	0.080	0.0056
68	Run361	MHL	Model 0	0.5	FW	17.5	0.58	0.5	1.000	36.25	1.46E+05	0.000	0.000	0.000	0.000	0.669	1.2641	0.56	0.8286	0.157	0.1512
69	Run362b	MHL	Model 0	0.5	FW	17.5	0.58	0.5	1.000	36.25	1.46E+05	0.000	0.000	0.000	0.000	0.557	1.9646	0.21	1.2146	0.156	0.2446
70	Run365	MHL	Model 0	0.5	FW	17.5	1.76	1.5	1.000	36.25	4.38E+05	0.000	0.000	0.000	0.000	0.461	0.3132	0.20	0.3890	0.073	0.0405
71	Run366	MHL	Model 0	0.5	FW	17.5	1.75	1.5	1.000	64.44	4.37E+05	0.000	0.000	0.000	0.000	0.460	0.2162	0.17	0.1557	0.075	0.0360
72	Run363	MHL	Model 0	0.5	FW	17.5	2.33	2	1.000	36.25	5.80E+05	0.000	0.000	0.000	0.000	0.383	0.1167	0.14	0.0854	0.082	0.0220
73	Run364	MHL	Model 0	0.5	FW	17.5	2.32	2	1.000	36.25	5.79E+05	0.000	0.000	0.000	0.000	0.376	0.1536	0.14	0.1147	0.083	0.0275
74	Run367	MHL	Model 0	0.5	FW	17.5	3.51	3	1.000	16.11	8.75E+05	0.000	0.000	0.000	0.000	0.349	0.0627	0.12	0.0452	0.089	0.0119
75	Run369	MHL	Model 0	0.5	FW	17.5	4.06	3.5	1.000	11.84	1.01E+06	0.000	0.000	0.000	0.000	0.338	0.0563	0.11	0.0385	0.089	0.0111
76	Run370	MHL	Model 0	0.5	FW	17.5	4.65	4	1.000	9.06	1.16E+06	0.000	0.000	0.000	0.000	0.336	0.0468	0.11	0.0306	0.089	0.0090

#	Run Name	Facility	Model	AR_h	Flow Regime	α, deg	Speed, m/s	Fn_h	Facility Pressure, bar	σ_v	Re_c	δ_{SC} at tip, m		θ at tip, deg		$C_{L,3D}$		$C_{D,3D}$		$C_{M,3D}$ (about 0.5c)	
												Mean	Std	Mean	Std	Mean	Std	Mean	Std	Mean	Std
77	Run368	MHL	Model 0	0.5	FW	17.5	5.79	5	1.000	5.80	1.44E+06	0.000	0.000	0.000	0.000	0.330	0.0328	0.11	0.0300	0.088	0.0058
78	Run368b	MHL	Model 0	0.5	FW	17.5	5.79	5	1.000	5.80	1.44E+06	0.000	0.000	0.000	0.000	0.331	0.0339	0.11	0.0297	0.087	0.0062
79	Run148	MHL	Model 0	0.5	FW	20	0.59	0.5	1.000	16.00	1.65E+05	0.000	0.000	0.000	0.000	0.566	0.4895	0.24	0.4861	0.125	0.0685
80	Run371	MHL	Model 0	0.5	FW	20	0.59	0.5	1.000	36.25	1.46E+05	0.000	0.000	0.000	0.000	1.163	1.1875	0.69	0.6880	0.180	0.1486
81	Run373	MHL	Model 0	0.5	FW	20	0.58	0.5	1.000	36.25	1.46E+05	0.000	0.000	0.000	0.000	0.549	1.1617	0.35	1.0497	0.143	0.1795
82	Run374	MHL	Model 0	0.5	FW	20	0.59	0.5	1.000	36.25	1.46E+05	0.000	0.000	0.000	0.000	0.682	0.4421	0.29	0.8499	0.122	0.0538
83	Run375	MHL	Model 0	0.5	FW	20	0.59	0.5	1.000	36.25	1.46E+05	0.000	0.000	0.000	0.000	0.660	0.8862	0.43	0.9569	0.148	0.0925
84	Run376	MHL	Model 0	0.5	FW	20	0.59	0.5	1.000	36.25	1.46E+05	0.000	0.000	0.000	0.000	0.394	0.9329	0.66	0.9971	0.200	0.2470
85	Run372	MHL	Model 0	0.5	FW	20	2.34	2	1.000	36.25	5.83E+05	0.000	0.000	0.000	0.000	0.432	0.1402	0.18	0.1038	0.087	0.0308
86	Run378	MHL	Model 0	0.5	FW	20	3.51	3	1.000	16.11	8.74E+05	0.000	0.000	0.000	0.000	0.418	0.0721	0.16	0.0498	0.096	0.0128
87	Run136	MHL	Model 0	0.5	FW	20	4.63	4	1.000	9.00	1.30E+06	0.000	0.000	0.000	0.000	0.388	0.0425	0.14	0.0342	0.089	0.0074
88	Run379	MHL	Model 0	0.5	FW	20	5.79	5	1.000	5.80	1.44E+06	0.000	0.000	0.000	0.000	0.403	0.0332	0.16	0.0275	0.095	0.0063
89	Run146	MHL	Model 0	0.5	FW	25	0.59	0.5	1.000	16.00	1.65E+05	0.000	0.000	0.000	0.000	0.667	0.3914	0.38	0.5608	0.125	0.0611
90	Run381	MHL	Model 0	0.5	FW	25	0.58	0.5	1.000	36.25	1.46E+05	0.000	0.000	0.000	0.000	0.711	1.3592	0.30	1.0362	0.111	0.1881
91	Run382	MHL	Model 0	0.5	FW	25	0.59	0.5	1.000	36.25	1.46E+05	0.000	0.000	0.000	0.000	0.811	0.6546	0.47	0.7813	0.129	0.0870
92	Run144	MHL	Model 0	0.5	FW	30	0.59	0.5	1.000	16.00	1.65E+05	0.000	0.000	0.000	0.000	1.014	0.3847	0.57	0.4279	0.165	0.0478
93	Run384	MHL	Model 0	0.5	FW	30	0.59	0.5	1.000	36.25	1.46E+05	0.000	0.000	0.000	0.000	0.907	1.4377	0.47	0.8486	0.137	0.1649
94	Run330	MHL	Model 0	0.5	PV	2.5	2.34	2	1.000	19.17	5.84E+05	0.000	0.000	0.000	0.000	0.045	0.1395	0.01	0.0783	0.014	0.0232
95	Run324	MHL	Model 0	0.5	PV	2.5	2.63	2.25	1.000	28.64	6.56E+05	0.000	0.000	0.000	0.000	0.050	0.1085	0.03	0.0749	0.014	0.0186
96	Run323	MHL	Model 0	0.5	PV	2.5	2.92	2.5	1.000	23.20	7.28E+05	0.000	0.000	0.000	0.000	0.048	0.0930	0.03	0.0595	0.012	0.0152
97	Run128b	MHL	Model 0	0.5	PV	5	1.75	1.5	1.000	16.00	4.94E+05	0.000	0.000	0.000	0.000	0.134	0.2068	0.03	0.1386	0.024	0.0324
98	Run336b	MHL	Model 0	0.5	PV	5	1.76	1.5	1.000	36.25	4.38E+05	0.000	0.000	0.000	0.000	0.134	0.2325	0.04	0.1184	0.024	0.0355
99	Run342	MHL	Model 0	0.5	PV	7.5	1.17	1	1.000	36.25	2.92E+05	0.000	0.000	0.000	0.000	0.305	0.3945	0.10	0.2459	0.045	0.0565
100	Run339	MHL	Model 0	0.5	PV	7.5	1.75	1.5	1.000	64.44	4.37E+05	0.000	0.000	0.000	0.000	0.196	0.2130	0.04	0.1286	0.040	0.0355
101	Run153	MHL	Model 0	0.5	PV	10	1.17	1	1.000	16.00	3.30E+05	0.000	0.000	0.000	0.000	0.372	0.3357	0.11	0.1644	0.051	0.0521
102	Run348	MHL	Model 0	0.5	PV	10	1.17	1	1.000	36.25	2.92E+05	0.000	0.000	0.000	0.000	0.373	0.3394	0.12	0.2845	0.065	0.0509
103	Run354	MHL	Model 0	0.5	PV	12.5	1.17	1	1.000	36.25	2.92E+05	0.000	0.000	0.000	0.000	0.460	0.4010	0.14	0.2512	0.075	0.0584
104	Run151	MHL	Model 0	0.5	PV	15	1.17	1	1.000	16.00	3.31E+05	0.000	0.000	0.000	0.000	0.570	0.3168	0.20	0.2008	0.083	0.0514
105	Run360	MHL	Model 0	0.5	PV	15	1.17	1	1.000	36.25	2.92E+05	0.000	0.000	0.000	0.000	0.536	0.3495	0.19	0.2209	0.086	0.0481
106	Run362b	MHL	Model 0	0.5	PV	17.5	0.59	0.5	1.000	36.25	1.46E+05	0.000	0.000	0.000	0.000	0.914	1.1820	0.19	1.0621	0.178	0.1721
107	Run363	MHL	Model 0	0.5	PV	17.5	0.59	0.5	1.000	36.25	1.46E+05	0.000	0.000	0.000	0.000	0.870	1.2165	0.10	0.8558	0.149	0.1572
108	Run364	MHL	Model 0	0.5	PV	17.5	0.59	0.5	1.000	36.25	1.46E+05	0.000	0.000	0.000	0.000	0.734	0.7729	0.16	0.6842	0.155	0.1302
109	Run365	MHL	Model 0	0.5	PV	17.5	0.59	0.5	1.000	36.25	1.46E+05	0.000	0.000	0.000	0.000	0.720	1.3002	0.18	0.8291	0.145	0.1766
110	Run361	MHL	Model 0	0.5	PV	17.5	1.17	1	1.000	36.25	2.91E+05	0.000	0.000	0.000	0.000	0.617	0.5014	0.33	0.3680	0.098	0.0708
111	Run149	MHL	Model 0	0.5	PV	20	0.59	0.5	1.000	16.00	1.65E+05	0.000	0.000	0.000	0.000	0.830	1.2875	0.17	0.9863	0.137	0.1543
112	Run371	MHL	Model 0	0.5	PV	20	0.59	0.5	1.000	36.25	1.46E+05	0.000	0.000	0.000	0.000	1.020	0.5688	-0.43	0.7774	0.294	0.1169
113	Run373	MHL	Model 0	0.5	PV	20	0.59	0.5	1.000	36.25	1.46E+05	0.000	0.000	0.000	0.000	1.018	0.9414	0.33	1.0663	0.145	0.1170
114	Run374	MHL	Model 0	0.5	PV	20	0.59	0.5	1.000	36.25	1.46E+05	0.000	0.000	0.000	0.000	0.885	0.9800	0.32	0.7841	0.151	0.1674

#	Run Name	Facility	Model	AR_h	Flow Regime	α, deg	Speed, m/s	Fn_h	Facility Pressure, bar	σ_v	Re_c	δ_{SC} at tip, m		θ at tip, deg		$C_{L,3D}$		$C_{D,3D}$		$C_{M,3D}$ (about 0.5c)	
												Mean	Std	Mean	Std	Mean	Std	Mean	Std	Mean	Std
115	Run376	MHL	Model 0	0.5	PV	20	0.58	0.5	1.000	36.25	1.46E+05	0.000	0.000	0.000	0.000	0.917	1.1759	0.19	0.7608	0.170	0.1543
116	Run148	MHL	Model 0	0.5	PV	20	1.17	1	1.000	16.00	3.30E+05	0.000	0.000	0.000	0.000	0.589	0.2778	0.27	0.2511	0.088	0.0441
117	Run375	MHL	Model 0	0.5	PV	20	1.17	1	1.000	36.25	2.92E+05	0.000	0.000	0.000	0.000	0.714	0.4215	0.30	0.3002	0.103	0.0628
118	Run380	MHL	Model 0	0.5	PV	22.5	1.15	1	1.000	36.25	2.87E+05	0.000	0.000	0.000	0.000	0.743	0.2608	0.35	0.2633	0.102	0.0411
119	Run147	MHL	Model 0	0.5	PV	25	0.59	0.5	1.000	16.00	1.65E+05	0.000	0.000	0.000	0.000	1.193	1.3825	0.42	0.9179	0.113	0.2259
120	Run382	MHL	Model 0	0.5	PV	25	0.58	0.5	1.000	36.25	1.46E+05	0.000	0.000	0.000	0.000	0.941	0.9571	0.41	0.8060	0.129	0.1346
121	Run146	MHL	Model 0	0.5	PV	25	1.17	1	1.000	16.00	3.30E+05	0.000	0.000	0.000	0.000	0.720	0.2621	0.39	0.2592	0.093	0.0419
122	Run381	MHL	Model 0	0.5	PV	25	1.17	1	1.000	36.25	2.91E+05	0.000	0.000	0.000	0.000	0.761	0.4542	0.41	0.3870	0.101	0.0651
123	Run325	MHL	Model 0	0.5	FV	2.5	3.51	3	1.000	16.11	8.74E+05	0.000	0.000	0.000	0.000	0.040	0.0689	0.02	0.0450	0.010	0.0112
124	Run326	MHL	Model 0	0.5	FV	2.5	4.09	3.5	1.000	11.84	1.02E+06	0.000	0.000	0.000	0.000	0.032	0.0564	0.02	0.0394	0.008	0.0089
125	Run327	MHL	Model 0	0.5	FV	2.5	4.68	4	1.000	9.06	1.17E+06	0.000	0.000	0.000	0.000	0.022	0.0448	0.02	0.0323	0.004	0.0070
126	Run328	MHL	Model 0	0.5	FV	2.5	5.26	4.5	1.000	7.16	1.31E+06	0.000	0.000	0.000	0.000	0.017	0.0387	0.02	0.0280	0.003	0.0066
127	Run329b	MHL	Model 0	0.5	FV	2.5	5.78	5	1.000	5.80	1.44E+06	0.000	0.000	0.000	0.000	0.011	0.0321	0.02	0.0290	0.002	0.0050
128	Run128b	MHL	Model 0	0.5	FV	5	2.92	2.5	1.000	16.00	8.24E+05	0.000	0.000	0.000	0.000	0.089	0.0809	0.03	0.0499	0.018	0.0127
129	Run333	MHL	Model 0	0.5	FV	5	2.92	2.5	1.000	23.20	7.28E+05	0.000	0.000	0.000	0.000	0.093	0.0938	0.03	0.0519	0.020	0.0148
130	Run125	MHL	Model 0	0.5	FV	5	3.52	3	1.000	11.76	9.91E+05	0.000	0.000	0.000	0.000	0.075	0.0879	0.01	0.0533	0.014	0.0124
131	Run334	MHL	Model 0	0.5	FV	5	3.51	3	1.000	16.11	8.74E+05	0.000	0.000	0.000	0.000	0.081	0.0690	0.03	0.0416	0.015	0.0112
132	Run126	MHL	Model 0	0.5	FV	5	4.68	4	1.000	9.00	1.32E+06	0.000	0.000	0.000	0.000	0.048	0.0378	0.02	0.0290	0.008	0.0063
133	Run127	MHL	Model 0	0.5	FV	5	5.26	4.5	1.000	7.11	1.48E+06	0.000	0.000	0.000	0.000	0.037	0.0355	0.02	0.0273	0.008	0.0061
134	Run335b	MHL	Model 0	0.5	FV	5	5.79	5	1.000	5.80	1.44E+06	0.000	0.000	0.000	0.000	0.035	0.0334	0.03	0.0214	0.008	0.0055
135	Run342	MHL	Model 0	0.5	FV	7.5	2.31	2	1.000	36.25	5.77E+05	0.000	0.000	0.000	0.000	0.166	0.1533	0.06	0.1069	0.034	0.0241
136	Run340	MHL	Model 0	0.5	FV	7.5	3.51	3	1.000	16.11	8.74E+05	0.000	0.000	0.000	0.000	0.117	0.0646	0.04	0.0472	0.020	0.0102
137	Run341b	MHL	Model 0	0.5	FV	7.5	5.78	5	1.000	5.80	1.44E+06	0.000	0.000	0.000	0.000	0.063	0.0318	0.03	0.0271	0.015	0.0051
138	Run348	MHL	Model 0	0.5	FV	10	1.76	1.5	1.000	36.25	4.37E+05	0.000	0.000	0.000	0.000	0.276	0.2046	0.08	0.1442	0.050	0.0351
139	Run345	MHL	Model 0	0.5	FV	10	1.75	1.5	1.000	64.44	4.37E+05	0.000	0.000	0.000	0.000	0.267	0.2280	0.08	0.1369	0.049	0.0363
140	Run153	MHL	Model 0	0.5	FV	10	2.92	2.5	1.000	16.00	8.23E+05	0.000	0.000	0.000	0.000	0.174	0.0829	0.06	0.0523	0.027	0.0127
141	Run346b	MHL	Model 0	0.5	FV	10	3.50	3	1.000	16.11	8.73E+05	0.000	0.000	0.000	0.000	0.154	0.0755	0.05	0.0468	0.025	0.0114
142	Run129	MHL	Model 0	0.5	FV	10	4.09	3.5	1.000	11.76	1.15E+06	0.000	0.000	0.000	0.000	0.120	0.0485	0.04	0.0334	0.022	0.0079
143	Run130	MHL	Model 0	0.5	FV	10	4.68	4	1.000	9.00	1.32E+06	0.000	0.000	0.000	0.000	0.112	0.0385	0.04	0.0249	0.021	0.0064
144	Run131	MHL	Model 0	0.5	FV	10	5.25	4.5	1.000	7.11	1.48E+06	0.000	0.000	0.000	0.000	0.103	0.0345	0.04	0.0250	0.020	0.0060
145	Run347b	MHL	Model 0	0.5	FV	10	5.79	5	1.000	5.80	1.44E+06	0.000	0.000	0.000	0.000	0.102	0.0338	0.04	0.0252	0.021	0.0058
146	Run354	MHL	Model 0	0.5	FV	12.5	1.76	1.5	1.000	36.25	4.38E+05	0.000	0.000	0.000	0.000	0.346	0.2106	0.10	0.1401	0.055	0.0355
147	Run352	MHL	Model 0	0.5	FV	12.5	3.51	3	1.000	16.11	8.74E+05	0.000	0.000	0.000	0.000	0.193	0.0696	0.07	0.0547	0.030	0.0105
148	Run353b	MHL	Model 0	0.5	FV	12.5	5.80	5	1.000	5.80	1.44E+06	0.000	0.000	0.000	0.000	0.133	0.0336	0.05	0.0268	0.025	0.0052
149	Run357	MHL	Model 0	0.5	FV	15	1.75	1.5	1.000	64.44	4.37E+05	0.000	0.000	0.000	0.000	0.419	0.2051	0.15	0.1329	0.056	0.0319
150	Run360	MHL	Model 0	0.5	FV	15	2.34	2	1.000	36.25	5.82E+05	0.000	0.000	0.000	0.000	0.302	0.1294	0.12	0.1035	0.043	0.0351
151	Run151	MHL	Model 0	0.5	FV	15	2.93	2.5	1.000	16.00	8.24E+05	0.000	0.000	0.000	0.000	0.254	0.0781	0.10	0.0501	0.035	0.0131
152	Run358	MHL	Model 0	0.5	FV	15	3.51	3	1.000	16.11	8.74E+05	0.000	0.000	0.000	0.000	0.231	0.0684	0.09	0.0441	0.035	0.0105

#	Run Name	Facility	Model	AR_h	Flow Regime	α, deg	Speed, m/s	Fn_h	Facility Pressure, bar	σ_v	Re_c	δ_{SC} at tip, m		θ at tip, deg		$C_{L,3D}$		$C_{D,3D}$		$C_{M,3D}$ (about 0.5c)	
												Mean	Std	Mean	Std	Mean	Std	Mean	Std	Mean	Std
153	Run132	MHL	Model 0	0.5	FV	15	4.09	3.5	1.000	11.76	1.15E+06	0.000	0.000	0.000	0.000	0.198	0.0457	0.08	0.0361	0.032	0.0075
154	Run133	MHL	Model 0	0.5	FV	15	4.67	4	1.000	9.00	1.32E+06	0.000	0.000	0.000	0.000	0.180	0.0385	0.07	0.0289	0.031	0.0064
155	Run134	MHL	Model 0	0.5	FV	15	5.25	4.5	1.000	7.11	1.48E+06	0.000	0.000	0.000	0.000	0.172	0.0354	0.07	0.0285	0.030	0.0062
156	Run359b	MHL	Model 0	0.5	FV	15	5.80	5	1.000	5.80	1.44E+06	0.000	0.000	0.000	0.000	0.174	0.0314	0.07	0.0227	0.031	0.0047
157	Run362b	MHL	Model 0	0.5	FV	17.5	1.76	1.5	1.000	36.25	4.38E+05	0.000	0.000	0.000	0.000	0.491	0.2017	0.17	0.1707	0.061	0.0339
158	Run365	MHL	Model 0	0.5	FV	17.5	1.76	1.5	1.000	36.25	4.37E+05	0.000	0.000	0.000	0.000	0.490	0.2216	0.19	0.1737	0.058	0.0391
159	Run366	MHL	Model 0	0.5	FV	17.5	1.75	1.5	1.000	64.44	4.37E+05	0.000	0.000	0.000	0.000	0.482	0.1996	0.19	0.1508	0.060	0.0324
160	Run361	MHL	Model 0	0.5	FV	17.5	2.33	2	1.000	36.25	5.81E+05	0.000	0.000	0.000	0.000	0.370	0.1246	0.18	0.0896	0.045	0.0222
161	Run363	MHL	Model 0	0.5	FV	17.5	2.34	2	1.000	36.25	5.83E+05	0.000	0.000	0.000	0.000	0.367	0.1215	0.15	0.0946	0.044	0.0226
162	Run364	MHL	Model 0	0.5	FV	17.5	2.34	2	1.000	36.25	5.83E+05	0.000	0.000	0.000	0.000	0.358	0.1270	0.15	0.0983	0.045	0.0212
163	Run367	MHL	Model 0	0.5	FV	17.5	3.51	3	1.000	16.11	8.74E+05	0.000	0.000	0.000	0.000	0.268	0.0638	0.11	0.0470	0.041	0.0103
164	Run369	MHL	Model 0	0.5	FV	17.5	4.09	3.5	1.000	11.84	1.02E+06	0.000	0.000	0.000	0.000	0.246	0.0548	0.11	0.0399	0.039	0.0092
165	Run370	MHL	Model 0	0.5	FV	17.5	4.68	4	1.000	9.06	1.17E+06	0.000	0.000	0.000	0.000	0.230	0.0410	0.10	0.0332	0.038	0.0069
166	Run368c	MHL	Model 0	0.5	FV	17.5	5.78	5	1.000	5.80	1.44E+06	0.000	0.000	0.000	0.000	0.214	0.0331	0.10	0.0258	0.036	0.0051
167	Run149	MHL	Model 0	0.5	FV	20	1.17	1	1.000	16.00	3.31E+05	0.000	0.000	0.000	0.000	0.700	0.2608	0.28	0.2141	0.094	0.0381
168	Run371	MHL	Model 0	0.5	FV	20	1.17	1	1.000	36.25	2.92E+05	0.000	0.000	0.000	0.000	0.812	0.3132	0.23	0.4369	0.118	0.0400
169	Run373	MHL	Model 0	0.5	FV	20	1.17	1	1.000	36.25	2.92E+05	0.000	0.000	0.000	0.000	0.723	0.2643	0.31	0.3009	0.102	0.0466
170	Run376	MHL	Model 0	0.5	FV	20	1.76	1.5	1.000	36.25	4.38E+05	0.000	0.000	0.000	0.000	0.559	0.2071	0.22	0.1387	0.058	0.0327
171	Run377	MHL	Model 0	0.5	FV	20	1.75	1.5	1.000	64.44	4.37E+05	0.000	0.000	0.000	0.000	0.562	0.1997	0.23	0.1419	0.059	0.0339
172	Run374	MHL	Model 0	0.5	FV	20	2.34	2	1.000	36.25	5.82E+05	0.000	0.000	0.000	0.000	0.409	0.1254	0.19	0.0857	0.048	0.0204
173	Run375	MHL	Model 0	0.5	FV	20	2.34	2	1.000	36.25	5.82E+05	0.000	0.000	0.000	0.000	0.402	0.1182	0.18	0.0972	0.048	0.0183
174	Run148	MHL	Model 0	0.5	FV	20	3.47	3	1.000	16.00	9.77E+05	0.000	0.000	0.000	0.000	0.287	0.0632	0.15	0.0548	0.042	0.0100
175	Run378	MHL	Model 0	0.5	FV	20	3.51	3	1.000	16.11	8.74E+05	0.000	0.000	0.000	0.000	0.314	0.0798	0.15	0.0514	0.046	0.0129
176	Run135	MHL	Model 0	0.5	FV	20	4.09	3.5	1.000	11.76	1.15E+06	0.000	0.000	0.000	0.000	0.270	0.0536	0.13	0.0470	0.041	0.0093
177	Run136	MHL	Model 0	0.5	FV	20	4.67	4	1.000	9.00	1.32E+06	0.000	0.000	0.000	0.000	0.263	0.0388	0.12	0.0324	0.040	0.0067
178	Run137	MHL	Model 0	0.5	FV	20	5.23	4.5	1.000	7.11	1.47E+06	0.000	0.000	0.000	0.000	0.245	0.0322	0.12	0.0296	0.039	0.0057
179	Run379b	MHL	Model 0	0.5	FV	20	5.80	5	1.000	5.80	1.45E+06	0.000	0.000	0.000	0.000	0.257	0.0346	0.13	0.0260	0.041	0.0054
180	Run380	MHL	Model 0	0.5	FV	22.5	1.19	1	1.000	36.25	2.96E+05	0.000	0.000	0.000	0.000	0.736	0.4085	0.35	0.3075	0.106	0.0573
181	Run147	MHL	Model 0	0.5	FV	25	1.17	1	1.000	16.00	3.30E+05	0.000	0.000	0.000	0.000	0.915	0.2142	0.45	0.2122	0.101	0.0433
182	Run382	MHL	Model 0	0.5	FV	25	1.17	1	1.000	36.25	2.92E+05	0.000	0.000	0.000	0.000	0.846	0.4058	0.44	0.3078	0.110	0.0631
183	Run146	MHL	Model 0	0.5	FV	25	1.76	1.5	1.000	16.00	4.96E+05	0.000	0.000	0.000	0.000	0.630	0.2417	0.34	0.2000	0.053	0.0417
184	Run381	MHL	Model 0	0.5	FV	25	2.33	2	1.000	36.25	5.81E+05	0.000	0.000	0.000	0.000	0.485	0.1144	0.27	0.0967	0.055	0.0188
185	Run138b	MHL	Model 0	0.5	FV	25	4.09	3.5	1.000	11.76	1.15E+06	0.000	0.000	0.000	0.000	0.360	0.0465	0.21	0.0395	0.049	0.0082
186	Run138	MHL	Model 0	0.5	FV	25	4.09	3.5	1.000	11.76	1.15E+06	0.000	0.000	0.000	0.000	0.362	0.0504	0.20	0.0352	0.049	0.0087
187	Run139	MHL	Model 0	0.5	FV	25	4.67	4	1.000	9.00	1.32E+06	0.000	0.000	0.000	0.000	0.337	0.0423	0.19	0.0326	0.048	0.0071
188	Run140	MHL	Model 0	0.5	FV	25	5.24	4.5	1.000	7.11	1.48E+06	0.000	0.000	0.000	0.000	0.330	0.0360	0.18	0.0326	0.047	0.0062
189	Run383b	MHL	Model 0	0.5	FV	25	5.80	5	1.000	5.80	1.45E+06	0.000	0.000	0.000	0.000	0.331	0.0300	0.19	0.0300	0.050	0.0051
190	Run144	MHL	Model 0	0.5	FV	30	1.17	1	1.000	16.00	3.30E+05	0.000	0.000	0.000	0.000	0.862	0.2878	0.52	0.2667	0.107	0.0461

#	Run Name	Facility	Model	AR_h	Flow Regime	α, deg	Speed, m/s	Fn_h	Facility Pressure, bar	σ_v	Re_c	δ_{SC} at tip, m		θ at tip, deg		$C_{L,3D}$		$C_{D,3D}$		$C_{M,3D}$ (about 0.5c)	
												Mean	Std	Mean	Std	Mean	Std	Mean	Std	Mean	Std
191	Run384	MHL	Model 0	0.5	FV	30	1.18	1	1.000	36.25	2.95E+05	0.000	0.000	0.000	0.000	0.869	0.3620	0.55	0.3741	0.112	0.0609
192	Run385	MHL	Model 0	0.5	FV	30	1.17	1	1.000	36.25	2.92E+05	0.000	0.000	0.000	0.000	0.990	0.3035	0.60	0.2757	0.125	0.0502
193	Run141	MHL	Model 0	0.5	FV	30	4.09	3.5	1.000	11.76	1.15E+06	0.000	0.000	0.000	0.000	0.434	0.0461	0.28	0.0431	0.056	0.0082
194	Run142	MHL	Model 0	0.5	FV	30	4.67	4	1.000	9.00	1.32E+06	0.000	0.000	0.000	0.000	0.422	0.0405	0.29	0.0361	0.055	0.0070
195	Run143	MHL	Model 0	0.5	FV	30	5.24	4.5	1.000	7.11	1.48E+06	0.000	0.000	0.000	0.000	0.412	0.0355	0.28	0.0333	0.053	0.0065
196	Run386	MHL	Model 0	0.5	FV	30	5.80	5	1.000	5.80	1.45E+06	0.000	0.000	0.000	0.000	0.418	0.0284	0.28	0.0264	0.057	0.0051
197	Run110	MHL	Model 0	1	FW	-5	2.49	1.5	1.000	18.01	7.01E+05	0.000	0.000	0.000	0.000	-0.139	0.0489	0.05	0.0393	-0.040	0.0097
198	Run224b	MHL	Model 0	1	FW	-5	3.31	2	1.000	18.12	8.33E+05	0.000	0.000	0.000	0.000	-0.121	0.0332	0.04	0.0262	-0.038	0.0062
199	Run224	MHL	Model 0	1	FW	-5	3.28	2	1.000	18.12	8.25E+05	0.000	0.000	0.000	0.000	-0.125	0.0339	0.04	0.0258	-0.039	0.0062
200	Run078	MHL	Model 0	1	FW	-5	4.13	2.5	1.000	11.52	1.16E+06	0.000	0.000	0.000	0.000	-0.124	0.0224	0.03	0.0177	-0.039	0.0047
201	Run079	MHL	Model 0	1	FW	-5	4.96	3	1.000	8.00	1.40E+06	0.000	0.000	0.000	0.000	-0.121	0.0184	0.03	0.0171	-0.038	0.0037
202	Run080	MHL	Model 0	1	FW	-5	5.74	3.5	1.000	5.88	1.62E+06	0.000	0.000	0.000	0.000	-0.119	0.0152	0.03	0.0181	-0.038	0.0027
203	Run226	MHL	Model 0	1	FW	0	2.03	1.25	1.000	8.05	5.12E+05	0.000	0.000	0.000	0.000	-0.012	0.0809	0.03	0.0675	0.001	0.0122
204	Run225	MHL	Model 0	1	FW	0	2.49	1.5	1.000	18.12	6.26E+05	0.000	0.000	0.000	0.000	0.010	0.0655	0.04	0.0516	0.004	0.0132
205	Run111	MHL	Model 0	1	FW	0	3.29	2	1.000	18.01	9.28E+05	0.000	0.000	0.000	0.000	0.008	0.0386	0.03	0.0511	0.003	0.0073
206	Run081	MHL	Model 0	1	FW	0	4.13	2.5	1.000	11.52	1.16E+06	0.000	0.000	0.000	0.000	0.006	0.0259	0.02	0.0180	0.003	0.0047
207	Run082	MHL	Model 0	1	FW	0	4.95	3	1.000	8.00	1.40E+06	0.000	0.000	0.000	0.000	0.006	0.0250	0.02	0.0122	0.003	0.0042
208	Run083	MHL	Model 0	1	FW	0	5.74	3.5	1.000	5.88	1.62E+06	0.000	0.000	0.000	0.000	0.007	0.0194	0.02	0.0121	0.003	0.0034
209	Run227	MHL	Model 0	1	FW	2.5	2.07	1.25	1.000	32.17	5.21E+05	0.000	0.000	0.000	0.000	0.080	0.0656	0.04	0.0747	0.024	0.0140
210	Run228	MHL	Model 0	1	FW	2.5	2.48	1.5	1.000	32.17	6.25E+05	0.000	0.000	0.000	0.000	0.070	0.0538	0.03	0.0431	0.024	0.0098
211	Run229	MHL	Model 0	1	FW	2.5	3.30	2	1.000	18.12	8.32E+05	0.000	0.000	0.000	0.000	0.068	0.0323	0.03	0.0229	0.024	0.0057
212	Run230	MHL	Model 0	1	FW	2.5	3.72	2.25	1.000	14.31	9.36E+05	0.000	0.000	0.000	0.000	0.072	0.0306	0.03	0.0192	0.023	0.0052
213	Run231	MHL	Model 0	1	FW	2.5	4.11	2.5	1.000	11.59	1.03E+06	0.000	0.000	0.000	0.000	0.071	0.0247	0.02	0.0161	0.024	0.0044
214	Run232	MHL	Model 0	1	FW	2.5	4.95	3	1.000	8.05	1.25E+06	0.000	0.000	0.000	0.000	0.071	0.0221	0.02	0.0145	0.024	0.0039
215	Run233	MHL	Model 0	1	FW	2.5	5.78	3.5	1.000	5.91	1.46E+06	0.000	0.000	0.000	0.000	0.069	0.0133	0.01	0.0133	0.024	0.0025
216	Run235	MHL	Model 0	1	FW	5	2.07	1.25	1.000	32.17	5.20E+05	0.000	0.000	0.000	0.000	0.173	0.0538	0.06	0.0516	0.042	0.0102
217	Run236	MHL	Model 0	1	FW	5	2.48	1.5	1.000	32.17	6.25E+05	0.000	0.000	0.000	0.000	0.139	0.0548	0.02	0.0466	0.043	0.0103
218	Run237	MHL	Model 0	1	FW	5	2.89	1.75	1.000	23.68	7.27E+05	0.000	0.000	0.000	0.000	0.135	0.0437	0.02	0.0309	0.043	0.0080
219	Run112	MHL	Model 0	1	FW	5	3.27	2	1.000	18.01	9.22E+05	0.000	0.000	0.000	0.000	0.135	0.0331	0.04	0.0228	0.038	0.0085
220	Run238	MHL	Model 0	1	FW	5	3.72	2.25	1.000	14.31	9.36E+05	0.000	0.000	0.000	0.000	0.141	0.0309	0.03	0.0201	0.045	0.0053
221	Run084	MHL	Model 0	1	FW	5	4.13	2.5	1.000	11.52	1.16E+06	0.000	0.000	0.000	0.000	0.136	0.0242	0.03	0.0169	0.043	0.0046
222	Run085	MHL	Model 0	1	FW	5	4.96	3	1.000	8.00	1.40E+06	0.000	0.000	0.000	0.000	0.135	0.0225	0.03	0.0136	0.043	0.0041
223	Run239	MHL	Model 0	1	FW	5	5.73	3.5	1.000	5.91	1.44E+06	0.000	0.000	0.000	0.000	0.138	0.0162	0.03	0.0165	0.044	0.0031
224	Run086	MHL	Model 0	1	FW	5	5.74	3.5	1.000	5.88	1.62E+06	0.000	0.000	0.000	0.000	0.133	0.0142	0.03	0.0114	0.043	0.0027
225	Run243	MHL	Model 0	1	FW	7.5	2.07	1.25	1.000	46.35	5.20E+05	0.000	0.000	0.000	0.000	0.234	0.0938	0.06	0.0594	0.060	0.0153
226	Run241	MHL	Model 0	1	FW	7.5	2.48	1.5	1.000	32.17	6.24E+05	0.000	0.000	0.000	0.000	0.232	0.0534	0.07	0.0443	0.063	0.0102
227	Run242	MHL	Model 0	1	FW	7.5	2.48	1.5	1.000	32.17	6.24E+05	0.000	0.000	0.000	0.000	0.223	0.0575	0.06	0.0418	0.062	0.0104
228	Run244	MHL	Model 0	1	FW	7.5	2.89	1.75	1.000	23.68	7.28E+05	0.000	0.000	0.000	0.000	0.210	0.0435	0.05	0.0326	0.063	0.0079

#	Run Name	Facility	Model	AR_h	Flow Regime	α, deg	Speed, m/s	Fn_h	Facility Pressure, bar	σ_v	Re_c	δ_{SC} at tip, m		θ at tip, deg		$C_{L,3D}$		$C_{D,3D}$		$C_{M,3D}$ (about 0.5c)	
												Mean	Std	Mean	Std	Mean	Std	Mean	Std	Mean	Std
229	Run245	MHL	Model 0	1	FW	7.5	3.30	2	1.000	18.12	8.32E+05	0.000	0.000	0.000	0.000	0.204	0.0335	0.05	0.0268	0.063	0.0070
230	Run246	MHL	Model 0	1	FW	7.5	3.71	2.25	1.000	14.31	9.34E+05	0.000	0.000	0.000	0.000	0.204	0.0288	0.05	0.0193	0.064	0.0051
231	Run247	MHL	Model 0	1	FW	7.5	4.11	2.5	1.000	11.59	1.04E+06	0.000	0.000	0.000	0.000	0.203	0.0240	0.04	0.0169	0.064	0.0047
232	Run248	MHL	Model 0	1	FW	7.5	4.91	3	1.000	8.05	1.24E+06	0.000	0.000	0.000	0.000	0.198	0.0202	0.04	0.0140	0.063	0.0037
233	Run249	MHL	Model 0	1	FW	7.5	5.78	3.5	1.000	5.91	1.46E+06	0.000	0.000	0.000	0.000	0.194	0.0123	0.03	0.0124	0.063	0.0025
234	Run114	MHL	Model 0	1	FW	10	0.83	0.5	1.000	18.01	2.33E+05	0.000	0.000	0.000	0.000	0.484	0.3358	0.16	0.2353	0.101	0.0510
235	Run253	MHL	Model 0	1	FW	10	2.07	1.25	1.000	46.35	5.20E+05	0.000	0.000	0.000	0.000	0.315	0.0820	0.08	0.0627	0.078	0.0142
236	Run251	MHL	Model 0	1	FW	10	2.48	1.5	1.000	32.17	6.25E+05	0.000	0.000	0.000	0.000	0.299	0.0556	0.09	0.0450	0.080	0.0099
237	Run252	MHL	Model 0	1	FW	10	2.48	1.5	1.000	32.17	6.25E+05	0.000	0.000	0.000	0.000	0.290	0.0607	0.07	0.0489	0.080	0.0114
238	Run407	MHL	Model 0	1	FW	10	2.50	1.5	1.000	32.07	6.69E+05	0.000	0.000	0.000	0.000	0.290	0.0424	0.07	0.0350	0.079	0.0072
239	Run254	MHL	Model 0	1	FW	10	2.89	1.75	1.000	23.68	7.28E+05	0.000	0.000	0.000	0.000	0.277	0.0450	0.07	0.0413	0.081	0.0084
240	Run255	MHL	Model 0	1	FW	10	3.30	2	1.000	19.16	8.31E+05	0.000	0.000	0.000	0.000	0.271	0.0354	0.06	0.0301	0.082	0.0067
241	Run087	MHL	Model 0	1	FW	10	4.13	2.5	1.000	11.52	1.16E+06	0.000	0.000	0.000	0.000	0.266	0.0243	0.05	0.0177	0.080	0.0047
242	Run400	MHL	Model 0	1	FW	10	4.15	2.5	1.000	11.55	1.11E+06	0.000	0.000	0.000	0.000	0.269	0.0233	0.06	0.0192	0.083	0.0039
243	Run256	MHL	Model 0	1	FW	10	4.51	2.75	1.000	9.59	1.14E+06	0.000	0.000	0.000	0.000	0.265	0.0200	0.05	0.0162	0.083	0.0036
244	Run257	MHL	Model 0	1	FW	10	4.96	3	1.000	8.05	1.25E+06	0.000	0.000	0.000	0.000	0.264	0.0197	0.05	0.0156	0.083	0.0036
245	Run088	MHL	Model 0	1	FW	10	4.96	3	1.000	8.00	1.40E+06	0.000	0.000	0.000	0.000	0.260	0.0212	0.05	0.0165	0.080	0.0039
246	Run258	MHL	Model 0	1	FW	10	5.73	3.5	1.000	5.91	1.44E+06	0.000	0.000	0.000	0.000	0.261	0.0151	0.05	0.0131	0.083	0.0029
247	Run266	MHL	Model 0	1	FW	12.5	1.65	1	1.000	72.51	4.12E+05	0.000	0.000	0.000	0.000	0.480	0.1259	0.12	0.0844	0.092	0.0203
248	Run260	MHL	Model 0	1	FW	12.5	2.48	1.5	1.000	32.17	6.24E+05	0.000	0.000	0.000	0.000	0.369	0.0550	0.10	0.0446	0.097	0.0101
249	Run261	MHL	Model 0	1	FW	12.5	2.48	1.5	1.000	32.17	6.24E+05	0.000	0.000	0.000	0.000	0.366	0.0558	0.10	0.0467	0.097	0.0103
250	Run262	MHL	Model 0	1	FW	12.5	2.48	1.5	1.000	32.17	6.24E+05	0.000	0.000	0.000	0.000	0.364	0.0566	0.10	0.0430	0.096	0.0103
251	Run263	MHL	Model 0	1	FW	12.5	2.48	1.5	1.000	32.17	6.24E+05	0.000	0.000	0.000	0.000	0.362	0.0536	0.10	0.0453	0.096	0.0098
252	Run264	MHL	Model 0	1	FW	12.5	2.48	1.5	1.000	32.19	6.18E+05	0.000	0.000	0.000	0.000	0.378	0.0543	0.11	0.0428	0.099	0.0099
253	Run265	MHL	Model 0	1	FW	12.5	2.48	1.5	1.000	32.19	6.18E+05	0.000	0.000	0.000	0.000	0.360	0.0595	0.08	0.0462	0.099	0.0108
254	Run267	MHL	Model 0	1	FW	12.5	2.89	1.75	1.000	23.69	7.21E+05	0.000	0.000	0.000	0.000	0.348	0.0483	0.09	0.0337	0.099	0.0092
255	Run268	MHL	Model 0	1	FW	12.5	4.13	2.5	1.000	11.59	1.03E+06	0.000	0.000	0.000	0.000	0.343	0.0243	0.08	0.0172	0.102	0.0047
256	Run269	MHL	Model 0	1	FW	12.5	4.92	3	1.000	8.06	1.23E+06	0.000	0.000	0.000	0.000	0.338	0.0194	0.08	0.0156	0.102	0.0038
257	Run270	MHL	Model 0	1	FW	12.5	5.36	3.25	1.000	6.86	1.34E+06	0.000	0.000	0.000	0.000	0.338	0.0191	0.07	0.0159	0.101	0.0037
258	Run271	MHL	Model 0	1	FW	12.5	5.74	3.5	1.000	5.92	1.43E+06	0.000	0.000	0.000	0.000	0.337	0.0177	0.07	0.0144	0.101	0.0034
259	Run310	MHL	Model 0	1	FW	14	0.83	0.5	1.000	32.19	2.07E+05	0.000	0.000	0.000	0.000	0.629	0.2997	0.17	0.2403	0.148	0.0348
260	Run309	MHL	Model 0	1	FW	14	2.07	1.25	1.000	32.19	5.16E+05	0.000	0.000	0.000	0.000	0.428	0.0743	0.13	0.0704	0.102	0.0107
261	Run308	MHL	Model 0	1	FW	14	2.47	1.5	1.000	32.19	6.15E+05	0.000	0.000	0.000	0.000	0.392	0.0677	0.11	0.0518	0.102	0.0127
262	Run402	MHL	Model 0	1	FW	14	4.16	2.5	1.000	11.55	1.12E+06	0.000	0.000	0.000	0.000	0.381	0.0240	0.10	0.0195	0.107	0.0044
263	Run405	MHL	Model 0	1	FW	14	4.16	2.5	1.000	11.55	1.11E+06	0.000	0.000	0.000	0.000	0.378	0.0242	0.09	0.0185	0.106	0.0046
264	Run311	MHL	Model 0	1	FW	14	5.75	3.5	1.000	5.92	1.43E+06	0.000	0.000	0.000	0.000	0.366	0.0156	0.09	0.0156	0.106	0.0031
265	Run286	MHL	Model 0	1	FW	15	2.48	1.5	1.000	5.92	6.19E+05	0.000	0.000	0.000	0.000	0.426	0.0474	0.14	0.0342	0.112	0.0091
266	Run091b	MHL	Model 0	1	FW	15	4.12	2.5	1.000	11.52	1.16E+06	0.000	0.000	0.000	0.000	0.415	0.0218	0.12	0.0164	0.110	0.0039

#	Run Name	Facility	Model	AR_h	Flow Regime	α, deg	Speed, m/s	Fn_h	Facility Pressure, bar	σ_v	Re_c	δ_{SC} at tip, m		θ at tip, deg		$C_{L,3D}$		$C_{D,3D}$		$C_{M,3D}$ (about 0.5c)	
												Mean	Std	Mean	Std	Mean	Std	Mean	Std	Mean	Std
267	Run091	MHL	Model 0	1	FW	15	4.13	2.5	1.000	11.52	1.16E+06	0.000	0.000	0.000	0.000	0.421	0.0246	0.11	0.0196	0.111	0.0049
268	Run092	MHL	Model 0	1	FW	15	4.93	3	1.000	8.00	1.39E+06	0.000	0.000	0.000	0.000	0.405	0.0162	0.10	0.0164	0.111	0.0031
269	Run234	MHL	Model 0	1	PV	2.5	2.07	1.25	1.000	18.12	5.22E+05	0.000	0.000	0.000	0.000	0.084	0.0711	0.03	0.0415	0.022	0.0115
270	Run240	MHL	Model 0	1	PV	5	2.07	1.25	1.000	18.12	5.22E+05	0.000	0.000	0.000	0.000	0.173	0.0705	0.05	0.0600	0.039	0.0119
271	Run250	MHL	Model 0	1	PV	7.5	1.66	1	1.000	23.68	4.17E+05	0.000	0.000	0.000	0.000	0.304	0.1360	0.08	0.0863	0.061	0.0190
272	Run243	MHL	Model 0	1	PV	7.5	2.07	1.25	1.000	46.35	5.20E+05	0.000	0.000	0.000	0.000	0.246	0.0873	0.07	0.0595	0.056	0.0127
273	Run259	MHL	Model 0	1	PV	10	0.83	0.5	1.000	32.17	2.08E+05	0.000	0.000	0.000	0.000	0.603	0.3975	0.12	0.2943	0.113	0.0588
274	Run251	MHL	Model 0	1	PV	10	1.66	1	1.000	32.17	4.18E+05	0.000	0.000	0.000	0.000	0.376	0.1332	0.13	0.1148	0.074	0.0220
275	Run253	MHL	Model 0	1	PV	10	2.07	1.25	1.000	46.35	5.20E+05	0.000	0.000	0.000	0.000	0.337	0.0767	0.09	0.0593	0.070	0.0119
276	Run272	MHL	Model 0	1	PV	12.5	0.83	0.5	1.000	32.19	2.06E+05	0.000	0.000	0.000	0.000	0.759	0.2963	0.20	0.2205	0.139	0.0386
277	Run307	MHL	Model 0	1	PV	14	0.83	0.5	1.000	32.19	2.06E+05	0.000	0.000	0.000	0.000	0.657	0.2490	0.16	0.1893	0.137	0.0341
278	Run308	MHL	Model 0	1	PV	14	0.83	0.5	1.000	32.19	2.06E+05	0.000	0.000	0.000	0.000	0.790	0.3402	0.21	0.2993	0.148	0.0455
279	Run310	MHL	Model 0	1	PV	14	1.66	1	1.000	32.19	4.14E+05	0.000	0.000	0.000	0.000	0.510	0.0977	0.16	0.0851	0.094	0.0137
280	Run406	MHL	Model 0	1	PV	14	1.66	1	1.000	72.24	4.45E+05	0.000	0.000	0.000	0.000	0.503	0.0943	0.15	0.0705	0.090	0.0143
281	Run289	MHL	Model 0	1	PV	15	0.83	0.5	1.000	32.19	2.06E+05	0.000	0.000	0.000	0.000	0.847	0.2474	0.14	0.1921	0.162	0.0341
282	Run273b	MHL	Model 0	1	PV	15	0.83	0.5	1.000	32.19	2.07E+05	0.000	0.000	0.000	0.000	0.706	0.5242	0.21	0.3043	0.145	0.0764
283	Run274	MHL	Model 0	1	PV	15	0.83	0.5	1.000	32.19	2.07E+05	0.000	0.000	0.000	0.000	0.679	0.3869	0.18	0.2458	0.145	0.0548
284	Run275	MHL	Model 0	1	PV	15	0.83	0.5	1.000	32.19	2.06E+05	0.000	0.000	0.000	0.000	0.694	0.4641	0.19	0.3273	0.152	0.0670
285	Run276	MHL	Model 0	1	PV	15	0.83	0.5	1.000	32.19	2.07E+05	0.000	0.000	0.000	0.000	0.683	0.1979	0.21	0.2764	0.145	0.0354
286	Run276b	MHL	Model 0	1	PV	15	0.83	0.5	1.000	32.19	2.06E+05	0.000	0.000	0.000	0.000	0.676	0.2374	0.20	0.4037	0.149	0.0257
287	Run278	MHL	Model 0	1	PV	15	1.65	1	1.000	72.51	4.12E+05	0.000	0.000	0.000	0.000	0.561	0.1226	0.15	0.0830	0.094	0.0201
288	Run292	MHL	Model 0	1	PV	17.5	0.83	0.5	1.000	32.19	2.07E+05	0.000	0.000	0.000	0.000	0.719	0.4397	0.26	0.2960	0.154	0.0588
289	Run295	MHL	Model 0	1	PV	20	0.83	0.5	1.000	32.19	2.06E+05	0.000	0.000	0.000	0.000	0.686	0.2971	0.26	0.2244	0.126	0.0435
290	Run409	MHL	Model 0	1	PV	20	0.92	0.5	1.000	236.67	2.47E+05	0.000	0.000	0.000	0.000	0.741	0.2166	0.30	0.1807	0.139	0.0318
291	Run298	MHL	Model 0	1	PV	20	1.65	1	1.000	72.51	4.12E+05	0.000	0.000	0.000	0.000	0.757	0.1148	0.30	0.0888	0.103	0.0174
292	Run299	MHL	Model 0	1	PV	25	0.83	0.5	1.000	32.19	2.07E+05	0.000	0.000	0.000	0.000	0.827	0.2389	0.39	0.2770	0.137	0.0327
293	Run301	MHL	Model 0	1	PV	25	1.65	1	1.000	72.51	4.12E+05	0.000	0.000	0.000	0.000	0.887	0.1048	0.44	0.0882	0.109	0.0156
294	Run302	MHL	Model 0	1	PV	30	0.83	0.5	1.000	32.19	2.06E+05	0.000	0.000	0.000	0.000	0.895	0.2719	0.52	0.2874	0.103	0.0458
295	Run303	MHL	Model 0	1	PV	30	0.83	0.5	1.000	32.19	2.06E+05	0.000	0.000	0.000	0.000	1.046	0.3072	0.62	0.3502	0.095	0.0467
296	Run229	MHL	Model 0	1	FV	2.5	3.30	2	1.000	18.12	8.32E+05	0.000	0.000	0.000	0.000	0.065	0.0360	0.03	0.0251	0.018	0.0057
297	Run230c	MHL	Model 0	1	FV	2.5	3.71	2.25	1.000	14.31	9.35E+05	0.000	0.000	0.000	0.000	0.067	0.0315	0.03	0.0193	0.017	0.0047
298	Run232b	MHL	Model 0	1	FV	2.5	4.96	3	1.000	8.05	1.25E+06	0.000	0.000	0.000	0.000	0.043	0.0218	0.02	0.0120	0.010	0.0036
299	Run237	MHL	Model 0	1	FV	5	2.89	1.75	1.000	23.68	7.28E+05	0.000	0.000	0.000	0.000	0.140	0.0462	0.03	0.0306	0.035	0.0072
300	Run240	MHL	Model 0	1	FV	5	3.31	2	1.000	18.12	8.32E+05	0.000	0.000	0.000	0.000	0.131	0.0356	0.04	0.0242	0.030	0.0058
301	Run238	MHL	Model 0	1	FV	5	3.72	2.25	1.000	14.31	9.36E+05	0.000	0.000	0.000	0.000	0.127	0.0323	0.04	0.0232	0.026	0.0050
302	Run084b	MHL	Model 0	1	FV	5	4.13	2.5	1.000	11.52	1.16E+06	0.000	0.000	0.000	0.000	0.109	0.0245	0.03	0.0164	0.021	0.0042
303	Run085b	MHL	Model 0	1	FV	5	4.95	3	1.000	8.00	1.39E+06	0.000	0.000	0.000	0.000	0.083	0.0188	0.03	0.0125	0.016	0.0033
304	Run239b	MHL	Model 0	1	FV	5	5.74	3.5	1.000	5.91	1.44E+06	0.000	0.000	0.000	0.000	0.068	0.0175	0.03	0.0124	0.014	0.0031

#	Run Name	Facility	Model	AR_h	Flow Regime	α, deg	Speed, m/s	Fn_h	Facility Pressure, bar	σ_v	Re_c	δ_{SC} at tip, m		θ at tip, deg		$C_{L,3D}$		$C_{D,3D}$		$C_{M,3D}$ (about 0.5c)	
												Mean	Std	Mean	Std	Mean	Std	Mean	Std	Mean	Std
305	Run086b	MHL	Model 0	1	FV	5	5.75	3.5	1.000	5.88	1.62E+06	0.000	0.000	0.000	0.000	0.065	0.0161	0.03	0.0127	0.013	0.0027
306	Run250	MHL	Model 0	1	FV	7.5	2.89	1.75	1.000	23.68	7.28E+05	0.000	0.000	0.000	0.000	0.209	0.0432	0.06	0.0304	0.044	0.0076
307	Run245	MHL	Model 0	1	FV	7.5	3.30	2	1.000	18.12	8.32E+05	0.000	0.000	0.000	0.000	0.191	0.0372	0.06	0.0261	0.036	0.0060
308	Run246	MHL	Model 0	1	FV	7.5	3.72	2.25	1.000	14.31	9.36E+05	0.000	0.000	0.000	0.000	0.173	0.0318	0.05	0.0215	0.031	0.0054
309	Run247	MHL	Model 0	1	FV	7.5	4.13	2.5	1.000	11.59	1.04E+06	0.000	0.000	0.000	0.000	0.152	0.0243	0.05	0.0183	0.027	0.0043
310	Run248	MHL	Model 0	1	FV	7.5	4.96	3	1.000	8.05	1.25E+06	0.000	0.000	0.000	0.000	0.118	0.0207	0.04	0.0151	0.022	0.0038
311	Run249	MHL	Model 0	1	FV	7.5	5.74	3.5	1.000	5.91	1.44E+06	0.000	0.000	0.000	0.000	0.100	0.0161	0.04	0.0120	0.021	0.0027
312	Run259	MHL	Model 0	1	FV	10	2.48	1.5	1.000	32.17	6.25E+05	0.000	0.000	0.000	0.000	0.293	0.0652	0.08	0.0503	0.059	0.0104
313	Run254	MHL	Model 0	1	FV	10	2.89	1.75	1.000	23.68	7.28E+05	0.000	0.000	0.000	0.000	0.272	0.0443	0.08	0.0318	0.048	0.0078
314	Run255	MHL	Model 0	1	FV	10	3.30	2	1.000	19.16	8.32E+05	0.000	0.000	0.000	0.000	0.241	0.0355	0.07	0.0272	0.041	0.0060
315	Run087b	MHL	Model 0	1	FV	10	4.13	2.5	1.000	11.52	1.16E+06	0.000	0.000	0.000	0.000	0.189	0.0240	0.06	0.0195	0.032	0.0042
316	Run401	MHL	Model 0	1	FV	10	4.15	2.5	1.000	11.55	1.11E+06	0.000	0.000	0.000	0.000	0.187	0.0249	0.06	0.0200	0.032	0.0037
317	Run256	MHL	Model 0	1	FV	10	4.54	2.75	1.000	9.59	1.14E+06	0.000	0.000	0.000	0.000	0.171	0.0216	0.05	0.0165	0.031	0.0037
318	Run257b	MHL	Model 0	1	FV	10	4.96	3	1.000	8.05	1.25E+06	0.000	0.000	0.000	0.000	0.156	0.0211	0.05	0.0156	0.029	0.0036
319	Run088b	MHL	Model 0	1	FV	10	4.96	3	1.000	8.00	1.40E+06	0.000	0.000	0.000	0.000	0.151	0.0202	0.05	0.0149	0.028	0.0036
320	Run272	MHL	Model 0	1	FV	12.5	2.07	1.25	1.000	32.19	5.15E+05	0.000	0.000	0.000	0.000	0.424	0.0714	0.13	0.0539	0.081	0.0120
321	Run267	MHL	Model 0	1	FV	12.5	2.89	1.75	1.000	23.69	7.21E+05	0.000	0.000	0.000	0.000	0.328	0.0465	0.11	0.0322	0.053	0.0076
322	Run268	MHL	Model 0	1	FV	12.5	4.13	2.5	1.000	11.59	1.03E+06	0.000	0.000	0.000	0.000	0.237	0.0266	0.08	0.0207	0.039	0.0045
323	Run269	MHL	Model 0	1	FV	12.5	4.96	3	1.000	8.06	1.24E+06	0.000	0.000	0.000	0.000	0.199	0.0207	0.07	0.0146	0.036	0.0037
324	Run270b	MHL	Model 0	1	FV	12.5	5.35	3.25	1.000	6.86	1.33E+06	0.000	0.000	0.000	0.000	0.186	0.0184	0.07	0.0142	0.035	0.0031
325	Run271b	MHL	Model 0	1	FV	12.5	5.74	3.5	1.000	5.92	1.43E+06	0.000	0.000	0.000	0.000	0.179	0.0162	0.06	0.0147	0.035	0.0027
326	Run307	MHL	Model 0	1	FV	14	2.07	1.25	1.000	32.19	5.17E+05	0.000	0.000	0.000	0.000	0.442	0.0632	0.15	0.0584	0.082	0.0107
327	Run308	MHL	Model 0	1	FV	14	2.48	1.5	1.000	32.19	6.18E+05	0.000	0.000	0.000	0.000	0.391	0.0665	0.13	0.0478	0.064	0.0104
328	Run309	MHL	Model 0	1	FV	14	2.48	1.5	1.000	32.19	6.18E+05	0.000	0.000	0.000	0.000	0.396	0.0489	0.13	0.0416	0.065	0.0079
329	Run310	MHL	Model 0	1	FV	14	2.47	1.5	1.000	32.19	6.16E+05	0.000	0.000	0.000	0.000	0.395	0.0572	0.14	0.0420	0.065	0.0089
330	Run403	MHL	Model 0	1	FV	14	4.16	2.5	1.000	11.55	1.11E+06	0.000	0.000	0.000	0.000	0.242	0.0245	0.09	0.0211	0.041	0.0038
331	Run278	MHL	Model 0	1	FV	15	1.65	1	1.000	72.51	4.12E+05	0.000	0.000	0.000	0.000	0.563	0.1189	0.15	0.0819	0.094	0.0197
332	Run289	MHL	Model 0	1	FV	15	2.07	1.25	1.000	32.19	5.16E+05	0.000	0.000	0.000	0.000	0.503	0.0830	0.16	0.0611	0.085	0.0123
333	Run288	MHL	Model 0	1	FV	15	2.48	1.5	1.000	32.19	6.18E+05	0.000	0.000	0.000	0.000	0.427	0.0639	0.15	0.0540	0.066	0.0129
334	Run291	MHL	Model 0	1	FV	15	2.48	1.5	1.000	32.19	6.18E+05	0.000	0.000	0.000	0.000	0.426	0.0580	0.14	0.0459	0.065	0.0099
335	Run290	MHL	Model 0	1	FV	15	2.48	1.5	1.000	32.19	6.18E+05	0.000	0.000	0.000	0.000	0.427	0.0595	0.14	0.0499	0.066	0.0106
336	Run273b	MHL	Model 0	1	FV	15	2.48	1.5	1.000	32.19	6.17E+05	0.000	0.000	0.000	0.000	0.435	0.0616	0.16	0.0420	0.066	0.0099
337	Run274	MHL	Model 0	1	FV	15	2.48	1.5	1.000	32.19	6.18E+05	0.000	0.000	0.000	0.000	0.436	0.0601	0.15	0.0419	0.066	0.0099
338	Run275	MHL	Model 0	1	FV	15	2.48	1.5	1.000	32.19	6.18E+05	0.000	0.000	0.000	0.000	0.436	0.0563	0.15	0.0425	0.067	0.0096
339	Run276	MHL	Model 0	1	FV	15	2.48	1.5	1.000	32.19	6.18E+05	0.000	0.000	0.000	0.000	0.430	0.0587	0.15	0.0428	0.066	0.0100
340	Run276b	MHL	Model 0	1	FV	15	2.48	1.5	1.000	32.19	6.18E+05	0.000	0.000	0.000	0.000	0.432	0.0576	0.15	0.0420	0.066	0.0100
341	Run277	MHL	Model 0	1	FV	15	2.48	1.5	1.000	32.19	6.18E+05	0.000	0.000	0.000	0.000	0.440	0.0565	0.16	0.0444	0.066	0.0098
342	Run273	MHL	Model 0	1	FV	15	2.48	1.5	1.000	32.19	6.18E+05	0.000	0.000	0.000	0.000	0.448	0.0569	0.16	0.0441	0.066	0.0098

#	Run Name	Facility	Model	AR_h	Flow Regime	α, deg	Speed, m/s	Fn_h	Facility Pressure, bar	σ_v	Re_c	δ_{SC} at tip, m		θ at tip, deg		$C_{L,3D}$		$C_{D,3D}$		$C_{M,3D}$ (about 0.5c)	
												Mean	Std	Mean	Std	Mean	Std	Mean	Std	Mean	Std
343	Run279	MHL	Model 0	1	FV	15	2.89	1.75	1.000	23.69	7.20E+05	0.000	0.000	0.000	0.000	0.367	0.0434	0.14	0.0323	0.054	0.0076
344	Run280	MHL	Model 0	1	FV	15	3.30	2	1.000	18.13	8.23E+05	0.000	0.000	0.000	0.000	0.330	0.0353	0.12	0.0276	0.049	0.0062
345	Run281	MHL	Model 0	1	FV	15	3.71	2.25	1.000	14.32	9.25E+05	0.000	0.000	0.000	0.000	0.291	0.0300	0.11	0.0230	0.046	0.0049
346	Run282	MHL	Model 0	1	FV	15	4.13	2.5	1.000	11.59	1.03E+06	0.000	0.000	0.000	0.000	0.263	0.0237	0.10	0.0190	0.044	0.0041
347	Run091b	MHL	Model 0	1	FV	15	4.13	2.5	1.000	11.52	1.16E+06	0.000	0.000	0.000	0.000	0.275	0.0230	0.10	0.0202	0.044	0.0040
348	Run283	MHL	Model 0	1	FV	15	4.53	2.75	1.000	9.59	1.13E+06	0.000	0.000	0.000	0.000	0.239	0.0206	0.09	0.0173	0.043	0.0035
349	Run284	MHL	Model 0	1	FV	15	4.95	3	1.000	8.06	1.23E+06	0.000	0.000	0.000	0.000	0.224	0.0208	0.09	0.0163	0.041	0.0036
350	Run285	MHL	Model 0	1	FV	15	5.35	3.25	1.000	6.86	1.33E+06	0.000	0.000	0.000	0.000	0.213	0.0167	0.09	0.0159	0.040	0.0030
351	Run285b	MHL	Model 0	1	FV	15	5.36	3.25	1.000	6.86	1.34E+06	0.000	0.000	0.000	0.000	0.215	0.0184	0.09	0.0193	0.041	0.0031
352	Run285c	MHL	Model 0	1	FV	15	5.33	3.25	1.000	6.86	1.33E+06	0.000	0.000	0.000	0.000	0.216	0.0172	0.09	0.0143	0.041	0.0031
353	Run093	MHL	Model 0	1	FV	15	5.77	3.5	1.000	5.88	1.62E+06	0.000	0.000	0.000	0.000	0.217	0.0153	0.08	0.0124	0.041	0.0026
354	Run093b	MHL	Model 0	1	FV	15	5.77	3.5	1.000	5.88	1.62E+06	0.000	0.000	0.000	0.000	0.216	0.0160	0.08	0.0126	0.040	0.0028
355	Run287	MHL	Model 0	1	FV	15	6.02	3.75	1.000	5.34	1.50E+06	0.000	0.000	0.000	0.000	0.223	0.0171	0.08	0.0226	0.042	0.0026
356	Run292	MHL	Model 0	1	FV	17.5	2.07	1.25	1.000	32.19	5.16E+05	0.000	0.000	0.000	0.000	0.568	0.0705	0.23	0.0542	0.083	0.0115
357	Run293	MHL	Model 0	1	FV	17.5	2.48	1.5	1.000	32.19	6.18E+05	0.000	0.000	0.000	0.000	0.490	0.0600	0.20	0.0492	0.066	0.0108
358	Run294	MHL	Model 0	1	FV	17.5	5.74	3.5	1.000	5.92	1.43E+06	0.000	0.000	0.000	0.000	0.246	0.0157	0.11	0.0173	0.046	0.0028
359	Run099	MHL	Model 0	1	FV	20	1.66	1	1.000	18.01	4.67E+05	0.000	0.000	0.000	0.000	0.823	0.1515	0.32	0.0898	0.116	0.0269
360	Run297	MHL	Model 0	1	FV	20	2.07	1.25	1.000	46.37	5.15E+05	0.000	0.000	0.000	0.000	0.638	0.0810	0.28	0.0631	0.080	0.0123
361	Run295	MHL	Model 0	1	FV	20	2.48	1.5	1.000	32.19	6.18E+05	0.000	0.000	0.000	0.000	0.531	0.0539	0.23	0.0511	0.065	0.0084
362	Run296	MHL	Model 0	1	FV	20	2.48	1.5	1.000	32.19	6.19E+05	0.000	0.000	0.000	0.000	0.522	0.0625	0.23	0.0485	0.064	0.0101
363	Run095	MHL	Model 0	1	FV	20	3.29	2	1.000	18.01	9.26E+05	0.000	0.000	0.000	0.000	0.408	0.0338	0.19	0.0293	0.057	0.0065
364	Run096	MHL	Model 0	1	FV	20	4.13	2.5	1.000	11.52	1.16E+06	0.000	0.000	0.000	0.000	0.345	0.0236	0.16	0.0192	0.055	0.0042
365	Run097	MHL	Model 0	1	FV	20	4.94	3	1.000	8.00	1.39E+06	0.000	0.000	0.000	0.000	0.309	0.0186	0.14	0.0165	0.052	0.0033
366	Run098	MHL	Model 0	1	FV	20	5.78	3.5	1.000	5.88	1.63E+06	0.000	0.000	0.000	0.000	0.287	0.0160	0.13	0.0153	0.051	0.0028
367	Run300	MHL	Model 0	1	FV	25	1.66	1	1.000	32.19	4.13E+05	0.000	0.000	0.000	0.000	0.960	0.1167	0.49	0.0897	0.115	0.0173
368	Run299	MHL	Model 0	1	FV	25	2.07	1.25	1.000	32.19	5.16E+05	0.000	0.000	0.000	0.000	0.746	0.0642	0.41	0.0627	0.078	0.0110
369	Run104	MHL	Model 0	1	FV	25	3.27	2	1.000	18.98	9.20E+05	0.000	0.000	0.000	0.000	0.475	0.0469	0.25	0.0487	0.064	0.0073
370	Run100	MHL	Model 0	1	FV	25	3.29	2	1.000	18.01	9.25E+05	0.000	0.000	0.000	0.000	0.487	0.0388	0.26	0.0381	0.065	0.0061
371	Run101	MHL	Model 0	1	FV	25	4.13	2.5	1.000	11.52	1.16E+06	0.000	0.000	0.000	0.000	0.426	0.0251	0.23	0.0213	0.063	0.0044
372	Run102	MHL	Model 0	1	FV	25	4.96	3	1.000	8.00	1.40E+06	0.000	0.000	0.000	0.000	0.391	0.0186	0.22	0.0162	0.062	0.0035
373	Run102b	MHL	Model 0	1	FV	25	4.95	3	1.000	8.00	1.39E+06	0.000	0.000	0.000	0.000	0.390	0.0179	0.22	0.0158	0.061	0.0032
374	Run103	MHL	Model 0	1	FV	25	5.78	3.5	1.000	5.88	1.63E+06	0.000	0.000	0.000	0.000	0.372	0.0154	0.21	0.0147	0.060	0.0026
375	Run303	MHL	Model 0	1	FV	30	1.66	1	1.000	32.19	4.12E+05	0.000	0.000	0.000	0.000	1.075	0.1011	0.68	0.0904	0.110	0.0137
376	Run304	MHL	Model 0	1	FV	30	1.65	1	1.000	72.51	4.12E+05	0.000	0.000	0.000	0.000	1.047	0.1027	0.66	0.0930	0.108	0.0159
377	Run302	MHL	Model 0	1	FV	30	2.07	1.25	1.000	32.19	5.15E+05	0.000	0.000	0.000	0.000	0.842	0.0680	0.55	0.0655	0.075	0.0111
378	Run105	MHL	Model 0	1	FV	30	3.29	2	1.000	18.01	9.27E+05	0.000	0.000	0.000	0.000	0.548	0.0393	0.36	0.0407	0.071	0.0062
379	Run106	MHL	Model 0	1	FV	30	4.13	2.5	1.000	11.52	1.16E+06	0.000	0.000	0.000	0.000	0.498	0.0229	0.33	0.0211	0.069	0.0041
380	Run107	MHL	Model 0	1	FV	30	4.95	3	1.000	8.00	1.40E+06	0.000	0.000	0.000	0.000	0.465	0.0183	0.31	0.0161	0.068	0.0035

#	Run Name	Facility	Model	AR_h	Flow Regime	α, deg	Speed, m/s	Fn_h	Facility Pressure, bar	σ_v	Re_c	δ_{SC} at tip, m		θ at tip, deg		$C_{L,3D}$		$C_{D,3D}$		$C_{M,3D}$ (about 0.5c)	
												Mean	Std	Mean	Std	Mean	Std	Mean	Std	Mean	Std
381	Run108	MHL	Model 0	1	FV	30	5.80	3.5	1.000	5.88	1.63E+06	0.000	0.000	0.000	0.000	0.446	0.0157	0.29	0.0146	0.066	0.0027
382	Run041	MHL	Model 0	1.5	FW	-5	3.03	1.5	1.000	21.33	8.53E+05	0.000	0.000	0.000	0.000	-0.172	0.0285	0.05	0.0205	-0.048	0.0130
383	Run001	MHL	Model 0	1.5	FW	-5	3.48	1.75	1.000	16.06	9.81E+05	0.000	0.000	0.000	0.000	-0.173	0.0179	0.05	0.0149	-0.048	0.0066
384	Run154	MHL	Model 0	1.5	FW	-5	4.04	2	1.000	12.02	1.12E+06	0.000	0.000	0.000	0.000	-0.170	0.0144	0.05	0.0126	-0.049	0.0057
385	Run002	MHL	Model 0	1.5	FW	-5	4.08	2	1.000	11.76	1.15E+06	0.000	0.000	0.000	0.000	-0.169	0.0152	0.04	0.0112	-0.048	0.0048
386	Run042	MHL	Model 0	1.5	FW	-5	4.04	2	1.000	12.01	1.14E+06	0.000	0.000	0.000	0.000	-0.169	0.0158	0.05	0.0131	-0.048	0.0061
387	Run003	MHL	Model 0	1.5	FW	-5	4.66	2.25	1.000	9.00	1.31E+06	0.000	0.000	0.000	0.000	-0.168	0.0159	0.04	0.0110	-0.048	0.0047
388	Run003b	MHL	Model 0	1.5	FW	-5	4.67	2.25	1.000	9.00	1.32E+06	0.000	0.000	0.000	0.000	-0.170	0.0136	0.04	0.0119	-0.048	0.0043
389	Run043	MHL	Model 0	1.5	FW	-5	5.05	2.5	1.000	7.68	1.42E+06	0.000	0.000	0.000	0.000	-0.166	0.0121	0.04	0.0097	-0.048	0.0037
390	Run034	MHL	Model 0	1.5	FW	-5	5.26	2.5	1.000	7.11	1.48E+06	0.000	0.000	0.000	0.000	-0.165	0.0105	0.04	0.0146	-0.047	0.0030
391	Run044	MHL	Model 0	1.5	FW	-5	6.05	3	1.000	5.34	1.70E+06	0.000	0.000	0.000	0.000	-0.161	0.0096	0.03	0.0091	-0.048	0.0035
392	Run035	MHL	Model 0	1.5	FW	-5	5.87	3	1.000	5.76	1.65E+06	0.000	0.000	0.000	0.000	-0.159	0.0094	0.03	0.0122	-0.048	0.0026
393	Run045	MHL	Model 0	1.5	FW	0	2.53	1.25	1.000	21.33	7.13E+05	0.000	0.000	0.000	0.000	0.011	0.0326	0.04	0.0320	0.004	0.0165
394	Run004	MHL	Model 0	1.5	FW	0	3.49	1.75	1.000	16.00	9.83E+05	0.000	0.000	0.000	0.000	0.006	0.0183	0.03	0.0144	0.004	0.0073
395	Run155	MHL	Model 0	1.5	FW	0	4.04	2	1.000	12.02	1.13E+06	0.000	0.000	0.000	0.000	0.008	0.0152	0.03	0.0126	0.005	0.0057
396	Run005	MHL	Model 0	1.5	FW	0	4.08	2	1.000	11.76	1.15E+06	0.000	0.000	0.000	0.000	0.007	0.0167	0.03	0.0120	0.004	0.0058
397	Run046	MHL	Model 0	1.5	FW	0	4.04	2	1.000	12.01	1.14E+06	0.000	0.000	0.000	0.000	0.013	0.0156	0.03	0.0137	0.005	0.0060
398	Run006	MHL	Model 0	1.5	FW	0	4.67	2.25	1.000	9.00	1.32E+06	0.000	0.000	0.000	0.000	0.008	0.0146	0.03	0.0110	0.004	0.0046
399	Run006b	MHL	Model 0	1.5	FW	0	4.68	2.25	1.000	9.00	1.32E+06	0.000	0.000	0.000	0.000	0.003	0.0137	0.03	0.0138	0.004	0.0040
400	Run047	MHL	Model 0	1.5	FW	0	5.04	2.5	1.000	7.68	1.42E+06	0.000	0.000	0.000	0.000	0.011	0.0121	0.03	0.0096	0.004	0.0041
401	Run036	MHL	Model 0	1.5	FW	0	5.24	2.5	1.000	7.11	1.48E+06	0.000	0.000	0.000	0.000	0.011	0.0095	0.02	0.0096	0.005	0.0029
402	Run048	MHL	Model 0	1.5	FW	0	6.04	3	1.000	5.34	1.70E+06	0.000	0.000	0.000	0.000	0.011	0.0105	0.02	0.0098	0.004	0.0029
403	Run037	MHL	Model 0	1.5	FW	0	5.84	3	1.000	5.76	1.64E+06	0.000	0.000	0.000	0.000	0.009	0.0097	0.02	0.0080	0.004	0.0024
404	Run156	MHL	Model 0	1.5	FW	2.5	2.54	1.25	1.000	12.02	7.06E+05	0.000	0.000	0.000	0.000	0.108	0.0296	0.04	0.0288	0.029	0.0105
405	Run157	MHL	Model 0	1.5	FW	2.5	3.03	1.5	1.000	21.34	8.44E+05	0.000	0.000	0.000	0.000	0.099	0.0372	0.04	0.0381	0.029	0.0265
406	Run158	MHL	Model 0	1.5	FW	2.5	4.04	2	1.000	12.02	1.12E+06	0.000	0.000	0.000	0.000	0.095	0.0155	0.03	0.0105	0.027	0.0050
407	Run159	MHL	Model 0	1.5	FW	2.5	4.53	2.25	1.000	9.50	1.26E+06	0.000	0.000	0.000	0.000	0.094	0.0122	0.03	0.0098	0.028	0.0045
408	Run160	MHL	Model 0	1.5	FW	2.5	5.02	2.5	1.000	7.69	1.40E+06	0.000	0.000	0.000	0.000	0.090	0.0110	0.03	0.0086	0.027	0.0035
409	Run161b	MHL	Model 0	1.5	FW	2.5	6.04	3	1.000	5.34	1.68E+06	0.000	0.000	0.000	0.000	0.092	0.0074	0.02	0.0054	0.028	0.0020
410	Run390	MHL	Model 0	1.5	FW	5	2.03	1	1.000	48.17	5.45E+05	0.000	0.000	0.000	0.000	0.203	0.0474	0.05	0.0402	0.050	0.0125
411	Run163	MHL	Model 0	1.5	FW	5	2.54	1.25	1.000	21.34	7.06E+05	0.000	0.000	0.000	0.000	0.186	0.0299	0.06	0.0284	0.052	0.0109
412	Run049	MHL	Model 0	1.5	FW	5	3.03	1.5	1.000	21.33	8.53E+05	0.000	0.000	0.000	0.000	0.194	0.0282	0.04	0.0197	0.053	0.0116
413	Run164	MHL	Model 0	1.5	FW	5	3.01	1.5	1.000	21.34	8.38E+05	0.000	0.000	0.000	0.000	0.180	0.0295	0.05	0.0251	0.052	0.0195
414	Run007	MHL	Model 0	1.5	FW	5	3.49	1.75	1.000	16.00	9.83E+05	0.000	0.000	0.000	0.000	0.188	0.0185	0.04	0.0155	0.054	0.0064
415	Run165	MHL	Model 0	1.5	FW	5	4.02	2	1.000	12.02	1.12E+06	0.000	0.000	0.000	0.000	0.177	0.0156	0.04	0.0146	0.052	0.0067
416	Run009	MHL	Model 0	1.5	FW	5	4.09	2	1.000	11.76	1.15E+06	0.000	0.000	0.000	0.000	0.190	0.0173	0.03	0.0135	0.054	0.0053
417	Run050	MHL	Model 0	1.5	FW	5	4.04	2	1.000	12.01	1.14E+06	0.000	0.000	0.000	0.000	0.190	0.0175	0.04	0.0159	0.053	0.0070
418	Run166	MHL	Model 0	1.5	FW	5	4.52	2.25	1.000	9.50	1.26E+06	0.000	0.000	0.000	0.000	0.178	0.0120	0.04	0.0105	0.052	0.0045

#	Run Name	Facility	Model	AR_h	Flow Regime	α, deg	Speed, m/s	Fn_h	Facility Pressure, bar	σ_v	Re_c	δ_{SC} at tip, m		θ at tip, deg		$C_{L,3D}$		$C_{D,3D}$		$C_{M,3D}$ (about 0.5c)	
												Mean	Std	Mean	Std	Mean	Std	Mean	Std	Mean	Std
419	Run010	MHL	Model 0	1.5	FW	5	4.67	2.25	1.000	9.00	1.31E+06	0.000	0.000	0.000	0.000	0.188	0.0151	0.03	0.0120	0.053	0.0045
420	Run010b	MHL	Model 0	1.5	FW	5	4.67	2.25	1.000	9.00	1.31E+06	0.000	0.000	0.000	0.000	0.182	0.0140	0.03	0.0102	0.053	0.0041
421	Run010c	MHL	Model 0	1.5	FW	5	4.68	2.25	1.000	9.00	1.32E+06	0.000	0.000	0.000	0.000	0.184	0.0139	0.03	0.0104	0.054	0.0044
422	Run010d	MHL	Model 0	1.5	FW	5	4.68	2.25	1.000	9.00	1.32E+06	0.000	0.000	0.000	0.000	0.181	0.0130	0.03	0.0099	0.053	0.0042
423	Run167	MHL	Model 0	1.5	FW	5	5.02	2.5	1.000	7.69	1.40E+06	0.000	0.000	0.000	0.000	0.176	0.0091	0.04	0.0083	0.052	0.0036
424	Run051	MHL	Model 0	1.5	FW	5	5.06	2.5	1.000	7.68	1.42E+06	0.000	0.000	0.000	0.000	0.185	0.0130	0.03	0.0093	0.054	0.0040
425	Run038	MHL	Model 0	1.5	FW	5	5.82	2.75	1.000	5.76	1.64E+06	0.000	0.000	0.000	0.000	0.179	0.0077	0.02	0.0067	0.052	0.0031
426	Run168	MHL	Model 0	1.5	FW	5	6.02	3	1.000	5.34	1.68E+06	0.000	0.000	0.000	0.000	0.175	0.0105	0.03	0.0091	0.053	0.0022
427	Run172	MHL	Model 0	1.5	FW	7.5	2.01	1	1.000	48.07	5.60E+05	0.000	0.000	0.000	0.000	0.309	0.0546	0.07	0.0410	0.076	0.0194
428	Run173	MHL	Model 0	1.5	FW	7.5	2.52	1.25	1.000	30.78	7.02E+05	0.000	0.000	0.000	0.000	0.284	0.0341	0.06	0.0275	0.076	0.0196
429	Run170	MHL	Model 0	1.5	FW	7.5	3.03	1.5	1.000	21.34	8.43E+05	0.000	0.000	0.000	0.000	0.270	0.0262	0.06	0.0181	0.076	0.0096
430	Run174	MHL	Model 0	1.5	FW	7.5	3.04	1.5	1.000	21.34	8.45E+05	0.000	0.000	0.000	0.000	0.272	0.0233	0.06	0.0191	0.075	0.0101
431	Run171	MHL	Model 0	1.5	FW	7.5	3.01	1.5	1.000	21.34	8.37E+05	0.000	0.000	0.000	0.000	0.268	0.0275	0.05	0.0225	0.076	0.0148
432	Run175	MHL	Model 0	1.5	FW	7.5	3.54	1.75	1.000	15.69	9.85E+05	0.000	0.000	0.000	0.000	0.272	0.0168	0.06	0.0147	0.076	0.0079
433	Run176	MHL	Model 0	1.5	FW	7.5	4.03	2	1.000	12.02	1.12E+06	0.000	0.000	0.000	0.000	0.267	0.0143	0.05	0.0104	0.076	0.0056
434	Run176b	MHL	Model 0	1.5	FW	7.5	4.04	2	1.000	12.02	1.12E+06	0.000	0.000	0.000	0.000	0.270	0.0145	0.05	0.0105	0.078	0.0045
435	Run177	MHL	Model 0	1.5	FW	7.5	4.52	2.25	1.000	9.50	1.26E+06	0.000	0.000	0.000	0.000	0.264	0.0124	0.05	0.0100	0.077	0.0042
436	Run178b	MHL	Model 0	1.5	FW	7.5	5.03	2.5	1.000	7.69	1.40E+06	0.000	0.000	0.000	0.000	0.269	0.0097	0.05	0.0091	0.079	0.0041
437	Run179	MHL	Model 0	1.5	FW	7.5	6.04	3	1.000	5.34	1.68E+06	0.000	0.000	0.000	0.000	0.264	0.0101	0.04	0.0092	0.078	0.0026
438	Run179b	MHL	Model 0	1.5	FW	7.5	6.05	3	1.000	5.34	1.68E+06	0.000	0.000	0.000	0.000	0.262	0.0088	0.04	0.0069	0.078	0.0026
439	Run179c	MHL	Model 0	1.5	FW	7.5	6.03	3	1.000	5.34	1.68E+06	0.000	0.000	0.000	0.000	0.261	0.0101	0.04	0.0073	0.078	0.0025
440	Run181	MHL	Model 0	1.5	FW	10	2.02	1	1.000	48.07	5.62E+05	0.000	0.000	0.000	0.000	0.413	0.0467	0.09	0.0351	0.101	0.0130
441	Run182	MHL	Model 0	1.5	FW	10	2.54	1.25	1.000	21.34	7.07E+05	0.000	0.000	0.000	0.000	0.374	0.0297	0.08	0.0243	0.101	0.0166
442	Run053	MHL	Model 0	1.5	FW	10	3.03	1.5	1.000	21.33	8.52E+05	0.000	0.000	0.000	0.000	0.367	0.0297	0.08	0.0237	0.100	0.0104
443	Run184	MHL	Model 0	1.5	FW	10	3.03	1.5	1.000	21.34	8.43E+05	0.000	0.000	0.000	0.000	0.365	0.0275	0.08	0.0238	0.100	0.0160
444	Run191	MHL	Model 0	1.5	FW	10	3.00	1.5	1.000	21.34	8.36E+05	0.000	0.000	0.000	0.000	0.365	0.0303	0.07	0.0227	0.099	0.0228
445	Run183	MHL	Model 0	1.5	FW	10	3.03	1.5	1.000	21.34	8.45E+05	0.000	0.000	0.000	0.000	0.369	0.0255	0.08	0.0181	0.101	0.0098
446	Run185	MHL	Model 0	1.5	FW	10	3.50	1.75	1.000	15.69	9.75E+05	0.000	0.000	0.000	0.000	0.359	0.0210	0.07	0.0179	0.101	0.0097
447	Run011	MHL	Model 0	1.5	FW	10	3.49	1.75	1.000	16.00	9.84E+05	0.000	0.000	0.000	0.000	0.375	0.0194	0.07	0.0160	0.104	0.0078
448	Run186	MHL	Model 0	1.5	FW	10	4.01	2	1.000	12.02	1.12E+06	0.000	0.000	0.000	0.000	0.356	0.0160	0.07	0.0155	0.101	0.0074
449	Run012	MHL	Model 0	1.5	FW	10	4.09	2	1.000	11.76	1.15E+06	0.000	0.000	0.000	0.000	0.379	0.0153	0.06	0.0137	0.105	0.0049
450	Run187	MHL	Model 0	1.5	FW	10	4.52	2.25	1.000	9.50	1.26E+06	0.000	0.000	0.000	0.000	0.353	0.0119	0.07	0.0112	0.102	0.0057
451	Run013	MHL	Model 0	1.5	FW	10	4.66	2.25	1.000	9.00	1.31E+06	0.000	0.000	0.000	0.000	0.371	0.0148	0.07	0.0119	0.104	0.0049
452	Run013d	MHL	Model 0	1.5	FW	10	4.73	2.25	1.000	9.00	1.33E+06	0.000	0.000	0.000	0.000	0.359	0.0114	0.05	0.0125	0.105	0.0045
453	Run188	MHL	Model 0	1.5	FW	10	5.03	2.5	1.000	7.69	1.40E+06	0.000	0.000	0.000	0.000	0.351	0.0097	0.07	0.0089	0.102	0.0039
454	Run055b	MHL	Model 0	1.5	FW	10	5.06	2.5	1.000	7.68	1.43E+06	0.000	0.000	0.000	0.000	0.359	0.0111	0.06	0.0090	0.103	0.0039
455	Run055	MHL	Model 0	1.5	FW	10	5.06	2.5	1.000	7.68	1.42E+06	0.000	0.000	0.000	0.000	0.358	0.0116	0.06	0.0094	0.103	0.0039
456	Run039	MHL	Model 0	1.5	FW	10	5.22	2.5	1.000	7.11	1.47E+06	0.000	0.000	0.000	0.000	0.362	0.0095	0.05	0.0111	0.104	0.0027

#	Run Name	Facility	Model	AR_h	Flow Regime	α, deg	Speed, m/s	Fn_h	Facility Pressure, bar	σ_v	Re_c	δ_{SC} at tip, m		θ at tip, deg		$C_{L,3D}$		$C_{D,3D}$		$C_{M,3D}$ (about 0.5c)	
												Mean	Std	Mean	Std	Mean	Std	Mean	Std	Mean	Std
457	Run040	MHL	Model 0	1.5	FW	10	5.81	2.75	1.000	5.76	1.64E+06	0.000	0.000	0.000	0.000	0.352	0.0072	0.06	0.0070	0.102	0.0030
458	Run189	MHL	Model 0	1.5	FW	10	5.56	2.75	1.000	6.35	1.55E+06	0.000	0.000	0.000	0.000	0.347	0.0078	0.06	0.0070	0.102	0.0030
459	Run190	MHL	Model 0	1.5	FW	10	6.07	3	1.000	5.34	1.69E+06	0.000	0.000	0.000	0.000	0.349	0.0083	0.06	0.0092	0.103	0.0024
460	Run194	MHL	Model 0	1.5	FW	12.5	2.02	1	1.000	48.07	5.63E+05	0.000	0.000	0.000	0.000	0.510	0.0478	0.11	0.0281	0.116	0.0176
461	Run195	MHL	Model 0	1.5	FW	12.5	2.53	1.25	1.000	30.78	7.04E+05	0.000	0.000	0.000	0.000	0.475	0.0352	0.10	0.0228	0.117	0.0194
462	Run195c	MHL	Model 0	1.5	FW	12.5	2.53	1.25	1.000	30.78	7.03E+05	0.000	0.000	0.000	0.000	0.472	0.0336	0.10	0.0296	0.118	0.0148
463	Run192	MHL	Model 0	1.5	FW	12.5	3.03	1.5	1.000	21.34	8.44E+05	0.000	0.000	0.000	0.000	0.463	0.0287	0.10	0.0196	0.118	0.0106
464	Run196	MHL	Model 0	1.5	FW	12.5	3.04	1.5	1.000	21.34	8.45E+05	0.000	0.000	0.000	0.000	0.457	0.0251	0.10	0.0217	0.119	0.0130
465	Run193	MHL	Model 0	1.5	FW	12.5	3.01	1.5	1.000	21.34	8.37E+05	0.000	0.000	0.000	0.000	0.458	0.0299	0.10	0.0202	0.118	0.0144
466	Run197	MHL	Model 0	1.5	FW	12.5	3.54	1.75	1.000	15.69	9.85E+05	0.000	0.000	0.000	0.000	0.455	0.0176	0.10	0.0152	0.121	0.0081
467	Run199	MHL	Model 0	1.5	FW	12.5	4.52	2.25	1.000	9.50	1.26E+06	0.000	0.000	0.000	0.000	0.447	0.0131	0.10	0.0113	0.123	0.0052
468	Run200b	MHL	Model 0	1.5	FW	12.5	6.07	3	1.000	5.34	1.69E+06	0.000	0.000	0.000	0.000	0.439	0.0084	0.09	0.0084	0.122	0.0026
469	Run062	MHL	Model 0	1.5	FW	15	2.54	1.25	1.000	21.33	7.16E+05	0.000	0.000	0.000	0.000	0.558	0.0430	0.16	0.0608	0.130	0.0114
470	Run059	MHL	Model 0	1.5	FW	15	4.04	2	1.000	12.01	1.14E+06	0.000	0.000	0.000	0.000	0.553	0.0184	0.14	0.0125	0.133	0.0078
471	Run016	MHL	Model 0	1.5	FW	15	4.08	2	1.000	11.76	1.15E+06	0.000	0.000	0.000	0.000	0.582	0.0197	0.16	0.0128	0.130	0.0060
472	Run395	MHL	Model 0	1.5	FW	15	4.06	2	1.000	12.04	1.09E+06	0.000	0.000	0.000	0.000	0.449	0.0190	0.12	0.0128	0.119	0.0042
473	Run017	MHL	Model 0	1.5	FW	15	4.68	2.25	1.000	9.00	1.32E+06	0.000	0.000	0.000	0.000	0.567	0.0175	0.15	0.0128	0.129	0.0063
474	Run017b	MHL	Model 0	1.5	FW	15	4.69	2.25	1.000	9.00	1.32E+06	0.000	0.000	0.000	0.000	0.547	0.0151	0.13	0.0136	0.130	0.0059
475	Run060	MHL	Model 0	1.5	FW	15	5.04	2.5	1.000	7.68	1.42E+06	0.000	0.000	0.000	0.000	0.532	0.0129	0.13	0.0088	0.132	0.0057
476	Run061	MHL	Model 0	1.5	FW	15	5.85	3	1.000	5.34	1.65E+06	0.000	0.000	0.000	0.000	0.534	0.0113	0.14	0.0068	0.132	0.0055
477	Run029b	MHL	Model 0	1.5	FW	15	5.89	3	1.000	5.76	1.66E+06	0.000	0.000	0.000	0.000	0.540	0.0106	0.14	0.0071	0.126	0.0043
478	Run162	MHL	Model 0	1.5	PV	2.5	4.03	2	1.000	12.02	1.12E+06	0.000	0.000	0.000	0.000	0.084	0.0154	0.03	0.0106	0.022	0.0030
479	Run159	MHL	Model 0	1.5	PV	2.5	4.55	2.25	1.000	9.50	1.27E+06	0.000	0.000	0.000	0.000	0.077	0.0131	0.03	0.0109	0.018	0.0024
480	Run169	MHL	Model 0	1.5	PV	5	2.54	1.25	1.000	21.34	7.06E+05	0.000	0.000	0.000	0.000	0.199	0.0283	0.04	0.0211	0.049	0.0092
481	Run172	MHL	Model 0	1.5	PV	7.5	2.02	1	1.000	48.07	5.63E+05	0.000	0.000	0.000	0.000	0.325	0.0466	0.07	0.0326	0.073	0.0161
482	Run173	MHL	Model 0	1.5	PV	7.5	2.53	1.25	1.000	30.78	7.03E+05	0.000	0.000	0.000	0.000	0.297	0.0305	0.07	0.0236	0.066	0.0087
483	Run181	MHL	Model 0	1.5	PV	10	2.02	1	1.000	48.07	5.63E+05	0.000	0.000	0.000	0.000	0.429	0.0537	0.10	0.0356	0.093	0.0168
484	Run191	MHL	Model 0	1.5	PV	10	2.53	1.25	1.000	21.34	7.05E+05	0.000	0.000	0.000	0.000	0.408	0.0316	0.09	0.0291	0.078	0.0196
485	Run201b	MHL	Model 0	1.5	PV	12.5	1.01	0.5	1.000	21.34	2.82E+05	0.000	0.000	0.000	0.000	0.730	0.1680	0.22	0.1725	0.139	0.0329
486	Run194	MHL	Model 0	1.5	PV	12.5	2.02	1	1.000	48.07	5.63E+05	0.000	0.000	0.000	0.000	0.542	0.0479	0.12	0.0261	0.102	0.0111
487	Run194b	MHL	Model 0	1.5	PV	12.5	2.02	1	1.000	48.36	5.63E+05	0.000	0.000	0.000	0.000	0.541	0.0502	0.12	0.0261	0.102	0.0128
488	Run195	MHL	Model 0	1.5	PV	12.5	2.53	1.25	1.000	30.78	7.03E+05	0.000	0.000	0.000	0.000	0.477	0.0358	0.12	0.0211	0.084	0.0099
489	Run195c	MHL	Model 0	1.5	PV	12.5	2.53	1.25	1.000	30.78	7.03E+05	0.000	0.000	0.000	0.000	0.476	0.0357	0.12	0.0288	0.084	0.0087
490	Run058	MHL	Model 0	1.5	PV	15	1.01	0.5	1.000	21.33	2.86E+05	0.000	0.000	0.000	0.000	0.751	0.1989	0.22	0.1466	0.153	0.0321
491	Run062	MHL	Model 0	1.5	PV	15	1.01	0.5	1.000	21.33	2.86E+05	0.000	0.000	0.000	0.000	0.982	0.1719	0.26	0.1074	0.162	0.0518
492	Run206	MHL	Model 0	1.5	PV	15	2.02	1	1.000	48.07	5.63E+05	0.000	0.000	0.000	0.000	0.657	0.0440	0.20	0.0395	0.105	0.0099
493	Run202	MHL	Model 0	1.5	PV	15	2.53	1.25	1.000	30.78	7.03E+05	0.000	0.000	0.000	0.000	0.557	0.0396	0.18	0.0305	0.089	0.0100
494	Run214	MHL	Model 0	1.5	PV	17.5	1.01	0.5	1.000	48.07	2.82E+05	0.000	0.000	0.000	0.000	0.924	0.0705	0.34	0.1061	0.176	0.0190

#	Run Name	Facility	Model	AR_h	Flow Regime	α, deg	Speed, m/s	Fn_h	Facility Pressure, bar	σ_v	Re_c	δ_{SC} at tip, m		θ at tip, deg		$C_{L,3D}$		$C_{D,3D}$		$C_{M,3D}$ (about 0.5c)	
												Mean	Std	Mean	Std	Mean	Std	Mean	Std	Mean	Std
495	Run212	MHL	Model 0	1.5	PV	17.5	2.52	1.25	1.000	30.78	7.02E+05	0.000	0.000	0.000	0.000	0.619	0.0353	0.23	0.0283	0.087	0.0072
496	Run220	MHL	Model 0	1.5	PV	20	2.53	1.25	1.000	21.34	7.04E+05	0.000	0.000	0.000	0.000	0.664	0.0316	0.28	0.0310	0.083	0.0078
497	Run223	MHL	Model 0	1.5	PV	25	1.02	0.5	1.000	21.34	2.83E+05	0.000	0.000	0.000	0.000	1.160	0.1675	0.53	0.1449	0.118	0.0311
498	Run068	MHL	Model 0	1.5	PV	25	1.02	0.5	1.000	84.96	2.86E+05	0.000	0.000	0.000	0.000	0.982	0.1350	0.48	0.1325	0.109	0.0310
499	Run222	MHL	Model 0	1.5	PV	25	2.54	1.25	1.000	21.34	7.07E+05	0.000	0.000	0.000	0.000	0.745	0.0267	0.40	0.0283	0.080	0.0072
500	Run033	MHL	Model 0	1.5	PV	25	2.49	1.25	1.000	5.76	7.02E+05	0.000	0.000	0.000	0.000	0.741	0.0274	0.40	0.0221	0.077	0.0049
501	Run073	MHL	Model 0	1.5	PV	30	1.51	0.75	1.000	84.96	4.25E+05	0.000	0.000	0.000	0.000	1.085	0.0846	0.73	0.0904	0.104	0.0357
502	Run160	MHL	Model 0	1.5	FV	2.5	5.06	2.5	1.000	7.69	1.41E+06	0.000	0.000	0.000	0.000	0.068	0.0116	0.03	0.0093	0.015	0.0021
503	Run161b	MHL	Model 0	1.5	FV	2.5	5.57	2.75	1.000	5.34	1.55E+06	0.000	0.000	0.000	0.000	0.059	0.0090	0.02	0.0083	0.013	0.0016
504	Run161	MHL	Model 0	1.5	FV	2.5	6.03	3	1.000	5.34	1.68E+06	0.000	0.000	0.000	0.000	0.050	0.0104	0.02	0.0110	0.011	0.0016
505	Run169	MHL	Model 0	1.5	FV	5	3.03	1.5	1.000	21.34	8.43E+05	0.000	0.000	0.000	0.000	0.178	0.0245	0.04	0.0223	0.043	0.0078
506	Run165	MHL	Model 0	1.5	FV	5	3.55	1.75	1.000	12.02	9.88E+05	0.000	0.000	0.000	0.000	0.174	0.0240	0.04	0.0210	0.038	0.0053
507	Run169b	MHL	Model 0	1.5	FV	5	4.04	2	1.000	12.02	1.12E+06	0.000	0.000	0.000	0.000	0.154	0.0148	0.04	0.0103	0.032	0.0028
508	Run166	MHL	Model 0	1.5	FV	5	4.55	2.25	1.000	9.50	1.27E+06	0.000	0.000	0.000	0.000	0.139	0.0133	0.04	0.0108	0.027	0.0023
509	Run010d	MHL	Model 0	1.5	FV	5	4.67	2.25	1.000	9.00	1.32E+06	0.000	0.000	0.000	0.000	0.136	0.0159	0.03	0.0084	0.026	0.0022
510	Run167	MHL	Model 0	1.5	FV	5	5.06	2.5	1.000	7.69	1.41E+06	0.000	0.000	0.000	0.000	0.119	0.0111	0.04	0.0096	0.022	0.0019
511	Run051b	MHL	Model 0	1.5	FV	5	5.06	2.5	1.000	7.68	1.43E+06	0.000	0.000	0.000	0.000	0.122	0.0137	0.03	0.0097	0.023	0.0020
512	Run027	MHL	Model 0	1.5	FV	5	5.86	3	1.000	7.11	1.65E+06	0.000	0.000	0.000	0.000	0.094	0.0123	0.03	0.0077	0.019	0.0016
513	Run052	MHL	Model 0	1.5	FV	5	6.06	3	1.000	5.34	1.71E+06	0.000	0.000	0.000	0.000	0.092	0.0101	0.03	0.0107	0.018	0.0016
514	Run168	MHL	Model 0	1.5	FV	5	6.03	3	1.000	5.34	1.68E+06	0.000	0.000	0.000	0.000	0.092	0.0105	0.03	0.0185	0.018	0.0015
515	Run038	MHL	Model 0	1.5	FV	5	5.85	3	1.000	5.76	1.65E+06	0.000	0.000	0.000	0.000	0.099	0.0106	0.03	0.0088	0.019	0.0015
516	Run174	MHL	Model 0	1.5	FV	7.5	3.04	1.5	1.000	21.34	8.45E+05	0.000	0.000	0.000	0.000	0.277	0.0286	0.07	0.0270	0.056	0.0219
517	Run175	MHL	Model 0	1.5	FV	7.5	3.54	1.75	1.000	15.69	9.85E+05	0.000	0.000	0.000	0.000	0.250	0.0194	0.07	0.0157	0.046	0.0065
518	Run176	MHL	Model 0	1.5	FV	7.5	4.05	2	1.000	12.02	1.13E+06	0.000	0.000	0.000	0.000	0.221	0.0144	0.06	0.0122	0.038	0.0029
519	Run177	MHL	Model 0	1.5	FV	7.5	4.55	2.25	1.000	9.50	1.27E+06	0.000	0.000	0.000	0.000	0.189	0.0138	0.05	0.0113	0.033	0.0023
520	Run178	MHL	Model 0	1.5	FV	7.5	5.05	2.5	1.000	7.69	1.41E+06	0.000	0.000	0.000	0.000	0.162	0.0108	0.05	0.0098	0.030	0.0018
521	Run191	MHL	Model 0	1.5	FV	10	3.04	1.5	1.000	21.34	8.45E+05	0.000	0.000	0.000	0.000	0.352	0.0277	0.09	0.0223	0.061	0.0069
522	Run183	MHL	Model 0	1.5	FV	10	3.03	1.5	1.000	21.34	8.44E+05	0.000	0.000	0.000	0.000	0.357	0.0259	0.10	0.0186	0.062	0.0113
523	Run185	MHL	Model 0	1.5	FV	10	3.54	1.75	1.000	15.69	9.85E+05	0.000	0.000	0.000	0.000	0.309	0.0192	0.09	0.0146	0.051	0.0042
524	Run186	MHL	Model 0	1.5	FV	10	4.05	2	1.000	12.02	1.13E+06	0.000	0.000	0.000	0.000	0.268	0.0151	0.08	0.0132	0.044	0.0027
525	Run012b	MHL	Model 0	1.5	FV	10	4.09	2	1.000	11.76	1.15E+06	0.000	0.000	0.000	0.000	0.279	0.0169	0.08	0.0131	0.045	0.0026
526	Run054	MHL	Model 0	1.5	FV	10	4.04	2	1.000	12.01	1.14E+06	0.000	0.000	0.000	0.000	0.262	0.0165	0.07	0.0126	0.043	0.0027
527	Run187	MHL	Model 0	1.5	FV	10	4.55	2.25	1.000	9.50	1.27E+06	0.000	0.000	0.000	0.000	0.233	0.0122	0.07	0.0105	0.039	0.0021
528	Run013c	MHL	Model 0	1.5	FV	10	4.66	2.25	1.000	9.00	1.31E+06	0.000	0.000	0.000	0.000	0.238	0.0147	0.07	0.0115	0.039	0.0020
529	Run013d	MHL	Model 0	1.5	FV	10	4.67	2.25	1.000	9.00	1.32E+06	0.000	0.000	0.000	0.000	0.224	0.0135	0.05	0.0107	0.039	0.0020
530	Run188	MHL	Model 0	1.5	FV	10	5.06	2.5	1.000	7.69	1.41E+06	0.000	0.000	0.000	0.000	0.205	0.0111	0.06	0.0098	0.036	0.0017
531	Run055c	MHL	Model 0	1.5	FV	10	5.06	2.5	1.000	7.68	1.42E+06	0.000	0.000	0.000	0.000	0.206	0.0136	0.06	0.0084	0.036	0.0020
532	Run039	MHL	Model 0	1.5	FV	10	5.25	2.5	1.000	7.11	1.48E+06	0.000	0.000	0.000	0.000	0.204	0.0118	0.06	0.0109	0.036	0.0017

#	Run Name	Facility	Model	AR_h	Flow Regime	α, deg	Speed, m/s	Fn_h	Facility Pressure, bar	σ_v	Re_c	δ_{SC} at tip, m		θ at tip, deg		$C_{L,3D}$		$C_{D,3D}$		$C_{M,3D}$ (about 0.5c)	
												Mean	Std	Mean	Std	Mean	Std	Mean	Std	Mean	Std
533	Run189	MHL	Model 0	1.5	FV	10	5.55	2.75	1.000	6.35	1.55E+06	0.000	0.000	0.000	0.000	0.184	0.0097	0.06	0.0089	0.035	0.0014
534	Run190b	MHL	Model 0	1.5	FV	10	6.08	3	1.000	5.34	1.69E+06	0.000	0.000	0.000	0.000	0.170	0.0086	0.05	0.0084	0.033	0.0013
535	Run056	MHL	Model 0	1.5	FV	10	6.07	3	1.000	5.34	1.71E+06	0.000	0.000	0.000	0.000	0.174	0.0098	0.05	0.0073	0.033	0.0015
536	Run040	MHL	Model 0	1.5	FV	10	5.86	3	1.000	5.76	1.65E+06	0.000	0.000	0.000	0.000	0.180	0.0100	0.05	0.0102	0.034	0.0015
537	Run201b	MHL	Model 0	1.5	FV	12.5	2.58	1.25	1.000	21.34	7.19E+05	0.000	0.000	0.000	0.000	0.473	0.0342	0.15	0.0302	0.082	0.0124
538	Run196	MHL	Model 0	1.5	FV	12.5	3.03	1.5	1.000	21.34	8.44E+05	0.000	0.000	0.000	0.000	0.422	0.0276	0.12	0.0207	0.065	0.0066
539	Run201	MHL	Model 0	1.5	FV	12.5	3.04	1.5	1.000	21.34	8.45E+05	0.000	0.000	0.000	0.000	0.415	0.0317	0.14	0.0277	0.065	0.0211
540	Run197	MHL	Model 0	1.5	FV	12.5	3.54	1.75	1.000	15.69	9.85E+05	0.000	0.000	0.000	0.000	0.360	0.0185	0.11	0.0154	0.054	0.0035
541	Run198	MHL	Model 0	1.5	FV	12.5	4.04	2	1.000	12.02	1.13E+06	0.000	0.000	0.000	0.000	0.309	0.0147	0.10	0.0126	0.047	0.0024
542	Run198b	MHL	Model 0	1.5	FV	12.5	4.05	2	1.000	12.02	1.13E+06	0.000	0.000	0.000	0.000	0.308	0.0151	0.10	0.0132	0.047	0.0025
543	Run199	MHL	Model 0	1.5	FV	12.5	4.55	2.25	1.000	9.50	1.27E+06	0.000	0.000	0.000	0.000	0.279	0.0130	0.09	0.0113	0.045	0.0021
544	Run200	MHL	Model 0	1.5	FV	12.5	6.07	3	1.000	5.34	1.69E+06	0.000	0.000	0.000	0.000	0.201	0.0097	0.07	0.0092	0.039	0.0014
545	Run211	MHL	Model 0	1.5	FV	15	2.54	1.25	1.000	21.34	7.06E+05	0.000	0.000	0.000	0.000	0.572	0.0318	0.18	0.0274	0.086	0.0072
546	Run204	MHL	Model 0	1.5	FV	15	3.04	1.5	1.000	21.34	8.45E+05	0.000	0.000	0.000	0.000	0.482	0.0280	0.17	0.0213	0.068	0.0050
547	Run058	MHL	Model 0	1.5	FV	15	3.03	1.5	1.000	21.33	8.52E+05	0.000	0.000	0.000	0.000	0.477	0.0335	0.17	0.0250	0.067	0.0109
548	Run203	MHL	Model 0	1.5	FV	15	3.03	1.5	1.000	21.34	8.44E+05	0.000	0.000	0.000	0.000	0.485	0.0328	0.18	0.0288	0.068	0.0142
549	Run205	MHL	Model 0	1.5	FV	15	3.04	1.5	1.000	21.34	8.45E+05	0.000	0.000	0.000	0.000	0.482	0.0253	0.17	0.0215	0.068	0.0048
550	Run207	MHL	Model 0	1.5	FV	15	3.54	1.75	1.000	15.69	9.85E+05	0.000	0.000	0.000	0.000	0.410	0.0181	0.15	0.0159	0.057	0.0030
551	Run015	MHL	Model 0	1.5	FV	15	3.49	1.75	1.000	16.00	9.84E+05	0.000	0.000	0.000	0.000	0.423	0.0204	0.15	0.0138	0.059	0.0032
552	Run015b	MHL	Model 0	1.5	FV	15	3.49	1.75	1.000	16.00	9.83E+05	0.000	0.000	0.000	0.000	0.423	0.0201	0.15	0.0143	0.059	0.0031
553	Run059b	MHL	Model 0	1.5	FV	15	4.04	2	1.000	12.01	1.14E+06	0.000	0.000	0.000	0.000	0.361	0.0161	0.13	0.0125	0.054	0.0026
554	Run016b	MHL	Model 0	1.5	FV	15	4.08	2	1.000	11.76	1.15E+06	0.000	0.000	0.000	0.000	0.374	0.0162	0.13	0.0118	0.055	0.0024
555	Run059	MHL	Model 0	1.5	FV	15	4.05	2	1.000	12.01	1.14E+06	0.000	0.000	0.000	0.000	0.368	0.0163	0.12	0.0126	0.055	0.0025
556	Run208	MHL	Model 0	1.5	FV	15	4.55	2.25	1.000	9.50	1.27E+06	0.000	0.000	0.000	0.000	0.311	0.0122	0.12	0.0109	0.051	0.0020
557	Run017	MHL	Model 0	1.5	FV	15	4.66	2.25	1.000	9.00	1.31E+06	0.000	0.000	0.000	0.000	0.332	0.0140	0.12	0.0110	0.052	0.0019
558	Run017b	MHL	Model 0	1.5	FV	15	4.67	2.25	1.000	9.00	1.32E+06	0.000	0.000	0.000	0.000	0.314	0.0143	0.10	0.0117	0.052	0.0021
559	Run060	MHL	Model 0	1.5	FV	15	5.06	2.5	1.000	7.68	1.42E+06	0.000	0.000	0.000	0.000	0.292	0.0135	0.10	0.0100	0.049	0.0021
560	Run028	MHL	Model 0	1.5	FV	15	5.28	2.5	1.000	7.11	1.49E+06	0.000	0.000	0.000	0.000	0.283	0.0105	0.09	0.0093	0.050	0.0017
561	Run209	MHL	Model 0	1.5	FV	15	5.57	2.75	1.000	6.35	1.55E+06	0.000	0.000	0.000	0.000	0.258	0.0093	0.10	0.0098	0.047	0.0015
562	Run210	MHL	Model 0	1.5	FV	15	6.14	3	1.000	5.34	1.71E+06	0.000	0.000	0.000	0.000	0.239	0.0080	0.09	0.0082	0.046	0.0014
563	Run061	MHL	Model 0	1.5	FV	15	6.09	3	1.000	5.34	1.72E+06	0.000	0.000	0.000	0.000	0.259	0.0104	0.10	0.0078	0.047	0.0019
564	Run061b	MHL	Model 0	1.5	FV	15	6.07	3	1.000	5.34	1.71E+06	0.000	0.000	0.000	0.000	0.239	0.0098	0.09	0.0124	0.045	0.0017
565	Run029	MHL	Model 0	1.5	FV	15	5.91	3	1.000	5.76	1.67E+06	0.000	0.000	0.000	0.000	0.267	0.0102	0.09	0.0072	0.049	0.0016
566	Run219	MHL	Model 0	1.5	FV	17.5	2.54	1.25	1.000	30.78	7.06E+05	0.000	0.000	0.000	0.000	0.656	0.0322	0.26	0.0272	0.086	0.0066
567	Run213	MHL	Model 0	1.5	FV	17.5	3.04	1.5	1.000	21.34	8.45E+05	0.000	0.000	0.000	0.000	0.527	0.0267	0.21	0.0212	0.069	0.0055
568	Run215	MHL	Model 0	1.5	FV	17.5	3.54	1.75	1.000	15.69	9.85E+05	0.000	0.000	0.000	0.000	0.450	0.0185	0.19	0.0168	0.062	0.0030
569	Run216	MHL	Model 0	1.5	FV	17.5	4.55	2.25	1.000	9.50	1.27E+06	0.000	0.000	0.000	0.000	0.347	0.0126	0.15	0.0119	0.056	0.0020
570	Run217	MHL	Model 0	1.5	FV	17.5	5.58	2.75	1.000	6.35	1.55E+06	0.000	0.000	0.000	0.000	0.292	0.0093	0.12	0.0086	0.053	0.0015

#	Run Name	Facility	Model	AR_h	Flow Regime	α, deg	Speed, m/s	Fn_h	Facility Pressure, bar	σ_v	Re_c	δ_{SC} at tip, m		θ at tip, deg		$C_{L,3D}$		$C_{D,3D}$		$C_{M,3D}$ (about 0.5c)	
												Mean	Std	Mean	Std	Mean	Std	Mean	Std	Mean	Std
571	Run218	MHL	Model 0	1.5	FV	17.5	6.12	3	1.000	5.34	1.70E+06	0.000	0.000	0.000	0.000	0.279	0.0096	0.12	0.0092	0.052	0.0014
572	Run221	MHL	Model 0	1.5	FV	20	2.54	1.25	1.000	21.34	7.06E+05	0.000	0.000	0.000	0.000	0.714	0.0312	0.31	0.0280	0.086	0.0067
573	Run220	MHL	Model 0	1.5	FV	20	3.03	1.5	1.000	21.34	8.44E+05	0.000	0.000	0.000	0.000	0.576	0.0259	0.25	0.0206	0.071	0.0042
574	Run063	MHL	Model 0	1.5	FV	20	3.03	1.5	1.000	21.33	8.53E+05	0.000	0.000	0.000	0.000	0.566	0.0299	0.24	0.0217	0.070	0.0089
575	Run019	MHL	Model 0	1.5	FV	20	3.49	1.75	1.000	16.00	9.84E+05	0.000	0.000	0.000	0.000	0.498	0.0178	0.21	0.0156	0.067	0.0028
576	Run022	MHL	Model 0	1.5	FV	20	3.66	1.75	1.000	16.00	1.03E+06	0.000	0.000	0.000	0.000	0.465	0.0231	0.21	0.0192	0.064	0.0034
577	Run020	MHL	Model 0	1.5	FV	20	4.08	2	1.000	11.76	1.15E+06	0.000	0.000	0.000	0.000	0.429	0.0153	0.19	0.0143	0.064	0.0024
578	Run064	MHL	Model 0	1.5	FV	20	4.05	2	1.000	12.01	1.14E+06	0.000	0.000	0.000	0.000	0.425	0.0164	0.19	0.0149	0.064	0.0026
579	Run021	MHL	Model 0	1.5	FV	20	4.65	2.25	1.000	9.00	1.31E+06	0.000	0.000	0.000	0.000	0.388	0.0129	0.17	0.0131	0.061	0.0021
580	Run021b	MHL	Model 0	1.5	FV	20	4.68	2.25	1.000	9.00	1.32E+06	0.000	0.000	0.000	0.000	0.382	0.0139	0.17	0.0097	0.061	0.0020
581	Run065	MHL	Model 0	1.5	FV	20	5.05	2.5	1.000	7.68	1.42E+06	0.000	0.000	0.000	0.000	0.357	0.0114	0.16	0.0090	0.060	0.0020
582	Run030	MHL	Model 0	1.5	FV	20	5.29	2.5	1.000	7.11	1.49E+06	0.000	0.000	0.000	0.000	0.351	0.0126	0.16	0.0132	0.059	0.0017
583	Run066	MHL	Model 0	1.5	FV	20	6.09	3	1.000	5.34	1.72E+06	0.000	0.000	0.000	0.000	0.319	0.0099	0.15	0.0087	0.057	0.0017
584	Run031	MHL	Model 0	1.5	FV	20	6.00	3	1.000	5.76	1.69E+06	0.000	0.000	0.000	0.000	0.326	0.0113	0.15	0.0078	0.058	0.0017
585	Run223	MHL	Model 0	1.5	FV	25	2.54	1.25	1.000	21.34	7.06E+05	0.000	0.000	0.000	0.000	0.800	0.0350	0.43	0.0309	0.086	0.0063
586	Run222	MHL	Model 0	1.5	FV	25	3.03	1.5	1.000	21.34	8.44E+05	0.000	0.000	0.000	0.000	0.647	0.0246	0.35	0.0203	0.077	0.0041
587	Run072	MHL	Model 0	1.5	FV	25	2.96	1.5	1.000	21.33	8.35E+05	0.000	0.000	0.000	0.000	0.642	0.0307	0.35	0.0247	0.077	0.0052
588	Run068	MHL	Model 0	1.5	FV	25	3.03	1.5	1.000	84.96	8.53E+05	0.000	0.000	0.000	0.000	0.646	0.0256	0.34	0.0226	0.076	0.0046
589	Run023	MHL	Model 0	1.5	FV	25	3.49	1.75	1.000	16.00	9.84E+05	0.000	0.000	0.000	0.000	0.564	0.0199	0.30	0.0194	0.074	0.0029
590	Run069	MHL	Model 0	1.5	FV	25	4.04	2	1.000	12.01	1.14E+06	0.000	0.000	0.000	0.000	0.497	0.0169	0.27	0.0148	0.072	0.0029
591	Run024	MHL	Model 0	1.5	FV	25	4.08	2	1.000	11.76	1.15E+06	0.000	0.000	0.000	0.000	0.498	0.0151	0.27	0.0134	0.072	0.0025
592	Run025	MHL	Model 0	1.5	FV	25	4.66	2.25	1.000	9.00	1.31E+06	0.000	0.000	0.000	0.000	0.454	0.0136	0.25	0.0120	0.069	0.0021
593	Run025b	MHL	Model 0	1.5	FV	25	4.65	2.25	1.000	9.00	1.31E+06	0.000	0.000	0.000	0.000	0.463	0.0126	0.26	0.0124	0.070	0.0020
594	Run070	MHL	Model 0	1.5	FV	25	5.06	2.5	1.000	7.68	1.43E+06	0.000	0.000	0.000	0.000	0.428	0.0113	0.23	0.0100	0.068	0.0021
595	Run032	MHL	Model 0	1.5	FV	25	5.28	2.5	1.000	7.11	1.49E+06	0.000	0.000	0.000	0.000	0.427	0.0092	0.23	0.0097	0.068	0.0017
596	Run071	MHL	Model 0	1.5	FV	25	6.07	3	1.000	5.34	1.71E+06	0.000	0.000	0.000	0.000	0.396	0.0123	0.22	0.0141	0.065	0.0019
597	Run033	MHL	Model 0	1.5	FV	25	6.10	3	1.000	5.76	1.72E+06	0.000	0.000	0.000	0.000	0.403	0.0078	0.22	0.0076	0.066	0.0015
598	Run077	MHL	Model 0	1.5	FV	30	2.97	1.5	1.000	21.33	8.38E+05	0.000	0.000	0.000	0.000	0.694	0.0282	0.44	0.0239	0.080	0.0059
599	Run073	MHL	Model 0	1.5	FV	30	3.01	1.5	1.000	84.96	8.49E+05	0.000	0.000	0.000	0.000	0.689	0.0248	0.44	0.0229	0.082	0.0046
600	Run074	MHL	Model 0	1.5	FV	30	4.03	2	1.000	12.01	1.14E+06	0.000	0.000	0.000	0.000	0.555	0.0160	0.37	0.0154	0.078	0.0030
601	Run075	MHL	Model 0	1.5	FV	30	5.06	2.5	1.000	7.68	1.43E+06	0.000	0.000	0.000	0.000	0.497	0.0121	0.33	0.0113	0.073	0.0019
602	Run076	MHL	Model 0	1.5	FV	30	6.08	3	1.000	5.34	1.71E+06	0.000	0.000	0.000	0.000	0.463	0.0121	0.31	0.0140	0.071	0.0021
603	RunF100	MHL	Model 1	0.5	FW	-5	1.76	1.5	1.000	64.27	4.64E+05	-0.001	0.000	-0.043	-0.043	-0.123	0.1822	0.04	0.1425	-0.022	0.0158
604	RunF101	MHL	Model 1	0.5	FW	-5	2.35	2	1.000	36.15	6.19E+05	-0.002	0.000	-0.049	-0.049	-0.095	0.1044	0.03	0.0957	-0.027	0.0106
605	RunF102	MHL	Model 1	0.5	FW	-5	2.94	2.5	1.000	23.14	7.74E+05	-0.003	0.000	-0.073	-0.073	-0.087	0.0753	0.02	0.0606	-0.028	0.0067
606	RunF103	MHL	Model 1	0.5	FW	-5	3.53	3	1.000	16.07	9.29E+05	-0.004	0.000	-0.111	-0.111	-0.086	0.0543	0.02	0.0475	-0.029	0.0047
607	RunF104	MHL	Model 1	0.5	FW	-5	4.70	4	1.000	9.04	1.24E+06	-0.006	0.000	-0.180	-0.180	-0.083	0.0278	0.02	0.0295	-0.029	0.0033
608	RunF105	MHL	Model 1	0.5	FW	-5	5.86	5	1.000	5.78	1.54E+06	-0.010	0.000	-0.262	-0.262	-0.082	0.0235	0.02	0.0175	-0.030	0.0029

#	Run Name	Facility	Model	AR_h	Flow Regime	α, deg	Speed, m/s	Fn_h	Facility Pressure, bar	σ_v	Re_c	δ_{SC} at tip, m		θ at tip, deg		$C_{L,3D}$		$C_{D,3D}$		$C_{M,3D}$ (about 0.5c)	
												Mean	Std	Mean	Std	Mean	Std	Mean	Std	Mean	Std
609	RunF106	MHL	Model 1	0.5	FW	0	1.77	1.5	1.000	64.27	4.65E+05	0.000	0.000	0.011	0.011	0.004	0.1905	0.03	0.1397	0.002	0.0167
610	RunF107	MHL	Model 1	0.5	FW	0	2.35	2	1.000	36.15	6.19E+05	0.000	0.000	0.013	0.013	-0.002	0.1020	0.03	0.0929	0.000	0.0100
611	RunF108	MHL	Model 1	0.5	FW	0	3.52	3	1.000	16.07	9.28E+05	0.000	0.000	0.013	0.013	0.000	0.0510	0.03	0.0474	0.002	0.0042
612	RunF109	MHL	Model 1	0.5	FW	0	4.70	4	1.000	9.04	1.24E+06	0.000	0.000	0.011	0.011	0.000	0.0285	0.02	0.0295	0.002	0.0029
613	RunF110	MHL	Model 1	0.5	FW	0	5.86	5	1.000	5.78	1.54E+06	0.000	0.000	0.017	0.017	0.001	0.0200	0.02	0.0188	0.002	0.0022
614	RunF111	MHL	Model 1	0.5	FW	5	1.77	1.5	1.000	64.27	4.65E+05	0.001	0.000	0.056	0.056	0.119	0.1847	0.05	0.1397	0.025	0.0140
615	RunF113	MHL	Model 1	0.5	FV	5	3.53	3	1.000	16.07	9.29E+05	0.003	0.000	0.100	0.100	0.074	0.0476	0.03	0.0527	0.014	0.0043
616	RunFC006	MHL	Model 1	1	FW	-12.5	2.49	1.5	1.000	32.09	6.60E+05	-0.014	0.000	-0.403	-0.403	-0.383	0.0470	0.10	0.0327	-0.101	0.0066
617	RunFC002	MHL	Model 1	1	FW	-12.5	3.06	1.75	1.000	21.32	8.10E+05	-0.021	0.000	-0.594	-0.594	-0.378	0.0388	0.10	0.0258	-0.106	0.0071
618	RunFC003	MHL	Model 1	1	FW	-12.5	3.32	2	1.000	18.07	8.80E+05	-0.025	0.000	-0.747	-0.747	-0.374	0.0324	0.10	0.0220	-0.107	0.0066
619	RunFC004	MHL	Model 1	1	FW	-12.5	4.15	2.5	1.000	11.56	1.10E+06	-0.039	0.000	-1.024	-1.024	-0.374	0.0302	0.10	0.0164	-0.108	0.0065
620	RunFC009	MHL	Model 1	1	FW	-12.5	4.14	2.5	1.000	11.56	1.10E+06	-0.037	0.000	-0.988	-0.988	-0.359	0.0307	0.09	0.0169	-0.105	0.0066
621	RunFC009D	MHL	Model 1	1	FW	-12.5	4.15	2.5	1.000	11.56	1.10E+06	-0.037	0.001	-1.001	-1.001	-0.364	0.0271	0.10	0.0173	-0.105	0.0052
622	RunFC009A	MHL	Model 1	1	FW	-12.5	4.15	2.5	1.000	11.56	1.10E+06	-0.039	0.000	-1.036	-1.036	-0.363	0.0249	0.10	0.0160	-0.106	0.0046
623	RunFC009B	MHL	Model 1	1	FW	-12.5	4.15	2.5	1.000	11.56	1.10E+06	-0.037	0.000	-0.999	-0.999	-0.369	0.0290	0.10	0.0175	-0.106	0.0057
624	RunFC009C	MHL	Model 1	1	FW	-12.5	4.16	2.5	1.000	11.56	1.10E+06	-0.037	0.001	-0.997	-0.997	-0.362	0.0258	0.10	0.0158	-0.105	0.0043
625	RunFC005	MHL	Model 1	1	FW	-12.5	4.96	3	1.000	8.03	1.31E+06	-0.055	0.000	-1.288	-1.288	-0.369	0.0234	0.10	0.0120	-0.107	0.0053
626	RunFC010	MHL	Model 1	1	FW	-12.5	5.88	3.5	1.000	5.90	1.56E+06	-0.077	0.001	-1.481	-1.481	-0.363	0.0248	0.10	0.0111	-0.108	0.0062
627	RunF049	MHL	Model 1	1	FW	-5	2.49	1.5	1.000	32.10	6.57E+05	-0.006	0.000	-0.212	-0.212	-0.147	0.0545	0.04	0.0418	-0.043	0.0063
628	RunF050	MHL	Model 1	1	FW	-5	3.32	2	1.000	18.08	8.78E+05	-0.009	0.000	-0.325	-0.325	-0.137	0.0280	0.03	0.0258	-0.043	0.0042
629	RunF051	MHL	Model 1	1	FW	-5	4.15	2.5	1.000	11.56	1.10E+06	-0.014	0.000	-0.497	-0.497	-0.139	0.0198	0.03	0.0164	-0.044	0.0022
630	RunF052	MHL	Model 1	1	FW	-5	4.99	3	1.000	8.03	1.32E+06	-0.021	0.000	-0.688	-0.688	-0.138	0.0156	0.03	0.0129	-0.044	0.0020
631	RunF053	MHL	Model 1	1	FW	0	2.49	1.5	1.000	32.10	6.58E+05	0.000	0.000	0.010	0.010	0.000	0.0581	0.03	0.0443	-0.002	0.0061
632	RunF054	MHL	Model 1	1	FW	0	3.32	2	1.000	18.08	8.77E+05	0.000	0.000	0.011	0.011	0.001	0.0275	0.03	0.0272	0.001	0.0034
633	RunF055	MHL	Model 1	1	FW	0	4.16	2.5	1.000	11.56	1.10E+06	0.000	0.000	0.024	0.024	0.001	0.0187	0.03	0.0190	0.001	0.0025
634	RunF056	MHL	Model 1	1	FW	0	4.99	3	1.000	8.03	1.32E+06	0.000	0.000	0.023	0.023	0.002	0.0145	0.02	0.0136	0.001	0.0015
635	RunF057	MHL	Model 1	1	FW	5	1.64	1	1.000	72.30	4.34E+05	0.003	0.000	0.119	0.119	0.187	0.1092	0.05	0.0880	0.038	0.0149
636	RunF058	MHL	Model 1	1	FW	5	2.49	1.5	1.000	32.10	6.59E+05	0.005	0.000	0.208	0.208	0.141	0.0588	0.04	0.0417	0.040	0.0054
637	RunF059	MHL	Model 1	1	FW	5	3.32	2	1.000	18.08	8.77E+05	0.009	0.000	0.335	0.335	0.139	0.0297	0.03	0.0261	0.042	0.0042
638	RunF060	MHL	Model 1	1	FW	5	4.15	2.5	1.000	11.56	1.10E+06	0.014	0.000	0.515	0.515	0.139	0.0196	0.03	0.0181	0.043	0.0023
639	RunF060B	MHL	Model 1	1	FW	5	4.18	2.5	1.000	11.56	1.10E+06	0.014	0.000	0.496	0.496	0.135	0.0210	0.03	0.0237	0.043	0.0028
640	RunF061	MHL	Model 1	1	FW	5	5.00	3	1.000	8.03	1.32E+06	0.020	0.000	0.671	0.671	0.138	0.0138	0.02	0.0120	0.044	0.0015
641	RunF065	MHL	Model 1	1	FW	10	2.49	1.5	1.000	32.10	6.59E+05	0.011	0.000	0.402	0.402	0.296	0.0538	0.07	0.0421	0.081	0.0061
642	RunF069	MHL	Model 1	1	FW	10	2.50	1.5	1.000	32.10	6.60E+05	0.011	0.000	0.370	0.370	0.292	0.0647	0.06	0.0514	0.081	0.0109
643	RunF066	MHL	Model 1	1	FW	10	3.32	2	1.000	18.08	8.78E+05	0.018	0.000	0.635	0.635	0.283	0.0273	0.06	0.0285	0.084	0.0043
644	RunF067	MHL	Model 1	1	FW	10	4.15	2.5	1.000	11.56	1.10E+06	0.028	0.000	0.777	0.777	0.282	0.0194	0.05	0.0179	0.086	0.0026
645	RunF068	MHL	Model 1	1	FW	10	4.99	3	1.000	8.03	1.32E+06	0.041	0.000	0.990	0.990	0.285	0.0142	0.05	0.0114	0.088	0.0026
646	RunF070	MHL	Model 1	1	FW	12.5	1.66	1	1.000	72.30	4.38E+05	0.008	0.000	0.269	0.269	0.478	0.0920	0.12	0.0936	0.092	0.0163

#	Run Name	Facility	Model	AR_h	Flow Regime	α, deg	Speed, m/s	Fn_h	Facility Pressure, bar	σ_v	Re_c	δ_{SC} at tip, m		θ at tip, deg		$C_{L,3D}$		$C_{D,3D}$		$C_{M,3D}$ (about 0.5c)	
												Mean	Std	Mean	Std	Mean	Std	Mean	Std	Mean	Std
647	RunF071	MHL	Model 1	1	FW	12.5	2.50	1.5	1.000	32.10	6.59E+05	0.014	0.000	0.490	0.490	0.374	0.0530	0.09	0.0401	0.098	0.0054
648	RunF075	MHL	Model 1	1	FW	12.5	2.47	1.5	1.000	32.10	6.52E+05	0.013	0.000	0.469	0.469	0.361	0.0522	0.09	0.0429	0.098	0.0072
649	RunF072	MHL	Model 1	1	FW	12.5	3.33	2	1.000	18.08	8.79E+05	0.023	0.000	0.692	0.692	0.357	0.0297	0.08	0.0282	0.103	0.0052
650	RunF072A	MHL	Model 1	1	FW	12.5	3.33	2	1.000	18.08	8.78E+05	0.023	0.000	0.687	0.687	0.350	0.0272	0.08	0.0284	0.101	0.0043
651	RunF073	MHL	Model 1	1	FW	12.5	4.16	2.5	1.000	11.56	1.10E+06	0.036	0.000	0.919	0.919	0.354	0.0172	0.08	0.0181	0.104	0.0031
652	RunF074	MHL	Model 1	1	FW	12.5	4.99	3	1.000	8.03	1.32E+06	0.052	0.000	1.286	1.286	0.355	0.0152	0.08	0.0119	0.105	0.0028
653	RunF098	MHL	Model 1	1	FW	13	2.49	1.5	1.000	32.10	6.56E+05	0.014	0.000	0.505	0.505	0.388	0.0428	0.10	0.0389	0.100	0.0058
654	RunFC012	MHL	Model 1	1	PV	-20	1.66	1	1.000	72.29	4.40E+05	-0.014	0.000	-0.384	-0.384	-0.798	0.0960	0.33	0.0720	-0.109	0.0129
655	RunFC011	MHL	Model 1	1	PV	-20	1.57	1	1.000	33.30	4.17E+05	-0.012	0.000	-0.348	-0.348	-0.818	0.1027	0.35	0.0777	-0.115	0.0161
656	RunFC013	MHL	Model 1	1	PV	-20	2.08	1.25	1.000	46.23	5.50E+05	-0.019	0.000	-0.475	-0.475	-0.680	0.0713	0.31	0.0514	-0.089	0.0093
657	RunF057	MHL	Model 1	1	PV	5	1.66	1	1.000	72.30	4.39E+05	0.003	0.000	0.121	0.121	0.188	0.1032	0.05	0.0787	0.039	0.0119
658	RunF070	MHL	Model 1	1	PV	12.5	1.66	1	1.000	72.30	4.39E+05	0.008	0.000	0.280	0.280	0.490	0.1036	0.12	0.0796	0.089	0.0169
659	RunF099	MHL	Model 1	1	PV	13	1.66	1	1.000	72.31	4.38E+05	0.008	0.000	0.284	0.284	0.504	0.0930	0.13	0.0818	0.091	0.0167
660	RunF076	MHL	Model 1	1	PV	15	1.66	1	1.000	72.31	4.38E+05	0.010	0.000	0.333	0.333	0.588	0.0995	0.17	0.0791	0.097	0.0147
661	RunF083	MHL	Model 1	1	PV	20	1.66	1	1.000	72.31	4.38E+05	0.012	0.000	-0.906	-0.906	0.792	0.1013	0.30	0.0827	0.105	0.0170
662	RunF089	MHL	Model 1	1	PV	25	1.66	1	1.000	72.31	4.39E+05	0.017	0.000	0.478	0.478	0.938	0.1057	0.46	0.0837	0.111	0.0167
663	RunFC007	MHL	Model 1	1	FV	-17.5	1.65	1	1.000	18.07	4.38E+05	-0.011	0.001	-0.303	-0.303	-0.731	0.0631	0.14	0.1043	-0.111	0.0236
664	RunFC008E	MHL	Model 1	1	FV	-17.5	3.32	2	1.000	18.07	8.80E+05	-0.027	0.000	-0.631	-0.631	-0.392	0.0347	0.15	0.0249	-0.057	0.0038
665	RunFC008	MHL	Model 1	1	FV	-17.5	4.15	2.5	1.000	11.56	1.10E+06	-0.034	0.000	-0.805	-0.805	-0.318	0.0259	0.13	0.0171	-0.054	0.0032
666	RunFC008A	MHL	Model 1	1	FV	-17.5	4.16	2.5	1.000	11.56	1.10E+06	-0.034	0.000	-0.816	-0.816	-0.317	0.0264	0.13	0.0173	-0.054	0.0033
667	RunFC008B	MHL	Model 1	1	FV	-17.5	4.15	2.5	1.000	11.56	1.10E+06	-0.034	0.000	-0.808	-0.808	-0.316	0.0228	0.13	0.0166	-0.054	0.0029
668	RunFC008C	MHL	Model 1	1	FV	-17.5	4.15	2.5	1.000	11.56	1.10E+06	-0.034	0.000	-0.794	-0.794	-0.315	0.0295	0.13	0.0179	-0.054	0.0035
669	RunFC008D	MHL	Model 1	1	FV	-17.5	4.15	2.5	1.000	11.56	1.10E+06	-0.034	0.000	-0.776	-0.776	-0.316	0.0245	0.13	0.0169	-0.054	0.0030
670	RunFC003	MHL	Model 1	1	FV	-12.5	3.32	2	1.000	18.07	8.80E+05	-0.021	0.000	-0.545	-0.545	-0.310	0.0317	0.11	0.0237	-0.050	0.0036
671	RunFC004	MHL	Model 1	1	FV	-12.5	4.16	2.5	1.000	11.56	1.10E+06	-0.027	0.000	-0.643	-0.643	-0.252	0.0210	0.09	0.0161	-0.043	0.0025
672	RunFC009	MHL	Model 1	1	FV	-12.5	4.15	2.5	1.000	11.56	1.10E+06	-0.026	0.000	-0.615	-0.615	-0.242	0.0250	0.08	0.0173	-0.042	0.0029
673	RunFC009D	MHL	Model 1	1	FV	-12.5	4.15	2.5	1.000	11.56	1.10E+06	-0.026	0.000	-0.628	-0.628	-0.247	0.0237	0.09	0.0174	-0.042	0.0025
674	RunFC009A	MHL	Model 1	1	FV	-12.5	4.15	2.5	1.000	11.56	1.10E+06	-0.028	0.000	-0.662	-0.662	-0.246	0.0222	0.09	0.0178	-0.042	0.0027
675	RunFC009C	MHL	Model 1	1	FV	-12.5	4.15	2.5	1.000	11.56	1.10E+06	-0.026	0.000	-0.620	-0.620	-0.246	0.0241	0.09	0.0184	-0.042	0.0027
676	RunFC005	MHL	Model 1	1	FV	-12.5	4.98	3	1.000	8.03	1.32E+06	-0.032	0.000	-0.720	-0.720	-0.208	0.0189	0.08	0.0127	-0.040	0.0026
677	RunFC010	MHL	Model 1	1	FV	-12.5	5.79	3.5	1.000	5.90	1.53E+06	-0.038	0.000	-0.782	-0.782	-0.184	0.0136	0.07	0.0091	-0.038	0.0017
678	RunF063	MHL	Model 1	1	FV	5	2.56	1.5	1.000	18.08	6.76E+05	0.006	0.000	0.214	0.214	0.149	0.0593	0.04	0.0386	0.036	0.0077
679	RunF059	MHL	Model 1	1	FV	5	3.32	2	1.000	18.08	8.77E+05	0.009	0.000	0.312	0.312	0.131	0.0323	0.04	0.0249	0.030	0.0045
680	RunF060B	MHL	Model 1	1	FV	5	4.16	2.5	1.000	11.56	1.10E+06	0.012	0.000	0.377	0.377	0.107	0.0195	0.03	0.0179	0.021	0.0025
681	RunF061	MHL	Model 1	1	FV	5	4.98	3	1.000	8.03	1.32E+06	0.013	0.000	0.411	0.411	0.082	0.0164	0.03	0.0136	0.016	0.0017
682	RunF064	MHL	Model 1	1	FV	10	1.66	1	1.000	72.30	4.39E+05	0.006	0.000	0.221	0.221	0.385	0.1065	0.09	0.0766	0.076	0.0147
683	RunF065	MHL	Model 1	1	FV	10	2.49	1.5	1.000	32.10	6.59E+05	0.012	0.000	0.407	0.407	0.304	0.0537	0.08	0.0391	0.061	0.0076
684	RunF066	MHL	Model 1	1	FV	10	3.33	2	1.000	18.08	8.78E+05	0.017	0.000	0.536	0.536	0.247	0.0294	0.07	0.0266	0.043	0.0035

#	Run Name	Facility	Model	AR_h	Flow Regime	α, deg	Speed, m/s	Fn_h	Facility Pressure, bar	σ_v	Re_c	δ_{SC} at tip, m		θ at tip, deg		$C_{L,3D}$		$C_{D,3D}$		$C_{M,3D}$ (about 0.5c)	
												Mean	Std	Mean	Std	Mean	Std	Mean	Std	Mean	Std
685	RunF067	MHL	Model 1	1	FV	10	4.15	2.5	1.000	11.56	1.10E+06	0.021	0.000	0.576	0.576	0.196	0.0189	0.06	0.0177	0.034	0.0025
686	RunF068	MHL	Model 1	1	FV	10	4.99	3	1.000	8.03	1.32E+06	0.024	0.000	0.604	0.604	0.158	0.0153	0.05	0.0131	0.031	0.0019
687	RunF071	MHL	Model 1	1	FV	12.5	2.50	1.5	1.000	32.10	6.59E+05	0.015	0.000	0.473	0.473	0.379	0.0553	0.11	0.0402	0.066	0.0069
688	RunF075	MHL	Model 1	1	FV	12.5	2.49	1.5	1.000	32.10	6.57E+05	0.014	0.000	0.459	0.459	0.360	0.0461	0.11	0.0446	0.065	0.0081
689	RunF072	MHL	Model 1	1	FV	12.5	3.32	2	1.000	18.08	8.78E+05	0.020	0.000	0.569	0.569	0.294	0.0304	0.09	0.0258	0.047	0.0036
690	RunF072A	MHL	Model 1	1	FV	12.5	3.32	2	1.000	18.08	8.77E+05	0.020	0.000	0.544	0.544	0.289	0.0316	0.09	0.0262	0.046	0.0035
691	RunF073	MHL	Model 1	1	FV	12.5	4.16	2.5	1.000	11.56	1.10E+06	0.025	0.000	0.621	0.621	0.234	0.0201	0.08	0.0190	0.040	0.0027
692	RunF074	MHL	Model 1	1	FV	12.5	4.98	3	1.000	8.03	1.31E+06	0.029	0.000	0.690	0.690	0.197	0.0143	0.07	0.0134	0.038	0.0020
693	RunF099	MHL	Model 1	1	FV	13	1.66	1	1.000	72.31	4.38E+05	0.008	0.000	0.285	0.285	0.505	0.0918	0.13	0.0804	0.091	0.0164
694	RunF098	MHL	Model 1	1	FV	13	2.49	1.5	1.000	32.10	6.57E+05	0.015	0.000	0.484	0.484	0.387	0.0404	0.12	0.0386	0.066	0.0072
695	RunF096	MHL	Model 1	1	FV	14	2.49	1.5	1.000	32.10	6.57E+05	0.016	0.000	0.503	0.503	0.412	0.0478	0.13	0.0395	0.066	0.0069
696	RunF097	MHL	Model 1	1	FV	14	4.14	2.5	1.000	8.03	1.09E+06	0.027	0.000	0.603	0.603	0.244	0.0201	0.09	0.0292	0.043	0.0034
697	RunF076	MHL	Model 1	1	FV	15	1.66	1	1.000	72.31	4.38E+05	0.010	0.000	0.334	0.334	0.589	0.1003	0.17	0.0789	0.097	0.0145
698	RunF082	MHL	Model 1	1	FV	15	2.47	1.5	1.000	32.10	6.51E+05	0.017	0.000	0.471	0.471	0.439	0.0489	0.14	0.0458	0.068	0.0079
699	RunF077	MHL	Model 1	1	FV	15	2.49	1.5	1.000	32.10	6.57E+05	0.017	0.000	0.510	0.510	0.441	0.0541	0.15	0.0442	0.068	0.0079
700	RunF078	MHL	Model 1	1	FV	15	3.32	2	1.000	18.08	8.76E+05	0.023	0.000	0.606	0.606	0.332	0.0292	0.12	0.0268	0.050	0.0037
701	RunF079	MHL	Model 1	1	FV	15	4.16	2.5	1.000	11.56	1.10E+06	0.029	0.000	0.688	0.688	0.269	0.0204	0.10	0.0187	0.046	0.0027
702	RunF080	MHL	Model 1	1	FV	15	4.98	3	1.000	8.03	1.31E+06	0.035	0.000	0.776	0.776	0.230	0.0137	0.09	0.0128	0.044	0.0019
703	RunF081	MHL	Model 1	1	FV	15	5.82	3.5	1.000	5.90	1.54E+06	0.043	0.000	0.913	0.913	0.211	0.0114	0.08	0.0090	0.044	0.0017
704	RunF086	MHL	Model 1	1	FV	20	1.68	1	1.000	11.56	4.42E+05	0.014	0.000	0.442	0.442	0.826	0.1013	0.28	0.0781	0.117	0.0172
705	RunF088	MHL	Model 1	1	FV	20	1.68	1	1.000	32.10	4.44E+05	0.014	0.001	0.292	0.292	0.818	0.1028	0.32	0.0770	0.117	0.0191
706	RunF083	MHL	Model 1	1	FV	20	1.66	1	1.000	72.31	4.38E+05	0.012	0.000	-0.906	-0.906	0.792	0.1012	0.30	0.0830	0.105	0.0170
707	RunF084	MHL	Model 1	1	FV	20	2.50	1.5	1.000	32.10	6.59E+05	0.019	0.000	-1.491	-1.491	0.559	0.0572	0.24	0.0443	0.069	0.0063
708	RunF085	MHL	Model 1	1	FV	20	3.32	2	1.000	18.08	8.76E+05	0.025	0.000	-2.068	-2.068	0.414	0.0293	0.18	0.0283	0.061	0.0035
709	RunF087	MHL	Model 1	1	FV	20	4.98	3	1.000	8.03	1.31E+06	0.048	0.000	0.990	0.990	0.316	0.0153	0.15	0.0132	0.058	0.0021
710	RunF089	MHL	Model 1	1	FV	25	1.66	1	1.000	72.31	4.39E+05	0.017	0.000	0.476	0.476	0.935	0.0995	0.46	0.0826	0.111	0.0171
711	RunF090	MHL	Model 1	1	FV	25	2.49	1.5	1.000	32.10	6.58E+05	0.026	0.000	0.587	0.587	0.639	0.0542	0.34	0.0445	0.074	0.0058
712	RunF094	MHL	Model 1	1	FV	25	2.49	1.5	1.000	32.10	6.57E+05	0.026	0.000	0.558	0.558	0.638	0.0467	0.34	0.0490	0.073	0.0068
713	RunF091	MHL	Model 1	1	FV	25	3.32	2	1.000	18.08	8.76E+05	0.034	0.000	0.712	0.712	0.482	0.0313	0.26	0.0283	0.070	0.0037
714	RunF092	MHL	Model 1	1	FV	25	4.15	2.5	1.000	11.56	1.10E+06	0.047	0.000	0.950	0.950	0.428	0.0219	0.24	0.0191	0.070	0.0030
715	RunF093	MHL	Model 1	1	FV	25	4.98	3	1.000	8.03	1.31E+06	0.062	0.000	1.285	1.285	0.396	0.0163	0.22	0.0136	0.070	0.0024
716	RunFC153	MHL	Model 1	1.5	FW	-12.5	5.09	2.5	1.000	7.71	1.35E+06	-0.101	0.001	-0.971	-0.971	-0.461	0.0309	0.13	0.0116	-0.123	0.0073
717	RunFC151	MHL	Model 1	1.5	FW	-10	2.03	1	1.000	48.20	5.39E+05	-0.012	0.000	-0.368	-0.368	-0.391	0.0417	0.08	0.0266	-0.095	0.0058
718	RunF001	MHL	Model 1	1.5	FW	-5	2.49	1.25	1.000	32.09	6.61E+05	-0.009	0.000	-0.277	-0.277	-0.190	0.0350	0.06	0.0297	-0.048	0.0048
719	RunF001A	MHL	Model 1	1.5	FW	-5	2.49	1.25	1.000	32.09	6.60E+05	-0.009	0.000	-0.275	-0.275	-0.193	0.0280	0.06	0.0280	-0.048	0.0051
720	RunF002	MHL	Model 1	1.5	FW	-5	3.32	1.75	1.000	18.07	8.79E+05	-0.016	0.000	-0.482	-0.482	-0.187	0.0222	0.06	0.0176	-0.050	0.0188
721	RunF003	MHL	Model 1	1.5	FW	-5	4.15	2	1.000	11.56	1.10E+06	-0.025	0.000	-0.711	-0.711	-0.189	0.0139	0.05	0.0120	-0.051	0.0030
722	RunF004	MHL	Model 1	1.5	FW	-5	4.98	2.5	1.000	8.03	1.32E+06	-0.036	0.000	-0.964	-0.964	-0.191	0.0100	0.04	0.0086	-0.052	0.0015

#	Run Name	Facility	Model	AR_h	Flow Regime	α, deg	Speed, m/s	Fn_h	Facility Pressure, bar	σ_v	Re_c	δ_{SC} at tip, m		θ at tip, deg		$C_{L,3D}$		$C_{D,3D}$		$C_{M,3D}$ (about 0.5c)	
												Mean	Std	Mean	Std	Mean	Std	Mean	Std	Mean	Std
723	RunFC152	MHL	Model 1	1.5	FW	-5	6.13	3	1.000	5.36	1.62E+06	-0.056	0.001	-1.244	-1.244	-0.187	0.0088	0.03	0.0073	-0.055	0.0019
724	RunF000	MHL	Model 1	1.5	FW	0	1.53	0.75	1.000	21.32	4.04E+05	0.000	0.000	0.011	0.011	0.004	0.0829	0.05	0.0640	0.003	0.0095
725	RunF005	MHL	Model 1	1.5	FW	0	2.49	1.25	1.000	32.09	6.60E+05	0.000	0.000	0.013	0.013	0.001	0.0305	0.04	0.0265	0.002	0.0044
726	RunF006	MHL	Model 1	1.5	FW	0	3.32	1.75	1.000	18.07	8.80E+05	0.000	0.000	0.013	0.013	0.000	0.0225	0.04	0.0175	-0.002	0.0156
727	RunF007	MHL	Model 1	1.5	FW	0	4.16	2	1.000	11.56	1.10E+06	0.000	0.000	0.009	0.009	-0.002	0.0112	0.03	0.0118	-0.002	0.0018
728	RunF008	MHL	Model 1	1.5	FW	0	4.98	2.5	1.000	8.03	1.32E+06	0.000	0.000	-0.001	-0.001	-0.002	0.0086	0.03	0.0085	-0.001	0.0009
729	RunF010	MHL	Model 1	1.5	FW	5	2.49	1.25	1.000	32.09	6.61E+05	0.009	0.000	0.285	0.285	0.203	0.0279	0.05	0.0258	0.054	0.0043
730	RunF041	MHL	Model 1	1.5	FW	5	3.06	1.5	1.000	21.40	8.07E+05	0.013	0.000	0.468	0.468	0.184	0.0201	0.04	0.0188	0.052	0.0086
731	RunF041A	MHL	Model 1	1.5	FW	5	3.05	1.5	1.000	21.40	8.07E+05	0.013	0.000	0.471	0.471	0.179	0.0263	0.04	0.0210	0.051	0.0097
732	RunF009A	MHL	Model 1	1.5	FW	5	3.32	1.75	1.000	18.07	8.81E+05	0.017	0.000	0.560	0.560	0.203	0.0205	0.04	0.0167	0.054	0.0167
733	RunF011	MHL	Model 1	1.5	FW	5	3.32	1.75	1.000	18.07	8.79E+05	0.017	0.000	0.654	0.654	0.198	0.0206	0.04	0.0173	0.056	0.0185
734	RunF009	MHL	Model 1	1.5	FW	5	3.32	1.75	1.000	18.07	8.80E+05	0.016	0.000	0.532	0.532	0.197	0.0205	0.04	0.0174	0.053	0.0170
735	RunF012A	MHL	Model 1	1.5	FW	5	4.15	2	1.000	11.56	1.10E+06	0.026	0.000	0.683	0.683	0.200	0.0124	0.04	0.0101	0.058	0.0042
736	RunF042	MHL	Model 1	1.5	FW	5	4.07	2	1.000	12.05	1.08E+06	0.024	0.000	0.700	0.700	0.188	0.0155	0.04	0.0136	0.055	0.0052
737	RunF043	MHL	Model 1	1.5	FW	5	5.07	2.5	1.000	7.71	1.34E+06	0.038	0.001	0.897	0.897	0.188	0.0101	0.03	0.0105	0.057	0.0015
738	RunF013	MHL	Model 1	1.5	FW	5	4.96	2.5	1.000	8.03	1.31E+06	0.038	0.000	0.825	0.825	0.204	0.0096	0.03	0.0071	0.060	0.0016
739	RunF015	MHL	Model 1	1.5	FW	10	2.49	1.25	1.000	32.09	6.60E+05	0.019	0.000	0.626	0.626	0.405	0.0356	0.08	0.0280	0.105	0.0037
740	RunF044	MHL	Model 1	1.5	FW	10	3.06	1.5	1.000	21.40	8.07E+05	0.027	0.000	0.736	0.736	0.374	0.0241	0.07	0.0212	0.104	0.0040
741	RunF016	MHL	Model 1	1.5	FW	10	3.32	1.75	1.000	18.07	8.81E+05	0.032	0.000	0.762	0.762	0.391	0.0186	0.08	0.0154	0.108	0.0050
742	RunF017	MHL	Model 1	1.5	FW	10	4.17	2	1.000	11.56	1.10E+06	0.052	0.000	1.134	1.134	0.395	0.0139	0.07	0.0101	0.112	0.0032
743	RunF045	MHL	Model 1	1.5	FW	10	4.07	2	1.000	12.05	1.08E+06	0.049	0.000	1.146	1.146	0.381	0.0135	0.07	0.0116	0.109	0.0037
744	RunF046	MHL	Model 1	1.5	FW	10	5.09	2.5	1.000	7.71	1.34E+06	0.079	0.001	2.329	2.329	0.393	0.0149	0.07	0.0076	0.113	0.0035
745	RunF018	MHL	Model 1	1.5	FW	10	4.96	2.5	1.000	8.03	1.32E+06	0.078	0.000	2.154	2.154	0.407	0.0104	0.07	0.0076	0.117	0.0019
746	RunF020	MHL	Model 1	1.5	FW	12.5	2.49	1.25	1.000	32.09	6.60E+05	0.024	0.000	0.670	0.670	0.509	0.0369	0.12	0.0273	0.122	0.0044
747	RunF024	MHL	Model 1	1.5	FW	12.5	3.05	1.5	1.000	21.40	8.08E+05	0.035	0.000	0.800	0.800	0.497	0.0244	0.11	0.0175	0.126	0.0050
748	RunF027	MHL	Model 1	1.5	FW	12.5	3.11	1.5	1.000	48.20	8.25E+05	0.036	0.000	0.790	0.790	0.473	0.0233	0.10	0.0201	0.124	0.0052
749	RunF021	MHL	Model 1	1.5	FW	12.5	3.32	1.75	1.000	18.07	8.81E+05	0.041	0.000	0.924	0.924	0.494	0.0195	0.11	0.0159	0.128	0.0059
750	RunF022	MHL	Model 1	1.5	FW	12.5	4.16	2	1.000	11.56	1.10E+06	0.067	0.000	1.672	1.672	0.502	0.0204	0.11	0.0110	0.129	0.0046
751	RunF025	MHL	Model 1	1.5	FW	12.5	4.07	2	1.000	12.05	1.08E+06	0.064	0.000	1.563	1.563	0.506	0.0184	0.12	0.0105	0.129	0.0046
752	RunF040	MHL	Model 1	1.5	FW	25	2.06	1	1.000	21.40	5.44E+05	0.031	0.001	0.622	0.622	0.890	0.0516	0.44	0.0391	0.081	0.0059
753	RunFC150	MHL	Model 1	1.5	PV	-15	2.03	1	1.000	48.20	5.39E+05	-0.021	0.000	-0.585	-0.585	-0.642	0.0548	0.20	0.0357	-0.105	0.0066
754	RunF010A	MHL	Model 1	1.5	PV	5	2.50	1.25	1.000	32.09	6.62E+05	0.010	0.000	0.204	0.204	0.210	0.0226	0.05	0.0244	0.051	0.0041
755	RunFC153	MHL	Model 1	1.5	FV	-12.5	5.09	2.5	1.000	7.71	1.35E+06	-0.055	0.000	-0.921	-0.921	-0.246	0.0174	0.09	0.0093	-0.047	0.0027
756	RunFC152	MHL	Model 1	1.5	FV	-5	5.99	3	1.000	5.36	1.59E+06	-0.028	0.000	-0.700	-0.700	-0.089	0.0071	0.02	0.0081	-0.019	0.0011
757	RunF014	MHL	Model 1	1.5	FV	5	3.28	1.5	1.000	18.07	8.70E+05	0.016	0.000	0.548	0.548	0.195	0.0214	0.04	0.0203	0.055	0.0168
758	RunF041A	MHL	Model 1	1.5	FV	5	3.05	1.5	1.000	21.40	8.06E+05	0.014	0.000	0.504	0.504	0.185	0.0228	0.04	0.0198	0.045	0.0052
759	RunF012A	MHL	Model 1	1.5	FV	5	4.15	2	1.000	11.56	1.10E+06	0.023	0.000	0.624	0.624	0.167	0.0127	0.04	0.0118	0.034	0.0025
760	RunF042A	MHL	Model 1	1.5	FV	5	4.07	2	1.000	12.05	1.08E+06	0.021	0.000	0.656	0.656	0.155	0.0131	0.04	0.0122	0.033	0.0032

#	Run Name	Facility	Model	AR_h	Flow Regime	α, deg	Speed, m/s	Fn_h	Facility Pressure, bar	σ_v	Re_c	δ_{SC} at tip, m		θ at tip, deg		$C_{L,3D}$		$C_{D,3D}$		$C_{M,3D}$ (about 0.5c)	
												Mean	Std	Mean	Std	Mean	Std	Mean	Std	Mean	Std
761	RunF043	MHL	Model 1	1.5	FV	5	5.09	2.5	1.000	7.71	1.34E+06	0.026	0.000	0.643	0.643	0.118	0.0093	0.03	0.0080	0.024	0.0012
762	RunF013	MHL	Model 1	1.5	FV	5	4.98	2.5	1.000	8.03	1.32E+06	0.027	0.000	0.604	0.604	0.132	0.0099	0.03	0.0097	0.026	0.0013
763	RunF015	MHL	Model 1	1.5	FV	10	2.49	1.25	1.000	32.09	6.60E+05	0.019	0.000	0.631	0.631	0.406	0.0270	0.08	0.0232	0.105	0.0038
764	RunF044	MHL	Model 1	1.5	FV	10	3.05	1.5	1.000	21.40	8.07E+05	0.027	0.000	0.707	0.707	0.356	0.0223	0.09	0.0197	0.066	0.0063
765	RunF016	MHL	Model 1	1.5	FV	10	3.32	1.75	1.000	18.07	8.80E+05	0.030	0.000	0.683	0.683	0.346	0.0222	0.09	0.0182	0.060	0.0085
766	RunF017	MHL	Model 1	1.5	FV	10	4.16	2	1.000	11.56	1.10E+06	0.038	0.000	0.704	0.704	0.273	0.0141	0.08	0.0115	0.048	0.0019
767	RunF045	MHL	Model 1	1.5	FV	10	4.07	2	1.000	12.05	1.07E+06	0.037	0.000	0.765	0.765	0.271	0.0144	0.07	0.0128	0.048	0.0021
768	RunF046	MHL	Model 1	1.5	FV	10	5.10	2.5	1.000	7.71	1.35E+06	0.045	0.000	0.947	0.947	0.211	0.0118	0.06	0.0090	0.041	0.0016
769	RunF018	MHL	Model 1	1.5	FV	10	4.99	2.5	1.000	8.03	1.32E+06	0.046	0.000	0.901	0.901	0.222	0.0124	0.06	0.0087	0.042	0.0016
770	RunF023	MHL	Model 1	1.5	FV	12.5	2.04	1	1.000	48.20	5.39E+05	0.018	0.000	0.571	0.571	0.571	0.0429	0.14	0.0321	0.105	0.0052
771	RunF020	MHL	Model 1	1.5	FV	12.5	2.49	1.25	1.000	32.09	6.60E+05	0.025	0.000	0.679	0.679	0.512	0.0275	0.14	0.0225	0.092	0.0066
772	RunF024	MHL	Model 1	1.5	FV	12.5	3.05	1.5	1.000	21.40	8.09E+05	0.033	0.000	0.729	0.729	0.446	0.0240	0.13	0.0198	0.071	0.0052
773	RunF021	MHL	Model 1	1.5	FV	12.5	3.32	1.75	1.000	18.07	8.80E+05	0.036	0.000	0.758	0.758	0.409	0.0228	0.12	0.0171	0.066	0.0046
774	RunF022	MHL	Model 1	1.5	FV	12.5	4.15	2	1.000	11.56	1.10E+06	0.046	0.000	0.896	0.896	0.326	0.0171	0.10	0.0115	0.055	0.0021
775	RunF025	MHL	Model 1	1.5	FV	12.5	4.07	2	1.000	12.05	1.08E+06	0.045	0.000	0.870	0.870	0.337	0.0184	0.11	0.0124	0.055	0.0022
776	RunF026	MHL	Model 1	1.5	FV	15	2.04	1	1.000	48.20	5.39E+05	0.022	0.000	0.613	0.613	0.674	0.0469	0.19	0.0331	0.107	0.0053
777	RunF028	MHL	Model 1	1.5	FV	15	2.03	1	1.000	48.21	5.36E+05	0.021	0.000	0.607	0.607	0.661	0.0473	0.18	0.0359	0.109	0.0052
778	RunF032	MHL	Model 1	1.5	FV	15	3.06	1.5	1.000	21.40	8.07E+05	0.037	0.000	0.736	0.736	0.474	0.0261	0.17	0.0235	0.071	0.0051
779	RunF029	MHL	Model 1	1.5	FV	15	3.05	1.5	1.000	21.40	8.06E+05	0.037	0.000	0.757	0.757	0.481	0.0213	0.16	0.0201	0.073	0.0045
780	RunF030	MHL	Model 1	1.5	FV	15	4.07	2	1.000	12.05	1.08E+06	0.049	0.000	1.007	1.007	0.357	0.0166	0.13	0.0123	0.059	0.0021
781	RunF031	MHL	Model 1	1.5	FV	15	5.09	2.5	1.000	7.71	1.34E+06	0.060	0.000	1.374	1.374	0.285	0.0126	0.11	0.0082	0.055	0.0018
782	RunF034	MHL	Model 1	1.5	FV	20	3.05	1.5	1.000	21.40	8.06E+05	0.046	0.000	0.902	0.902	0.588	0.0257	0.26	0.0204	0.079	0.0035
783	RunF036	MHL	Model 1	1.5	FV	20	3.05	1.5	1.000	21.40	8.07E+05	0.045	0.001	0.830	0.830	0.579	0.0274	0.26	0.0248	0.079	0.0042
784	RunF037	MHL	Model 1	1.5	FV	25	2.04	1	1.000	48.21	5.38E+05	0.028	0.001	0.593	0.593	0.840	0.0546	0.42	0.0365	0.075	0.0056
785	RunF038	MHL	Model 1	1.5	FV	25	3.06	1.5	1.000	21.40	8.09E+05	0.052	0.000	1.027	1.027	0.643	0.0232	0.35	0.0199	0.085	0.0032
786	RunF040	MHL	Model 1	1.5	FV	25	3.08	1.5	1.000	21.40	8.13E+05	0.052	0.001	0.971	0.971	0.627	0.0291	0.34	0.0246	0.083	0.0040
787	RunF039	MHL	Model 1	1.5	FV	25	4.07	2	1.000	12.05	1.08E+06	0.071	0.001	1.710	1.710	0.501	0.0202	0.28	0.0140	0.081	0.0025
788	RunS046	MHL	Model 2	1	FW	0	2.47	1.5	1.000	11.55	6.67E+05	0.000	0.000	0.011	0.011	0.008	0.0493	0.04	0.0440	0.007	0.0211
789	RunS047	MHL	Model 2	1	FW	5	3.32	2	1.000	18.06	8.96E+05	0.007	0.000	0.204	0.204	0.143	0.0300	0.03	0.0242	0.042	0.0139
790	RunS048	MHL	Model 2	1	FW	5	4.15	2.5	1.000	11.55	1.12E+06	0.010	0.000	0.337	0.337	0.145	0.0193	0.03	0.0124	0.045	0.0067
791	RunS049	MHL	Model 2	1	FW	5	4.98	3	1.000	8.02	1.34E+06	0.015	0.000	0.547	0.547	0.149	0.0196	0.02	0.0129	0.046	0.0067
792	RunS051	MHL	Model 2	1	FW	10	3.32	2	1.000	18.06	8.96E+05	0.013	0.000	0.453	0.453	0.293	0.0344	0.06	0.0272	0.082	0.0144
793	RunS052	MHL	Model 2	1	FW	10	4.16	2.5	1.000	11.55	1.12E+06	0.020	0.000	0.738	0.738	0.287	0.0246	0.05	0.0201	0.084	0.0116
794	RunS053	MHL	Model 2	1	FW	10	4.98	3	1.000	8.02	1.34E+06	0.029	0.000	1.010	1.010	0.289	0.0184	0.05	0.0134	0.086	0.0077
795	RunS055	MHL	Model 2	1	FW	12.5	2.48	1.5	1.000	18.06	6.68E+05	0.010	0.000	0.284	0.284	0.373	0.0285	0.13	0.0206	0.103	0.0089
796	RunS056	MHL	Model 2	1	FW	12.5	4.15	2.5	1.000	11.55	1.12E+06	0.025	0.000	0.821	0.821	0.365	0.0250	0.08	0.0201	0.100	0.0105
797	RunS056A	MHL	Model 2	1	FW	12.5	4.16	2.5	1.000	11.55	1.12E+06	0.025	0.000	0.827	0.827	0.361	0.0207	0.08	0.0168	0.100	0.0087
798	RunS057	MHL	Model 2	1	FW	12.5	4.96	3	1.000	8.02	1.34E+06	0.036	0.000	1.071	1.071	0.365	0.0191	0.08	0.0147	0.102	0.0082

#	Run Name	Facility	Model	AR_h	Flow Regime	α, deg	Speed, m/s	Fn_h	Facility Pressure, bar	σ_v	Re_c	δ_{SC} at tip, m		θ at tip, deg		$C_{L,3D}$		$C_{D,3D}$		$C_{M,3D}$ (about 0.5c)	
												Mean	Std	Mean	Std	Mean	Std	Mean	Std	Mean	Std
799	RunS061	MHL	Model 2	1	FW	15	2.49	1.5	1.000	8.02	6.73E+05	0.012	0.000	0.367	0.367	0.460	0.0365	0.16	0.1118	0.116	0.0432
800	RunS050	MHL	Model 2	1	PV	5	1.67	1	1.000	18.06	4.52E+05	0.002	0.000	0.049	0.049	0.214	0.0983	0.04	0.0958	0.035	0.0442
801	RunS047	MHL	Model 2	1	FV	5	3.32	2	1.000	18.06	8.95E+05	0.006	0.000	0.169	0.169	0.137	0.0312	0.04	0.0267	0.028	0.0157
802	RunS050	MHL	Model 2	1	FV	5	3.28	2	1.000	18.06	8.85E+05	0.006	0.000	0.183	0.183	0.143	0.0342	0.04	0.0303	0.030	0.0177
803	RunS048	MHL	Model 2	1	FV	5	4.15	2.5	1.000	11.55	1.12E+06	0.008	0.000	0.216	0.216	0.114	0.0201	0.03	0.0170	0.021	0.0095
804	RunS049A	MHL	Model 2	1	FV	5	4.98	3	1.000	8.02	1.34E+06	0.009	0.000	0.262	0.262	0.088	0.0153	0.03	0.0098	0.017	0.0051
805	RunS051	MHL	Model 2	1	FV	10	3.32	2	1.000	18.06	8.95E+05	0.011	0.000	0.331	0.331	0.255	0.0335	0.07	0.0281	0.039	0.0164
806	RunS052	MHL	Model 2	1	FV	10	4.15	2.5	1.000	11.55	1.12E+06	0.014	0.000	0.408	0.408	0.198	0.0240	0.06	0.0203	0.031	0.0114
807	RunS053	MHL	Model 2	1	FV	10	4.98	3	1.000	8.02	1.34E+06	0.016	0.000	0.525	0.525	0.160	0.0206	0.05	0.0137	0.029	0.0073
808	RunS058	MHL	Model 2	1	FV	12.5	2.51	1.5	1.000	18.06	6.77E+05	0.010	0.000	0.253	0.253	0.387	0.0520	0.12	0.0437	0.055	0.0256
809	RunS055	MHL	Model 2	1	FV	12.5	3.32	2	1.000	18.06	8.95E+05	0.014	0.000	0.351	0.351	0.295	0.0333	0.09	0.0276	0.040	0.0156
810	RunS056A	MHL	Model 2	1	FV	12.5	4.15	2.5	1.000	11.55	1.12E+06	0.017	0.000	0.504	0.504	0.237	0.0242	0.08	0.0211	0.037	0.0119
811	RunS057	MHL	Model 2	1	FV	12.5	4.98	3	1.000	8.02	1.34E+06	0.021	0.000	0.601	0.601	0.202	0.0212	0.07	0.0144	0.036	0.0081
812	RunS062	MHL	Model 2	1	FV	15	2.55	1.5	1.000	18.06	6.88E+05	0.012	0.000	0.327	0.327	0.448	0.0422	0.14	0.0370	0.055	0.0235
813	RunS061	MHL	Model 2	1	FV	15	2.51	1.5	1.000	8.02	6.78E+05	0.013	0.000	0.320	0.320	0.482	0.0483	0.13	0.0490	0.052	0.0299
814	RunS059	MHL	Model 2	1	FV	15	3.29	2	1.000	18.06	8.87E+05	0.016	0.000	0.352	0.352	0.344	0.0362	0.12	0.0289	0.044	0.0156
815	RunS060	MHL	Model 2	1	FV	15	4.15	2.5	1.000	11.55	1.12E+06	0.020	0.000	0.574	0.574	0.277	0.0241	0.10	0.0204	0.042	0.0114
816	RunS065	MHL	Model 2	1	FV	17.5	2.56	1.5	1.000	18.06	6.90E+05	0.014	0.000	0.397	0.397	0.514	0.0402	0.19	0.0389	0.053	0.0239
817	RunS063	MHL	Model 2	1	FV	17.5	3.32	2	1.000	18.06	8.96E+05	0.018	0.000	0.485	0.485	0.383	0.0365	0.15	0.0322	0.048	0.0178
818	RunS064	MHL	Model 2	1	FV	17.5	4.15	2.5	1.000	11.55	1.12E+06	0.023	0.000	0.633	0.633	0.318	0.0241	0.13	0.0198	0.048	0.0116
819	RunS066	MHL	Model 2	1	FV	20	2.49	1.5	1.000	18.06	6.70E+05	0.015	0.000	0.421	0.421	0.576	0.0484	0.24	0.0441	0.053	0.0229
											1.34E+05										
820	RunA00_U1P3_FW_AL_S_OFF_006	INSEAN	Model 0	1	FW	2	1.30	0.75	1.086	117.27	3.39E+05	0.000	0.000	0.000	0.000	0.071	0.0932	-0.18	0.0149	-0.051	0.0151
821	RunA00_U2P5_FW_AL_S_OFF_002	INSEAN	Model 0	1	FW	2	2.50	1.5	1.086	31.73	6.46E+05	0.000	0.000	0.000	0.000	0.047	0.0312	-0.02	0.0330	-0.004	0.0166
822	RunA00_U4P2_FW_AL_S_OFF_004	INSEAN	Model 0	1	FW	2	4.20	2.5	1.087	11.25	1.06E+06	0.000	0.000	0.000	0.000	0.048	0.0312	0.01	0.0266	0.008	0.0107
823	RunA05_U0P0_FW_AL_S_OFF_029	INSEAN	Model 0	1	FW	7	0.00	0	1.096	Inf	0.00E+00	0.000	0.000	0.000	0.000	NaN	NaN	NaN	NaN	NaN	NaN
824	RunA05_U1P0_FW_AL_S_OFF_030	INSEAN	Model 0	1	FW	7	1.00	0.5	1.096	198.16	2.62E+05	0.000	0.000	0.000	0.000	0.331	0.0609	0.09	0.0477	0.061	0.0332
825	RunA05_U2P5_FW_AL_S_OFF_032	INSEAN	Model 0	1	FW	7	2.50	1.5	1.096	31.71	6.54E+05	0.000	0.000	0.000	0.000	0.216	0.0557	0.06	0.0206	0.050	0.0101
826	RunA05_U3P0_FWFV_AL_S_OFF_P200_051	INSEAN	Model 0	1	FW	7	3.00	1.75	0.199	4.03	7.95E+05	0.000	0.000	0.000	0.000	0.205	0.0279	0.04	0.0215	0.051	0.0081
827	RunA05_U3P0_FWFV_AL_S_OFF_P150_052	INSEAN	Model 0	1	FW	7	3.00	1.75	0.152	2.91	7.95E+05	0.000	0.000	0.000	0.000	0.209	0.0289	0.04	0.0196	0.051	0.0084
828	RunA05_U3P0_FWPC_AL_S_OFF_P100_055	INSEAN	Model 0	1	FW	7	3.00	1.75	0.086	1.78	7.95E+05	0.000	0.000	0.000	0.000	0.197	0.0351	0.03	0.0201	0.048	0.0097
829	RunA05_U3P5_FW_AL_S_OFF_P250_043	INSEAN	Model 0	1	FW	7	3.50	2	0.250	3.79	9.27E+05	0.000	0.000	0.000	0.000	0.187	0.0227	0.05	0.0075	0.052	0.0063

#	Run Name	Facility	Model	AR_h	Flow Regime	α, deg	Speed, m/s	Fn_h	Facility Pressure, bar	σ_v	Re_c	δ_{SC} at tip, m		θ at tip, deg		$C_{L,3D}$		$C_{D,3D}$		$C_{M,3D}$ (about 0.5c)	
												Mean	Std	Mean	Std	Mean	Std	Mean	Std	Mean	Std
830	RunA05_U4P2_FWFV_AL_S_OFF_036	INSEAN	Model 0	1	FW	7	4.20	2.5	1.097	11.23	1.10E+06	0.000	0.000	0.000	0.000	0.181	0.0207	0.04	0.0205	0.051	0.0072
831	RunA05_U4P2_FW_AL_S_OFF_034	INSEAN	Model 0	1	FW	7	4.20	2.5	1.097	11.23	1.10E+06	0.000	0.000	0.000	0.000	0.165	0.0268	0.04	0.0150	0.047	0.0076
832	RunA05_U4P2_FW_AL_S_OFF_P250_044	INSEAN	Model 0	1	FW	7	4.20	2.5	0.250	2.63	1.11E+06	0.000	0.000	0.000	0.000	0.207	0.0259	0.05	0.0310	0.057	0.0104
833	RunA05_U4P2_FW_AL_S_OFF_P200_045	INSEAN	Model 0	1	FW	7	4.20	2.5	0.201	2.06	1.11E+06	0.000	0.000	0.000	0.000	0.208	0.0279	0.04	0.0289	0.057	0.0104
834	RunA10_U0P0_FW_AL_S_OFF_025	INSEAN	Model 0	1	FW	12	0.00	0	1.097	Inf	0.00E+00	0.000	0.000	0.000	0.000	NaN	NaN	NaN	NaN	NaN	NaN
835	RunA10_U1P0_FW_AL_S_OFF_027	INSEAN	Model 0	1	FW	12	1.00	0.5	1.097	198.16	2.62E+05	0.000	0.000	0.000	0.000	0.632	0.0501	0.14	0.0325	0.103	0.0198
836	RunA10_U1P5_FW_AL_S_OFF_P050_088	INSEAN	Model 0	1	FW	12	1.50	1	0.051	2.22	4.02E+05	0.000	0.000	0.000	0.000	0.600	0.0762	0.12	0.0193	0.084	0.0104
837	RunA10_U2P0_FW_AL_S_OFF_P045_089	INSEAN	Model 0	1	FW	12	2.00	1.25	0.050	1.20	5.36E+05	0.000	0.000	0.000	0.000	0.424	0.0424	0.09	0.0152	0.076	0.0079
838	RunA10_U2P0US_PC_AL_S_OFF_P045_090	INSEAN	Model 0	1	FW	12	2.00	1.25	0.050	1.15	5.36E+05	0.000	0.000	0.000	0.000	0.466	0.0412	0.10	0.0149	0.088	0.0096
839	RunA10_U2P5_FW_AL_S_OFF_009	INSEAN	Model 0	1	FW	12	2.50	1.5	1.086	31.71	6.52E+05	0.000	0.000	0.000	0.000	0.437	0.0293	0.05	0.0322	0.050	0.0109
840	RunA10_U3P0_FW_AL_S_OFF_P250_076	INSEAN	Model 0	1	FW	12	3.00	1.75	0.250	5.14	8.03E+05	0.000	0.000	0.000	0.000	0.324	0.0376	0.08	0.0503	0.083	0.0127
841	RunA10_U3P3_FW_AL_S_OFF_P250_077	INSEAN	Model 0	1	FW	12	3.30	2	0.249	4.25	8.83E+05	0.000	0.000	0.000	0.000	0.337	0.0276	0.08	0.0284	0.089	0.0094
842	RunA10_U3P3_FW_AL_S_OFF_P200_082	INSEAN	Model 0	1	FW	12	3.30	2	0.200	3.32	8.85E+05	0.000	0.000	0.000	0.000	0.332	0.0309	0.09	0.0413	0.088	0.0112
843	RunA10_U3P3_FW_AL_S_OFF_P200US_083	INSEAN	Model 0	1	FW	12	3.30	2	0.170	3.32	8.85E+05	0.000	0.000	0.000	0.000	0.330	0.0314	0.08	0.0423	0.087	0.0114
844	RunA10_U3P3_FW_AL_S_OFF_P150_084	INSEAN	Model 0	1	FW	12	3.30	2	0.152	2.39	8.83E+05	0.000	0.000	0.000	0.000	0.331	0.0271	0.08	0.0434	0.087	0.0111
845	RunA10_U3P3_FW_AL_S_OFF_P150US_085	INSEAN	Model 0	1	FW	12	3.30	2	0.143	2.39	8.83E+05	0.000	0.000	0.000	0.000	0.345	0.0313	0.09	0.0417	0.090	0.0113
846	RunA10_U4P2_FW_AL_S_OFF_011	INSEAN	Model 0	1	FW	12	4.20	2.5	1.086	11.23	1.10E+06	0.000	0.000	0.000	0.000	0.396	0.0303	0.08	0.0259	0.087	0.0121
847	RunA10_U4P2_FW_AL_S_OFF_P250_079	INSEAN	Model 0	1	FW	12	4.20	2.5	0.249	2.62	1.12E+06	0.000	0.000	0.000	0.000	0.331	0.0260	0.08	0.0158	0.091	0.0077
848	RunA05_U2P5_FWPV_AL_S_OFF_039	INSEAN	Model 0	1	PV	7	2.50	1.5	1.096	31.71	6.54E+05	0.000	0.000	0.000	0.000	0.235	0.0482	0.08	0.0199	0.046	0.0083
849	RunA10_U1P0_FWPV_AL_S_OFF_P050_087	INSEAN	Model 0	1	PV	12	1.00	0.5	0.054	5.59	2.68E+05	0.000	0.000	0.000	0.000	0.809	0.0289	0.10	0.0136	0.100	0.0116
850	RunA15_U1P0_PV_AL_S_OFF_017	INSEAN	Model 0	1	PV	17	1.00	0.5	1.097	198.13	2.62E+05	0.000	0.000	0.000	0.000	0.288	0.0770	0.32	0.0325	0.062	0.0166
851	RunA15_U1P5_PV_AL_S_OFF_018	INSEAN	Model 0	1	PV	17	1.50	1	1.096	88.07	3.92E+05	0.000	0.000	0.000	0.000	0.530	0.0818	0.27	0.0309	0.079	0.0117
852	RunA05_U3P0_FWFV_AL_S_OFF_P200_051	INSEAN	Model 0	1	FV	7	3.00	1.75	0.198	4.03	7.95E+05	0.000	0.000	0.000	0.000	0.207	0.0371	0.05	0.0216	0.037	0.0071

#	Run Name	Facility	Model	AR_h	Flow Regime	α, deg	Speed, m/s	Fn_h	Facility Pressure, bar	σ_v	Re_c	δ_{SC} at tip, m		θ at tip, deg		$C_{L,3D}$		$C_{D,3D}$		$C_{M,3D}$ (about 0.5c)	
												Mean	Std	Mean	Std	Mean	Std	Mean	Std	Mean	Std
853	RunA05_U3P0_FWFV_AL_S_OFF_P150_052	INSEAN	Model 0	1	FV	7	3.00	1.75	0.152	2.91	7.95E+05	0.000	0.000	0.000	0.000	0.218	0.0283	0.05	0.0203	0.037	0.0060
854	RunA05_U3P5_FV_AL_S_OFF_P200_049	INSEAN	Model 0	1	FV	7	3.50	2	0.202	2.96	9.27E+05	0.000	0.000	0.000	0.000	0.192	0.0206	0.05	0.0104	0.031	0.0094
855	RunA05_U3P5_FV_AL_S_OFF_P44_071	INSEAN	Model 0	1	FV	7	3.50	2	0.048	0.39	9.27E+05	0.000	0.000	0.000	0.000	0.191	0.0179	0.04	0.0096	0.029	0.0093
856	RunA05_U4P2_FWFV_AL_S_OFF_036	INSEAN	Model 0	1	FV	7	4.20	2.5	1.097	11.23	1.10E+06	0.000	0.000	0.000	0.000	0.142	0.0160	0.05	0.0214	0.022	0.0061
857	RunA05_U4P2_FV_AL_S_OFF_P150_047	INSEAN	Model 0	1	FV	7	4.20	2.5	0.152	1.48	1.11E+06	0.000	0.000	0.000	0.000	0.163	0.0149	0.05	0.0411	0.025	0.0106
858	RunA05_U4P2_FW_AL_S_OFF_P150_046	INSEAN	Model 0	1	FV	7	4.20	2.5	0.149	1.48	1.11E+06	0.000	0.000	0.000	0.000	0.161	0.0136	0.04	0.0301	0.024	0.0080
859	RunA10_U2P5_FV_AL_S_OFF_015	INSEAN	Model 0	1	FV	12	2.50	1.5	1.087	31.71	6.54E+05	0.000	0.000	0.000	0.000	0.467	0.0274	0.09	0.0313	0.025	0.0102
860	RunA10_U2P9_FV_AL_S_OFF_P044_105	INSEAN	Model 0	1	FV	12	2.90	1.75	0.049	0.54	7.78E+05	0.000	0.000	0.000	0.000	0.302	0.0326	0.09	0.0183	0.040	0.0055
861	RunA10_U3P3_FV_AL_S_OFF_P132_086	INSEAN	Model 0	1	FV	12	3.30	2	0.135	2.06	8.83E+05	0.000	0.000	0.000	0.000	0.306	0.0179	0.10	0.0321	0.043	0.0078
862	RunA10_U3P3_FV_AL_S_OFF_P044_108	INSEAN	Model 0	1	FV	12	3.30	2	0.049	0.42	8.85E+05	0.000	0.000	0.000	0.000	0.318	0.0209	0.10	0.0126	0.043	0.0048
863	RunA10_U4P2_FV_AL_S_OFF_013	INSEAN	Model 0	1	FV	12	4.20	2.5	1.087	11.23	1.10E+06	0.000	0.000	0.000	0.000	0.273	0.0254	0.08	0.0272	0.024	0.0115
864	RunA10_U4P2_FV_AL_S_OFF_P250_080	INSEAN	Model 0	1	FV	12	4.20	2.5	0.250	2.62	1.12E+06	0.000	0.000	0.000	0.000	0.227	0.0155	0.08	0.0152	0.034	0.0053
865	RunA10_U4P2_FV_AL_S_OFF_P044_109	INSEAN	Model 0	1	FV	12	4.20	2.5	0.052	0.26	1.13E+06	0.000	0.000	0.000	0.000	0.236	0.0176	0.08	0.0480	0.034	0.0132
866	RunA15_U2P0_FV_AL_S_OFF_019	INSEAN	Model 0	1	FV	17	2.00	1.25	1.096	49.54	5.23E+05	0.000	0.000	0.000	0.000	0.495	0.0725	0.23	0.0283	0.065	0.0082
867	RunA15_U4P0_FV_AL_S_OFF_021	INSEAN	Model 0	1	FV	17	4.00	2.5	1.096	12.39	1.05E+06	0.000	0.000	0.000	0.000	0.295	0.0263	0.14	0.0227	0.041	0.0096
868	RunA05_U3P0_FWPC_AL_S_OFF_P70_056	INSEAN	Model 0	1	PC	7	3.00	1.75	0.075	1.11	7.95E+05	0.000	0.000	0.000	0.000	0.207	0.0352	0.04	0.0196	0.051	0.0098
869	RunA05_U3P0_PC_AL_S_OFF_P68_059	INSEAN	Model 0	1	PC	7	3.00	1.75	0.064	1.06	7.95E+05	0.000	0.000	0.000	0.000	0.197	0.0351	0.03	0.0197	0.048	0.0098
870	RunA05_U3P0_PC_AL_S_OFF_P50_060	INSEAN	Model 0	1	PC	7	3.00	1.75	0.055	0.66	7.95E+05	0.000	0.000	0.000	0.000	0.198	0.0358	0.03	0.0191	0.048	0.0098
871	RunA05_U3P0_PC_AL_S_OFF_P50_061	INSEAN	Model 0	1	PC	7	3.00	1.75	0.052	0.66	7.95E+05	0.000	0.000	0.000	0.000	0.200	0.0351	0.03	0.0190	0.048	0.0097
872	RunA05_U3P1_PC_AL_S_OFF_P45_063	INSEAN	Model 0	1	PC	7	3.10	1.75	0.049	0.51	8.21E+05	0.000	0.000	0.000	0.000	0.208	0.0285	0.03	0.0188	0.052	0.0098
873	RunA05_U3P4_PC_AL_S_OFF_P44_068	INSEAN	Model 0	1	PC	7	3.40	2	0.048	0.41	9.01E+05	0.000	0.000	0.000	0.000	0.210	0.0266	0.03	0.0106	0.055	0.0094
874	RunA05_U3P5_PC_AL_S_OFF_P43_072	INSEAN	Model 0	1	PC	7	3.50	2	0.048	0.37	9.27E+05	0.000	0.000	0.000	0.000	0.197	0.0301	0.03	0.0099	0.053	0.0093
875	RunA05_U4P2_FW_AL_S_OFF_P150_046	INSEAN	Model 0	1	PC	7	4.20	2.5	0.151	1.48	1.11E+06	0.000	0.000	0.000	0.000	0.204	0.0254	0.04	0.0337	0.055	0.0107

#	Run Name	Facility	Model	AR_h	Flow Regime	α, deg	Speed, m/s	Fn_h	Facility Pressure, bar	σ_v	Re_c	δ_{SC} at tip, m		θ at tip, deg		$C_{L,3D}$		$C_{D,3D}$		$C_{M,3D}$ (about 0.5c)	
												Mean	Std	Mean	Std	Mean	Std	Mean	Std	Mean	Std
876	RunA10_U2P2_PC_AL_S_OFF_P044_091	INSEAN	Model 0	1	PC	12	2.20	1.25	0.050	0.95	5.90E+05	0.000	0.000	0.000	0.000	0.406	0.0323	0.09	0.0125	0.081	0.0081
877	RunA10_U2P2US_PC_AL_S_OFF_P044_092	INSEAN	Model 0	1	PC	12	2.20	1.25	0.049	0.95	5.90E+05	0.000	0.000	0.000	0.000	0.434	0.0368	0.10	0.0160	0.089	0.0102
878	RunA10_U2P3_PC_AL_S_OFF_P044_093	INSEAN	Model 0	1	PC	12	2.30	1.5	0.049	0.87	6.17E+05	0.000	0.000	0.000	0.000	0.415	0.0327	0.09	0.0152	0.085	0.0098
879	RunA10_U2P4_PC_AL_S_OFF_P044_095	INSEAN	Model 0	1	PC	12	2.40	1.5	0.049	0.80	6.44E+05	0.000	0.000	0.000	0.000	0.401	0.0405	0.09	0.0137	0.085	0.0103
880	RunA10_U2P5_PC_AL_S_OFF_P044_097	INSEAN	Model 0	1	PC	12	2.50	1.5	0.049	0.73	6.71E+05	0.000	0.000	0.000	0.000	0.384	0.0448	0.09	0.0152	0.084	0.0099
881	RunA10_U2P6_PC_AL_S_OFF_P044_099	INSEAN	Model 0	1	PC	12	2.60	1.5	0.049	0.68	6.97E+05	0.000	0.000	0.000	0.000	0.382	0.0469	0.09	0.0201	0.087	0.0100
882	RunA10_U2P7_PC_AL_S_OFF_P044_101	INSEAN	Model 0	1	PC	12	2.70	1.75	0.049	0.63	7.24E+05	0.000	0.000	0.000	0.000	0.386	0.0354	0.09	0.0183	0.090	0.0087
883	RunA10_U2P8_PC_AL_S_OFF_P044_103	INSEAN	Model 0	1	PC	12	2.80	1.75	0.044	0.58	7.51E+05	0.000	0.000	0.000	0.000	0.396	0.0342	0.09	0.0173	0.093	0.0089
884	RunAN05_U1P6_FW_PVC_S_OFF_P1000_135	INSEAN	Model 2	1	FW	-3	1.60	1	0.970	77.05	4.53E+05	-0.001	0.000	-0.037	-0.037	0.075	0.0349	-0.06	0.0101	0.054	0.0067
885	RunAN05_U2P5_FW_PVC_S_OFF_P1000_136	INSEAN	Model 2	1	FW	-3	2.50	1.5	0.970	31.56	7.08E+05	-0.003	0.001	0.043	0.043	-0.016	0.0286	-0.01	0.0236	0.002	0.0069
886	RunAN05_U3P3_FW_PVC_S_OFF_P1000_137	INSEAN	Model 2	1	FW	-3	3.30	2	0.971	18.11	9.34E+05	-0.006	0.001	0.279	0.279	-0.076	0.0297	0.01	0.0308	-0.020	0.0117
887	RunAN05_U4P2_FW_PVC_S_OFF_P1000_138	INSEAN	Model 2	1	FW	-3	4.20	2.5	0.971	11.18	1.19E+06	-0.008	0.002	0.290	0.290	-0.059	0.0250	0.01	0.0160	-0.018	0.0085
888	RunA00_U0P5_FW_PVC_S_OFF_P1000_006	INSEAN	Model 2	1	FW	2	0.50	0.25	0.970	791.55	1.34E+05	0.000	0.000	0.008	0.008	0.156	0.1275	-0.02	0.0286	0.012	0.0225
889	RunA00_U1P6_FW_PVC_S_OFF_P1000_008	INSEAN	Model 2	1	FW	2	1.60	1	0.971	77.30	4.29E+05	0.000	0.000	0.003	0.003	0.067	0.0329	-0.01	0.0161	0.004	0.0061
890	RunA00_U2P5_FW_PVC_S_OFF_P1000_011	INSEAN	Model 2	1	FW	2	2.50	1.5	0.971	31.66	6.71E+05	0.001	0.001	-0.005	-0.005	0.052	0.0350	0.01	0.0216	0.009	0.0080
891	RunA00_U3P5_FW_PVC_S_OFF_P1000_019	INSEAN	Model 2	1	FW	2	3.50	2	0.971	16.15	9.39E+05	0.002	0.001	-0.026	-0.026	0.036	0.0217	0.02	0.0264	0.008	0.0113
892	RunA00_U3P3_FW_PVC_S_OFF_P1000_013	INSEAN	Model 2	1	FW	2	3.30	2	0.971	18.17	8.85E+05	0.003	0.001	-0.001	-0.001	0.053	0.0277	0.02	0.0420	0.013	0.0104
893	RunA00_U4P2_FW_PVC_S_OFF_P1000_130	INSEAN	Model 2	1	FW	2	4.20	2.5	0.971	11.18	1.19E+06	0.003	0.002	-0.036	-0.036	0.038	0.0251	0.02	0.0151	0.012	0.0086
894	RunA05_U1P6_FW_PVC_S_OFF_P1000_021	INSEAN	Model 2	1	FW	7	1.60	1	0.970	77.25	4.35E+05	0.002	0.000	0.028	0.028	0.531	0.0377	-0.02	0.0110	0.091	0.0072
895	RunA05_U1P6_FW_PVC_S_OFF_P050_046	INSEAN	Model 2	1	FW	7	1.60	1	0.052	2.18	4.38E+05	0.003	0.000	0.133	0.133	0.273	0.0343	0.07	0.0119	0.050	0.0066
896	RunA05_U1P6_FW_PVC_S_OFF_P045_048	INSEAN	Model 2	1	FW	7	1.60	1	0.047	1.79	4.38E+05	0.003	0.000	0.215	0.215	0.293	0.0354	0.04	0.0118	0.048	0.0067

#	Run Name	Facility	Model	AR_h	Flow Regime	α, deg	Speed, m/s	Fn_h	Facility Pressure, bar	σ_v	Re_c	δ_{SC} at tip, m		θ at tip, deg		$C_{L,3D}$		$C_{D,3D}$		$C_{M,3D}$ (about 0.5c)	
												Mean	Std	Mean	Std	Mean	Std	Mean	Std	Mean	Std
897	RunA05_U2P5_FW_PVC_S_OFF_P1000_026	INSEAN	Model 2	1	FW	7	2.50	1.5	0.970	31.64	6.79E+05	0.006	0.001	-0.013	-0.013	0.214	0.0299	0.06	0.0256	0.051	0.0076
898	RunA05_U3P3_FW_PVC_S_OFF_P1000_027	INSEAN	Model 2	1	FW	7	3.30	2	0.970	18.16	8.96E+05	0.010	0.001	-0.023	-0.023	0.197	0.0293	0.05	0.0312	0.053	0.0109
899	RunA05_U3P3_FW_PVC_S_OFF_P1000_037	INSEAN	Model 2	1	FW	7	3.30	2	0.969	18.16	8.96E+05	0.010	0.001	0.059	0.059	0.178	0.0271	0.06	0.0267	0.047	0.0094
900	RunA05_U4P2_FWFV_PVC_S_OFF_P1000_030	INSEAN	Model 2	1	FW	7	4.20	2.5	0.970	11.21	1.14E+06	0.016	0.002	0.260	0.260	0.192	0.0305	0.05	0.0123	0.055	0.0097
901	RunA05_U4P2_FW_PVC_S_OFF_P1000_028	INSEAN	Model 2	1	FW	7	4.20	2.5	0.970	11.21	1.14E+06	0.015	0.002	0.238	0.238	0.185	0.0293	0.04	0.0141	0.053	0.0094
902	RunA08_U1P6_FW_PVC_S_OFF_P1000_069	INSEAN	Model 2	1	FW	10	1.60	1	0.971	77.20	4.40E+05	0.004	0.000	0.121	0.121	0.409	0.0420	0.09	0.0102	0.072	0.0073
903	RunA08_U3P3_FWFV_PVC_S_OFF_P1000_071	INSEAN	Model 2	1	FW	10	3.30	2	0.971	18.15	9.07E+05	0.012	0.001	0.213	0.213	0.254	0.0285	0.06	0.0343	0.072	0.0109
904	RunA08_U3P3_FW_PVC_S_OFF_P1000_070	INSEAN	Model 2	1	FW	10	3.30	2	0.971	18.15	9.07E+05	0.012	0.001	0.230	0.230	0.257	0.0272	0.06	0.0345	0.073	0.0106
905	RunA10_U1P6_FW_PVC_S_OFF_P1000_079	INSEAN	Model 2	1	FW	12	1.60	1	0.971	77.19	4.41E+05	0.005	0.000	0.064	0.064	0.481	0.0399	0.13	0.0132	0.080	0.0064
906	RunA10_U2P0_PVFV_PVC_S_OFF_P047_098	INSEAN	Model 2	1	FW	12	2.00	1.25	0.048	1.22	5.53E+05	0.007	0.001	0.346	0.346	0.412	0.0321	0.12	0.0154	0.078	0.0059
907	RunA10_U2P5_FW_PVC_S_OFF_P1000_080	INSEAN	Model 2	1	FW	12	2.50	1.5	0.971	31.62	6.89E+05	0.010	0.001	0.086	0.086	0.366	0.0362	0.10	0.0276	0.089	0.0075
908	RunA10_U2P5_FW_PVC_S_OFF_P150_108	INSEAN	Model 2	1	FW	12	2.50	1.5	0.146	4.09	6.97E+05	0.009	0.001	0.241	0.241	0.344	0.0332	0.09	0.0208	0.086	0.0072
909	RunA10_U3P3_FW_PVC_S_OFF_P1000_082	INSEAN	Model 2	1	FW	12	3.30	2	0.971	18.14	9.09E+05	0.016	0.001	0.279	0.279	0.329	0.0313	0.08	0.0371	0.091	0.0109
910	RunA10_U3P3_FW_PVC_S_OFF_P150_109	INSEAN	Model 2	1	FW	12	3.30	2	0.143	2.35	9.21E+05	0.016	0.001	0.623	0.623	0.343	0.0312	0.08	0.0238	0.095	0.0098
911	RunA10_U4P2_FW_PVC_S_OFF_P1000_084	INSEAN	Model 2	1	FW	12	4.20	2.5	0.972	11.20	1.16E+06	0.024	0.002	0.640	0.640	0.285	0.0285	0.07	0.0132	0.084	0.0093
912	RunA10_U1P6_PV_PVC_S_OFF_P1000_134	INSEAN	Model 2	1	PV	12	1.60	1	0.970	77.05	4.53E+05	0.006	0.000	-0.014	-0.014	0.493	0.0382	0.14	0.0132	0.073	0.0067
913	RunA10_U2P0_PVFV_PVC_S_OFF_P047_098	INSEAN	Model 2	1	PV	12	2.00	1.25	0.048	1.22	5.53E+05	0.007	0.001	0.346	0.346	0.412	0.0321	0.12	0.0154	0.078	0.0059
914	RunA15_U1P6_PV_PVC_S_OFF_P1000_144	INSEAN	Model 2	1	PV	17	1.60	1	0.968	76.99	4.58E+05	0.008	0.000	0.159	0.159	0.709	0.0396	0.26	0.0168	0.109	0.0062
915	RunA05_U3P3_FV_PVC_S_OFF_P1000_036	INSEAN	Model 2	1	FV	7	3.30	2	0.969	18.16	8.96E+05	0.010	0.001	0.038	0.038	0.172	0.0234	0.06	0.0274	0.029	0.0071
916	RunA05_U3P3_PCFV_PVC_S_OFF_P061_065	INSEAN	Model 2	1	FV	7	3.30	2	0.065	0.71	9.07E+05	0.009	0.001	0.495	0.495	0.187	0.0230	0.04	0.0198	0.034	0.0088
917	RunA05_U3P8_FV_PVC_S_OFF_P047_060	INSEAN	Model 2	1	FV	7	3.80	2.25	0.048	0.36	1.04E+06	0.010	0.001	0.425	0.425	0.152	0.0184	0.04	0.0158	0.026	0.0061
918	RunA05_U4P2_FWFV_PVC_S_OFF_P1000_030	INSEAN	Model 2	1	FV	7	4.20	2.5	0.970	11.21	1.14E+06	0.013	0.001	0.033	0.033	0.140	0.0218	0.05	0.0133	0.023	0.0060

#	Run Name	Facility	Model	AR_h	Flow Regime	α, deg	Speed, m/s	Fn_h	Facility Pressure, bar	σ_v	Re_c	δ_{SC} at tip, m		θ at tip, deg		$C_{L,3D}$		$C_{D,3D}$		$C_{M,3D}$ (about 0.5c)	
												Mean	Std	Mean	Std	Mean	Std	Mean	Std	Mean	Std
919	RunA05_U4P2_FWFV_PVC_S_OFF_P1000_033	INSEAN	Model 2	1	FV	7	4.20	2.5	0.970	11.21	1.14E+06	0.013	0.001	0.087	0.087	0.138	0.0160	0.05	0.0138	0.022	0.0064
920	RunA05_U4P2_FV_PVC_S_OFF_P048_061	INSEAN	Model 2	1	FV	7	4.20	2.5	0.049	0.29	1.15E+06	0.011	0.001	0.577	0.577	0.147	0.0173	0.04	0.0259	0.026	0.0101
921	RunA08_U3P3_FV_PVC_S_OFF_P1000_073	INSEAN	Model 2	1	FV	10	3.30	2	0.972	18.15	9.07E+05	0.011	0.001	0.147	0.147	0.222	0.0190	0.07	0.0346	0.036	0.0093
922	RunA08_U3P3_FV_PVC_S_OFF_P1000_072	INSEAN	Model 2	1	FV	10	3.30	2	0.972	18.15	9.07E+05	0.012	0.001	0.132	0.132	0.231	0.0232	0.07	0.0350	0.038	0.0093
923	RunA08_U3P3_FWFV_PVC_S_OFF_P1000_071	INSEAN	Model 2	1	FV	10	3.30	2	0.971	18.15	9.07E+05	0.011	0.001	0.101	0.101	0.217	0.0184	0.06	0.0342	0.035	0.0092
924	RunA10_U2P2_FV_PVC_S_OFF_P047_099	INSEAN	Model 2	1	FV	12	2.20	1.25	0.048	1.01	6.08E+05	0.009	0.001	0.478	0.478	0.401	0.0292	0.12	0.0175	0.074	0.0061
925	RunA10_U2P0_PVFV_PVC_S_OFF_P047_098	INSEAN	Model 2	1	FV	12	2.00	1.25	0.048	1.22	5.53E+05	0.007	0.001	0.346	0.346	0.412	0.0321	0.12	0.0154	0.078	0.0059
926	RunA10_U2P5_FV_PVC_S_OFF_P212_092	INSEAN	Model 2	1	FV	12	2.50	1.5	0.212	7.34	6.92E+05	0.011	0.001	0.127	0.127	0.390	0.0309	0.12	0.0196	0.065	0.0060
927	RunA10_U3P3_FV_PVC_S_OFF_P1000_088	INSEAN	Model 2	1	FV	12	3.30	2	0.972	18.14	9.09E+05	0.015	0.001	0.138	0.138	0.267	0.0221	0.10	0.0325	0.043	0.0080
928	RunA10_U3P3_FV_PVC_S_OFF_P1000_133	INSEAN	Model 2	1	FV	12	3.30	2	0.971	18.11	9.34E+05	0.016	0.001	0.173	0.173	0.307	0.0287	0.11	0.0346	0.048	0.0093
929	RunA10_U3P3_FV_PVC_S_OFF_P1000_142	INSEAN	Model 2	1	FV	12	3.30	2	0.970	18.11	9.34E+05	0.015	0.001	-0.004	-0.004	0.283	0.0285	0.10	0.0347	0.045	0.0093
930	RunA10_U3P3_FV_PVC_S_OFF_P050_100	INSEAN	Model 2	1	FV	12	3.30	2	0.051	0.52	9.12E+05	0.015	0.001	0.568	0.568	0.288	0.0239	0.10	0.0164	0.045	0.0065
931	RunA10_U3P3_FV_PVC_S_OFF_P050_116	INSEAN	Model 2	1	FV	12	3.30	2	0.050	0.49	9.25E+05	0.015	0.001	0.164	0.164	0.297	0.0231	0.07	0.0316	0.043	0.0086
932	RunA10_U4P2_FV_PVC_S_OFF_P1000_086	INSEAN	Model 2	1	FV	12	4.20	2.5	0.972	11.20	1.16E+06	0.017	0.001	0.190	0.190	0.185	0.0218	0.07	0.0135	0.033	0.0064
933	RunA15_U1P6_PV_PVC_S_OFF_P1000_144	INSEAN	Model 2	1	FV	17	1.60	1	0.968	76.99	4.58E+05	0.008	0.000	0.159	0.159	0.709	0.0395	0.26	0.0168	0.109	0.0062
934	RunA15_U2P5_FV_PVC_S_OFF_P1000_145	INSEAN	Model 2	1	FV	17	2.50	1.5	0.967	31.54	7.16E+05	0.016	0.001	0.171	0.171	0.521	0.0284	0.21	0.0229	0.072	0.0058
935	RunA15_U2P5_FV_PVC_S_OFF_P1000_148	INSEAN	Model 2	1	FV	17	2.50	1.5	0.966	31.54	7.16E+05	0.017	0.001	0.208	0.208	0.560	0.0280	0.22	0.0216	0.076	0.0055
936	RunA15_U3P3_FV_PVC_S_OFF_P1000_146	INSEAN	Model 2	1	FV	17	3.30	2	0.967	18.10	9.45E+05	0.020	0.001	0.396	0.396	0.392	0.0310	0.17	0.0368	0.057	0.0086
937	RunA15_U4P2_FV_PVC_S_OFF_P1000_147	INSEAN	Model 2	1	FV	17	4.20	2.5	0.967	11.17	1.20E+06	0.024	0.001	0.417	0.417	0.271	0.0203	0.12	0.0159	0.047	0.0060
938	RunA05_U2P5_PC_PVC_S_OFF_P044_049	INSEAN	Model 2	1	PC	7	2.50	1.5	0.048	0.73	6.84E+05	0.005	0.001	0.210	0.210	0.210	0.0328	0.04	0.0207	0.052	0.0075
939	RunA05_U3P3_PC_PVC_S_OFF_P061_063	INSEAN	Model 2	1	PC	7	3.30	2	0.065	0.71	9.07E+05	0.009	0.001	0.514	0.514	0.192	0.0269	0.04	0.0199	0.053	0.0095
940	RunA05_U3P3_PC_PVC_S_OFF_P048_052	INSEAN	Model 2	1	PC	7	3.30	2	0.050	0.42	9.05E+05	0.008	0.001	0.229	0.229	0.176	0.0265	0.03	0.0159	0.052	0.0091

#	Run Name	Facility	Model	AR_h	Flow Regime	α, deg	Speed, m/s	Fn_h	Facility Pressure, bar	σ_v	Re_c	δ_{SC} at tip, m		θ at tip, deg		$C_{L,3D}$		$C_{D,3D}$		$C_{M,3D}$ (about 0.5c)	
												Mean	Std	Mean	Std	Mean	Std	Mean	Std	Mean	Std
941	RunA05_U3P5_PC_PVC_S_OFF_P048_055	INSEAN	Model 2	1	PC	7	3.50	2	0.050	0.37	9.60E+05	0.011	0.001	0.458	0.458	0.214	0.0287	0.04	0.0143	0.062	0.0103
942	RunA05_U3P6_PC_PVC_S_OFF_P047_057	INSEAN	Model 2	1	PC	7	3.60	2.25	0.049	0.38	9.87E+05	0.010	0.001	0.460	0.460	0.190	0.0262	0.03	0.0140	0.056	0.0090
943	RunA10_U2P5_PC_PVC_S_OFF_P050_111	INSEAN	Model 2	1	PC	12	2.50	1.5	0.050	0.85	6.99E+05	0.010	0.001	0.036	0.036	0.398	0.0345	0.07	0.0214	0.088	0.0083
944	RunA10_U3P0_PC_PVC_S_OFF_P050_114	INSEAN	Model 2	1	PC	12	3.00	1.75	0.050	0.59	8.39E+05	0.014	0.001	0.155	0.155	0.366	0.0337	0.07	0.0330	0.092	0.0112
945	RunA10_U3P3_PC_PVC_S_OFF_P070_119	INSEAN	Model 2	1	PC	12	3.30	2	0.068	0.86	9.25E+05	0.016	0.001	0.616	0.616	0.331	0.0310	0.09	0.0458	0.096	0.0132

APPENDIX D

Order-of-Magnitude Analysis of the Re-Entrant Jet Thickness

In order for the re-entrant jet to propagate upstream in the manner described in this work, the jet must possess sufficient momentum to overcome wall-friction. The following rough-order-of-magnitude argument is intended to show that for the conditions of interest to this work, the effect of wall friction is immaterial. Consider a cavity with a re-entrant jet, as shown in figure D.1. Suppose that a control volume is placed around the re-entrant jet, as shown in the figure.

The momentum flux per unit span through the control volume's upstream and downstream surfaces, when wall friction is acting on the lower surface is,

$$\int_0^{L_c} \frac{1}{2}\rho C_f U^2 dx = \delta_1 \rho U_1^2 - \delta_2 \rho U_2^2, \tag{D.1}$$

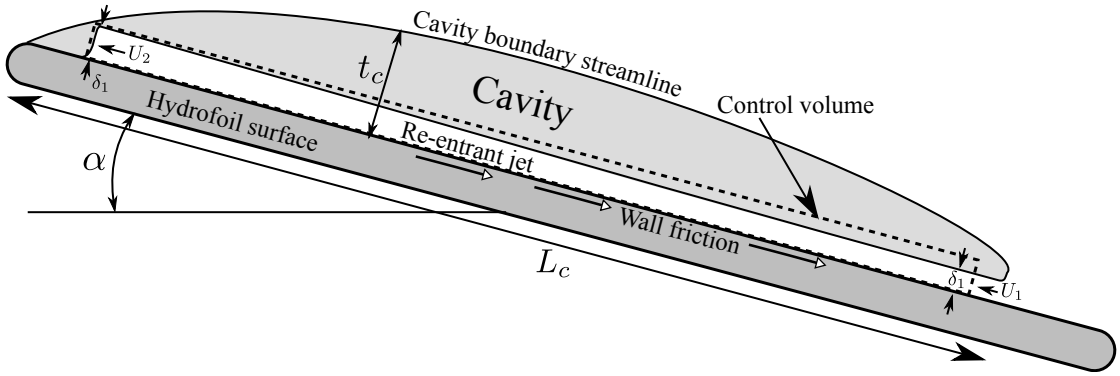

Figure D.1: Re-entrant jet and control volume.

where δ_1, δ_2, U_1, and U_2 are defined in figure D.1. Suppose that the wall friction coefficient, C_f is sufficient to stagnate the flow just before the re-entrant jet exits the upstream surface of the control volume, such that $U_2 = 0$. The momentum balance becomes,

$$\int_0^{L_c} \frac{1}{2}\rho C_f U^2 dx = \delta_1 \rho U_1^2. \tag{D.2}$$

The thickness of a re-entrant jet is given by *Callenaere et al.* (2001) to be,

$$\delta_1 = \frac{1}{2}\left(1 - \frac{1}{\overline{(1+\sigma_c)}}\right) t_c, \tag{D.3}$$

where the maximum cavity thickness, t_c is roughly approximated by,

$$t_c \approx \alpha \frac{L_c}{2}. \tag{D.4}$$

The right hand side of equation D.2 becomes,

$$\delta_1 \rho U_1^2 = \frac{1}{4}\left(1 - \frac{1}{\overline{(1+\sigma_c)}}\right) \rho U_1^2 \alpha L_c \tag{D.5}$$

The integral on the left-hand side of equation D.2 is replaced by a mid-point approximation, giving,

$$\int_0^{L_c} \frac{1}{2}\rho C_f U^2 dx \approx \frac{L_c}{4}\rho \bar{C_f} U_1^2, \tag{D.6}$$

Note that this is an inexact application of the mean value theorem, but is sufficient for order-of-magnitude analysis. Combining equations D.2, D.5, and D.6 yields,

$$C_f \approx \mathrm{O} \quad 1 - \frac{1}{\sqrt{1+\sigma_c}} \quad \alpha \quad , \tag{D.7}$$

which represents the order of magnitude of the wall-friction coefficient required to stagnate the jet flow.

The minimum angle of attack at which the re-entrant jet is proposed to be a washout mechanisms is $\alpha = 5°$. Washout typically occurs at $Fn_h \approx 1$, for which $\sigma_c = \frac{2}{Fn_h^2}\frac{z'}{h} \approx 1$ near mid-span ($\frac{z'}{h} = 0.5$). For these conditions, the skin friction coefficient required to stagnate the jet flow is roughly $\bar{C_f} \approx 2.5 \times 10^-2 = \mathrm{O}\,(10^-2)$. This is an

unusually high friction coefficient – though not an unreasonable one. Larger angles of attack, however, lead to un-physically large values of $\bar{C_f}$. This result supports the hypothesis presented in the text, that for $\alpha \geq 5^\circ$, skin friction should not prevent the re-entrant jet from impinging on a cavity's leading edge.

APPENDIX E

Order-of-Magnitude Analysis of Added-Mass Effect on Measured Loads

The following order-of-magnitude analysis is intended to show that the component of instantaneous measured lift and drag due to hydrodynamic added-mass is negligible above certain speeds.

Consider a representative section of the hydrofoil as a Two-Dimensional (2-D) flat plate at an angle of attack α, in an infinite domain, with an instantaneous inflow velocity of $U = \dot{X}$, and accelerating at a constant rate of $\ddot{X} = a$. The lift and drag on the plate can be approximately decomposed as,

$$\begin{aligned} L &= L_{unsteady} + L_{steady}, \\ D &= D_{unsteady} + D_{steady}. \end{aligned} \tag{E.1}$$

The unsteady forces in this case are limited to the inertial influence of the fluid as the body accelerates. Potential flow can be used to show that the inertial component in the Y direction due to accelerations in X is,

$$\begin{aligned} L_{unsteady} &= m_{21}\ddot{X} \\ &= \frac{1}{2}\pi\rho \left(\frac{c}{2}\right)^2 sin(2\alpha)\ddot{X}. \end{aligned} \tag{E.2}$$

The inertial component in the X direction is,

$$\begin{aligned} D_{unsteady} &= m_{11}\ddot{X} \\ &= \pi\rho \left(\frac{c}{2}\right)^2 sin^2(\alpha)\ddot{X}, \end{aligned} \tag{E.3}$$

where m_{21} and m_{11} are components of the added-mass tensor $\boldsymbol{m}$.

Equation E.1 becomes,

$$\begin{aligned} L &= \frac{\pi}{2}\rho \left(\frac{c}{2}\right)^2 sin(2\alpha)\ddot{X} + C_{L_{3D}}\frac{1}{2}\rho\dot{X}^2 c, \\ D &= \pi\rho \left(\frac{c}{2}\right)^2 sin^2(\alpha)\ddot{X} + C_{D_{3D}}\frac{1}{2}\rho\dot{X}^2 c. \end{aligned} \tag{E.4}$$

Given that $Fn_h = \dot{X}/\sqrt{gh}$, the ratio of unsteady to steady lift can be expressed as,

$$\begin{aligned} R_L = \frac{L_{unsteady}}{L_{steady}} &= \frac{\frac{1}{2}\pi\rho \left(\frac{c}{2}\right)^2 \sin(2\alpha)\ddot{X}}{C_{L_{3D}}\frac{1}{2}\rho\dot{X}^2 c} \\ &= \frac{\pi}{4AR_h}\frac{\sin(2\alpha)}{C_{L_{3D}}}\frac{\ddot{X}}{g}\frac{1}{Fn_h^2}. \end{aligned} \tag{E.5}$$

The ratio of unsteady to steady drag is written,

$$\begin{aligned} R_D = \frac{D_{unsteady}}{D_{steady}} &= \frac{\pi\rho \left(\frac{c}{2}\right)^2 \sin^2(\alpha)\ddot{X}}{C_{D_{3D}}\frac{1}{2}\rho\dot{X}^2 c} \\ &= \frac{\pi}{2AR_h}\frac{\sin^2(\alpha)}{C_{D_{3D}}}\frac{\ddot{X}}{g}\frac{1}{Fn_h^2}. \end{aligned} \tag{E.6}$$

The quantities of equations E.5 and E.6 may be estimated by order of magnitude as follows.

- $\sin^2(\alpha) = \mathrm{O}\left(10^{-1}\right)$ for $\alpha < 30°$.
- $\sin(2\alpha) = \mathrm{O}\left(1\right)$ for $\alpha < 30°$.
- $\frac{\ddot{X}}{g} = \mathrm{O}\left(10^{-2}\right)$, assuming $\ddot{X} = a \approx \mathrm{O}\left(1\right)$ ft s^{-2}.
- $AR_h = \mathrm{O}\left(1\right)$
- $C_{L_{3D}} = \mathrm{O}\left(1\right)$
- $C_{D_{3D}} = \mathrm{O}\left(10^{-1}\right)$

The resulting ratios become, after simplification,

$$R_L \approx \frac{\pi}{4} \times 10^{-2} \frac{1}{Fn_h^2} = \mathrm{O} \quad \frac{1}{Fn_h^2} \times 10^{-2} \tag{E.7}$$

$$R_D \approx \frac{\pi}{2} \times 10^{-2} \frac{1}{Fn_h^2} = \mathrm{O} \quad \frac{1}{Fn_h^2} \times 10^{-2} \quad . \tag{E.8}$$

This result suggests that for $Fn_h << 1$ only, inertial forces are on the same order as the steady lift and drag. The relative magnitude of the inertial components vanishes quickly as the speed – and Fn_h – increase, and may be neglected for $Fn_h > 1$.

APPENDIX F

Validation of Rational Fraction Polynomial Modal Analysis

A 6-by-6 model was created with known natural frequencies, mode shapes, and viscous and structural damping ratios. Frequency Response Function (FRF) matrices were synthesized from the known values and used to test the system-ID approach described in the preceding sections.

A single row of the FRF matrix was retained at each frequency, simulating the case of a multiply-instrumented test specimen with a single excitation point. For all cases, the modal viscous damping ratio was set to a constant $\xi_v = 2.5\%$. The structural damping was defined as $[\boldsymbol{\eta_s}] = \xi_h/(2\omega_{0,n}^2)$, so that the equivalent viscous damping ratio ξ_h would be constant for all modes. Finally, uniformly distributed random error $\epsilon \in [0, 1]$ was added to the real and imaginary parts of the FRF. The random signal was generated with an Root Mean Square (RMS) proportional to the RMS of the FRF. Mode shapes were defined as

$$[\boldsymbol{\Theta}] = [\sin\{\boldsymbol{\phi}\} \quad \cos\{\boldsymbol{\phi}\} \quad \tan\{\boldsymbol{\phi}\} \quad \sinh\{\boldsymbol{\phi}\} \quad \cosh\{\boldsymbol{\phi}\} \quad \tanh\{\boldsymbol{\phi}\}],$$

where $\{\boldsymbol{\phi}\} = [0.1\pi \ldots 0.9\pi]^T$. The undamped natural frequencies may be found in table F.1.

Three test cases were considered:

1. $\xi_v = 0.025$ viscous damping for all modes; $\eta_s = 0$ structural damping for all modes; no noise added to spectrum.

2. $\xi_v = 0.025$ viscous damping for all modes; $\eta_s = 0.025/(2\omega_{0,n}^2)$ structural damping for all modes; no noise added to spectrum.

3. $\xi_v = 0.025$ viscous damping for all modes; $\eta_s = 0.025/(2\omega_{0,n}^2)$ structural damping for all modes; random noise added to spectrum.

F.1 Test Case 1: Proportional Viscous Damping

A litmus test of any system identification procedure is whether or not the algorithm can recover prescribed system parameters under perfectly ideal conditions, *i.e.* no noise or nonlinearities. The first test of the Rational Fraction Polynomial (RFP) modal used only the linear viscous damping coefficient. The entire simulated frequency range was used to perform identification with $N = 6$ (all modes being identified). The resulting sythesized FRF magnitude, fitted FRF, and contribution of each identified mode are shown in figure F.1. As shown in table F.1 and figure F.1, the quantitative identification is excellent. One might expect the natural frequencies and damping ratios to be recovered to within machine precision, appreciable numerical errors accumulate during the generation of the FRF, so it's unsurprising that the fidelity is limited.

	ξ_v	ξ_h	$\frac{RMS_{noise}}{RMS_{FRF}}$			
	0.025	0	0			
	ω_n, rad/s			ξ_e		
	Truth	ID	% Error	Truth	ID	% Error
Mode 1	1.2	'1.2±1.16e-06'	-3.8E-07	0.03	'0.025±7.78e-07'	-1.2E-05
Mode 2	2.24	'2.24±1.95e-07'	-4.2E-08	0.03	'0.025±1.23e-08'	-2.3E-07
Mode 3	7.2	'7.2±3.73e-05'	-2.0E-06	0.03	'0.025±3.43e-07'	-3.2E-06
Mode 4	8	'8±1.46e-06'	6.9E-08	0.03	'0.025±1.05e-07'	-2.0E-06
Mode 5	10	'10±1.33e-08'	5.0E-11	0.03	'0.025±3.42e-10'	8.4E-09
Mode 6	12.3	'12.3±7.48e-09'	-1.5E-10	0.03	'0.025±1.21e-09'	1.3E-08

Table F.1: Summary of results for test case 1 with viscous damping only.

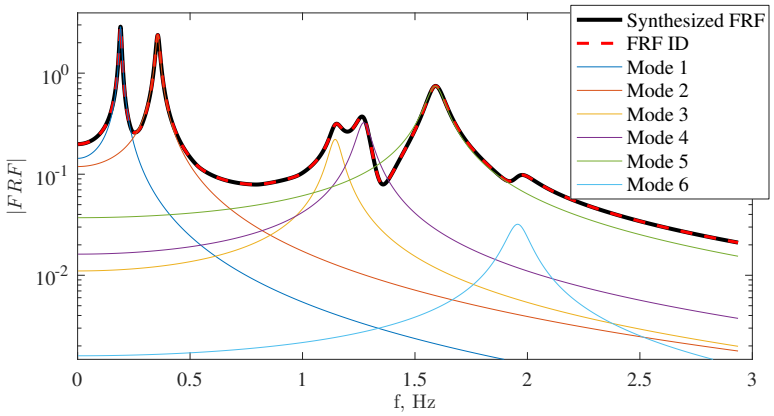

Figure F.1: Test case #1: FRF Reconstruction with $\xi_v = 2.5\%; \xi_h = 0\%$

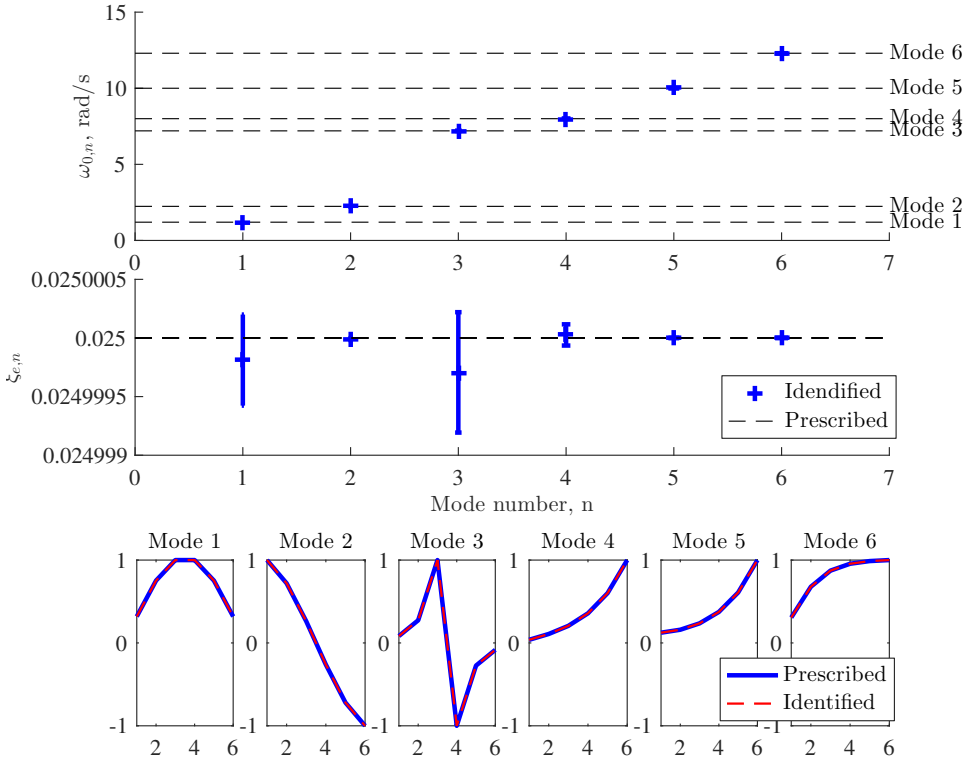

Figure F.2: Test case #1: Parameter ID with $\xi_v = 2.5\%; \xi_h = 0\%$. Blue markers indicate means and standard deviations of identified values. Grey dashed lines indicate the "true" prescribed values. Mode shapes along the bottom of the figure are plotted with the degree of freedom on the X-axis and the unscaled modal participation factor on the Y-axis.

F.2 Test Case 2: Proportional Viscous Damping and Hysteretic Damping

For the second test, $\eta_n = 0.05/\omega_{0,n}$ was used, which translates to a constant equivalent viscous damping ratio of $\xi_h = 2.5\%$, and a total effective viscous damping ratio of $\xi_e = 5\%$. Results in this case were obtained by setting the RFP numerator order to $N + 1$, providing one additional term for fitting the nonlinear contribution of the hysteretic damping.

Table F.2 shows that very good fidelity is achieved in the case of mixed linear-nonlinear damping. The resulting effective modal damping (constant $\xi_e = 5\%$) is actually quite large, which causes the peaks at 7.2 and 8 rad/s to merge together in the FRF portrayed in figure F.3. The RFP system identification extracts all modes with good accuracy, regardless.

Table F.2: Summary of results for test case 2 with viscous and hysteretic damping. In general, the results remain quite good, with the exception that the frequencies of modes

	ξ_v	ξ_h	$\frac{RMS_{noise}}{RMS_{FRF}}$			
	0.025	0.025	0			
	ω_n			ξ_e		
	Truth	ID	% Error	Truth	ID	% Error
Mode 1	1.2	'1.19±0.00969'	-0.78%	0.05	'0.0502±0.00349'	0.41%
Mode 2	2.24	'2.24±0.00387'	0.07%	0.05	'0.0496±0.00298'	-0.73%
Mode 3	7.2	'7.22±0.0621'	0.24%	0.05	'0.0481±0.00473'	-3.79%
Mode 4	8	'8.03±0.0103'	0.36%	0.05	'0.051±0.0013'	2.00%
Mode 5	10	'10±4.3e-05'	0.12%	0.05	'0.05±2.92e-05'	0.05%
Mode 6	12.3	'12.3±0.000517'	0.12%	0.05	'0.05±1.06e-05'	-0.09%

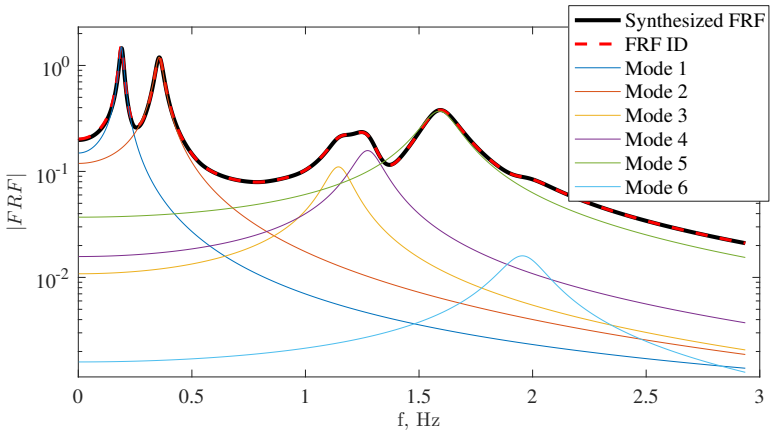

Figure F.3: Test case #2: FRF Reconstruction with $\xi_v = 2.5\%; \xi_h = 2.5\%$. The curve shown in the mean FRF, averaged across the six components in one row of the FRF matrix.

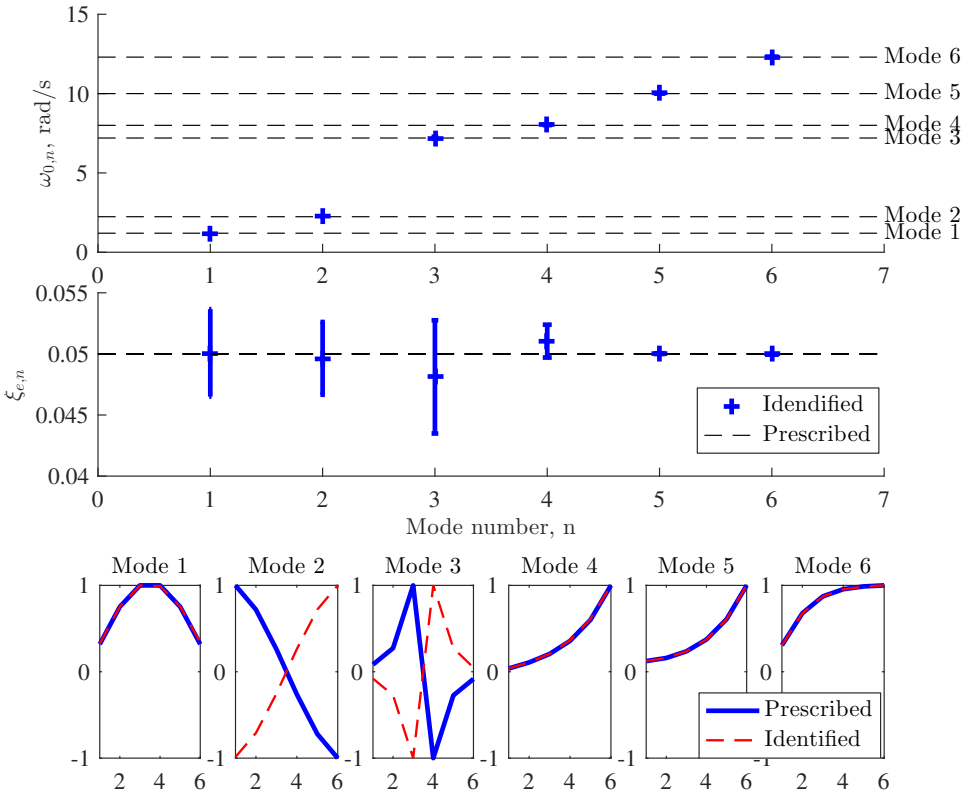

Figure F.4: Test case #2: Parameter ID with $\xi_v = 2.5\%; \xi_h = 2.5\%$. Blue markers indicate means and standard deviations of identified values. Grey dashed lines indicate the "true" prescribed values. Mode shapes along the bottom of the figure are plotted with the degree of freedom on the X-axis and the unscaled modal participation factor on the Y-axis.

F.3 Test Case 3: Proportional Viscous Damping, Hysteretic Damping, and Spectral Noise

The results in table F.3, show a degradation in the quality of the identified parameters when spectral noise is added. Modes 4 and 6 are missed by the algorithm, probably because their peaks are ill-defined in the presence of high damping and noise. Figure F.5 shows the reconstructed FRF magnitudes, and indicates the fitting of some spurious modes. Figure F.6 also portrays a degradations of the identified natural frequencies, equivalent damping ratios, and mode shapes.

Table F.3: Summary of results for test case 3 with viscous damping, hysteretic damping and spectral noise ($\xi_v = 2.5\%; \xi_h = 0\%; RMS(\epsilon) = 0.05RMS(|FRF|)$). A degradation of the identified parameters occurs where modes are indistinct.

	ξ_v	ξ_h	$\frac{RMS_{noise}}{RMS_{FRF}}$			
	0.025	0.025	0.025			
	ω_n			ξ_e		
	Truth	ID	% Error	Truth	ID	% Error
Mode 1	1.2	1.207±0.032	5.8E-03	0.05	0.0538±0.011	7.6E-02
Mode 2	2.24	2.369±0.183	5.7E-02	0.05	0.061±0.041	2.2E-01
Mode 3	7.2	7.619±0.330	5.8E-02	0.05	0.058±0.024	1.6E-01
Mode 4	8	10.005±0.009	2.5E-01	0.05	0.045±0.003	-9.7E-02
Mode 5	10	12.827±0.199	2.8E-01	0.05	0.019±0.007	-6.2E-01
Mode 6	12.3	14.725±0.0789	2.0E-01	0.05	0.000±0.0012	-1.0E+00

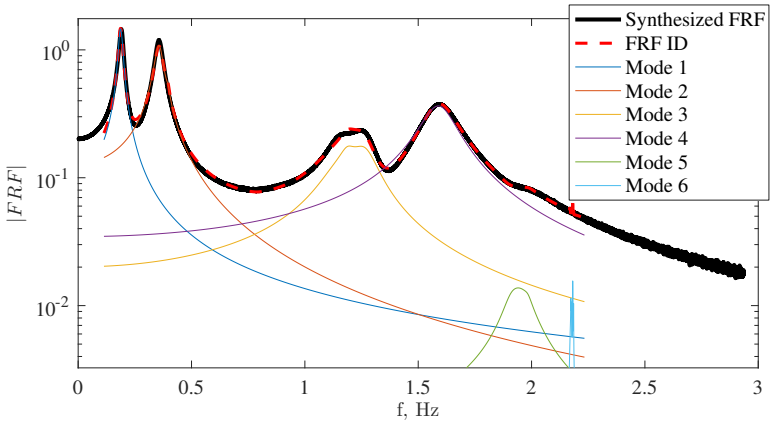

Figure F.5: Test case #3: FRF Reconstruction with $\xi_v = 2.5\%; \xi_h = 2.5\%$ 2.5% noise added to spectrum.

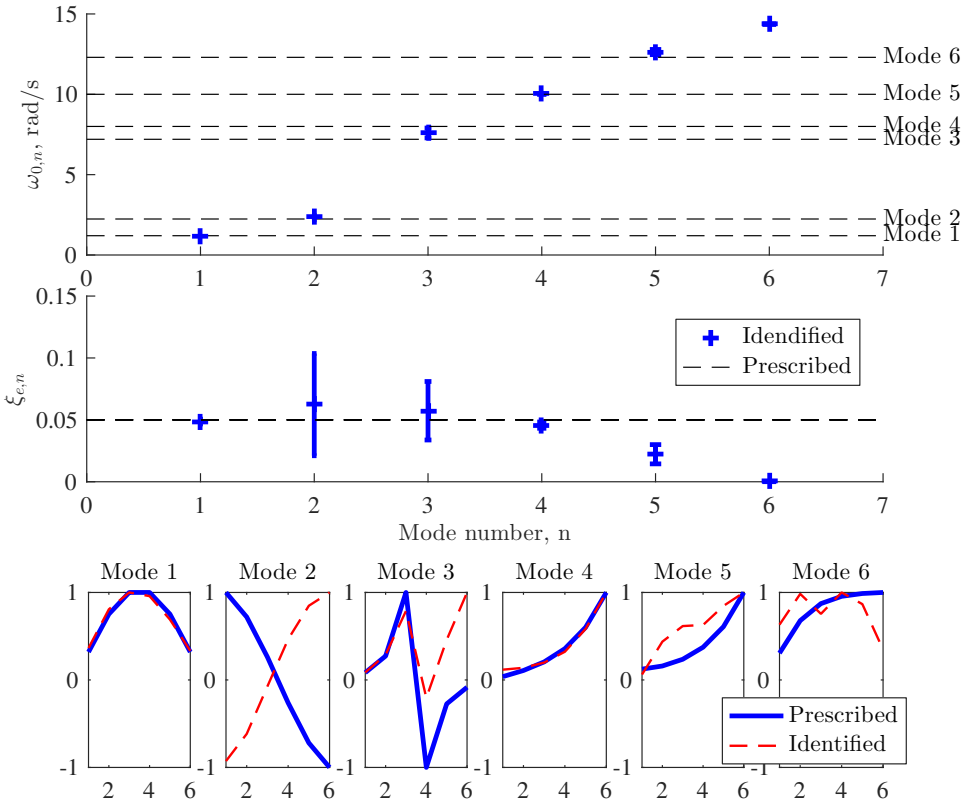

Figure F.6: Test case #3: Parameter ID with $\xi_v = 2.5\%; \xi_h = 2.5\%$; 2.5% noise added to spectrum.

F.4 Robust Estimation of Noisy Spectra

§F demonstrates that an attempt to identify all six modes at once results in significant errors when spurious spectral content is added. However, a sequential estimation of modal parameters over truncated portions of the frequency axis yields improved identification by reducing the size of the optimization problem. As verification, consider figure F.7, which shows the FRF of case #3, but fitted in three separate operations. The respective parameter estimates in figure F.8 confirm that by querying smaller domains of the frequency axis in a sequential manner, the identification can be made more robust when a contaminated signal is being considered. Thus, while the fitting algorithm is sensitive to noise, robust performance can be achieved by sequentially performing identification only on localized portions of the frequency domain. Additionally, the signal-to-noise ratio is unlikely to be uniform across all measured channels. Some additional robustness can be gained by rejecting outliers in the natural frequency and damping vectors, $\{\boldsymbol{\omega_0}\}$ and $\{\boldsymbol{\xi}_e\}$, for each identified mode.

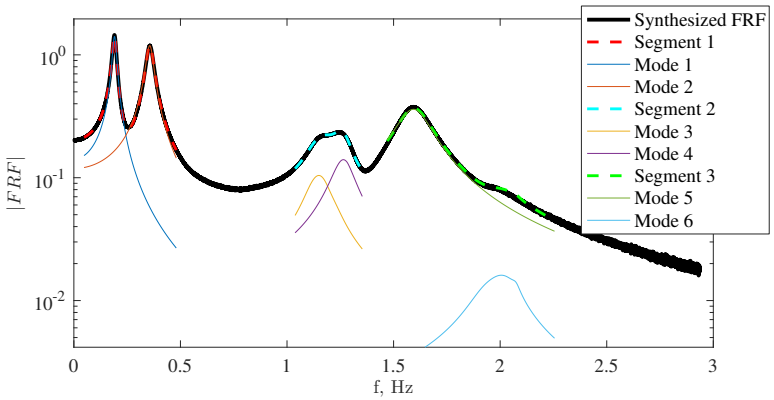

Figure F.7: Test case #3: FRF Reconstruction with $\xi_v = 2.5\%; \xi_h = 2.5\%$; 2.5% Noise

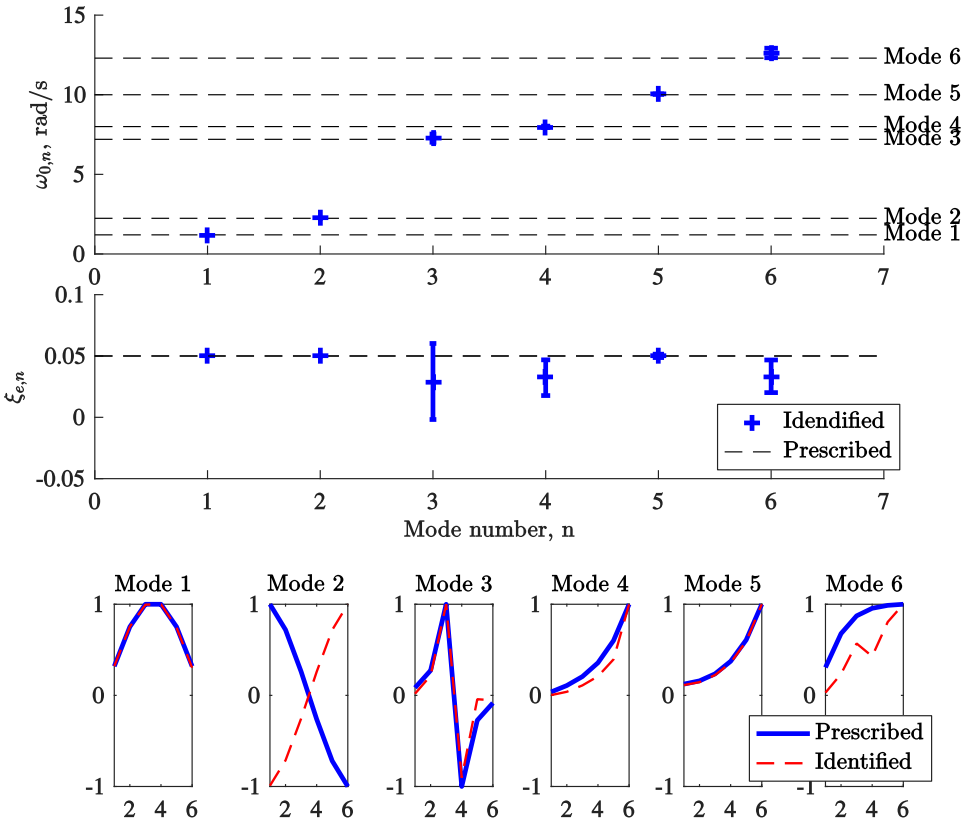

Figure F.8: Test case #3, refitted in three operations. The estimates of modal parameters are significantly improved by reducing the size of the identification.

APPENDIX G

Frequency Response Functions and Mode Shapes of Model 2 in Five Flow Conditions

G.1 Dry Conditions

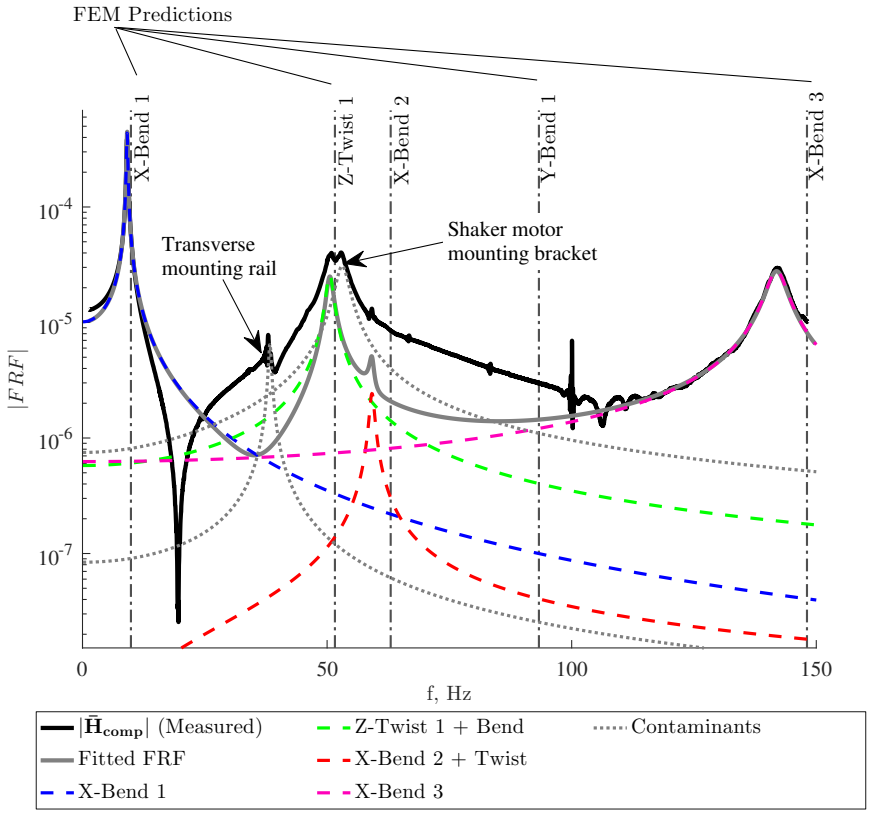

Figure G.1: Mean magnitudes of compliance FRF $|\overline{\mathbf{H}^{\mathbf{comp}}}|$ for model 2 in dry conditions.

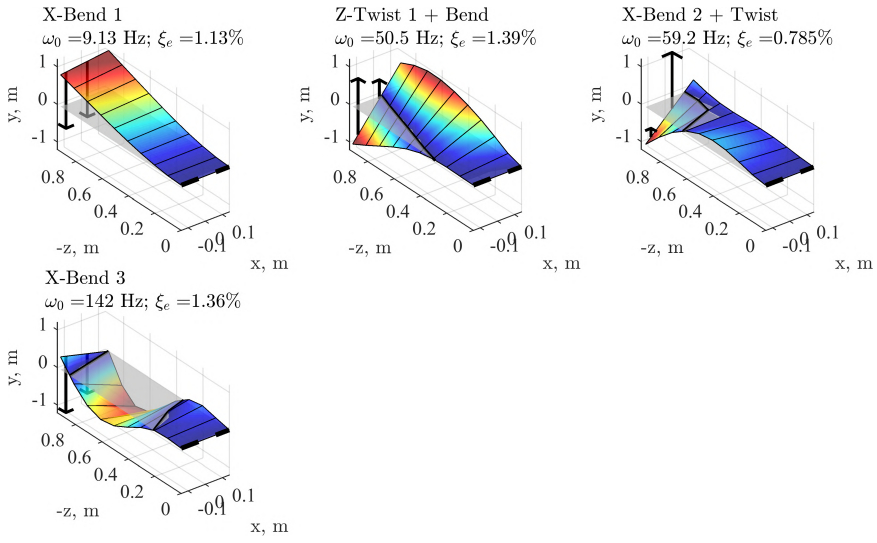

Figure G.2: Normalized mode shapes of model 2 in dry conditions.

G.2 Still-Water Conditions at $AR_h = 1.0$

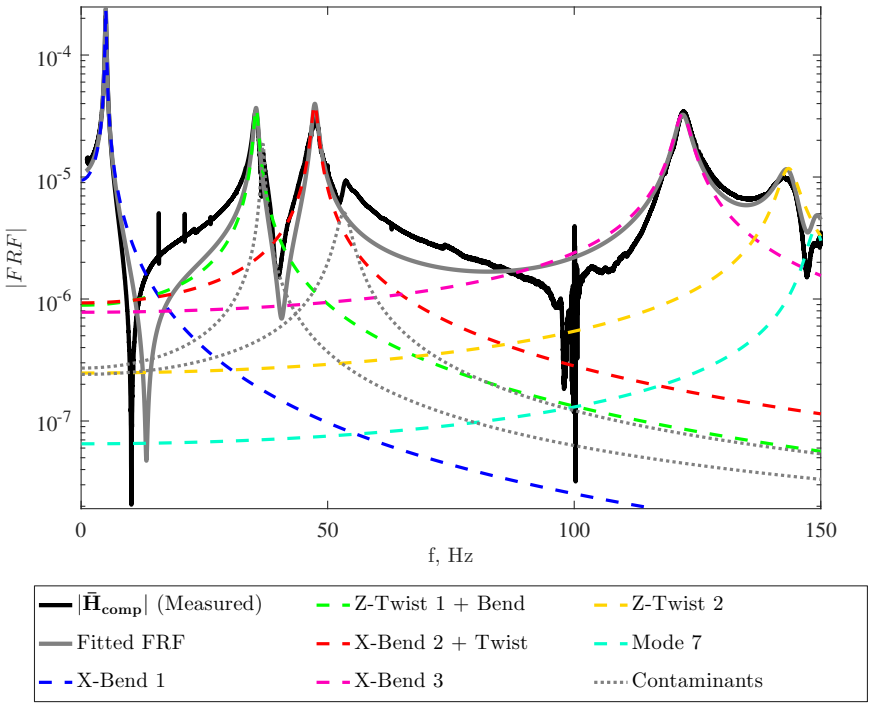

Figure G.3: Mean magnitudes of compliance FRF $|\overline{\mathbf{H}^{\mathbf{comp}}}|$ for model 2 in still water at $AR_h = 1.0$.

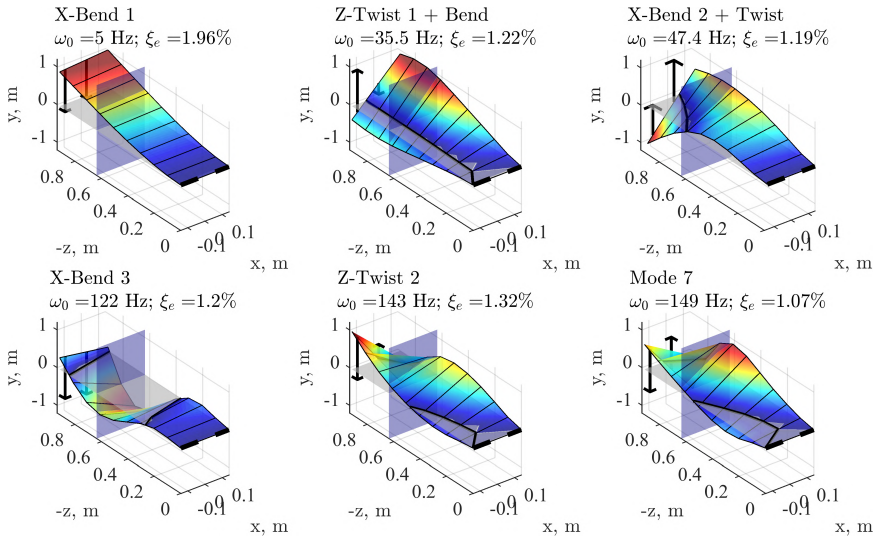

Figure G.4: Normalized mode shapes of model 2 in still water at $AR_h = 1.0$

G.3 Forward Speed in Fully Wetted Flow at $\alpha = 0°$; $Fn_h = 1.5$; $AR_h = 1.0$

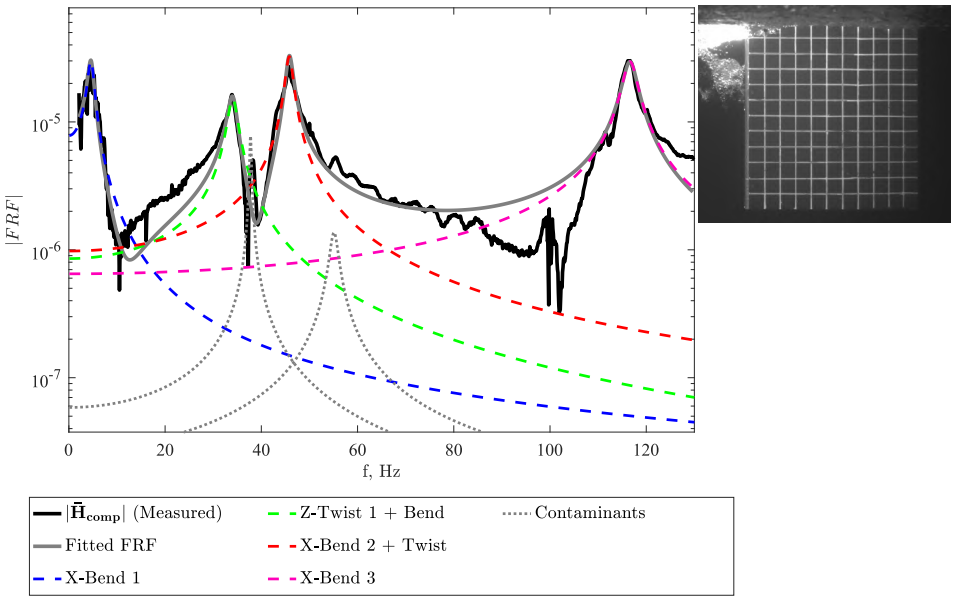

Figure G.5: Mean magnitudes of compliance FRF $|\overline{\mathbf{H}^{\mathbf{comp}}}|$ for model 2 in fully wetted flow at $\alpha = 0°$; $Fn_h = 1.5$; $AR_h = 1.0$

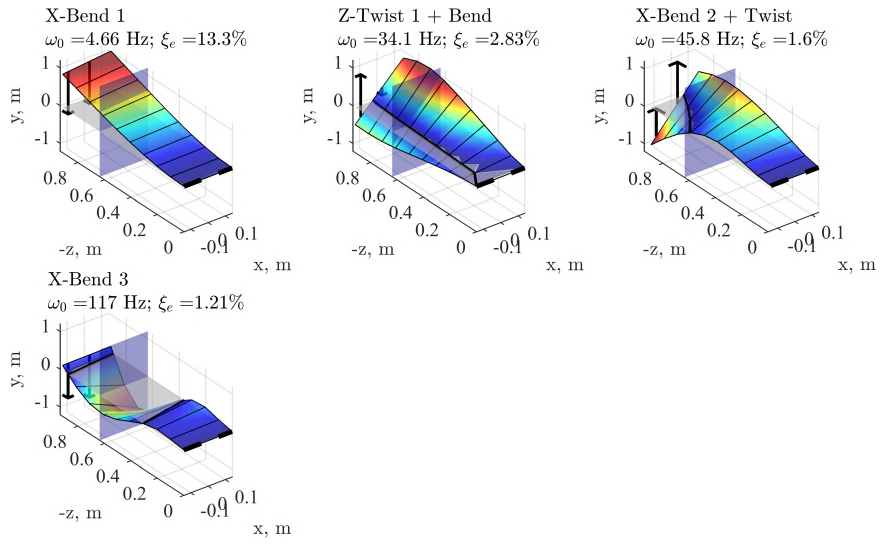

Figure G.6: Normalized mode shapes of model 2 in fully wetted flow at $\alpha = 0°$; $Fn_h = 1.5$; $AR_h = 1.0$.

G.4 Forward Speed in Fully Ventilated Flow at $\alpha = 0°$; $Fn_h = 1.5$; $AR_h = 1.0$

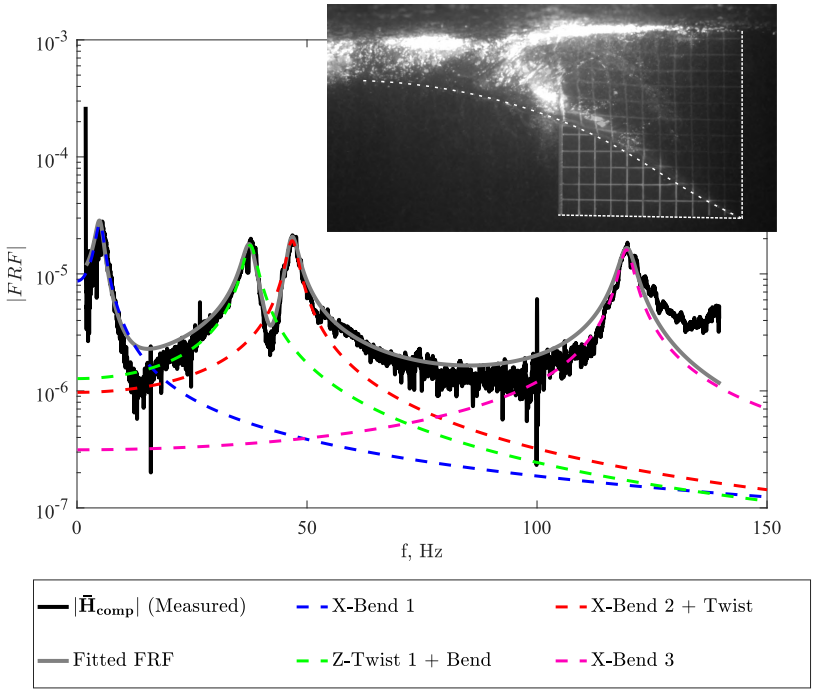

Figure G.7: Mean magnitudes of compliance FRF $|\overline{\mathbf{H}^{\mathbf{comp}}}|$ for model 2 in fully ventilated flow at $\alpha = 10°$; $Fn_h = 1.5$; $AR_h = 1.0$.

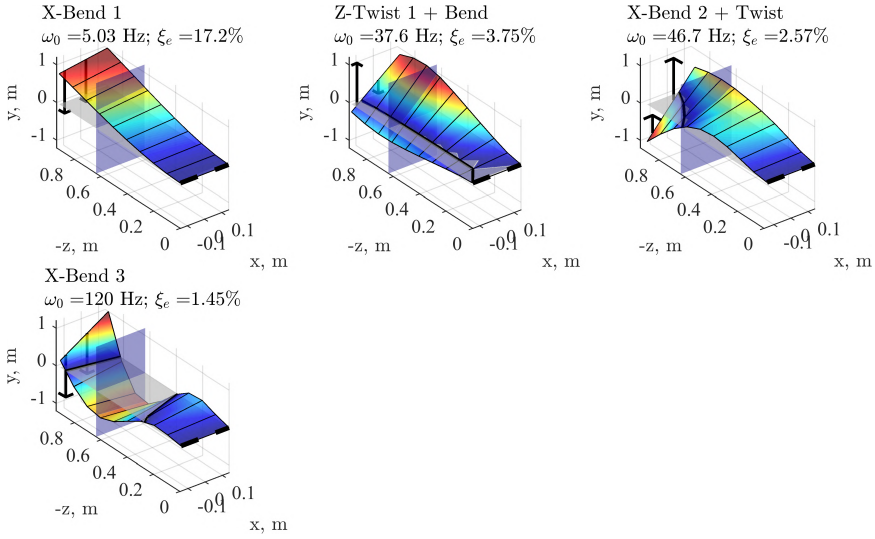

Figure G.8: Normalized mode shapes of model 2 in fully ventilated flow at $\alpha = 0°$; $Fn_h = 1.5$; $AR_h = 1.0$.

G.5 Forward Speed in Partially Cavitating Flow at $\alpha = 10°$; $Fn_h = 1.5$; $AR_h = 1.0$; $\sigma_v = 0.85$

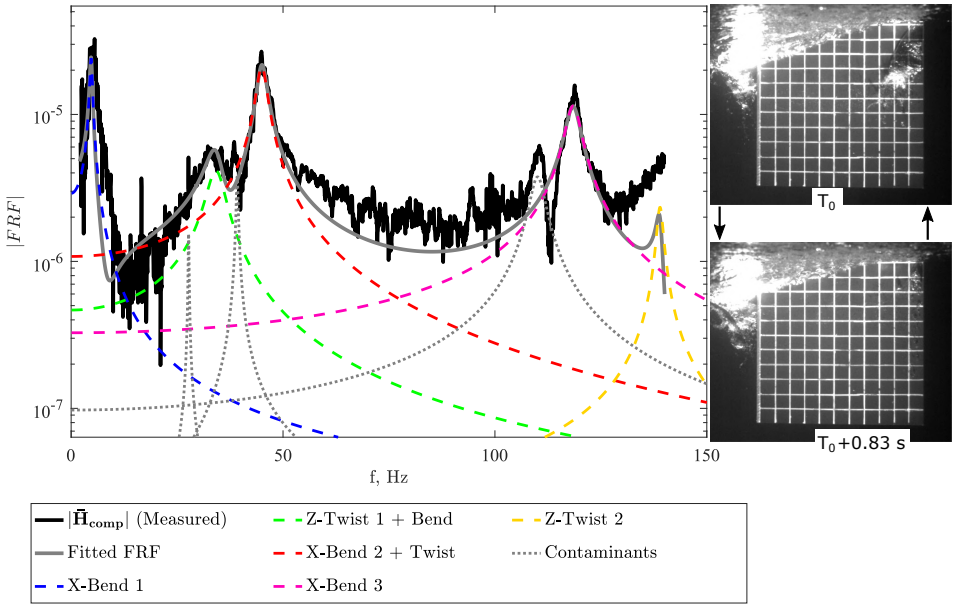

Figure G.9: Mean magnitudes of compliance FRF $|\overline{\mathbf{H}^{\mathbf{comp}}}|$ for model 2 in partially cavitating flow at $\alpha = 10°; Fn_h = 1.5; AR_h = 1.0; \sigma_v = 0.85$.

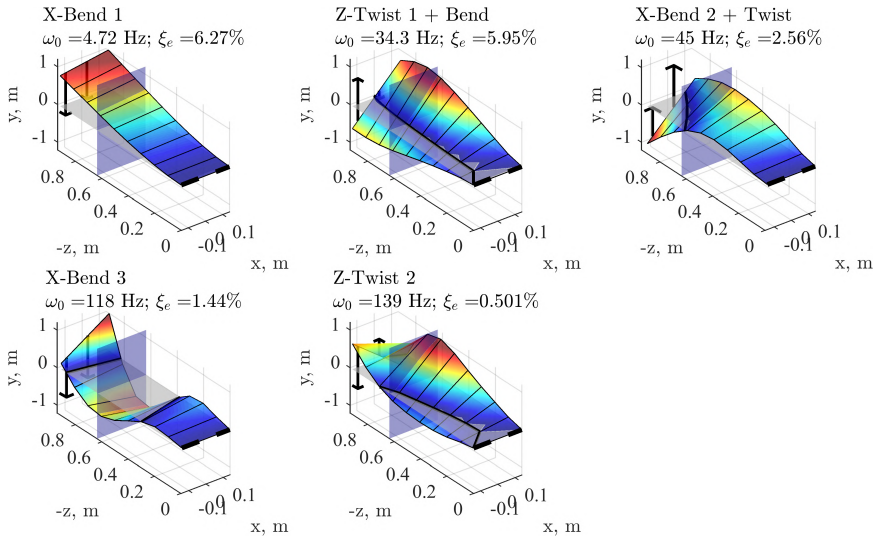

Figure G.10: Normalized mode shapes of model 2 in partially cavitating flow at $\alpha = 10°; Fn_h = 1.5; AR_h = 1.0; \sigma_v = 0.85$.

BIBLIOGRAPHY

BIBLIOGRAPHY

Abbott, I. H., and A. E. Von Doenhoff (1959), *Theory of wing sections, including a summary of airfoil data*, Dover.

Abramson, H. N. (1969), Hydroelasticity: a review of hydrofoil flutter, *Applied Mechanics Reviews*, *22*(2), 115–121.

Abramson, H. N., and W. H. Chu (1959), A discussion of the flutter of submerged hydrofoils, *Journal of Ship Research*, *3*(2), 5–13.

Acosta, A. J. (1955), Note on partial cavitation of flat plate hydrofoils, *Tech. Rep. E-19.9*, California Institute of Technology.

Acosta, A. J. (1979), Hydrofoils and hydrofoil crafts, *Annual Review on Fluid Mechanics*, *5*(5), 161–184, doi:10.1146/annurev.fl.05.010173.001113.

Adhikari, S. (2006), Damping modelling using generalized proportional damping, *Journal of Sound and Vibration*, *293*(1-2), 156–170, doi:10.1016/j.jsv.2005.09.034.

Akcabay, D. T., and Y. L. Young (2014), Influence of cavitation on the hydroelastic stability of hydrofoils, *J. Fluids and Structures*, *49*(0), 170–185, doi: 10.1016/j.jfluidstructs.2014.04.010.

Akcabay, D. T., and Y. L. Young (2015), Parametric excitations and lock-in of flexible hydrofoils in two-phase flow, *Journal of Fluids and Structures*, *57*, 344–356.

Akcabay, D. T., E. J. Chae, Y. L. Young, A. Ducoin, and J. A. Astolfi (2014a), Cavity induced vibration of flexible hydrofoils, *Journal of Fluids and Structures*, *49*, 463–484.

Akcabay, D. T., Y. L. Young, A. Lelong, and J. A. Astolfi (2014b), Cavity-induced vibrations of flexible hydrofoils and their susceptibility to lock-in and parametric excitations, in *Proceedings of the 2014 Symposium on Naval Hydrodynamics*.

Amromin, E. (2007), Determination of cavity detachment for sheet cavitation, *Transactions of the ASME. Journal of Fluids Engineering*, *129*(9), 1105–1111, doi: 10.1115/1.2754312.

Amromin, E. (2015), Ships with ventilated cavitation in seaways and active flow control, *Applied Ocean Research*, *50*, 163–172, doi:10.1016/j.apor.2015.01.017.

Arndt, R., C. Ellis, and S. Paul (1995), Preliminary investigation of the use of air injection to mitigate cavitation erosion, *Transactions of the ASME. Journal of Fluids Engineering*, *117*(3), 498–504, doi:10.1115/1.2817290.

Arndt, R., W. Hambleton, E. Kawakami, and E. Amromin (2009), Creation and maintenance of cavities under horizontal surfaces in steady and gust flows, *Journal of Fluids Engineering*, *131*(11).

Bearman, P. W. (1967), On vortex street wakes, *Journal of Fluid Mechanics*, *28*(4), 625–641, doi:10.1017/S0022112067002368.

Bert, C. (1973), Material damping, *Journal of Sound and Vibration*, *29*(2), 129–153, doi:10.1016/S0022-460X(73)80131-2.

Besch, P. K., and Y. Liu (1971), Flutter and divergence characteristics of four low mass ratio hydrofoils, *Tech. Rep. 3410*, Naval Ship Research and Development Center.

Besch, P. K., and Y. N. Liu (1973), Bending flutter and torsional flutter of flexible hydrofoil struts, *Tech. rep.*, Naval Ship Research and Development Center.

Besch, P. K., and Y. N. Liu (1974), Hydroelastic design of subcavitating and cavitating hydrofoil strut systems, *Tech. rep.*, Naval Ship Research and Development Center.

Bisplinghoff, R., H. Ashley, and R. Halfman (2013), *Aeroelasticity*, Dover Books on Aeronautical Engineering, Dover Publications.

Blake, W. K. (1972), On the damping of transverse motion of free-free beams in dense, stagnant fluids, *Shock and Vibration Bulletin*, (Pt4).

Blake, W. K., and L. J. Maga (1975), On the flow-excited vibrations of cantilever struts in water. i. flow-induced damping and vibration, *Journal of the Acoustical Society of America*, *57(3)*, 610–625.

Brennen, C. E. (1995), *Cavitation and bubble dynamics*, Oxford University Press.

Breslin, J. P. (1958), Discussion of paper by K. L. wadlin, in *Proc. Second Symp. Nav. Hydrodyn.*, vol. 1, pp. 434–440, U.S. Office of Naval Research.

Breslin, J. P., and R. Skalak (1959), Exploratory study of ventilated flows about yawed surface-piercing struts, *Tech. Rep. 2-23-59W*, NASA Tech. Mem., Washington, DC, USA.

Brizzolara, S., and Y. Young (2012), Physical and theoretical modeling of surface-piercing hydrofoils for a high-speed unmanned surface vessel., in *31th International Conference on Ocean, Offshore and Arctic Engineering (OMAE 2012), Rio de Janeiro, Brazil, June 10-15.*, ASME, Rio de Janeiro, Brazil.

Brucker, K., D. Dommermuth, T. O'Shea, D. Yue, K. Hendrickson, and G. Weymouth (2010), Computational naval ship hydrodynamics, in *Proceedings of the 2010 DoD High Performance Computing Modernization Program Users Group Conference (HPCMP-UGC 2010)*, pp. 64–70, doi:10.1109/HPCMP-UGC.2010.62.

Budynas, R. G., J. K. Nisbett, and J. E. Shigley (2011), *Shigley's mechanical engineering design*, McGraw-Hill, New York.

Callenaere, M., J.-P. Franc, J.-M. Michael, and M. Riondet (2001), The cavitation instability induced by the development of a re-entrant jet, *Journal of Fluid Mechanics*, *444*, 223–255.

Caverly, R. J., C. Li, E. J. Chae, J. R. Forbes, and Y. L. Young (2016), Modeling and control of flow-induced vibrations of a flexible hydrofoil in viscous flow, *Smart Materials and Structures*, *25*(6), 065,007.

Ceccio, S. L. (2010), Friction drag reduction of external flows with bubble and gas injection, *Annual Review of Fluid Mechanics*, *42*, 183–203, doi:10.1146/annurev-fluid-121108-145504.

Chae, E., D. Akcabay, A. Lelong, J. Astolfi, and Y. Young (2016), Numerical and experimental investigation of natural flow-induced vibrations of flexible hydrofoils, *Physics of Fluids*, *28*, 075,102.

Chae, E. J. (2015), Dynamic response and stability of flexible hydrofoils in incompressible and viscous flow, Ph.D. thesis, University of Michigan.

Chae, E. J., D. T. Akcabay, and Y. L. Young (2013), Dynamic response and stability of a flapping foil in a dense and viscous fluid, *Physics of Fluids*, *25*(10), 104106, doi:10.1063/1.4825136.

Chang, P. K. (1960), Laminar separation of flow around symmetrical struts at zero angle of attack, *J. Frankl. Inst.*, *270*(5), 382–396, doi:10.1016/0016-0032(60)90842-5.

Chang, P. K. (1961), Separation of flow, *J. Frankl. Inst.*, *272*(6), 433–448.

Coffee, J., C. W., and R. E. McKann (1953), Hydrodynamic drag of 12- and 21-percent-thick surface-piercing struts, *Tech. Rep. 3093*, NACA Tech. Note.

Crandall, S. (1970), The role of damping in vibration theory, *Journal of Sound and Vibration*, *11*(1), 3–18, doi:10.1016/S0022-460X(70)80105-5.

de Graaf, K., B. Pearce, and P. Brandner (2016), The influence of nucleation on cloud cavitation about a sphere, in *Proceedings of the International Symposium on Transport Phenomena and Dynamics of Rotating Machinery*.

De Lange, D. F., and G. J. De Bruin (1998), Sheet cavitation and cloud cavitation, re-entrant jet and three-dimensionality, in *In Fascination of Fluid Dynamics*, pp. 91–114, Springer.

Dommermuth, D., T. O'Shea, D. Wyatt, M. Sussman, G. Weymouth, D. K. Yue, P. Adams, and R. Hand (2006), The numerical simulation of ship waves using cartesian-grid and volume-of-fluid methods, in *Proceedings of the 26th Symposium on Naval Hydrodynamics*, Rome, Italy.

Dommermuth, D., L. Rhymes, and J. Rottman (2013), Direct simulations of breaking ocean waves with data assimilation, in *OCEANS 2013 MTS/IEEE - San Diego: An Ocean in Common*, San Diego, California, USA.

Dommermuth, D., et al. (2007), An application of cartesian-grid and volume-of-fluid methods to numerical ship hydrodynamics, in *NSH 2007 - 9th International Conference on Numerical Ship Hydrodynamics*, Ann Arbor, Michigan, USA.

Dowell, E. H., R. Clark, D. Cox, et al. (2004), *A modern course in aeroelasticity*, vol. 3, Springer.

Drela, M. (1989), Xfoil: an analysis and design system for low reynolds number airfoils, in *Low Reynolds Number Aerodynamics: Proceedings of the Conference Notre Dame, Indiana, USA, 5–7 June 1989*, *Lecture Notes in Engineering*, vol. 54, edited by T. J. Mueller, 1 ed., chap. 1, pp. 1–12, Springer Berlin Heidelberg, doi: 10.1007/978-3-642-84010-4_1.

Ducoin, A., Y. L. Young, and J. F. Sigrist (2010), Hydroelastic responses of a flexible hydrofoil in turbulent, cavitating flow, in *American Society of Mechanical Engineers, Fluids Engineering Division (Publication) FEDSM*, vol. **3**, pp. 493–502, Montreal, QC, Canada.

Ducoin, A., J. A. Astolfi, and M. Gobert (2012a), An experimental study of boundary-layer transition induced vibrations on a hydrofoil, *Journal of Fluids and Structures*, *32*, 37–51.

Ducoin, A., J. A. Astolfi, and J. F. Sigrist (2012b), An experimental analysis of fluid structure interaction on a flexible hydrofoil in various flow regimes including cavitating flow, *European Journal of Mechanics - B/Fluids*, *36*(0), 63–74, doi:10.1016/j.euromechflu.2012.03.009.

Duttweiler, M. E., and C. E. Brennen (1998), Partial cavity instabilities, in *1998 US-Japan Seminar on Abnormal Flow Phenomena in Turbomachines*, Unpublished.

Elata, C. (1967), Choking of strut-ventilated foil cavities., *Tech. Rep. 605-2*, Hydronautics, inc.

Emmons, H., C. Chang, and B. Watson (1960), Taylor instability of finite surface waves, *Journal of Fluid Mechanics*, *7*, 177–193.

Faltinsen, O. M. (2005), *Hydrodynamics of high-speed marine vehicles*, Cambridge university press.

Franc, J.-P., and J.-M. Michel (2004), *Fundamentals of cavitation*, Kluwer Academic Publishers.

Fridsma, G. (1963), Ventilation inception on a surface piercing dihedral hydrofoil with plane surface wedge section, *Tech. rep.*, Stevens Institute of Technology, Davidson Laboratory.

Fu, Y., and W. Price (1987), Interactions between a partially or totally immersed vibrating cantilever plate and the surrounding fluid, *Journal of Sound and Vibration*, *118*(3), 495–513.

Fung, Y. (2002), *An introduction to the theory of aeroelasticity*, Dover Phoenix Edition: Engineering, Dover Publications.

Fuwa, T., N. Hirata, T. Hori, and J. Fujisawa (1993), Experimental study on spray shape, spray drag and flow field of surface-piercing vertical strut advancing at high speed, *Senpaku Gijutsu Kenkyusho Hokoku/Papers of Ship Research Institute*, *30*(6), 1–31.

Ganesh, H. (2015), Bubbly shock propagation as a cause of sheet to cloud transition of partial cavitation and stationary cavitation bubbles forming on a delta wing vortex, Ph.D. thesis, University of Michigan.

Ganesh, H., S. A. Mäkiharju, and S. L. Ceccio (2016), Bubbly shock propagation as a mechanism for sheet-to-cloud transition of partial cavities, *Journal of Fluid Mechanics*, *802*, 37–78, doi:10.1017/jfm.2016.425.

Gault, D. A. (1957), A correlation of low-speed, airfoil-section stalling characteristics with reynolds number and airfoil geometry, *Tech. Rep. 3963*, NACA Tech. Note.

Glauert, H. (1943), *The elements of aerofoil and airscrew theory*, Cambridge University Press.

Green, S. (1988), Tip vortices–single phase and cavitating flow phenomena, Ph.D. thesis, California Institute of Technology.

Green, S., and A. Acosta (1991), Unsteady flow in trailing vortices, *Journal of Fluid Mechanics*, *227*, 107–34, doi:10.1017/S0022112091000058.

Grubbs, F. E. (1969), Procedures for detecting outlying observations in samples, *Technometrics*, *11*(1), 1–21.

Harwood, C. M., and Y. L. Young (2014), A physics-based gap-flow model for potential flow solvers, *Ocean Engineering*, *88*, 578–587.

Harwood, C. M., K. A. Brucker, F. Miguel, Y. L. Young, and S. L. Ceccio (2014), Experimental and numerical investigation of ventilation inception and washout mechanisms of a surface-piercing hydrofoil, in *Proc. 30th Symp. Nav. Hydrodyn.*, U.S. Office of Naval Research.

Harwood, C. M., A. J. Stankovich, Y. L. Young, and S. L. Ceccio (2016a), Combined experimental and numerical study of the free vibration of surface-piercing struts, in *Proceedings of the International Symposium on Transport Phenomena and Dynamics of Rotating Machinery*.

Harwood, C. M., J. C. Ward, Y. L. Young, and S. L. Ceccio (2016b), Experimental investigation of the hydro-elastic response of a surface-piercing hydrofoil in multiphase flow, in *Proceedings of the 31st Symposium on Naval Hydrodynamics*.

Harwood, C. M., Y. L. Young, and S. L. Ceccio (2016c), Ventilated cavities on a surface-piercing hydrofoil at moderate froude numbers: cavity formation, elimination and stability, *Journal of Fluid Mechanics*, *800*, 5–56, doi:10.1017/jfm.2016.373.

Hecker, R., and G. Ober (1974), Flow separation, reattachment, and ventilation of foils with sharp leading edge at low reynolds number, *Tech. Rep. AD-787500*, Naval Ship Research and Development Center.

Helmbold, H. (1942), Der unverwundene ellipsenflugel als tragende flanche, *Jahrbuch*, pp. 111–113.

Henry, C. J., J. Dugundji, and H. Ashley (1959), Aeroelastic stability of lifting surfaces in high-density fluids, *Journal fo Ship Research*, pp. 10–21.

Hilborne, D. V. (1958), The hydroelastic stability of struts, *Tech. rep.*, Rept. No. ARL/R1/G/HY/5/3 Admiralty Reseach Laboratory.

Iafrati, A., S. Grizzi, M. Siemann, and L. B. M. nés (2015), High-speed ditching of a flat plate: experimental data and uncertainty assessment, *Journal of Fluids and Structures*, *55*, 501–525, doi:10.1016/j.jfluidstructs.2015.03.019.

ITTC (2002), *Ittc international towing tank conference catalogue of facilities: towing tanks, seakeeping and manoeuvring basins, circulating water channels, cavitation tunnels*, International Towing Tank Conference.

Kaplan, P. (1962), Hydroelastic instabilities of partially cavitated hydrofoils, in *Fourth Symposium on Naval Hydrodynamics*.

Kaplan, P., and C. J. Henry (1960), A study of the hydroelastic instabilities of supercavitating hydrofoils, *Journal of Ship Research*, *4*(3), 28–38.

Kaplan, P., and A. F. Lehman (1966), An experimental study of hydroelastic instabilities of finite span hydrofoils under cavitating conditions, *AIAA Journal of Aircraft*, *3*(3), 262–269.

Kaplan, P., and L. J. Zeckendorf (1964), A study of hydroelastic stability of partially cavitated hydrofoils by application of quasi-steady theory, *Tech. rep.*, Rept. 64010, Oceanics, Inc.

Kawakami, D. T., A. Fuji, Y. Tsujimoto, and R. E. A. Arndt (2008), An assessment of the influence of environmental factors on cavitation instabilities, *Journal of Fluids Engineering*, *130*(3), 1–8, doi:10.1115/1.2842146.

Kennedy, R. C. (2015), A reduced-order model for an oscillating hydrofoil near the free surface, in *13th International Conference on Fast Sea Transportation*, Washington DC.

Kerwin, J. E., and J. B. Hadler (2010), *Principles of naval architecture series - propulsion*, Society of Naval Architects and Marine Engineers (SNAME).

Kiceniuk, T. (1954), A preliminary experimental study of vertical hydrofoils of low aspect ratio piercing a water surface, *Tech. Rep. E-55.2*, California Instute of Technology.

Kramer, M., Z. Liu, and Y. Young (2013), Free vibration of cantilevered composite plates in air and in water, *Composite Structures*, *95*, 254–263, doi:10.1016/j.compstruct.2012.07.017.

Laberteaux, K., and S. Ceccio (2001a), Partial cavity flows. 1. cavities forming on models without spanwise variation, *Journal of Fluid Mechanics*, *431*, 1–41, doi:10.1017/S0022112000002925.

Laberteaux, K., and S. Ceccio (2001b), Partial cavity flows. 2. cavities forming on test objects with spanwise variation, *Journal of Fluid Mechanics*, *431*, 43–63, doi:10.1017/S0022112000002937.

Lee, I.-h. R. (2015), Scaling of gas diffusion into limited partial cavity and interaction of vertical jet with cross-flow beneath horizontal surface, Ph.D. thesis, Universit of Michigan.

Leonard, B. (1997), Bounded higher-order upwind multidimensional finite-volume convection-diffusion algorithms, in *Advances in Numerical Heat Transfer*, vol. 1, pp. 1–57.

Liu, Z., and Y. L. Young (2010), Static divergence of self-twisting composite rotors, *Journal of Fluids and Structures*, *26*(5), 841–847, doi:10.1016/j.jfluidstructs.2010.05.002.

McCroskey, W., L. Carr, and K. McAlister (1976), Dynamic stall experiments on oscillating airfoils, *AIAA Journal*, *14*(1), 57–63.

McCroskey, W. J. (1982), Unsteady airfoils, *Annual Review of Fluid Mechanics*, *14*(1), 285–311.

McCroskey, W. J., K. W. McAlister, L. W. Carr, S. L. Pucci, O. Lambert, and R. F. Indergrand (1981), Dynamic stall on advanced airfoil sections, *Journal of the American Helicopter Society*, *26*(3), 40–50.

McCroskey, W. J., K. W. McAlister, L. W. Carr, and S. L. Pucci (1982), An experimental study of dynamic stall on advanced airfoil sections. volume 1. summary of the experiment., *Technical Memorandum 84245*, NASA.

Mcgregor, R. C., A. J. Wright, P. D. Swales, and G. D. Crapper (1973), An examination of the influence of waves on the ventilation of surface-piercing struts, *Journal of Fluid Mechanics*, *61*, 85–96, doi:10.1017/S0022112073000583.

Milne-Thomson, L. M. (1973), *Theoretical aerodynamics*, 4 ed., Dover.

Morch, K. (2009), Cavitation nuclei: experiments and theory, *Journal of Hydrodynamics*, *21*(2), 176–189.

Motley, M., and Y. Young (2011), Performance-based design and analysis of flexible composite propulsors, *Journal of Fluids and Structures*, *27*(8), 1310–1325, doi:10.1016/j.jfluidstructs.2011.08.004.

Motley, M., Z. Liu, and Y. Young (2009), Utilizing fluid-structure interactions to improve energy efficiency of composite marine propellers in specially varying wake, *Composite Structures*, *90*(3), 304–313.

Motley, M. R., M. R. Kramer, and Y. L. Young (2013), Free surface and solid boundary eeffect on the free vibration of composite plates, *Composite Structures*, *95*, 365–375.

Münch, C., P. Ausoni, O. Braun, M. Farhat, and F. Avellan (2010), Fluid-structure coupling for an oscillating hydrofoil, *Journal of Fluids and Structures*, *26*(6), 1018–1033, doi:10.1016/j.jfluidstructs.2010.07.002.

Munk, M. M. (1923), General theory of thin wing sections, *Tech. Rep. 142*, National Advisory Committee for Aeronautics.

Munkres, J. (1957), Algorithms for the assignment and transportation problems, *Journal of the society for industrial and applied mathematics*, *5*(1), 32–38.

Newman, J. N. (1977), *Marine hydrodynamics*, MIT Press.

Olofsson, N. (1996), Force and flow characteristics of a partially submerged propeller, Ph.D. thesis, Chalmers University of Technology, Department of Naval Architecture and Ocean Engineering.

O'Shea, T., K. Brucker, D. Dommermuth, and D. Wyatt (2008), A numerical formulation for simulating free-surface hydrodynamics, in *Proceedings of the 27th Symposium on Naval Hydrodynamics*, Seoul, Korea.

Pearce, B. W., and P. A. Brandner (2012), Experimental investigation of a base-ventilated supercavitating hydrofoil with interceptor, in *Proceedings of the Eighth International Symposium on Cavitation-Cav2012*, pp. 14–16.

Perry, B. (1955), Experiments on struts piercing the water surface, *Tech. Rep. E-55.1*, California Instute of Technology.

Pogozelski, E. M., J. Katz, and T. T. Huang (1997), The flow structure around a surface piercing strut, *Physics of Fluids*, *9*(5), 1387–1399.

Prandtl, L. (1918), Tragflügeltheorie, *Nachrichten von der Gesellschaft der Wissenschaften zu Göttingen, Mathematisch-Physikalische Klasse*, (pts. 1-2).

Ramsen, J. A. (1957), An experimental hydrodynamic investigation of the inception of vortex ventilation, *Tech. Rep. 3903*, National Advisory Committee for Aeronautics.

Rayleigh, L. (), *The theory of sound*, Dover, New York, reissued in 1945.

Reese, M. C. (2010), Vibration and damping of hydrofoils in uniform flow, Master thesis, Pennsylvania State University.

Richardson, M., and D. Formenti (1982), Parameter estimation from frequency response measurements using rational fraction polynomials, in *Proceedings of the International Modal Analysis Conference*, pp. 167–182.

Rodriguez, O. d. l. T. (2012), Influence of cavitation on the dynamic response of hydrofoils, Ph.D. thesis, Technical University of Catalonia, Barcelona.

Rothblum, R. S. (1977a), Scale effect in models with forced or natural ventilation near the free water surface, in *Proc. 18th Gen. Mtg. Am. Towing Tank Conf.*, vol. 2, edited by B. Johnson and B. Nehrling, pp. 349–360, American Towing Tank Conference.

Rothblum, R. S. (1977b), Investigation of methods of delayiing or controlling ventilation on surface-piercing struts, Ph.D. thesis, University of Leeds.

Rothblum, R. S., D. A. Mayer, and G. M. Wilburn (1969), Ventilation, cavitation and other characteristics of high speed surface-piercing strut, *Tech. Rep. 3023*, Naval Ship Research and Development Center.

Rothblum, R. S., R. C. McGregor, and P. D. Swales (1974), Effect of roughness, wettability and speed on the ventilation characteristics of surface piercing hydrofoil struts, in *Proc. Intl Hovering Craft, Hydrofoil, and Adv. Transit Sys. Conf.*, pp. 235–243.

Rothblum, R. S., M. F. Jeffers, and R. P. Smith (1976), Methods for controlling the sideforce on surface-piercing hydrofoil struts, *Tech. Rep. SPD-700-1*, DTIC Document.

Rottman, J., K. Brucker, D. muth, and D. Broutman (2010), Parameterization of the internal wave field generated by a submarine and its turbulent wake in a uniformly stratified fluid, in *Proceeding of the 28th Symposium on Naval Hydrodynamics*, Pasadena, California, USA.

Rowe, W. S., and T. B. Marvin (1968), A program of theoretical research on hydroelastic stability., *Tech. Rep. AD0679632*, DTIC Document.

Sallet, D. W. (1969), On the spacing of karman vortices, *Journal of Applied Mechanics*, *36*(2), 370–372, doi:10.1115/1.3564657.

Scherer, J., and J. Auslaender (1964), Experimental and theoretical performance of a supercavitating hydrofoil operating near a free surface, *Journal of Aircraft*, *2*, 144–152.

Schiebe, F. R., and J. M. Wetzel (1961), Ventilated cavities on submerged three-dimensional hydrofoils, *Tech. Rep. 36, Series B*, DTIC Document.

Schwarz, B. J., and M. H. Richardson (1999), Experimental modal analysis, in *CSI Reliability Week*.

Sears, W. R. (1941), Some aspects of non-stationary airfoil theory and its practical application, *Journal of the Aeronautical Sciences(Institute of the Aeronautical Sciences)*, *8(3)*, 104–108.

Shoelson, B. (2011), Deleteoutliers, MATLAB Central File Exchange.

Soroka, W. W. (1949), Note on the Relations Between Viscous and Structural Damping Coefficients, *Journal of the Aeronautical Sciences (Institute of the Aeronautical Sciences)*, *16*(7), 409–410, doi:10.2514/8.11822.

Swales, P., A. Wright, R. McGregor, and B. Cole (1973), Pressure, flow visualisation and ventilation, *Hovering Craft and Hydrofoil*, *13*(1), 11–16.

Swales, P., A. Wright, R. McGregor, and R. Rothblum (1974), Mechanism of ventilation inception on surface piercing foils., *Journal of Mechanical Engineering Science*, *16*(1), 18–24.

Tassin Leger, A., and S. Ceccio (1998), Examination of the flow near the leading edge of attached cavitation. part 1. detachment of two-dimensional and axisymmetric cavities, *Journal of Fluid Mechanics*, *376*, 61–90, doi:10.1017/S0022112098002766.

Taylor, G. (1950), The instability of liquid surfaces when accelerated in a direction perpendicular to their planes i, *P. Roy. Soc. A - Math Phy.*, *201*, 192–196.

Terentiev, A., I. N. Kirschner, and J. S. Uhlman (2011), *The hydrodynamics of cavitating flows*, Backbone Publishing Company.

Theodorsen, T. (1935), General theory of aerodynamic instability and the mechanism of flutter, *Tech. Rep. 496*, National Advisory Committee for Aeronautics.

Tineves, J.-Y. (2016), Simple tracker, MATLAB Central File Exchange.

Tulin, H. P. (1953), Steady two-dimensional cavity flows about slender bodies, *Tech. Rep. 834*, United States Navy Department - David W Taylor Model Basin.

Tulin, M. (1956), Supercavitating flow past foils and struts, in *Proc. Symp. on Cavitation in Hydrodynamics, NPL*.

Tulin, M. P. (1964), Supercavitating flows – small perturbation theory, *J. Ship Res.*, *7*(January), 16–37.

Wade, R., and A. Acosta (1966), Experimental observations on the flow past a plano-convex hydrofoil, *Journal of Basic Engineering*, *88*(1), 273–282.

Wadlin, K. (1958), Mechanics of ventilation inception, in *Second Symposium on Naval Hydrodynamics*, vol. 1, pp. 425–446, U.S. Office of Naval Research.

Wadlin, K. (1959), Ventilated flows with hydrofoils, in *Twelfth General Meeting of the American Towing Tank Conference*, Berkeley, California, USA.

Wagner, H. (1925), *Über die entstehung des dynamischen auftriebes von tragflügeln*, VDI-Verl.

Waid, R. L. (1968), Experimental investigation of the ventilation of vertical surface-piercing struts in the presence of cavitation, *Tech. Rep. AD0738493*, Naval Ship Research and Development Center.

Ward, J. C., C. M. Harwood, and Y. L. Young (2016), Inverse method for determination of the in situ hydrodynamic load distribution in multi-phase flow, in *Proceedings of the 31st Symposium on Naval Hydrodynamics*.

Wetzel, J. (1957), Experimental studies of air ventilation of vertical, semi-submerged bodies, *Tech. Rep. 57*, St. Anthony Falls Hydraulic Laboratory, University of Minnesota.

Woolston, D. S., and G. E. Castile (1951), Some effects of variations in several parameters including fluid density on the flutter speed of light uniform cantilever wings, *Tech. Rep. 2558*, National Advisory Committee for Aeronautics.

Wu, T. Y.-T. (1962), A wake model for free-streamline flow theory part 1. fully and partially developed wake flows past an oblique flat plate, *Journal of Fluid Mechanics*, *13*, 161–181, doi:10.1017/S0022112062000609.

Wu, T. Y.-T. (1972), Cavity and wake flows, *Annual Review of Fluid Mechanics*, *4*(1), 243–284.

Young, Y. (2010), Dynamic hydroelastic scaling of self-adaptive composite marine rotors, *Composite Structures*, pp. 97–106.

Young, Y., and S. Brizzolara (2013), Numerical and physical investigation of a surface-piercing hydrofoil, in *Proc. Third Intl Symp. Marine Propulsors*, edited by J. Binns, R. Brown, and N. Bose, pp. 1–8, SMP, Australian Maritime College, University of Tasmania, Launceston.

Young, Y., and S. Kinnas (2003a), Analysis of supercavitating and surface-piercing propeller flows via BEM, *Computational Mechanics*, *32*, 269–280.

Young, Y., and S. Kinnas (2003b), Numerical modeling of supercavitating propeller flows, *Journal of Ship Research*, *47*(1), 48–62.

Young, Y., J. Baker, and M. Motley (2010), Reliability-based design and optimization of adaptive marine structures, *Composite Structures*, *92*(2), 244–253.

Young, Y. L., and B. R. Savander (2011), Numerical analysis of large-scale surface-piercing propellers, *Ocean Engineering*, *38*(13), 1368–1381, doi:10.1016/j.oceaneng.2011.05.019.

Young, Y. L., C. M. Harwood, F. M. Montero, J. C. Ward, and S. L. Ceccio (2016), Ventilation of lifting surfaces: review of the physics and scaling relations, *Applied Mechanics Reviews*, accepted.